

# **Modifizierte Thiostannate durch Integration von Übergangsmetallkationen**

**Solvothermale Synthesen sowie  
in-situ-EDXRD-Untersuchungen  
ausgewählter Verbindungen**

Kumulative Dissertation  
zur Erlangung des Doktorgrades  
der Mathematisch-Naturwissenschaftlichen Fakultät  
der Christian-Albrechts-Universität  
zu Kiel

vorgelegt von  
**Nicole Pienack**

Kiel  
2008



Referent/in:.....

Koreferent/in:.....

Tag der Prüfung:.....

Zum Druck genehmigt: Kiel, .....

Der Dekan



# **Modifizierte Thiostannate durch Integration von Übergangsmetallkationen**

## **Solvothermale Synthese sowie in-situ-EDXRD-Untersuchungen ausgewählter Verbindungen**

Ein wesentliches Ziel dieser Arbeit war die Darstellung und Charakterisierung neuer Thiostannate durch die Integration von Übergangsmetallkationen. Dadurch kann die Ladungsneutralität erreicht werden und die chemisch-physikalischen Eigenschaften können modifiziert werden. Zusätzlich wird die strukturelle Vielfalt der Thiostannate erweitert. Unter solvothermalen Bedingungen wurden insgesamt 13 neue Verbindungen erhalten, wobei ein Schwerpunkt bei den Synthesen auf die Elemente Kupfer und Mangan gelegt wurde. In den kupferhaltigen Thiostannaten  $(\text{DBUH})\text{CuSnS}_3$  (DBU = 1,8-Diazabicyclo[5.4.0]undec-7-en),  $(1,4\text{-dabH})_2\text{Cu}_2\text{SnS}_4$  (1,4-dab = 1,4-Diaminobutan),  $(\text{DBNH})_2\text{Cu}_6\text{Sn}_2\text{S}_8$  (DBN = 1,5-Diazabicyclo[4.3.0]non-5-en) und  $(\text{dienH}_2)\text{Cu}_2\text{Sn}_2\text{S}_6$  (dien = Diethylentriamin) spiegelt sich die strukturelle Vielfalt der Thiostannate wider. In den beiden ersten Verbindungen sind die wesentlichen Strukturmerkmale unterschiedliche eindimensionale Ketten und ladungskompensierende, protonierte Aminmoleküle. Im Gegensatz zu den gerade erwähnten Verbindungen werden in  $(\text{DBNH})_2\text{Cu}_6\text{Sn}_2\text{S}_8$  (Raumgruppe  $\text{Pca}2_1$ ) und  $(\text{dienH}_2)\text{Cu}_2\text{Sn}_2\text{S}_6$  (Raumgruppe  $\bar{1}4m2$ ) unterschiedliche Schichtanionen gefunden. Ein gewisser Nachteil der Synthesen mit Kupfer ist die Verunreinigung der Reaktionsprodukte mit binären oder ternären Sulfiden. Obwohl umfangreiche Variationen der Reaktionsbedingungen durchgeführt wurden, konnte dies nicht beseitigt werden. Weniger problematisch waren die Synthesen mit Mangan, welches eine vergleichbare Affinität zu Schwefel und Stickstoff aufweist. Mit Mangan konnten die Thiostannate  $(1,4\text{-dabH}_2)\text{MnSnS}_4$ ,  $[\text{Mn}(1,2\text{-dach})_2(\text{H}_2\text{O})]_2\text{Sn}_2\text{S}_6$ ,  $[\text{Mn}(1,2\text{-dach})_2]\text{Sn}_2\text{S}_6 \cdot 2(1,2\text{-dach})$  (1,2-dach = 1,2-Diaminocyclohexan) und  $[\text{Mn}(\text{trien})]_2\text{SnS}_4 \cdot 4 \text{H}_2\text{O}$  (trien = Triethylentetramin) dargestellt und charakterisiert werden. Zusätzlich wurden die Verbindungen  $(1,4\text{-dabH})_2\text{Ag}_2\text{SnS}_4$  und  $[\text{M}(\text{tepa})]_2\text{Sn}_2\text{S}_6$  (M = Co, Ni, Fe; tepa = Tetraethylenpentamin) synthetisiert und charakterisiert. Bei den Synthesen von  $(\text{DBNH})_2\text{Cu}_6\text{Sn}_2\text{S}_8$  wurde das gemischtvalente Sn(II)/Sn(IV)-Thiostannat  $(\text{DBNH})_2\text{Sn}_3\text{S}_6$  als zweites Produkt erhalten. Um die simultane Kristallisation dieser beiden Verbindungen besser zu verstehen, wurden in-situ-Untersuchungen mit energiedispersiver Röntgenbeugung (EDXRD) durchgeführt. Solche EDXRD-Experimente wurden in Kooperation mit Fr. Prof. G. Patzke an anderen Systemen durchgeführt.

# Modified Thiostannates by Integration of Transition Metal Cations

## Solvothermal Syntheses and in-situ EDXRD Investigations

### of Selected Compounds

The preparation and characterisation of new thiostannates by the integration of transition metal cations was the main aim of this work. With this approach charge neutrality of the thiostannate compounds may be achieved, the physico-chemical properties are modified and the structural variety is enhanced. Applying the solvothermal synthesis method, 13 new compounds were obtained with the main focus on the elements copper and manganese. The structural diversity is reflected in the Cu containing thiostannates (DBUH)CuSnS<sub>3</sub> (DBU = 1,8-diazabicyclo[5.4.0]undec-7-ene), (1,4-dabH)<sub>2</sub>Cu<sub>2</sub>SnS<sub>4</sub> (1,4-dab = 1,4-diaminobutane), (DBNH)<sub>2</sub>Cu<sub>6</sub>Sn<sub>2</sub>S<sub>8</sub> (DBN = 1,5-diazabicyclo[4.3.0]non-5-ene) and (dienH<sub>2</sub>)Cu<sub>2</sub>Sn<sub>2</sub>S<sub>6</sub> (dien = diethylenetriamine). The first two compounds exhibit different one-dimensional anionic chains and charge compensating protonated amine molecules as structural features. In contrast, (DBNH)<sub>2</sub>Cu<sub>6</sub>Sn<sub>2</sub>S<sub>8</sub> (space group Pca2<sub>1</sub>) and (dienH<sub>2</sub>)Cu<sub>2</sub>Sn<sub>2</sub>S<sub>6</sub> (space group  $\bar{1}4m2$ ) feature different anionic layers. A disadvantage of the syntheses with Cu is the contamination of the reaction products with binary and ternary sulfides. Fewer problems occurred with manganese which is believed to have a similar binding affinity to sulphur and nitrogen. The syntheses of the Mn containing thiostannates (1,4-dabH<sub>2</sub>)MnSnS<sub>4</sub>, [Mn(1,2-dach)<sub>2</sub>(H<sub>2</sub>O)]<sub>2</sub>Sn<sub>2</sub>S<sub>6</sub>, [Mn(1,2-dach)<sub>2</sub>]Sn<sub>2</sub>S<sub>6</sub> · 2 (1,2-dach) (1,2-dach = 1,2-diaminocyclohexane) and [Mn(trien)]<sub>2</sub>SnS<sub>4</sub> · 4 H<sub>2</sub>O (trien = triethylenetetramine) confirm this assumption. In addition, the new compounds (1,4-dabH)<sub>2</sub>Ag<sub>2</sub>SnS<sub>4</sub> and [M(tepa)]<sub>2</sub>Sn<sub>2</sub>S<sub>6</sub> (M = Co, Ni, Fe; tepa = tetraethylenepentamine) could be obtained. During the formation of (DBNH)<sub>2</sub>Cu<sub>6</sub>Sn<sub>2</sub>S<sub>8</sub> the mixed-valent Sn(II)/Sn(IV)-thiostannate (DBNH)<sub>2</sub>Sn<sub>3</sub>S<sub>6</sub> was obtained as a second product. For a better understanding of the reactions occurring during the solvothermal synthesis, in-situ energy dispersive X-ray diffraction (EDXRD) investigations were performed to shed light onto the formation and the crystallisation kinetics. Some EDXRD experiments were conducted in collaboration with Prof. G. Patzke.





## Inhaltsverzeichnis

1. Einleitung.....	1
1.1. Motivation und Zielsetzung.....	1
1.2. Thiostannate.....	2
1.2.1. Anorganische Thiostannate.....	2
1.2.2. Thiostannate mit organischen, strukturdirigierenden Reagenzien.....	3
1.3. Modifizierung der Thiostannate durch Integration von Übergangsmetallen (ÜM) .....	9
1.4. In-situ-Untersuchungen zur Bildung von Thiostannaten unter solvothermalen Bedingungen.....	15
2. Untersuchungsmethoden.....	19
2.1. Untersuchungen mit Synchrotronstrahlung: energiedispersive Röntgenbeugung (Energy Dispersive X-Ray Diffraction EDXRD) und Röntgenabsorptionsspektroskopie (X-Ray Absorption Spectroscopy XAS) .....	19
2.1.1. Synchrotronstrahlung .....	19
2.1.2. Energiedispersive Röntgenbeugung (EDXRD) .....	21
2.1.3. Röntgenabsorptionsspektroskopie (XAS).....	23
2.2. Impedanzanalyse .....	26
3. Experimentelles .....	27
3.1. Solvothermale Synthese .....	27
3.2. In-situ-Syntheseapparatur .....	29
3.3. Messplatz F3 am Hasylab, Desy, Hamburg .....	31
3.4. Messplatz X1 am Hasylab, Desy, Hamburg.....	32
3.5. Verwendete Chemikalien .....	33
3.6. Geräte.....	34
3.7. Verwendete Programme .....	35

---

4. Ergebnisse (kumulativer Hauptteil).....	37
4.1. Ergebnisse und Publikationen der übergangsmetallhaltigen Thiostannate.....	37
4.1.1. Die Verbindungen (DBUH)CuSnS <sub>3</sub> und (1,4-dabH <sub>2</sub> )Cu <sub>2</sub> SnS <sub>4</sub> .....	37
4.1.2. Die Verbindung (1,4-dabH <sub>2</sub> )Ag <sub>2</sub> SnS <sub>4</sub> .....	48
4.1.3. Die Verbindung (1,4-dabH) <sub>2</sub> MnSnS <sub>4</sub> .....	61
4.1.4. Die Verbindung (dienH <sub>2</sub> )Cu <sub>2</sub> Sn <sub>2</sub> S <sub>6</sub> .....	69
4.1.5. Die Verbindungen [Mn(1,2-dach) <sub>2</sub> (H <sub>2</sub> O)] <sub>2</sub> Sn <sub>2</sub> S <sub>6</sub> und [Mn(1,2-dach) <sub>2</sub> ]Sn <sub>2</sub> S <sub>6</sub> · 2 (1,2-dach) .....	78
4.1.6. Die Verbindungen [Co(tepa)] <sub>2</sub> Sn <sub>2</sub> S <sub>6</sub> , [Fe(tepa)] <sub>2</sub> Sn <sub>2</sub> S <sub>6</sub> und [Ni(tepa)] <sub>2</sub> Sn <sub>2</sub> S <sub>6</sub> .....	104
4.1.7. Die Verbindung [Mn(trien)] <sub>2</sub> SnS <sub>4</sub> · 4 H <sub>2</sub> O .....	123
4.2. Ergebnisse und Publikationen der in-situ-Untersuchungen mit EDXRD und EXAFS .....	128
4.2.1. Synthesen, Strukturen und EDXRD-Untersuchungen zur Bildung der Thiostannate (DBNH) <sub>2</sub> Sn <sub>3</sub> S <sub>6</sub> und (DBNH) <sub>2</sub> Cu <sub>6</sub> Sn <sub>2</sub> S <sub>8</sub> .....	128
4.2.2. EXAFS-Untersuchungen zur Bildung von [Co(C <sub>6</sub> H <sub>18</sub> N <sub>4</sub> )] [Sb <sub>2</sub> S <sub>4</sub> ] .....	144
4.3. Ergebnisse und Publikationen aus Kooperationen .....	157
4.3.1. EDXRD-Untersuchungen zur Bildung von W/Mo-Oxiden .....	157
4.3.2. EDXRD-Untersuchungen zur Bildung von Bi <sub>2</sub> O <sub>3</sub> -Nanodrähten sowie nanostrukturierter W/Mo-HTB-Oxide .....	171
5. Zusammenfassung und Ausblick.....	175
6. Anhang .....	183
6.1. Publikationsliste.....	183
6.1.1. Publikationen.....	183
6.1.2. Tagungsbeiträge.....	185
6.2. Strukturdaten / Messprotokolle .....	187
6.2.1. Messprotokoll für die Verbindung (DBUH)CuSnS <sub>3</sub> .....	187
6.2.2. Messprotokoll für die Verbindung (DBNH) <sub>2</sub> Sn <sub>3</sub> S <sub>6</sub> .....	190
6.2.3. Messprotokoll für die Verbindung (1,4-dabH <sub>2</sub> )Cu <sub>2</sub> SnS <sub>4</sub> .....	194

6.2.4. Messprotokoll für die Verbindung (1,4-dabH <sub>2</sub> )Ag <sub>2</sub> SnS <sub>4</sub> .....	197
6.2.5. Messprotokoll für die Verbindung (1,4-dabH) <sub>2</sub> MnSnS <sub>4</sub> .....	200
6.2.6. Messprotokoll für die Verbindung (DBNH) <sub>2</sub> Cu <sub>6</sub> Sn <sub>2</sub> S <sub>8</sub> .....	203
6.2.7. Messprotokoll für die Verbindung (dienH <sub>2</sub> )Cu <sub>2</sub> Sn <sub>2</sub> S <sub>6</sub> .....	208
6.2.8. Messprotokoll für die Verbindung [Mn(trien)] <sub>2</sub> SnS <sub>4</sub> · 4 H <sub>2</sub> O.....	211
6.2.9. Messprotokoll für die Verbindung [Mn(1,2-dach) <sub>2</sub> (H <sub>2</sub> O)] <sub>2</sub> Sn <sub>2</sub> S <sub>6</sub> .....	216
6.2.10. Messprotokoll für die Verbindung [Mn(C <sub>6</sub> N <sub>2</sub> H <sub>14</sub> ) <sub>2</sub> ]Sn <sub>2</sub> S <sub>6</sub> · 2 C <sub>6</sub> N <sub>2</sub> H <sub>15</sub>	221
6.2.11. Messprotokoll für die Verbindung [Co(tepa)] <sub>2</sub> Sn <sub>2</sub> S <sub>6</sub> .....	227
6.2.12. Messprotokoll für die Verbindung [Fe(tepa)] <sub>2</sub> Sn <sub>2</sub> S <sub>6</sub> .....	231
6.2.13. Messprotokoll für die Verbindung [Ni(tepa)] <sub>2</sub> Sn <sub>2</sub> S <sub>6</sub> .....	235
6.3. Programmroutine calf3.....	239
Danksagung .....	241
Erklärung.....	242
7. Literatur.....	243



# 1. Einleitung

## 1.1. Motivation und Zielsetzung

In der Festkörperchemie hat sich in den vergangenen Jahren die Synthese von Materialien mit definierten Porengrößen als ein sehr wichtiger Forschungszweig etabliert. Dabei stehen zumeist die Materialien mit offenporigen, dreidimensionalen Gerüststrukturen im Fokus, da ein besonderes Potential für Anwendungen wie Gasspeicherung oder heterogener Katalyse erwartet werden kann [1]. So finden z. B. die Zeolithe Na-A in Waschmitteln Verwendung und bei der Lufttrennung, wo eine Trennung von  $N_2$  und  $O_2$  erfolgt, werden Li-ausgetauschte Zeolithe eingesetzt. Eine weitere wichtige Anwendung stellt das katalytische Cracken der Benzinherstellung mit Zeolith Y Derivaten dar.

Zu den porösen Materialien gehören neben den klassischen Zeolithen die Alumophosphate sowie eine große Anzahl an Verbindungen, die inzwischen mit mehr als 25 Elementen des Periodensystems dargestellt werden [1]. Neben den bekannten oxidischen Materialien lassen sich offene Gerüstmaterialien auch auf Grundlage von Chalkogeniden darstellen. In den letzten Jahren hat sich die Gruppe der Thiometallate in dem Bereich poröser Materialien entwickelt. Das große Interesse an Thiometallaten, insbesondere an Thiostannaten, wird unter anderem durch die Erwartungen begründet, die typischen Eigenschaften der Zeolithe (Ionenaustauscher, Trennverfahren, heterogene Katalyse) mit den elektronischen und optischen Eigenschaften dieser Halbleitermaterialien zu kombinieren [1]. Potentiellen Anwendungen steht jedoch oft entgegen, dass es nicht möglich ist, die in den Kanälen oder zwischen den Schichten lokalisierten Strukturdirektoren ohne Verlust der Kristallinität und dem Kollaps der Strukturen zu entfernen.

Das Hauptziel dieser Arbeit besteht darin, neue Übergangsmetallhaltige Thiostannate darzustellen und zu charakterisieren. Dabei sollten Struktur-Eigenschafts-Beziehungen ermittelt werden, was nur durch eine entsprechende Anzahl an „Studienobjekten“ möglich ist. Außerdem sollten die Synthesen optimiert werden, um hohe Ausbeuten und gut kristalline Produkte zu erhalten. Um dies zu erreichen, sollten Untersuchungen zur Aufklärung der Bildungsmechanismen der Thiometallate unter solvothermalen Bedingungen mit in-situ-Methoden durchgeführt werden.

## 1.2. Thiostannate

Das große Interesse an Thiostannaten beruht vor allem auf der strukturellen Flexibilität der Koordinationsfähigkeit des Zinns sowohl trigonal-pyramidale (Koordinationszahl 3), tetraedrische (Koordinationszahl 4), trigonal-bipyramidale (Koordinationszahl 5) als auch oktaedrische (Koordinationszahl 6) Polyeder auszubilden, so dass durch die Verknüpfung dieser primären Baueinheiten zwei- und dreidimensionale Strukturen gebildet werden können. Die maximale Koordinationszahl nimmt von 6 mit Schwefel über 5 mit Selen zu 4 mit Tellur hin ab [2]. Bemerkenswert ist, dass Sn(II) meistens trigonal-pyramidal koordiniert vorliegt. In der Mehrzahl der Thiostannate wird jedoch Sn(IV) gefunden, was auf die hohe Oxidationskraft des Schwefels zurückgeführt werden kann. In wässriger Lösung können die verschiedenen  $\text{SnS}_x$ -Polyeder in Abhängigkeit des pH-Wertes nachgewiesen werden. Neben den  $[\text{SnS}_4]^{4-}$ -Ionen können unterschiedliche Kondensationsprodukte wie  $[\text{Sn}_2\text{S}_6]^{4-}$  oder  $[\text{Sn}_2\text{S}_7]^{6-}$  [3, 4, 5] sowie deren Oligomere  $[\text{Sn}_m\text{S}_n]^{(2n-4m)-}$  auftreten [6].

„Thiostannate“ ist ein sehr umfangreicher Begriff, der bereits im Chemiestudium im Rahmen der qualitativen Analyse (Freiberger Aufschluss) das erste Mal erwähnt wird. Aufgrund der Vielfältigkeit der Thiostannate wird im folgenden zunächst zwischen den rein anorganischen Verbindungen und den anorganisch-organischen Hybridmaterialien unterschieden.

### 1.2.1. Anorganische Thiostannate

Krebs berichtete 1983 in einem Übersichtsartikel über Thioverbindungen der Hauptgruppenelemente und die vielseitigen Koordinationsmöglichkeiten von Zinn und Schwefel. Dabei prägte er den Begriff der Thiostannate [3]: „Die Bezeichnung „Thiosalz“ mit „Thioanionen“ im Gegensatz zur Bezeichnung „ternäres Sulfid“ für eine feste Phase  $\text{A}_x\text{B}_y\text{S}_z$  ist dann sinnvoll, wenn diskrete (auch polymere)  $\text{B}_y\text{S}_z$ -Struktureinheiten erkennbar sind; Kriterien hierfür sind signifikant stärkere (und meist stärker kovalente) B-S-Bindungen relativ zu (stärker heteropolaren) schwächeren  $\text{A}\cdots\text{S}$ -Bindungen.“ Aus diesem Grund ist die Verbindung  $\text{Na}_6\text{Sn}_2\text{S}_7$  [4] ein Natriumthiostannat mit  $[\text{Sn}_2\text{S}_7]^{6-}$ -Anionen und „ $\text{ZnAl}_2\text{S}_4$  eher ein Zinkaluminiumsulfid“ [3].

Weitere Beispiele für rein anorganische Thiostannate mit typischen Anionen bzw. Grundelementen sind die Verbindungen  $\text{Na}_4\text{Sn}_2\text{S}_6 \cdot 14 \text{H}_2\text{O}$  mit isolierten  $[\text{Sn}_2\text{S}_6]^{4-}$ -Anionen [4],  $\text{Na}_4\text{SnS}_4 \cdot 14 \text{H}_2\text{O}$  [7],  $[\text{K}_4(\text{H}_2\text{O})_4]\text{SnS}_4$ ,  $[\text{Ba}_4(\text{H}_2\text{O})_{11}]\text{SnS}_4$  [8] mit  $[\text{SnS}_4]^{4-}$ -Anionen,  $\text{Cs}_4\text{Sn}_5\text{S}_{12} \cdot 2 \text{H}_2\text{O}$  mit  $[\text{Sn}_5\text{S}_{12}]^{4-}$ -Baugruppen [9],  $\text{Rb}_2\text{Sn}_3\text{S}_7 \cdot 2 \text{H}_2\text{O}$  mit  $[\text{Sn}_3\text{S}_7]^{2-}$ -Anionen [10], die Schichtstrukturen  $\text{A}_2\text{Cu}_2\text{Sn}_2\text{S}_6$  (A = Na, K, Rb, Cs) mit  $\text{SnS}_4$ -Tetraedern [11] sowie die Thiostannate  $\text{K}_2\text{Sn}_2\text{S}_5$  [12] und  $\text{Na}_4\text{Sn}_3\text{S}_8$  [13] mit dreidimensionaler Gerüststruktur.

Die ersten anorganischen Thiostannate wurden durch Hochtemperatursynthesen oder aus Alkali-Polychalkogenidschmelzen erhalten. Allerdings wurde z. B.  $\text{Cs}_4\text{Sn}_5\text{S}_{12} \cdot 2 \text{H}_2\text{O}$  bereits unter hydrothermalen Bedingungen aus  $\text{Cs}_2\text{CO}_3$  und  $\text{SnS}_2$  bei 130 °C dargestellt [9]. Mit fortschreitender Entwicklung solvothormaler Methoden konnten mit Methanol als Solvens Selenido- und Telluridostannate wie z. B. die Verbindung  $\text{Rb}_2\text{Sn}_2\text{Se}_5$  mit dreidimensionaler Gerüststruktur dargestellt werden [6].

Die relativ milden Bedingungen solvothormaler Synthesen haben der Festkörperchemie einen weiteren präparativen Zugang zu neuen Materialien eröffnet [6]. Unter diesen Bedingungen werden unterschiedlichste Lösungsmittel wie Wasser, Alkohole sowie Amine bei relativ niedrigen Temperaturen zwischen 100 – 200 °C eingesetzt. Solvothermale Bedingungen begünstigen das Kristallwachstum und molekulare Baueinheiten bleiben intakt, so dass diese durch Polymerisieren höherdimensionale Strukturen ausbilden können. Der Einsatz organischer Moleküle, insbesondere Amine, als strukturdirigierende Reagenzien ermöglicht die Synthese von anorganisch-organischen Hybridmaterialien, zu denen auch die in dieser Arbeit vorgestellten Thiostannate gehören.

### 1.2.2. Thiostannate mit organischen, strukturdirigierenden Reagenzien

Bedard und Mitarbeiter konnten 1989 unter Verwendung von Alkylammoniumkationen die ersten Schichtthiostannate mit großen Poren in den Schichten synthetisieren [14, 15, 16]. Auch werden Alkylammoniumkationen und Amine als strukturdirigierende Reagenzien bei der Synthese poröser Materialien eingesetzt, um „zeotype“ Halbleitermaterialien auf Chalkogenbasis darzustellen. Oft wurden Metalle und Halbmetalle verwendet, die mit Schwefelatomen eine tetraedrische Koordination eingehen, um die Kristallchemie der Zeolithe und Alumophosphate imitieren zu können [1].

Bedard führte die Nomenklatur R-M'MS-n für die Gruppe der neuen Thiometallate ein. Das organische Molekül R dient sowohl als strukturdirigierendes Reagenz als auch als ladungskompensierendes Kation (sofern notwendig). M' repräsentiert ein 3d- oder 4d-Metall und M = Ge, Sn, Sb, In. Die verschiedenen Strukturtypen werden durch das angehängte „n“ unterschieden. Die Synthese der Thiometallate erfolgt unter solvothormalen Bedingungen aus den Metallsulfiden oder aus den Metallen und Schwefel und den entsprechenden Aminen oder Alkylammoniumionen. Die organischen Moleküle werden oft zur Lenkung der Selbstorganisation polymerer, anionischer Baueinheiten eingesetzt, und in den finalen Strukturen spiegeln sich häufig die Größe und Geometrie der Strukturdirektoren wider [6]. Da verschiedene Alkylammoniumionen zur Bildung eines ganz bestimmten Strukturtyps oder einzelne Alkylammoniumionen zur Ausbildung unterschiedlicher Strukturtypen führen können, wird von strukturdirigierender Wirkung, nicht aber von Templaten oder dem Templateffekt gesprochen.

Bei den Thiostannaten werden nur wenige Verbindungen mit dreidimensionalen Gerüststrukturen beobachtet, da meist lamellare Strukturen ausgebildet werden. Typische Koordinationspolyeder wie trigonale SnS<sub>5</sub>-Bipyramiden, SnS<sub>4</sub>-Tetraeder sowie resultierende Baueinheiten wie Sn<sub>3</sub>S<sub>4</sub>-Halbwürfel und [Sn<sub>2</sub>S<sub>6</sub>]<sup>4-</sup>-Anionen sind in Abb. 1.1 dargestellt.

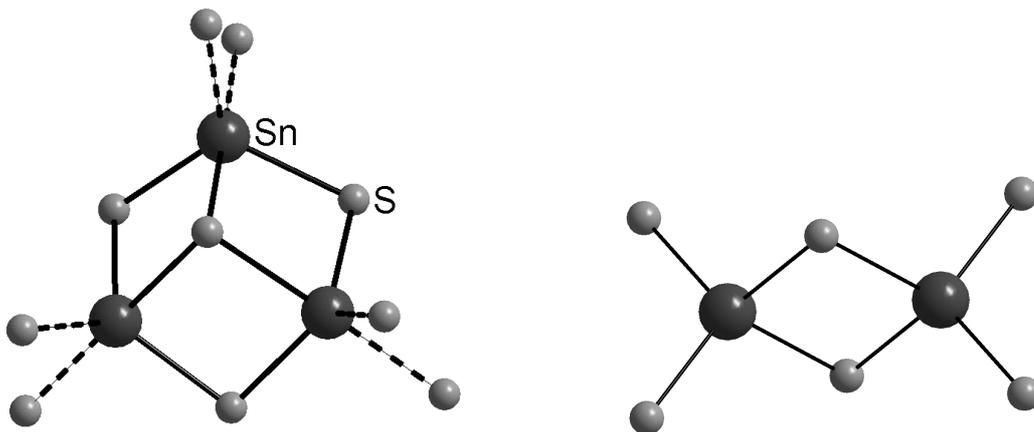


**Abb. 1.1:** Typische Koordinationspolyeder in Thiostannaten (dunkelgrau: Sn-Atome, grau: S-Atome), links: Sn<sub>3</sub>S<sub>4</sub>-Halbwürfel mit trigonal-bipyramidal koordinierten Sn-Atomen, rechts: [Sn<sub>2</sub>S<sub>6</sub>]<sup>4-</sup>-Anion mit Sn in tetraedrischer Umgebung.

Die beiden „klassischen“ Thiostannatstrukturtypen R-SnS-1 und R-SnS-3 bestehen aus zweidimensionalen [Sn<sub>3</sub>S<sub>7</sub>]<sup>2-</sup>- bzw. [Sn<sub>4</sub>S<sub>9</sub>]<sup>2-</sup>-Schichten (vgl. Abb. 1.2). In den Schichten werden Sn<sub>3</sub>S<sub>4</sub>-Baueinheiten beobachtet, welche die Gestalt

eines Würfels mit einer fehlenden Ecke bzw. eines so genannten Halbwürfels aufweisen (siehe Abb. 1.1, links). Diese Halbwürfel sind über zweifach verbrückende  $\text{Sn}(\mu\text{-S})_2\text{Sn}$ -Schwefelbindungen verbunden und bilden so das Schichtanion aus.

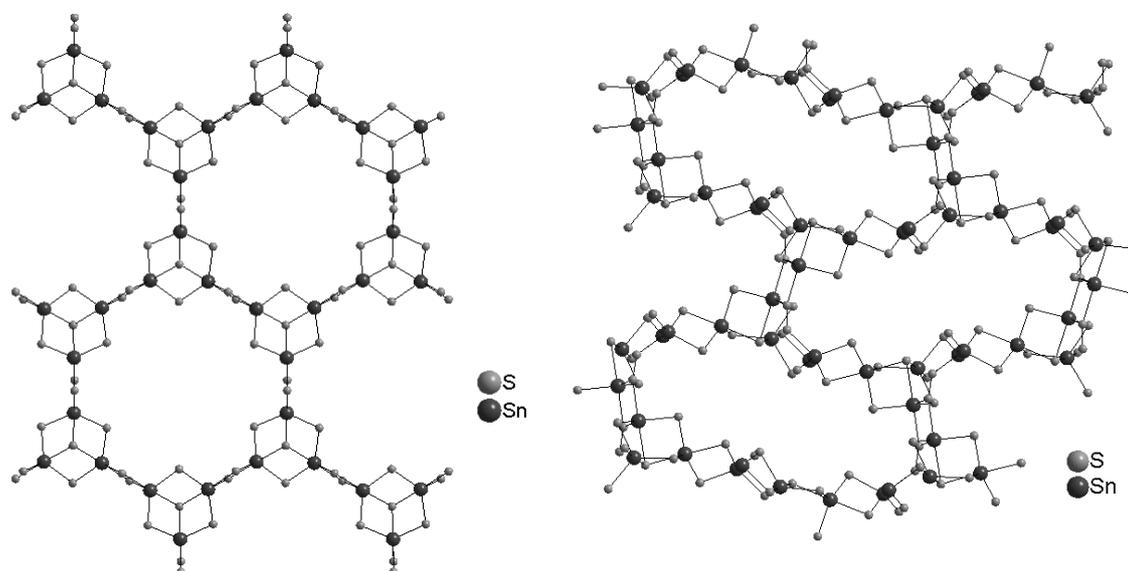


**Abb. 1.2:** Die anionischen Schichten der R-SnS-n-Materialien, links:  $[\text{Sn}_3\text{S}_7]^{2-}$  mit hexagonalen Poren, rechts:  $[\text{Sn}_4\text{S}_9]^{2-}$  mit annähernd elliptischen Poren. Die organischen Kationen sind zur besseren Übersicht nicht dargestellt.

In den R-SnS-1-Schichten liegen als primäre Baueinheiten (primary building units PBU) trigonale Bipyramiden  $\text{SnS}_5$  (z. B. in Abb. 1.1, links) vor, die sekundären Baueinheiten (secondary building units SBU) stellen die  $\text{Sn}_3\text{S}_4$ -Halbwürfel dar (Abb. 1.1, links). Die Verknüpfung der Halbwürfel über  $(\mu\text{-S})_2^-$  und  $(\mu\text{-S}_2\text{SnS}_2)$ -Einheiten führt zur Ausbildung hexagonaler, 24-atomiger Ringe in den Schichten. Die Struktur der R-SnS-3-Materialien wird ebenfalls durch Verknüpfung von  $\text{Sn}_3\text{S}_4$ -Halbwürfeln über  $(\mu\text{-S})_2^-$  und  $(\mu\text{-S}_2\text{SnS}_2)$ -Einheiten gebildet, dabei werden jedoch 32-atomige Ringe mit annähernd elliptischer Form ausgebildet. Im Gegensatz zum R-SnS-1-Typ werden hier als PBU  $\text{SnS}_4$ -Tetraeder und  $\text{SnS}_5$ -Bipyramiden beobachtet. Die ladungskompensierenden Kationen sind zwischen den Schichten und/oder in den Poren lokalisiert. Die typischen Schichtabstände liegen zwischen 8 und 9 Å für R-SnS-1 und bei etwa 14 Å für R-SnS-3 [17]. Einige Thiostannate finden bereits Anwendungen in der Katalyse, als Absorber und Molekülsensoren sowie Ionenaustauscher [17, 18, 19, 20, 21, 22].

In der folgenden Tabelle sind ausgewählte Beispiele sowie Eigenschaften (Tab. 1.1) von Thioannaten stichwortartig zusammengestellt. Detaillierte Informationen können den entsprechenden Literaturstellen sowie zahlreichen Übersichtsartikeln entnommen werden [1, 2, 6, 17].

**Tab. 1.1: Ausgewählte Thioannate sowie einige Eigenschaften und Besonderheiten**

<b>Verbindung</b>	<b>Eigenschaften / Besonderheiten</b>
R-SnS-1: [Me <sub>4</sub> N] <sub>2</sub> Sn <sub>3</sub> S <sub>7</sub> [18]	Lamellare Strukturen (vgl. Text); Me <sub>4</sub> N <sup>+</sup> -Kation kann gegen Alkali- bzw. Erdalkali-Kationen ausgetauscht werden; Abstimmen der optischen Bandlücke durch partielle Substitution von S durch Se [24]; Untersuchungen zum Einfluss der Schwerkraft auf das Kristallwachstum [25]; Untersuchungen der Intermediate der Thioannatbildung [26]; Sensitiv für CO <sub>2</sub> und H <sub>2</sub> O [20].
[Et <sub>4</sub> N] <sub>2</sub> Sn <sub>3</sub> S <sub>7</sub> [23]	Dehydrierte Varianten absorbieren reversibel H <sub>2</sub> O, H <sub>2</sub> S, CO <sub>2</sub> und Ar [27].
[DABCO] <sub>2</sub> Sn <sub>3</sub> S <sub>7</sub> [23] (DABCO = 1,4-Diazabicyclo[2.2.2]oktan)	Untersuchungen zur pH-Wert-Abhängigkeit der Kristallbildung [19].
R-SnS-3: [Pr <sub>4</sub> N] <sub>2</sub> Sn <sub>4</sub> S <sub>9</sub> [28]	Lamellare Strukturen (vgl. Text); Untersuchungen der Intermediate der Thioannatbildung [26].
[Bu <sub>4</sub> N] <sub>2</sub> Sn <sub>4</sub> S <sub>9</sub> [28]	Untersuchungen zum Einfluss der Schwerkraft auf das Kristallwachstum [25].
[(C <sub>3</sub> H <sub>7</sub> ) <sub>4</sub> N]·[(CH <sub>3</sub> ) <sub>3</sub> NH]Sn <sub>4</sub> S <sub>9</sub> [29]	In-situ-Bildung von (CH <sub>3</sub> ) <sub>3</sub> NH <sup>+</sup> aus (C <sub>3</sub> H <sub>7</sub> ) <sub>4</sub> N <sup>+</sup> .
[C <sub>4</sub> H <sub>11</sub> N <sub>2</sub> ] <sub>2</sub> [C <sub>10</sub> N <sub>4</sub> H <sub>24</sub> ]Sn <sub>5</sub> S <sub>12</sub> [30]	Synthese mit DABCO liefert C <sub>4</sub> H <sub>11</sub> N <sub>2</sub> und C <sub>10</sub> N <sub>4</sub> H <sub>24</sub> zwischen den anorganischen Schichten.
<sup>1</sup> [SnS <sub>2</sub> ·en] [31] (en = Ethylendiamin)	Das Amin ist direkt an Sn koordiniert, so dass SnS <sub>4</sub> N <sub>2</sub> -Oktaeder gebildet werden; 1D-Struktur.
[enH] <sub>4</sub> Sn <sub>2</sub> S <sub>6</sub> [32]	Diskrete [Sn <sub>2</sub> S <sub>6</sub> ] <sup>4-</sup> -Anionen.
[C <sub>6</sub> H <sub>20</sub> N <sub>4</sub> ] <sub>2</sub> Sn <sub>2</sub> S <sub>6</sub> · 2 H <sub>2</sub> O [33]	Diskrete [Sn <sub>2</sub> S <sub>6</sub> ] <sup>4-</sup> -Anionen.
[enH <sub>2</sub> ][enH] <sub>2</sub> Sn <sub>2</sub> S <sub>6</sub> [34]	Diskrete [Sn <sub>2</sub> S <sub>6</sub> ] <sup>4-</sup> -Anionen und sowohl einfach- als auch zweifach protonierte Ethylendiaminmoleküle.

Ein Schwerpunkt bei den Untersuchungen der Eigenschaften lag auf der thermischen Stabilität. Die Thiostannate sind in der Regel nur bis etwa 200 °C thermisch stabil, was ihre mögliche Anwendung stark einschränkt. Oberhalb von ca. 200 °C reagieren chemisorbiertes Wasser sowie die strukturdirigierenden Moleküle mit den Konstituenten der Anionenschichten. Dabei erfolgt eine Reorganisation bzw. der Kollaps der Festkörperstruktur und diverse Zinnsulfide wie Berndtit  $\text{SnS}_2$ , Herzenbergit  $\text{SnS}$  und Ottemannit  $\text{Sn}_2\text{S}_3$  werden als Abbauprodukte beobachtet [35]. Um die Stabilität der Thiostannate zu erhöhen und ein Kollabieren der Strukturen zu verhindern, wurden 1994 von Parise und Mitarbeitern erste Versuche unternommen, die organischen Kationen gegen Alkali- und Erdalkalimetall-Kationen auszutauschen [18].

Die strukturelle Vielfalt der Thiostannate beruht auf der Koordinationsvariabilität von Sn und S, der Tendenz des Schwefels zur Ketten- und Ringbildung, und den Möglichkeiten von Sn, sowohl in den Oxidationsstufen +II und +IV aufzutreten als auch gemischtvalente Verbindungen zu bilden. In den Thiostannaten werden tetraedrische  $[\text{SnS}_4]^{4-}$ -Monomere,  $[\text{Sn}_2\text{S}_6]^{4-}$ - und  $[\text{Sn}_2\text{S}_7]^{6-}$ -Dimere mit kanten- bzw. eckenverknüpften  $\text{SnS}_4$ -Tetraedern sowie adamantanartige  $[\text{Sn}_4\text{S}_{10}]^{4-}$ -Tetramere beobachtet [17]. Das Polythiostannat-Anion  $[\text{Sn}_5\text{S}_{12}]^{4-}$  wurde bereits von Sheldrick 1988 in der Verbindung  $\text{Cs}_4\text{Sn}_5\text{S}_{12} \cdot 2 \text{H}_2\text{O}$  beschrieben [9] und wird auch in  $[\text{C}_4\text{H}_{11}\text{N}_2]_2[\text{C}_{10}\text{N}_4\text{H}_{24}]\text{Sn}_5\text{S}_{12}$  [30] beobachtet. In diesem Anion ist Sn sowohl trigonal-bipyramidal als auch oktaedrisch koordiniert und die Anionenschicht wird durch Kantenverknüpfung der Polyeder gebildet. Die 1985 von Müller vorgestellten Polysulfido-Anionen  $\text{SnS}_x^{2-}$  (mit  $x = 4, 5, 6, 9$ ) werden beispielsweise in  $[\text{Et}_4\text{N}]_3[\text{Sn}(\text{S}_4)_2]_{0.4}[\text{Sn}(\text{S}_4)_2(\text{S}_6)]_{0.6}$  [36] und in  $\text{Cs}_2\text{SnS}_{14}$  (mit  $\text{S}_4^{2-}$ - und  $\text{S}_6^{2-}$ -Einheiten) [12] beobachtet.

Prinzipiell können drei Arten von Gegenionen zu den Thiostannat-Anionen unterschieden werden. Die einfachsten sind die Metallkationen (siehe Kap. 1.2.1). Bei der zweiten Gruppe wird der Ladungsausgleich durch organische Moleküle erreicht, zu denen auch die protonierten Amine gehören. Zu dieser Gruppe können auch Übergangsmetallkomplexe gezählt werden. Drittens kann die Ladungskompensation durch die Integration von Übergangsmetallen in das Netzwerk erreicht werden. Diese Art der Ladungskompensation ist bisher eher

weniger untersucht worden und wird im folgenden Kapitel beschrieben. Zusätzlich wird auf Thiostannate eingegangen, bei denen Übergangsmetallkomplexe Teil der Struktur sind.

### **1.3. Modifizierung der Thiostannate durch Integration von Übergangsmetallen (ÜM)**

Das Interesse, Übergangsmetallkationen in Thiostannate einzubauen besteht nicht allein darin, Ladungsneutralität zu erreichen, sondern in der Modifizierung der chemisch-physikalischen Eigenschaften. Zusätzlich sollte die strukturelle Vielfalt durch die Integration von ÜM-Kationen deutlich erweitert werden können. Rein anorganische Thiostannate sind schon seit längerer Zeit bekannt und bei dieser Verbindungsklasse ist die Integration einiger ÜM erfolgreich:  $\text{Cu}_2\text{SrSnS}_4$  [37],  $\text{BaCdSnS}_4$  [38],  $\text{A}_2\text{Cu}_2\text{Sn}_2\text{S}_6$  (A = Na, K, Rb, Cs),  $\text{Rb}_2\text{Cu}_2\text{SnS}_4$  [11],  $\text{Cu}_2\text{CdSn}_3\text{S}_8$  [39],  $\text{K}_{10}\text{M}_4\text{Sn}_4\text{S}_{17}$  (M = Mn, Fe, Co, Zn) [40],  $\text{K}_6\text{Sn}[\text{Zn}_4\text{Sn}_4\text{S}_{17}]$  [41] und  $\text{R}_3\text{Ag}_{1-\delta}\text{SnS}_7$  (R = La, Ce;  $\delta = 0.18 - 0.19$ ) [42] sind nur ausgewählte Beispiele aus der Vielzahl an Verbindungen.

Solvothermale Synthesen mit Übergangsmetallen in Gegenwart organischer strukturdirigierender Reagenzien führen meist zur Bildung von Übergangsmetall-Komplexen als ladungskompensierende Kationen, welche keine Bindung zu dem Thiostannatgerüst haben. Obwohl die Integration der Übergangsmetalle in die anorganischen Netzwerke bzw. Schichten damit nicht gelungen ist, wird durch die ggfs. auftretende Schichtaufweitung die Eigenschaft der Verbindung verändert.

Wie bereits weiter oben erwähnt, variiert bei den R-SnS-n-Materialien je nach Alkylammoniumionen der Interschichtabstand von 8 bis 14 Å [17, 23]. 1997 beschrieben Ozin und Mitarbeiter die Synthese von „mesolamellaren“ Thiostannaten mit Alkylamin-Doppelschichten zwischen den anorganischen Schichten mit einem Schichtabstand von 51 Å [43]. Außerdem wurde versucht, die Schichtaufweitung mit größeren Kationen wie z. B. Übergangsmetall-Komplexen zu erzwingen. Kanatzidis und Mitarbeiter berichteten 2002 über die mesostrukturierte Phase  $(\text{CP})_x\text{M}_y\text{Sn}_2\text{S}_6$  (M = Zn, Cd, Ga; CP = Cetylpyridinium) [44]. Durch die Integration der Übergangsmetalle sowie die Aufweitung der Schichtabstände (auf ca. 35 - 36 Å) wurden Anwendungen in der Photokatalyse und der Adsorption erhofft, obgleich die genaue Struktur nicht geklärt werden konnte.

Die erfolgreiche Integration von Übergangsmetallen in Thiometallate gelang in unserer Arbeitsgruppe 1996 bei den Thioantimonaten  $\text{Mn}_2\text{Sb}_2\text{S}_5(\text{CH}_3\text{NH}_2)_2$  und  $\text{Mn}_2\text{Sb}_2\text{S}_5(\text{NH}_2(\text{CH}_2)_3\text{NH}_2)$  [45]. 2003 wurde neben  $[\text{Ni}(\text{en})_3]_2\text{Sn}_2\text{S}_6$  (en =

Ethylendiamin) und  $[\text{Ni}(\text{dap})_3]_2\text{Sn}_2\text{S}_6 \cdot 2 \text{H}_2\text{O}$  (dap = 1,2-Diaminopropan) auch das Thiostannat  $[\text{Co}(\text{tren})]_2\text{Sn}_2\text{S}_6$  (tren = Tris-(2-aminoethyl)-amin) [46] publiziert, in dem das  $\text{Co}^{2+}$ -Ion sowohl Bindungen zu den Thiostannat-Anionen als auch zu den Aminen ausbildet. Während in  $[\text{Co}(\text{tren})]_2\text{Sn}_2\text{S}_6$  die  $[\text{Co}(\text{tren})]^{2+}$ -Komplexe mit den Thiostannat-Anionen verknüpft sind, werden in  $[\text{Ni}(\text{en})_3]_2\text{Sn}_2\text{S}_6$  und  $[\text{Ni}(\text{dap})_3]_2\text{Sn}_2\text{S}_6 \cdot 2 \text{H}_2\text{O}$  nur diskrete  $[\text{Sn}_2\text{S}_6]^{4-}$ -Anionen gefunden. Weitere Beispiele mit isolierten, ladungskompensierenden  $[\text{ÜM}(\text{Amin})_x]^{y+}$ -Kationen stellen die Thiostannate  $[\text{M}(\text{en})_3]_2\text{Sn}_2\text{S}_6$  (M = Mn, Co, Zn) [47],  $[\text{Ni}(\text{en})_3]_2\text{Sn}_2\text{S}_6$ ,  $[\text{Ni}(\text{dien})_2]_2\text{Sn}_2\text{S}_6$  (dien = Diethylentriamin) [48],  $[\text{Mn}(\text{en})_3]_2\text{Sn}_2\text{S}_6 \cdot 2 \text{H}_2\text{O}$  und  $[\text{Mn}(\text{dien})_2]_2\text{Sn}_2\text{S}_6$  [49] dar.

Erst in den letzten Jahren wurde über Thiostannate berichtet, in denen die Übergangsmetalle in den anionischen Ketten oder Schichten integriert sind. In der Verbindung  $(\text{NH}_4)_2\text{Ag}_6\text{Sn}_3\text{S}_{10}$  werden die  $[\text{Ag}_6\text{SnS}_4]^{2+}$ -Kationenschichten von  $[\text{SnS}_3]^{2-}$ -Zickzackketten durchzogen und die  $\text{NH}_4^+$ -Kationen befinden sich in den eindimensionalen Kanälen [50].  $[\text{HgSnS}_4]_\infty^{2-}$ -Säulen werden in  $(\text{enH}_2)\text{HgSnS}_4$  durch  $(\text{enH}_2)^{2+}$ -Säulen unterbrochen [51]. Auch für diese Verbindungen wurden mögliche Anwendungen als neuartige Molekülsiebe mit Eigenschaften von Halbleitermaterialien postuliert. Im Gegensatz zu  $(\text{enH}_2)\text{HgSnS}_4$  handelt es sich bei der Verbindung  $(\text{enH}_2)\text{Ag}_2\text{SnS}_4$  um eine zweidimensionale, chirale Struktur mit  $[\text{Ag}_2\text{SnS}_4]^{2-}$ -Schichten [52]. Im Jahr 2007 erschienen die ersten Veröffentlichungen mit Lanthanoidionen-Komplexen als ladungskompensierende Kationen der diskreten Thiostannat-Anionen [53, 54].

Im Rahmen dieser Arbeit sollten neue übergangsmetallhaltige Thiostannate dargestellt und charakterisiert werden. Das finale Ziel war die Übergangsmetallkationen in die anionischen Thiostannatstrukturen zu integrieren. Wie bereits erwähnt, tritt unter solvothermalen Bedingungen bei Verwendung von Aminen als Strukturdirektoren und Lösungsmittel als Konkurrenz die Bildung isolierter Komplexe auf. Zusätzlich konkurrieren auch die stabileren, dichten binären oder ternären Phasen. Bei der Synthesedurchführung müssen daher oft sehr mühselig die optimalen Bedingungen gefunden werden. Diese Optimierungen basieren einerseits auf Erfahrungen, andererseits handelt es sich jedoch um ein „trial and error“ Vorgehen bis sich der Erfolg einstellt.

Die in-situ-Experimente mit energiedispersiver Röntgenbeugung (EDXRD) (vgl. Kap. 1.4, S. 15 und Kap. 2.1.2, S. 21) stellen einen eleganten Weg dar, diese Optimierung zu erzielen. Aufgrund der Vorteile dieser Methode und unserer (langjährigen) Erfahrung sind zudem einige Kooperationen durchgeführt worden, deren Ergebnisse in Kapitel 4.3 (S. 157) vorgestellt werden.

Im Rahmen der Dissertation konnten zwölf übergangsmetallhaltige Thiostannate sowie eine übergangsmetallfreie Verbindung synthetisiert und charakterisiert werden. Bei den Synthesen wurde ein Schwerpunkt auf die Elemente Kupfer und Mangan gelegt.

Kupfer ist ebenso wie Silber chalkophil und bildet unter Konkurrenzbedingungen bevorzugt Bindungen zu Chalkogenanionen anstatt zu beispielsweise Stickstoff oder Sauerstoff aus. Daher kann angenommen werden, dass Kupfer eher in Thiostannate integriert wird als dass  $[\text{Cu}(\text{Amin})_x]^{y+}$ -Kationen gebildet werden. Die Verbindungen  $(\text{DBUH})\text{CuSnS}_3$  (DBU = 1,8-Diazabicyclo[5.4.0]undec-7-en) und  $(1,4\text{-dabH})_2\text{Cu}_2\text{SnS}_4$  (1,4-dab = 1,4-Diaminobutan) sind die ersten Beispiele dafür, dass diese Überlegungen richtig sind. Die Synthesen und Strukturen werden in der Veröffentlichung in Kapitel 4.1.1 (S. 37) vorgestellt. In beiden Verbindungen fungiert das Amin als ladungskompensierendes Kation, während Kupfer in die anionischen Thiostannat-Ketten integriert ist.

Erstaunlich ist, dass bei Synthesen mit DBU keine anderen ÜM-haltigen Thiostannate synthetisiert werden konnten. Bei der Verwendung von 1,4-Diaminobutan (1,4-dab) konnten jedoch zwei weitere Thiostannate erhalten werden, die zu  $(1,4\text{-dabH})_2\text{Cu}_2\text{SnS}_4$  isostrukturelle Verbindung  $(1,4\text{-dabH})_2\text{Ag}_2\text{SnS}_4$  (Kap. 4.1.2, S. 48) sowie  $(1,4\text{-dabH}_2)\text{MnSnS}_4$ , dem ersten Thiostannat mit  $\text{Mn}^{2+}$ -Kationen in den anionischen Ketten (Kap. 4.1.3, S. 61).

Unter Verwendung von 1,5-Diazabicyclo[4.3.0]non-5-en (DBN) statt DBU wurden in einer Synthese zwei neue Thiostannate erhalten. Die kupferhaltige Verbindung  $(\text{DBNH})_2\text{Cu}_6\text{Sn}_2\text{S}_8$  sowie das gemischtvalente Thiostannat  $(\text{DBNH})_2\text{Sn}_3\text{S}_6$  koexistieren unter den gewählten Bedingungen. Um phasenreine Produkte zu kristallisieren, wurden verschiedene Syntheseparameter (Zeit, Temperatur, Konzentration) variiert. Allerdings konnte bei Verwendung von Kupfer immer nur ein Phasengemisch erhalten werden, während das gemischtvalente Thiostannat bei Verzicht auf Kupfer im Eduktgemisch phasenrein zugänglich ist. Diese

Beobachtung belegt wiederum, dass solvothermale Synthesen sehr komplex und immer noch schlecht verstanden sind (vgl. Kap. 1.4, S. 15). Um ein besseres Verständnis dieser Reaktion zu erarbeiten, wurde die Bildung dieser beiden Verbindungen unter solvothermalen Bedingungen mit energiedispersiver Röntgenbeugung untersucht. Wesentliches Ziel dieser in-situ-Untersuchungen war, den/die Parameter zu identifizieren, welcher/welche geändert werden muss/müssen, um zu phasenreinen Produkten zu gelangen. Die Ergebnisse dieser Untersuchungen werden in Kapitel 4.2.1 (S. 128) präsentiert.

Kupferhaltige Thiostannate  $(\text{Amin})_x\text{Cu}_a\text{Sn}_b\text{S}_c$  kombinieren die Eigenschaften von Halbleitern mit denen der Zeolithe und zeichnen sich außerdem durch einen möglichen Vorteil als photoleitende Substanzen aus. Das Material mit der besten Effizienz in der Photovoltaik ist  $\text{Cu}(\text{In,Ga})\text{Se}_2$  (CIGS) [55, 56], wobei der wesentliche Nachteil der hohe Preis für In darstellt. Kanatzidis und Mitarbeiter berichteten in der Veröffentlichung zu  $\text{A}_2\text{Cu}_2\text{Sn}_2\text{S}_6$  ( $\text{A} = \text{Na, K, Rb, Cs}$ ), dass Chalkogenide der Übergangsmetalle und Hauptgruppenelemente für Anwendungen in den Bereichen der nicht-linearen Optik, in Batterien sowie in der heterogenen Katalyse geeignet sein sollten, aber insbesondere für die Umwandlung der Sonnenenergie in elektrische Energie nützlich sein könnten [11]. Das Interesse an Materialien für die „Solar Energy Conversion“ zeigt sich an der großen Zahl an Publikationen aus den unterschiedlichsten Bereichen der Naturwissenschaften. Vor kurzem konnten unter solvothermalen Bedingungen  $\text{CuIn}(\text{Se}_x\text{S}_{1-x})_2$  „Nanokristallite“ hergestellt werden [57], die eine lineare Abhängigkeit der Absorptionsenergie vom Selengehalt aufweisen und damit dem Sonnenspektrum besser angepasst werden können. Allerdings wird aufgrund des stetig steigenden Preises für Indium nach neuen Materialien gesucht, in denen Indium durch z. B. Zinn substituiert ist, welche aber dennoch photovoltaische Eigenschaften aufweisen. Dass dies möglich ist, wurde kürzlich mit der photoaktiven Verbindung  $\text{Cu}_2\text{Sn}_{1-x}\text{Si}_x\text{S}_3$  demonstriert [58].

Bereits im Rahmen meiner Diplomarbeit konnte die Verbindung  $(\text{dienH}_2)\text{Cu}_2\text{Sn}_2\text{S}_6$  synthetisiert werden. Es stellte sich heraus, dass dieses Thiostannat eine optischen Bandlücke von 1.5 eV aufweist, was für photovoltaische Materialien der optimale Wert ist. Aufgrund der schlechten Kristallqualität konnte die Struktur allerdings erst im letzten Jahr bestimmt werden. Die Ergebnisse auch der

Untersuchungen zu den photoelektrischen Eigenschaften werden in der Veröffentlichung in Kapitel 4.1.4 (S. 69) vorgestellt.

Obwohl Silber einmal erfolgreich in ein Thiostannat eingebaut werden konnte (Kap. 4.1.2, S. 48), wurde der Schwerpunkt der synthetischen Arbeiten auf das Element Mangan gelegt. Die Synthesen mit chalkophilen Übergangsmetallen waren nicht immer erfolgreich, da die Tendenz zur Ausbildung binärer Sulfide sehr stark ausgeprägt ist. Zahlreiche Veröffentlichungen belegen, dass solvothermale Synthesen mit z. B. Ni, Co oder Zn in Gegenwart von Aminen oft zu anorganischen Anionen und  $[\text{ÜM}(\text{Amin})_x]^{y+}$ -Kationen führen. Dies ist nicht verwunderlich, da selbst Ammoniak mit diesen Übergangsmetallen stabile Komplexe ausbildet. Sobald das Metallion vollständig komplexiert ist, steht keine Bindungsstelle für den Schwefel zur Verfügung und es entstehen isolierte Baueinheiten. Bei multidentaten Aminen wie beispielsweise Tris-(2-Aminoethyl)-amin (tren) werden die Koordinationsbedürfnisse einiger Übergangsmetallkationen nicht befriedigt, so dass ein oder zwei Bindungsstellen am Kation unbesetzt bleiben. Mit dieser Synthesestrategie konnten Übergangsmetalle in die anorganischen Gerüststrukturen integriert werden wie z. B. in  $[\text{Co}(\text{tren})]_2\text{Sn}_2\text{S}_6$  [46] oder  $[\text{M}(\text{tren})]\text{Sb}_4\text{S}_7$  (M = Mn, Fe, Co, Zn) [59]. Eine interessante Beobachtung im Gebiet der Thioantimonatchemie ist, dass sich  $\text{Mn}^{2+}$  völlig anders verhält als z. B.  $\text{Co}^{2+}$  oder  $\text{Ni}^{2+}$ .  $\text{Mn}^{2+}$  bildet Bindungen zu den S-Atomen der Thioantimonat-Anionen aus, ohne dass das Kation gewissermaßen mit einem multidentaten Amin dazu „gezwungen“ werden muss. Das deutet darauf hin, dass  $\text{Mn}^{2+}$  im Vergleich zu den anderen Übergangsmetallkationen eine ähnliche Affinität zu Schwefel und Stickstoff aufweist. Beispiele dafür sind z. B.  $[\text{Mn}(\text{C}_6\text{H}_{14}\text{N}_2)_3]_2[\text{Mn}(\text{C}_6\text{H}_{14}\text{N}_2)_2(\text{SbS}_4)_2] \cdot 6 \text{H}_2\text{O}$  [60] oder die  $\text{Mn}_2(\text{Amin})\text{Sb}_2\text{S}_5$ -Familie [45, 61, 62, 63, 64].

Die Anzahl manganhaltiger Thiostannate ist deutlich geringer. In  $[\text{Mn}(\text{en})_3]_2\text{Sn}_2\text{S}_6$  [47] und  $[\text{Mn}(\text{dien})_2]_2\text{Sn}_2\text{S}_6$  [49] liegen isolierte  $[\text{Sn}_2\text{S}_6]^{4-}$ -Anionen vor, in  $[\text{Mn}(\text{tepa})]_2(\mu_2\text{-Sn}_2\text{S}_6)$  (tepa = Tetraethylenpentamin) [65] verbinden die  $[\text{Sn}_2\text{S}_6]^{4-}$ -Anionen als bidentate Liganden die  $[\text{Mn}(\text{tepa})]^{2+}$ -Komplexe zu neutralen  $\{[\text{Mn}(\text{tepa})]_2\text{Sn}_2\text{S}_6\}$ -Einheiten und in der Verbindung  $\{[\text{Mn}(\text{en})_2]_2(\mu\text{-en})(\mu\text{-Sn}_2\text{S}_6)\}_\infty$  werden eine Mn-S-Bindung sowie 5 Mn-N-Bindungen beobachtet [66]. Das oben bereits erwähnte Thiostannat  $(1,4\text{-dabH}_2)\text{MnSnS}_4$  ist das erste mit  $\text{Mn}^{2+}$ -Kationen in den anionischen Ketten. Synthesen mit Triethyltetramin (trien) und

1,2-Diaminocyclohexan (1,2-dach) führten zur Bildung der neuen Verbindungen  $[\text{Mn}(1,2\text{-dach})_2(\text{H}_2\text{O})]_2\text{Sn}_2\text{S}_6$ ,  $[\text{Mn}(1,2\text{-dach})_2]\text{Sn}_2\text{S}_6 \cdot 2(1,2\text{-dach})$  und  $[\text{Mn}(\text{trien})]_2\text{SnS}_4 \cdot 4 \text{H}_2\text{O}$ , über deren Strukturen und Eigenschaften in den Veröffentlichungen in Kapitel 4.1.5 (S. 78) sowie Kapitel 4.1.7 (S. 123) berichtet wird.

Solvothermale Synthesen mit Diethylentriamin waren sowohl mit Kupfer ( $(\text{dienH}_2)\text{Cu}_2\text{Sn}_2\text{S}_6$ ) als auch mit Mangan ( $[\text{Mn}(\text{dien})_2]_2\text{Sn}_2\text{S}_6$  [49]) erfolgreich. In  $(\text{dienH}_2)\text{Cu}_2\text{Sn}_2\text{S}_6$  befinden sich die Aminmoleküle zwischen den anorganischen  $[\text{Cu}_2\text{Sn}_2\text{S}_6]^{2-}$ -Schichten. Die Versuche, das organische Molekül „zu vergrößern“ und damit den Interschichtabstand zu verändern, schlugen bei den Synthesen mit Kupfer in Gegenwart von Triethylentetramin bzw. Tetraethylenpentamin als Strukturdirektoren bislang fehl. Im Gegensatz dazu waren die Synthesen mit Mangan erfolgreich und die Verbindung  $[\text{Mn}(\text{tepa})]_2(\mu_2\text{-Sn}_2\text{S}_6)$  wurde bereits publiziert [65]. Mit den Kationen  $\text{Co}^{2+}$ ,  $\text{Ni}^{2+}$  und  $\text{Fe}^{2+}$  konnten die neuen Verbindungen  $[\text{M}(\text{tepa})]_2\text{Sn}_2\text{S}_6$  (M = Co, Ni, Fe) synthetisiert und charakterisiert werden, wobei  $[\text{Fe}(\text{tepa})]_2\text{Sn}_2\text{S}_6$  das erste eisenhaltige Thiostannat darstellt. Die Synthesen dieser Verbindungen sowie ausgewählte spektroskopische Eigenschaften werden in der Veröffentlichung in Kapitel 4.1.6 (S. 104) präsentiert.

### **1.4. In-situ-Untersuchungen zur Bildung von Thiostannaten unter solvothermalen Bedingungen**

Untersuchungen zur Aufklärung der Bildungsmechanismen von Thiometallaten unter solvothermalen Bedingungen sind essentiell, um gezielt Parameter verändern und damit eine Synthese optimieren zu können. Das Problem solvothormaler Synthesen ist, dass bei den heterogenen Reaktionen viele Parameter wie z. B. Temperatur, Zeit, Solvens, pH-Wert, Konzentration usw. die Produktbildung in nicht verstandener Weise beeinflussen. Deshalb gibt es bis jetzt nur ein rudimentäres Verständnis der unter solvothermalen Bedingungen ablaufenden Reaktionen, obwohl sich weltweit mehrere Arbeitsgruppen damit beschäftigen [67]. Um diese solvothermalen „Black-Box-Reaktionen“ etwas zu beleuchten, sind in-situ-Experimente notwendig. Mit solchen Untersuchungen werden unter realen Bedingungen kristalline Vorläufer oder Intermediate sowie deren Umwandlung in die Produkte erfasst und bei ausreichender Zeitauflösung des Experiments kann die Kristallisationskinetik ausgewertet werden.

Zeitaufgelöste in-situ energiedispersive Röntgenbeugung (in-situ-EDXRD; vgl. Kap. 2.1.2, S. 21) wurde 1996 von O'Hare und Mitarbeitern eingesetzt, um die hydrothermale Bildung von Thiostannaten zu untersuchen [68].

Der auf der Basis der Ergebnisse vorgeschlagene Mechanismus der Bildung von  $[\text{Me}_4\text{N}]_2\text{Sn}_3\text{S}_7$  ist in Abb. 1.3 dargestellt. Nach Auflösen der Edukte entstehen die Thiostannat-Anionen, welche kondensieren und die anionischen Schichten bilden. Diese sind zunächst ungeordnet und erst einige Zeit später erfolgt eine dreidimensionale Ausordnung der Schichten.

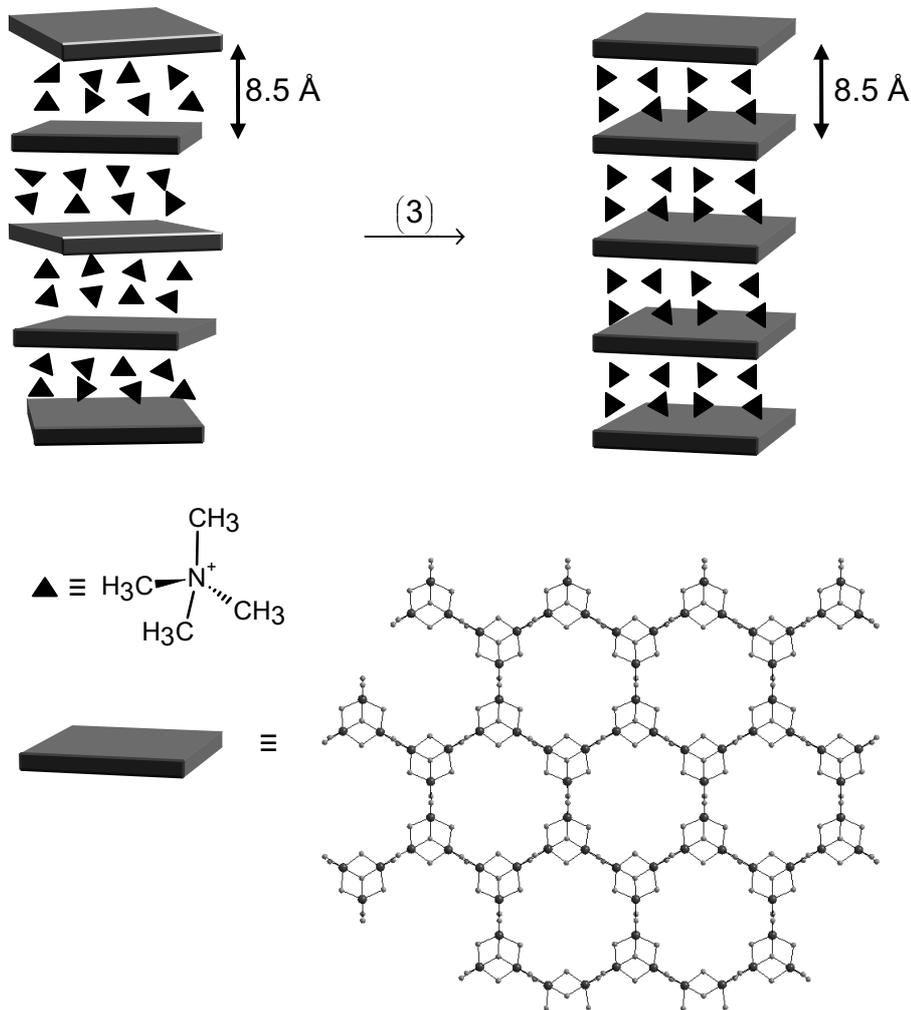
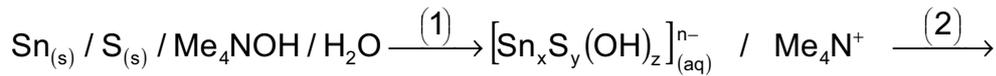


**Abb. 1.3:** Schematische Darstellung des vorgeschlagenen Mechanismus zur Bildung von  $[\text{Me}_4\text{N}]_2\text{Sn}_3\text{S}_7$ : (1) Auflösung der festen Edukte unter Bildung der Thiostannat-Anionen und Methylammonium-Kationen, (2) Kondensation der Ionen und Präorganisation eines Schichtverbands, (3) Organisation der Schichten und Ausbildung einer 3D-geordneten Struktur.

Da die R-SnS-n-Materialien nur schlecht kristallisieren und kleine Kristalle bilden, wurden von Ozin und Mitarbeitern mit  $^{119}\text{Sn}$  NMR- und UV/Vis-Spektroskopie die Reaktionslösungen untersucht [26]. Die abgefangenen Intermediate wurden mit Pulverdiffraktometrie und Einkristallstrukturanalysen charakterisiert. Bei diesen Untersuchungen konnten verschiedene Intermediate während der Reaktionen beobachtet werden:  $[\text{Sn}_2\text{S}_6]^{4-}$ , die Polysulfide  $[\text{Sn}(\text{S}_4)_3]^{2-}$  bzw.  $[\text{Sn}(\text{S}_4)_2(\text{S}_6)]^{2-}$  sowie  $[\text{S}_2\text{O}_3]^{2-}$ , wobei die Ergebnisse belegen, dass  $[\text{Sn}_2\text{S}_6]^{4-}$  die dominierende Spezies ist.

Eine schematische Darstellung des postulierten Mechanismus der Bildung von  $[\text{Me}_4\text{N}]_2\text{Sn}_3\text{S}_7$  ist in Abb. 1.4 gezeigt. Nach Auflösung der Edukte unter basischen, solvothermalen Bedingungen findet eine Adsorption an Zinn statt, wo der Elektronentransfer von Sn zu S stattfindet. Nach Komplexierung des Zinns wird das Intermediat  $[\text{Sn}_2\text{S}_6]^{4-}$  gebildet und mit strukturdirigierender Wirkung der Alkylammoniumionen erfolgt Keimbildung und anschließendes Kristallwachstum [26].

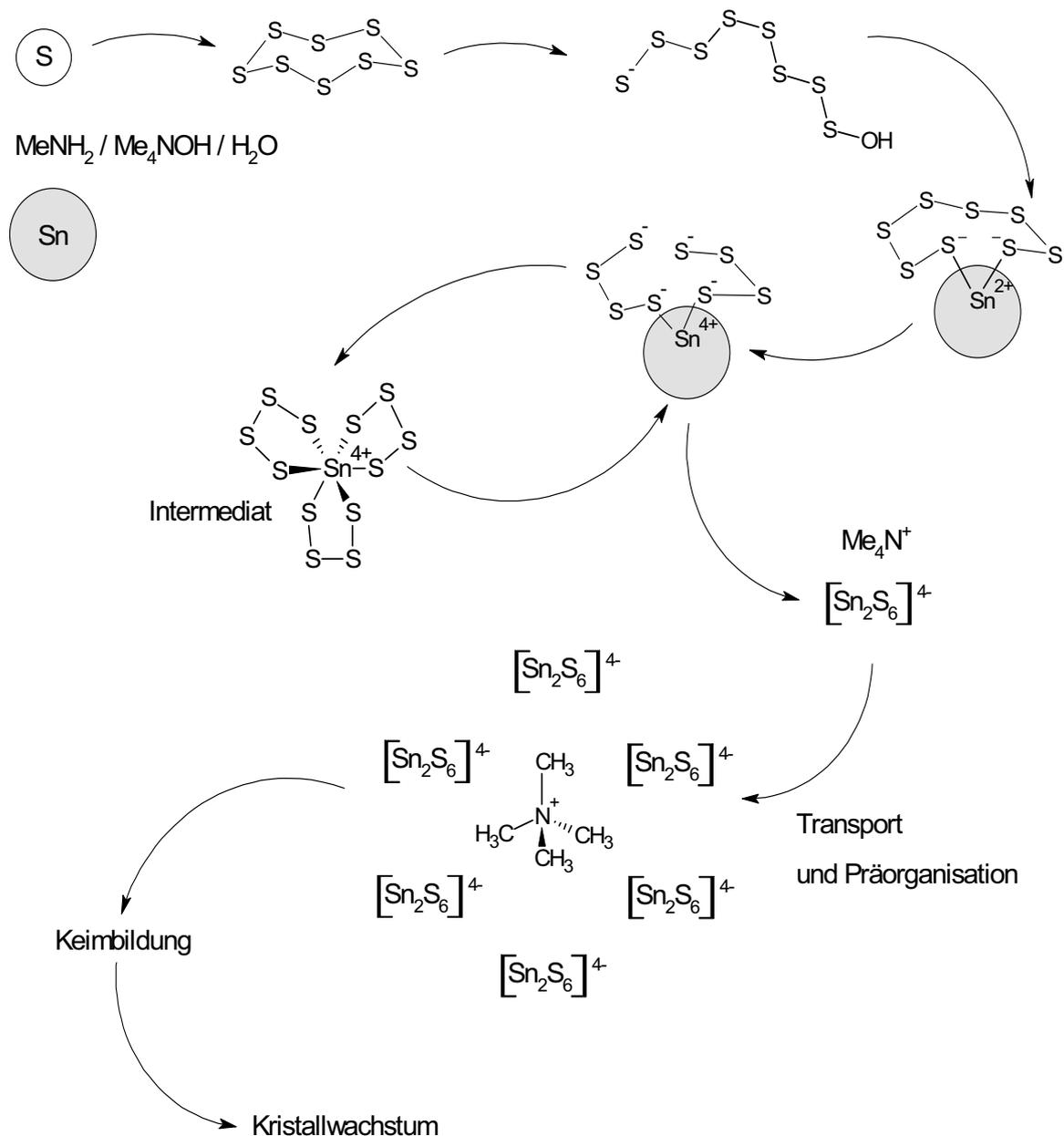


Abb. 1.4: Übersichtsschema der Bildung von R-SnS-n-Materialien aus Zinn und Schwefel unter solvothermalen Bedingungen in Gegenwart organischer Moleküle als strukturdirigierende Reagenzien am Beispiel von  $[\text{Me}_4\text{N}]_2\text{Sn}_3\text{S}_7$ .

In den letzten Jahren haben wir zeitaufgelöste in-situ-Untersuchungen mit energiedispersiver Röntgenbeugung erfolgreich bei solvothermalen Synthesen verschiedener Übergangsmetallhaltiger Thioantimonate eingesetzt [69, 70, 71]. Die Leistungsfähigkeit, aber auch Notwendigkeit der Untersuchung solvothermalen Synthesen mit in-situ-EDXRD wird an dem Beispiel der Reaktionen von Kupfer, Zinn und Schwefel in 1,5-Diazabicyclo[4.3.0]non-5-en (DBN) deutlich. Die Beobachtung, dass zwei Thiostannate  $((\text{DBNH})_2\text{Sn}_3\text{S}_6$  und  $(\text{DBNH})_2\text{Cu}_6\text{Sn}_2\text{S}_8$ ) unter den gewählten Bedingungen koexistieren, ist an sich schon interessant. Aber besonders bemerkenswert ist, dass  $(\text{DBNH})_2\text{Sn}_3\text{S}_6$  gemischtvalent ist und  $(\text{DBNH})_2\text{Cu}_6\text{Sn}_2\text{S}_8$  ein Thiostannat(IV) darstellt. D. h., bei der solvothermalen Synthese finden komplexe Redoxreaktionen statt und welches Produkt zuerst gebildet wird, ist völlig unklar. Die Ergebnisse dieser Untersuchungen sowie die Strukturen und weitere Eigenschaften der beiden Thiostannate werden in der Veröffentlichung in Kapitel 4.2.1 (S. 128) detailliert beschrieben.

## 2. Untersuchungsmethoden

Die Methoden, die zur Untersuchung und Charakterisierung der Produkte zum Einsatz gekommen sind, sollen in diesem Kapitel kurz vorgestellt werden. Dabei werden die in der anorganischen Festkörperchemie etablierten Methoden nicht näher diskutiert. Dazu zählen die Pulverdiffraktometrie, die Einkristallstrukturanalyse, die spektroskopischen Methoden wie Raman-, IR- und UV/Vis-Spektroskopie, die Elementaranalyse, die Elektronenmikroskopie und die thermischen Methoden. Die für diese Untersuchungen eingesetzten Geräte sind in Kapitel 3 in Tab. 3.3 kurz dargestellt. Es sollen jedoch die Methoden, die nicht zum Standardrepertoire gehören bzw. die üblicherweise nicht in jedem Laboratorium zugänglich sind, kurz dargestellt werden.

### ***2.1. Untersuchungen mit Synchrotronstrahlung: energiedispersive Röntgenbeugung (Energy Dispersive X-Ray Diffraction EDXRD) und Röntgenabsorptionsspektroskopie (X-Ray Absorption Spectroscopy XAS)***

#### **2.1.1. Synchrotronstrahlung**

Die Synchrotronstrahlung als Quelle elektromagnetischer Strahlung ist eine der erfolgreichsten, wenn auch zufälligen Entdeckungen. Jede beschleunigte bewegte elektrische Ladung stellt eine Quelle elektromagnetischer Strahlung dar. Werden Elektronen von einem Teilchenbeschleuniger oder einem Synchrotron in ein Magnetfeld injiziert, so entsteht bei der Umlaufbewegung dieser Elektronen Synchrotronstrahlung. Durch die mit nahezu Lichtgeschwindigkeit bewegten Elektronen erhält die Synchrotronstrahlung einige Besonderheiten. Die Abstrahlung erfolgt tangential zur Bewegungsrichtung in kurzen Pulsen (alle 800 ns mit einer Pulsdauer von 0.3 ns). Der diskontinuierliche Verlauf ist in Abb. 2.1 dargestellt.

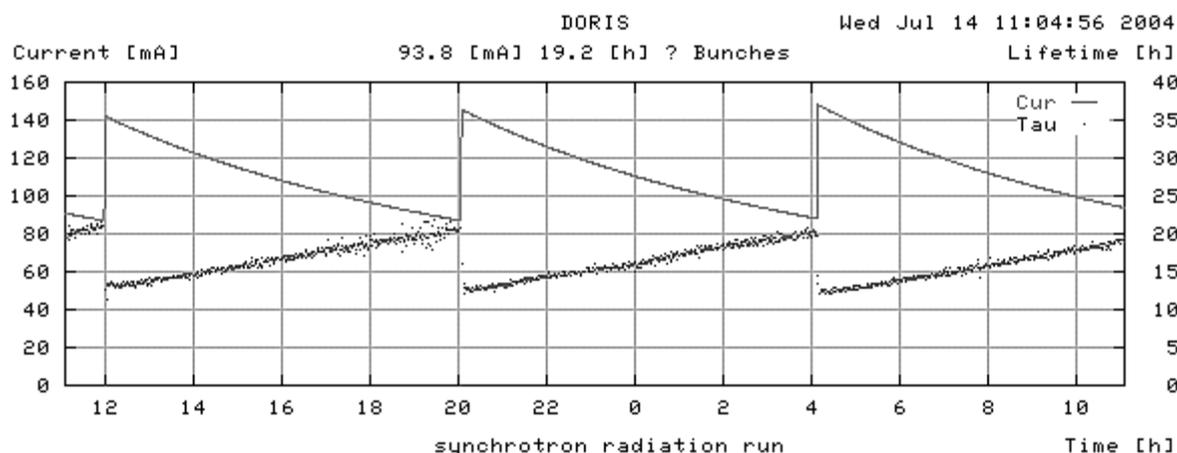


**Abb. 2.1: Schematischer Verlauf des Stromes der Synchrotronstrahlung des Speicherrings DORIS III des Hasylabs (Abkürzungen siehe Text; Verlauf vom 14.07.04) [72].**

Bei der ausgesandten, polarisierten Strahlung handelt es sich um weiße, polychromatische Strahlung mit einem Wellenlängenbereich vom Infrarot- bis zum harten Röntgen- und Gammastrahlenbereich, wobei der Energiebereich jedoch vom Speicherring abhängig ist.

Die Synchrotronstrahlung bietet neben der hohen Primärintensität eine Reihe von Vorteilen wie die Durchstimmbbarkeit der Wellenlänge, so dass durch geeignete Monochromatoren verschiedene Wellenlängen ausgewählt und somit auf Anforderungen des Experiments zugeschnitten werden können. Die Synchrotronstrahlung weist eine sehr hohe Kollimation auf, wodurch sehr scharfe Beugungsmaxima z. B. bei der Röntgenbeugung erhalten werden können.

Um den Abfall der Intensität nach bestimmter Zeit zu kompensieren, werden in die Speicherringe Teilchenpakete, die so genannten bunches, injiziert. Deshalb hat die emittierte Strahlung eine Zeitstruktur im Nanosekundenbereich (s. o.), wodurch auch Untersuchungen dynamischer Prozesse ermöglicht werden. Aufgrund der Vorteile der Synchrotronstrahlung wurden für verschiedene Forschungsarbeiten eine große Anzahl an Quellen eingerichtet, unter anderem das Hasylab (Hamburger Synchrotronstrahlungslabor) am DESY (Deutsches Elektronen Synchrotron). Der große Nachteil der Forschung mit Synchrotronstrahlung liegt in der Tatsache, dass solche Experimente nur in Großforschungseinrichtungen realisierbar sind.

Alle Experimente mit Synchrotronstrahlung dieser Arbeit wurden am Hasylab, DESY in Hamburg durchgeführt. Der Speicherring DORIS III (Doppel-Ring-Speicher; Positronen) liefert Synchrotronstrahlung mit Wellenlängen im harten

Röntgenbereich. Sein Umfang von 289 m ermöglicht eine Energie der Positronen von 4.45 GeV und einen Anfangsstrom von bis zu 120 mA. Die Synchrotronstrahlung wird allerdings nicht allein in den Ablenkmagneten in den Kurven des Speicherrings erzeugt, welche die beschleunigten Positronen auf ihrer Kreisbahn halten. Weitaus intensivere Strahlung wird in zusätzlich eingebauten Spezialmagneten erzeugt. Diese so genannten Wiggler und Undulatoren bestehen aus einer Reihe sich abwechselnder magnetischer Nord- und Südpole, wodurch die Positronen auf eine Art Slalomkurs gezwungen werden. Aufgrund der vielen, aufeinander folgenden Magnetpole wird eine viel intensivere Strahlung ausgesendet. Wiggler erzeugen im Vergleich zu Ablenkmagneten bis zu hundertfach intensivere Synchrotronstrahlung und Undulatoren können aufgrund der konstruktiven Überlagerung der Wellenzüge sogar eine tausendfache Verstärkung erreichen.

Durch spezielle Strahlführungen (die so genannten Beamlines) wird die Synchrotronstrahlung zu den verschiedenen Experimentierhallen und zu den Experimentierplätzen geleitet (Abb. 2.2).

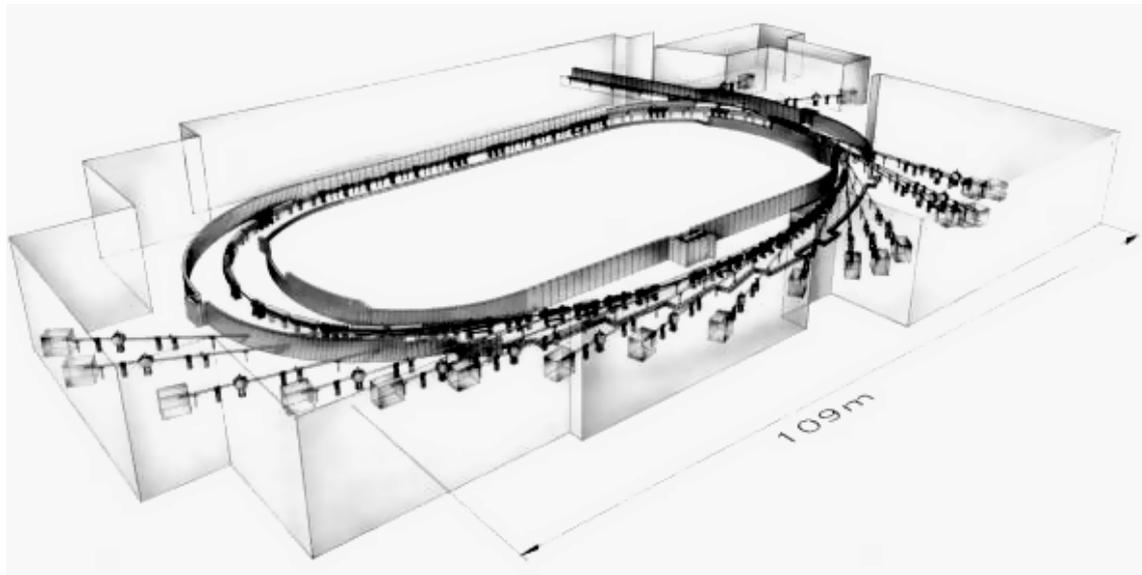


Abb. 2.2: Schema des Speicherrings DORIS III des Hasylabs [73].

### 2.1.2. Energiedispersive Röntgenbeugung (EDXRD)

Die Synchrotronstrahlung kann für energiedispersive Röntgenbeugungsexperimente eingesetzt werden. Aus dem einfallenden weißen Synchrotron-

spektrum wird ein energetisch kleiner Teil gebeugt. Je nach Orientierung der Kristallite einer polykristallinen Probe finden sich immer Wellenlängen bzw. Photonenenergien, welche die Bragg'sche Gleichung erfüllen. Die Energie ergibt sich nach

$$E_{hkl} = n \frac{h \cdot c}{2 \cdot d_{hkl} \sin \theta}$$

mit der Beugungsordnung  $n$ , der Planck'schen Konstante  $h$ , der Lichtgeschwindigkeit  $c$ , dem Netzebenenabstand  $d_{hkl}$  und dem Bragg'schen Winkel  $\theta$ .

Vereinfacht dargestellt besteht ein Experiment aus der Strahlung, die auf die Probe trifft und einem Detektor, der die gebeugte Strahlung winkelabhängig aufnimmt. Durch die Primärstrahlung können gleichzeitig zu den Beugungslinien Röntgenfluoreszenzen angeregt werden, die zusätzliche Informationen erhalten. Durch Variation des Bragg'schen Winkels  $\theta$  können die Braggreflexe bzw. ihre Lage im Energiespektrum verschoben werden, so dass diese im Idealfall nicht von den Fluoreszenzen überdeckt werden.

Die hohe Intensität der Synchrotronstrahlung ermöglicht eine gute Zeitauflösung (von wenigen Minuten pro Spektrum) im Vergleich zu mehreren Stunden bei Verwendung einer „herkömmlichen“ Röntgenquelle. Zusätzlich ist die Intensität der Synchrotronstrahlung ausreichend, um Wände der Reaktionsgefäße (z. B. Edelstahlautoklaven) zu durchdringen und ermöglicht damit in-situ-Untersuchungen von Reaktionen unter solvothermalen Bedingungen (vgl. Kap. 3.1, S. 27). Da es sich bei Solvothermalsynthesen um heterogene Reaktionen handelt, bei denen eine große Anzahl an Faktoren die Produktbildung beeinflusst, sind in-situ-Untersuchungen unverzichtbar. Mit den laborüblichen analytischen Methoden können solvothermale Reaktionen nur bedingt untersucht und eventuell auftretende Zwischenprodukte, Intermediate oder Precursoren nicht detektiert oder abgefangen werden. Besonders elegant ist, dass der Einfluss verschiedener Reaktionsparameter auf den Reaktionsverlauf und die Produktbildung gezielt untersucht werden kann [74]. Ein geringer Nachteil der verwendeten Messzelle ist jedoch, dass die Auflösung der Spektren relativ gering ist. Trotzdem erlauben die Daten eine recht detaillierte Beschreibung des Reaktionsablaufs und der Kristallisationskinetik.

### 2.1.3. Röntgenabsorptionsspektroskopie (XAS)

Die Röntgenabsorptionsspektroskopie ist der Oberbegriff für mehrere Messverfahren, zu denen auch die Röntgenabsorptionsfeinstrukturanalyse („EXAFS-Methode“, Extended X-Ray Absorption Fine Structure) sowie die kernnahe Röntgenstrukturanalyse (X-Ray Absorption Near Edge Structure XANES) zählen. Bei der EXAFS-Spektroskopie wird der Absorptionskoeffizient  $\mu$  eines Elements als Funktion der Photonenenergie  $E$  oberhalb der Absorptionskante gemessen. Das Prinzip beruht auf der Absorption von Röntgenstrahlen durch kernnahe Elektronen. Wird eine Probe mit Röntgenstrahlung durchstimmbarer Energie bestrahlt, so wird bei der so genannten Schwellenenergie  $E_0$  ein inneres Elektron aus der Atomhülle entfernt und gelangt in das Kontinuum, was zu einem sprunghaften Anstieg des Absorptionskoeffizienten führt. Diese Schwellenenergie ist von der chemischen Umgebung des Absorberatoms abhängig. Bei einem solchen Absorptionsexperiment wird ein Absorptionsspektrum wie beispielsweise in Abb. 2.3 dargestellt gemessen, in dem die Änderung des Absorptionskoeffizienten für ausgewählte Absorberatome energieabhängig erfasst wird. Aus der Interferenz der ausgehenden Photoelektronenwellen des Absorberatoms mit den rückgestreuten Photoelektronenwellen benachbarter Atome entsteht das Röntgenabsorptionsspektrum und macht sich als komplexe Feinstruktur (Modulationen) bemerkbar, in welcher die Art, die Anzahl und der Abstand der Nachbaratome verborgen sind [75]. Je nach Gangunterschied zwischen den Photoelektronenwellen treten konstruktive und destruktive Interferenzen auf, die im Röntgenabsorptionsspektrum als Maxima und Minima oberhalb der Absorptionskante auftreten (vgl. Abb. 2.3).

Die Grundlage für die Analyse der Röntgenabsorptionsspektren legten u. a. die Arbeiten von Stern, Sayers, Lytle und Pendry in den achtziger Jahren [76, 77, 78, 79, 80], welche weitere Entwicklungen nach sich zogen (z. B. von B.K. Teo [81]).

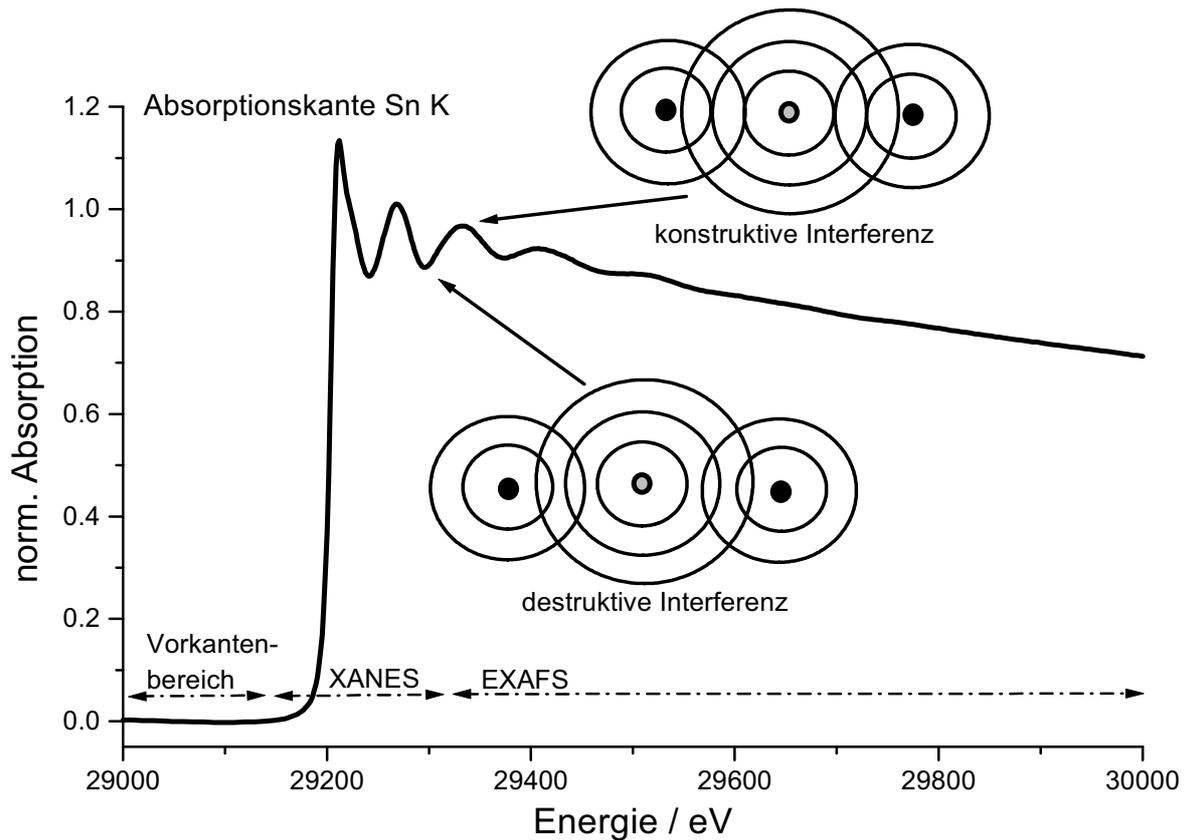


**Abb. 2.3:** Röntgenabsorptionsspektrum einer Thiostannatlösung, aufgenommen am Messplatz X1, Hasylab, Desy, an der Sn-K-Kante (29.2 keV) in Transmission. (Weitere Details im Text.)

Die Abb. 2.3 zeigt ein typisches Röntgenabsorptionsspektrum. Der Energiebereich wird entsprechend für das Atom um die Absorptionskante (hier: Sn-K-Kante) gewählt. EXAFS-Spektren werden in der Regel in einem Bereich von 40-1000 eV oberhalb der Absorptionskante gemessen [81]. Der Vorkantenbereich ( $E < E_0$ ) enthält Informationen über Bindungen und Oxidationsstufen des Absorberatoms, da Elektronenübergänge zwischen den inneren und höheren halb- oder unbesetzten Schalen wie z. B.  $1s \rightarrow 4p$  oder  $1p \rightarrow 3d$  auftreten können (Dipolübergänge). Die Lage der Kante erlaubt durch den Vergleich mit Referenzsubstanzen eine Abschätzung der Elektronendichte (= Ladung) des Absorberatoms.

Zwischen Vorkanten- und EXAFS-Bereich befindet sich die XANES-Region, in der Effekte wie Mehrfachstreuung, das Vielkörperproblem, Verzerrungen der Übergangszustandswellenfunktionen durch Coulomb-Felder oder Bandstrukturen die theoretische Beschreibung sowie das exakte Verständnis erschweren [81].

Für die Analyse der Röntgenabsorptionsspektren wird der Absorptionsquerschnitt des jeweiligen Atoms in die lokale Struktur mit Hilfe von Fourier-Transformationen überführt. Die resultierenden Peaks in der radialen Abstandsverteilung entsprechen in erster Näherung den unterschiedlichen Abständen des Absorberatoms zu benachbarten Atomen, müssen allerdings durch Simulationen an ein Strukturmodell angepasst werden. Diese Simulationen basieren auf der EXAFS-Gleichung, welche einen Zusammenhang zwischen den Strukturparametern und den Modulationsfrequenzen herstellt [81]:

$$\chi(k) = \sum_j N_j S_i(k) F_j(k) \exp(-2\sigma_j^2 k^2) \exp\left(-\frac{2r_j}{\lambda_j(k)}\right) \left(\frac{\sin(2kr_j + \varphi_{ij}(k))}{kr_j^2}\right).$$

Der Index der Schalen der benachbarten Atome um das Absorberatom wird mit  $j$  bezeichnet,  $N$  ist die Koordinationszahl,  $S(k)$  ein Dämpfungsfaktor,  $F(k)$  die Rückstreuamplitude bzw. Streukraft des rückstreuenden Atoms,  $r$  der mittlere Abstand,  $\sigma$  der Debye-Waller-Faktor,  $\lambda$  die mittlere freie Weglänge des Elektrons

(der Ausdruck  $\exp\left(-\frac{2r_j}{\lambda_j(k)}\right)$  entspricht der Dämpfung des Spektrums),  $\varphi$  die

Phasenverschiebung der Photoelektronenwelle und  $k$  der Wellenvektor nach  $k = \sqrt{(2m/\hbar^2)(E - E_0)}$  (mit  $m$  der Masse des Elektrons,  $\hbar$  dem reduzierten Planck'schen Wirkungsquantum und der Schwellenenergie  $E_0$ ).

Die Röntgenabsorptionsspektroskopie eignet sich besonders für Analysen der lokalen Struktur um das Absorberatom, die außerdem bei einer homogenen Probe nicht vom Aggregatzustand abhängig ist. Die Informationen über den Abstand und über die Anzahl und Art benachbarter Atome werden aus Amplitude und Phase erhalten. Die Lage der Absorptionskante ist von der Ladungsabschirmung der Rumpfelektronen des Absorberatoms abhängig, welche sowohl von der Oxidationsstufe des Absorberatoms als auch vom Kovalenzgrad der chemischen Bindungen zu seinen Nachbarn beeinflusst wird. Daher wird immer auf den elementaren Zustand des untersuchten Absorberatoms referenziert. Zwar sind die Röntgenabsorptionsspektren elementspezifisch, stellen aber nur einen Mittelwert über die Absorptionen aller Atome des gleichen Elements dar. Befindet sich ein Absorberatom in unterschiedlichen lokalen Umgebungen, so kann die lokale Struktur nur schwierig ohne bekanntes Strukturmodell aufgeklärt werden.

## 2.2. Impedanzanalyse

Mit dieser elektrochemischen Untersuchungsmethode können die elektrische Leitfähigkeit, der Widerstand, die Kapazität, die Beweglichkeiten von Ladungsträgern sowie Aktivierungsenergien gemessen werden [82, 83, 84].

Bei der Impedanzanalyse wird der Wechselstromwiderstand als Funktion der Frequenz gemessen. Die Impedanz  $Z$  ist der komplexe Quotient aus der Wechselspannung  $U$  und der Wechselstromstärke  $I$ . Der Betrag der Impedanz wird Scheinwiderstand genannt. Der komplexe Wert setzt sich aus einem Realteil  $Z'$  und einem Imaginärteil  $Z''$  zusammen ( $Z = Z' - iZ''$ ). Der Verlauf der Impedanz wird in den so genannten Nyquist-Plots dargestellt, in denen der Imaginärteil  $-Z''$  über dem Realteil  $Z'$  des komplexen Widerstandes aufgetragen wird. Die Ersatzschaltbilder aus unterschiedlichen Kombinationen von Ohm'schen Widerständen  $R$  und Kondensatoren  $C$  beschreiben die Messanordnungen ausreichend gut, so dass das Impedanzverhalten erfasst und beschrieben werden kann.

Die Impedanzanalysen wurden mit Hilfe der Kieler Zelle [85] durchgeführt, in welche die untersuchten Verbindungen in Form von Presslingen eingebracht wurden. Zur elektrischen Kontaktierung wurde Gold- bzw. Platinfolie verwendet und die Messzelle an eine Impedanzbrücke (HP 4192 Impedance-Analyzer) angeschlossen, die einen Frequenzbereich von 5 Hz – 13 MHz überstreicht. Die Integration der Anordnung in die Kieler Zelle ermöglicht aufgrund des gasdichten Duranglaszylinders das Einstellen einer definierten Schutzgasatmosphäre, so dass z. B. Oxidation vermieden werden kann. Ein externer Ofen sowie ein in die Zelle integriertes Cr/CrNi-Thermoelement erlauben die Durchführung der Impedanzmessungen bei verschiedenen Temperaturen z. B. für die Ermittlung der Aktivierungsenergie.

## 3. Experimentelles

### 3.1. Solvothermale Synthese

Die solvothermale Synthese ist die Präparationsmethode der Wahl für die Darstellung poröser Materialien, mit welcher der überwiegende Teil neuer Verbindungen mit offenen Netzwerkstrukturen synthetisiert wurde. Seit Rabenau 1985 die wichtige Rolle der Hydrothermalsynthese in der präparativen Chemie beschrieb [86], wurde die Entwicklung hydro-, aber auch solvothermalen Methoden vorangetrieben. Die Eigenschaften und Vorteile wurden und werden von verschiedenen Arbeitsgruppen genutzt, auf unterschiedliche Verbindungsklassen wie z. B. die Chalkogenidometallate übertragen und diskutiert [1, 6].

Die Solvothermalsynthese wird seit Jahren in unserer Arbeitsgruppe eingesetzt und kam daher auch im Rahmen dieser Arbeit für die Präparation neuer Thiostannate zum Einsatz.

Zur Durchführung solvothermalen Synthesen wurden aus Teflon gefertigte Becher mit einem inneren Volumen von ca. 30 mL und einem schließenden Deckel als Reaktionsgefäße benutzt. Teflon wurde ausgewählt, da es gegenüber Säuren und Basen weitgehend inert ist und eine entsprechende Stabilität im erforderlichen Temperatur- und Druckbereich aufweist. Die Teflonbecher werden als so genannte schwimmende Einsätze in einen druckfesten Edelstahlautoklaven eingesetzt (Abb. 3.1).

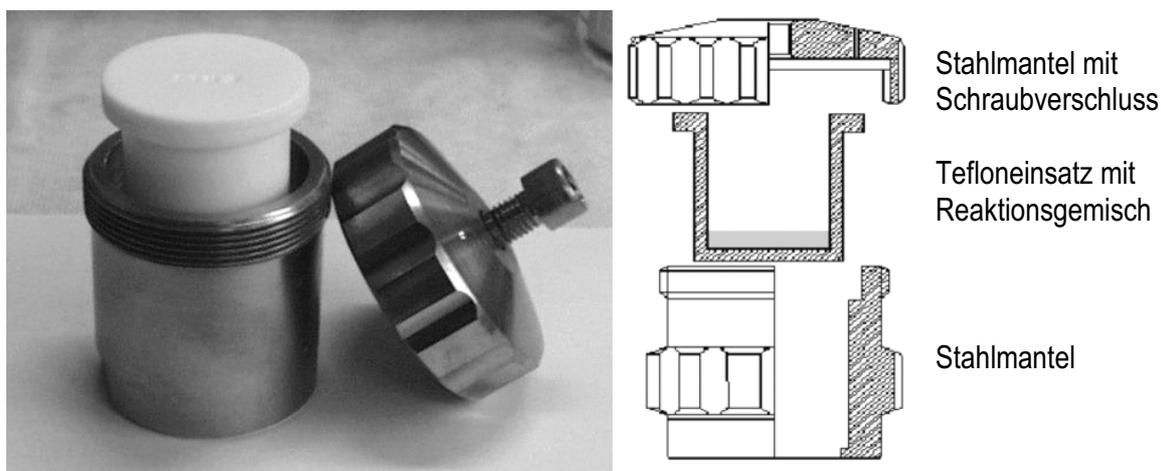


Abb. 3.1: Edelstahlautoklav mit Tefloneinsatz (links) sowie eine schematische Darstellung (rechts).

Im allgemeinen wurden für die Synthesen der Thiostannate Reaktionsgemische aus elementarem Zinn (oder aber auch eine andere Zinnquelle), einer Übergangsmetallquelle (oft die entsprechenden Metalle) und Schwefel in einer (wässrigen) Aminlösung verwendet. Die Reaktionsgemische wurden bei Temperaturen zwischen 110 und 190 °C in der Regel mehrere Tage getempert, anschließend aufgearbeitet, mit Wasser und Ethanol gewaschen und im Vakuum getrocknet. Die Reaktionsparameter wie Temperatur, Reaktionsdauer, Edukteinwaagen und -Verhältnisse, Konzentrationen der Amine und Füllhöhen wurden variiert, um die optimalen Synthesebedingungen für eine bestimmte Verbindung festzustellen.

Neben der statischen Reaktionsführung, bei der die Reaktionsgemische bei der entsprechenden Temperatur für die Reaktionszeit in einen Ofen gestellt werden, ist auch die dynamische Durchführung möglich. Bei dieser wird dem Reaktionsgemisch ein magnetischer Rührstab hinzugefügt und der Autoklav mittels eines speziellen Aluminium-Blockes, unter dem sich ein Magnetrührer mit Heizplatte befindet, erhitzt (Abb. 3.3, Kap. 3.2), so dass während der Reaktion das Gemisch kontinuierlich gerührt und eine homogene Verteilung der Reaktionsspezies erreicht wird. Im Vergleich zur statischen Reaktionsführung wird die Reaktionszeit stark verringert und die Reaktionen laufen oft vollständig ab, so dass phasenreine Produkte erhalten werden können. Liegt das mikrokristalline Produkt jedoch nicht phasenrein vor, so besteht keine Möglichkeit der Trennung, was oft einen Nachteil darstellt.

### 3.2. In-situ-Syntheseapparatur

Für die in-situ-Untersuchungen am Hasylab, Desy, Hamburg sind die in Abb. 3.1 vorgestellten Edelstahlautoklaven aufgrund der zu dicken Wandstärke ungeeignet. Daher war die Konstruktion einer speziellen Syntheseapparatur erforderlich. An diese waren einige Anforderungen zu stellen: sie muss die Sicherheitsstandards erfüllen und zudem für die Synchrotronstrahlung ohne große Streu- oder Absorptionsverluste transparent sein.

Eine schematische Darstellung dieser in-situ-Apparatur mit Strahlengang befindet sich in Abb. 3.2, in welcher ebenfalls die Skizze eines Edelstahlautoklaven für die statische Reaktionsführung zum Vergleich abgebildet wird.

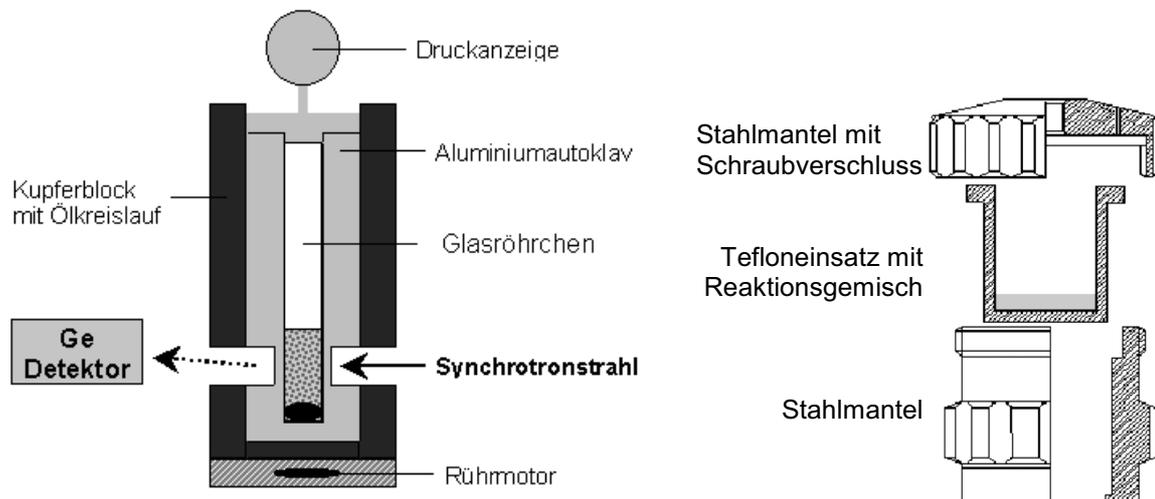


**Abb. 3.2:** Schematische Darstellung der in-situ-Apparatur mit skizziertem Strahlenverlauf (links) sowie der Aufbau für die statische Reaktionsführung gegenübergestellt (rechts).

Die im Labor verwendete Apparatur für dynamische Reaktionsführungen ist in Abb. 3.3 (links) dargestellt. Im Vergleich dazu befindet sich auf dem mittleren Foto (Abb. 3.3) die für den Messplatz F3 (Hasylab, Desy) konstruierte in-situ-Apparatur; ein typischer Autoklav mit Druckanzeige außerhalb der Apparatur ist auf dem rechten Foto abgebildet.

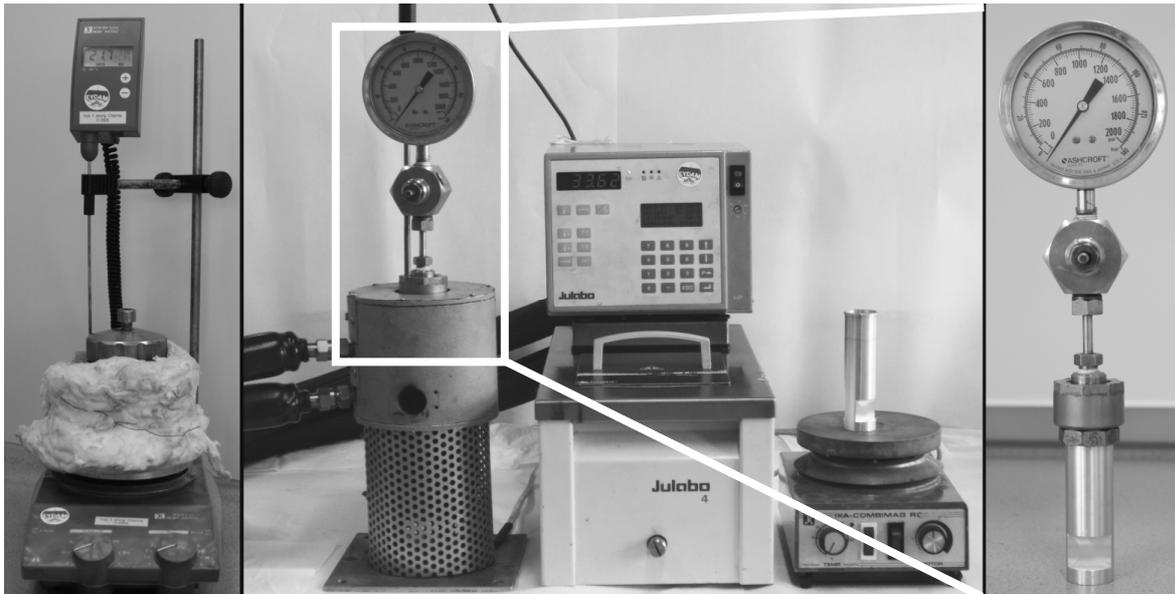


**Abb. 3.3:** Links: Apparatur zur dynamischen Reaktionsführung (Labor), Mitte: In-situ-Apparatur für den Messplatz F3 für Untersuchungen mit energiedispersiver Röntgenbeugung, rechts: Aluminiumautoklav mit Druckanzeige (vergrößerte Darstellung des markierten Bereichs ohne Heizblock).

Die wesentlichen Bestandteile stellen der Aluminiumautoklav und die Ölheizung dar. Als Material für den Autoklaven wurde Aluminium aufgrund der guten Wärmeleitfähigkeit sowie der geringen Absorption der Synchrotronstrahlung sowie der gebeugten Strahlung ausgewählt, so dass eine ausreichende Qualität der Spektren gewährleistet ist. Der Druck im Inneren des Autoklaven wird mit einem Druckmesser kontrolliert. Für die Versuche steht ein Temperaturbereich von 100 bis 200 °C zur Verfügung, der mit Hilfe einer selbst regelnden Ölheizung eingestellt wird. Zur Verbesserung des Messsignals werden bei den Experimenten kleinere Autoklaven verwendet, die einen geringeren Streuuntergrund verursachen. Die verwendeten Teflonbecher sind nur ca. 10 cm hoch mit einem Volumen von ca. 7 mL. Anstelle der Tefloneinsätze können auch Kulturröhrchen aus Glas gleicher Dimensionen eingesetzt werden. Um eine bessere Reproduzierbarkeit zu erreichen, werden diese Kulturröhrchen entweder nur einmal verwendet oder aber Vergleichsmessungen mit neuen und gebrauchten Gläsern durchgeführt, damit Einflüsse z. B. durch Oberflächenveränderung hervorgerufen durch Reinigungsprozesse oder Kristallisationskeime ausgeschlossen werden können. Für die Messungen erfordern die kleineren Volumina meistens eine Anpassung der Reaktionsparameter der untersuchten Reaktionen.

### 3.3. Messplatz F3 am Hasylab, Desy, Hamburg

Der für Untersuchungen mit energiedispersiver Röntgenbeugung optimierte Messplatz F3 wird mit weißer Synchrotronstrahlung wie in Abb. 3.4 dargestellt versorgt.

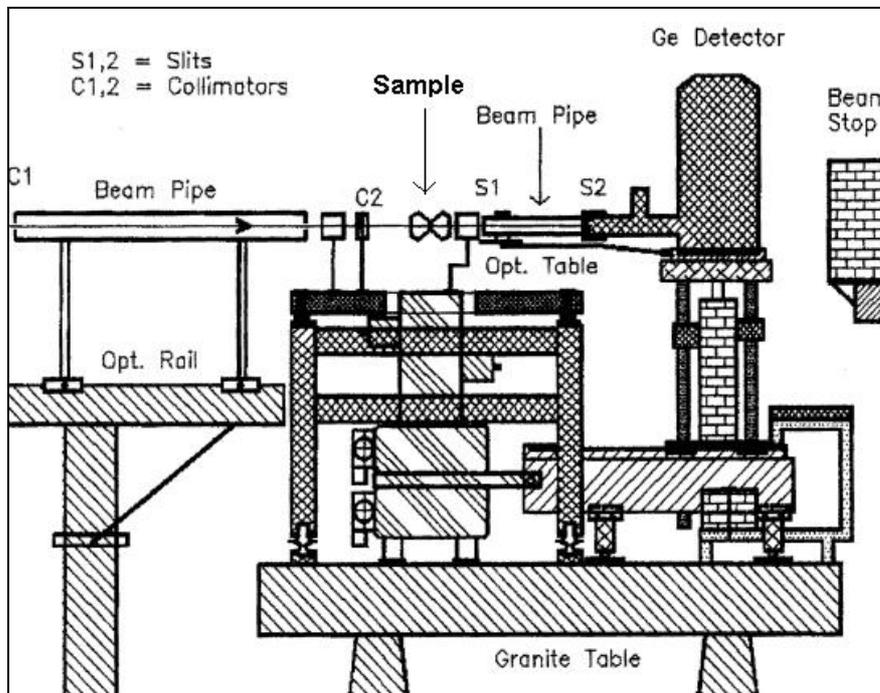


Abb. 3.4: Schematischer Aufbau des Messplatzes F3 am Hasylab, Desy, Hamburg [87].

Mit Hilfe eines Kollimators wird die Synchrotronstrahlung auf die gewünschte Intensität und Geometrie (Höhe und Breite) eingestellt, die maximalen Abmessungen betragen  $6 \cdot 6 \text{ mm}^2$ . Die zu untersuchende Probe bzw. die in-situ-Apparatur ist auf einem motorisierten, in x-, y- und z-Richtung verschiebbaren Tisch fixiert. Nach Durchstrahlung der Probe wird die gebeugte Strahlung energiedispersiv von einem beweglichen Germaniumdetektor (Auflösung der gestreuten Strahlung  $\sim 1 \%$ ) registriert. Die rechnergestützte Steuerung aller Motoren und Spaltsysteme erfolgt über die Software SPECTRA [88] (Standard des Hasylabs). Die Position des Detektors wird bei einem bestimmten Winkel derart fixiert, dass alle interessierenden Braggreflexe der Verbindung beobachtet werden können. Der Bereich der Netzebenenabstände  $d$  kann nach  $E = \frac{6.199}{d \cdot \sin\theta}$  ermittelt werden. Weitere Details sind in den Referenzen [69, 70] sowie in den Dissertationen von M. Schaefer [89], L. Engelke [90] und R. Kiebach [91] zu finden.

### 3.4. Messplatz X1 am Hasylab, Desy, Hamburg

Der Messplatz X1 ist für Untersuchungen mit Röntgenabsorptionsspektroskopie optimiert und der Aufbau schematisch in Abb. 3.5 dargestellt. Im Gegensatz zu dem Messplatz F3, der mit weißer Synchrotronstrahlung beliefert wird, kann am Messplatz X1 die Strahlung mit Hilfe von Monochromatoren auf die gewünschten Wellenlängen variabel eingestellt werden.

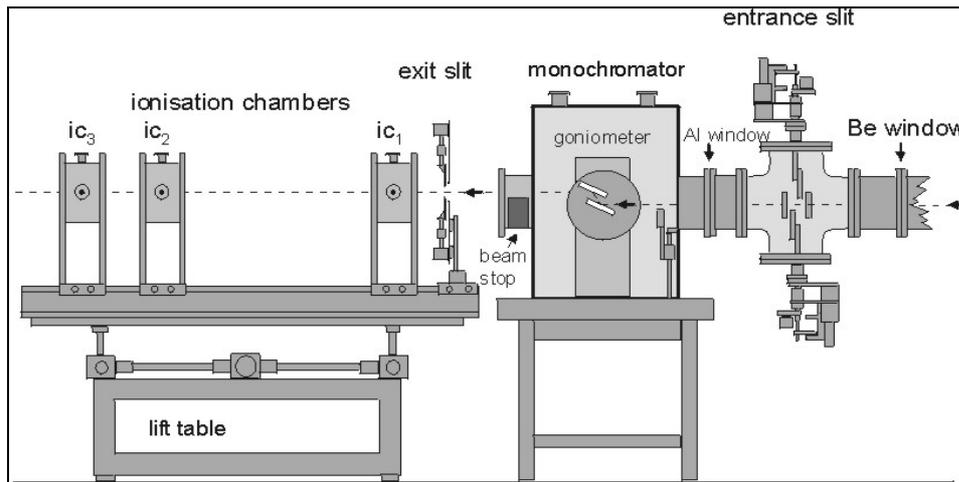


Abb. 3.5: Schematischer Aufbau des Messplatzes X1 am Hasylab, Desy, Hamburg [92].

Der Messplatz bietet einen Energiebereich von 6 - 80 keV mit hoher Auflösung. Nachdem die Synchrotronstrahlung durch einen verstellbaren Eintrittsspalt in die Monochromatorkammer eingetreten ist, wird durch einen auf einem Goniometer fixierten Si-Doppelkristall die gewünschte Wellenlänge aus der weißen Strahlung extrahiert. Die Strahlmessungen und damit die Intensität können beim Austritt aus der Monochromatorkammer durch ein zweites Spaltsystem eingestellt werden. Die rechnergestützte Steuerung aller Motoren, Monochromator- und Spaltsysteme erfolgt auch hier über die Software SPECTRA [88]. Die Intensitäten der Strahlung werden durch die Gas-Ionisationskammern ( $ic_1$ ,  $ic_2$ ,  $ic_3$ ) gemessen, die je nach eingestelltem Energiebereich mit verschiedenen Inertgasen unterschiedlicher Drücke befüllt sein müssen. Durch den experimentellen Aufbau – die Probe befindet sich zwischen erster und zweiter und die Referenz zwischen zweiter und dritter Ionisationskammer – können die Intensitäten von Probe und Referenz gleichzeitig gemessen und miteinander verglichen werden. Die in-situ-EXAFS-Untersuchungen wurden an der Sb-K-Kante bei 30.49 keV in Transmissionsgeometrie durchgeführt.

### 3.5. Verwendete Chemikalien

Tab. 3.1: Verwendete Elemente und Verbindungen

Chemikalien	Summenformel	Reinheitsgrad / %	Hersteller
Zinn	Sn	99 99.5	Merck Aldrich
Kupfer	Cu	99.5	Alfa Aesar
Silber	Ag	99.99	Fluka
Eisen	Fe	99	Alfa Aesar
Mangan	Mn	99.5	Alfa Aesar
Schwefel	S	sublimiert	Aldrich
Cobalt(II)chloridhexahydrat	CoCl <sub>2</sub> · 6 H <sub>2</sub> O	z. A.	Merck
Nickel(II)chloridhexahydrat	NiCl <sub>2</sub> · 6 H <sub>2</sub> O	z. A.	Merck
Zinn(II)chloriddihydrat	SnCl <sub>2</sub> · 2 H <sub>2</sub> O	98	Alfa Aesar

Tab. 3.2: Verwendete Amine

Chemikalien	Summenformel	Reinheitsgrad / %	Hersteller
Diethylentriamin	C <sub>4</sub> H <sub>13</sub> N <sub>3</sub>	≥ 97 ≥ 98.5	Fluka Acros Organics
1,4-Diaminobutan	C <sub>4</sub> H <sub>12</sub> N <sub>2</sub>	≥ 98	Fluka
1,5-Diazabicyclo[4.3.0] non-5-en	C <sub>7</sub> H <sub>12</sub> N <sub>2</sub>	≥ 98	Fluka
1,8-Diazabicyclo[5.4.0] undec-7-en	C <sub>9</sub> H <sub>16</sub> N <sub>2</sub>	≥ 98	Fluka
1,2-Diaminocyclohexan	C <sub>6</sub> H <sub>14</sub> N <sub>2</sub>	≥ 99 ( <i>cis / trans</i> )	Aldrich
Triethylentetramin	C <sub>6</sub> H <sub>18</sub> N <sub>4</sub>	~ 60 (techn.)	ABCR
Tetraethylenpentamin	C <sub>8</sub> H <sub>23</sub> N <sub>5</sub>	≥ 95 techn.	Merck Acros Organics

### 3.6. Geräte

Tab. 3.3: Im Rahmen der vorliegenden Arbeit eingesetzte analytische Geräte mit einigen Kenndaten.

Methoden	Gerät	Kenndaten
ESEM / EDX	Philips ESEM XL 30	Rasterelektronenmikroskop mit EDX-Aufsatz der Fa. EDAX
Pulverdiffraktometrie	STOE Stadi-p	Transmissionsgeometrie, Cu-K $_{\alpha}$ (1.54051 Å), Germanium-Monochromator, IP-PSD bzw. lin. PSD
Einkristallstruktur-analyse	STOE IPDS-1  Philips PW1100	Mo-K $_{\alpha}$ (0.71073 Å), Graphit-Monochromator; Mo-K $_{\alpha}$ (0.71073 Å), Graphit-Monochromator
DTA – TG	Netzsch STA 409 CD	Pt-Pt/Rh-Thermoelement, Gasstrom 75 mL/min, Heizrate 4 K/min
TG – MS	Balzer QMG 422	Quadrupol Massenspektrometer
MIR	ATI Mattson Genesis	In KBr-Matrix, 450-3000 cm $^{-1}$ , Auflösung 1 cm $^{-1}$
FIR	Bruker IFS 66	In Polyethylen-Matrix, 80-500 cm $^{-1}$ , 1 cm $^{-1}$ Auflösung
Raman	Bruker IFS 66	100-3500 cm $^{-1}$ , 2 cm $^{-1}$ Auflösung
Elementaranalyse	Eurovektor EuroEA Elemental Analyzer	CHNS-Analyse, Trägergas He, Verbrennung in O $_2$ bei 1010 °C, Detektion über Wärmeleitzelle
Diffuse Reflektion	Cary5Varian TechtronPty. Darmstadt	250-2000 nm, BaSO $_4$ als Referenzmaterial

### **3.7. Verwendete Programme**

Für die vorliegende Arbeit wurden die folgenden Programme zur Auswertung unterschiedlicher Messdaten verwendet:

1. *STOE WinXPow* [93]: Programmpaket zur Datensammlung von Pulverdiffraktogrammen, zur Auswertung sowie zur Berechnung von Pulverdiffraktogrammen aus Einkristallstrukturdaten.
2. *SHELXS 97* [94]: Programm zur Strukturlösung aus Messdaten der Einkristallstrukturanalyse.
3. *SHELXL 97* [95]: Programm zur Strukturverfeinerung aus Einkristallstrukturdaten.
4. *STOE X-RED*, Version 1.11 [96] sowie *X-SHAPE*, Version 1.03 [97]: Programme zur Durchführung einer numerischen Absorptionskorrektur.
5. *PLATON* [98]: Programmpaket zur Überprüfung der Berechnungen der Kristallstrukturen.
6. *Diamond*, Versionen 2.1e und 3.1f [99]: Programm zur Erstellung von Strukturbildern der Verbindungen.
7. *Netzsch TA4* [100]: Programmpaket zur Datensammlung und Auswertung thermischer Untersuchungen (DTA-TG).
8. *QUADSTAR 422* [101]: Programmpaket zur Datensammlung und Auswertung thermischer Untersuchungen (TG-MS).
9. *EDXPowd*, Version 3.155 [102]: Programm zur Ermittlung der Reflexintensitäten bzw. Reflexintegrale der Spektren der in-situ-Untersuchungen mit EDXRD.
10. *calf3* [s. Kap. 6.3, S. 239]: Programm zur Ermittlung der Reflexintegrale der Spektren der in-situ-Untersuchungen mit EDXRD.
11. *WinXAS*, Version 3.1 [103]: Programm zur Auswertung der XAS-Spektren.
12. *FEFF* [104]: Programm zur Erstellung theoretischer XAS-Spektren.
13. *Iffeffit*, Version 1.2.2 [105]: Programmpaket zur Auswertung und Simulation von XAS-Daten.



## 4. Ergebnisse (kumulativer Hauptteil)

### 4.1. Ergebnisse und Publikationen der Übergangsmetallhaltigen Thiostannate

#### 4.1.1. Die Verbindungen (DBUH)CuSnS<sub>3</sub> und (1,4-dabH<sub>2</sub>)Cu<sub>2</sub>SnS<sub>4</sub>

Zusammenfassung der Veröffentlichung „Two new copper thiostannates synthesized under solvothermal conditions: Crystal structures, spectroscopic and thermal properties of (DBUH)CuSnS<sub>3</sub> and (1,4-dabH<sub>2</sub>)Cu<sub>2</sub>SnS<sub>4</sub>“.

In der Veröffentlichung werden die Synthesen, die Strukturen sowie die spektroskopischen und thermischen Eigenschaften der neuen Verbindungen (DBUH)CuSnS<sub>3</sub> (I) (DBU = 1,8-Diazabicyclo[5.4.0]undec-7-en, C<sub>9</sub>N<sub>2</sub>H<sub>17</sub>) und (1,4-dabH<sub>2</sub>)Cu<sub>2</sub>SnS<sub>4</sub> (II) (1,4-dab = 1,4-Diaminobutan, C<sub>4</sub>N<sub>2</sub>H<sub>14</sub>) präsentiert. Die Verbindungen wurden unter solvothermalen Bedingungen aus den Edukten Sn, Cu und S im Verhältnis 1:1:3.3 (I) bzw. 1:1:3 (II) mmol in 5 mL DBU (I) bzw. 3 mL 1,4-dab (II) bei 170 °C (I) bzw. 150 °C (II) in fünf Tagen in Edelstahlautoklaven (Kap. 3.1, S. 27) synthetisiert.

Die Verbindung (DBUH)CuSnS<sub>3</sub> (I) kristallisiert in der monoklinen Raumgruppe P2<sub>1</sub>/n mit vier Formeleinheiten in der Elementarzelle. In der Struktur sind zwei SnS<sub>4</sub>-Tetraeder über gemeinsame Kanten zu einer Sn<sub>2</sub>S<sub>6</sub>-Einheit verknüpft. Ungewöhnliche, fast schon lineare CuS<sub>2</sub>-Hanteln verbrücken die Sn<sub>2</sub>S<sub>6</sub>-Gruppen, wodurch eine eindimensionale [CuSnS<sub>3</sub>]-Kette gebildet wird (Abb. 4.1, links). Jede dieser Anionenketten ist von sechs einfach protonierten Aminmolekülen umgeben (Abb. 4.1, rechts).

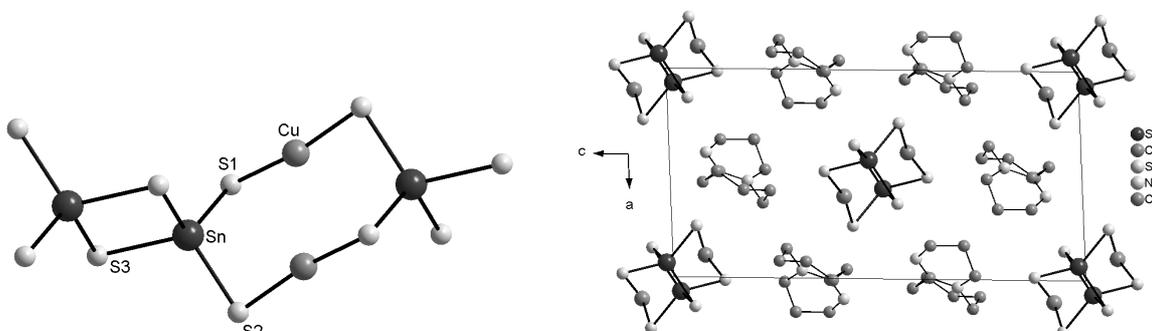
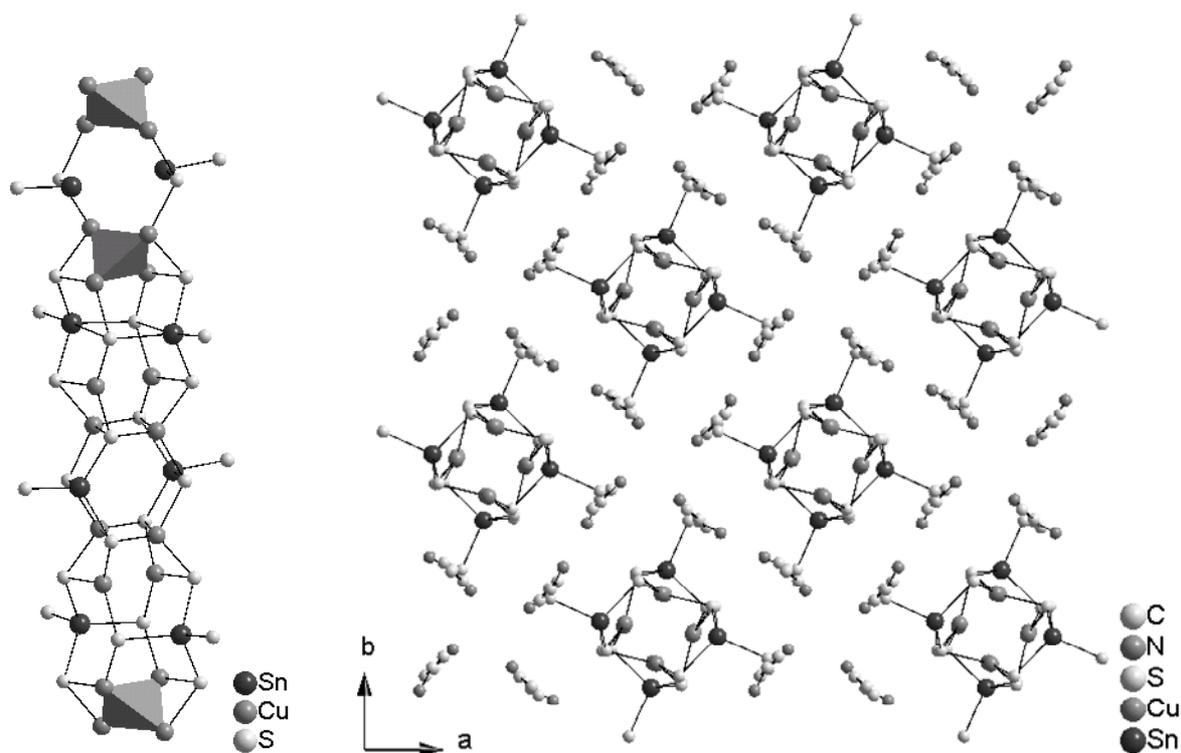


Abb. 4.1: Ausschnitt der Anionenkette (links) mit SnS<sub>4</sub>-Tetraedern und CuS<sub>2</sub>-Hanteln, rechts: Anordnung der Anionenketten und Kationen (Blick entlang [010], die Wasserstoffatome wurden zur besseren Übersicht entfernt).

Die zweite Verbindung  $(1,4\text{-dabH}_2)\text{Cu}_2\text{SnS}_4$  (II) kristallisiert in der tetragonalen Raumgruppe  $P4_2/n$  mit acht Formeleinheiten in der Elementarzelle.  $\text{SnS}_4$ -Tetraeder bilden mit  $\text{CuS}_3$ -Dreiecken eindimensionale Ketten der Zusammensetzung  $[\text{Cu}_2\text{SnS}_4]^{2-}$ . In diesen Ketten werden verzerrte  $\text{Cu}_4\text{S}_4$ - und  $\text{Cu}_2\text{Sn}_2\text{S}_4$ -Würfel beobachtet, die über gemeinsame Kanten verknüpft sind. Eine alternative Beschreibung beginnt mit zwei  $\text{Cu}_4$ -Tetraedern, welche zusammen mit zwei S-Atomen  $\text{Cu}_8\text{S}_2$ -Einheiten bilden, die über zwei  $\text{SnS}_4$ -Tetraeder zu der Anionenkette verknüpft sind (Abb. 4.2, links). Auch in dieser Verbindung umgeben die ladungskompensierenden Kationen die anionischen Ketten (Abb. 4.2, rechts).



**Abb. 4.2:** Links: Verzerrte Würfel in den Anionenketten von II mit  $\text{Cu}_4$ -Tetraedern. Packungsbild der Struktur (rechts; Blick entlang [001], die Wasserstoffatome sind zur besseren Übersicht weggelassen).

Die optischen Bandlücken wurden zu 3.06 eV (I) bzw. 2.15 eV (II) bestimmt, so dass beide Verbindungen als optische Halbleiter bezeichnet werden können. Die Raman-Spektren weisen Sn-S-Schwingungen in dem für Thiostannate typischen Bereich auf, wobei die Unterschiede der beiden Strukturen sich in den Lagen bzw. Verschiebungen der einzelnen Resonanzen widerspiegeln. Bei ca.  $380\text{ cm}^{-1}$  werden symmetrische  $\text{Sn-S}_{\text{terminal}}$ -Streckschwingungen der  $[\text{Sn}_2\text{S}_6]$ -Einheiten beobachtet. Aufgrund der kürzeren Sn-S-Bindung ist das Signal in I zu höheren Wellenzahlen ( $385\text{ cm}^{-1}$ ) verschoben. Zwischen  $350$  und  $310\text{ cm}^{-1}$  treten die  $\text{Sn-S}_{\text{bridging}}$ -Moden auf. Eine Schwingung des  $\text{Sn}_2\text{S}_2$ -Rings wird bei  $280\text{ cm}^{-1}$

gefunden. Da keine  $[\text{Sn}_2\text{S}_6]$ -Einheit in **II** vorhanden ist, wird auch kein Signal bei etwa  $380\text{ cm}^{-1}$  beobachtet. Die Schwingung bei  $334\text{ cm}^{-1}$  kann einer  $\text{Sn-S}_{\text{bridging}}$ -Mode zugeschrieben werden. In den Spektren beider Thiostannate treten Signale unterhalb von  $200\text{ cm}^{-1}$  auf, die durch das so genannte  $\text{SnS}_2$  „wagging and twisting“ hervorgerufen werden könnten. Eine detaillierte Zuordnung in diesem Bereich kann aufgrund möglicher Gerüstschwingungen nicht getroffen werden.

Die Verbindung  $(\text{DBUH})\text{CuSnS}_3$  (**I**) wird ab  $T_{\text{Onset}} = 246\text{ °C}$  in drei Stufen zersetzt. Der Massenabbau von insgesamt 43.1 % wird von endothermen Ereignissen in der DTA-Kurve begleitet ( $T_{\text{Peak 1}} = 264\text{ °C}$ ,  $T_{\text{Peak 2}} = 319\text{ °C}$ ,  $T_{\text{Peak 3}} = 377\text{ °C}$ ). Das Abbauprodukt ist weitgehend frei von organischen Komponenten und im Pulverdiffraktogramm können die Reflexe der Verbindungen  $\text{Cu}_2\text{SnS}_3$  und  $\text{SnS}$  identifiziert werden. Die Verbindung  $(1,4\text{-dabH}_2)\text{Cu}_2\text{SnS}_4$  (**II**) ist bis  $T_{\text{Onset}} = 227\text{ °C}$  ( $T_{\text{Peak}} = 254\text{ °C}$ ) stabil. Die Zersetzung erfolgt in einem Schritt mit einem Gesamtmassenverlust von 24.9 %, der von einem endothermen Signal in der DTA-Kurve begleitet ist. Im Abbauprodukt können die Verbindungen  $\text{Cu}_2\text{SnS}_3$ ,  $\text{Cu}_4\text{SnS}_4$  und  $\text{SnS}$  identifiziert werden.

Available online at [www.sciencedirect.com](http://www.sciencedirect.com)

Solid State Sciences 9 (2007) 100–107

[www.elsevier.com/locate/sss](http://www.elsevier.com/locate/sss)

## Two new copper thioannates synthesised under solvothermal conditions: Crystal structures, spectroscopic and thermal properties of (DBUH)CuSnS<sub>3</sub> and (1,4-dabH<sub>2</sub>)Cu<sub>2</sub>SnS<sub>4</sub>

Nicole Pienack, Christian Näther, Wolfgang Bensch\*

*Institut für Anorganische Chemie, Christian-Albrechts-Universität zu Kiel, Olshausenstr. 40-60, 24098 Kiel, Germany*

Received 29 March 2006; received in revised form 3 November 2006; accepted 10 November 2006

Available online 19 January 2007

### Abstract

The new compounds (DBUH)CuSnS<sub>3</sub> (**1**) (DBU = 1,8-diazabicyclo[5.4.0]undec-7-ene) and (1,4-dabH<sub>2</sub>)Cu<sub>2</sub>SnS<sub>4</sub> (**2**) (1,4-dab = 1,4-diaminobutane) were prepared under solvothermal conditions. In compound **1** two SnS<sub>4</sub> tetrahedra share common edges yielding an Sn<sub>2</sub>S<sub>6</sub> moiety. Unusual nearly linear CuS<sub>2</sub> dumbbells interconnect the Sn<sub>2</sub>S<sub>6</sub> groups forming an one-dimensional [CuSnS<sub>3</sub>]<sup>−</sup> chain. Every anionic chain is surrounded by mono-protonated organic cations. In compound **2** SnS<sub>4</sub> tetrahedra are joined by CuS<sub>3</sub> triangles to form an one-dimensional anionic [Cu<sub>2</sub>SnS<sub>4</sub>]<sup>2−</sup> chain. Central motifs of the chain are distorted Cu<sub>4</sub>S<sub>4</sub> and Cu<sub>2</sub>Sn<sub>2</sub>S<sub>4</sub> cubes sharing common faces. Four edges of the former cube are capped by two Sn and two S atoms whereas the latter cube is capped by two Cu and two S atoms. An alternative description is based on the interconnection of two Cu<sub>4</sub> tetrahedra by two S atoms to form a Cu<sub>8</sub>S<sub>2</sub> unit. This unit is then joined in an alternating way by two SnS<sub>4</sub> tetrahedra yielding the anionic chains. Both compounds were characterised by UV/Vis and Raman spectroscopies as well as thermoanalysis.

© 2006 Elsevier Masson SAS. All rights reserved.

*Keywords:* Solvothermal synthesis; Crystal structure; Spectroscopic properties; Thermal properties; Copper (I) thioannates

### 1. Introduction

Among the class of main group thiometalates, the thioannates are an interesting group of compounds which in part behave like zeolites [1–4]. Some of these materials have structures which are characterised by pore sizes up to 13 Å in diameter, and these thioannates are candidates for applications in catalysis and chemical sensing [5–9]. Several materials with interesting structural features and ‘unusual’ properties were prepared under solvothermal conditions [10–14]. Until now two different structure types are distinguished [6,7,15–19]. These are the so-called R-SnS-1 and R-SnS-3 type (R is an organic component) structures with two-dimensional anionic layers of composition [Sn<sub>3</sub>S<sub>7</sub>]<sup>2−</sup> and [Sn<sub>4</sub>S<sub>9</sub>]<sup>4−</sup>, respectively.

In R-SnS-1 compounds SnS<sub>4</sub> tetrahedra form the primary building units (PBU) which are condensed to form Sn<sub>3</sub>S<sub>4</sub> semi-cubes as secondary building units (SBU). The Sn<sub>3</sub>S<sub>4</sub> semi-cubes are joined via two S<sup>2−</sup> anions forming anionic layers with pores consisting of 24 atoms. The size of the pores measures about 10 Å in diameter. The organic components like tetramethylammonium (TMA) [7] or tetrapropylammonium (TPA) [20] act as charge compensating cations, and are located between the anionic layers above and below the pores. The Sn<sub>3</sub>S<sub>4</sub> semi-cubes are joined by SnS<sub>4</sub> tetrahedra to form [Sn<sub>4</sub>S<sub>9</sub>]<sup>4−</sup> anionic layers in the R-SnS-3 compounds. Elliptical pores with a size of about 13–15 Å are the main structural feature [16]. Other thioannates containing alkali metals instead of organic templates were also reported [21–23].

It can be expected that the physical and chemical properties of such compounds can be enhanced if transition metal atoms are integrated into the thioannate networks [24]. Recently, we presented four new thioannates containing Ni and Co as

\* Corresponding author. Tel.: +49 431 880 2419; fax: +49 431 880 1520.  
E-mail address: [wbensch@ac.uni-kiel.de](mailto:wbensch@ac.uni-kiel.de) (W. Bensch).

transition metals [25]. In general only a few thioannates containing transition metals were reported until now [24,26–28] and copper containing thioannates are quite rare. In our ongoing work in the field of the solvothermal syntheses of main group thiometalates with integrated transition metal cations we started to explore the Cu–Sn–S amine system. As a first result we present the two new thioannates (DBUII)CuSnS<sub>3</sub> (**1**) (DBU – 1,8-diazabicyclo[5.4.0]undec-7-ene) and (1,4-dabH<sub>2</sub>)Cu<sub>2</sub>SnS<sub>4</sub> (**2**) (1,4-dab = 1,4-diaminobutane).

## 2. Experimental details

### 2.1. Synthesis

**General:** all reactions were performed under solvothermal conditions in teflon-lined steel autoclaves with an inner volume of 30 mL. After the reaction the crystalline products were filtered off, washed with water and ethanol and dried in vacuum.

**Synthesis of (DBUII)CuSnS<sub>3</sub> (1):** 118.7 mg (1 mmol) Sn (99%, Merck), 63.9 mg (1.005 mmol) Cu (99%, Alfa Aesar), 105.6 mg (3.294 mmol) S and 5 mL of 1,8-diazabicyclo[5.4.0]undec-7-ene (98%, Fluka) were reacted for 120 h at 170 °C, followed by cooling to 25 °C for 30 h. Light yellow needles of compound **1** are obtained in 20% yield based on Sn. The composition was confirmed by EDX (Sn/Cu/S ratio: 1:1:3) and by elemental analysis. (Results in %: found: C 25.02, H 3.96, N 6.36, S 22.49; calculated: C 25.04, H 3.97, N 6.49, S 22.28.)

**Synthesis of (1,4-dabH<sub>2</sub>)Cu<sub>2</sub>SnS<sub>4</sub> (2):** 118.8 mg (1 mmol) Sn (99%, Merck), 64.7 mg (1.018 mmol) Cu (99%, Alfa Aesar), 96.8 mg (3.025 mmol) S and 3 mL of 1,4-diaminobutane (98%, Fluka) were mixed and reacted for 120 h at 150 °C. Yellow needles of compound **2** were obtained in 30% yield based on Sn. The composition was confirmed by EDX (Sn/Cu/S ratio: 2:1:4) and by elemental analysis (data in %: found: C 10.31, H 2.85, N 5.92, S 27.93; calculated: C 10.35, H 3.04, N 6.03, S 27.63).

Table 1  
Selected crystal data and details of the structure refinement for (DBUII)-CuSnS<sub>3</sub> (**1**) and (1,4-dabH<sub>2</sub>)Cu<sub>2</sub>SnS<sub>4</sub> (**2**)

	(DBUII)CuSnS <sub>3</sub>	(1,4-dabH <sub>2</sub> )Cu <sub>2</sub> SnS <sub>4</sub>
<i>a</i> /Å	9.2541(10)	14.5392(15)
<i>b</i> /Å	8.6190(7)	14.5392(15)
<i>c</i> /Å	18.135(2)	11.4776(12)
$\beta$ /°	92.803(16)	—
<i>V</i> /Å <sup>3</sup>	1444.7(3)	2426.2(4)
Crystal system	Monoclinic	Tetragonal
Space group	<i>P</i> 2 <sub>1</sub> / <i>n</i>	<i>P</i> 4 <sub>2</sub> / <i>n</i>
<i>Z</i>	4	8
<i>D</i> <sub>calc</sub> /g cm <sup>-3</sup>	1.985	2.542
$\mu$ /mm <sup>-1</sup>	3.61	6.163
Scan range	4.5° ≤ 2 $\theta$ ≤ 60.08°	4.52° ≤ 2 $\theta$ ≤ 50.04°
Measured reflections	8629	5424
Independent reflections	4215	2135
<i>R</i> <sub>int</sub>	0.0230	0.0751
<i>R</i> 1 for all <i>F</i> <sub>0</sub> > 4 $\sigma$ <i>F</i> <sub>0</sub>	0.0208	0.1132
<i>wR</i> 2 for all data	0.0496	0.1988
Res. electron density/eÅ <sup>-3</sup>	0.362/–0.383	1.687/–2.321

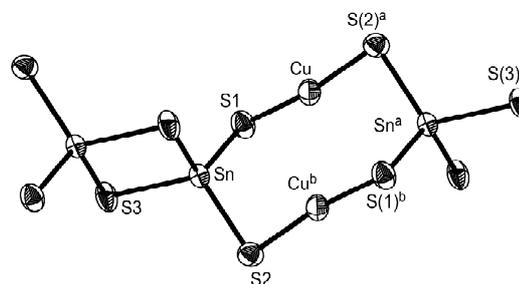


Fig. 1. View of the connection of the SnS<sub>4</sub> tetrahedra and CuS<sub>2</sub> dumbbells in compound **1** with labelling and displacement ellipsoids drawn at the 50% probability level. Symmetry transformations used to generate equivalent atoms: <sup>a</sup>  $-x + 2, -y, -z + 1$ ; <sup>b</sup>  $-x + 2, -y + 1, -z + 1$ .

### 2.2. Structure determination

The single crystal X-ray intensities were collected using a PW 1100 diffractometer for compound **1** and an STOE-1 Imaging Plate Diffraction System (IPDS-1) for compound **2** at room temperature using Mo K $\alpha$  radiation. The intensities were corrected for Lorentz, polarisation effects and for compound **1** an absorption correction was also applied. The structures were solved with direct methods using SHELXS 97 [29] and refined against *F*<sup>2</sup> with SHELXL 97 [30]. All non-hydrogen atoms were refined anisotropically. The H atoms were positioned with idealised geometry and were refined using a riding model. Details of data acquisition and some selected results of the refinements are summarised in Table 1.

Crystallographic data (excluding structure factors) for the structures reported in this paper have been deposited with the Cambridge Crystallographic Data Centre as supplementary publication no. CCDC613370 (**1**) and CCDC613369 (**2**). Copies of the data can be obtained, free of charge, on application to CCDC, 12 Union Road, Cambridge CB2 1EZ, UK (fax: +44 (0) 1223 336033 or email: deposit@ccdc.cam.ac.uk).

### 2.3. Thermal investigations

DTA–TG analyses were performed using a Netzsch STA 429 DTA–TG device. The samples were heated to 600 °C

Table 2  
Selected bond lengths [Å] and angles [°] for (DBUII)CuSnS<sub>3</sub> (**1**)

Sn(1)–S(1)	2.3508(6)	Sn(1)–S(3) <sup>a</sup>	2.4332(6)
Sn(1)–S(2)	2.3715(6)	Sn(1)–S(3)	2.4399(6)
Cu(1)–S(1)	2.1419(6)	Cu(1)–S(2) <sup>b</sup>	2.1496(6)
S(1)–Sn(1)–S(2)	111.25(2)	S(3) <sup>a</sup> –Sn(1)–S(3)	93.76(2)
S(1)–Sn(1)–S(3) <sup>a</sup>	115.24(2)	S(1)–Sn(1)–S(3)	108.86(2)
S(2)–Sn(1)–S(3) <sup>a</sup>	113.91(2)	S(2)–Sn(1)–S(3)	112.59(2)
S(1)–Cu(1)–S(2) <sup>b</sup>	166.27(2)	Cu(1) <sup>b</sup> –S(2)–Sn(1)	92.39(2)
Cu(1)–S(1)–Sn(1)	99.59(2)	Sn(1) <sup>a</sup> –S(3)–Sn(1)	86.24(2)

Symmetry transformations used to generate equivalent atoms: <sup>a</sup>  $x + 2, y, -z + 1$ ; <sup>b</sup>  $-x + 2, -y + 1, -z + 1$ .

in  $\text{Al}_2\text{O}_3$  crucibles at a rate of  $4 \text{ K min}^{-1}$  under a flow of argon ( $75 \text{ mL min}^{-1}$ ). The TG–MS measurements (heating rate: of  $4 \text{ K min}^{-1}$ ,  $\text{Al}_2\text{O}_3$  crucibles, dynamic helium atmosphere, flow-rate:  $75 \text{ mL min}^{-1}$ ) were conducted simultaneously using a STA-409CD device (Netzsch) with Skimmer coupling, which is equipped with a Balzers QMA 400 Quadrupole Mass Spectrometer (max. 512 amu). The MS data were recorded in the analogue and trend scan modes. The TG data were corrected for buoyancy and current effects.

#### 2.4. Spectroscopic experiments

*Raman:* Raman spectra were recorded in the region  $100\text{--}3500 \text{ cm}^{-1}$  with a Bruker IFS 66 Fourier Transform Raman spectrometer (wavelength: 541.5 nm).

*UV/Vis:* UV/Vis spectroscopic investigations were conducted at room temperature using a UV–VIS–NIR two-channel spectrometer Cary 5 from Varian Techtron Pty., Darmstadt. The optical properties of the compounds were investigated by studying the UV/Vis reflectance spectrum of the powdered

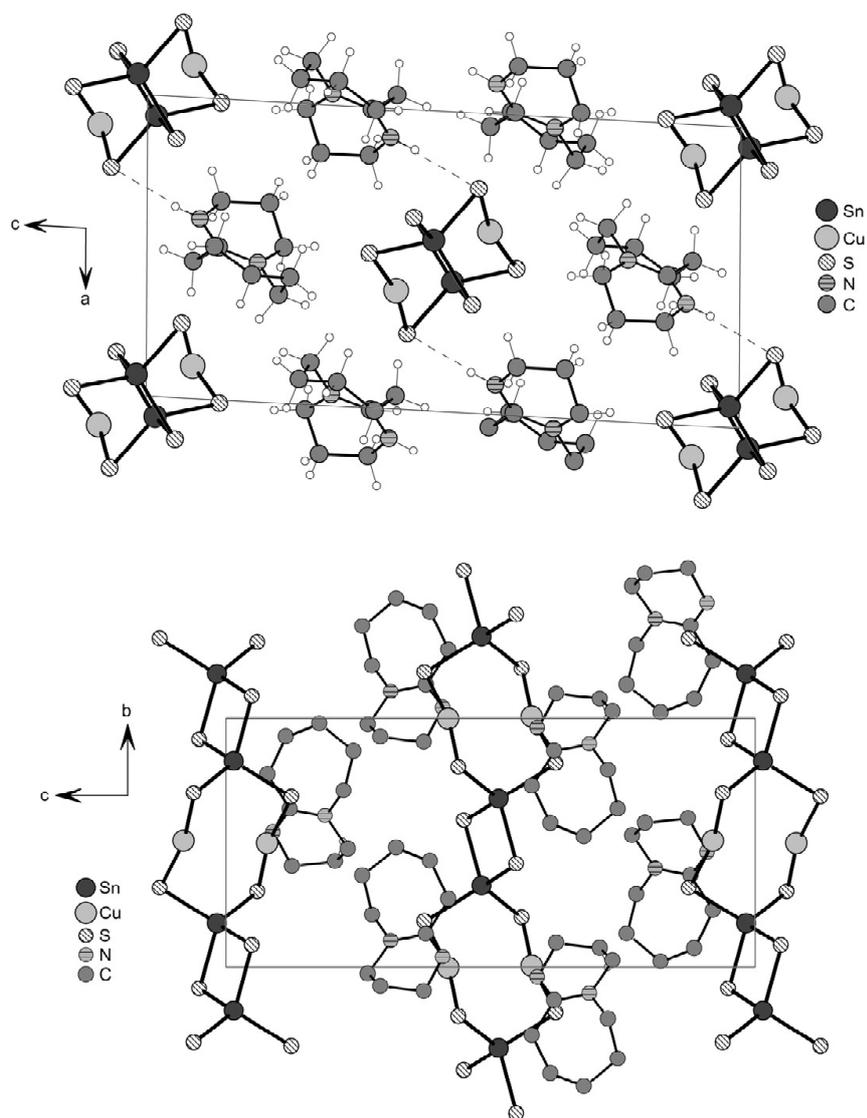


Fig. 2. Arrangement of the anionic chains and the cations in compound 1. Top: view along the *b*-axis with N–H...S bonds shown as dashed lines; bottom: anionic chains along [010] showing the different sequence of the rings of neighbored anions.

samples. The absorption data were calculated with the Kubelka–Munk relation for diffuse reflectance data. BaSO<sub>4</sub> powder was used as reference material.

### 2.5. Scanning electron microscopy (SEM)/energy dispersive X-ray fluorescence (EDX)

EDX analyses were done with a Philips ESEM XL30 equipped with an EDAX detector.

### 2.6. Elemental analysis

CHN analysis has been performed using a EURO EA Elemental Analyzer, fabricated by EURO VECTOR Instruments and Software.

## 3. Results and discussion

### 3.1. Crystal structures

The new compound (DBUH)CuSnS<sub>3</sub> (**1**) crystallises in the monoclinic space group *P2<sub>1</sub>/n* with all unique atoms being located on general positions. The one-dimensional anions are separated by protonated amine molecules. The Sn atom is in a tetrahedral environment of four S atoms and the Cu atom has only bonds to two S atoms in a nearly linear geometry (S–Cu–S: 166.27(2)°) (Fig. 1).

Linear CuS<sub>2</sub> groups are not very common and examples are the compounds CsCu<sub>5</sub>S<sub>3</sub> [31], TiCu<sub>7</sub>S<sub>4</sub> [32] or RbCu<sub>3</sub>S<sub>2</sub> [33]. In RbCu<sub>3</sub>S<sub>2</sub> the two-coordinated Cu atom has two additional S atoms at about 2.836 Å, and in the former compound this Cu atom has a contact to another S atom of 2.708 Å. In the present material no S atom is in the environment of Cu up to about 4.1 Å. In contrast to the S–Cu–S angle in the title compound in all these compounds the angles S–Cu–S are about 120°.

The Sn–S distances from 2.3508(6) to 2.4399(6) Å and the corresponding S–Sn–S angles (108.86(2)°–115.24(2)°) indicate a slight distortion of the SnS<sub>4</sub> tetrahedron (Table 2), but all geometric parameters are in the range reported in the literature [25,34,35]. The Cu–S bond lengths are 2.1496(6) and 2.1419(6) Å, very similar to the values observed in Cu<sub>2</sub>SnS<sub>3</sub> and Cu<sub>4</sub>SnS<sub>7</sub> [36,37]. Two symmetry related SnS<sub>4</sub> tetrahedra share a common edge to form the well known [Sn<sub>2</sub>S<sub>6</sub>]<sup>4-</sup> moiety [16,17], with the resulting Sn<sub>2</sub>S<sub>2</sub> ring being planar. The double tetrahedral groups are then interconnected via the CuS<sub>2</sub> units to form the [CuSnS<sub>3</sub>]<sup>-</sup> chains running along [010], and the sequence of the two building units is ...Sn<sub>2</sub>S<sub>6</sub>–2 CuS<sub>2</sub>–Sn<sub>2</sub>S<sub>6</sub>–2 CuS<sub>2</sub>... (Fig. 1).

The chains contain a Cu<sub>2</sub>Sn<sub>2</sub>S<sub>8</sub> ring in chair conformation with dimensions of 5.8–3.4 Å (Fig. 1). Along the *b*-axis the anionic chains are surrounded by six cations, and one short S...N separation of 3.413 Å indicating weak hydrogen bonding (Fig. 2, top). A view along [100] reveals that neighbored chains proceed in an opposite manner, i.e. the sequence of rings along [001] is ...Sn<sub>2</sub>S<sub>6</sub>...Sn<sub>2</sub>Cu<sub>2</sub>S<sub>4</sub>...Sn<sub>2</sub>S<sub>6</sub>... (Fig. 2, bottom).

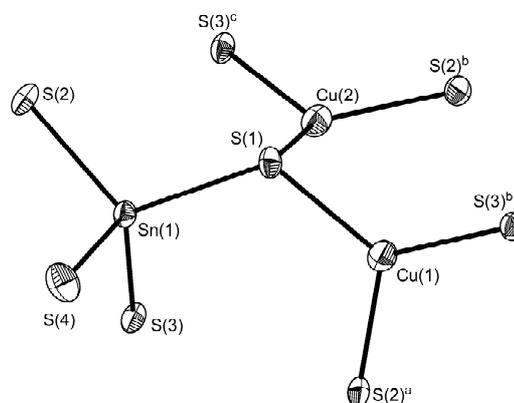


Fig. 3. View of the connection of the SnS<sub>4</sub> tetrahedron and the two CuS<sub>3</sub> triangles in compound **2** with labelling and displacement ellipsoids drawn at the 50% probability level. Symmetry transformations used to generate equivalent atoms: <sup>a</sup>  $-x+2, -y, -z+1$ ; <sup>b</sup>  $-x+2, -y+1, -z+1$ ; <sup>c</sup>  $-x+1/2, -y+3/2, z$ .

The new compound (1,4-dabH<sub>2</sub>)Cu<sub>2</sub>SnS<sub>4</sub> (**2**) crystallises in the tetragonal space group *P4<sub>2</sub>/n* with all unique atoms being located on general positions. The structure consists of a one-dimensional chain [Cu<sub>2</sub>SnS<sub>4</sub>]<sup>2-</sup> anion and charge compensating protonated cations. The Sn atom is surrounded by four S atoms in a slightly distorted tetrahedral geometry with S–Sn–S angles varying from 105.03(16)° to 113.08(14)° (Fig. 3, Table 3).

The Sn–S bond lengths are between 2.367(4) and 2.401(4) Å (Table 3) and are nearly in the same range like in compound **1**.

Table 3  
Bond lengths [Å] and angles [°] of (1,4-dabH<sub>2</sub>)Cu<sub>2</sub>SnS<sub>4</sub> (**2**)

Sn(1)–S(4)	2.367(4)	Sn(1)–S(1)	2.397(4)
Sn(1)–S(2)	2.380(4)	Sn(1)–S(3)	2.401(4)
Cu(1)–S(2) <sup>a</sup>	2.246(5)	Cu(2)–S(1)	2.265(4)
Cu(1)–S(1)	2.290(5)	Cu(2)–S(2) <sup>b</sup>	2.272(5)
Cu(1)–S(3) <sup>b</sup>	2.305(5)	Cu(2)–S(3) <sup>c</sup>	2.323(5)
Cu(1)–Cu(2)	2.718(3)	Cu(2)–Cu(1) <sup>c</sup>	2.845(3)
Cu(1)–Cu(2) <sup>c</sup>	2.845(3)	Cu(2)–Cu(2) <sup>c</sup>	2.991(4)
Cu(1)–Cu(1) <sup>c</sup>	3.057(4)	S(2)–Cu(1) <sup>d</sup>	2.246(5)
S(3)–Cu(1) <sup>e</sup>	2.305(5)	S(2)–Cu(2) <sup>e</sup>	2.272(5)
S(3)–Cu(2) <sup>e</sup>	2.323(5)		
S(4)–Sn(1)–S(2)	105.03(16)	S(4)–Sn(1)–S(3)	109.99(15)
S(4)–Sn(1)–S(1)	108.95(15)	S(2)–Sn(1)–S(3)	110.03(14)
S(2)–Sn(1)–S(1)	113.08(14)	S(1)–Sn(1)–S(3)	109.65(14)
S(2) <sup>b</sup> –Cu(1)–S(1)	123.22(17)	S(1)–Cu(2)–S(2) <sup>b</sup>	126.93(17)
S(2) <sup>a</sup> –Cu(1)–S(3) <sup>b</sup>	119.52(17)	S(1)–Cu(2)–S(3) <sup>c</sup>	121.29(16)
S(1)–Cu(1)–S(3) <sup>b</sup>	112.37(16)	S(2) <sup>b</sup> –Cu(2)–S(3) <sup>e</sup>	107.52(16)
Cu(2)–S(1)–Cu(1)	73.26(14)	Cu(1) <sup>a</sup> –S(2)–Cu(2) <sup>c</sup>	78.07(15)
Cu(2)–S(1)–Sn(1)	99.82(15)	Cu(1) <sup>a</sup> –S(2)–Sn(1)	103.00(16)
Cu(1)–S(1)–Sn(1)	114.49(18)	Cu(2) <sup>e</sup> –S(2)–Sn(1)	112.66(18)
Cu(1) <sup>e</sup> –S(3)–Cu(2) <sup>c</sup>	117.68(18)	Cu(2) <sup>e</sup> –S(3)–Sn(1)	100.18(16)
Cu(1) <sup>e</sup> –S(3)–Sn(1)	96.39(15)		

Symmetry transformations used to generate equivalent atoms: <sup>a</sup>  $y-1/2, -x+1, z-1/2$ ; <sup>b</sup>  $-y+1, x+1/2, z-1/2$ ; <sup>c</sup>  $-x+1/2, -y+3/2, z$ ; <sup>d</sup>  $-y+1, x+1/2, z+1/2$ ; <sup>e</sup>  $y-1/2, -x+1, z+1/2$ .

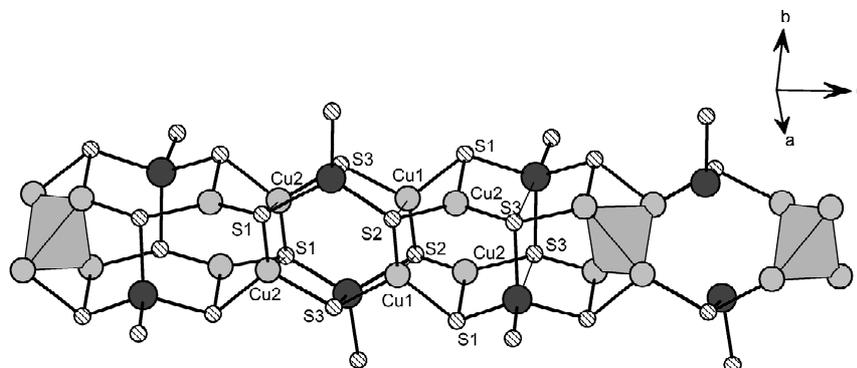


Fig. 4. The distorted cubes in the structure of compound **2** with the  $\text{Cu}_4$  tetrahedra shown as polyhedra.

The Cu atoms have bonds to three S atoms forming distorted trigonal planar polyhedra. The angles for S–Cu(1)–S are  $123.22(17)^\circ$ ,  $119.52(17)^\circ$  and  $112.37(16)^\circ$  and for S–Cu(2)–S the values are  $126.93(17)^\circ$ ,  $121.29(16)^\circ$  and  $107.52(16)^\circ$ , showing a different degree of distortion for the two unique Cu atoms. The Cu–S distances amount to 2.246(5), 2.290(5) and 2.305(5) Å for Cu(1) and they are 2.265(4), 2.272(5) and 2.323(5) Å for Cu(2) (Table 3). The bond lengths are in the

typical range reported for other copper and sulfur containing compounds [36,37]. With the exception of S(4) all S atoms are bound to one Sn and two Cu atoms. The S(1), S(2), and S(3) atoms of the  $\text{SnS}_4$  tetrahedron have bonds to six  $\text{CuS}_3$  triangles, whereas S(4) is terminal explaining the short Sn–S(4) bond length. Central motifs of the chain are alternating distorted cubes  $\text{Cu}(1)_2\text{Cu}(2)_2\text{S}(1)_2\text{S}(2)_2$  and  $\text{Cu}(1)_2\text{Sn}_2\text{S}(2)_2\text{S}(3)_2$ . In the first cube two Sn and two S(3) atoms are nearly above four

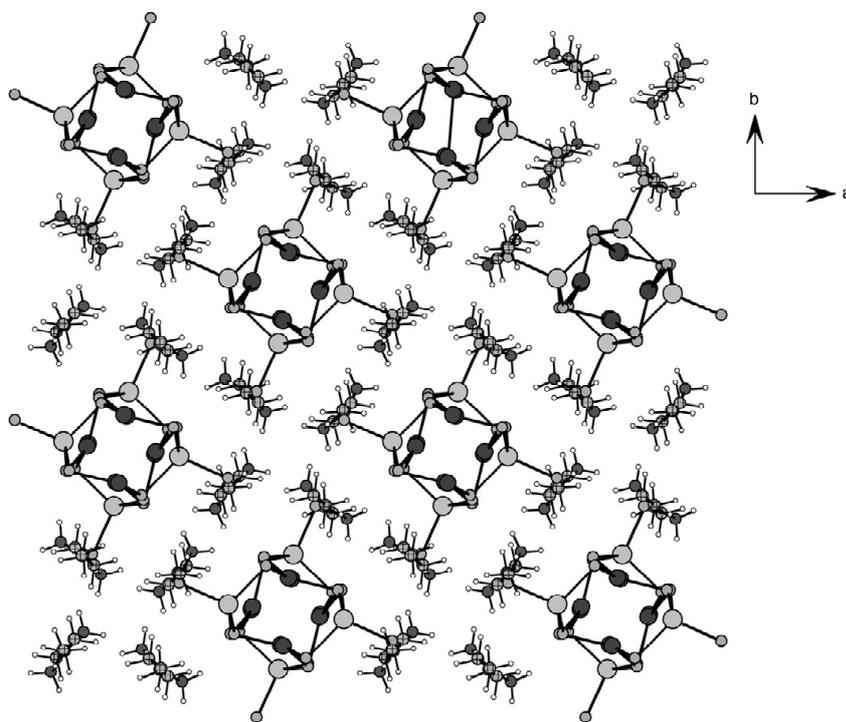


Fig. 5. Crystal structure of compound **2** with view along the *c*-axis.

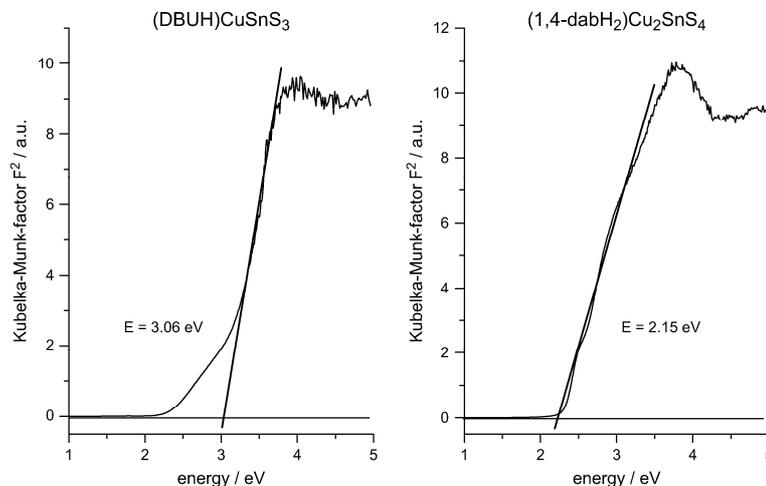


Fig. 6. Kubelka–Munk plots for compound **1** (left) and **2** (right).

edges whereas in the latter cube two S(1) atoms are above two edges and two Cu(2) atoms are located slightly above two distorted rectangular planes (Fig. 4).

Another description starts with Cu atoms which are arranged as tetrahedra with Cu–Cu distances in the range of 2.718(3)–3.057(4) Å, which are longer than in elemental Cu. But comparable separations were found for example in  $(C_6N_4H_{20})_{0.5}Cu_3Sb_2S_5$  [38]. Two neighbored  $Cu_4$  groups are joined via two S(3) atoms. These  $Cu_8S_2$  groups are interconnected in an alternating fashion by two  $SnS_4$  tetrahedra to form a chain running along [001] (Fig. 4).

Eight cations are arranged in a square like fashion to form tunnels which host the anionic chains (Fig. 5).

The N(1) atom has a short contact to S(4) (N(1)⋯S(4): 3.124 Å; angle: 167.4°) and N(2) has two such contacts, one to S(4) (distance: 3.127 Å; angle: 166.9°) and to S(1) (distance: 3.269 Å; angle: 166.2°) which indicate hydrogen bonding interactions.

### 3.2. Spectroscopic properties

#### 3.2.1. UV/Vis spectroscopy

The optical band gaps were calculated by the Kubelka–Munk method from UV/Vis data, and the value of 3.06 eV (405 nm) for compound **1** (Fig. 6, left) is in agreement with the light yellow colour of the material. For compound **2**

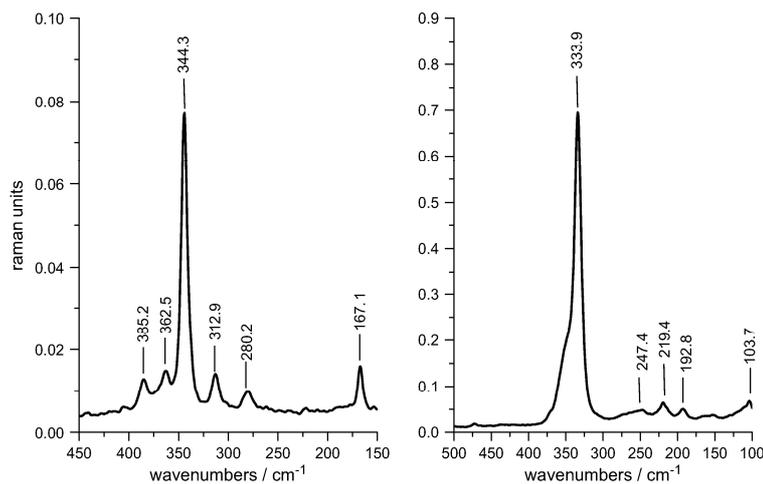


Fig. 7. Raman spectra for compounds **1** (left) and **2** (right).

a significant lower value of 2.15 eV (577 nm) was estimated (Fig. 6, right).

### 3.2.2. Raman spectroscopy

The region of interest in the Raman spectra ranges from 400 to 100  $\text{cm}^{-1}$  where the Sn–S resonances are located [14,39]. A comparison of the spectra of compounds **1** (Fig. 7, left) and **2** (Fig. 7, right) directly displays the differences between the two structures. Around 380  $\text{cm}^{-1}$  the modes of the symmetric Sn–S<sub>terminal</sub> stretching vibrations are located, and for isolated  $[\text{Sn}_2\text{S}_6]^{4-}$  anions the values range from 372 to 377  $\text{cm}^{-1}$  [40]. In compound **1** the signal is shifted to slightly higher wavenumbers (385.2  $\text{cm}^{-1}$ ) due to the somewhat shorter terminal Sn–S bond of 2.3508(6) Å. The resonance for the Sn–S(2) bond is found at 362.5  $\text{cm}^{-1}$ . Between 350 and 310  $\text{cm}^{-1}$  the Sn–S<sub>bridging</sub> modes occur [40,41]. A vibration of the  $\text{Sn}_2\text{S}_2$  ring is at 280  $\text{cm}^{-1}$  in the spectrum of compound **1**. The deformation vibrations are found below 200  $\text{cm}^{-1}$ . The signal at 167  $\text{cm}^{-1}$  may be due to the  $\text{SnS}_2$  wagging and twisting modes, but the detailed assignment in this region is quite ambiguous due to resonances from lattice vibrations.

In compound **2** no  $[\text{Sn}_2\text{S}_6]^{4-}$  anions are present and no signal is found around 380  $\text{cm}^{-1}$ . The resonance at 333.9  $\text{cm}^{-1}$  could be due to the Sn–S<sub>bridging</sub> mode and deformation vibrations are usually detected below 200  $\text{cm}^{-1}$ . The signals at 192 and 104  $\text{cm}^{-1}$  could be associated with the  $\text{SnS}_2$  wagging and twisting modes, but again an unambiguous assignment is not possible.

### 3.3. Thermal properties

The thermal decomposition of  $(\text{DBUH})\text{CuSnS}_3$  (**1**) occurs in three close steps (Fig. 8). The first step ( $T_{\text{onset}} = 246^\circ\text{C}$ ;  $T_p = 264^\circ\text{C}$ ) is accompanied by a mass loss of 27.1%. The second thermal reaction occurs at 304 °C with a mass change of 8.6%. The last thermal event ( $T_{\text{onset}} = 363^\circ\text{C}$ ;  $T_p = 377^\circ\text{C}$ ) is accompanied by an additional mass loss of 7.4%. The theoretical mass loss for the emission of one molecule of DBU and  $\text{H}_2\text{S}$  is 42.9% (DBU = 35.5%;  $\text{H}_2\text{S}$  = 7.4%), i.e. this value matches well with the experimental data. Further TG–MS investigations prove that DBU and  $\text{H}_2\text{S}$  are emitted simultaneously. At the different peak temperatures, mass signals of  $\text{H}_2\text{S}$  and DBU are detected showing that DBU is decomposed during thermal reaction. Chemical analysis of the residue demonstrates that the product is almost free of organic components and the X-ray powder pattern showed reflections of  $\text{Cu}_2\text{SnS}_3$  and SnS.

The compound  $(1,4\text{-dabH}_2)\text{Cu}_2\text{SnS}_4$  (**2**) decomposes in one step at  $T_{\text{onset}} = 227^\circ\text{C}$  ( $T_p = 254^\circ\text{C}$ ) (Fig. 9). The corresponding mass loss of 24.9% is lower than the value expected for the emission of 1,4-diaminobutane (19%) and one  $\text{H}_2\text{S}$  (7.3%). After heating to 600 °C the residue is almost free of organic components and in the X-ray powder pattern  $\text{Cu}_2\text{SnS}_3$ ,  $\text{Cu}_4\text{SnS}_4$  and SnS could be identified.

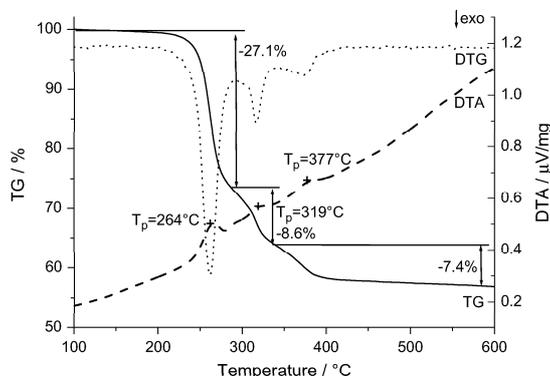


Fig. 8. DTA–TG curves for compound **1**. The weight losses and peak temperatures  $T_p$  are indicated.

## 4. Conclusion

In the present work we demonstrated that new copper containing thiostannates can be prepared reacting the elements in amine solutions under solvothermal conditions. For both compounds the ratio of starting material was about 1:1:3 mmol for Cu/Sn/S but in the crystalline products different building units are observed. In compound **1** two  $\text{SnS}_4$  tetrahedra share a common edge to form the well established  $\text{Sn}_2\text{S}_6$  group. Adjacent  $\text{Sn}_2\text{S}_6$  moieties are joined by two nearly linear  $\text{CuS}_2$  dumbbells to form the one-dimensional anionic  $[\text{CuSnS}_3]^-$  chains. The  $\text{SnS}_4$  tetrahedron is also found in the structure of compound **2**, but in this case the tetrahedron is interconnected by two  $\text{CuS}_3$  triangles into the final  $[\text{Cu}_2\text{SnS}_4]^{2-}$  anion. A possible explanation for the occurrence of the two different structure types may be that DBU can only be monoprotonated whereas 1,4-dab can carry two positive charges. But the influence of amines on the product formation and crystal structures is not well understood, and other factors like time, temperature, and pH-value are also important

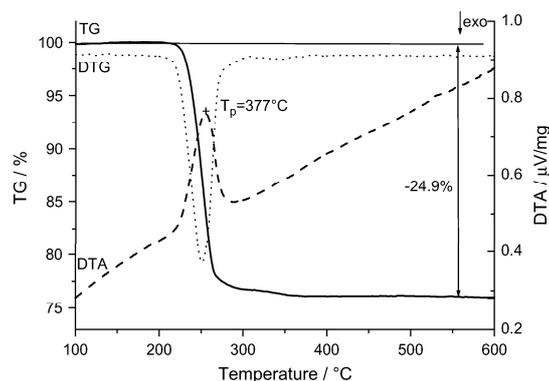


Fig. 9. DTA–TG curves for compound **2**. The weight loss and peak temperature  $T_p$  are indicated.

synthetic parameters. Systematic studies are needed for a better understanding of how the different parameters influence product formation. More copper(I) thiostannates should be prepared in the presence of amines as structure directing molecules to explore the structural flexibility and variability of such inorganic–organic hybrid compounds.

#### References

- [1] H. Ahari, C.L. Bowes, T. Jiang, A. Lough, G.A. Ozin, R.L. Bedard, S. Petrov, D. Young, *Adv. Mater.* 7 (1995) 375.
- [2] H. Ahari, G.A. Ozin, R.L. Bedard, S. Petrov, D. Young, *Adv. Mater.* 7 (1995) 370.
- [3] P. Enzel, G.S. Henderson, G.A. Ozin, R.L. Bedard, *Adv. Mater.* 7 (1995) 64.
- [4] T. Jiang, G.A. Ozin, R.L. Bedard, *Adv. Mater.* 7 (1995) 166.
- [5] R.W.J. Scott, M.J. MacLachlan, G.A. Ozin, *Curr. Opin. Solid State Mater. Sci.* 4 (1999) 113.
- [6] T. Jiang, A. Lough, G.A. Ozin, *Adv. Mater.* 10 (1998) 42.
- [7] J.B. Parise, Y. Ko, J. Rijssenbeek, D.M. Nellis, K. Tan, S. Koch, *J. Chem. Soc., Chem. Commun.* (1994) 527.
- [8] R.J. Francis, S.J. Price, J.S.O. Evans, S. O'Brien, D. O'Hare, S.M. Clark, *Chem. Mater.* 8 (1996) 2102.
- [9] T. Jiang, G.A.J. Ozin, *Mater. Chem.* 7 (1997) 2213.
- [10] W.S. Sheldrick, M. Wachhold, *Angew. Chem.* 109 (1997) 214.
- [11] W.S. Sheldrick, *J. Chem. Soc., Dalton Trans.* (2000) 3041.
- [12] T. Jiang, G.A. Ozin, A. Verma, R.L. Bedard, *J. Mater. Chem.* 8 (1998) 1649.
- [13] I. Sokolov, T. Jiang, G.A. Ozin, *Adv. Mater.* 10 (1998) 942.
- [14] C.L. Bowes, S. Petrov, G. Vovk, D. Young, G.A. Ozin, R.L. Bedard, *J. Mater. Chem.* 8 (1998) 711.
- [15] Y. Ko, K. Tan, D.M. Nellis, S. Koch, J.B. Parise, *J. Solid State Chem.* 114 (1995) 506.
- [16] T. Jiang, A. Lough, G.A. Ozin, R.L. Bedard, R. Broach, *J. Mater. Chem.* 8 (1998) 721.
- [17] T. Jiang, A. Lough, G.A. Ozin, R.L. Bedard, *J. Mater. Chem.* 8 (1998) 733.
- [18] H. Ahari, Ö. Dag, S. Petrov, G.A. Ozin, *J. Phys. Chem. B* 102 (1998) 2356.
- [19] G.A. Marking, M. Evain, V. Petricek, M.G. Kanatzidis, *J. Solid State Chem.* 141 (1998) 17.
- [20] T. Jiang, A.J. Lough, G.A. Ozin, D. Young, R.L. Bedard, *Chem. Mater.* 7 (1995) 245.
- [21] W.S. Sheldrick, B. Schaaf, *Z. Anorg. Allg. Chem.* 620 (1994) 1041.
- [22] J. Li, B. Marler, H. Kessler, M. Soular, S. Kallus, *Inorg. Chem.* 36 (1997) 4697.
- [23] J.H. Liao, C. Varotsis, M.G. Kanatzidis, *Inorg. Chem.* 32 (1993) 2453.
- [24] K.K. Rungan, P.N. Trikalitis, C. Canlas, T. Bakas, D.P. Weliky, M.G. Kanatzidis, *Nano Lett.* 2 (2002) 513.
- [25] M. Behrens, S. Scherb, C. Näther, W. Bensch, *Z. Anorg. Allg. Chem.* 629 (2003) 1367.
- [26] D.X. Jia, J. Dai, Q.Y. Zhu, Y. Zhang, X.M. Gu, *Polyhedron* 23 (2004) 937.
- [27] Y. An, M. Ji, M. Baiyin, X. Liu, C. Jia, D. Wang, *Inorg. Chem.* 14 (2003) 4248.
- [28] O. Palchik, R.G. Iyer, J.H. Liao, M.G. Kanatzidis, *Inorg. Chem.* 42 (2003) 5052.
- [29] G.M. Sheldrick, SHELXS 97, Program for the Solution of Crystal Structures, University of Göttingen, Germany, 1997.
- [30] G.M. Sheldrick, SHELXL 97, Program for the Refinement of Crystal Structures, University of Göttingen, Germany, 1997.
- [31] J. Huster, W. Bronger, *Z. Anorg. Allg. Chem.* 627 (2001) 1395.
- [32] L. Noren, K. Larsson, R.G. Delaplane, R. Berger, *J. Alloys Compd.* 314 (2001) 114.
- [33] K.O. Klepp, M. Sing, *Z. Kristallogr. NCS* 217 (2002) 474.
- [34] T. Jiang, G.A. Ozin, *Adv. Mater.* 8 (1998) 1099.
- [35] T. Jiang, G.A. Ozin, R.L. Bedard, *J. Mater. Chem.* 8 (1998) 1641.
- [36] X. Chen, H. Wada, A. Sato, M. Mieno, *J. Solid State Chem.* 139 (1998) 144.
- [37] X. Chen, H. Wada, A. Sato, *Mater. Res. Bull.* 34 (1999) 239.
- [38] V. Spetzler, C. Näther, W. Bensch, *Inorg. Chem.* 44 (2005) 5805.
- [39] Ö. Dag, H. Ahari, N. Coombs, J. Jiang, P.P. Aroca-Quellette, S. Petrov, *Adv. Mater.* 9 (1997) 1133.
- [40] B. Krebs, W. Schiwy, *Z. Anorg. Allg. Chem.* 398 (1973) 63.
- [41] B. Krebs, S. Pohl, W. Schiwy, *Angew. Chem.* 82 (1970) 884.

#### 4.1.2. Die Verbindung (1,4-dabH<sub>2</sub>)Ag<sub>2</sub>SnS<sub>4</sub>

*Zusammenfassung der Veröffentlichung „The New Silver Thiostannate (1,4-dabH<sub>2</sub>)Ag<sub>2</sub>SnS<sub>4</sub>: Solvothermal Synthesis, Crystal Structure and Spectroscopic Properties“.*

Das neue Thiostannat (1,4-dabH<sub>2</sub>)Ag<sub>2</sub>SnS<sub>4</sub> (1,4-dab = 1,4-Diaminobutan, C<sub>4</sub>N<sub>2</sub>H<sub>14</sub>) wurde unter solvothermalen Bedingungen aus den Elementen dargestellt: Ag, Sn und S im Verhältnis 1:1:3 mmol werden in 3 mL 1,4-Diaminobutan für 145 h bei 150 °C zur Reaktion gebracht.

Die Verbindung kristallisiert in der tetragonalen Raumgruppe P4<sub>2</sub>/n mit acht Formeleinheiten in der Elementarzelle und ist isostrukturell zu der Verbindung (1,4-dabH<sub>2</sub>)Cu<sub>2</sub>SnS<sub>4</sub> (Kap. 4.1.1). In der Struktur werden die SnS<sub>4</sub>-Tetraeder und trigonalen AgS<sub>3</sub>-Polyeder derart verknüpft, dass eindimensionale [Ag<sub>2</sub>SnS<sub>4</sub>]<sup>2-</sup>-Ketten gebildet werden. In den Ketten werden als strukturelle Merkmale verzerrte Ag<sub>4</sub>S<sub>4</sub>- und Ag<sub>2</sub>Sn<sub>2</sub>S<sub>4</sub>-Würfel beobachtet. Eine alternative Beschreibung geht von Ag<sub>4</sub>-Tetraedern aus. Zwei Ag<sub>4</sub>-Tetraeder bilden mit zwei Schwefel-Atomen Ag<sub>8</sub>S<sub>2</sub>-Einheiten und durch weitere Verknüpfung mit SnS<sub>4</sub>-Tetraedern werden die anionischen Ketten gebildet, die von protonierten Aminmolekülen umgeben sind.

In dem Raman-Spektrum werden Sn-S<sub>bridging</sub>-Resonanzen bei 349 und 336 cm<sup>-1</sup> sowie weitere Moden bei 254, 224, 200 und 119 cm<sup>-1</sup> beobachtet.

Das Interessante an dieser Verbindung ist, dass sie isostrukturell zu der in Kapitel 4.1.1. vorgestellten kupferhaltigen Verbindung (1,4-dabH<sub>2</sub>)Cu<sub>2</sub>SnS<sub>4</sub> ist. Dies ist für Thiometallate eher unüblich. So kristallisieren beispielsweise silberhaltige Thioantimonate in anderen Strukturtypen als die kupferhaltigen [84]. Interessant ist, dass bei (1,4-dabH<sub>2</sub>)Ag<sub>2</sub>SnS<sub>4</sub> und (1,4-dabH<sub>2</sub>)Cu<sub>2</sub>SnS<sub>4</sub> die Gitterparameter recht ähnlich und auch die Anordnung der SnS<sub>4</sub>-Tetraeder annähernd identisch sind, wenngleich die Ag<sub>3</sub>S-Gruppen stärker verzerrt sind als die entsprechenden CuS<sub>3</sub>-Dreiecke.

N. Pienack, W. Bensch: The New Silver Thiostannate  $(1,4\text{-dabH}_2)\text{Ag}_2\text{SnS}_4$ : Solvothermal Synthesis, Crystal Structure and Spectroscopic Properties.

*Z. Anorg. Allg. Chem.* **2006**, *632*, 1733-1736.

Copyright Wiley-VCH Verlag GmbH & Co. KGaA.

Reproduced with permission.

The New Silver Thiostannate  $(1,4\text{-dabH}_2)\text{Ag}_2\text{SnS}_4$ : Solvothermal Synthesis,  
Crystal Structure and Spectroscopic Properties

Nicole Pienack and Wolfgang Bensch\*

Kiel, Institut für Anorganische Chemie der Christian-Albrechts Universität

*Dedicated to Prof. Dr. H.-G. von Schnering on the occasion of his 75<sup>th</sup> birthday*

\* Prof. Dr. W. Bensch, Institut für Anorganische Chemie der Universität Kiel, Olshausenstr.  
40, D-24098 Kiel

Fax: +49 (0)431/880 –1520, e-Mail: wbensch@ac.uni-kiel.de

**Abstract:** The new compound  $(1,4\text{-dabH}_2)\text{Ag}_2\text{SnS}_4$  (1,4-dab = 1,4-diaminobutane) was prepared under solvothermal conditions and crystallizes in the tetragonal space group  $P4_2/n$  with lattice parameters  $a = 14.7847(8) \text{ \AA}$ ,  $c = 11.9087(6) \text{ \AA}$ ,  $V = 2603.1(2) \text{ \AA}^3$ ,  $Z = 8$ . In the structure  $\text{SnS}_4$  tetrahedra and  $\text{AgS}_3$  triangles are joined to form an one-dimensional  $[\text{Ag}_2\text{SnS}_4]^{2-}$  anionic chain. Prominent structural features of the chains are distorted  $\text{Ag}_4\text{S}_4$  and  $\text{Ag}_2\text{Sn}_2\text{S}_4$  cubes sharing common faces. Four edges of the  $\text{Ag}_4\text{S}_4$  cube are capped by two Sn and two S atoms whereas the latter cube is capped by two Ag and two S atoms. Another description base on the interconnection of two  $\text{Ag}_4$  tetrahedra by two S atoms to form an  $\text{Ag}_8\text{S}_2$  unit which is joined by two  $\text{SnS}_4$  tetrahedra yielding the anionic chains. The compound was characterized with Raman spectroscopy.

**Keywords:** Solvothermal Synthesis, Silverthiostannate; Crystal Structure, Raman Spectroscopy

## Introduction

In recent years, the interest in the synthesis of open-framework materials on the basis of interconnected thiometallate building units increased markedly. The incorporation of transition metals into thioannate frameworks is a promising strategy to enhance the functionality of such material and applications for molecule-separating catalysis and chemical sensing were reported [1-4]. The thioannates exhibit a complex structural chemistry due to the ability of the Sn atom to coordinate four, five or six sulfur atoms and due to the condensation of the polyhedra via vertices or edges [1, 5-10]. Thioannate compounds with new network topologies and promising electrical properties can be expected if Ag can be integrated into the networks because Ag shows also various coordination polyhedra with S like  $\text{AgS}_2$  dumbbells,  $\text{AgS}_3$  triangles or  $\text{AgS}_4$  tetrahedra. Until now only a few examples for Ag containing thioannates prepared under solvothermal synthesis conditions are known like  $(\text{NH}_4)_2\text{Ag}_6\text{Sn}_3\text{S}_{10}$  [11],  $\text{K}_2\text{Ag}_6\text{Sn}_3\text{S}_{10}$  [12] or  $(\text{NH}_3\text{CH}_2\text{CH}_2\text{NH}_3)\text{Ag}_2\text{SnS}_4$  which contains chiral layers [13]. The relatively mild solvothermal conditions are ideal for the preparation of new phases which may be thermodynamically metastable and due to the presence of organic structure directing molecules often open networks are obtained. The power of the solvothermal route was impressively demonstrated in the past and thiometallates with unusual structural features and possible interesting properties were reported [14-18].

Recently, we presented two new copper-containing thioannates [19] synthesized under solvothermal conditions. In our continuing work on the solvothermal syntheses of transition metal containing thioannates, the silver containing compound  $(1,4\text{-dabH}_2)\text{Ag}_2\text{SnS}_4$  (1,4-dab = 1,4-diaminobutane) was obtained. In the report we present the synthesis, crystal structure and Raman data of this new thioannate.

## Experimental Section

### *Synthesis*

The new compound (1,4-dabH<sub>2</sub>)Ag<sub>2</sub>SnS<sub>4</sub> was prepared under solvothermal conditions in a teflon-lined steel autoclave (inner volume: 30 mL). 118.3 mg (1 mmol) Sn (99.5 %, Aldrich), 107.0 mg (1 mmol), Ag (99.9 %, Fluka), 96.3 mg (3 mmol) S and 3 mL of 1,4-diaminobutane (98 %, Fluka) were mixed and reacted for 145 h at 150 °C. The crystalline product was filtered off, washed with water and ethanol and dried in vacuum. Single crystals of (1,4-dabH<sub>2</sub>)Ag<sub>2</sub>SnS<sub>4</sub> were obtained in form of pale yellow needles. The yield based on Sn was always low and a large number of syntheses with varying conditions were performed to increase the yield. But all attempts failed and the yield was always only a few percent. The of the sample composition was confirmed with EDX (Sn/Ag/S ratio 2 : 1 : 4) and by elemental analysis (found %: C 8.81, H 2.25, N 4.97, S 23.13; calculated %: C 8.69, H 2.55, N 5.07, S 23.20).

### *Structure refinement details*

For the compound the single crystal X-ray intensities were collected on an Imaging Plate Diffraction System (IPDS-1) at room temperature using MoK<sub>α</sub> radiation. The intensities were corrected for Lorentz, polarization effects and an absorption correction was also applied. The structure was solved with direct methods using the program SHELXS-97 [20] and refined against  $F^2$  with SHELXL-97 [21]. Anisotropic displacement parameters were used for Sn, Ag, S, C and N atoms. The H atoms were positioned with idealized geometry and refined using a riding model with a fixed isotropic displacement parameter. The details of data acquisition and some selected results of the refinement are summarized in Table 1.

Crystallographic data (excluding structure factors) for the structure reported in this paper have been deposited with the Cambridge Crystallographic Data Center as supplementary publication no. CCDC 608047. Copies of the data can be obtained, free of charge, on

application to CCDC, 12 Union Road, Cambridge CB2 1 EZ, UK. (fax: +44-(0)1223-336033 or email: deposit@ccdc.ca.ac.uk).

#### **Scanning electron microscopy (SEM)/ energy dispersive X-ray fluorescence (EDX):**

EDX analyses were done with a Philips ESEM XL30 equipped with an EDAX detector.

#### **Raman Spectroscopy:**

The spectrum was recorded in the region 100 to 3500  $\text{cm}^{-1}$  with a Bruker IFS 66 Fourier Transform Raman spectrometer (wavelength: 541.5 nm).

#### **Results and Discussion**

The new compound  $(1,4\text{-dabH}_2)\text{Ag}_2\text{SnS}_4$  crystallizes in the tetragonal space group  $P4_2/n$ . All unique atoms are located on general positions. The structure contains an one-dimensional anionic chain  $[\text{Ag}_2\text{SnS}_4]^{2-}$  and charge compensating protonated diammoniumbutane cations. The Sn atom is coordinated by four S atoms in a tetrahedral geometry with S-Sn-S angles varying from 105.73(3) to 112.81(4)  $^\circ$  (Fig. 1, Tab. 2). The Sn-S bond lengths (2.3826(9) - 2.3982(9)  $\text{\AA}$ , Tab. 2) and the S-Sn-S angles indicate a slight distortion of the  $\text{SnS}_4$  tetrahedron, but all geometric parameters are in the range reported in the literature [11-13, 19, 22-24]. The Ag atoms have bonds to 3 S atoms forming distorted trigonal pyramidal units. The values for the Ag(1)-S bonds scatter from 2.4514(10) to 2.6019(10)  $\text{\AA}$  and they are between 2.4921(10) and 2.5829(10)  $\text{\AA}$  for Ag(2) (Tab. 2). The angles around Ag(1) (106.27(3) - 130.48(3)  $^\circ$ ) and Ag(2) (100.83(3) - 133.97(3)  $^\circ$ ) show a distortion of the environment around the two unique Ag atoms. Furthermore, for each Ag atom two of the bonds are short and one bond is long indicating a distortion of the trigonal geometry towards a linear arrangement. As a consequence wide S-Ag-S angles of 130.48(3)  $^\circ$  (Ag(1)) and of 133.97(3)  $^\circ$  (Ag(2)) are observed between the shorter Ag-S bonds. The Ag atoms are located above the trigonal plane formed by the S atoms (Ag(1): 0.1241  $\text{\AA}$ , Ag(2): 0.1195  $\text{\AA}$ ) indicating a second distortion

towards a pyramidal arrangement. The bond lengths and the angles are in the typical range reported for other  $\text{AgS}_3$  groups containing compounds [11-13, 25-27]. All S atoms except S(4) which is terminal are surrounded by one Sn and two Ag atoms. The  $\text{SnS}_4$  tetrahedron and the  $\text{AgS}_3$  triangles are joined to form an one-dimensional chain which may be described as alternating distorted cubes composed of  $\text{Ag}(1)_2\text{Ag}(2)_2\text{S}(1)_2\text{S}(2)_2$  and  $\text{Ag}(1)_2\text{Sn}_2\text{S}(2)_2\text{S}(3)_2$ . In the former cube, two Sn and two S(3) atoms are nearly above four edges whereas in the second cube two S(1) atoms are above two edges and two Ag(2) atoms are located slightly above two distorted rectangular planes (Fig. 2). A different view of the structure base on the interconnection of  $\text{Ag}_4$  tetrahedra by S(3) atoms forming  $\text{Ag}_8\text{S}_2$  groups with Ag-Ag distances in the range of 2.9926(5) to 3.1378(5) Å, which are longer than in elemental Ag. Nevertheless, these Ag-Ag separations are not unusual and comparable values could be found in the compounds  $\text{Ag}_{3.8}\text{Sn}_3\text{S}_8$  [27] and  $\text{Ag}_8\text{SnS}_6$  [28]. Two neighbored  $\text{Ag}_4$  groups are joined via two S(3) atoms. The resulting  $\text{Ag}_8\text{S}_2$  units and the intervening two  $\text{SnS}_4$  tetrahedra form the chain running along [001] (Fig. 2). We note that the connection mode of the different building units in the title compound is very similar to that found for  $(1,4\text{-dabH}_2)\text{Cu}_2\text{SnS}_4$ .

The charge compensating diammoniumbutane molecules are arranged in a square like manner around the anions to form tunnels hosting the chains (Fig. 3). Every anionic chain is surrounded by 8 cations. The N(1) atom has two short contacts ((N(1)··S(4): 3.300 Å; angle: 172.0 °; N(1)··S(3): 3.346 Å; angle: 168.0 °) and N(2) has one such contact to S(4) (3.234 Å; angle: 161.0 °) which indicate hydrogen bonding interactions.

The region of interest in the Raman spectra ranges from 400 to 100  $\text{cm}^{-1}$  where the Sn-S resonances are located [18, 29]. The spectrum is shown in Fig. 4. At 349 and 336  $\text{cm}^{-1}$  the Sn-S<sub>bridging</sub> modes are located [30, 31]. The deformation vibrations are found below 200  $\text{cm}^{-1}$ . The signals at 200  $\text{cm}^{-1}$  and 119  $\text{cm}^{-1}$  may be due to the  $\text{SnS}_2$  wagging and twisting modes, but the detailed assignment in this region is quite ambiguously because of the resonances from lattice vibrations.

The successful synthesis of the new silver containing thiostannate is a promising result and further work is in progress to prepare more compounds. An interesting observation is that the title compound is not isostructural to  $(\text{NH}_3\text{CH}_2\text{CH}_2\text{NH}_3)\text{Ag}_2\text{SnS}_4$  [13] which crystallizes in the monoclinic space group  $C2/c$  with a layered anion. In this compound the geometry of the  $\text{AgS}_3$  triangle is much more distorted than in  $(1,4\text{-dabH}_2)\text{Ag}_2\text{SnS}_4$  with Ag-S bond lengths between 2.416 and 2.772 Å and S-Ag-S angles from 93.1 to 161.5°. Central motifs of the anionic layers are condensed  $\text{Ag}_2\text{Sn}_2\text{S}_4$  and  $\text{Ag}_2\text{SnS}_3$  rings. Another unusual result is that the title compound is isostructural to the analogous copper compound. This is not often the case for thiometallates and for instance thioantimonates containing Ag crystallize in a different structure compared to the Cu thioantimonates. The main differences like lattice parameters and unit cell volumes between the Ag and Cu thiostannate are caused by the larger ionic radius of  $\text{Ag}^+$ . The geometry of the  $\text{SnS}_4$  tetrahedra is nearly identical in both compounds but the  $\text{CuS}_3$  groups are less distorted than the  $\text{AgS}_3$  units.

#### ***Acknowledgements***

This work has been supported by the State of Schleswig-Holstein and the Deutsche Forschungsgemeinschaft (DFG).

## References

- [1] R.W.J. Scott, M.J. MacLachlan, G.A. Ozin, *Curr. Op. Solid State Mater. Sci.* **1999**, *4*, 113.
- [2] T. Jiang, A. Lough, G.A. Ozin, *Adv. Mater.* **1998**, *10*, 42.
- [3] J.B. Parise, Y. Ko, J. Rijssenbeek, D.M. Nellis, K. Tan, S. Koch, *J. Chem. Soc., Chem. Commun.* **1994**, 527.
- [4] R.J. Francis, S.J. Price, J.S.O. Evans, S. O'Brien, D. O'Hare, S.M. Clark, *Chem. Mater.* **1996**, *8*, 2102.
- [5] T. Jiang, G.A. Ozin, *J. Mater. Chem.* **1997**, *7*, 2213.
- [6] W.S. Sheldrick, *Z. Anorg. Allg. Chem.* **1998**, 562, 23.
- [7] Y. Ko, K. Tan, D.M. Nellis, S. Koch, J.B. Parise, *J. Solid State Chem.* **1995**, *114*, 506.
- [8] T. Jiang, A. Lough, G.A. Ozin, R.L. Bedard, R. Broach, *J. Mater. Chem.* **1998**, *8*, 721.
- [9] W.S. Sheldrick, B. Schaaf, *Z. Anorg. Allg. Chem.* **1994**, 620, 1041.
- [10] J. Li, B. Marler, H. Kessler, M. Soulard, S. Kallus, *Inorg. Chem.* **1997**, *36*, 4697.
- [11] M.H. Baiyin, L. Ye, Y. L. An, X. Liu, C.Y. Jia, G.L. Ning, *Bull. Chem. Soc. Jpn.* **2005**, *78*, 1283.
- [12] M.H. Baiyin, Y. L. An, X. Liu, M. Ji, C.Y. Jia, G.L. Ning, *Inorg. Chem.* **2004**, *43*, 3764.
- [13] Y. An, B. Menghe, L. Ye, M. Ji, X. Liu, G. Ning, *Inorg. Chem. Comm.* **2005**, *8*, 301.
- [14] W.S. Sheldrick, M. Wachhold, *Angew. Chem.* **1997**, *109*, 241.
- [15] W.S. Sheldrick, *J. Chem. Soc. Dalton Trans.* **2000**, 3041.
- [16] T. Jiang, G.A. Ozin, A. Verma, R.L. Bedard, *J. Mater. Chem.* **1998**, *8*, 1649.
- [17] I. Sokolov, T. Jiang, G.A. Ozin, *Adv. Mater.* **1998**, *10*, 942.
- [18] C.L. Bowes, S. Petrov, G. Vovk, D. Young, G.A. Ozin, R.L. Bedard, *J. Mater. Chem.* **1998**, *8*, 711.
- [19] N. Pienack, C. Näther, W. Bensch, *Solid State Sci.* **2006**, submitted.

- [20] G. M. Sheldrick, SHELXS 97, *Program for the Solution of Crystal Structures* **1997**  
Universität Göttingen.
- [21] G. M. Sheldrick, SHELXL 97, *Program for the Refinement of Crystal Structures* **1997**,  
Universität Göttingen.
- [22] M. Behrens, S. Scherb, C. Näther, W. Bensch, *Z. Anorg. Allg. Chem.* **2003**, 629, 1367.
- [23] T. Jiang, G.A. Ozin, *Adv. Mater.* **1998**, 8, 1099.
- [24] T. Jiang, G.A. Ozin, R.L. Bedard, *J. Mater. Chem.* **1998**, 8, 1641.
- [25] P. Rahls, *Z. Physikal. Chem.* **1936**, B 31, 157.
- [26] S. Kashida, N. Watanabe, T. Hasegawa, H. Iida, M. Mori, S. Savrasov, *Solid State Ionics* **2003**, 158, 167.
- [27] O. Amiel, D.C. Frankel, H. Wada, *J. Solid State Chem.* **1995**, 116, 409.
- [28] N. Wang, *Neues Jhb. Miner.* **1978**, 269.
- [29] Ö. Dag, H. Ahari, N. Coombs, J. Jiang, P.P. Aroca-Quellette, S. Petrov, *Adv. Mater.* **1997**, 9, 1133.
- [30] B. Krebs, W. Schiwy, *Z. Anorg. Allg. Chem.* **1973**, 398, 63.
- [31] B. Krebs, S. Pohl, W. Schiwy, *Angew. Chem.* **1970**, 82, 884.

Table 1: Details of the structure determination of (1,4-dabH<sub>2</sub>)Ag<sub>2</sub>SnS<sub>4</sub> and selected results of the structure refinement. Estimated standard deviations are given in parentheses.

	(1,4-dabH <sub>2</sub> )Ag <sub>2</sub> SnS <sub>4</sub>
Formula	(C <sub>4</sub> H <sub>14</sub> N <sub>2</sub> )Ag <sub>2</sub> SnS <sub>4</sub>
a / Å	14.7847(8)
c / Å	11.9087(6)
V / Å <sup>3</sup>	2603.1(2)
Crystal system	Tetragonal
Space group	P4 <sub>2</sub> /n
Z	8
FW / g·mol <sup>-1</sup>	552.84
D <sub>calc</sub> / g·cm <sup>-3</sup>	2.821
μ / mm <sup>-1</sup>	5.486
Scan range / 2θ°	5.18 to 56.1
Measured reflections	24124
Independent reflections	3143
Reflection with I > 2σ(I)	2717
R <sub>int</sub>	0.0426
No. refined parameters	119
R1 for all F <sub>0</sub> > 4σF <sub>0</sub>	0.0269
wR2 for all data	0.0711
Goodness of fit	1.042
Res. electron density / eÅ <sup>-3</sup>	1.599 / -1.342

Tab. 2: Bond lengths [Å] and angles [°] with the estimated standard deviations given in parentheses.

Sn(1)-S(2)	2.3826(9)	Ag(2)-Ag(1a)	3.1378(5)
Sn(1)-S(4)	2.3846(9)	S(2)-Sn(1)-S(4)	105.73(3)
Sn(1)-S(3)	2.3919(9)	S(2)-Sn(1)-S(3)	112.81(4)
Sn(1)-S(1)	2.3982(9)	S(4)-Sn(1)-S(3)	108.63(3)
Ag(1)-S(2a)	2.4514(10)	S(2)-Sn(1)-S(1)	110.53(3)
Ag(1)-S(1)	2.5029(10)	S(4)-Sn(1)-S(1)	108.52(4)
Ag(1)-S(3b)	2.6019(10)	S(3)-Sn(1)-S(1)	110.41(3)
Ag(1)-Ag(2)	2.9926(5)	S(2a)-Ag(1)-S(1)	130.48(3)
Ag(1)-Ag(1a)	3.1021(7)	S(2a)-Ag(1)-S(3b)	117.92(3)
Ag(1)-Ag(2a)	3.1377(5)	S(1)-Ag(1)-S(3b)	106.27(3)
Ag(2)-S(3b)	2.4921(10)	S(3b)-Ag(2)-S(1c)	133.97(3)
Ag(2)-S(1c)	2.5099(10)	S(3b)-Ag(2)-S(2)	120.16(3)
Ag(2)-S(2)	2.5829(10)	S(1c)-Ag(2)-S(2)	100.83(3)
Ag(2)-Ag(2a)	3.0117(6)		

Symmetry transformations used to generate equivalent atoms: a: -x+3/2,-y+1/2,z; b: -y+1,x-1/2,z-1/2; c: y+1/2,-x+1,z-1/2; d: -y+1,x-1/2,z+1/2; e: y+1/2,-x+1,z+1/2

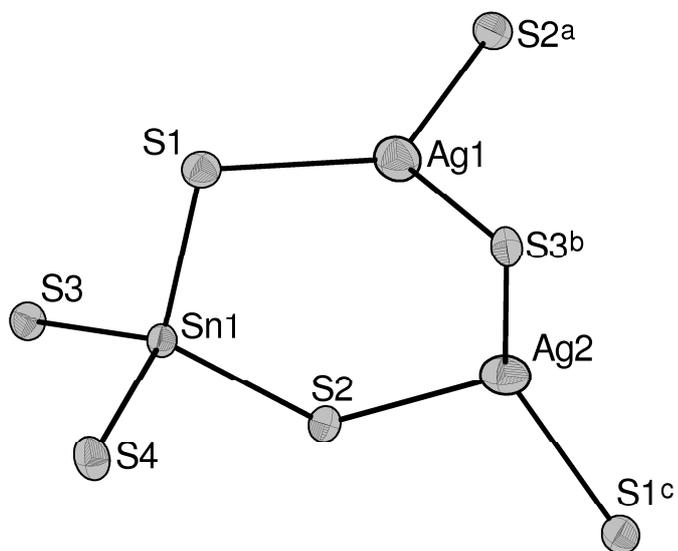


Fig. 1: The  $\text{SnS}_4$  tetrahedron and the two  $\text{AgS}_3$  triangles with labelling. Probability ellipsoids are drawn at the 50% level.

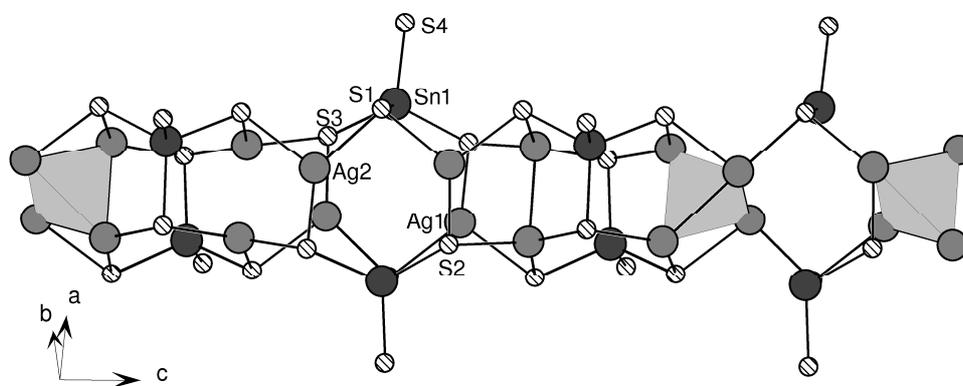


Fig. 2: The one-dimensional anionic chains with the distorted cubes (see text) and some  $\text{Ag}_4$  tetrahedra shown as polyhedron.

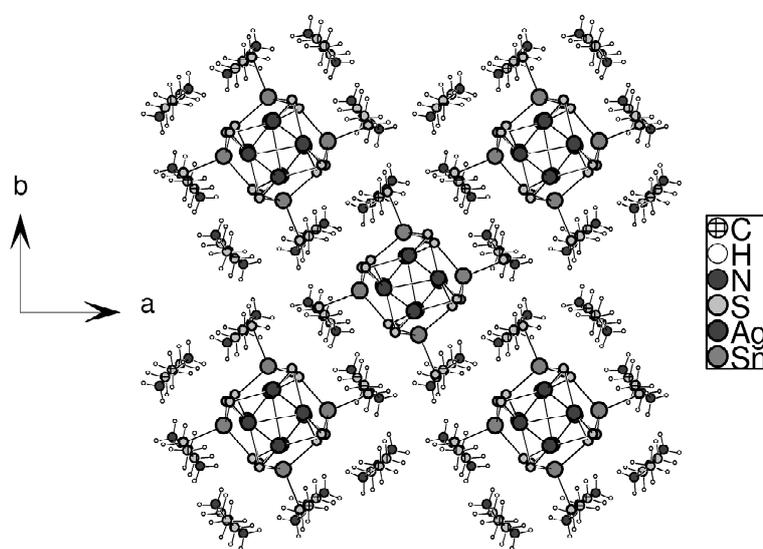


Fig. 3: Arrangement of anionic chains and the cations.

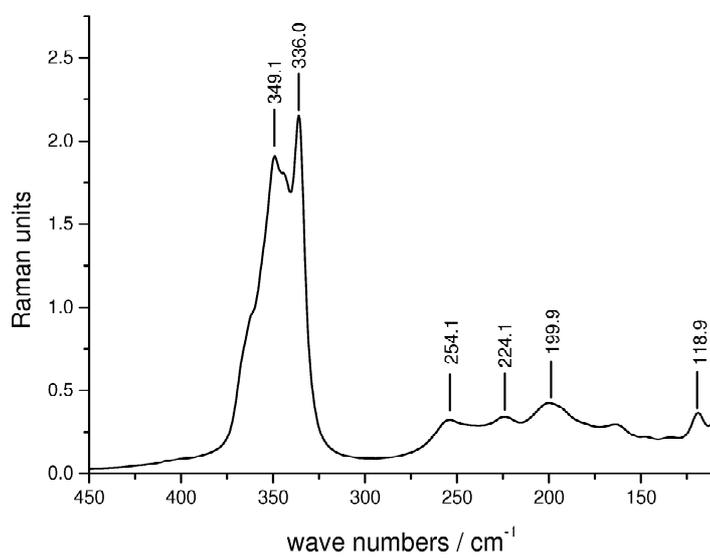
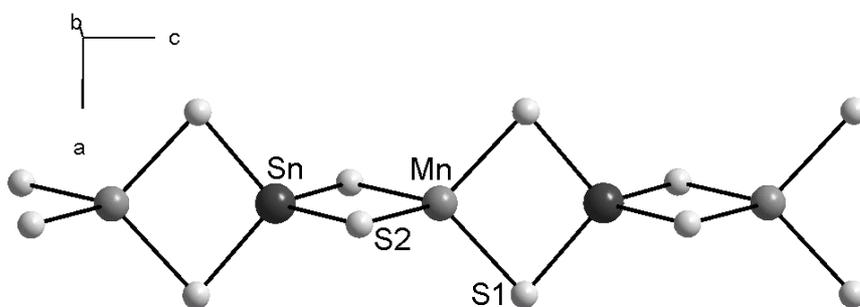


Fig. 4: Raman spectrum for  $(1,4\text{-dabH}_2)\text{Ag}_2\text{SnS}_4$

### 4.1.3. Die Verbindung $(1,4\text{-dabH})_2\text{MnSnS}_4$

*Zusammenfassung der Veröffentlichung “(1,4-dabH)<sub>2</sub>MnSnS<sub>4</sub>: The first thioannate with integrated Mn<sup>2+</sup> ions in an anionic chain structure”.*

Bei der Verwendung von Zinn, Mangan und Schwefel im Verhältnis 1:1:3.3 mmol in 3 mL 1,4-Diaminobutan (1,4-dab, C<sub>4</sub>N<sub>2</sub>H<sub>14</sub>) wird bei 150 °C (120 h) mit anschließender kontrollierter Abkühlung (in 30 h auf 25 °C) das neue Thiostannat  $(1,4\text{-dabH})_2\text{MnSnS}_4$  erhalten. Die Verbindung kristallisiert in der nicht-zentrosymmetrischen orthorhombischen Raumgruppe Fdd2 mit acht Formeleinheiten in der Elementarzelle. Die eindimensionalen anionischen Ketten sind durch einfach protonierte Aminmoleküle getrennt. Sowohl die Sn- als auch die Mn-Atome sind jeweils von vier S-Atomen tetraedrisch umgeben. Das resultierende Strukturmotiv  $[\text{MnSnS}_6]$  ist analog wie das Thiostannat-Anion  $[\text{Sn}_2\text{S}_6]^{4-}$  aufgebaut, wobei ein SnS<sub>4</sub>-Tetraeder durch ein MnS<sub>4</sub>-Tetraeder ersetzt ist. Durch Kantenverknüpfung der  $[\text{MnSnS}_6]$ -Einheiten werden eindimensionale Ketten entlang [001] gebildet (Abb. 4.3).



**Abb. 4.3:** Ausschnitt der eindimensionalen Kette mit Blick entlang [010].

$(1,4\text{-dabH})_2\text{MnSnS}_4$  ist das erste eindimensionale Thiostannat, das Mn<sup>2+</sup>-Ionen in den anionischen Ketten aufweist. Ein weiteres strukturelles Merkmal stellt das Netzwerk der protonierten strukturdirigierenden Aminmoleküle dar. Die Kationen bilden über Wasserstoffbrücken wellenförmige Ketten entlang [100], wobei diese derart angeordnet sind, dass Tunnel in [001]-Richtung entstehen, in denen die anionischen Ketten verlaufen (Abb. 4.4).

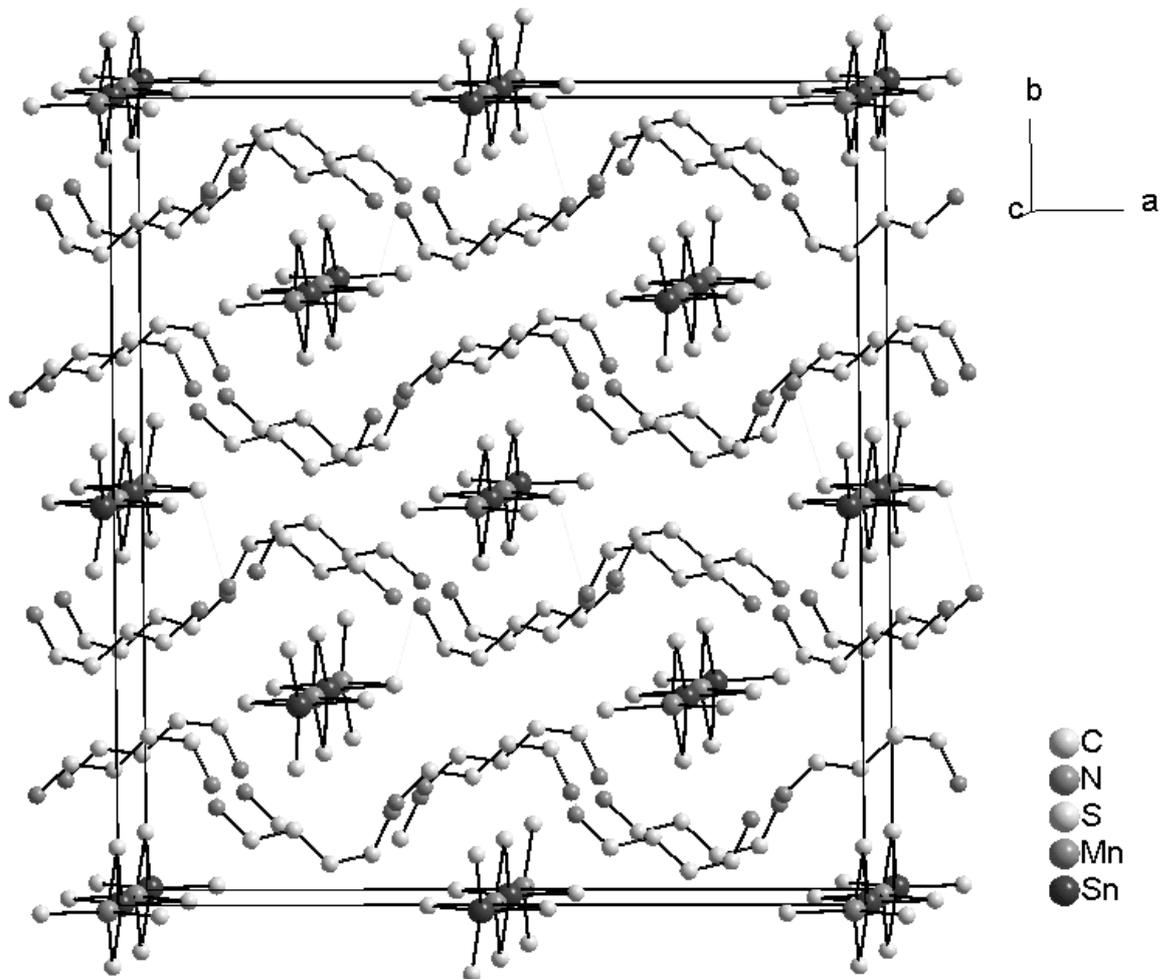


**Abb. 4.4:** Anordnung der anionischen Ketten in den Kanälen der protonierten Aminmoleküle in  $(1,4\text{-dabH})_2\text{MnSnS}_4$ . Die Wasserstoffatome sind zur besseren Übersicht nicht abgebildet.

Das MIR-Spektrum zeigt Absorptionen von Ammonium-Aminobutan, d. h. die Aminmoleküle sind einfach protoniert und damit wird Ladungsneutralität erreicht. Die im Raman-Spektrum beobachteten Schwingungen liegen in dem für Thiostannate typischen Bereich zwischen  $400$  und  $100\text{ cm}^{-1}$ . Bei  $374\text{ cm}^{-1}$  tritt die symmetrische Sn-S-Streckschwingung und bei  $348\text{ cm}^{-1}$  der symmetrische Sn-S<sub>bridging</sub>-Mode auf. Die Resonanz bei  $249\text{ cm}^{-1}$  kann durch eine  $\text{MnS}_2$ -Vibration hervorgerufen werden. Eine genaue Zuordnung der Signale unterhalb von  $200\text{ cm}^{-1}$  ist aufgrund von Gerüstschwingungen in diesem Bereich schwierig und wird deshalb nicht vorgenommen.

Die Auswertung des UV/Vis-Spektrums (diffuse Reflektanz) mit der Kubelka-Munk-Methode ergibt eine optische Bandlücke von  $2.9\text{ eV}$  ( $428\text{ nm}$ ), entsprechend der gelben Farbe der Kristalle.

Die Zersetzung beginnt bei  $T_{\text{Onset}} = 194 \text{ }^{\circ}\text{C}$ . Der Abbau erfolgt in zwei gut aufgelösten, endothermen Stufen ( $T_{\text{Peak1}} = 208 \text{ }^{\circ}\text{C}$ ,  $T_{\text{Peak2}} = 268 \text{ }^{\circ}\text{C}$ ) mit einem Gesamtmassenverlust von 42.5 % entsprechend einer Emission von zwei Molekülen Diaminobutan und einem Molekül Schwefelwasserstoff. Der Rückstand ist weitgehend frei von organischen Komponenten und es können Reflexe von MnS und SnS im Pulverdiffraktogramm identifiziert werden. Wird die thermische Zersetzung bei  $208 \text{ }^{\circ}\text{C}$  unterbrochen, so entspricht der korrespondierende Massenverlust von 24.8 % formal 1.3 Molekülen Diaminobutan. Das röntgenographisch amorphe Pulver hat die über Elementaranalyse ermittelte Zusammensetzung  $(1,4\text{-dabH})_{0.7}\text{MnSnS}_4$ .

Mit magnetischen Untersuchungen konnte die Anwesenheit von  $\text{Mn}^{2+}$  bestätigt werden. Die Curie-Konstante von 4.39 entspricht  $5.92 \mu_{\text{B}}/\text{Mn}^{2+}$  was exakt dem spin-only-Wert von  $\text{Mn}^{2+} d^5$  entspricht. Die Weiss'sche Konstante von -31 K deutet auf antiferromagnetische Austauschwechselwirkungen zwischen den  $\text{Mn}^{2+}$ -Zentren hin (nicht Bestandteil der Veröffentlichung).

Available online at [www.sciencedirect.com](http://www.sciencedirect.com)

Solid State Sciences 9 (2007) 1110–1114

[www.elsevier.com/locate/ssscie](http://www.elsevier.com/locate/ssscie)

## (1,4-dabH)<sub>2</sub>MnSnS<sub>4</sub>: The first thiostannate with integrated Mn<sup>2+</sup> ions in an anionic chain structure

Nicole Pienack, Karina Möller, Christian Näther, Wolfgang Bensch\*

*Institute of Inorganic Chemistry, Christian-Albrechts-University of Kiel, Olshausenstr. 40, 24098 Kiel, Germany*

Available online 6 August 2007

### Abstract

The new thiostannate (1,4-dabH)<sub>2</sub>MnSnS<sub>4</sub> (1,4-dab = 1,4-diaminobutane) was synthesized under solvothermal conditions. The compound crystallizes in the non-centrosymmetric space group *Fdd2* with  $a = 22.8124(15)$  Å,  $b = 24.7887(16)$  Å,  $c = 6.4153(6)$  Å,  $Z = 8$ , and  $V = 3627.8(5)$  Å<sup>3</sup>. The structure consists of one-dimensional straight anionic chains composed of alternating SnS<sub>4</sub> and MnS<sub>4</sub> tetrahedra sharing common edges. The chains are directed along [001] and are surrounded by the organic cations which form undulated chains along [100] by strong intermolecular N–H⋯N hydrogen bonding interactions. Several S⋯H contacts suggest weak interactions between the anionic chains and the cations. The band gap amounts to 2.9 eV indicating that the compound is a photo-conductor. The compound is stable up to about 190 °C and decomposes in two distinct steps above this temperature.

© 2007 Elsevier Masson SAS. All rights reserved.

**Keywords:** Solvothermal synthesis; Crystal structure; Spectroscopic properties; Thermal properties; Thiostannates

### 1. Introduction

The great potential of open-framework thiometalates was impressively demonstrated very recently. New materials were reported which may be suitable as ion-exchangers [1,2], as quantum dots [3] or for photo catalytic applications [4]. In these compounds the semi-conducting properties of chalcogenides are combined with the properties of zeolite-like materials [5–8]. The most common way to synthesize such compounds is the solvothermal approach. Thiostannates containing a transition metal (TM) in the inorganic network should expand the physical and chemical properties of thiometalates [9]. In the past, several TM containing thiostannates were reported, e.g. [Ni(en)<sub>3</sub>]<sub>2</sub>Sn<sub>2</sub>S<sub>6</sub>, [Co(tren)<sub>3</sub>]<sub>2</sub>Sn<sub>2</sub>S<sub>6</sub> [10], [Mn(en)<sub>3</sub>]<sub>2</sub>Sn<sub>2</sub>S<sub>6</sub> [11], [Mn(dien)<sub>2</sub>]<sub>2</sub>Sn<sub>2</sub>S<sub>6</sub> [12] or [Mn(en)<sub>2</sub>]<sub>2</sub>(μ-en)(μ-Sn<sub>2</sub>S<sub>6</sub>)<sub>∞</sub> [13]. In the compounds with ethylenediamine and diethylenetriamine, the structures are composed of discrete [Sn<sub>2</sub>S<sub>6</sub>]<sup>4−</sup> anions and charge compensating cations. This observation is not surprising because these amines form

stable TM<sup>n+</sup> complexes and the central ions are saturated leaving no free binding site to the thiostannate network. Applying the tetrapodal amine tren (tren = tris(2-aminoethyl)-amine), transition metal cations are surrounded by four N atoms leaving one or two binding positions free for bonds to the thiometalate network. The potential of such multidentate amines was previously demonstrated and examples are the thioantimonates [Fe(tren)]Sb<sub>4</sub>S<sub>7</sub> [14], [Co(tren)]<sub>2</sub>Sb<sub>2</sub>S<sub>5</sub> [15] and [Ni(tren)](Sb<sub>2</sub>S<sub>4</sub>) [16]. For Mn<sup>2+</sup>, the situation seems to be different compared with ions like Co<sup>2+</sup>, Ni<sup>2+</sup>, or Fe<sup>2+</sup>. In a number of thiometalates Mn<sup>2+</sup> is part of the inorganic network even when mono- or bidentate amines are applied. Some examples are Mn<sub>2</sub>Sb<sub>2</sub>S<sub>5</sub>(CH<sub>3</sub>NH<sub>2</sub>)<sub>2</sub> [17], Mn<sub>2</sub>(H<sub>2</sub>N(CH<sub>2</sub>)<sub>2</sub>NH<sub>2</sub>)<sub>2</sub>Sb<sub>2</sub>S<sub>5</sub> [18], Mn<sub>2</sub>(C<sub>2</sub>H<sub>5</sub>NH<sub>2</sub>)<sub>2</sub>Sb<sub>2</sub>S<sub>5</sub> [19] and Mn<sub>2</sub>(C<sub>4</sub>H<sub>12</sub>N<sub>2</sub>)Sb<sub>2</sub>S<sub>5</sub> [20]. It can be assumed that Mn<sup>2+</sup> has a comparable tendency to form bonds to S and N atoms and the application of multidentate amines is not required to incorporate Mn<sup>2+</sup> into the inorganic network.

Here we reported the synthesis, crystal structure, spectroscopic and thermal properties of (1,4-dabH)<sub>2</sub>MnSnS<sub>4</sub> (1,4-dab = 1,4-diaminobutane) which is the first one-dimensional thiostannate compound containing Mn<sup>2+</sup> as part of the anionic chains.

\* Corresponding author. Tel.: +49 431 880 2419, fax: +49 431 880 1520.  
E-mail address: [wbensch@ac.uni-kiel.de](mailto:wbensch@ac.uni-kiel.de) (W. Bensch).

## 2. Experimental details

### 2.1. Synthesis

**General:** the compound was prepared under solvothermal conditions in Teflon-lined steel autoclaves (inner volume: 30 mL) reacting manganese, tin and sulfur. The crystalline product was filtered off after the reaction, washed with water and ethanol, and dried in vacuum.

Synthesis of (1,4-dabH)<sub>2</sub>MnSnS<sub>4</sub>: 1 mmol Sn (99.5%, Aldrich), 1 mmol Mn (99.5%, Alfa Aesar), 3.3 mmol S in 3 mL of 1,4-diaminobutane (≥98.0%, Fluka) were reacted for 120 h at 150 °C, then cooled to 25 °C in 30 h. Yellow rods in 10% yield were found in the reaction product. The main products were Sn and Mn sulfides. All attempts to improve the yield of the title compound by variation of synthesis parameters like reaction temperature, time, addition of water, heating and cooling procedure were not successful. The yield was always low and in best syntheses gave about 10% (based on Sn). The X-ray powder patterns of hand-picked crystals are in full accordance with the pattern calculated from single crystal data. Elemental analysis of the yellow rods (%): found: C 20.28, H 5.54, N 11.57, S 25.31; calculated: C 20.01, H 5.46, N 11.67, S 24.72.

### 2.2. Structure determination

The intensity data were collected using a PHILIPS PW 1100 diffractometer with Mo K $\alpha$  radiation ( $\lambda = 0.7107 \text{ \AA}$ ) at room temperature. The structure was solved with direct methods using the program SHELXS 97 [21] and the refinement was done against  $F^2$  with SHELXL 97 [22]. Anisotropic displacement parameters were used for C, N, Mn, Sn and S atoms. The H atoms of the amine were positioned with idealized geometry and refined using a riding model and a fixed isotropic displacement parameter. The absolute structure was determined and is in agreement with the selected setting (Flack  $x$ -parameter:  $-0.01(2)$ ). Some selected refinement results are summarized in Table 1. Further crystallographic information has been deposited with the Cambridge Crystallographic Data Centre as publication no. CCDC 637210. Copies of the data can be obtained, free of charge, on application to CCDC, 12 Union Road, Cambridge CB2 1EZ, UK (e-mail: deposit@ccdc.ca.ac.uk).

### 2.3. Thermal investigations

DTA–TG analyses were done using a Netzsch STA 429 DTA–TG device. The samples were heated to 600 °C at a rate of 4 K min<sup>-1</sup> under a flow of argon (75 mL min<sup>-1</sup>) in Al<sub>2</sub>O<sub>3</sub> crucibles. The TG data were corrected for buoyancy and current effects.

### 2.4. Spectroscopy

**Raman:** The Raman spectra were measured in the region from 100 to 3500 cm<sup>-1</sup> with a Bruker IFS 66 Fourier transform Raman spectrometer (wavelength: 541.5 nm).

Table 1

Selected technical details of data collection and results of the structure refinement of the title compound

(1,4-dabH) <sub>2</sub> MnSnS <sub>4</sub>	
Crystal system	Orthorhombic
Space group	<i>Fdd2</i>
<i>a</i> /Å	22.8124(15)
<i>b</i> /Å	24.7887(16)
<i>c</i> /Å	6.4153(6)
<i>V</i> /Å <sup>3</sup>	3627.8(5)
<i>Z</i>	8
<i>D</i> <sub>calc</sub> /g cm <sup>-3</sup>	1.758
$\mu$ /mm <sup>-1</sup>	2.524
Scan range	2.43° ≤ 2 $\theta$ ≤ 30.02°
Reflections collected	3122
Refl. with $F_o > 4\sigma(F_o)$	1928
Independent reflections	2632
GOF	1.046
Final <i>R</i> indices	
[ <i>I</i> > 2 $\sigma(I)$ ]	<i>R</i> 1 = 0.0184, <i>wR</i> 2 = 0.0494
<i>R</i> indices (all data)	<i>R</i> 1 = 0.0217, <i>wR</i> 2 = 0.0504
Res. Elec. Dens./eÅ <sup>-3</sup>	0.476/−0.732
Flack <i>x</i> -parameter	−0.01(2)

**UV/vis:** UV/vis spectroscopic investigations were conducted at room temperature using an UV–vis–NIR two-channel spectrometer Cary 5 from Varian Techtron Pty., Darmstadt. The absorption data were calculated with the Kubelka–Munk relation for diffuse reflectance data. BaSO<sub>4</sub> powder was used as reference material.

### 2.5. Scanning electron microscopy (SEM)/energy dispersive X-ray fluorescence (EDX)

The EDX analyses have been carried out with a Philips ESEM XL30 equipped with an EDAX detector.

### 2.6. Elemental analysis

CHNS analyses were done using a EURO EA elemental analyzer, fabricated by EURO VECTOR Instruments and Software.

## 3. Results and discussion

### 3.1. Crystal structure

The new compound (1,4-dabH)<sub>2</sub>MnSnS<sub>4</sub> crystallizes in the non-centrosymmetric, orthorhombic space group *Fdd2* with Sn and Mn being located on special positions, whereas all other atom are on general positions. The one-dimensional anionic chains are separated by the single-protonated amine molecules. The Sn atoms as well as the Mn atoms are in a tetrahedral environment of four S atoms. SnS<sub>4</sub> tetrahedra are very common and can be found in many compounds containing discrete [Sn<sub>2</sub>S<sub>6</sub>]<sup>2-</sup> anions like [Mn(en)<sub>3</sub>]<sub>2</sub>Sn<sub>2</sub>S<sub>6</sub> [11]. The Sn–S distances (2.3832(7)–2.3958(7) Å) and the corresponding S–Sn–S angles (99.66(4)–115.467(15)°) suggest a slight distortion (Table 2), but all parameters are in the range

1112

N. Pienack et al. / Solid State Sciences 9 (2007) 1110–1114

Table 2  
Selected bond lengths [Å] and angles [°] for (1,4-dabH)<sub>2</sub>MnSnS<sub>4</sub>

Sn(1)–S(1)	2.3832(7)	S(1) <sup>a</sup> –Mn(1)–S(1)	95.09(7)
Sn(1)–S(2)	2.3958(7)	S(1)–Mn(1)–S(2) <sup>c</sup>	117.928(14)
Sn(1)–Mn(1)	3.2027(13)	S(1)–Mn(1)–S(2) <sup>d</sup>	116.145(14)
Sn(1)–Mn(1) <sup>b</sup>	3.2126(13)	S(2) <sup>c</sup> –Mn(1)–S(2) <sup>d</sup>	95.36(7)
Mn(1)–S(1)	2.4724(14)		
Mn(1)–S(2) <sup>c</sup>	2.4761(14)	S(1)–Sn(1)–Mn(1)	49.942(18)
N(1)–C(1)	1.485(3)	S(2)–Sn(1)–Mn(1)	130.170(19)
N(2)–C(4)	1.482(3)	S(1)–Sn(1)–Mn(1) <sup>b</sup>	130.058(19)
C(3)–C(4)	1.510(3)	S(2)–Sn(1)–Mn(1) <sup>b</sup>	49.830(19)
C(3)–C(2)	1.528(3)	S(1)–Mn(1)–Sn(1)	47.54(3)
C(1)–C(2)	1.511(3)	S(2) <sup>c</sup> –Mn(1)–Sn(1)	132.32(4)
		S(1)–Mn(1)–Sn(1) <sup>d</sup>	132.46(3)
S(1) <sup>a</sup> –Sn(1)–S(1)	99.88(4)	S(2) <sup>c</sup> –Mn(1)–Sn(1) <sup>d</sup>	47.68(4)
S(1) <sup>a</sup> –Sn(1)–S(2)	115.467(15)	Sn(1)–S(1)–Mn(1)	82.51(3)
S(1)–Sn(1)–S(2)	113.595(15)	Mn(1)–Sn(1)–Mn(1) <sup>b</sup>	180.000(1)
S(2) <sup>a</sup> –Sn(1)–S(2)	99.66(4)	Sn(1)–Mn(1)–Sn(1) <sup>d</sup>	180.0

Symmetry transformations used to generate equivalent atoms:

$$^a -x + 1, -y + 1, z.$$

$$^b x, y, z + 1.$$

$$^c -x + 1, -y + 1, z - 1.$$

$$^d x, y, z - 1.$$

reported in the literature [10,23]. Mn<sup>2+</sup> is in a tetrahedral environment of S atoms which is less common than the octahedral surrounding and some examples with MnS<sub>4</sub> tetrahedra are [Mn(tren)]<sub>4</sub>Mn<sub>2</sub>Sb<sub>4</sub>S<sub>12</sub> [24] and [Mn(tren)]<sub>2</sub>Mn<sub>2</sub>Sb<sub>4</sub>S<sub>10</sub> [25]. The Mn–S bond lengths are 2.4724(14) and 2.4761(14) Å being very similar to those reported for K<sub>10</sub>Mn<sub>4</sub>Sn<sub>4</sub>S<sub>17</sub> [26], [Mn(tren)]<sub>4</sub>Mn<sub>2</sub>Sb<sub>4</sub>S<sub>12</sub> or [Mn(tren)]<sub>2</sub>Mn<sub>2</sub>Sb<sub>4</sub>S<sub>10</sub>. The observed S–Mn–S angles vary between 95.09(7)° and 117.928(14)° indicative for a pronounced distortion of the tetrahedron.

The [Sn<sub>2</sub>S<sub>6</sub>]<sup>4-</sup> moiety composed of two edge-sharing SnS<sub>4</sub> tetrahedra is a well known structural motif [27,28]. In the title compound, one SnS<sub>4</sub> tetrahedron is substituted by one MnS<sub>4</sub> tetrahedron to form a MnSnS<sub>6</sub> unit. A linear one-dimensional chain along [001] is formed by condensation of [MnSnS<sub>2</sub>S<sub>4/2</sub>]<sup>2-</sup> groups. The central non-centrosymmetric MnSnS<sub>2</sub> rings of the chains are planar like the Sn<sub>2</sub>S<sub>2</sub> rings in the [Sn<sub>2</sub>S<sub>6</sub>]<sup>4-</sup> anions (Fig. 1). The rings of neighboring units are rotated by 90° to each other. The distances between Sn<sup>4+</sup> and Mn<sup>2+</sup> are 3.2027(13) and 3.2126(13) Å, which are too long for interatomic interactions.

The anionic chains are surrounded by six protonated cations (Fig. 2). In a solvothermal synthesis applying amines as solvents, the reaction with sulfur yields polysulfide anions, polysulfide radicals, thiosulfate ions and so on. Furthermore, the amines are redox active and it is not surprising that

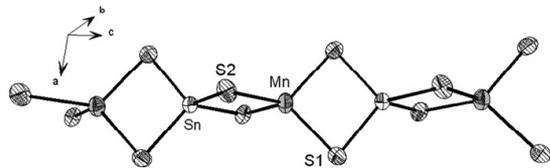


Fig. 1.

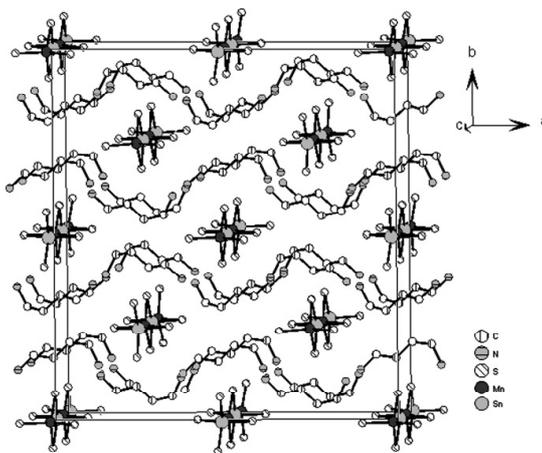


Fig. 2.

protonated amine molecules occur in the resulting structures. Interestingly, the cations form a network and undulated chains propagating along [100] are observed due to the strong N–H···N bond (N1–H1a···N2 distance: 1.962 Å, angle: 164.11°) between protonated and unprotonated N atoms (Fig. 3). The chains are arranged in a way that tunnels directed along [001] are generated which host the anionic chains. The atom S2 has two contacts to H atoms of two amine molecules (S2···H: 2.474, 2.734 Å; N–H···S angles: 165.3°, 152.2°) and S1 has one such interaction (S<sub>1</sub>···H: 2.498 Å, N–H···S angle: 154.3°). The relatively short S···H distances as well as the angles indicate hydrogen bonding interactions between the anionic chains and the cations (Fig. 4).

### 3.2. Spectroscopic properties

Charge neutrality of the material requires that the amine molecules are single protonated. In the MIR spectra, all absorptions can be assigned to the ammonium–aminobutane molecule. Primary amines produce two N–H stretching absorptions at 3470 and 3320 cm<sup>-1</sup> and the absorptions located at 1540, 1600 and 3240 cm<sup>-1</sup> are caused by R–NH<sub>3</sub><sup>+</sup> groups. In the Raman spectrum, the resonances at 374, 348 and 249 cm<sup>-1</sup> are in the typical region for Sn–S resonances [29,30]. The symmetric Sn–S stretching vibration is located at 374 cm<sup>-1</sup> and the resonance at 348 cm<sup>-1</sup> can be assigned

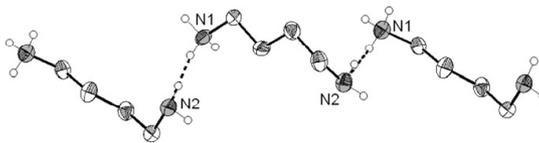


Fig. 3.

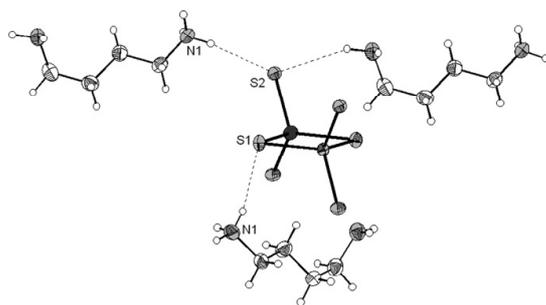


Fig. 4.

to a symmetric Sn–S bridging mode. The resonance at  $249\text{ cm}^{-1}$  may be caused by a  $\text{MnS}_2$  vibration [31]. The assignment of the last two modes is difficult due to the lattice vibrations.

### 3.3. UV/vis spectroscopy

The optical band gap was determined from transformed UV/vis diffuse reflectance spectra (Kubelka–Munk method). The value of  $2.9\text{ eV}$  ( $428\text{ nm}$ ) (Fig. 5) is in agreement with the yellow color of the crystals.

### 3.4. Thermal stability

The DTA–TG–DTG curves are shown in Fig. 6. The compound starts to decompose at  $T_{\text{onset}} = 194\text{ }^\circ\text{C}$  with an endothermic signal at  $T_p = 208\text{ }^\circ\text{C}$ . The associated mass loss is 30%. A second step occurs at  $T_{\text{onset}} = 249\text{ }^\circ\text{C}$  ( $T_p = 268\text{ }^\circ\text{C}$ ) which is accompanied by a further weight change of 12.5%. The total weight loss of 42.5% is in good agreement with the theoretical value for the emission of two diaminobutane molecules and one  $\text{H}_2\text{S}$  molecule. The residue is nearly free of organic contaminants (CHN:  $\sim 2\%$ ). In the X-ray powder

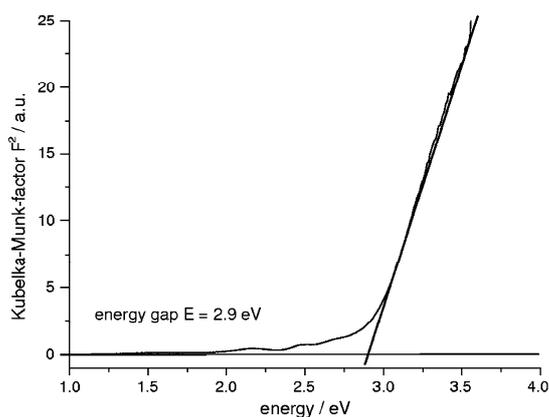


Fig. 5.

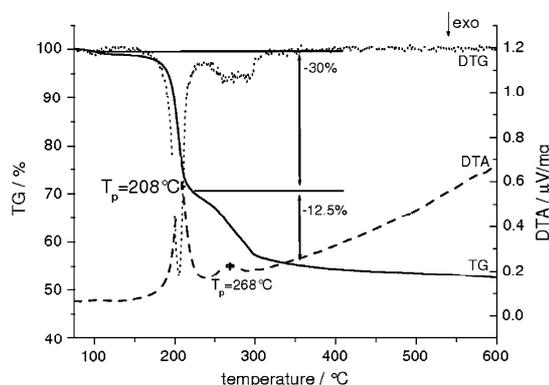
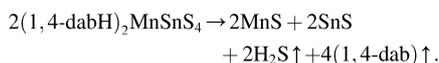


Fig. 6.

pattern  $\text{MnS}$  and  $\text{SnS}$  could be identified and the reaction pathway probably proceeds as:



Interrupting the thermal decomposition at  $208\text{ }^\circ\text{C}$  the powder changed the color to dark yellow. The mass loss of 24.8% corresponds to the emission of about 1.3 molecules of 1,4-diaminobutane. In the powder pattern no reflections are observed and the elemental analysis yields the composition  $(1,4\text{-dabH})_{0.7}\text{MnSnS}_4$ .

## 4. Conclusion

In this work we presented the solvothermal synthesis of a new manganese containing thiostannate. There are two interesting structural features in the structure of  $(1,4\text{-dabH})_2\text{MnSnS}_4$ . The  $\text{SnS}_4$  tetrahedron shares an edge with the  $\text{MnS}_4$  tetrahedron yielding the high negatively charged  $[\text{MnSnS}_6]^{6-}$  anion. The one-dimensional chains running along  $[001]$  are made of  $[\text{MnSnS}_6]^{6-}$  groups sharing two edges with adjacent units. The second structural highlight is the network of the protonated structure directing molecules. Until now there are only few examples for thiometalates, e.g. (*trans*-1,4- $\text{C}_6\text{N}_2\text{H}_{15}$ ) $\text{Sb}_3\text{S}_5$  and (*trans*-1,2- $\text{C}_6\text{N}_2\text{H}_{15}$ ) $\text{Sb}_3\text{S}_5$  [32], where hydrogen bonds join the protonated amine molecules to form chains or layers.

Recently, we published two new thiostannates with 1,4-diaminobutane as structure directing molecule  $(1,4\text{-dabH}_2)\text{-Cu}_2\text{SnS}_4$  [33] and  $(1,4\text{-dabH}_2)\text{Ag}_2\text{SnS}_4$  [34]. In these compounds the Cu/Ag atoms form distorted tetrahedral  $\text{Cu}_4$  respectively  $\text{Ag}_4$  units. Two such units are joined via two S atoms yielding  $\text{Cu}_8\text{S}_2$  ( $\text{Ag}_8\text{S}_2$ ) groups which are interconnected by two  $\text{SnS}_4$  tetrahedra to form chains. While these two compounds are isostructural, the title compound adopts a new structure type. It is interesting to note that all three compounds were synthesized under analogous synthesis conditions. An obvious difference between the three compounds

is the fact that Cu and Ag occur always as  $\text{Cu}^{\text{I}}/\text{Ag}^{\text{I}}$  in an environment of S atoms, whereas  $\text{Mn}^{2+}$  is the most stable oxidation state in sulfides and/or thiometalates. Therefore, the ratio of M/Sn (M = Cu, Ag, Mn) is 1:1 in the present compound and 2:1 in the former thioannates. Another interesting difference between the compounds is the occurrence of a double-protonated amine molecule in the Cu/Ag containing thioannates, whereas the title compound contains a single-protonated amine. Further experiments are under way to elucidate whether a larger amount of  $\text{Mn}^{2+}$  can be incorporated into thioannate networks.

## References

- [1] M.J. Manos, R.G. Iyer, E. Quarez, J.H. Liao, M.G. Kanatzidis, *Angew. Chem.* 117 (2005) 3618.
- [2] M.J. Manos, K. Chrissafis, M.G. Kanatzidis, *J. Am. Chem. Soc.* 128 (2006) 8875.
- [3] N. Zheng, X. Bu, H. Lu, Q. Zhang, P. Feng, *J. Am. Chem. Soc.* 127 (2005) 11963.
- [4] N. Zheng, X. Bu, H. Vu, P. Feng, *Angew. Chem.* 117 (2005) 5433.
- [5] H. Ahari, C.L. Bowes, T. Jiang, A. Lough, G.A. Ozin, R.L. Bedard, S. Petrov, D. Young, *Adv. Mater.* 7 (1995) 375.
- [6] H. Ahari, G.A. Ozin, R.L. Bedard, S. Petrov, D. Young, *Adv. Mater.* 7 (1995) 370.
- [7] T. Jiang, G.A. Ozin, R.L. Bedard, *Adv. Mater.* 7 (1995) 166.
- [8] P. Enzel, G.S. Henderson, G.A. Ozin, R.L. Bedard, *Adv. Mater.* 7 (1995) 64.
- [9] T. Jiang, A. Lough, G.A. Ozin, *Adv. Mater.* 10 (1998) 42.
- [10] M. Behrens, S. Scherb, C. Näther, W. Bensch, *Z. Anorg. Allg. Chem.* 629 (2003) 1367.
- [11] D.-X. Jia, Y. Zhang, J. Dai, Q.-Y. Zhu, X.-M. Gu, *Z. Anorg. Allg. Chem.* 630 (2004) 313.
- [12] M.-L. Fu, G.-C. Guo, B. Liu, A.-Q. Wu, J.-S. Huang, *Chin. J. Inorg. Chem.* 21 (2005) 21.
- [13] X.-M. Gu, J. Dai, D.-X. Jia, Y. Zhang, Q.-Y. Zhu, *Cryst. Growth Des.* 5 (2005) 1845.
- [14] M. Schaefer, R. Stähler, R. Kiebach, C. Näther, W. Bensch, *Z. Anorg. Allg. Chem.* 630 (2004) 1816.
- [15] R. Stähler, W. Bensch, *J. Chem. Soc., Dalton Trans.* (2001) 2518.
- [16] R. Stähler, W. Bensch, *Eur. J. Inorg. Chem.* (2001) 3073.
- [17] W. Bensch, M. Schur, *Eur. J. Solid State Inorg. Chem.* 33 (1996) 1149.
- [18] M. Schur, W. Bensch, *Z. Naturforsch.* 57b (2002) 1.
- [19] M. Schur, C. Näther, W. Bensch, *Z. Naturforsch.* 56b (2001) 79.
- [20] L. Engelke, R. Stähler, M. Schur, C. Näther, W. Bensch, R. Pöttgen, M.H. Möller, *Z. Naturforsch.* 59b (2004) 869.
- [21] G.M. Sheldrick, SHELXS 97, Program for the Solution of Crystal Structures, University of Göttingen, Germany, 1997.
- [22] G.M. Sheldrick, SHELXL 97, Program for the Refinement of Crystal Structures, University of Göttingen, Germany, 1997.
- [23] T. Jiang, G.A. Ozin, R.L. Bedard, *J. Mater. Chem.* 8 (1998) 1641.
- [24] M. Schaefer, C. Näther, W. Bensch, *Solid State Sci.* 5 (2003) 1135.
- [25] M. Schaefer, C. Näther, N. Lehnert, W. Bensch, *Inorg. Chem.* 43 (2004) 2914.
- [26] O. Palchik, R.G. Iyer, J.H. Liao, M.G. Kanatzidis, *Inorg. Chem.* 42 (2003) 5052.
- [27] T. Jiang, A. Lough, G.A. Ozin, R.L. Bedard, R. Broach, *J. Mater. Chem.* 8 (1998) 721.
- [28] T. Jiang, A. Lough, G.A. Ozin, R.L. Bedard, *J. Mater. Chem.* 8 (1998) 733.
- [29] B. Krebs, W. Schiwy, *Z. Anorg. Allg. Chem.* 398 (1973) 63.
- [30] B. Krebs, S. Pohl, W. Schiwy, *Angew. Chem.* 82 (1970) 884.
- [31] J.L. Verble, F.M. Humphrey, *Solid State Commun.* 15 (1974) 1693.
- [32] L. Engelke, C. Näther, W. Bensch, *Eur. J. Inorg. Chem.* (2002) 2936.
- [33] N. Pienack, C. Näther, W. Bensch, *Solid State Sci.* 9 (2007) 100.
- [34] N. Pienack, W. Bensch, *Z. Anorg. Allg. Chem.* 632 (2006) 1733.

#### 4.1.4. Die Verbindung $(\text{dienH}_2)\text{Cu}_2\text{Sn}_2\text{S}_6$

Zusammenfassung der Veröffentlichung "The Layered Thiostannate  $(\text{dienH}_2)\text{Cu}_2\text{Sn}_2\text{S}_6$  – a Photoconductive Inorganic-Organic Hybrid Compound".

Die Verbindung  $(\text{dienH}_2)\text{Cu}_2\text{Sn}_2\text{S}_6$  (dien = Diethylentriamin,  $\text{C}_4\text{N}_3\text{H}_{13}$ ) wird unter solvothermalen Bedingungen aus den Elementen  $\text{Cu}:\text{Sn}:\text{S} = 0.5:0.5:2$  mmol in 6 mL Diethylentriamin erhalten. Das Reaktionsgemisch wird entweder für 120 h bei  $170\text{ }^\circ\text{C}$  getempert und anschließend in 30 h auf  $25\text{ }^\circ\text{C}$  abgekühlt oder unter Rühren für 30 h auf  $170\text{ }^\circ\text{C}$  erhitzt. Die Verbindung kristallisiert in Form schwarzer Plättchen in der tetragonalen Raumgruppe  $\bar{1}4m2$  mit vier Formeleinheiten in der Elementarzelle. Die Struktur besteht aus anionischen  $[\text{Cu}_2\text{Sn}_2\text{S}_6]^{2-}$ -Schichten in der (001)-Ebene und protonierten Aminmolekülen als ladungskompensierende Kationen, die zwischen den Schichten angeordnet sind (Abb. 4.5). Das  $[\text{Cu}_2\text{Sn}_2\text{S}_6]^{2-}$ -Schichtanion besteht aus einer Schicht, welche durch allseitig eckenverknüpfte  $\text{CuS}_4$ -Tetraeder (mit  $\text{Cu}_4\text{S}_4$ -Ringen) gebildet wird und aus Ketten eckenverknüpfter  $\text{SnS}_4$ -Tetraeder, welche diese Schicht sandwichartig umgeben.

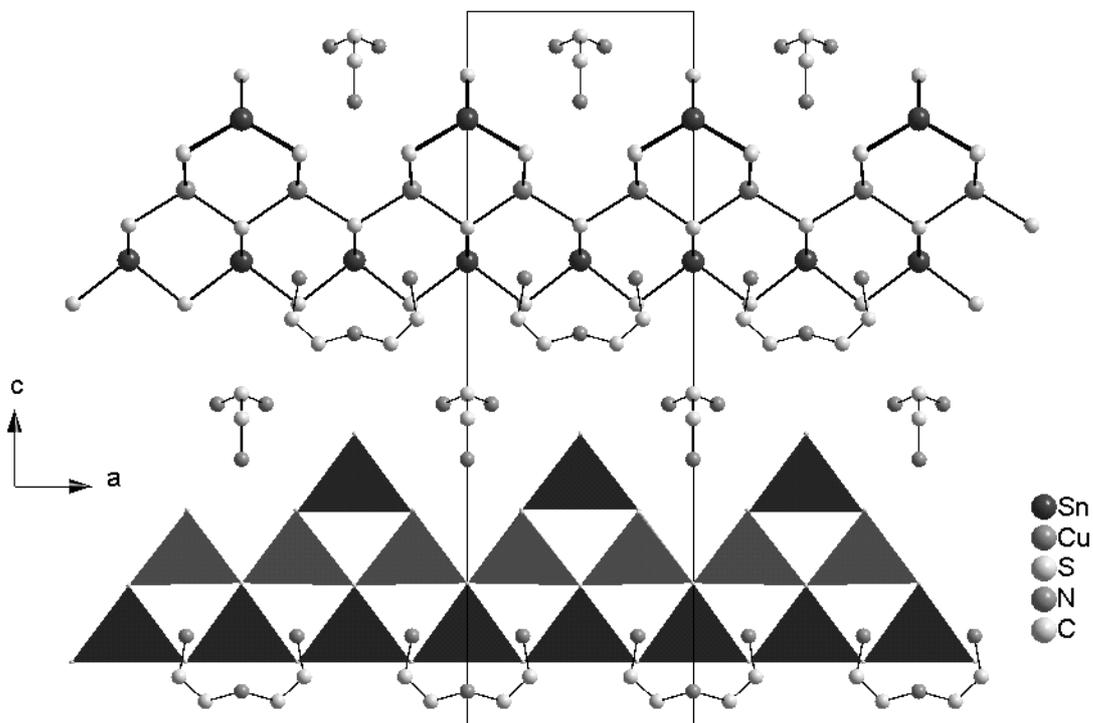


Abb. 4.5: Anordnung der  $[\text{Cu}_2\text{Sn}_2\text{S}_6]^{2-}$ -Schichten und der Kationen in den Zwischenschichten. In der unteren anionischen Schicht sind die  $\text{CuS}_4$ - (grau) und  $\text{SnS}_4$ -Tetraeder (dunkelgrau) als Polyeder dargestellt. Die H-Atome sind zur besseren Übersicht nicht abgebildet.

Die Ladungsneutralität verlangt zweifach protonierte Aminmoleküle zur Ladungskompensation der Anionenschichten, was im MIR-Spektrum durch die typischen Absorptionen primärer, protonierter Amine nachgewiesen werden konnte. Im Raman-Spektrum werden Resonanzen zwischen 400 und 100  $\text{cm}^{-1}$  beobachtet, wobei die symmetrische Sn-S-Streckschwingung bei 373  $\text{cm}^{-1}$  auftritt, bei 301  $\text{cm}^{-1}$  der Sn-S<sub>bridging</sub>-Mode und bei 233  $\text{cm}^{-1}$  das SnS<sub>2</sub> „wagging and twisting“. Cu-S-Vibrationen können dem Signal bei 267  $\text{cm}^{-1}$  zugeordnet werden. Die Verbindung ist ein Halbleiter mit einer optischen Bandlücke von 1.51 eV. Dieser Wert entspricht dem optimalen Bandlückenabstand photoleitender Materialien (zum Vergleich: CdTe 1.5 eV, GaAs 1.4 eV). Die Auswertung der UV/Vis-Spektren (Auftragung  $((\alpha/S) \cdot E)^2$  gegen Energie) lässt den Schluss zu, dass es sich um einen direkten Halbleiter handelt. Widerstands- bzw. Leitfähigkeitsmessungen mittels Impedanzspektroskopie ergeben einen spezifischen Widerstand von  $R_{\text{RT}} = 7.22 \cdot 10^6 \Omega \cdot \text{cm}$  bzw. eine Leitfähigkeit von  $\sigma_{\text{RT}} = 1.38 \cdot 10^{-7} \Omega^{-1} \cdot \text{cm}^{-1}$ . Diese Werte liegen in der Größenordnung von undotiertem GaAs ( $10^8 \Omega \cdot \text{cm}$ ) und CdTe ( $10^9 \Omega \cdot \text{cm}$ ) [106]. Viel interessanter ist die Beobachtung, dass das Material photoleitende Eigenschaften aufzeigt. Die Bestrahlung der Probe mit UV-Licht führt zu einer (reversiblen) Abnahme des spezifischen Widerstands um den Faktor 3 (vgl. Abb. 4.6).

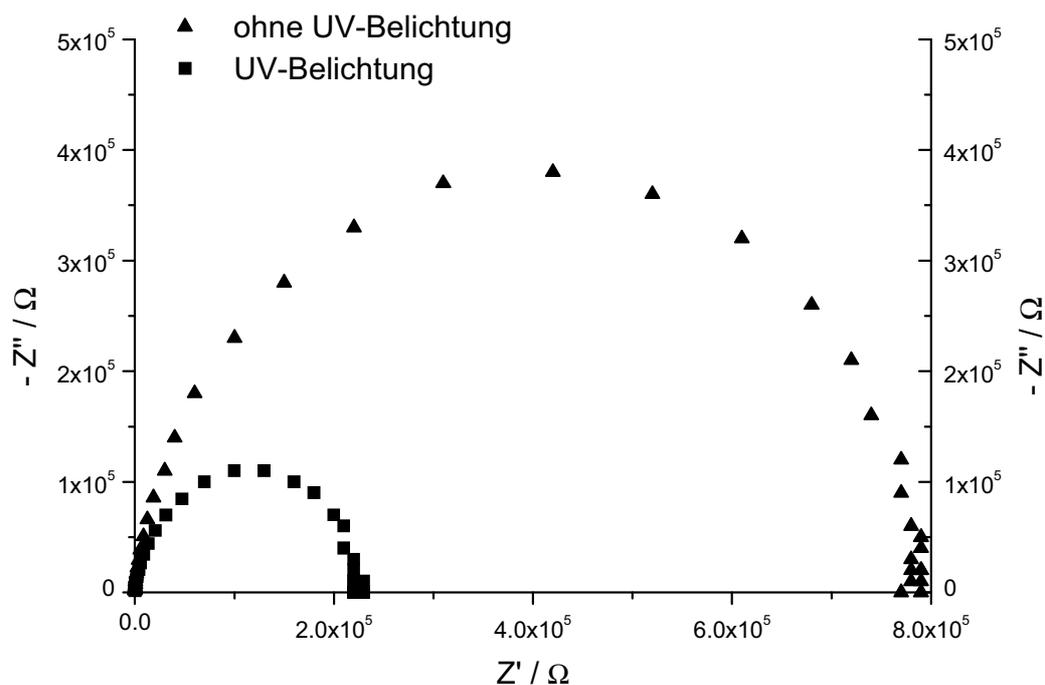


Abb. 4.6: Nyquist-Plots der Impedanzmessungen ohne und unter UV-Belichtung.

Die vorläufigen Ergebnisse der Untersuchungen zur Photoleitfähigkeit sind viel versprechend; vor weiteren Messungen müssen allerdings einige Schwierigkeiten behoben werden. Die recht geringe Leitfähigkeit muss durch Dotieren mit geeigneten Fremdatomen verbessert werden.

Wird die Verbindung unter Schutzgasatmosphäre erhitzt, so beginnt die Zersetzung bei  $T_{\text{Onset}} = 256 \text{ °C}$ . Der Abbau erfolgt in einer (endothermen) Stufe mit einer Peaktemperatur von  $262 \text{ °C}$ , die mit einem Gesamtmassenverlust von  $23.5 \%$  einhergeht. Die Reflexe von SnS und  $\text{Cu}_2\text{SnS}_3$  können im Pulverdiffraktogramm des Rückstands identifiziert werden.

Reproduced with permission from N. Pienack, A. Puls, C. Näther, W. Bensch: The Layered Thiostannate  $(\text{dienH}_2)\text{Cu}_2\text{Sn}_2\text{S}_6$  – a Photoconductive Inorganic–Organic Hybrid Compound; *Inorg. Chem.*, accepted 30.07.08.

Copyright 2008 American Chemical Society.

ohio2/yic-yic/yic-yic/99907/yic4753d07z	xppws	23:ver.5	8/27/08	15:50	Msc: ic-2008-00118z	TEID: lrk00	BATID: ic10b27
---	-------	----------	---------	-------	---------------------	-------------	----------------

*Inorg. Chem.* XXXX, xx, 0

**Inorganic Chemistry**  
: Article

## The Layered Thiostannate $(\text{dienH}_2)\text{Cu}_2\text{Sn}_2\text{S}_6$ : a Photoconductive Inorganic–Organic Hybrid Compound

Nicole Pienack, Angela Puls, Christian Näther, and Wolfgang Bensch\*

*Institute of Inorganic Chemistry, Christian-Albrechts-University of Kiel, Olshausenstrasse 40-60, 24098 Kiel, Germany*

Received January 22, 2008

The new inorganic–organic hybrid compound  $(\text{dienH}_2)\text{Cu}_2\text{Sn}_2\text{S}_6$  (dien = diethylenetriamine) was synthesized under solvothermal conditions. It crystallizes in the tetragonal space group  $I4m2$  with  $a = 7.8793(3)$  Å,  $c = 24.9955(15)$  Å, and  $V = 1551.80(13)$  Å<sup>3</sup>. The structure consists of anionic  $[\text{Cu}_2\text{Sn}_2\text{S}_6]^{2-}$  layers extending in the (001) plane and protonated amine molecules as charge compensating ions sandwiched between the layers. The layered  $[\text{Cu}_2\text{Sn}_2\text{S}_6]^{2-}$  anion is composed of a single layer of edge-sharing  $\text{CuS}_4$  tetrahedra which is joined above and below to straight chains constructed by corner-sharing  $\text{SnS}_4$  tetrahedra. The material is a semiconductor with an optical band gap of 1.51 eV. More interestingly, preliminary results demonstrate that the compound exhibits photoconductive properties with an increase of the conductivity by a factor of 3 when irradiated with UV light. Upon heating in an inert atmosphere the compound starts to decompose at about 256 °C.

### Introduction

In recent years many efforts have been under way in the search of new and inexpensive photovoltaic materials. The materials presently used for the production of photovoltaic devices are mainly based on Si (about 90%), and thin-film materials like GaAs, amorphous Si, CdTe, or chalcopyrite compounds containing Cu, In, Ga, S, or Se<sup>1</sup> play only a minor but important part. Thin-film chalcogenide materials could lead to increased efficiencies and a reduction of the costs of solar cells.<sup>2</sup> A material with interesting structural and optical properties for thin-film photovoltaic applications is  $\text{Cu}(\text{In,Ga})\text{Se}_2$  (CIGS)<sup>2,3</sup> which belongs to the group of chalcopyrites. Such quaternary chalcopyrite semiconductors can be synthesized by applying different chemical synthetic methods like chemical vapor transport or the Bridgman technique.<sup>4</sup> Recently, the solvothermal synthesis of  $\text{CuIn}(\text{Se}_x\text{S}_{1-x})_2$  nanocrystallites was reported.<sup>5</sup> During the past decade the price for indium increased dramatically. Therefore it is necessary to search for new less costly compounds with

appropriate band gaps for sunlight absorption. In addition, such materials should generate electrons and holes due to the light absorption. Combinations of different semiconductor layers establish the so-called third generation solar cells to achieve efficiencies of about 30%. Typically applied layered devices consist of materials such as semiconducting polymers and nanostructured systems.<sup>6</sup>

Compounds with semiconductor properties are copper-containing thiostannates  $(\text{R})_x\text{Cu}_a\text{Sn}_b\text{S}_c$  (with R = organic compound) among the group of porous thiometalates. In such compounds typical properties of zeolites like gas adsorption or catalytic activity are combined with that of semiconductors or photocatalysts. Several thiostannates prepared under solvothermal conditions exhibit interesting properties.<sup>7–10</sup> Two different structure types are distinguished: R–SnS–1 and R–SnS–3.<sup>11–14</sup> R is an organic

\* To whom correspondence should be addressed. E-mail: wbensch@ac.uni-kiel.de. Phone: +49 431 880-2419. Fax: +49 431 880-1520.

(1) Lux-Steiner, M. C.; Willeke, G. *Phys. Bl.* **2001**, *37*, 47–53.  
 (2) Compaan, A. D. *Sol. Energy Mater. Sol. Cells* **2006**, *90*, 2170–2180.  
 (3) Goetzberger, A.; Hebling, C.; Schock, H. W. *Mater. Sci. Eng.* **2003**, *R40*, 1–46.  
 (4) Tomm, Y.; Fiechter, S. *J. Ceram. Proc. Res.* **2005**, *6*, 141–145.  
 (5) Xiao, J.; Xie, Y.; Xiong, Y.; Tang, R.; Qian, Y. *J. Mater. Chem.* **2001**, *11*, 1417–1420.

(6) Barnham, K. W. J.; Mazzer, M.; Clive, B. *Nat. Mater.* **2006**, *5*, 161–164.  
 (7) Ahari, H.; Bowes, C. L.; Jiang, T.; Lough, A.; Ozin, G. A.; Bedard, R. L.; Petrov, S.; Young, D. *Adv. Mater.* **1995**, *7*, 375–377.  
 (8) Ahari, H.; Ozin, G. A.; Bedard, R. L.; Petrov, S.; Young, D. *Adv. Mater.* **1995**, *7*, 370–374.  
 (9) Enzel, P.; Henderson, G. S.; Ozin, G. A.; Bedard, R. L. *Adv. Mater.* **1995**, *7*, 64–68.  
 (10) Jiang, T.; Ozin, G. A.; Bedard, R. L. *Adv. Mater.* **1995**, *7*, 166–170.  
 (11) Jiang, T.; Lough, A.; Ozin, G. A. *Adv. Mater.* **1998**, *10*, 42–46.  
 (12) Parise, J. B.; Ko, Y.; Rijssenbeek, J.; Nellis, D. M.; Tan, K.; Koch, S. *J. Chem. Soc., Chem. Commun.* **1994**, 527.  
 (13) Ko, Y.; Tan, K.; Nellis, D. M.; Koch, S.; Parise, J. B. *J. Solid State Chem.* **1995**, *114*, 506–511.

ohio2/yic-yic/yic-yic/yic99907/yic4753d07z	xppws	23:ver.5	8/27/08	15:50	Msc: ic-2008-00118z	TEID: lrk00	BATID: ic10b27
--	-------	----------	---------	-------	---------------------	-------------	----------------

Pienack et al.

52 component acting as a structure directing molecule. The  
 53 structures are composed of two-dimensional anionic layers  
 54 with compositions  $[\text{Sn}_3\text{S}_7]^{2-}$  and  $[\text{Sn}_4\text{S}_6]^{4-}$  for R-SnS-1 and  
 55 R-SnS-3, respectively. In R-SnS-1 the primary building units  
 56 (PBUs) are  $\text{SnS}_4$  tetrahedra which are combined to form  
 57  $\text{Sn}_3\text{S}_4$  semicubes as secondary building units (SBUs). Two  
 58  $\text{S}^{2-}$  anions connect the semicubes to form the anionic layers  
 59  $[\text{Sn}_3\text{S}_7]^{2-}$  with pores consisting of 24 atoms (diameter: 10  
 60 Å × 10 Å). The organic components, like for example,  
 61 tetraethylammonium, act as charge compensating cations and  
 62 are located below/above the pores between the layers.<sup>15</sup> In  
 63 R-SnS-3 the SBUs are joined by  $\text{SnS}_4$  tetrahedra to form  
 64  $[\text{Sn}_4\text{S}_6]^{4-}$  anionic layers. The pores are elliptical with a size  
 65 of about 13 Å × 15 Å.<sup>14</sup> Instead of organic structure directors  
 66 alkali metals were used to prepare 2D compounds like  
 67  $\text{Rb}_2\text{Sn}_3\text{S}_7 \cdot 2\text{H}_2\text{O}$  or  $\text{Cs}_4\text{Sn}_5\text{S}_{12} \cdot 2\text{H}_2\text{O}$ .<sup>16,17</sup>

68 Many compounds prepared under solvothermal conditions  
 69 have been studied in recent years, but most of them are wide  
 70 band gap semiconductors. Thiostannates are candidates for  
 71 catalytic applications, chemical sensing,<sup>11,12,18–20</sup> and with  
 72 the integration of transition metals (TM) into the network  
 73 the physical and chemical properties are altered.<sup>21</sup> Some TM  
 74 containing thiostannates were reported until now,<sup>21–24</sup> and  
 75 we recently presented two new compounds with copper  
 76 integrated into the thiostannate network.<sup>25</sup> The promising  
 77 photochemical properties of Cu and Sn containing sulfides  
 78 were demonstrated recently on the substitution series  
 79  $\text{Cu}_2\text{Sn}_{1-x}\text{Si}_x\text{S}_3$ <sup>26</sup> which were prepared using the classical high  
 80 temperature route. The results of this study motivated us to  
 81 perform syntheses with Cu, Sn, and S applying an amine as  
 82 structure director. One goal of the experiments is the search  
 83 for materials where the rare indium is replaced by tin  
 84 exhibiting potential photovoltaic properties. In this paper we  
 85 present the synthesis, crystal structure, and selected properties  
 86 of the new thiostannate  $(\text{dienH}_2)\text{Cu}_2\text{Sn}_2\text{S}_6$  (dien = diethyl-  
 87 entriamine,  $\text{C}_4\text{N}_3\text{H}_{13}$ ). We also report the first results of  
 88 experiments concerning photoconductive properties of the  
 89 compound.

- (14) Jiang, T.; Lough, A.; Ozin, G. A.; Bedard, R. L.; Broach, R. *J. Mater. Chem.* **1998**, *8*, 721–732.  
 (15) Jiang, T.; Lough, A.; Ozin, G. A.; Bedard, R. L. *J. Mater. Chem.* **1998**, *8*, 733–741.  
 (16) Jiang, T.; Ozin, G. A.; Bedard, R. L. *J. Mater. Chem.* **1998**, *8*, 1641–1648.  
 (17) Sheldrick, W. S.; Schaaf, B. Z. *Anorg. Allg. Chem.* **1994**, *620*, 1041–1045.  
 (18) Scott, R. W. J.; MacLachlan, M. J.; Ozin, G. A. *Curr. Opin. Solid State Mater. Sci.* **1999**, *4*, 113–121.  
 (19) Jiang, T.; Ozin, G. A. *J. Mater. Chem.* **1997**, *7*, 2213–2222.  
 (20) Francis, R. J.; Price, S. J.; Evans, J. S. O.; O'Brien, S.; O'Hare, D.; Clark, S. M. *Chem. Mater.* **1996**, *8*, 2102–2108.  
 (21) An, Y.; Ji, M.; Baiyin, M.; Liu, X.; Jia, C.; Wang, D. *Inorg. Chem.* **2003**, *42*, 4248–4249.  
 (22) Palchik, O.; Iyer, R. G.; Liao, J. H.; Kanatzidis, M. G. *Inorg. Chem.* **2003**, *42*, 5052–5054.  
 (23) Dag, Ö.; Ahari, H.; Coombs, N.; Jiang, J.; Aroca-Quellette, P. P.; Petrov, S. *Adv. Mater.* **1997**, *9*, 1133–1149.  
 (24) Bowes, C. L.; Petrov, S.; Vovk, G.; Young, D.; Ozin, G. A.; Bedard, R. L. *J. Mater. Chem.* **1998**, *8*, 711–720.  
 (25) Pienack, N.; Näther, C.; Bensch, W. *Solid State Sci.* **2007**, *9*, 100–107.  
 (26) Lafond, A.; Cody, J. A.; Souilah, M.; Guillot-Deudon, C.; Kiebach, R.; Bensch, W. *Inorg. Chem.* **2007**, *46*, 1502–1506, vorher.

B Inorganic Chemistry, Vol. xx, No. x, XXXX

**Table 1.** Selected Details of Data Collection and Results of the Refinement of  $(\text{dienH}_2)\text{Cu}_2\text{Sn}_2\text{S}_6$

compound	$(\text{dienH}_2)\text{Cu}_2\text{Sn}_2\text{S}_6$
crystal system	tetragonal
space group	$I4m2$
<i>a</i> /Å	7.8793(3)
<i>b</i> /Å	7.8793(3)
<i>c</i> /Å	24.9955(15)
<i>V</i> /Å <sup>3</sup>	1551.80(13)
<i>Z</i>	4
<i>D</i> <sub>calculated</sub> /g/cm <sup>3</sup>	2.834
$\mu$ /mm <sup>-1</sup>	6.673
scan range	$2.71 \leq 2\theta \leq 28.03^\circ$
reflections collected	6243
refl. with $F_o > 4\sigma(F_o)$	1256
independent reflections	1078
goodness-of-fit on $F^2$	1.052
final <i>R</i> indices [ $I > 2\sigma(I)$ ]	<i>R</i> 1 = 0.0417, <i>wR</i> 2 = 0.0979
<i>R</i> indices (all data)	<i>R</i> 1 = 0.0471, <i>wR</i> 2 = 0.1018
res. elec. dens./e Å <sup>-3</sup>	3.923/–1.949
Flack <i>x</i> parameter	0.02(6)

#### Experimental Details

90

**Synthesis. General Information.** All reactions were performed  
 91 under solvothermal conditions in Teflon-lined steel autoclaves (inner  
 92 volume, 30 mL). The crystalline products were filtered off after  
 93 the reactions, washed with water and ethanol, and dried in vacuum.

**Synthesis of  $(\text{dienH}_2)\text{Cu}_2\text{Sn}_2\text{S}_6$ .** A 0.5 mmol portion of Sn  
 95 (99.5%, Aldrich), 0.5 mmol of Cu (99.5%, Alfa Aesar), 2 mmol of  
 96 S, and 6 mL of diethylenetriamine ( $\geq 97.0\%$ , Fluka) were heated  
 97 to 170 °C in 2 h and then reacted for 120 h at this temperature,  
 98 followed by cooling to 25 °C in 30 h. The synthesis was performed  
 99 in a diffusion cell to separate Cu from Sn and S by a membrane.  
 100 The advantage of such a cell is that the dissolved Sn and Cu species  
 101 must diffuse through the membrane keeping the concentration of  
 102 the reacting species low at the site of crystallization. Thin black  
 103 plates of the title compound were obtained in 15% yield based on  
 104 Sn, which were slightly contaminated with sulfides on the surface.  
 105 Performing the synthesis under stirring, we received the black  
 106 powder in a 60% yield (based on Sn). The composition was  
 107 confirmed by EDX (Sn/Cu/S ratio, 1:1:3) and by elemental analysis  
 108 (results in %; found: C 7.29, H 2.05, N 6.04; calculated: C 7.23, H  
 109 2.58, N 6.33).

**Structure Determination.** Intensity data were collected using  
 111 a STOE IPDS-1 (Imaging Plate Diffraction System) with Mo *K* $\alpha$   
 112 radiation at room temperature. The structure was solved with direct  
 113 methods using the program SHELXS-97<sup>27</sup> and the refinement was  
 114 done against  $F^2$  with SHELXL-97.<sup>28</sup> All atoms except H were  
 115 refined with anisotropic displacement parameters. The  $\text{dienH}_2$   
 116 molecule is located on a crystallographic mirror plane with the  
 117 nitrogen atom N2 disordered over two positions. The N–H and  
 118 the C–H hydrogen atoms were positioned with idealized geometry  
 119 and were refined using a riding model with  $U_{\text{eq}}(\text{H}) = 1.2$  or  $1.5$   
 120  $U_{\text{eq}}(\text{C,N})$ . Crystal data and selected refinement results are sum-  
 121 marized in Table 1. Further structural details have been deposited  
 122 with the Cambridge Crystallographic Data Centre (CCDC) as  
 123 publication no. CCDC xxxx (I). Copies of the data can be obtained,  
 124 free of charge, on application to CCDC, 12 Union Road, Cambridge  
 125 CB2 1EZ, U.K. (mail: deposit@ccdc.ac.uk).

**Thermal Investigations.** Differential thermal analysis-thermo-  
 127 gravimetry (DTA-TG) analyses were performed using a Netzsch  
 128 STA 429 DTA-TG device. The samples were heated to 600 °C at  
 129

- (27) Sheldrick, G. M. *SHELXS 97, Program for the Solution of Crystal Structures*; University of Göttingen: Göttingen, Germany, 1997.  
 (28) Sheldrick, G. M. *SHELXL 97, Program for the Refinement of Crystal Structures*; University of Göttingen: Göttingen, Germany, 1997.

ohio2/yic-yic/yic-yic/yic99907/yic4753d07z | xppws | 23:ver.5 | 8/27/08 | 15:50 | Msc: ic-2008-00118z | TEID: lrk00 | BATID: ic10b27

#### Photoconductive Inorganic–Organic Hybrid Compound

130 a rate of  $4 \text{ K} \cdot \text{min}^{-1}$  under a flow of argon ( $75 \text{ mL} \cdot \text{min}^{-1}$ ) in  $\text{Al}_2\text{O}_3$   
 131 crucibles. The TG-MS measurements with a heating rate of  $4$   
 132  $\text{K} \cdot \text{min}^{-1}$  in  $\text{Al}_2\text{O}_3$  crucibles and in a dynamic helium atmosphere  
 133 with a flow rate of  $75 \text{ mL} \cdot \text{min}^{-1}$  were conducted simultaneously  
 134 using a STA-409CD device (Netzsch) with Skimmer coupling,  
 135 which is equipped with a Balzers QMA 400 Quadrupole Mass  
 136 Spectrometer (max. 512 amu). The MS data were recorded in the  
 137 analogue and trend scan modes. The TG data were corrected for  
 138 buoyancy and current effects. An isothermal experiment was  
 139 performed at  $150 \text{ }^\circ\text{C}$  for 5 h in Ar atmosphere.

140 **Spectroscopic Experiments. Raman.** The Raman spectra were  
 141 recorded in the region from 100 to  $3500 \text{ cm}^{-1}$  with a Bruker IFS  
 142 66 Fourier Transform Raman spectrometer (wavelength: 541.5 nm).

143 **UV/vis.** UV/vis spectroscopic investigations were conducted at  
 144 room temperature using a UV–vis–NIR two-channel spectrometer  
 145 Cary 5 from Varian Techtron Pty., Darmstadt. The optical properties  
 146 of the compound were investigated by studying the UV/vis  
 147 reflectance spectrum of a powdered sample. The absorption data  
 148 were calculated with the Kubelka–Munk relation for diffuse  
 149 reflectance data.  $\text{BaSO}_4$  powder was used as reference material.

150 **Scanning Electron Microscopy (SEM)/Energy Dispersive**  
 151 **X-ray Fluorescence (EDX).** The EDX analyses have been carried  
 152 out with a Philips ESEM XL30 equipped with an EDAX detector.

153 **Elemental Analysis.** CHNS analyses were done using a EURO  
 154 EA Elemental Analyzer, fabricated by EURO VECTOR Instruments  
 155 and Software.

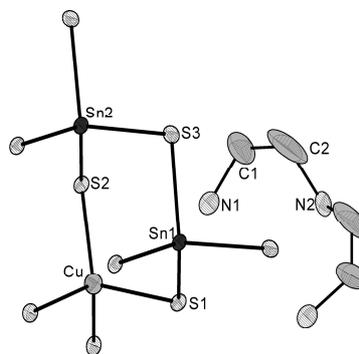
156 **Impedance Spectroscopy.** The impedance measurements were  
 157 done on a pressed pellet with the so-called “Kielcer cell” in argon  
 158 atmosphere using a HP 4192 Impedance-Analyzer at 5–13 MHz  
 159 with gold electrodes. The temperature was controlled with a Cr/  
 160 CrNi thermocouple. The equivalent circuit diagram contains a  
 161 resistance ( $R$ ) and a capacitance ( $C$ ) in parallel. The resulting  
 162 semicircle, the so-called Nyquist plot, has a high frequency limit  
 163 at the origin and a low frequency limit at  $Z' = R$ . The values for  
 164 the resistance from the Nyquist plot were converted using the  
 165 dimensions of the pressed pellet ( $d = 0.55 \text{ mm}$ , area =  $50.3 \text{ mm}^2$ )  
 166 to obtain the values for the resistivity. The capacitance could  
 167 be obtained from the maximum of the semicircle. For the photocon-  
 168 ductivity measurements a UV lamp ( $\lambda = 300\text{--}400 \text{ nm}$ ) was used.

#### Results and Discussion

170 **Crystal Structures.** The new compound  $(\text{dichH}_2)\text{Cu}_2\text{Sn}_2\text{S}_6$   
 171 crystallizes in the non-centrosymmetric tetragonal space  
 172 group  $I\bar{4}m2$  with 4 formula units in the unit cell. All non-H  
 173 atoms are located on special positions. The structure consists  
 174 of anionic  $[\text{Cu}_2\text{Sn}_2\text{S}_6]^{2-}$  layers which are separated by the  
 175 charge compensating cations, that is, the protonated amine  
 176 molecules. The two crystallographically independent Sn  
 177 atoms and the Cu atom are in a tetrahedral environment of  
 178 S atoms (Figure 1).

179  $\text{SnS}_4$  tetrahedra are common in thioannates and the  
 180 observed Sn–S distances (2.357(2)–2.486(3) Å, Table 2)  
 181 as well as the S–Sn–S angles (103.59(11)–117.98(10)°,  
 182 Table 2) indicate a slight distortion.

183 The geometric parameters are in good agreement with data  
 184 published in the literature.<sup>16,29,30</sup> The Cu–S bond lengths  
 185 in the  $\text{CuS}_4$  tetrahedron are 2.3464(13) and 2.3555(12) Å,



186 **Figure 1.** Connection of the  $\text{SnS}_4$  and  $\text{CuS}_4$  tetrahedra together with the  
 187 amine molecule and labeling of the atoms of the asymmetric unit. The  
 188 displacement ellipsoids are drawn at the 50% probability level. The hydrogen  
 189 atoms and the disorder of N2 are not shown for clarity.

190 **Table 2.** Selected Bond Lengths and Angles of ( $\text{I}^a$ )

Sn(1)–S(1)	2.357(2)	S(2)–Sn(2)–S(3)	107.44(4)
Sn(1)–S(3)	2.485(3)	S(3)–Sn(2)–S(3) <sup>c</sup>	106.13(12)
Sn(2)–S(2)	2.359(2)	S(2)–Cu–S(2) <sup>d</sup>	113.04(11)
Sn(2)–S(3)	2.486(3)	S(2)–Cu–S(1) <sup>e</sup>	106.61(7)
Cu–S(2)	2.3464(13)	S(2)–Cu–S(1)	113.88(5)
Cu–S(1)	2.3555(12)	S(2) <sup>d</sup> –Cu–S(1)	106.61(7)
S(1)–Cu <sup>f</sup>	2.3555(12)	S(1) <sup>f</sup> –Cu–S(1)	102.51(11)
S(2)–Cu <sup>g</sup>	2.3464(13)	Cu–S(1)–Cu <sup>f</sup>	116.43(8)
		Cu–S(1)–Sn(1)	103.93(6)
S(1)–Sn(1)–S(1) <sup>b</sup>	117.98(10)	Cu <sup>g</sup> –S(2)–Cu	111.32(8)
S(1)–Sn(1)–S(3)	108.58(4)	Cu–S(2)–Sn(2)	103.95(6)
S(3) <sup>b</sup> –Sn(1)–S(3)	103.59(11)	Sn(1)–S(3)–Sn(2)	104.86(8)
S(2)–Sn(2)–S(2) <sup>c</sup>	120.16(11)		

191 <sup>a</sup> The symmetry transformations used to generate equivalent atoms are  
 192 indicated in the footnotes. <sup>b</sup>  $-x, -y, z$ ; <sup>c</sup>  $-x + 1, -y, z$ ; <sup>d</sup>  $-y + 1/2, x - 1/2,$   
 193  $-z + 1/2$ ; <sup>e</sup>  $-y + 1/2, x + 1/2, -z + 1/2$ ; <sup>f</sup>  $y - 1/2, -x + 1/2, -z + 1/2$ ; <sup>g</sup>  $y +$   
 194  $1/2, -x + 1/2, -z + 1/2$ .

186 being longer than in  $\text{CuInS}_2$ <sup>31</sup> but similar to values observed  
 187 in the compounds presented below. The S–Cu–S angles  
 188 vary between 102.51(11) and 113.88(5)° indicating a pro-  
 189 nounced distortion of the tetrahedron. Such a distortion is  
 190 uncommon, and similar values were reported in the  
 191 literature. For instance, in the compounds  $\text{Rb}_2\text{CuMS}_4$  ( $M =$   
 192  $\text{Nb}, \text{V}$ )<sup>32</sup> linear chains are constructed by edge-sharing of  
 193  $\text{CuS}_4$  and  $\text{MS}_4$  tetrahedra and also in  $\text{RbCu}_2\text{VS}_4$  Cu is in  
 194 a distorted tetrahedral environment.<sup>33</sup> Analyzing the structures  
 195 of different thiometalates the occurrence of  $\text{CuS}_4$  tetrahedra  
 196 in copper thioannates is quite unusual, whereas in Cu  
 197 thioantimonates  $\text{CuS}_4$  tetrahedra are more common like,  
 198 for example,  $(\text{C}_4\text{N}_3\text{H}_{14})\text{Cu}_3\text{Sb}_2\text{S}_5$  ( $\text{C}_4\text{N}_3\text{H}_{13}$  = diethylenetriamine)  
 199 and  $(\text{C}_6\text{N}_4\text{H}_{20})_{0.5}\text{Cu}_3\text{Sb}_2\text{S}_5$  ( $\text{C}_6\text{N}_4\text{H}_{18}$  = triethylenetetramine).<sup>34</sup>  
 200 All S atoms of the  $\text{CuS}_4$  tetrahedron share a corner with  
 201 neighboring  $\text{CuS}_4$  tetrahedra to form a single puckered layer  
 202  $[\text{CuS}_{4/4}]$  within the (001) plane containing  $\text{Cu}_4\text{S}_4$  rings as a  
 203 special structural feature (Figure 2, bottom).

(31) Hahn, H.; Frank, G.; Klingler, W.; Meyer, A. D.; Stoerger, G. *Z. Anorg. Allg. Chem.* **1953**, *271*, 153.

(32) Rumpf, C.; Tillinski, R.; Näther, C.; Dürichen, P.; Jess, I.; Bensch, W. *Eur. J. Solid State Inorg. Chem* **1997**, *34*, 1187–1198.

(33) Tillinski, R.; Näther, C.; Bensch, W. *Acta Crystallogr.* **2001**, *C57*, 333–334.

(34) Spetzler, V.; Näther, C.; Bensch, W. *Inorg. Chem.* **2005**, *44*, 5805–5812.

(29) Behrens, M.; Scherb, S.; Näther, C.; Bensch, W. *Z. Anorg. Allg. Chem.* **2003**, *629*, 1367–1373.

(30) Jiang, T.; Ozin, G. A. *J. Mater. Chem.* **1998**, *8*, 1099–1108.

ohio2/yic-yic/yic-yic/yic99907/yic4753d07z | xppws | 23:ver.5 | 8/27/08 | 15:50 | Msc: ic-2008-00118z | TEID: lrk00 | BATID: ic10b27

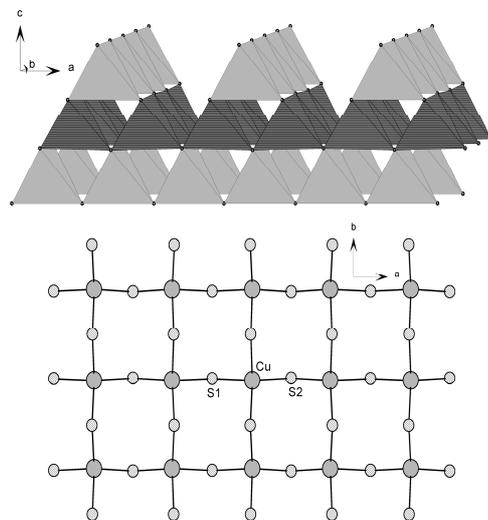


**Figure 2.** Polyhedral representation of the layered  $[\text{Cu}_2\text{Sn}_2\text{S}_6]^{2-}$  anion (top:  $\text{SnS}_4$  tetrahedra light gray and  $\text{CuS}_4$  tetrahedra dark gray) and a layer in the (001) plane formed by corner-sharing of  $\text{CuS}_4$  tetrahedra (bottom).

204 The different positions of the Sn atoms (Sn(1) and Sn(2))  
205 do not correspond neither to two different sheets nor to  
206 different chains. The  $\text{Sn}(1)\text{S}_4$  and  $\text{Sn}(2)\text{S}_4$  tetrahedra  
207 are joined via common corners into one-dimensional chains  
208  $[\text{SnS}_4]_2$  running along [100] and [010]. The chains are bound  
209 to the  $[\text{CuS}_4]_2$  layer via S(1) and S(2) yielding the layered  
210  $[\text{Cu}_2\text{Sn}_2\text{S}_6]^{2-}$  anion (Figure 2, top). As a consequence of the  
211 connection mode the two atoms S(1) and S(2) have bonds  
212 to two Cu and one Sn centers whereas S(3) is only bound to  
213 two Sn atoms. The Cu–Sn distances are about 3.7 Å which  
214 are too long for any significant interactions.

215 The layers are stacked perpendicular to [001] with the  
216 protonated amine molecules residing in the void space with  
217 neighboring amines being rotated by 90° (Figure 3).

218 The terminal N(1) atom has two contacts to S atoms (3.292  
219 Å to S(1) and 3.275 Å to S(2)) indicating weak  $\text{N}(1)\text{---H}\cdots\text{S}$   
220 bonding interactions. The shortest interlayer distance of 5.3  
221 Å is determined by the arrangement of the organic molecules.

222 From a formal point of view the title compound belongs  
223 to a group of compounds with general composition  $\text{M}_2^{\text{I}}\text{M}^{\text{IV}}\text{Q}_3$   
224 with  $\text{M}^{\text{I}} = \text{Cu}$ ,  $\text{M}^{\text{IV}} = \text{Si}$ ,  $\text{Ge}$ ,  $\text{Sn}$  and  $\text{Q} = \text{S}$ ,  $\text{Se}$ .<sup>26,35–39</sup> and  
225  $\text{K}_2\text{MM}'_3\text{Se}_6$  ( $\text{M} = \text{Cu}$ ,  $\text{Ag}$ ;  $\text{M}' = \text{Ga}$ ,  $\text{In}$ ).<sup>40</sup> The structures  
226 of the members of the  $\text{M}_2^{\text{I}}\text{M}^{\text{IV}}\text{Q}_3$  series can be viewed as  
227 derivatives of the cubic sphalerite type structure, that is, the

(35) Chen, X. A.; Wada, H.; Sato, A.; Nozaki, H. *J. Alloys Compd.* **1999**, *290*, 91–96.

(36) Marcano, G.; Rincon, C.; Chalbaud, L. M. de; Brancho, D. B.; Sanchez Perez, G. *J. Appl. Phys.* **2001**, *90*, 1847–1853.

(37) Delgado, G. E.; Mora, A. J.; Marcona, G.; Rincon, C. *Mater. Res. Bull.* **2003**, *38*, 1949–1955.

(38) Onoda, M.; Chen, X. A.; Sato, A.; Wada, H. *Mater. Res. Bull.* **2000**, *35*, 1563–1570.

(39) Chalbaud, L. M. de; Delgado, G. Diaz de; Delgado, J. M.; Mora, A. E.; Sagredo, V. *Mater. Res. Bull.* **1997**, *32*, 1371–1376.

(40) Ma, H.-W.; Guo, G. C.; Wang, M.-S.; Zhou, G.-W.; Lin, S.-H.; Dong, Z.-C.; Huang, J.-S. *Inorg. Chem.* **2003**, *42*, 1366–1370.

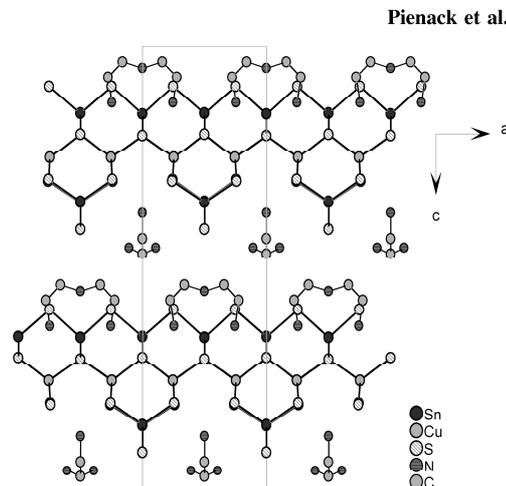


**Figure 3.** Arrangement of the  $[\text{Cu}_2\text{Sn}_2\text{S}_6]^{2-}$  layers and the amine molecules in the interlayer galleries. The hydrogen atoms are omitted for clarity.

228 tetrahedra form a three-dimensional network. The structures  
229 of the latter series of compounds are layered. A sublayer  
230 is composed by  $\text{InS}_4$  and  $\text{CuS}_4$  tetrahedra sharing all four  
231 corners leading to a topology which is similar to that of the  
232 title compound. This sublayer is sandwiched by parallel  
233 corner-sharing  $[\text{InS}_4]$  tetrahedral chains. Another structurally  
234 related compound is  $\text{Rb}_2\text{Cu}_2\text{Sn}_2\text{S}_6$ <sup>41</sup> which may be regarded  
235 as a derivative of the  $\text{M}_2^{\text{I}}\text{M}^{\text{IV}}\text{Q}_3$  structure by substituting one  
236  $\text{Cu}^+$  by a  $\text{Rb}^+$  ion yielding a layered structure. In this  
237 structure a layer constructed by corner-sharing  $\text{CuS}_4$  tetra-  
238 hedra is sandwiched by two layers composed of  $\text{SnS}_4$   
239 tetrahedra. In the two Sn containing layers  $1/2$  of the Sn sites  
240 are empty so that chains are formed running perpendicularly  
241 below and above the Cu layer. The interlayer separation in  
242  $\text{Rb}_2\text{Cu}_2\text{Sn}_2\text{S}_6$  amounts to 4.8 Å which is shorter than in the  
243 title compound.

244 **Spectroscopy.** Charge neutrality of the title compound  
245 requires that the amine molecule is diprotonated. In diethyl-  
246 ylenetriamine usually the primary amino groups are protonated.  
247 In this case, the IR spectra show the absorptions  
248 located at 1530, 1630, and 3430  $\text{cm}^{-1}$  which are excited by  
249  $\text{R-NH}_3^+$  groups.

250 In the Raman spectrum (Figure 4) vibrations occur at 373,  
251 301, 267, and 233  $\text{cm}^{-1}$  which is the typical region for Sn–S  
252 resonances.<sup>42,43</sup> The symmetric Sn–S stretching vibration  
253 is located at 373  $\text{cm}^{-1}$  and a symmetric Sn–S bridging mode  
254 at 301  $\text{cm}^{-1}$ . The signal at 233  $\text{cm}^{-1}$  could be assigned to  
255 the  $\text{SnS}_2$  wagging and twisting mode, and the resonance at  
256 267  $\text{cm}^{-1}$  is caused by Cu–S vibrations.<sup>44</sup>

257 The optical band gap  $E_g$  was determined from transformed  
258 UV/vis diffuse reflectance spectra by the Kubelka–Munk  
259 method. The value of 1.51 eV (821 nm, Figure 5) is in  
260 agreement with the black color of the crystals. The band gap

(41) Liao, J.-H.; Kanatzidis, M. G. *Chem. Mater.* **1993**, *5*, 1561–1569.

(42) Krebs, B.; Schiwy, W. *Z. Anorg. Allg. Chem.* **1973**, *398*, 63–71.

(43) Krebs, B.; Pohl, S.; Schiwy, W. *Angew. Chem.* **1970**, *82*, 884–885.

(44) Müller, A.; Menge, R. *Z. Anorg. Allg. Chem.* **1972**, *393*, 259–265.

ohio2/yic-yic/yic-yic/yic99907/yic4753d07z | xppws | 23:ver.5 | 8/27/08 | 15:50 | Msc: ic-2008-00118z | TEID: lrk00 | BATID: ic10b27

*Photoconductive Inorganic–Organic Hybrid Compound*

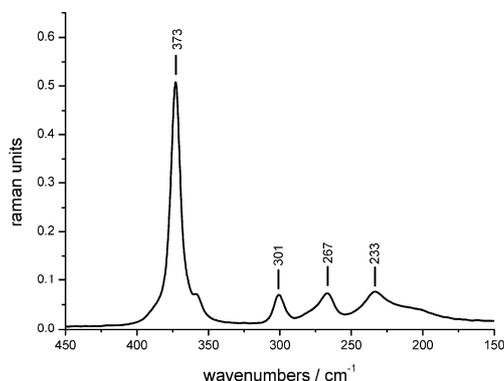


**Figure 4.** Raman spectrum of  $(\text{dienH}_2)\text{Cu}_2\text{Sn}_2\text{S}_6$  with the centers of the resonances given in  $\text{cm}^{-1}$ .

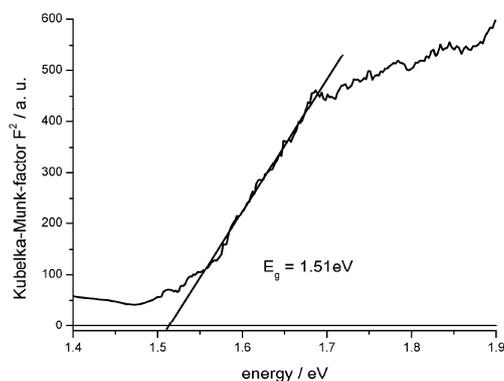


**Figure 5.** Determination of the optical band gap of  $(\text{dienH}_2)\text{Cu}_2\text{Sn}_2\text{S}_6$  from UV/vis diffuse reflectance spectrum using the Kubelka–Munk method.

261 of the title compound is comparable to that of CdTe (1.5  
262 eV) or GaAs (1.4 eV) which are together with CIS or CIGS  
263 (copper indium gallium selenide) efficient photovoltaic  
264 materials.<sup>45,46</sup> We note that the value for  $E_g$  of  $(\text{dienH}_2)$ -  
265  $\text{Cu}_2\text{Sn}_2\text{S}_6$  is slightly larger than that for the structurally related  
266 compound  $\text{Rb}_2\text{Cu}_2\text{Sn}_2\text{S}_6$  which was reported to be 1.44 eV.<sup>41</sup>  
267 Plotting  $((\alpha/S) \cdot E)^2$  versus the energy  $((\alpha/S)$  is the Kubelka–  
268 Munk factor) shows a linear behavior so that the band gap  
269 can be assumed to be direct.<sup>41</sup>

270 **Thermo Analytical Measurements.** The DTA-TG-DTG  
271 and MS trend scan curves are shown in Figure 6. The  
272 compound starts to decompose at  $T_{\text{onset}} = 256^\circ\text{C}$  with an  
273 endothermic signal at  $T_p = 262^\circ\text{C}$ . TG-MS investigations  
274 show that the amine and  $\text{H}_2\text{S}$  are emitted simultaneously at  
275 the decomposition temperature. The total weight loss of  
276 23.5% is slightly lower than the calculated value for the  
277 emission of the amine and two  $\text{H}_2\text{S}$  molecules ( $-\Delta m_{\text{theo}} =$   
278 25.7%). The residue is black and contains nearly 2% of CHN.  
279 In the X-ray powder pattern of the residue the compounds  
280  $\text{SnS}$  and  $\text{Cu}_2\text{SnS}_3$  could be identified.

(45) Miles, R. W.; Zoppi, G.; Forbes, I. *Mater. Today* **2007**, *10*, 20–27.  
(46) Conibeer, G. *Mater. Today* **2007**, *10*, 42–50.

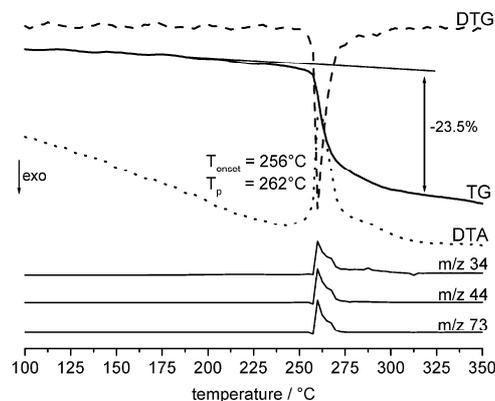


**Figure 6.** DTA-TG-MS trend scan curves of  $(\text{dienH}_2)\text{Cu}_2\text{Sn}_2\text{S}_6$ . Intensities of the signals are in arbitrary units,  $m/z$  34 =  $\text{H}_2\text{S}$ ;  $m/z$  44 and  $m/z$  73 are fragments of diethylenetriamine.

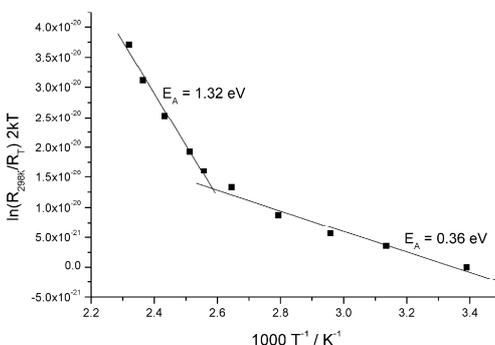


**Figure 7.** Arrhenius plot displaying two different regions for the activation energy (for details, see text).

281 An isothermal experiment performed for 5 h at  $150^\circ\text{C}$  in  
282 Ar atmosphere exhibits a very small mass loss of about 2%.  
283 The X-ray powder pattern recorded after this experiment  
284 shows only the reflections of the title compound. In addition,  
285 chemical analysis (6.1% N, 7.3% C, and 2.1% H) gives no  
286 hints for a significant decomposition, and we therefore  
287 assume that surface water was emitted.

288 **Impedance Spectroscopy.** The resistivity, the conductivity,  
289 and the capacitance at room temperature were estimated  
290 from the Nyquist plot as  $R_{\text{RT}} = 7.22 \times 10^6 \Omega \cdot \text{cm}$ ,  $\sigma_{\text{RT}} =$   
291  $1.38 \times 10^{-7} \Omega^{-1} \text{cm}^{-1}$ , and  $C_{\text{RT}} = 0.135 \text{ nF}$ . The resistivity  
292 decreases with increasing temperature reaching  $3.02 \times 10^5$   
293  $\Omega \cdot \text{cm}$  at  $158^\circ\text{C}$ .

294 Applying the Arrhenius equation the activation energy was  
295 determined as  $E_A = 0.36 \text{ eV}$  for the extrinsic and  $E_A = 1.32$   
296 eV for the intrinsic conductivity (Figure 7). Impurities or  
297 point defects in the material could explain the discrepancy  
298 between the optical band gap and the activation energy  
299 determined with impedance spectroscopy.

300 Exposing the material to UV light for some minutes leads  
301 to a strong decrease of the resistivity (Figure 8) exhibiting  
302 the difference between the dark and the photo current. After

ohio2/yic\_yic/yic\_yic/yic99907/yic4753d07z xppws 23:ver.5 8/27/08 15:50 Msc: ic 2008 00118z TFID: lrk00 BATID: ic10h27

PAGE EST: 5.6

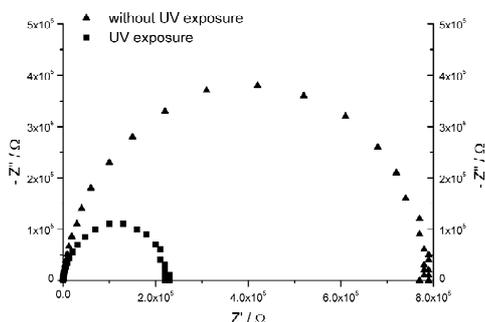


**Figure 8.** Nyquist plots from impedance measurements showing the resistance with and without UV light exposure.

303 20 min exposure a minimum of  $R_{UV} = 2.01 \times 10^6 \Omega \cdot \text{cm}$   
 304 was reached, and further irradiation with UV light does not  
 305 change the resistivity. The increase of the conductivity is  
 306 larger than a factor of 3. After switching-off the UV  
 307 irradiation the resistivity increased to  $7.22 \times 10^6 \Omega \cdot \text{cm}$   
 308 which is the value measured without UV light.

### 309 Conclusions

310 The new copper thioannate  $(\text{dienH}_2)\text{Cu}_2\text{Sn}_2\text{S}_6$  was ob-  
 311 tained as thin black plates under solvothermal conditions.  
 312 Under static conditions the yield is low but can be increased  
 313 by a factor of 4 by stirring the starting mixture. The structure  
 314 is constructed by alternate stacking of  $[\text{Cu}_2\text{Sn}_2\text{S}_6]^{2-}$  layers  
 315 and protonated amine molecules. The structural motif of the  
 316 anionic layer is related to a series of compounds with  
 317 compositions  $\text{M}^{\text{I}}\text{M}^{\text{IV}}\text{Q}_3$  with  $\text{M}^{\text{I}} = \text{Cu}$ ,  $\text{M}^{\text{IV}} = \text{Si}$ ,  $\text{Ge}$ ,  $\text{Sn}$   
 318 and  $\text{Q} = \text{S}$ ,  $\text{Se}$  and  $\text{K}_2\text{MM}'_3\text{Sc}_6$  ( $\text{M} = \text{Cu}$ ,  $\text{Ag}$ ;  $\text{M}' = \text{Ga}$ ,  
 319  $\text{In}$ ). All these compounds contain only inorganic constituents.  
 320 Replacement of a part of the small  $\text{M}^{\text{I}}$  ions by the protonated

Pienack et al.

321 dien molecule yields an inorganic–organic hybrid compound  
 322 exhibiting an inorganic substructure very similar to that  
 323 observed in the other compounds. The preliminary results  
 324 of the impedance measurements evidence the semiconducting  
 325 character of the title compound with a band gap typical for  
 326 photoconductors. First experiments indicate that the electrical  
 327 properties of the compound can be influenced by irradiating  
 328 the material with UV light leading to a reduction of the  
 329 resistivity by a factor of 3. Recently, we demonstrated that  
 330 the optical band gap of  $\text{Cu}_2\text{Sn}_{1-x}\text{Si}_x\text{S}_3$  can be altered from  
 331 1.25 to 1.45 eV through a substitution of Sn by Si.<sup>26</sup> For the  
 332 title compound challenging questions are whether the material  
 333 can be prepared applying different amines and how these  
 334 organic molecules influence the electric properties. In addition,  
 335 doping experiments are necessary to alter the conductivity  
 336 of the compound, that is, a distinct doping level would  
 337 allow controlling the conductivity. Such experiments are  
 338 currently under way. Copper thioannates are flexible with  
 339 respect to the crystal structure and the chemical composition,  
 340 and it can be assumed that more Cu/Sn based inorganic–  
 341 organic hybrid compounds are accessible using different  
 342 synthesis conditions. Further studies are needed to elucidate  
 343 whether the compound is a candidate for further applications.

**Acknowledgment.** We thank Dr. C. Knittlmayer and Prof.  
 344 Dr. W. Weppner (Tech. Faculty, University of Kiel) for the  
 345 possibility and their help during the impedance measure-  
 346 ments. We also thank Dr. G. Popkurov (Tech. Faculty,  
 347 University of Kiel) for fruitful discussions about photovoltaic  
 348 materials.  
 349

**Supporting Information Available:** X-ray crystallographic file  
 350 (in CIF format) of the title compound. This material is available  
 351 free of charge via the Internet at <http://pubs.acs.org>.  
 352

IC800118Z 353

#### 4.1.5. Die Verbindungen $[\text{Mn}(1,2\text{-dach})_2(\text{H}_2\text{O})]_2\text{Sn}_2\text{S}_6$ und $[\text{Mn}(1,2\text{-dach})_2]\text{Sn}_2\text{S}_6 \cdot 2(1,2\text{-dach})$

*Zusammenfassung der Veröffentlichung „The Influence of the Amine Concentration onto Product Formation: Crystal Structures, Thermal Stability and Spectroscopic Properties of Two New Manganese Thiostannates Obtained under Solvothermal Conditions“.*

Die beiden Thiostannate  $[\text{Mn}(1,2\text{-dach})_2(\text{H}_2\text{O})]_2\text{Sn}_2\text{S}_6$  (I) und  $[\text{Mn}(1,2\text{-dach})_2]\text{Sn}_2\text{S}_6 \cdot 2(1,2\text{-dach})$  (II) (1,2-dach = 1,2-Diaminocyclohexan,  $\text{C}_6\text{H}_{14}\text{N}_2$ ) zeigen den Einfluss der Aminkonzentration auf die Produkte der solvothermalen Synthese. Aus konzentrierten 1,2-Diaminocyclohexanlösungen kristallisiert die Verbindung  $[\text{Mn}(1,2\text{-dach})_2]\text{Sn}_2\text{S}_6 \cdot 2(1,2\text{-dach})$  (II) und die Verringerung der Aminkonzentration führt zur Bildung von  $[\text{Mn}(1,2\text{-dach})_2(\text{H}_2\text{O})]_2\text{Sn}_2\text{S}_6$  (I). Beide Thiostannate werden aus 1 mmol Mn, 1 mmol Sn und 4 mmol S in 5 mL 1,2-Diaminocyclohexanlösung der entsprechenden Konzentration (50 % für I, 99 % für II) nach Erhitzen auf 130 °C für 98 h erhalten.

$[\text{Mn}(1,2\text{-dach})_2(\text{H}_2\text{O})]_2\text{Sn}_2\text{S}_6$  (I) kristallisiert in der monoklinen Raumgruppe C2/c mit acht Formeleinheiten in der Elementarzelle und  $[\text{Mn}(1,2\text{-dach})_2]\text{Sn}_2\text{S}_6 \cdot 2(1,2\text{-dach})$  (II) in der triklinen Raumgruppe  $P\bar{1}$  mit  $Z = 1$ . In beiden Strukturen werden  $[\text{Sn}_2\text{S}_6]^{4-}$ -Anionen beobachtet, die als bidentate Liganden die oktaedrisch koordinierten  $\text{Mn}^{2+}$ -Kationen verbinden. Im Gegensatz zu den diskreten Molekülen in I wird in II ein eindimensionales Koordinationspolymer beobachtet. Die Koordination der  $\text{Mn}^{2+}$ -Kationen unterscheidet sich ebenfalls: in I bildet  $\text{Mn}^{2+}$  Bindungen zu vier Stickstoffatomen zweier Aminliganden, einem Schwefelatom der  $[\text{Sn}_2\text{S}_6]^{4-}$ -Einheit und einem Wassermolekül aus. Die  $[\text{Sn}_2\text{S}_6]^{4-}$ -Anionen liegen auf Symmetriezentren und verbrücken zwei  $\text{Mn}^{2+}$ -Oktaeder zu diskreten Einheiten (Abb. 4.7, links). Vier Stickstoffatome zweier Aminliganden und zwei Schwefelatome zweier benachbarter  $[\text{Sn}_2\text{S}_6]^{4-}$ -Einheiten koordinieren in II die  $\text{Mn}^{2+}$ -Kationen, was zur Ausbildung negativ geladener Ketten mit  $\text{Mn}^{2+}$ -Oktaedern als Knoten und  $[\text{Sn}_2\text{S}_6]^{4-}$ -Anionen als Linker führt. Hervorzuheben ist, dass bisher noch nie ein Thiometallat dargestellt werden konnte, in dem das integrierte Übergangsmetallkation Bindungen zu drei unterschiedlichen Liganden ausbildet. Insofern ist die Verbindung I einmalig. Zusätzlich belegt die erfolgreiche Isolierung

der beiden Verbindungen, dass eine Veränderung der Aminkonzentration einen großen Einfluss auf die Produktbildung ausübt. Einfach protonierte Aminmoleküle, erkennbar im MIR-Spektrum durch die Absorptionen primärer, protonierter Amine, umgeben zur Ladungskompensation die anionischen Ketten des Koordinationspolymers (Abb. 4.7, rechts).

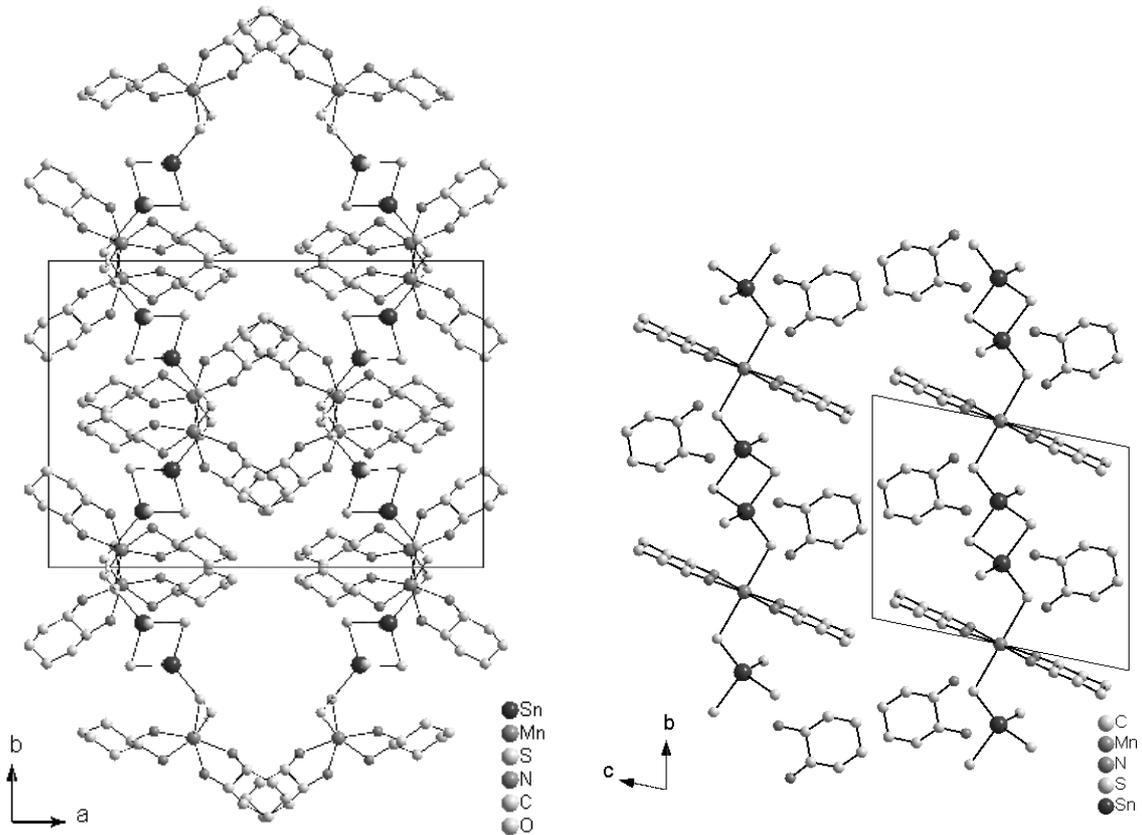


**Abb. 4.7:** Links: Packungsbild der Struktur von  $[\text{Mn}(1,2\text{-dach})_2(\text{H}_2\text{O})]_2\text{Sn}_2\text{S}_6$  (I) mit diskreten Molekülen. Die Anordnung der anionischen Ketten der Verbindung II ist auf der rechten Seite dargestellt. Die Wasserstoffatome sind zur besseren Übersicht nicht dargestellt.

Im Raman-Spektrum treten die für  $[\text{Sn}_2\text{S}_6]^{4-}$ -Einheiten typischen Resonanzen zwischen  $400$  und  $100\text{ cm}^{-1}$  auf. Aufgrund der Unterschiede in den Bindungslängen und -winkeln werden Verschiebungen der Banden beobachtet. Bei  $385\text{ cm}^{-1}$  (I) bzw.  $379\text{ cm}^{-1}$  (II) wird die symmetrische Sn-S-Streckschwingung und bei  $347\text{ cm}^{-1}$  (I) bzw.  $345\text{ cm}^{-1}$  (II) der Sn-S<sub>bridging</sub>-Mode beobachtet. Die Signale bei  $285\text{ cm}^{-1}$  (I) bzw.  $289\text{ cm}^{-1}$  (II) werden durch eine Schwingung des  $\text{Sn}_2\text{S}_2$ -Rings hervorgerufen.

Die optischen Bandlücken betragen  $2.6\text{ eV}$  ( $477\text{ nm}$ ) (I) bzw.  $3.1\text{ eV}$  ( $400\text{ nm}$ ) (II). Die Untersuchungen zur thermischen Stabilität zeigen, dass die Verbindung I bis  $115\text{ °C}$  stabil ist bzw. bis  $269\text{ °C}$ , wenn die Entfernung des Wassermoleküls vernachlässigt wird, und II sich ab  $198\text{ °C}$  zersetzt. Der thermische Abbau von I

verläuft in drei Stufen mit einem Gesamtmassenverlust von 48.6 %, der von endothermen Ereignissen mit Peaktemperaturen von  $T_p = 121, 286$  und  $321$  °C ( $T_{\text{Onset}} = 115, 269$  und  $313$  °C) begleitet ist. Das Zersetzungsprodukt ist weitgehend frei von organischen Bestandteilen und durch die Identifizierung der Reflexe von MnS und SnS im Pulverdiffraktogramm kann ein Abbau nach der formalen Gleichung  $[\text{Mn}(\text{C}_6\text{H}_{14}\text{N}_2)_2(\text{H}_2\text{O})]_2\text{Sn}_2\text{S}_6 \rightarrow 2 \text{MnS} + 2 \text{SnS} + 2 \text{H}_2\text{O} + 2 \text{H}_2\text{S} + 4 \text{C}_6\text{H}_{12}\text{N}_2$  postuliert werden. Die zweite Verbindung zersetzt sich in zwei Stufen mit einem Gesamtmassenverlust von 47.9 %. Die zugehörigen endothermen Ereignisse finden bei  $T_p = 220$  und  $316$  °C ( $T_{\text{Onset}} = 198$  und  $284$  °C) statt. Bei der ersten Stufe ( $T_{\text{Onset}} = 198$  °C) wird ein begleitender Massenverlust von ca. 25 % beobachtet, welcher der Emission zweier Aminmoleküle entspricht. Nach der zweiten Stufe (Massenverlust 22.9 %) treten im Pulverdiffraktogramm des Abbauprodukts die Reflexe von MnS und SnS auf. Wird die thermische Zersetzung nach der ersten Stufe (bei  $220$  °C) abgebrochen, so wird ein hellbraunes Pulver erhalten, dessen Pulverdiffraktogramm neben den Reflexen von MnS und SnS auch weitere, nicht zuordenbare aufweist. Mit CHN-Analyse kann der verbliebene organische Anteil bestimmt werden, was zu der formalen Zusammensetzung  $[\text{Mn}(1,2\text{-dach})_2]\text{SnS}_3$  führt. Die Annahme, dass zunächst die protonierten Aminmoleküle, die um die anionischen Ketten lokalisiert sind, abgebaut werden, konnte mittels MIR-Spektroskopie bestätigt werden. Die durch protonierte Amine hervorgerufenen Absorptionen konnten nicht mehr in den Spektren beobachtet werden. Allerdings ist dies noch kein Beweis und kombinierte DTA-TG-MS-Untersuchungen sind notwendig, um den Zersetzungsmechanismus aufzuklären.

The Influence of the Amine Concentration onto Product Formation:  
Crystal Structures, Thermal Stability and Spectroscopic Properties of  
Two New Manganese Thiostannates Obtained under Solvothermal  
Conditions

Nicole Pienack, Christian Näther, and Wolfgang Bensch

Institute of Inorganic Chemistry  
Christian-Albrechts-University of Kiel  
Max-Eyth-Str. 2  
24118 Kiel  
Germany

Reprints request to Wolfgang Bensch. E-mail: [wbensch@ac.uni-kiel.de](mailto:wbensch@ac.uni-kiel.de). Phone: +49 431 880-2419. Fax: +49 431 880-1520

Two new thiostannates with  $\text{Mn}^{2+}$  ions were obtained under solvothermal conditions applying different amine concentrations.  $[\text{Mn}(\text{C}_6\text{H}_{14}\text{N}_2)_2(\text{H}_2\text{O})]_2\text{Sn}_2\text{S}_6$  (**1**) ( $\text{C}_6\text{H}_{14}\text{N}_2$  = 1,2-diaminocyclohexane, 1,2-dach) crystallizes in the monoclinic space group  $C2/c$  (with  $a = 23.7500(18)$ ,  $b = 15.5655(16)$ ,  $c = 12.1072(9)$  Å,  $\beta = 113.532(8)^\circ$ ,  $Z = 8$ ). The second compound,  $[\text{Mn}(\text{C}_6\text{H}_{14}\text{N}_2)_2]\text{Sn}_2\text{S}_6 \cdot 2 \text{C}_6\text{H}_{15}\text{N}_2$  (**2**) crystallizes in the triclinic space group  $P\bar{1}$  with  $a = 7.3019(6)$ ,  $b = 11.1798(9)$ ,  $c = 13.2837(11)$  Å,  $\alpha = 76.877(10)$ ,  $\beta = 74.719(9)$ ,  $\gamma = 82.972(10)^\circ$ ,  $Z = 1$ . Both structures feature  $[\text{Sn}_2\text{S}_6]^{4-}$  anions acting as bidentate ligands joining the octahedrally coordinated  $\text{Mn}^{2+}$  cations, but in **1** a molecular complex is formed, whereas in **2** a one-dimensional coordination polymer is observed. In **1** the  $\text{Mn}^{2+}$  cation has bonds to four N atoms of two 1,2-dach ligands, to one  $\text{H}_2\text{O}$  molecule, and to one S atom of the  $[\text{Sn}_2\text{S}_6]^{4-}$  anion. The  $[\text{Sn}_2\text{S}_6]^{4-}$  anion is located on an inversion center joining two symmetry related complexes. In **2**  $\text{Mn}^{2+}$  is surrounded by four N atoms of two 1,2-dach ligands and by two S atoms of two neighboring  $[\text{Sn}_2\text{S}_6]^{4-}$  anions. In contrast to **1** a negatively charged coordination polymer is formed with  $[\text{Sn}_2\text{S}_6]^{4-}$  anions acting as linkers and the  $\text{Mn}^{2+}$  centered complexes being the nodes. The co-crystallized 1,2-dach molecules are protonated, and they are located between the chains. The first compound was obtained in an aqueous solution of 1,2-dach, and **2** crystallized from a concentrated 1,2-dach solution. In both compounds several short  $\text{S}\cdots\text{H}$  distances indicate weak hydrogen bonding interactions. Compound **1** is stable up to 121 °C and **2** up to 220 °C. In the Raman spectra of **1** and **2** resonances which are typical for  $[\text{Sn}_2\text{S}_6]^{4-}$  units could be observed. The band gaps are found to be 2.6 eV (477 nm) and 3.1 eV (400 nm) for **1** and **2**, respectively.

*Key words:* Thiostannates, Solvothermal Syntheses, Crystal Structure, Thermal and Spectroscopic Properties

## Introduction

During the last decade new open-framework thiometalate compounds were synthesized following the solvothermal route, and the potential of this approach was recently reviewed [1 - 3]. The structural features as well as the physical and chemical properties of thiometalate networks can be altered by the integration of transition metal (*TM*) ions. Whereas it is not surprising that chalcophilic elements like copper and silver can easily be integrated into thiometalate networks [4 - 8], the incorporation of other transition metal cations is more challenging. Using  $\text{Co}^{2+}$ ,  $\text{Ni}^{2+}$  or  $\text{Fe}^{2+}$  and amines as solvents and structure directing molecules, in most of the cases inorganic anions and  $[\text{TM}(\text{amine})_x]^{n+}$  complexes as charge compensating cations are found in the reaction products as for example in  $[\text{Ni}(\text{en})_3]_2\text{Sn}_2\text{S}_6$  (en = ethylenediamine) and  $[\text{Ni}(\text{dap})_3]_2\text{Sn}_2\text{S}_6 \cdot 2 \text{H}_2\text{O}$  (dap = diaminopropane) [9]. A few years ago we established a new synthesis strategy using multidentate amines like tren (tren = tris(2-aminoethyl)amine) which form unsaturated transition metal complexes. Such unsaturated  $[\text{TM}(\text{amine})_x]^{n+}$  complexes can form one or two bonds to the thiometalate network [e. g.  $[\text{Co}(\text{tren})]_2\text{Sn}_2\text{S}_6$  [9],  $[\text{Ni}(\text{tren})]\text{Sb}_2\text{S}_4$  [10] and  $[\text{TM}(\text{tren})]\text{Sb}_4\text{S}_7$  ( $\text{TM} = \text{Mn}, \text{Fe}, \text{Co}, \text{Zn}$ ) [11]]

Compared to other transition metals,  $\text{Mn}^{2+}$  behaves differently and is often integrated into thiometalate networks without usage of a multidentate amine. It seems that  $\text{Mn}^{2+}$  has a comparable affinity to S and N atoms. A prominent example is the thioantimonate structure family  $\text{Mn}_2(\text{L})\text{Sb}_2\text{S}_5$  with L = methylamine (ma), ethylamine (ea), diaminopropane (dap), diethylenetriamine (dien), *N*-methyl-1,3-diaminopropane (mdap) [12 - 14], ethylenediamine (en) [15] or diaminopentane (dape) [16] where one of the two independent  $\text{Mn}^{2+}$  ions is coordinated by four S and two N atoms whereas the second is surrounded by six S atoms.

Another interesting example is the thioantimonate  $[\text{Mn}(\text{C}_6\text{H}_{14}\text{N}_2)_3]_2[\text{Mn}(\text{C}_6\text{H}_{14}\text{N}_2)_2(\text{SbS}_4)_2] \cdot 6 \text{H}_2\text{O}$  ( $\text{C}_6\text{H}_{14}\text{N}_2 = 1,2\text{-diaminocyclohexane}, 1,2\text{-dach}$ ) with one  $\text{Mn}^{2+}$  ion in an isolated  $[\text{Mn}(1,2\text{-dach})_3]^{2+}$  cation and another  $\text{Mn}^{2+}$  ion surrounded by two 1,2-dach ligands and two monodentate  $[\text{SbS}_4]^{3-}$  units [17]. In the literature only a few Mn thioantimonates were reported

like  $[\text{Mn}(\text{en})_3]_2\text{Sn}_2\text{S}_6$  [18] and  $[\text{Mn}(\text{dien})_2]_2\text{Sn}_2\text{S}_6$  [19] with isolated  $[\text{Sn}_2\text{S}_6]^{4-}$  anions, or  $([\text{Mn}_2(\text{en})_5]\text{Sn}_2\text{S}_6)_n$  in which  $\text{Mn}^{2+}$  has bonds to one S atom and 5 N atoms [20]. Recently, we published the first  $\text{Mn}^{2+}$  containing thiostannate  $(1,4\text{-dabH})_2\text{MnSnS}_4$  crystallizing in an anionic chain structure with protonated amine molecules as charge compensating cations [21]. During our investigation of the Mn-Sn-S 1,2-diaminocyclohexane system we obtained two thiostannates  $[\text{Mn}(\text{C}_6\text{H}_{14}\text{N}_2)_2(\text{H}_2\text{O})]_2\text{Sn}_2\text{S}_6$  and  $[\text{Mn}(\text{C}_6\text{H}_{14}\text{N}_2)_2]\text{Sn}_2\text{S}_6 \cdot 2 \text{C}_6\text{H}_{15}\text{N}_2$ . Here we report the syntheses, crystal structures, spectroscopic and thermal properties of the new compounds.

## Experimental

### *Synthesis*

#### *General:*

All chemicals were purchased (see below for purity and company) and used without further purifications. All compounds were prepared under solvothermal conditions in Teflon-lined steel autoclaves (inner volume: 30 mL) using manganese, tin and sulfur. The crystalline products were filtered off after the reactions, washed with water and ethanol and dried in vacuum.

#### *Synthesis of $[Mn(C_6H_{14}N_2)_2(H_2O)]_2Sn_2S_6$ (1):*

1 mmol Sn (99.5 %, Aldrich), 1 mmol Mn (99.5 %, Alfa Aesar) and 4 mmol S in 2.5 mL of 1,2-diaminocyclohexane ( $C_6H_{14}N_2$ , 1,2-dach) ( $\geq 99$  %, Aldrich) and 2.5 mL of water were reacted for 98 h at 130 °C. In the reaction products dark-brown rods as well as several Mn and Sn sulfides were found. The yield of  $[Mn(C_6H_{14}N_2)_2(H_2O)]_2Sn_2S_6$  was about 15 % (based on tin).

#### *Synthesis of $[Mn(C_6H_{14}N_2)]Sn_2S_6 \cdot 2 C_6H_{15}N_2$ (2):*

1 mmol Sn, 1 mmol Mn and 4 mmol S in 5 mL of 1,2-dach were reacted for 98 h at 130 °C. In the reaction products yellow needles were found in a yield of approximately 15 % (based on Sn) whereas Mn and Sn sulfides formed the main part of the products.

The crystals were manually separated, and the homogeneity of the compounds was confirmed by X-ray powder diffraction and CHN analyses. Results in %: **1**: found C 26.4, H 5.7, N 10.4; calcd. C 27.9, H 5.8, N 10.9; **2**: found: C 30.1, H 6.2, N 11.6; calcd. C 30.6, H 6.2, N 11.9.

### Structure determination

The intensity data for the compounds were collected using a Stoe IPDS-1 (Imaging Plate Diffraction System) with Mo- $K_{\alpha}$  radiation at room temperature for **1** and **2**. The structures were solved with Direct Methods using the program SHELXS-97 [22], and the refinements were done against  $F^2$  with SHELXL-97 [23]. For all non-hydrogen atoms anisotropic displacement parameters were used. The hydrogen atoms of the amines and of the water molecules in **1** were positioned with idealized geometry and refined using a riding model and a fixed isotropic displacement parameter. Some disorder of the amine is present in compound **2**, and the structure refinement was done using a split model. Selected refinement results are summarized in Table 1. Structural data for **1** and **2** have been deposited with The Cambridge Crystallographic Data Centre as publication no. CCDC 701654 (**1**) and CCDC 701655 (**2**). Copies of the data can be obtained, free of charge, via [www.ccdc.cam.ac.uk/data\\_request/cif](http://www.ccdc.cam.ac.uk/data_request/cif).

Table 1. Selected details of the data collection and structure refinement results of the title compounds.

	[Mn(C <sub>6</sub> H <sub>14</sub> N <sub>2</sub> ) <sub>2</sub> (H <sub>2</sub> O)] <sub>2</sub> Sn <sub>2</sub> S <sub>6</sub> ( <b>1</b> )	[Mn(C <sub>6</sub> N <sub>2</sub> H <sub>14</sub> ) <sub>2</sub> ]Sn <sub>2</sub> S <sub>6</sub> · 2 C <sub>6</sub> N <sub>2</sub> H <sub>15</sub> ( <b>2</b> )
Crystal system	monoclinic	triclinic
Space group	<i>C</i> 2/ <i>c</i>	<i>P</i> $\bar{1}$
<i>a</i> , Å	23.7500(18)	7.3019(6)
<i>b</i> , Å	15.5655(16)	11.1798(9)
<i>c</i> , Å	12.1072(9)	13.2837(11)
$\alpha$ , deg	90	76.877(10)
$\beta$ , deg	113.532(8)	74.719(9)
$\gamma$ , deg	90	82.872(10)
<i>V</i> , Å <sup>3</sup>	4103.6(6)	1016.36(14)
<i>Z</i>	4	1
$D_{\text{calculated}}$ , g cm <sup>-3</sup>	1.67	1.54
$\mu$ , mm <sup>-1</sup>	2.1	1.9

Scan range	$2.62 \leq \theta \leq 28.16^\circ$	$2.72 \leq \theta \leq 28.00^\circ$
Reflections collected	25198	10307
Refl. with $F_o \geq 4\sigma(F_o)$	2088	479
Independent reflections	4943	4838
Goodness-of-fit on $F^2$	1.049	0.937
Final $R$ indices [ $I \geq 2\sigma(I)$ ]	$RI = 0.0381,$ $wR2 = 0.0923$	$RI = 0.0370,$ $wR2 = 0.0793$
$R$ indices (all data)	$RI = 0.0457,$ $wR2 = 0.0958$	$RI = 0.0622,$ $wR2 = 0.0873$
Res. elec. dens., $e \text{ \AA}^{-3}$	1.39 / -1.20	0.83 / -1.21

#### *Thermal investigations*

The thermal measurements were performed on a Netzsch STA 429 DTA-TG device. The samples were heated to 600 °C at a rate of 4 K·min<sup>-1</sup> under a flow of argon (75 mLmin<sup>-1</sup>) in Al<sub>2</sub>O<sub>3</sub> crucibles. The TG data were corrected for buoyancy and current effects.

#### *Infrared spectroscopy*

MIR spectra (450-3000 cm<sup>-1</sup>) were recorded with an ATI Mattson Genesis spectrometer. In the IR spectra the absorptions located at 3271 (m, -NH stretch, -NH<sub>2</sub>), 3199 (w, -NH stretch, -NH<sub>2</sub>), 3118 (m, -NH stretch, -NH<sub>2</sub>), 2927 (s, -CH<sub>2</sub>; m-s, -NH stretch), 2852 (m, -NH stretch), 1625 (m, -CC), 1574 (s, -NH<sub>2</sub>), 1444 (s, -CH, -CH<sub>2</sub>), 1349 (m, -CN), 1227 (w, -CN), 1139 (w, -CN), 1108 (m, -CN) and 1008 (s, -CN) cm<sup>-1</sup> for **1** can be assigned to the diaminocyclohexane and in a similar way for **2**: 3443 (m, -NH stretch (asym), -NH<sub>2</sub>), 3299 (s, -NH stretch, -NH<sub>2</sub>), 3243 (s, -NH stretch, -NH<sub>2</sub>), 3137 (m, -NH stretch, -NH<sub>3</sub><sup>+</sup>), 2924 (s, -CH<sub>2</sub>; m-s, -NH stretch), 2852 (s, -CH<sub>2</sub>; m-s, -NH stretch), 2720 (m, -NH stretch, -NH<sub>3</sub><sup>+</sup>), 2645 (m, -NH stretch, -NH<sub>3</sub><sup>+</sup>), 2503 (s, -NH stretch (asym), -NH<sub>3</sub><sup>+</sup>), 2022 (m, -NH<sub>3</sub><sup>+</sup> overtone), 1580 (s, -NH<sub>2</sub>), 1508 (s, -NH<sub>3</sub><sup>+</sup> deformation (sym)), 1451 (s, -CH, -CH<sub>2</sub>), 1379 (s, -CN), 1119 (s, -CN) and 1004 (s, -CN) cm<sup>-1</sup>.

*Raman spectroscopy*

Raman spectra were recorded with a Bruker IFS 66 Fourier transform Raman spectrometer (wavelength: 541.5 nm) in the region from 100 to 3500  $\text{cm}^{-1}$ .

*UV/Vis spectroscopy*

UV/Vis spectroscopic investigations were carried out at room temperature using an UV/Vis/NIR two-channel spectrometer Cary 5 from Varian Techtron Pty., Darmstadt. The optical properties of the compounds were investigated by analyzing the UV/Vis reflectance spectra of the powdered samples (with  $\text{BaSO}_4$  powder used as reference material). The absorption data were calculated applying the Kubelka-Munk relation for diffuse reflectance data. For **1**  $E_g$  amounts to 2.6 eV (477 nm), and the value for **2** is 3.1 eV (400 nm).

*EDX experiments*

Scanning electron microscopy investigations and energy dispersive analysis of X-rays (EDX) were done with a Philips Environmental Scanning Electron Microscope ESEM XL30 equipped with an EDAX detector.

## Results and Discussion

### *Syntheses*

Despite a large number of syntheses varying several experimental parameters like temperature or time, the yield of the two new compounds was relatively low. This observation is not unusual, and several other reaction parameters should be also varied. But such further variations are time consuming, and one cannot be sure that the yield is significantly enhanced. Nevertheless, the title compounds are interesting examples demonstrating the influence of the concentration of the amine onto the product. In concentrated 1,2-dach solution the compound  $[\text{Mn}(\text{C}_6\text{H}_{14}\text{N}_2)_2]\text{Sn}_2\text{S}_6 \cdot 2 \text{C}_6\text{H}_{15}\text{N}_2$  (**2**) is formed with the  $\text{Mn}^{2+}$  cation being octahedrally surrounded by four N and two S atoms. Dilution of 1,2-dach with water results in the crystallization of  $[\text{Mn}(\text{C}_6\text{H}_{14}\text{N}_2)_2(\text{H}_2\text{O})_2]\text{Sn}_2\text{S}_6$  (**1**) where the octahedral environment of the  $\text{Mn}^{2+}$  ion contains four N atoms, one O and one S atom. In the concentration range from 12.5 up to 62.5 % aqueous 1,2-dach solution only **1** is obtained, and a mixture of both compounds is formed applying a 75 % 1,2-dach solution. Above this concentration the water containing thiostannate is not observed, and **2** crystallizes.

### *Crystal structures*

$[\text{Mn}(\text{C}_6\text{H}_{14}\text{N}_2)_2(\text{H}_2\text{O})_2]\text{Sn}_2\text{S}_6$  (**1**) crystallizes in the monoclinic space group  $C2/c$  with eight formula units in the unit cell and  $[\text{Mn}(\text{C}_6\text{H}_{14}\text{N}_2)_2]\text{Sn}_2\text{S}_6 \cdot 2 \text{C}_6\text{H}_{15}\text{N}_2$  (**2**) crystallizes in the triclinic space group  $P\bar{1}$  with one formula unit in the unit cell. Both structures consist of  $[\text{Sn}_2\text{S}_6]^{4-}$  anions and charge compensating  $\text{Mn}^{2+}$  centered complexes. All atoms are located on general positions except Mn in **2** which is located on a special position. The  $[\text{Sn}_2\text{S}_6]^{4-}$  bi-tetrahedron (Fig. 1) is formed by two symmetry related edge-sharing  $\text{SnS}_4$  tetrahedra, and this anion is very common for thiostannates [9, 18 - 20].

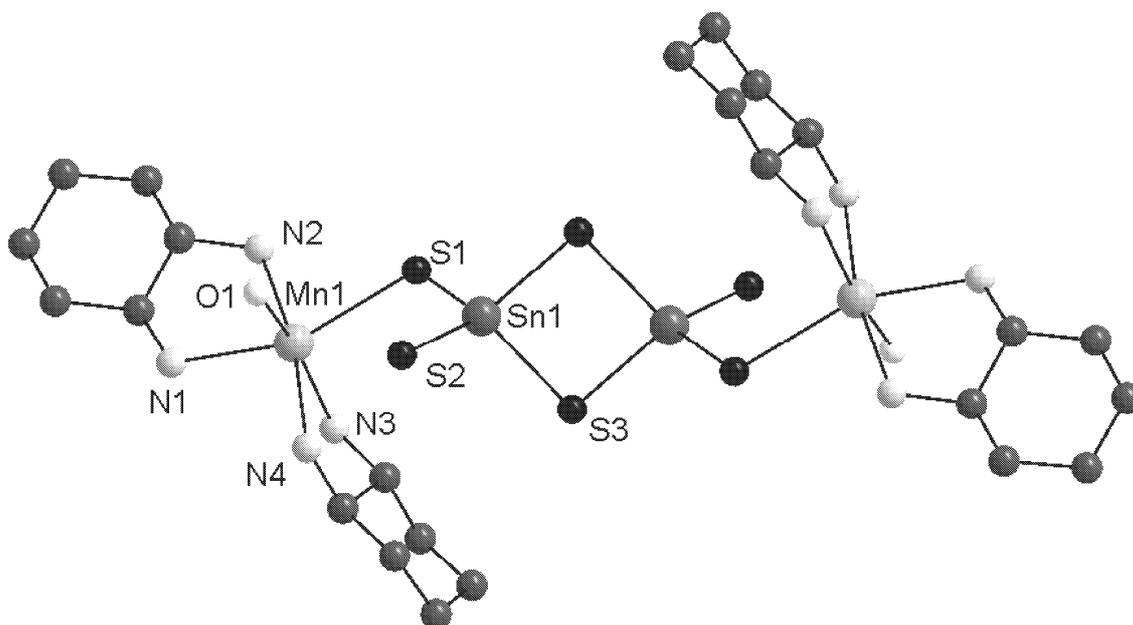


Fig. 1. The structure of  $[\text{Mn}(\text{C}_6\text{H}_{14}\text{N}_2)(\text{H}_2\text{O})]_2\text{Sn}_2\text{S}_6$  (**1**) with atom labeling. Note that H atoms are omitted and C atoms are not labeled.

The values for the terminal Sn-S<sub>t</sub> bond lengths are 2.3294(10) and 2.3373(10) Å and are shorter than the bridging Sn-S<sub>b</sub> bonds with values from 2.4415(9) to 2.4582(10) Å (Table 2).

Table 2. Selected bond lengths (Å) and angles (deg) of compounds **1** and **2**.

	<b>1</b>	<b>2</b>
Sn – S1	2.3561(9)	2.3432(10)
Sn – S2	2.3294(10)	2.3373(10)
Sn – S3	2.4582(10)	2.4462(11)
Sn – S3 <sup>a</sup>	2.4415(9)	2.4454(12)
S1 – Sn – S2	112.25(3)	117.27(4)
S1 – Sn – S3	109.37(4)	108.22(4)
S2 – Sn – S3	114.76(4)	111.68(4)
S1 – Sn – S3 <sup>a</sup>	113.02(4)	112.59(4)
S2 – Sn – S3 <sup>a</sup>	113.07(3)	110.78(4)

S3 – Sn – S3 <sup>a</sup>	92.99(3)	93.82(4)
Sn – S3 – Sn <sup>a</sup>	87.01(3)	86.18(4)
Mn1 – N1	2.279(3)	2.267(3)
Mn1 – N2	2.297(4)	2.266(4)
Mn1 – N3	2.268(3)	
Mn1 – N4	2.281(3)	
Mn1 – S1	2.5707(10)	2.6888(11)
Mn1 – O1	2.302(3)	

The S(1) atoms have a bond to the Mn<sup>2+</sup> cation but the Sn-S bond lengths of 2.3561(9) (**1**) and 2.3432(10) Å (**2**) are not affected, and the values are in the same range like those reported for discrete [Sn<sub>2</sub>S<sub>6</sub>]<sup>4-</sup> anions. The S<sub>b</sub>-Sn-S<sub>b</sub> angles of the Sn<sub>2</sub>S<sub>2</sub> rings are 92.99(3) (**1**) and 93.82(4)° (**2**) and are larger than the Sn-S<sub>b</sub>-Sn angles (87.01 (**1**) and 86.18° (**2**)). The other angles around the Sn<sup>4+</sup> ions range from 108.24(5) to 117.27(4)° (Table 2) indicating a severe deviation from the ideal geometry, but all values match well with those reported in literature [9, 24].

In both compounds the Mn<sup>2+</sup> cations are in a distorted octahedral coordination. In **1** the Mn<sup>2+</sup> ion is surrounded by four N atoms of two amine molecules, one S atom of the [Sn<sub>2</sub>S<sub>6</sub>]<sup>4-</sup> anion and one O atom of a water molecule giving the formula [Mn(C<sub>6</sub>H<sub>14</sub>N<sub>2</sub>)<sub>2</sub>(H<sub>2</sub>O)]<sup>2+</sup> (Fig. 1). In contrast, in **2** the Mn<sup>2+</sup> cation is in the environment of four N atoms of two ligands and two S atoms of neighboring [Sn<sub>2</sub>S<sub>6</sub>]<sup>4-</sup> anions yielding [Mn(C<sub>6</sub>H<sub>14</sub>N<sub>2</sub>)<sub>2</sub>S<sub>2</sub>] as the formula. In **1** the [Sn<sub>2</sub>S<sub>6</sub>]<sup>4-</sup> anion is located on an inversion centre and acts as a bidentate ligand connecting two symmetry related [Mn(C<sub>6</sub>H<sub>14</sub>N<sub>2</sub>)<sub>2</sub>(H<sub>2</sub>O)]<sup>2+</sup> complexes forming neutral [Mn(C<sub>6</sub>H<sub>14</sub>N<sub>2</sub>)<sub>2</sub>(H<sub>2</sub>O)]<sub>2</sub>Sn<sub>2</sub>S<sub>6</sub> moieties. In **2** the position of the H<sub>2</sub>O molecule is empty allowing bond formation to another [Sn<sub>2</sub>S<sub>6</sub>]<sup>4-</sup> anion yielding a coordination polymer with the Mn<sup>2+</sup> complexes as nodes and the anions as linkers (Fig. 2).

In compound **1** the Mn-N bond lengths (2.268(3) - 2.297(4) Å, Table 2), the Mn-N-Mn angles ranging from 74.85(13) to 168.43(14)°, the Mn-S bond of 2.5707(10) Å as well as the Mn-O bond of 2.302(3) Å (Table 2) are in the range as reported for other compounds like  $C_9H_{23}N_3OMnS_4$  [25],  $[Mn(C_6H_{18}N_4)(C_6H_{19}N_4)]SbS_4$  ( $C_6H_{18}N_4 = tren$ ) and  $[Mn(C_6H_{14}N_2)_3]_2[Mn(C_6H_{14}N_2)_2(SbS_4)_2] \cdot 6 H_2O$  [17].

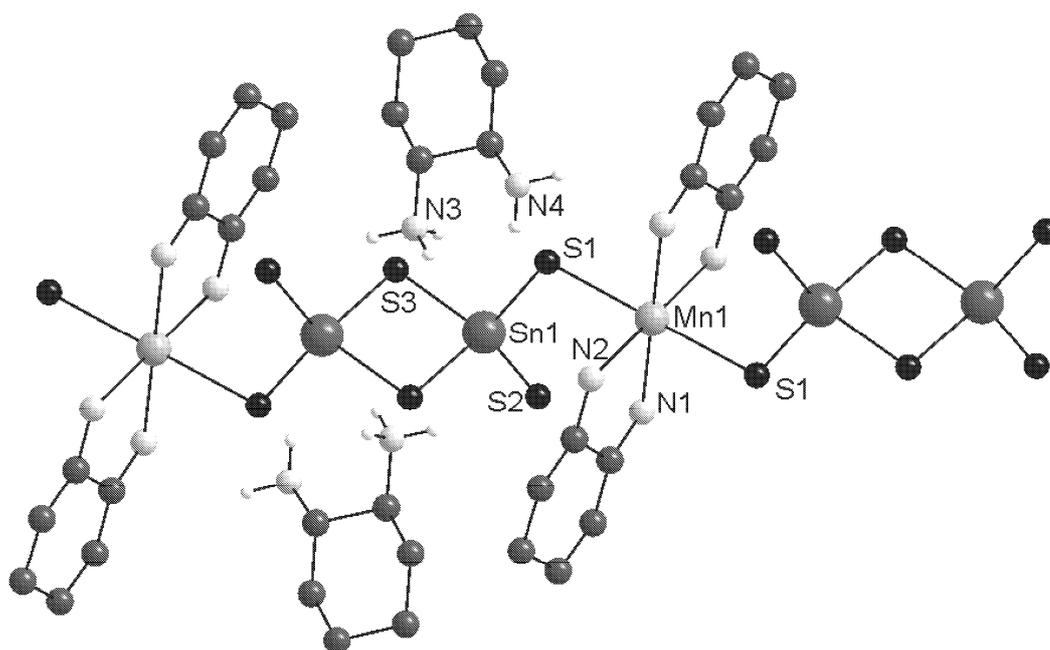


Fig. 2. Part of the crystal structure of compound **2** showing the  $\{[Mn(C_6H_{14}N_2)_2]Sn_2S_6\}$  chain and the isolated 1,2-dach molecules. Note that only the H atoms of the isolated 1,2-dach molecules are shown.

In **2** the Mn-N bonds are identical (2.266(4) and 2.267(3) Å, bite angle N-Mn-N: 77.76(13)°) and shorter than in **1**. In contrast, the Mn-S bond length of 2.6888(11) Å (Table 2) is about 0.12 Å longer than in **1**. Sterical requirements of the amine may explain the weakening of the Mn-S interaction. The enlargement of the Mn-S bond length is accompanied by shorter Mn-N bonds. A similar phenomenon was observed in the thioantimonate family  $Mn_2(L)Sb_2S_5$  [12, 13, 16] where Mn-S distances up to 3.185 Å for  $L = mdap$  were observed [14, 16]. The N-

Mn-S angles are in the range from 84.60(9) to 95.40(9) ° evidencing a severe distortion of the octahedral environment.

In **1** the  $[\text{Mn}(\text{C}_6\text{H}_{14}\text{N}_2)_2(\text{H}_2\text{O})]_2\text{Sn}_2\text{S}_6$  moieties are stacked onto each other to form rods along  $[\bar{1}10]$  and along  $[001]$ . Within the (001) plane a layer-like arrangement of the complexes occurs with neighboring molecules being rotated by 90° (Fig. 3). The dimensions of the channels formed by four complexes (see center of the unit cell) are about 6.2 · 5.2 Å.

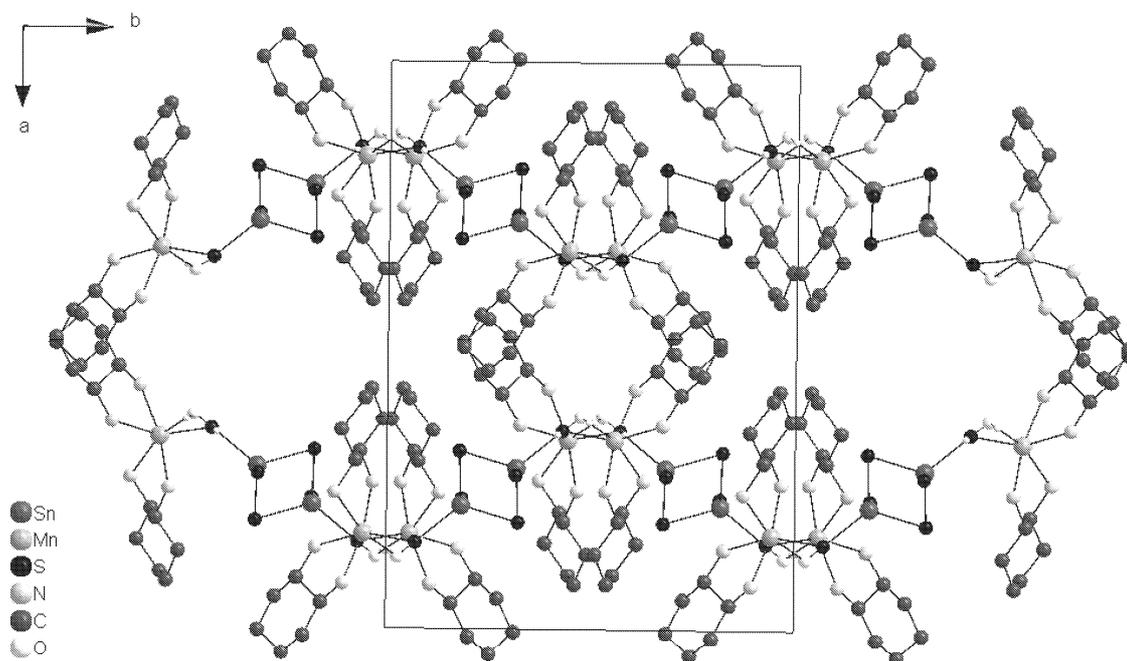


Fig. 3. Arrangement of the  $[\text{Mn}(\text{C}_6\text{H}_{14}\text{N}_2)_2(\text{H}_2\text{O})]_2\text{Sn}_2\text{S}_6$  units in compound **1** (view along the  $c$  axis). H atoms are omitted for clarity.

In **1** the  $\text{H}_2\text{O}$  molecules and N(1), N(3), and N(4) are involved in intra- and intermolecular hydrogen bonding interactions (see Table 3). One of the H atoms of  $\text{H}_2\text{O}$  has a short distance to the terminal S(2) atom and the other an interaction with S(1) of a neighboring molecule. The S(2) atom is involved in five  $\text{S}\cdots\text{H}$  interactions of which two are intramolecular and three

connect to two adjacent  $[\text{Mn}(\text{C}_6\text{H}_{14}\text{N}_2)_2(\text{H}_2\text{O})]_2\text{Sn}_2\text{S}_6$  units. The bridging S(3) atom has only one such interaction to a neighboring moiety, and S(1) has also one contact to this neighbor.

In **2** the anionic chains are running along [010]. The void space generated by neighboring chains is occupied by the 1,2-dach molecules. Charge neutrality requires protonated amine molecules in the second compound where these are located next to the  $[\text{Sn}_2\text{S}_6]^{4-}$  anions (Fig. 4).

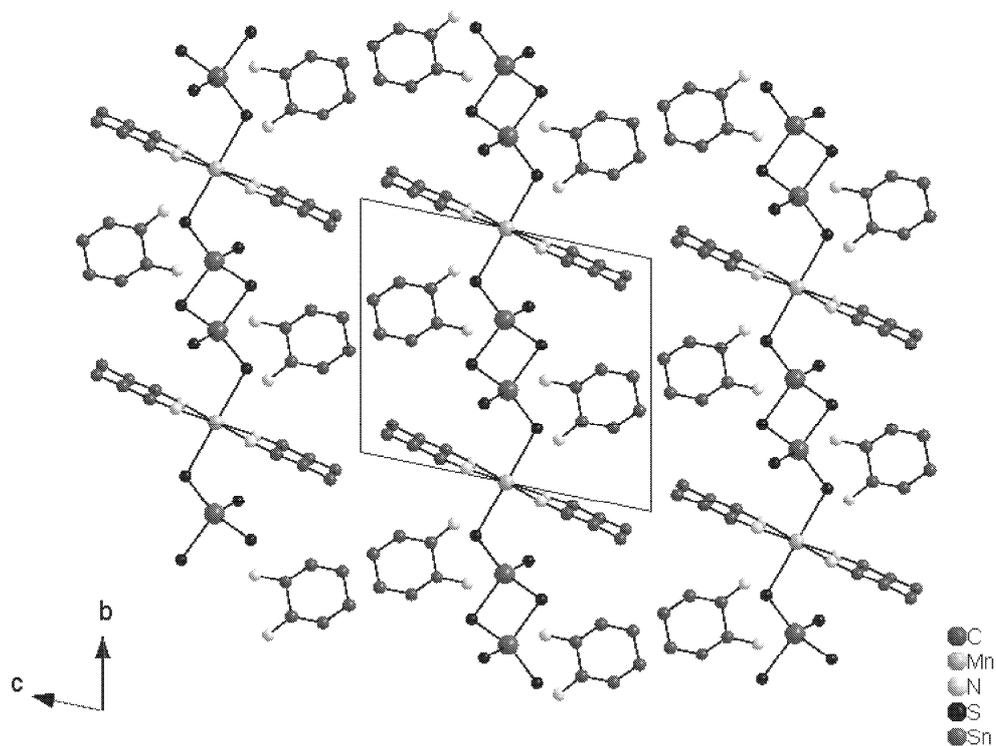


Fig. 4. Arrangement of the chains and the amine molecules in compound **2** (view along [100]). Hydrogen atoms are omitted for clarity.

It is obvious that the different arrangements are due to the spatial requirements of the cations and anions. Like for **1** several S atoms of **2** are involved in  $\text{S}\cdots\text{H}$  interactions (Table 3), but the bridging S(3) atom is not part of such contacts. All three H atoms of the  $\text{N}(3)\text{H}_3$  group show  $\text{S}\cdots\text{H}$  bonding interactions with S atoms of two adjacent chains, whereas only one H atom of  $\text{N}(4)\text{H}_2$  has such a contact (Table 3).

Table 3. Interatomic S...H distances (Å) and angles (deg) indicating hydrogen bonding interactions.

Distances			Angles		
	<b>1</b>	<b>2</b>		<b>1</b>	<b>2</b>
S1 ... H-N1	2.750	-	S1-H-N1	158.75	-
S1...H-O1	2.267	-	S1-H-O1	166.30	-
S1 ... H-N3	-	2.522	S1-H-N3	-	147.48
S2 ... H-N1	2.743	2.686 (intramolecular)	S2-H-N1	167.23	170.41
S2...H-N2	-	2.799	S2-H-N2	-	155.29
S2 ... H-N3	2.681	2.449	S2-H-N3	163.82	168.33
S2...H-N3	2.664	2.427	S2-H-N3	156.86	163.79
S2...H-N4	2.628 (intramolecular)	2.917	S2-H-N4	157.04	136.05
S2...H-O1	2.243 (intramolecular)	-	S2-H-O1	169.41	-
S3 ... H-N4	2.953	-	S3-H-N4	149.49	-

### *Spectroscopic Properties*

#### *Raman spectroscopy*

The interesting region of the Raman spectra ranges from 400 to 100  $\text{cm}^{-1}$  where the Sn-S resonances are located (Fig. 5). Spectral data for the  $[\text{Sn}_2\text{S}_6]^{4-}$  anion are well documented and were reported in many publications, as for example in [9] or for  $\text{Na}_4\text{Sn}_2\text{S}_6 \cdot 14 \text{H}_2\text{O}$  in ref. [26]. The assignment of the modes was made based on these published data (Table 4).

Table 4. Data of the Raman lines of  $\text{Na}_4\text{Sn}_2\text{S}_6 \cdot 14 \text{H}_2\text{O}$ ,  $[\text{Mn}(\text{C}_6\text{H}_{14}\text{N}_2)_2(\text{H}_2\text{O})]_2\text{Sn}_2\text{S}_6$  (**1**) and  $[\text{Mn}(\text{C}_6\text{N}_2\text{H}_{14})_2]\text{Sn}_2\text{S}_6 \cdot 2 \text{C}_6\text{N}_2\text{H}_{15}$  (**2**) in  $\text{cm}^{-1}$ .

$\text{Na}_4\text{Sn}_2\text{S}_6 \cdot 14 \text{H}_2\text{O}$ [26]	<b>1</b>	<b>2</b>
377	385	379
341	347	345
281	285	289
190	-	198
151	153	152
136	137	132

The resonances of the symmetric Sn-S<sub>t</sub> stretching modes are found around 380 cm<sup>-1</sup>. In compounds **1** and **2** the Sn-S<sub>t</sub> bond lengths range from 2.3294(10) to 2.3375(11) Å, and therefore the lines observed in the spectra are slightly shifted (385 cm<sup>-1</sup> (**1**) and 379 cm<sup>-1</sup> (**2**)). The Sn-S<sub>b</sub> vibrations are located at lower wave numbers at about 347 cm<sup>-1</sup> (**1**) and 345 cm<sup>-1</sup> (**2**). The resonances at 285 cm<sup>-1</sup> (**1**) and 289 cm<sup>-1</sup> (**2**) are caused by a Sn<sub>2</sub>S<sub>2</sub> ring vibration. The energetic differences between the resonances in I and II as well as to the data reported for Na<sub>4</sub>Sn<sub>2</sub>S<sub>6</sub> · 14 H<sub>2</sub>O are caused by slightly differing bond lengths and angles. Below 200 cm<sup>-1</sup> deformation vibrations occur as well as resonances for lattice vibrations. A detailed assignment is not unambiguous, but in the literature the lines at about 190 and 130 cm<sup>-1</sup> were interpreted as SnS<sub>2</sub> wagging and twisting modes.

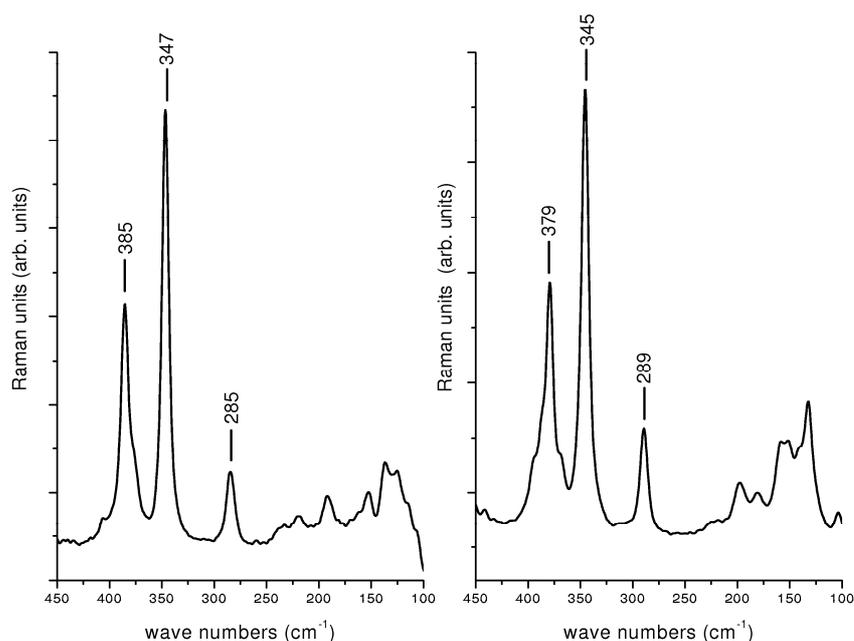


Fig. 5. The Raman spectra of compounds **1** and **2**. The wave numbers of the most prominent lines are given in the spectra.

### Thermal investigations

Compound **1** decomposes in three steps with a total weight loss of 48.6 % which is accompanied by three endothermic signals with peak temperatures at  $T_p = 121$ , 286 and 321 °C (Fig. 6).

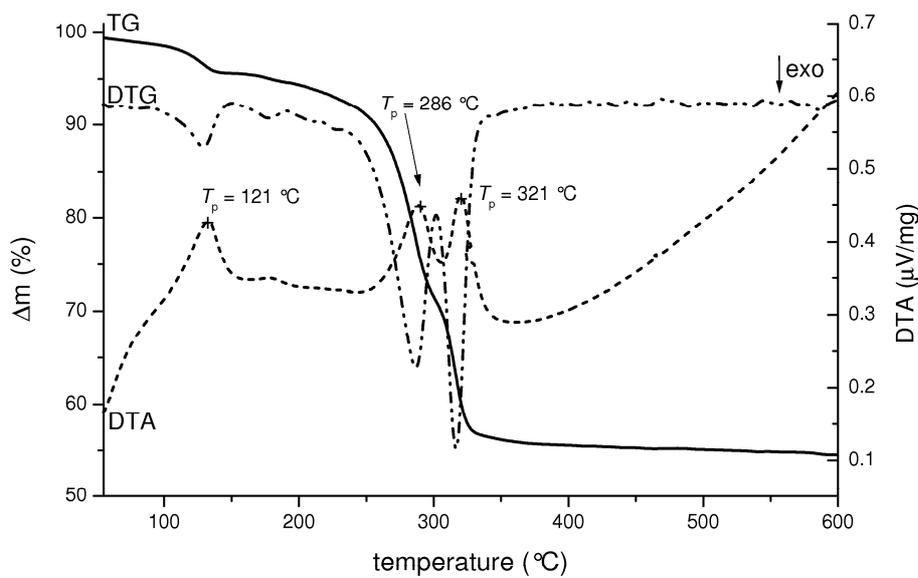
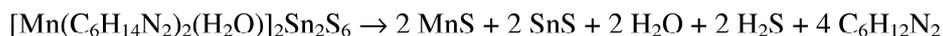


Fig. 6. DTA-TG-DTG curves of compound **1**. The peak temperatures  $T_p$  are indicated for the three thermal events.

The first step corresponds to the removal of water. Unfortunately, the following two thermal reactions are very close preventing a more detailed study of the decomposition mechanism. In the X-ray powder pattern of the decomposition product obtained at 600 °C MnS and SnS could be identified and the elemental analysis shows a few percent of CHN in the residue. The calculated weight loss of 53.5 % for the decomposition according to the formal equation



is larger than the observed value of 48.6 % which could be explained with the CHN contamination of the decomposition product.

Compound **2** decomposes in two steps with a total weight loss of 47.9 % with corresponding endothermic events at  $T_p = 220$  and 316 °C (Fig. 7).

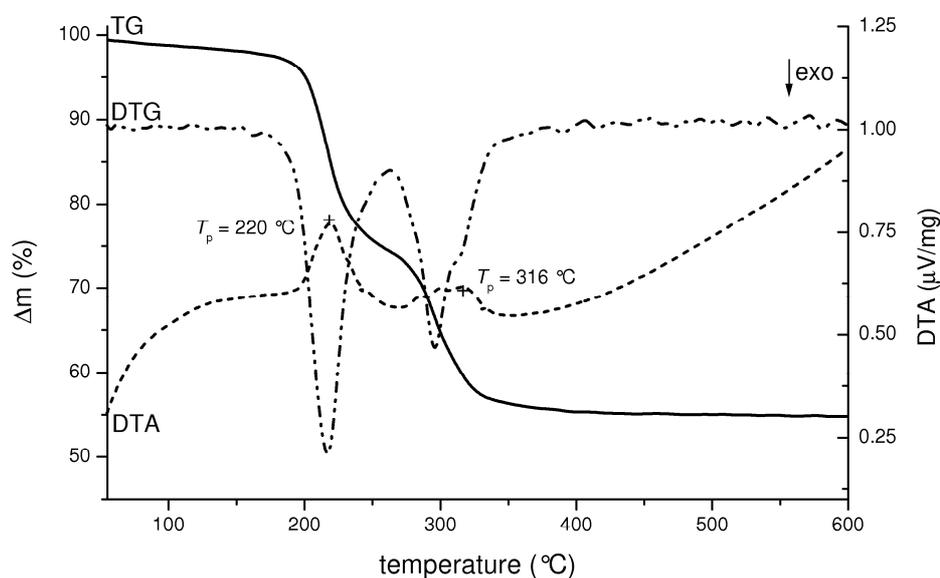


Fig.7. DTA-TG-DTG curves of compound **2**. The peak temperatures for the two endothermic events are indicated.

The first step with an onset temperature of  $T_{\text{onset}} = 198$  °C and a weight loss of approximately 25 % matches with the loss of two molecules 1,2-dach. The second step is accompanied by a mass loss of about 22.9 % and a broad endothermic signal indicating that there are some very close steps which cannot be resolved. Again, only reflections of MnS and SnS are present in the X-ray powder pattern after the decomposition and a few percent of CHN can be found in the final black residue. One can expect that the weight loss is due to the emission of 1,2-dach molecules and H<sub>2</sub>S. The moderate deviation of the experimentally determined mass loss from the expected value (55.4 %) can be explained with the contamination of the residue. An interruption of the thermal reaction at 220 °C yields a light brownish powder. In the X-ray powder pattern reflections of MnS and SnS were found as well as some reflections which cannot be identified. The elemental analysis gives an overall formula “[Mn(C<sub>6</sub>H<sub>14</sub>N<sub>2</sub>)<sub>2</sub>]SnS<sub>3</sub>” It can be assumed that in the first step the previously protonated amine molecules are removed. Indeed, in the IR spectrum (Fig. 8) of the intermediate of the thermal decomposition

reaction the absorptions corresponding to the protonated amino groups ( $-\text{NH}_3^+$ ) are missing, but the following modes observed at 3292 (w), 3207 (w), 3134 (w), 2923 (s), 2855 (s), 1688 (m), 1575 (s), 1445 (s), 1396 (m), 1354 (w) and 1110 (s)  $\text{cm}^{-1}$  can be assigned to the diaminocyclohexane (see Experimental Section infrared spectroscopy).

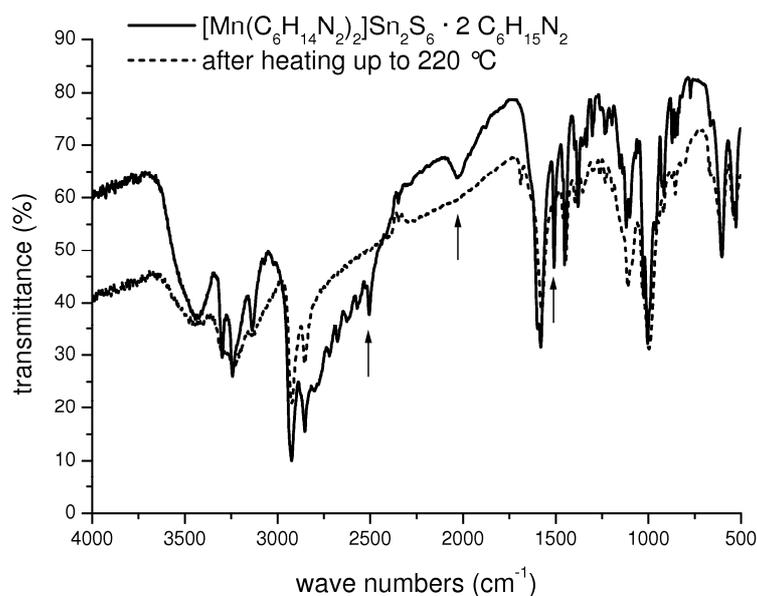


Fig. 8. Comparison of MIR spectra of compound **2** as synthesized and after heating up to 220 °C. Absorptions of the protonated amino groups ( $-\text{NH}_3^+$ ) in the starting material are marked.

## Conclusions

The successful isolation of the title compounds highlights the synthetic power of the solvothermal approach. From a diluted 1,2-dach solution,  $[\text{Mn}(\text{C}_6\text{H}_{14}\text{N}_2)_2(\text{H}_2\text{O})]_2\text{Sn}_2\text{S}_6$  (**1**) was obtained with the  $\text{Mn}^{2+}$  cation coordinated to three different ligands. The coordination of  $\text{H}_2\text{O}$  to  $\text{Mn}^{2+}$  is a highly interesting observation and to the best of our knowledge was not previously observed in transition metal thioantimonate chemistry. Normally water co-crystallizes as crystal water, and the transition metal cations have only bonds to the N atoms of the amine and/or to S atoms of the thioantimonate units. The  $\text{Mn}^{2+}$  cation seems to be unique in the series of transition metal cations with respect to bonding affinities to N and S, as mentioned in the introduction. The isolation of compound **1** further suggests that under special synthetic conditions  $\text{Mn}^{2+}$  also coordinates to O atoms. Whereas in **1** discrete molecules are observed, the structure of compound **2** can be viewed as a one-dimensional coordination polymer with the  $\text{Mn}^{2+}$ -centered cations as the nodes and the  $[\text{Sn}_2\text{S}_6]^{4-}$  anions acting as linkers. Comparing the two structures it appears that the removal of the  $\text{H}_2\text{O}$  ligand opens a second binding site for an S atom of the dissolved  $[\text{Sn}_2\text{S}_6]^{4-}$  anions. The  $\{[\text{Mn}(\text{C}_6\text{H}_{14}\text{N}_2)_2]\text{Sn}_2\text{S}_6\}^{2-}$  chain requires charge compensation which is achieved by the presence of protonated amine molecules. The isolation of two new thioantimonates by simply changing the concentration of the structure directing molecules in the solvent highlights the large synthetic potential of the solvothermal route. Often such dilution experiments are performed to increase the yield of a compound. But new compounds can also be formed and prominent examples are the series of  $[\text{Ni}(\text{dien})]^{2+}$  complexes (dien = diethylenetriamine) containing thioantimonates(III) [27-30]. These thioantimonates were obtained at the same temperature by varying the concentration of the amine. The reason for this finding is that the dilution of an amine not only changes the pH value but also several other important factors like viscosity, redox potential, boiling point *etc.* More syntheses with a systematic variation of the amine concentration may also yield new

thiostannates. Such experiments with different amines are currently under way in our laboratory.

*Acknowledgements*

Financial support by the State of Schleswig-Holstein and the Fonds der Chemischen Industrie is gratefully acknowledged.

- [1] W. S. Sheldrick, M. Wachhold, *Angew. Chem.* **1997**, *109*, 214-234; *Angew. Chem. Int. Ed. Engl.* **1997**, *36*, 206-224.
- [2] A. K. Cheetham, G. Férey, T. Loiseau, *Angew. Chem.* **1999**, *111*, 3466-3492; *Angew. Chem. Int. Ed. Engl.* **1999**, *38*, 3268-3292.
- [3] T. Jiang, G. A. Ozin, *J. Mater. Chem.* **1998**, *8*, 1099-1108.
- [4] N. Pienack, W. Bensch, *Z. Anorg. Allg. Chem.* **2006**, *632*, 1733-1736.
- [5] N. Pienack, C. Näther, W. Bensch, *Solid State Sci.* **2007**, *9*, 100-107.
- [6] V. Spetzler, H. Rijnberk, C. Näther, W. Bensch, *Z. Anorg. Allg. Chem.* **2004**, *630*, 142-148.
- [7] V. Spetzler, C. Näther, W. Bensch, *Inorg. Chem.* **2005**, *44*, 5805-5812.
- [8] V. Spetzler, C. Näther, W. Bensch, *J. Solid State Chem.* **2006**, *179*, 3541-3549.
- [9] M. Behrens, S. Scherb, C. Näther, W. Bensch, *Z. Anorg. Allg. Chem.* **2003**, *629*, 1367-1373.
- [10] R. Stähler, W. Bensch, *Eur. J. Inorg. Chem.* **2001**, 3073-3078.
- [11] M. Schaefer, R. Stähler, W. R. Kiebach, C. Näther, W. Bensch, *Z. Anorg. Allg. Chem.* **2004**, *630*, 1816-1822.
- [12] W. Bensch, M. Schur, *Eur. J. Solid State Inorg. Chem.* **1996**, *33*, 1149-1160.
- [13] M. Schur, C. Näther, W. Bensch, *Z. Naturforsch.* **2001**, *56b*, 79-84.
- [14] L. Engelke, R. Stähler, M. Schur, C. Näther, W. Bensch, R. Pöttgen, M. H. Möller, *Z. Naturforsch.* **2004**, *59b*, 869-876.
- [15] M. Schur, W. Bensch, *Z. Naturforsch.* **2002**, *57b*, 1-7.
- [16] A. Puls, C. Näther, W. Bensch, *Z. Anorg. Allg. Chem.* **2006**, *632*, 1239-1243.
- [17] M. Schaefer, L. Engelke, W. Bensch, *Z. Anorg. Allg. Chem.* **2003**, *629*, 1912-1918.
- [18] D. X. Jia, Y. Zhang, J. Dai, Q. Y. Zhu, X. M. Gu, *Z. Anorg. Allg. Chem.* **2004**, *630*, 313-318.

- [19] M. L. Fu, G. C. Guo, B. Liu, A. Q. Wu, J. S. Huang, *Chin. J. Inorg. Chem.* **2005**, *21*, 25-29.
- [20] X. M. Gu, J. Dai, D. X. Jia, Y. Zhang, Q. Y. Zhu, *Cryst. Growth Des.* **2005**, *5*, 1845-1848.
- [21] N. Pienack, K. Möller, C. Näther, W. Bensch, *Solid State Sci.* **2007**, *9*, 1110-1114.
- [22] G. M. Sheldrick, SHELXS-97, Program for the Solution of Crystal Structures, University of Göttingen, Göttingen (Germany) **1997**.
- [23] G. M. Sheldrick, SHELXL-97, Program for the Refinement of Crystal Structures, University of Göttingen, Göttingen (Germany) **1997**.
- [24] J. Li, B. Marler, H. Kessler, M. Soulard, S. Kallus, *Inorg. Chem.* **1997**, *36*, 4697-4701.
- [25] K. Wieghardt, U. Bossek, B. Nuber, J. Weiss, *Inorg. Chim. Acta* **1987**, *126*, 39-42.
- [26] B. Krebs, S. Pohl, W. Schiwy, *Angew. Chem.* **1970**, *21*, 884-885; *Angew. Chem. Int. Ed. Engl.* **1970**, *9*, 897-898.
- [27] W. Bensch, C. Näther, R. Stähler, *Chem. Commun.* **2001**, 477-478.
- [28] R. Stähler, W. Bensch, *Z. Anorg. Allg. Chem.* **2002**, *628*, 1657-1662.
- [29] R. Stähler, B.-D. Mosel, H. Eckert, W. Bensch, *Angew. Chem.* **2002**, *114*, 4671-4673; *Angew. Chem. Int. Ed.* **2002**, *41*, 4487-4489.
- [30] R. Stähler, C. Näther, W. Bensch, *J. Solid State Chem.* **2003**, *174*, 264-275.

#### 4.1.6. Die Verbindungen $[\text{Co}(\text{tepa})]_2\text{Sn}_2\text{S}_6$ , $[\text{Fe}(\text{tepa})]_2\text{Sn}_2\text{S}_6$ und $[\text{Ni}(\text{tepa})]_2\text{Sn}_2\text{S}_6$

*Zusammenfassung der Veröffentlichung „Solvothormal syntheses, crystal structures and selected optical properties of  $[\text{M}(\text{C}_8\text{N}_5\text{H}_{23})]_2\text{Sn}_2\text{S}_6$  ( $\text{M} = \text{Co}, \text{Fe}, \text{Ni}$ ;  $\text{C}_8\text{N}_5\text{H}_{23} = \text{tetraethylenepentamine}$ )“.*

In der Veröffentlichung werden die Thiostannate  $[\text{Co}(\text{tepa})]_2\text{Sn}_2\text{S}_6$  (I),  $[\text{Fe}(\text{tepa})]_2\text{Sn}_2\text{S}_6$  (II) und  $[\text{Ni}(\text{tepa})]_2\text{Sn}_2\text{S}_6$  (III) (tepa = Tetraethylenpentamin,  $\text{C}_8\text{N}_5\text{H}_{23}$ ) vorgestellt. Dabei stellt II das erste eisenhaltige Thiostannat dar. Die Verbindungen werden unter solvothormalen Bedingungen aus Gemischen von  $\text{SnCl}_2 \cdot 2 \text{H}_2\text{O}$ ,  $\text{CoCl}_2 \cdot 6 \text{H}_2\text{O}$  bzw. Fe bzw.  $\text{NiCl}_2 \cdot 6 \text{H}_2\text{O}$  und S (0.2:0.2:0.5 mmol) in 2.5 mL Tetraethylenpentamin nach 25 h bei 160 °C erhalten. In allen drei Strukturen werden  $[\text{Sn}_2\text{S}_6]^{4-}$ -Anionen beobachtet, die entweder als bidentater oder  $\mu_2$ -Ligand zwei  $[\text{M}(\text{tepa})]^{2+}$ -Kationen verknüpfen. Trotzdem sind nur die Verbindungen I und II isostrukturell. I/II und III weisen interessanterweise verschiedene Symmetrien auf und kristallisieren in unterschiedlichen Raumgruppen. I und II kristallisieren in der tetragonalen Raumgruppe  $I4_1/a$  mit acht Formeleinheiten in der Elementarzelle. III kristallisiert in der monoklinen Raumgruppe  $P2_1/n$  mit  $Z = 2$ . Das Übergangsmetall-Kation  $[\text{M}(\text{tepa})]^{2+}$  ist in allen Verbindungen sechsfach koordiniert und weist eine Bindung zu einem Schwefelatom der  $[\text{Sn}_2\text{S}_6]^{4-}$ -Einheit auf (vgl. Abb. 4.8). Intermolekulare Wechselwirkungen können die Unterschiede erklären. In I und II sind nur die terminalen S-Atome der  $[\text{Sn}_2\text{S}_6]^{4-}$ -Anionen an den Wasserstoffbrückenbindungen beteiligt. Aufgrund der unterschiedlichen Wechselwirkungen der S...H-Brücken wird in III eine andere Anordnung der Moleküle beobachtet.

Die unterschiedliche Bindungssituation der  $[\text{Sn}_2\text{S}_6]^{4-}$ -Anionen in I/II und III spiegelt sich in den Raman-Spektren wider. Die Resonanzen für die ersten beiden Thiostannate sind identisch und weichen leicht von denen der dritten Verbindung ab. In I und II sind die Sn-S-Bindungslängen ähnlich lang, wohingegen die Werte in III über einen weiteren Bereich streuen, was sich in der Lage der Signale bemerkbar macht (vgl. Tab. 4.1).

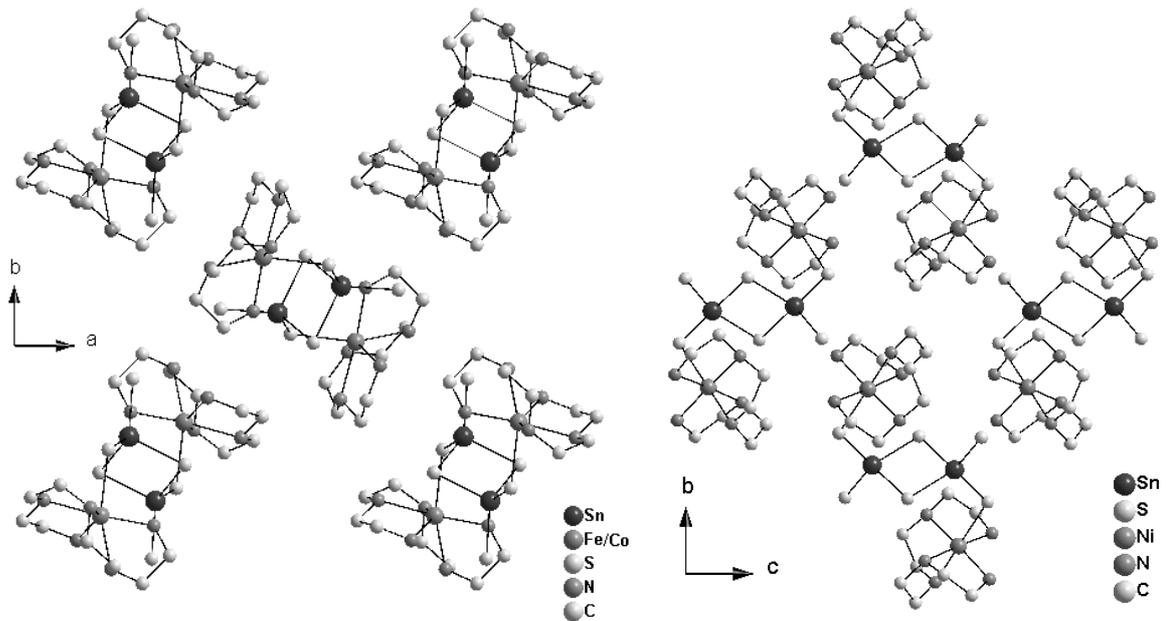


Abb. 4.8: Anordnung der  $[M(\text{tepa})]_2\text{Sn}_2\text{S}_6$ -Einheiten in I und II (links) mit Blick entlang  $[001]$  sowie III mit Blick entlang  $[100]$  (rechts). Die Wasserstoffatome sind zur besseren Übersicht nicht dargestellt.

Zuordnungen	I	II	III
symm. Sn-S-Streckschwingung	372	371	386
Sn-S <sub>bridging</sub>	341	340	334
Sn <sub>2</sub> S <sub>2</sub> -Ring	280	279	271

Tab. 4.1: Vergleich der Signale der Raman-Spektren der drei Verbindungen. Lage der Banden in  $\text{cm}^{-1}$ .

Die optischen Bandlücken (3.2 eV für I, 2.3 eV für II, 2.8 eV für III) wurden aus UV/Vis-Spektren (diffuse Reflektanz) mit der Kubelka-Munk-Methode ermittelt. Die UV/Vis-Spektren zeigen zudem d-d-Übergänge unterhalb der Absorptionskante.

N. Pienack, S. Lehmann, H. Lühmann, M. El-Madani, C. Näther, W. Bensch: Solvothermal syntheses, crystal structures and selected optical properties of  $[M(C_8N_5H_{23})]_2Sn_2S_6$  ( $M = Co, Fe, Ni$ ;  $C_8N_5H_{23}$  = tetraethylenepentamine).

*Z. Anorg. Allg. Chem.* **2008**, accepted 02.07.08.

Copyright Wiley-VCH Verlag GmbH & Co. KGaA.

Reproduced with permission.

**Solvothermal syntheses, crystal structures and selected optical properties of**  
 **$[M(C_8N_5H_{23})]_2Sn_2S_6$  ( $M = Co, Fe, Ni$ ;  $C_8N_5H_{23}$  = tetraethylenepentamine)**

Nicole Pienack, Stefanie Lehmann, Henning Lühmann, Marzog El-Madani, Christian Näther,  
Wolfgang Bensch\*

*Dedicated to Professor Bernt Krebs on the Occasion of his 70<sup>th</sup> Birthday*

Institut für Anorganische Chemie  
Christian-Albrechts-Universität zu Kiel

Olshausenstr. 40-60  
24098 Kiel  
Germany

\* Corresponding author, email: [wbesch@ac.uni-kiel.de](mailto:wbesch@ac.uni-kiel.de), phone: +49 431 880-2419, fax: +49 431 880-1520

**Abstract**

The three new thioannates  $[\text{Co}(\text{C}_8\text{N}_5\text{H}_{23})]_2\text{Sn}_2\text{S}_6$  (**I**),  $[\text{Fe}(\text{C}_8\text{N}_5\text{H}_{23})]_2\text{Sn}_2\text{S}_6$  (**II**) and  $[\text{Ni}(\text{C}_8\text{N}_5\text{H}_{23})]_2\text{Sn}_2\text{S}_6$  (**III**) were synthesized under solvothermal conditions. In all compounds the  $[\text{Sn}_2\text{S}_6]^{4-}$  anion acts as a bidentate or  $\mu_2$  ligand bridging two symmetry related  $[\text{M}(\text{C}_8\text{N}_5\text{H}_{23})]^{2+}$  cations. Despite the identical building units only compounds **I** and **II** are isostructural crystallizing in the tetragonal space group  $I4_1/a$ , whereas compound **III** crystallizes in space group  $P2_1/n$ . A detailed analysis of the intermolecular interactions reveals remarkable differences between **I/II** and **III** which may be responsible for the crystallization in different symmetries and space groups. The slightly different bonding situation in the  $[\text{Sn}_2\text{S}_6]^{4-}$  anion in **I/II** and **III** are reflected in the Raman spectra. For all three compounds the UV/Vis spectra show d-d transitions energetically below the absorption edge.

**Keywords:** Solvothermal Synthesis, Crystal Structure, Spectroscopic Properties, Thioannates

## Introduction

Thiostannates with inorganic cations as charge balancing ions are known since a long time [1], whereas the thiostannate chemistry with organic cations started only a couple of years ago [2, 3, 4]. During the last few years we investigated the reactions of several transition metal (TM) - Sn - S - amine combinations with the aim to synthesize new thiostannates with  $\text{TM}^{n+}$  ions being part of the inorganic networks. In compounds like  $[\text{Ni}(\text{en})_3]_2\text{Sn}_2\text{S}_6$ ,  $[\text{Co}(\text{tren})]_2\text{Sn}_2\text{S}_6$  and  $[\text{Ni}(\text{tren})_3]_2\text{Sn}_2\text{S}_6$  (en = ethylenediamine, tren = tris-(2-aminoethyl)amine) the  $\text{TM}^{2+}$  cations are bound to the  $[\text{Sn}_2\text{S}_6]^{4-}$  anion via one S atom [5]. Recently we successfully synthesized the first thiostannate chain anion containing a  $\text{Mn}^{2+}$  cation [6]. But in the overwhelming cases  $[\text{TM}(\text{amine})_x]^{n+}$  complexes and thiostannate anions are separated [5, 7, 8] and only a few thiostannates containing transition metals were reported until now [5, 9, 10]. One reason may be that the  $[\text{TM}(\text{amine})_x]^{n+}$  complexes are very stable under the synthesis conditions and the  $\text{TM}^{n+}$  is also coordinatively saturated preventing bond formation to the anionic network. Applying the chalcophilic elements Cu or Ag, the pronounced tendency to Cu-S/Ag-S bond formation and the higher stability of these bonds compared to Cu-N/Ag-N bonds yields thiostannates with  $\text{Cu}^+/\text{Ag}^+$  as part of the inorganic network like (DBUH) $\text{CuSnS}_3$  (DBU = 1,8-diazabicyclo[5.4.0]-undec-7-ene), (1,4-dabH<sub>2</sub>) $\text{CuSnS}_4$  [11] and (1,4-dabH<sub>2</sub>) $\text{AgSnS}_4$  [12] (1,4-dab = 1,4-diaminobutane). In these compounds the organic molecules act as structure directors and charge compensating cations. In very rare cases the Sn atom is coordinated by N atoms of the amine and to the best of our knowledge  $[\text{SnS}_2 \cdot \text{en}]$  [13] and  $[\text{2SnSe}_2 \cdot \text{en}]$  [14] are the only examples. Several thiostannates with the  $[\text{Sn}_2\text{S}_6]^{4-}$  anion and charge compensating organic ammonium cations were also reported like (tea)<sub>4</sub> $[\text{Sn}_2\text{S}_6] \cdot 2\text{H}_2\text{O}$  [15], (enH)<sub>4</sub> $[\text{Sn}_2\text{S}_6]$  [16] or (tma)<sub>4</sub> $[\text{Sn}_2\text{S}_6]$  [17] (tea = tetraethylamine, tma = tetramethylamine).

Some thiostannates have attracted attention due to their interesting structural features and in part unusual properties [10]. They can be prepared successfully under solvothermal conditions in the presence of organic ammonia salts or amines. The final products may be viewed as inorganic-organic hybrid compounds exhibiting for instance pores with sizes up to 13 Å in diameter [18]. These compounds have several potential applications, e.g. in catalysis or as chemical sensors [18, 19, 20, 21, 22].

The transition metal ion seems to influence the crystal structure of thiostannates like for example in  $[\text{TM}(\text{en})_3]_2\text{Sn}_2\text{S}_6$  with TM = Mn, Co or Zn [8]. The Mn containing compound crystallizes monoclinic in space group *C2/c*, whereas the Co and Zn thiostannates are

isostructural crystallizing in space group *Pbca*. In our ongoing work in the field of explorative solvothermal syntheses of transition metal containing thioannates we successfully obtained the three new compounds  $[\text{Co}(\text{C}_8\text{N}_5\text{H}_{23})]_2\text{Sn}_2\text{S}_6$  (**I**),  $[\text{Fe}(\text{C}_8\text{N}_5\text{H}_{23})]_2\text{Sn}_2\text{S}_6$  (**II**) and  $[\text{Ni}(\text{C}_8\text{N}_5\text{H}_{23})]_2\text{Sn}_2\text{S}_6$  (**III**) where to the best of our knowledge compound **II** presents the first Fe containing thioannate.

## Experimental Details

### Syntheses:

*General:* All three compounds were synthesized under solvothermal conditions in teflon-lined steel autoclaves with an inner volume of 30 mL reacting elemental transition metals or transition metal salts, tin chloride, sulfur and tetraethylenepentamine ( $\text{C}_8\text{N}_5\text{H}_{23}$ , tepa). The crystalline products were filtered off after the reactions, washed with water, ethanol and dried in vacuum.

#### *Synthesis of $[\text{Co}(\text{C}_8\text{N}_5\text{H}_{23})]_2\text{Sn}_2\text{S}_6$ (**I**):*

0.2 mmol  $\text{CoCl}_2 \cdot 6\text{H}_2\text{O}$ , 0.2 mmol  $\text{SnCl}_2 \cdot 2\text{H}_2\text{O}$  and 0.5 mmol S in 2.5 mL of 80 % tepa (>95 %, Merck) were reacted for 25 h at 160 °C, followed by cooling to room temperature. In the reaction product,  $[\text{Co}(\text{C}_8\text{N}_5\text{H}_{23})]_2\text{Sn}_2\text{S}_6$  was found as light red needles in a yield of about 15 % whereas the main products were Co and Sn sulfides. It can also be synthesized varying the amount of moles of starting materials and the reaction time as well as decreasing the temperature to 150 °C. Nevertheless the yield could not be significantly improved.

The reaction product was separated manually and the homogeneity of the crystalline part was checked by X-ray powder diffraction and elemental analysis (results in %; found: C 20.8, H 4.6, N 15.3; calculated: C 20.8, H 5.0, N 15.1).

#### *Synthesis of $[\text{Fe}(\text{C}_8\text{N}_5\text{H}_{23})]_2\text{Sn}_2\text{S}_6$ (**II**):*

0.2 mmol Fe powder, 0.2 mmol  $\text{SnCl}_2 \cdot 2\text{H}_2\text{O}$ , 0.5 mmol S, 2 mL tepa were mixed with 0.5 mL water and reacted for 25 h at 160 °C, followed by cooling to room temperature. The product  $[\text{Fe}(\text{C}_8\text{N}_5\text{H}_{23})]_2\text{Sn}_2\text{S}_6$  crystallized as yellow needles. The yield was low (about 10 % based on Sn) and could not be increased by varying the amount of educts, reaction time or changing the temperature.

Crystals of **II** were separated manually and the homogeneity was checked by X-ray powder diffraction and elemental analysis (results in %; found: C 20.8, H 5.2, N 14.7; calculated: C 20.9, H 5.0, N 15.2).

*Synthesis of [Ni(C<sub>8</sub>N<sub>5</sub>H<sub>23</sub>)]<sub>2</sub>Sn<sub>2</sub>S<sub>6</sub> (III):*

0.18 mmol SnCl<sub>2</sub> · 2H<sub>2</sub>O, 0.16 mmol NiCl<sub>2</sub> · 6H<sub>2</sub>O and 0.62 mmol S in 2 mL tepa and 0.5 mL H<sub>2</sub>O were reacted at 160 °C for 25 h. **III** was found in the reaction product as purple colored “fish bones” in a yield of 30 %. The homogeneity of hand selected crystals was confirmed by X-ray powder diffraction and elemental analysis (results in %; found: C 20.9, H 5.1, N 14.9; calculated: C 20.8, H 5.0, N 15.1).

**Structure determination:**

Intensity data were collected using a STOE IPDS-1 (Imaging Plate Diffraction System, Mo-K $\alpha$  radiation,  $\lambda = 0.71073 \text{ \AA}$ ) at room temperature. The structures were solved with direct methods using the program SHELXS-97 [23] and the refinements were done against F<sup>2</sup> with SHELXL-97 [24]. Anisotropic displacement parameters were used for all non-H atoms. The C-H and N-H H atoms were positioned with idealized geometry and refined using a riding model with U<sub>iso</sub>(H) = 1.2 x U<sub>eq</sub>(C, N) (1.5 for methyl H atoms). Some selected refinement results are summarized in Table 1. The crystallographic data for compounds **I**, **II** and **III** have been deposited with the Cambridge Crystallographic Data Centre as publication no. CCDC 691400 (**I**), CCDC 691401 (**II**) and CCDC 691399 (**III**). Copies of the data can be obtained, free of charge, on application to CCDC, 12 Union Road, Cambridge CB2 1 EZ, UK (mail: deposit@ccdc.ca.ac.uk).

**Spectroscopy**

*Raman:* The Raman spectra were measured in the region from 100 to 3500 cm<sup>-1</sup> with a Bruker IFS 66 Fourier Transform Raman spectrometer (wavelength: 541.5 nm).

*UV/Vis:* UV/Vis spectroscopic investigations were conducted at room temperature using a UV-VIS-NIR two-channel spectrometer Cary 5 from Varian Techtron Pty., Darmstadt. The absorption data were calculated with the Kubelka-Munk relation for diffuse reflectance data. BaSO<sub>4</sub> powder was used as reference material.

*Infrared spectroscopy*

Compound **I**: 3441 (s, -NH<sub>2</sub>), 3220 (s, -NH<sub>2</sub>), 3130 (m, -NH), 2917 (m, -CH<sub>2</sub>), 2839 (m, -CH<sub>2</sub>-deformation), 1635 (w, -NH<sub>2</sub>-deformation), 1442 (w, -CH<sub>2</sub>-deformation), 1314 (w, -CN) and 1076 (w, -CN-deformation) cm<sup>-1</sup>.

Compound **III**: 3210 (s, -NH<sub>2</sub>), 3070 (m, -NH), 2865 (m, -CH<sub>2</sub>-deformation), 1632 (w, -NH<sub>2</sub>-deformation), 1476 (w, -CH<sub>2</sub>-deformation), 1337 (w, -CN), 1120 and 1051 (w, -CN-deformation).

**Scanning electron microscopy (SEM) and energy dispersive X-ray fluorescence (EDX):**

The EDX analyses have been carried out with a Philips ESEM XL30 equipped with an EDAX detector.

**Elemental analysis:**

CHNS analyses were done using a EURO EA Elemental Analyzer, fabricated by EURO VECTOR Instruments and Software.

**Results and Discussion***Crystal structures*

The isostructural compounds **I** and **II** crystallize in the centrosymmetric tetragonal space group  $I4_1/a$  with eight formula units in the unit cell. Compound **III** crystallizes in the monoclinic space group  $P2_1/n$  with two formula units in the unit cell. In all three compounds the transition metal cation  $[M(\text{tepa})]^{2+}$  is in a six fold coordination of five N atoms of the tepa ligand ( $C_8N_5H_{23}$ ) and one S atom of the  $[Sn_2S_6]^{4-}$  anion. The presence of M, Sn and S in the ratio 2:2:6 could be unambiguously determined with EDX.

*[Co(C<sub>8</sub>N<sub>5</sub>H<sub>23</sub>)<sub>2</sub>Sn<sub>2</sub>S<sub>6</sub> (I) and [Fe(C<sub>8</sub>N<sub>5</sub>H<sub>23</sub>)<sub>2</sub>Sn<sub>2</sub>S<sub>6</sub> (II):*

In compounds **I** and **II** the Sn atoms are tetrahedrally coordinated by four S atoms with Sn-S bond lengths ranging from 2.3174(7) to 2.4602(7) Å and from 2.3192(8) to 2.4655(8) Å respectively. The terminal Sn-S<sub>t</sub> bonds of 2.3174(7) and 2.3192(8) Å are shorter than the bridging Sn-S<sub>b</sub> distance (Tables 2 and 3). All values are in good agreement with literature data [5, 13]. The  $[Sn_2S_6]^{4-}$  anion is composed of two SnS<sub>4</sub> tetrahedra sharing a common edge and the anion is located on a center of inversion. In **I** the Co<sup>2+</sup> cation is in a six fold coordination of S(1) (Co-S: 2.5826(8) Å) and the five N atoms of the tepa ligand (Co-N: 2.138(8) - 2.242(2) Å). The Fe<sup>2+</sup> cation of **II** is in a similar chemical environment with Fe-N distances from 2.188(3) to 2.2889(3) Å and a Fe-S(1) bond length of 2.5786(9) Å. The angles around the central cations (N-Co-N: 76.71(10) - 115.04(12) °; N-Fe-N: 75.46(12) - 117.07(13) °) indicate an appreciable distortion of the octahedral geometry. The  $[Sn_2S_6]^{4-}$  anion connects two  $[M(\text{tepa})]^{2+}$  (M = Co, Fe) units via the *trans* terminal S atoms forming neutral  $[M(\text{tepa})_2Sn_2S_6]$  moieties (Fig. 1). All distances and angles are in the same range like in  $[M'(\text{en})_3]_2Sn_2S_6$  (M' = Mn, Co, Zn) [8],  $[Fe(\text{tren})]FeSbS_4$ ,  $[Fe(\text{dien})_2]Fe_2Sb_4S_{10}$  (dien = diethylenetriamine) [25],  $[Co(\text{tren})]Sb_2S_5$  [26],  $[TM(\text{tren})]Sb_4S_7$  (TM = Mn, Fe, Co, Zn) [27] or  $[Ni(\text{en})_3]_2Sn_2S_6$ ,  $[Co(\text{tren})]_2Sn_2S_6$  and  $[Ni(\text{tren})_3]_2Sn_2S_6$  [5].

*[Ni(C<sub>8</sub>N<sub>5</sub>H<sub>23</sub>)]<sub>2</sub>Sn<sub>2</sub>S<sub>6</sub> (III):*

In compound **III** the Sn atoms are also tetrahedrally coordinated by S atoms. The Sn-S bond lengths vary from 2.3129(12) to 2.4832(11) Å with bridging Sn-S<sub>b</sub> distances between 2.4556(11) and 2.4832(11) Å being longer than the terminal Sn-S<sub>t</sub> bonds (2.3129(12) Å, 2.3420(10) Å, see Tab. 4). These values match well with literature data [5, 13] and the values observed for **I** and **II**.

The [Sn<sub>2</sub>S<sub>6</sub>]<sup>4-</sup> anion is composed of two SnS<sub>4</sub> tetrahedra sharing a common edge joining two [Ni(tepa)]<sup>2+</sup> complex ions via the *trans* terminal S atoms to form the neutral [Ni(tepa)]<sub>2</sub>Sn<sub>2</sub>S<sub>6</sub> moieties (Fig. 2). The Ni<sup>2+</sup> cation is in an octahedral environment of one S atom (Ni-S(1): 2.5698(12) Å) and five N atoms of the tepa ligand (Ni-N: 2.099(3) - 2.145(3) Å), with the longest Ni-N bond being in *trans* position to the Ni-S bond. Like in **I** and **II** the octahedron is severely distorted (Table 4). The Ni-S and Ni-N bond lengths match well with literature data [5, 28]. A distinct packing of the [M(tepa)]<sub>2</sub>Sn<sub>2</sub>S<sub>6</sub> (M = Co, Fe, Ni) moieties is observed in compounds **I/II** and **III**. In compounds **I** and **II** the individual complex molecules are stacked in rods along the crystallographic *c*-axis, and along [100] and [010] neighbored [M(tepa)]<sub>2</sub>Sn<sub>2</sub>S<sub>6</sub> moieties point always in the same direction. Every molecule is surrounded by six other molecules (Fig. 3).

In compound **III** the individual complex molecules are also stacked in rods running along all three axes (Fig. 4).

Short intermolecular S...N distances between the terminal S atoms and N atoms of neighbored molecules are observed in all three compounds indicating weak hydrogen bonding interactions connecting the molecules into a three-dimensional network. In **I** the two S(3)...N separations are 3.309 Å (S(3)-N(4); angle: 150.98 °) and 3.589 Å (S(3)-N(1); angle: 168.14 °). In addition, S(3) has two intramolecular contacts to N(5) (3.595 Å; angle: 158.12 °) and to N(1) (3.600 Å; angle: 149.08 °). S...N distances in the same range are found in the structure of **II**.

The hydrogen bonding pattern is different in **III** where the terminal S atom has only one intermolecular contact (S(2)-N(1): 3.340 Å, angle: 159.56 °). In contrast to **I** and **II** the bridging atom S(1) has one intermolecular (S(1)-N(5): 3.597 Å, angle: 121.67 °) and an intramolecular H bond (S(1)-N(4): 3.480 Å; angle: 147.69 °). The S...H bonding pattern in **III** leads to a denser packing of the molecules than in **I** and **II** (see Table 1). The N...S separations and corresponding angles found in **I** to **III** were also observed in other thioannates [5, 8, 29].

## Spectroscopic Properties

### *Raman spectroscopy*

In the Raman spectra (Fig. 5) the absorptions for **I** are located at 372, 341, 280, 194 and 158  $\text{cm}^{-1}$ , (**II**: 371, 340, 279, 191 and 152; **III**: 386, 334, 271, 182, 138 and 109  $\text{cm}^{-1}$ ) in the typical region for Sn-S resonances [30, 31]. The Co-S and Ni-S vibrations are observed at 226 and 269  $\text{cm}^{-1}$  respectively [28].

The symmetric stretching vibration for the  $[\text{Sn}_2\text{S}_6]^{4-}$  anion is located at 372  $\text{cm}^{-1}$  in **I** (371  $\text{cm}^{-1}$  (**II**); 386  $\text{cm}^{-1}$  (**III**)) and the SnS bridging mode occurs at 341  $\text{cm}^{-1}$  (340  $\text{cm}^{-1}$  (**II**); 334  $\text{cm}^{-1}$  (**III**)). The vibration of the  $\text{Sn}_2\text{S}_2$  ring is located 280  $\text{cm}^{-1}$  (279  $\text{cm}^{-1}$  (**II**); 271  $\text{cm}^{-1}$  (**III**)). The deformation vibrations are found below 200  $\text{cm}^{-1}$  and an unambiguous assignment in this region is not straightforward due to resonances from lattice vibrations which are also located in this region. The resonances observed for **I** and **II** are identical and differ slightly from the data obtained for **III**. These findings can be explained on the basis of the Sn-S bond lengths which are very similar for **I** and **II** but scatter over a larger range for **III** (see Tables 2 – 4).

### *UV/Vis spectroscopy*

The optical band gaps were determined from transformed UV/Vis diffuse reflectance spectra (Kubelka-Munk-method) and the values are 3.2 eV for **I**, 2.3 eV for **II** and 2.8 eV for **III** (Fig. 6). In the spectrum of **I** two broad peaks at 1.2 eV ( $\sim 1030$  nm; 9700  $\text{cm}^{-1}$ ) and 2.5 eV ( $\sim 500$  nm; 20000  $\text{cm}^{-1}$ ) are observed. These absorptions are caused by  $\text{Co}^{2+}$  d-d transitions  ${}^4T_{1g}(F) \rightarrow {}^4T_{1g}(P)$  at about 20000  $\text{cm}^{-1}$  and  ${}^4T_{1g}(F) \rightarrow {}^4T_{2g}$  around 10000  $\text{cm}^{-1}$  (1.24 eV) [32]. The weak shoulder at about 2 eV ( $\sim 16000$   $\text{cm}^{-1}$ ,  $\sim 620$  nm) may be due to the  ${}^4T_{1g}(F) \rightarrow {}^4A_{2g}$  transition. For compound **II** the d-d transitions are less pronounced but can still be seen below the absorption edge. For  $\text{Fe}^{2+}$  the transition of the  ${}^5T_{2g} \rightarrow {}^5E_g$  type is at around 11000  $\text{cm}^{-1}$  (1.36 eV). For the last compound two well resolved d-d transitions occur below the absorption edge. For  $\text{Ni}^{2+}$  such d-d transitions occur between 13000-19000  $\text{cm}^{-1}$  ( $\sim 770$ -530 nm; 1.6-2.4 eV;  ${}^3A_{2g} \rightarrow {}^3T_{1g}(F)$ ) and 24000-26000  $\text{cm}^{-1}$  ( $\sim 420$ -380 nm; 3.0-3.2 eV;  ${}^3A_{2g} \rightarrow {}^3T_{1g}(P)$ ) [32]. For compound **III** these transitions are located at about 1.3 and 2.3 eV.

## Conclusions

Three new compounds were synthesized under solvothermal conditions. Interestingly, compounds **I** and **II** are isostructural, whereas **III** crystallizes in a different space group. The

packing of the molecules is different in **III** which may be caused by the different types of intermolecular S...H bonding interactions. Whereas in **I** and **II** only the terminal S atoms of the  $[\text{Sn}_2\text{S}_6]^{4-}$  anion are involved in hydrogen bonding, in **III** the bridging S atoms have also such S...H bonds. The analogous selenidostannates  $[\text{M}(\text{tepa})]_2\text{Sn}_2\text{Se}_6$  (M = Mn, Fe, Co) [33, 34] and  $[\text{Mn}(\text{tepa})]_2\text{Sn}_2\text{S}_6$  [33] all crystallize in space group  $I4_1/a$  and are isostructural to compounds **I** and **II**. These chalcogenostannates were synthesized using  $\text{SnCl}_4 \cdot 5 \text{H}_2\text{O}$  as tin source, whereas the title compounds were obtained applying  $\text{SnCl}_2 \cdot 2 \text{H}_2\text{O}$ . Obviously, the  $[\text{Sn}_2\text{S}_6]^{4-}$  anions in the title compounds are formed via a redox reaction. But the results presented in [33, 34] indicate that such a reaction is not necessary for the formation of the chalcogenostannate anion. An interesting observation was made in the system Mn/Sn/Se/tepa [33]. Prolongation of the reaction time under identical conditions leads to a transformation of the isolated  $[\text{Mn}(\text{tepa})]_2\text{Sn}_2\text{Se}_6$  into the 1D chiral chain compound  $[\text{Mn}(\text{tepa})\text{Sn}_3\text{Se}_7]$ . Long time syntheses with the title compounds are under way to explore whether such a phenomenon occurs also for the thiostannates.

### Acknowledgements

Financial support by the State of Schleswig-Holstein and by the Fonds der Chemischen Industrie (FCI) is grateful acknowledged.

## Figures

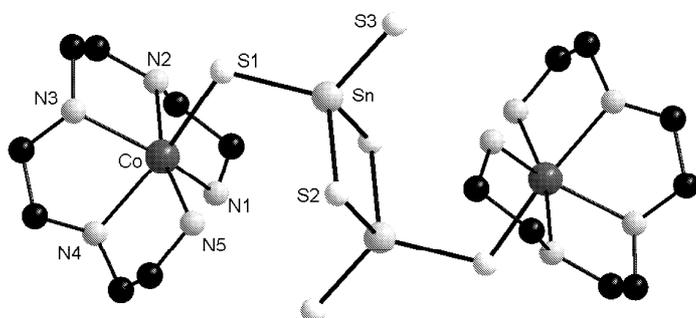


Fig. 1: View of the  $[M(\text{tepa})]_2\text{Sn}_2\text{S}_6$  ( $M = \text{Co}, \text{Fe}$ ) moieties. Some selected atoms are labeled and the hydrogen atoms are omitted for clarity.

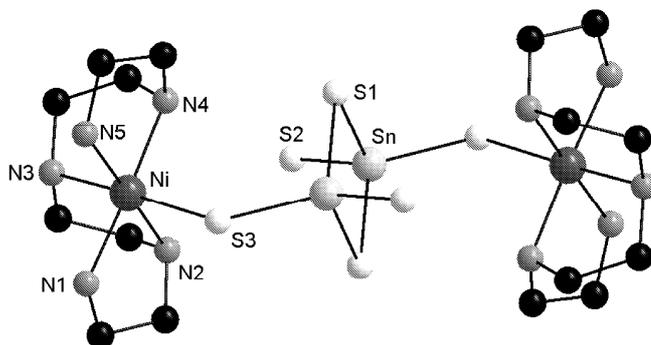


Fig. 2: View of the  $[\text{Ni}(\text{tepa})]_2\text{Sn}_2\text{S}_6$  molecule of compound **III**. Note that only selected atoms are labeled and H atoms are omitted for clarity.

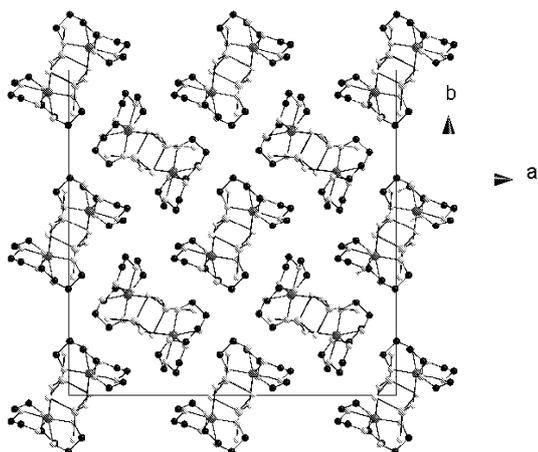


Fig. 3: Packing of  $[M(\text{tepa})]_2\text{Sn}_2\text{S}_6$  moieties in compounds **I** and **II** with view along  $[001]$ . The hydrogen atoms are omitted for clarity.

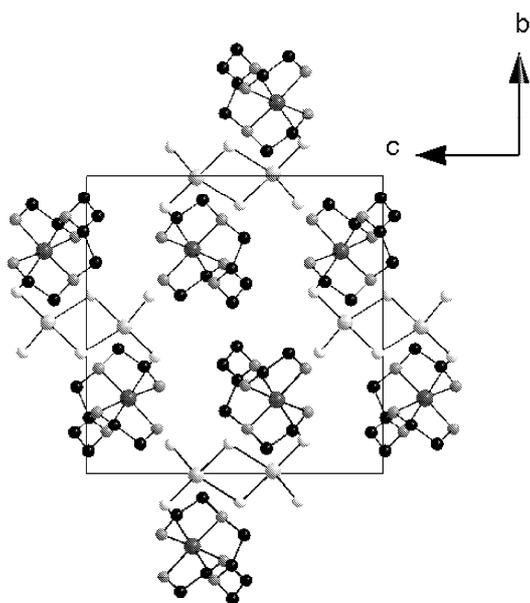


Fig. 4: Packing of  $[\text{Ni}(\text{tepa})]_2\text{Sn}_2\text{S}_6$  molecules in compound **III** with view along  $[100]$ . The hydrogen atoms are omitted for clarity.

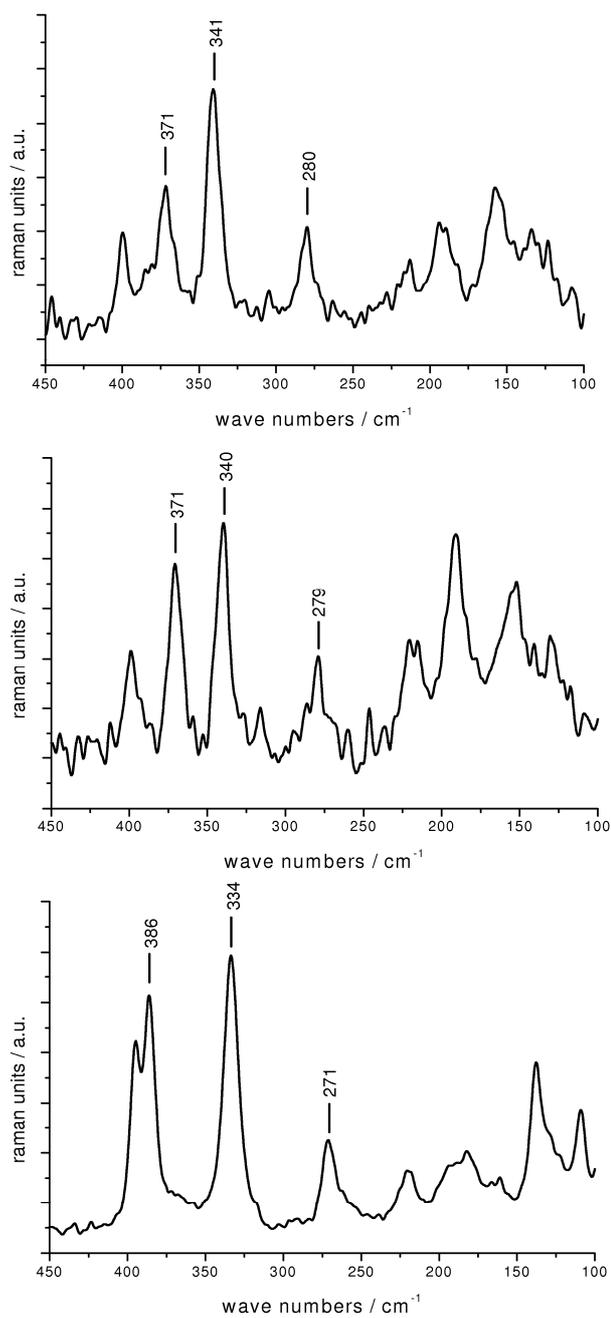


Fig. 5: The Raman spectra of compounds **I** (top), **II** (middle) and **III** (bottom).

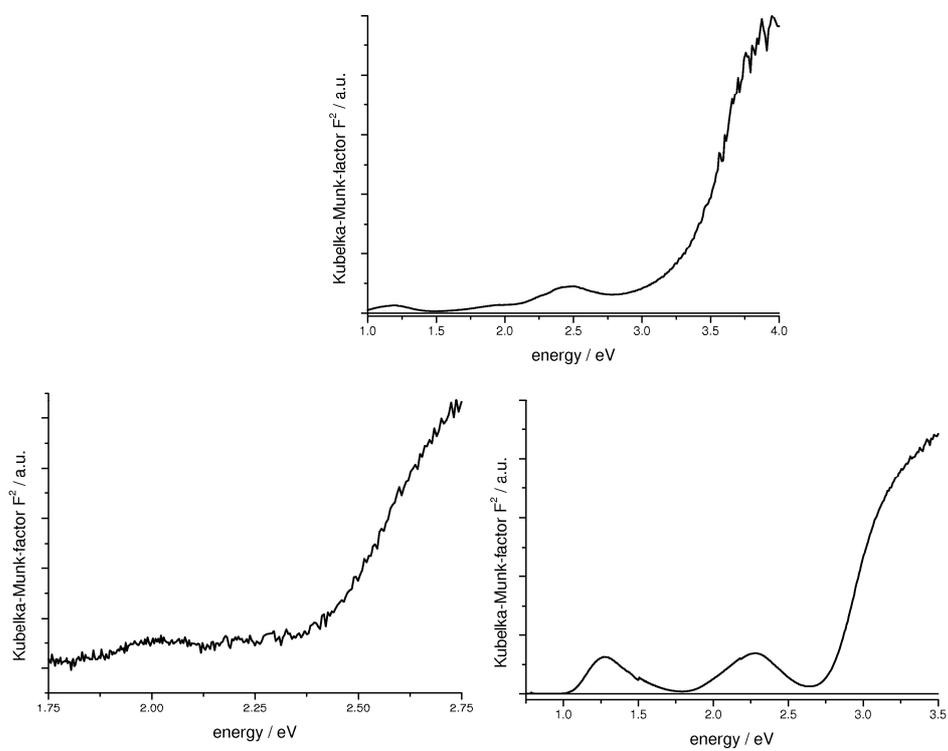


Fig. 6: The UV/Vis spectra of compounds **I** (top), **II** (left) and **III** (right).

## Tables

Table 1: Selected technical details of data collection and results of the structure refinement of the title compounds.

	[Co(tepa)] <sub>2</sub> Sn <sub>2</sub> S <sub>6</sub>	[Fe(tepa)] <sub>2</sub> Sn <sub>2</sub> S <sub>6</sub>	[Ni(tepa)] <sub>2</sub> Sn <sub>2</sub> S <sub>6</sub>
Crystal system	Tetragonal	Tetragonal	Monoclinic
Space group	I4 <sub>1</sub> /a	I4 <sub>1</sub> /a	P2 <sub>1</sub> /n
a / Å	25.9729(15)	25.9640(16)	9.1425(7)
b / Å	25.9729(15)	25.9640(16)	13.1394(7)
c / Å	9.8942(5)	9.9936(6)	13.0750(10)
β	90	90	93.002(9)
V / Å <sup>3</sup>	6674.5(6)	6737.0(7)	1568.50(19)
Z	8	8	2
D <sub>calculated</sub> / g/cm <sup>3</sup>	1.843	1.814	1.960
μ / mm <sup>-1</sup>	2.858	2.708	3.183
Scan Range	2.20 ≤ θ ≤ 28.08	2.69 ≤ θ ≤ 28.12°	2.72 ≤ θ ≤ 28.12
Reflections collected	37804	31747	10386
Refl. with Fo > 4σ (Fo)	3696	3680	928
Independent reflections	3922 [R(int) = 0.0445]	4080 [R(int) = 0.0487]	3027 [R(int) = 0.0529]
Goodness-of-fit on F <sup>2</sup>	1.050	1.005	1.028
Final R indices [I > 2σ(I)]	R1 = 0.0270 wR2 = 0.0633	R1 = 0.0368 wR2 = 0.0870	R1 = 0.0347 wR2 = 0.0881
R indices (all data)	R1 = 0.0372, wR2 = 0.0665	R1 = 0.0462, wR2 = 0.0915	R1 = 0.0434, wR2 = 0.0920
Res. Elec. Dens. / e.Å <sup>-3</sup>	0.427 / -0.824	0.485 / -1.370	0.803 / -0.895

Table 2: Bond lengths [ $\text{\AA}$ ] and angles [ $^\circ$ ] for **I**.

Sn-S(3)	2.3174(7)	Co-N(5)	2.138(3)
Sn-S(1)	2.3582(8)	Co-N(1)	2.170(3)
Sn-S(2)	2.4558(7)	Co-N(3)	2.196(3)
Sn-S(2)	2.4602(7)	Co-N(4)	2.239(2)
Co-S(1)	2.5826(8)	Co-N(2)	2.242(2)
S(3)-Sn-S(1)	119.06(3)	N(1)-Co-S(1)	111.96(7)
S(3)-Sn-S(2)	108.76(3)	N(3)-Co-N(2)	76.71(10)
S(1)-Sn-S(2)	110.10(3)	N(4)-Co-N(2)	113.46(9)
S(3)-Sn-S(2)	111.47(3)	N(1)-Co-N(2)	77.06(10)
S(1)-Sn-S(2)	110.57(3)	N(5)-Co-N(1)	95.59(12)
S(2)-Sn-S(2)	93.97(2)	N(5)-Co-N(3)	115.04(12)
N(5)-Co-S(1)	90.45(8)	N(1)-Co-N(3)	141.83(10)
N(3)-Co-S(1)	90.99(7)	N(5)-Co-N(4)	77.58(10)
N(4)-Co-S(1)	158.12(7)	N(1)-Co-N(4)	87.65(10)
N(2)-Co-S(1)	81.59(7)	N(3)-Co-N(4)	77.98(10)
		N(5)-Co-N(2)	166.07(11)

Table 3: Bond lengths [ $\text{\AA}$ ] and angles [ $^\circ$ ] for **II**.

Sn(1)-S(3)	2.3192(8)	Fe(1)-N(1)	2.188(3)
Sn(1)-S(1)	2.3605(9)	Fe(1)-N(5)	2.206(3)
Sn(1)-S(2)	2.4573(8)	Fe(1)-N(3)	2.254(3)
Sn(1)-S(2)	2.4655(8)	Fe(1)-N(2)	2.266(3)
Fe(1)-S(1)	2.5786(9)	Fe(1)-N(4)	2.289(3)
S(3)-Sn-S(1)	118.91(3)	N(4)-Fe-S(1)	82.05(8)
S(3)-Sn-S(2)	108.89(3)	N(1)-Fe-N(5)	95.53(13)
S(1)-Sn-S(2)	109.95(3)	N(1)-Fe-N(3)	117.07(13)
S(3)-Sn-S(2)	111.63(3)	N(5)-Fe-N(3)	140.44(11)
S(1)-Sn-S(2)	110.67(3)	N(1)-Fe-N(2)	77.18(12)
S(2)-Sn-S(2)	93.90(3)	N(5)-Fe-N(2)	90.23(11)
N(1)-Fe-S(1)	91.48(9)	N(3)-Fe-N(2)	76.92(12)
N(5)-Fe-S(1)	110.86(8)	N(1)-Fe-N(4)	166.18(13)
N(3)-Fe-S(1)	91.16(8)	N(5)-Fe-N(4)	75.62(11)
N(2)-Fe-S(1)	157.10(8)	N(3)-Fe-N(4)	75.46(12)
		N(2)-Fe-N(4)	112.94(11)

Table 4: Bond lengths [ $\text{\AA}$ ] and angles [ $^\circ$ ] for **III**.

Sn(1)-S(2)	2.3129(12)	Ni-N(1)	2.099(3)
Sn(1)-S(3)	2.3420(10)	Ni-N(2)	2.112(3)
Sn(1)-S(1)	2.4556(11)	Ni-N(4)	2.114(3)
Sn(1)-S(1)	2.4832(11)	Ni-N(5)	2.125(3)
Ni-S(3)	2.5698(12)	Ni-N(3)	2.145(3)
S(2)-Sn-S(3)	116.18(5)	N(1)-Ni-N(2)	83.50(13)
S(2)-Sn-S(1)	113.35(4)	N(1)-Ni-N(4)	177.23(14)
S(3)-Sn-S(1)	113.65(4)	N(2)-Ni-N(4)	97.37(14)
S(2)-Sn-S(1)	110.42(5)	N(2)-Ni-N(5)	177.38(15)
S(3)-Sn-S(1)	107.90(4)	N(1)-Ni-N(5)	96.94(14)
S(1)-Sn-S(1)	92.65(3)	N(5)-Ni-N(3)	94.45(16)
N(4)-Ni-N(5)	82.06(14)	N(1)-Ni-S(3)	84.63(10)
N(1)-Ni-N(3)	93.58(14)	N(2)-Ni-S(3)	96.64(10)
N(2)-Ni-N(3)	82.94(15)	N(4)-Ni-S(3)	97.85(11)
N(4)-Ni-N(3)	83.94(15)	N(5)-Ni-S(3)	85.97(12)
		N(3)-Ni-S(3)	178.20(11)

## References

- [1] B. Krebs, *Angew. Chem.* **1983**, *95*, 113.
- [2] W.S. Sheldrick, M. Wachhold, *Angew. Chem.* **1997**, *109*, 214.
- [3] W.S. Sheldrick, M. Wachhold, *Coord. Chem. Rev.* **1998**, *176*, 211.
- [4] W.S. Sheldrick, *J. Chem. Soc. Dalton Trans.* **2000**, 3041.
- [5] M. Behrens, S. Scherb, C. Näther, W. Bensch, *Z. Anorg. Allg. Chem.* **2003**, *629*, 1367.
- [6] N. Pienack, K. Möller, C. Näther, W. Bensch, *Solid State Sci.* **2007**, *9*, 1110.
- [7] D.X. Jia, J. Dai, Q.Y. Zhu, Y. Zhang, X.M. Gu, *Polyhedron* **2004**, *23*, 937.
- [8] D.X. Jia, Y. Zhang, J. Dai, Q.Y. Zhu, X.M. Gu, *Z. Anorg. Allg. Chem.* **2004**, *630*, 313.
- [9] Y. Wang, M. Baiyin, S. Ji, X. Liu, Y. An, G. Ning, *Chem. Res. Chin. Univ.* **2006**, *22*, 411.
- [10] X.M. Gu, J. Dai, D.X. Jia, Y. Zhang, Q.Y. Zhu, *Cryst. Growth Design* **2005**, *5*, 1845.
- [11] N. Pienack, C. Näther, W. Bensch, *Solid State Sci.* **2007**, *9*, 100.
- [12] N. Pienack, W. Bensch, *Z. Anorg. Allg. Chem.* **2006**, *632*, 1733.
- [13] M. Behrens, C. Näther, W. Bensch *Z. Anorg. Allg. Chem.* **628**, 2160, 2002.
- [14] W. S. Sheldrick, H. G. Braunbeck, *Z. Anorg. Allg. Chem.* **1993**, *619*, 1300.
- [15] J. Li, B. Marler, H. Kessler, M. Soulard, S. Kallus, *Inorg. Chem.* **1997**, *36*, 4697.
- [16] S. Dehnen, C. Zimmermann, *Z. Anorg. Allg. Chem.* **2002**, *628*, 2463.
- [17] T. Jiang, A. Lough, G.A. Ozin, R.L. Bedard, R. Broach, *J. Mater. Chem.* **1998**, *8*, 721.
- [18] R.W.J. Scott, M.J. MacLachlan, G.A. Ozin, *Cur. Op. Solid State Mater. Sci.* **1999**, *4*, 113.
- [19] T. Jiang, A. Lough, G.A. Ozin, *Adv. Mater.* **1998**, *10*, 42.
- [20] J.B. Parise, Y. Ko, J. Rijssenbeek, D.M. Nellis, K. Tan, S. Koch, *J. Chem. Soc., Chem. Commun.*, **1994**, 527.
- [21] R.J. Francis, S.J. Price, J.S.O. Evans, S. O'Brien, D. O'Hare, S.M. Clark, *Chem. Mater.* **1996**, *8*, 2102.
- [22] T. Jiang, G.A. Ozin, *J. Mater. Chem.* **1997**, *7*, 2213.
- [23] G.M. Sheldrick, *SHELXS 97, Program for the Solution of Crystal Structures*, University of Göttingen, Germany, **1997**.
- [24] G.M. Sheldrick, *SHELXL 97, Program for the Refinement of Crystal Structures*, University of Göttingen, Germany, **1997**.
- [25] R. Kiebach, W. Bensch, R.D. Hoffmann, R. Pöttgen, *Z. Anorg. Allg. Chem.* **2003**, *629*, 532.

- 
- [26] R. Stähler, W. Bensch, *J. Chem. Soc., Dalton Trans.* **2001**, 2518.
- [27] M. Schaefer, R. Stähler, R. Kiebach, C. Näther, W. Bensch, *Z. Anorg. Allg. Chem.* **2004**, *630*, 1816.
- [28] R. Stähler, W. Bensch, *Eur. J. Inorg. Chem.* **2001**, 3073.
- [29] C. Näther, S. Scherb, W. Bensch, *Acta Cryst.* **2003**, *E59*, m280.
- [30] B. Krebs, W. Schiwy, *Z. Anorg. Allg. Chem.* **1973**, *398*, 63.
- [31] B. Krebs, S. Pohl, W. Schiwy, *Angew. Chem.* **1970**, *82*, 884.
- [32] A.F. Hollemann, E. Wiberg, *Lehrbuch der Anorganischen Chemie*, Walter de Gruyter, Berlin, New York, **1995**.
- [33] J. Zhou, G.Q. Bian, J. Dai, Y. Zhang, A. Tang, Q.Y. Zhu, *Inorg. Chem.* **2007**, *46*, 1541.
- [34] J. Zhou, Y. Zhang, A. Tang, D.Q. Bian, D.X. Jia, J. Dai, *Inorg. Chem. Comm.* **2007**, *10*, 348.

#### 4.1.7. Die Verbindung $[\text{Mn}(\text{trien})]_2\text{SnS}_4 \cdot 4 \text{H}_2\text{O}$

Zusammenfassung der Veröffentlichung „The thiostannate coordination polymer  $\{[\text{Mn}(\text{trien})]_2\text{SnS}_4\} \cdot 4 \text{H}_2\text{O}$  exhibiting a hitherto unknown binding mode of the  $[\text{SnS}_4]^{4-}$  tetrahedron“.

Das Thiostannat  $[\text{Mn}(\text{trien})]_2\text{SnS}_4 \cdot 4 \text{H}_2\text{O}$  (trien = Triethyltetramin,  $\text{C}_6\text{H}_{18}\text{N}_4$ ) wird unter solvothermalen Bedingungen aus 1 mmol Sn, 1 mmol Mn und 2.5 mmol S in 2 mL 60%iger Triethyltetraminlösung und 3 mL Wasser nach 20 Tagen bei 140 °C gebildet. Die Verbindung kristallisiert in der monoklinen Raumgruppe  $P2_1/c$  mit vier Formeleinheiten in der Elementarzelle. Die Struktur besteht aus neutralen  $\{[\text{Mn}(\text{trien})]_2\text{SnS}_4\}_\infty$ -Ketten und Kristallwassermolekülen. In der Struktur verknüpfen  $\text{SnS}_4$ -Tetraeder auf bisher unbekannte Weise oktaedrisch koordinierte  $\text{Mn}^{2+}$ -Kationen zu den Ketten. Die  $\text{Mn}^{2+}$ -Kationen sind von vier Stickstoffatomen des Triethyltetraminliganden und zwei Schwefelatomen von zwei  $\text{SnS}_4$ -Tetraedern koordiniert. Zwei Schwefelatome des  $\text{SnS}_4$ -Tetraeders haben Bindungen zu zwei  $\text{Mn}^{2+}$ -Ionen, d. h. diese beiden S-Atome wirken  $\mu_3$ -verbrückend. Zwei  $\text{MnS}_2\text{N}_4$ -Oktaeder sind über eine gemeinsame Kante zu einem  $\text{Mn}_2\text{S}_2\text{N}_8$ -Doppeloktaeder verknüpft. Das Verknüpfungsmuster führt zur Bildung von  $\text{Mn}_2\text{S}_2$ -Ringen, welche abwechselnd mit  $\text{SnS}_4$ -Tetraedern zur Ausbildung der ungeladenen Kette des Koordinationspolymers entlang [001] führt (Abb. 4.9).

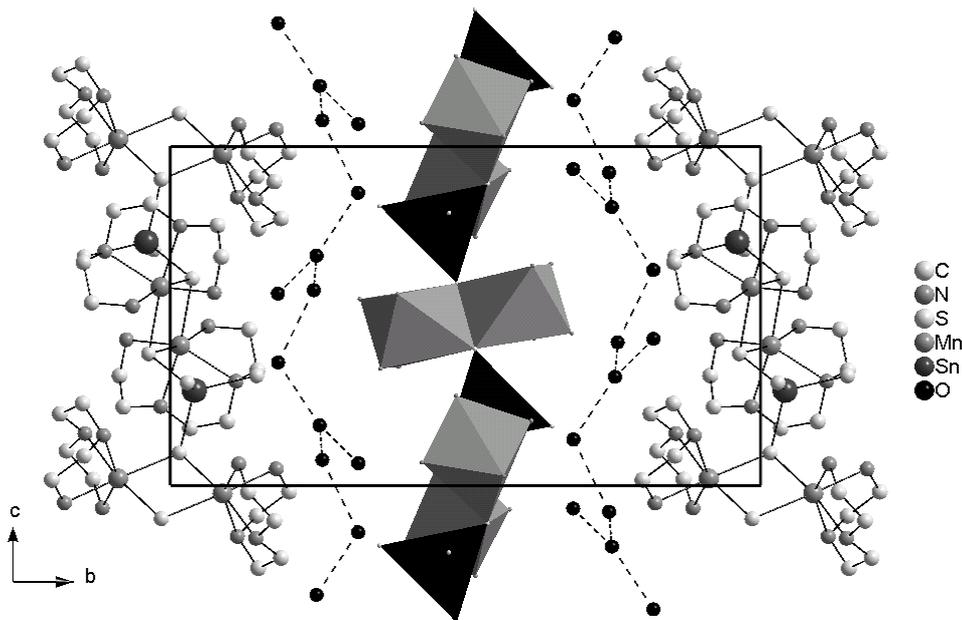


Abb. 4.9: Packungsbild von  $[\text{Mn}(\text{trien})]_2\text{SnS}_4 \cdot 4 \text{H}_2\text{O}$  in der  $bc$ -Ebene mit Blick entlang [100]. In der mittleren Kette sind die  $\text{SnS}_4$ -Tetraeder (schwarz) sowie die  $\text{MnS}_2\text{N}_4$ -Oktaeder (grau) als Polyeder dargestellt. Die Wasserstoffatome sowie die Kohlenstoff- und Stickstoffatome der Aminmoleküle der mittleren Kette sind zur besseren Übersicht nicht abgebildet.

Die Wassermoleküle  $\text{H}_2\text{O}(2)$ ,  $\text{H}_2\text{O}(3)$  und  $\text{H}_2\text{O}(4)$  sind über starke H-Brückenbindungen zu einer Kette verbunden, welche parallel zu der Polymerkette verläuft (vgl. Abb. 4.9). Das letzte  $\text{H}_2\text{O}$ -Molekül ist über eine H-Bindung an die Wasserkette gebunden. Neben den Wasserstoffbrückenbindungen zwischen den  $\text{H}_2\text{O}$ -Molekülen werden auch  $\text{S}\cdots\text{H}$ -Bindungen sowohl zu H-Atomen von Wasser als auch zu H-Atomen der Stickstoffatome beobachtet. Unter Berücksichtigung von  $\text{O-H}\cdots\text{S}$ -Bindungen kann als weiteres strukturelles Detail ein  $(\text{H}_2\text{O})_4\text{S}$ -Ring identifiziert werden.

Die Ausbeute ist gering und die Verbindung auch unter Luftausschluss und im Vakuum nicht stabil. Daher konnten bisher keine weiteren Untersuchungen durchgeführt werden.

1  
2  
3  
4  
5  
6  
7  
8  
9  
10  
11  
12  
13  
14  
15  
16  
17  
18  
19  
20  
21  
22  
23  
24  
25  
26  
27  
28  
29  
30  
31  
32  
33  
34  
35  
36  
37  
38  
39  
40  
41  
42  
43  
44  
45  
46  
47  
48  
49  
50  
51  
52  
53  
54  
55  
56  
57  
58  
59  
60

## The coordination polymer $\{[\text{Mn}(\text{trien})_2\text{SnS}_4] \cdot 4 \text{H}_2\text{O}\}$ exhibiting a hitherto unknown binding mode of the $[\text{SnS}_4]^{4-}$ tetrahedron

Nicole Pienack, Christian Näther, Wolfgang Bensch\*

*Institute of Inorganic Chemistry, Christian-Albrechts-University of Kiel,*

*Max-Eyth-Str. 2, 24118 Kiel, Germany*

RECEIVED DATE (will be automatically inserted after manuscript is accepted)

The new compound  $\{[\text{Mn}(\text{C}_6\text{H}_{18}\text{N}_4)]_2\text{SnS}_4\} \cdot 4 \text{H}_2\text{O}$  ( $\text{C}_6\text{H}_{18}\text{N}_4$  = triethylenetetramine) was obtained under solvothermal conditions. In the structure of the  $\{[\text{Mn}(\text{C}_6\text{H}_{18}\text{N}_4)]_2\text{SnS}_4\}_\infty$  chain two S atoms of the  $[\text{SnS}_4]^{4-}$  anion act in a hitherto never observed  $\mu_3$  bridging mode connecting  $\text{Mn}_2\text{S}_2\text{N}_8$  bioctahedra. The  $\text{Mn}^{2+}$  ions are octahedrally coordinated by 4 N and two S atoms and two symmetry related octahedra share a common S-S edge. Three of the  $\text{H}_2\text{O}$  molecules are joined into chains via H bonding interactions.

Thiostannates are an attractive group of compounds among the main group thiometalates which in part exhibit zeolite-like properties. Some materials with interesting structural features and properties were prepared under solvothermal conditions. The  $\text{Sn(II)/Sn(IV)}$  ions exhibit a flexible coordination behavior and typical polyhedra are  $\text{SnS}_3$  trigonal pyramids,  $\text{SnS}_4$  tetrahedra,  $\text{SnS}_5$  trigonal bipyramids or  $\text{SnS}_6$  octahedra. Different connection modes of these primary building blocks lead to the formation of discrete molecules, one-dimensional chains or two dimensional layered structures. Compounds with the  $[\text{SnS}_4]^{4-}$  monomer are known, but more often the  $[\text{Sn}_2\text{S}_6]^{4-}$  bitetrahedron is found in thiostannates [1, 2]. The integration of transition metals (TM) into the thiostannate networks alters the physical and chemical properties of such compounds and some of these compounds have interesting properties for different applications [3, 4]. Until now, several TM thiostannates were reported reflecting the variable and flexible connection modes of the building units. Recently we published the new copper and manganese thiostannates  $(\text{DBUH})\text{CuSnS}_3$  (DBU = 1,8-diazabicyclo[5.4.0]undec-7-ene),  $(1,4\text{-dabH})_2\text{Cu}_2\text{SnS}_4$  (1,4-dab = 1,4-diaminobutane) [5] and  $(1,4\text{-dabH}_2)\text{MnSnS}_4$  [6] with  $\text{SnS}_4$  tetrahedra and  $\text{Cu}^+/\text{Mn}^{2+}$  as part of the anionic chains. In  $(\text{enH}_2)\text{HgSnS}_4$  the  $[\text{HgSnS}_4]_\infty$  columns consist of  $\text{SnS}_4$  tetrahedra and  $\text{HgS}_3$  triangles [3]. The 2D compound  $(\text{enH}_2)\text{Ag}_2\text{SnS}_4$  contains  $[\text{Ag}_2\text{SnS}_4]^{2-}$  layers with  $\text{SnS}_4$

tetrahedra where each S atom has bonds to  $\text{Ag}_2\text{S}_2$  dumbbells forming twisted chains [7].

But most inorganic organic hybrid compounds are composed of transition metal complexes  $[\text{TM}(\text{amine})_x]^{y+}$  as charge compensating cations for the  $[\text{Sn}_2\text{S}_6]^{4-}$  anions, e.g. in  $[\text{Ni}(\text{en})_3]_2\text{Sn}_2\text{S}_6$  (en = ethylenediamine),  $[\text{Ni}(\text{dap})_3]_2\text{Sn}_2\text{S}_6 \cdot 2\text{H}_2\text{O}$  (dap = 1,2-diaminopropane) [8],  $[\text{M}(\text{en})_3]_2\text{Sn}_2\text{S}_6$  (M = Mn, Co, Zn) [9],  $[\text{Ni}(\text{en})_3]_2\text{Sn}_2\text{S}_6$ ,  $[\text{Ni}(\text{dien})_2]_2\text{Sn}_2\text{S}_6$  (dien = diethylenetriamine) [10],  $[\text{Mn}(\text{en})_3]_2\text{Sn}_2\text{S}_6 \cdot 2\text{H}_2\text{O}$ ,  $[\text{Mn}(\text{dien})_2]_2\text{Sn}_2\text{S}_6$  [11] and  $\{[\text{Mn}(\text{en})_2]_2(\mu\text{-en})(\mu\text{-Sn}_2\text{S}_6)\}_x$  [12]. Very recently, the first thiostannates with lanthanoid containing cations were reported [13, 14], but even here  $[\text{Sn}_2\text{S}_6]^{4-}$  anions are observed. Herein, we present the new thiostannate  $\{[\text{Mn}(\text{trien})_2\text{SnS}_4] \cdot 4\text{H}_2\text{O}\}$  (trien = triethylenetetramine,  $\text{C}_6\text{H}_{18}\text{N}_4$ ) [15]. The compound features  $\text{SnS}_4$  tetrahedra connected with bi-octahedral  $\text{Mn}_2\text{N}_8\text{S}_2$  units in a novel coordination mode.

$\{[\text{Mn}(\text{trien})_2\text{SnS}_4] \cdot 4\text{H}_2\text{O}\}$  crystallizes in the monoclinic space group  $P2_1/c$  with four formula units in the unit cell and all atoms being located on general positions [16, 17, 18, see Table 1]. The structure consists of neutral  $\{[\text{Mn}(\text{trien})_2\text{SnS}_4]\}_\infty$  chains running along [001] and water molecules. The asymmetrical unit is depicted in Fig. 1. The Sn-S distances in the  $\text{SnS}_4$  tetrahedron ranging from 2.3736(9) to 2.4275(9) Å and S-Sn-S angles between 102.21(3) and 111.71(3)° (Table 1) indicate a moderate deviation from ideal tetrahedral geometry. These values match well with data published in literature [8, 19]. The  $\text{Mn}^{2+}$  cations are six-fold coordinated by four N atoms of the triethylenetetramine and two S atoms of two  $\text{SnS}_4$  tetrahedra. In the octahedra two N and two S atoms form the base and two further N atoms are at the apices. Hence a severe distortion is observed and is evidenced by the Mn-S/Mn-N bond lengths scattering (2.5359(11) to 2.7115(10) resp. 2.259(3) and 2.370(3) Å) as well as by the N-Mn-N/S-Mn-N angles (Table 2). Two symmetry related  $\text{MnN}_4\text{S}_2$  octahedra share a common edge and the resulting building units may be represented as  $\text{Mn}(1)_2\text{S}_2\text{N}_8/\text{Mn}(2)_2\text{S}_2\text{N}_8$

\* To whom correspondence should be addressed: email: wbensch@ac.uni-kiel.de.

bioctahedra (Fig. 2). Due to the edge-sharing the  $Mn^{2+}$  ions are significantly shifted away from the centers of the octahedra giving rise for the observed strong distortion. The Mn-N/S bond lengths are in the range like those reported in literature [11,12, 20, 21]. We note that compounds with  $Mn_2S_2X_8$  bi-octahedra are known but only as discrete molecules like e.g. in  $C_{18}O_{16}Mn_4S_6$  [22] or  $C_{20}H_{10}Mn_2O_8S_2$  [23] and not as structural motif in extended structures. Whereas two S atoms of the  $[SnS_4]^{4-}$  anion (S(3) and S(4)) are terminal, S(1) and S(2) act in a  $\mu_3$  fashion each having bonds to two symmetry related  $Mn^{2+}$  ions, i.e., these two S atoms join two bi-octahedra. Therefore, the compound may be viewed as a one-dimensional coordination polymer with the bi-octahedra being the nodes and the  $[SnS_4]^{4-}$  anions acting as the linkers.

Three water molecules (O(2), O(3), O(4)) are joined by strong hydrogen bonds to form a chain running parallel to the coordination polymer chain. The last  $H_2O$  molecule is attached to the water chain via a O(3)-H...O(1) bond. Several short S...H-N separations (see Table 2) indicate weak hydrogen bonding interactions between the water molecules and the  $[Mn(C_6H_{18}N_4)]_2SnS_4$  chain, but there are also some intra- and interchain N-H...S contacts.

**Supporting Information Available:** X-ray crystallographic data in CIF format for the title compound. This material is available free of charge at <http://pubs.acs.org>.

## FIGURES

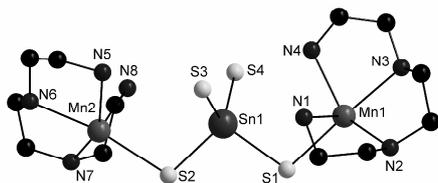


**Figure 1:** Detail of a chain of the title compound together with atom labeling. The H atoms of the amine molecules are omitted for clarity.

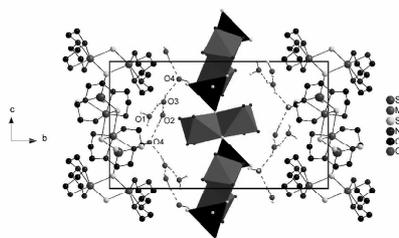


**Figure 2:** Packing of  $[Mn(trien)]_2SnS_4 \cdot 4 H_2O$  in the bc-plane with chains along  $[001]$ . H atoms are omitted for clarity and in the middle chain the C and N atoms of triethylenetetramine are also omitted for better presentation.

## TABLES

**Table 1** Selected details of the data collection and structure refinement results of the title compound.

[Mn(trien)] <sub>2</sub> SnS <sub>4</sub> · 4 H <sub>2</sub> O	
Crystal system	Monoclinic
Space group	P2 <sub>1</sub> /c
a / Å	10.8446(9)
b / Å	20.9740(10)
c / Å	13.2746(9)
β / °	113.487(8)
V / Å <sup>3</sup>	2769.2(3)
Z	4
D <sub>calculated</sub> / g/cm <sup>3</sup>	1.730
μ / mm <sup>-1</sup>	2.128
Scan Range	2.28 ≤ θ ≤ 28.11°
Reflections collected	15023
Refl. with Fo > 4σ (Fo)	1472
Independent reflections	6549
Goodness-of-fit on F <sup>2</sup>	0.984
Final R indices [I > 2σ(I)]	R1 = 0.0369, wR2 = 0.0854
R indices (all data)	R1 = 0.0584, wR2 = 0.0924
Res. Elec. Dens. / e.Å <sup>-3</sup>	0.669 / -0.955

**Table 2** Selected bond lengths, angles and geometric parameters indicating hydrogen bonding interactions.

Sn-S	distances / Å	S-Sn-S	angles / °
Sn-S1	2.4275(9)	S1-Sn-S2	102.21(3)
Sn-S2	2.4070(10)	S1-Sn-S3	111.49(3)
Sn-S3	2.3736(9)	S2-Sn-S3	111.71(3)
Sn-S4	2.3782(10)	S1-Sn-S4	110.50(3)
		S2-Sn-S4	109.05(3)
		S3-Sn-S4	111.50(3)

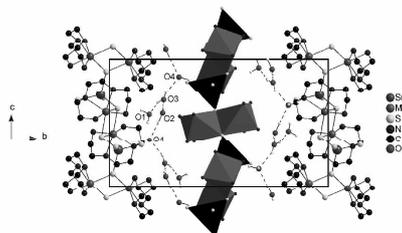
  

Mn-N/S	distances / Å	N/S-Mn-N/S	angles / °
Mn1-N1	2.317(3)	N4-Mn1-N1	82.90(13)
Mn1-N2	2.370(3)	N3-Mn1-N1	107.90(12)
Mn1-N3	2.315(3)	N4-Mn1-N3	76.67(13)
Mn1-N4	2.271(3)	N4-Mn1-N2	134.10(12)
		N3-Mn1-N2	74.09(12)
		N1-Mn1-N2	73.56(12)
Mn1-S1	2.5874(11)	S1-Mn1-N1	86.95(9)
Mn1-S1 <sup>a</sup>	2.7115(10)	S1-Mn1-N2	113.56(9)
		S1-Mn1-N3	164.98(9)
		S1-Mn1-N4	103.64(9)
Mn2-N5	2.259(3)	N5-Mn2-N6	77.38(13)
Mn2-N6	2.298(3)	N5-Mn2-N7	148.79(13)
Mn2-N7	2.299(3)	N6-Mn2-N7	76.20(12)
Mn2-N8	2.341(3)	N5-Mn2-N8	89.47(13)
		N6-Mn2-N8	93.69(13)
		N7-Mn2-N8	76.00(12)
Mn2-S2	2.5359(11)	S2-Mn2-N5	110.71(10)
Mn2-S2 <sup>a</sup>	2.6581(11)	S2-Mn2-N6	170.20(9)
		S2-Mn2-N7	97.45(9)
		S2-Mn2-N8	91.94(9)

S...H/O/N	distances / Å	angles / °
S1...H-O1	2.448	159.39
S2...H-N3	2.870	158.24
S3...H-N1	2.610	153.21
S3...H-N4	2.848	154.33
S3...H-O4	2.355	167.41
S4...H-O1	2.388	172.59
S4...H-O4	2.382	162.66
S4...H-N2	2.505	147.56
S4...H-N8	2.560	163.41

1  
2  
3  
4  
5  
6  
7  
8  
9  
10  
11  
12  
13  
14  
15  
16  
17  
18  
19  
20  
21  
22  
23  
24  
25  
26  
27  
28  
29  
30  
31  
32  
33  
34  
35  
36  
37  
38  
39  
40  
41  
42  
43  
44  
45  
46  
47  
48  
49  
50  
51  
52  
53  
54  
55  
56  
57  
58  
59  
60

$Mn_2S_2N_6$  bi-octahedra are connected into a one-dimensional chain by  $\mu_3$  acting S atoms of the  $[SnS_4]^{4-}$  anion. The  $\{[Mn(\text{trien})]_2SnS_4\}_n$  chain may be viewed as a coordination polymer with the bioctahedra as nodes and the  $[SnS_4]^{4-}$  anion acting as linkers. Water chains surround the coordination polymer.



- [1] Krebs, B. *Angew. Chem.* **1983**, *95*, 113; *Angew. Chem. Int. Ed. Engl.* **1983**, *22*, 113.  
 [2] Jiang, T.; Ozin, G.A. *J. Mater. Chem.* **1998**, *8*, 1099.  
 [3] Liao, J.; Kanatzidis, M.G. *Chem. Mater.* **1993**, *5*, 1561.  
 [4] Wang, Y.; Baiyin, M.; Li, S.; Liu, X.; An, Y.; Ning, G. *Chem. Res. Chinese U.* **2006**, *22*, 411.  
 [5] Pienack, N.; Näther, C.; Bensch, W. *Solid State Sci.* **2007**, *9*, 100.  
 [6] Pienack, N.; Möller, K.; Näther, C.; Bensch, W. *Solid State Sci.* **2007**, *9*, 1110.  
 [7] An, Y.; Menghe, B.; Ye, L.; Ji, M.; Liu, X.; Ning, G. *Inorg. Chem. Commun.* **2005**, *8*, 301.  
 [8] Behrens, M.; Scherb, S.; Näther, C.; Bensch, W. *Z. Anorg. Allg. Chem.* **2003**, *629*, 1367.  
 [9] Jia, D.X.; Zhang, Y.; Dai, J.; Zhu, Q.Y.; Gu, Y.M. *Z. Anorg. Allg. Chem.* **2004**, *630*, 313.  
 [10] Jia, D.X.; Dai, J.; Zhu, Q.Y.; Zhang, Y.; Gu, X.M. *Polyhedron* **2004**, *23*, 937.  
 [11] Fu, M.L.; Guo, G.C.; Liu, B.; Wu, A.Q.; Huang, J.S. *Chin. J. Inorg. Chem.* **2005**, *21*, 25.  
 [12] Gu, X.M.; Dai, J.; Jia, D.X.; Zhang, Y.; Zhu, Q.Y. *Cryst. Growth & Design* **2005**, *5*, 1845.  
 [13] Zhao, Q.; Jia, D.; Zhang, Y.; Song, L.; Dai, J. *Inorg. Chim. Acta* **2007**, *360*, 1895.  
 [14] Jia, D.X.; Zhu, A.M.; Deng, J.; Zhang, Y. *Z. Anorg. Allg. Chem.* **2007**, *633*, 1246.  
 [15] Synthesis of  $[Mn(\text{trien})]_2SnS_4 \cdot 4 H_2O$ : 1 mmol Sn (99.5 %, Aldrich), 1 mmol Mn (99.5 %, Alfa Aesar) and 2.5 mmol S in 2 mL triethylenetetramine (trien) ( $\geq 60$  %, ABCR) and 3 mL  $H_2O$  were reacted in teflon-lined steel autoclaves (inner volume: 30 mL) for 480 h at 140 °C. The crystalline products were filtered off after the reactions and washed with water and ethanol. We want to note that the yield was always low despite a broad variation of the synthesis conditions. The compound is not stable on air or in vacuum. The crystals were manually separated and the homogeneity of the compounds was confirmed by X-ray powder diffraction and CHN analysis Results in %: found: C 21.3, H 5.9, N 15.8; calculated: C 20.0, H 6.2, N 15.5.  
 [16] For single crystal structure determination, the intensity data were collected using a STOE IPDS-1 (Imaging Plate Diffraction System) with  $Mo K\alpha$  radiation at 170 K. The structure was solved with direct methods using the program SHELXS-97 [17] and the refinements were done against  $F^2$  with SHELXL-97 [18]. For all non-hydrogen atoms anisotropic displacement parameters were used. The hydrogen atoms of the amine were positioned with idealized geometry and refined using a riding model and a fixed isotropic displacement parameter. The O-H hydrogen atoms were located in the difference map, their bond lengths set to an ideal value and finally they were refined using a riding model. Selected refinement results are summarized in Table 1. The compound reported here has been deposited with the Cambridge Crystallographic Data Centre as publication no. CCDC XXX. Copies of the data can be obtained, free of charge, on application to CCDC, 12 Union Road, Cambridge CB2 1EZ, UK (mail: deposit@ccdc.ca.ac.uk).  
 [17] Sheldrick, G.M. SHELXS-97, Program for the Solution of Crystal Structures, University of Göttingen, Göttingen, Germany, **1997**.  
 [18] Sheldrick, G.M. SHELXL-97, Program for the Refinement of Crystal Structures, University of Göttingen, Göttingen, Germany, **1997**.  
 [19] Jiang, T.; Ozin, G.A.; Bedard, R.L. *J. Mater. Chem.* **1998**, *8*, 1641.  
 [20] Schur, M.; Näther, C.; Bensch, W. *Z. Naturforsch.* **2001**, *56b*, 79.  
 [21] Schur, M.; Bensch, W. *Z. Naturforsch.* **2002**, *57b*, 1.  
 [22] Mace, W.J.; Main, L.; Nicholson, B.K.; Hagyard, M. *J. Organomet.Chem.* **2002**, *664*, 288.  
 [23] Choi, D.S.; Hong, S.H.; Lee, S.S.; Chung, Y.K. *J. Organomet.Chem.* **1999**, *579*, 385.

## **4.2. Ergebnisse und Publikationen der in-situ-Untersuchungen mit EDXRD und EXAFS**

### **4.2.1. Synthesen, Strukturen und EDXRD-Untersuchungen zur Bildung der Thiostannate $(\text{DBNH})_2\text{Sn}_3\text{S}_6$ und $(\text{DBNH})_2\text{Cu}_6\text{Sn}_2\text{S}_8$**

*Zusammenfassung der Veröffentlichung „Solvothormal syntheses of two new thiostannates and an in-situ energy dispersive X-ray scattering study of their formation“.*

Die Verbindungen  $(\text{DBNH})_2\text{Sn}_3\text{S}_6$  (**I**) und  $(\text{DBNH})_2\text{Cu}_6\text{Sn}_2\text{S}_8$  (**II**) kristallisieren unter solvothormalen Bedingungen aus den Elementen mit einem Verhältnis Cu : Sn : S = 1 : 1 : 3.3 mmol in 3 mL DBN (DBN = 1,5-Diazabicyclo[4.3.0]non-5-en,  $\text{C}_7\text{N}_2\text{H}_{12}$ ) bei 170 °C. Kristalle von **I** und **II** werden auch nach einer Synthesedauer von fünf Tagen erhalten, jedoch sind diese sehr klein und von geringer Qualität, so dass zunächst keine Einkristallstrukturbestimmungen durchgeführt werden konnten. Die Synthesedauer musste bis auf 27 Tage verlängert werden, um Kristalle guter Qualität zu erhalten und die Strukturen bestimmen zu können.

Das gemischtvalente Sn(II)/Sn(IV)-Thiostannat  $(\text{DBNH})_2\text{Sn}_3\text{S}_6$  (**I**) kristallisiert in Form gelber Nadeln in der monoklinen Raumgruppe  $P2_1/n$ . In der Struktur werden anionische Ketten gebildet aus alternierenden  $\text{Sn}_3\text{S}_4$ -Halbwürfeln und  $\text{Sn}_2\text{S}_2$ -Ringen gefunden. Da das Sn(II)-Atom trigonal-pyramidal koordiniert ist, unterscheidet sich die  $\text{Sn}_3\text{S}_4$ -Einheit von den  $\text{Sn}_3\text{S}_4$ -Baugruppen der R-SnS-n-Materialien (vgl. Kap. 1.2.2). Die protonierten Aminmoleküle sind in den Ausbuchtungen benachbarter Ketten lokalisiert (Abb. 4.10, links).

Die zweite Verbindung, das kupferhaltige Thiostannat  $(\text{DBNH})_2\text{Cu}_6\text{Sn}_2\text{S}_8$  (**II**), kristallisiert in Form roter Plättchen in der nicht-zentrosymmetrischen Raumgruppe  $Pca2_1$ . Das Schichtanion kann als verzerrte  $6^3$ -Graphitschicht angesehen werden, die durch Verknüpfung von  $\text{CuS}_3$ -Einheiten und  $\text{SnS}_4$ -Tetraeder gebildet wird. Dieses Strukturmotiv kondensierter, sechsgliedriger Ringe wurde bisher bei Thiostannaten noch nicht beobachtet. Die protonierten Aminmoleküle befinden sich in der Struktur zwischen wellenförmigen Anionenschichten (Abb. 4.10, rechts).

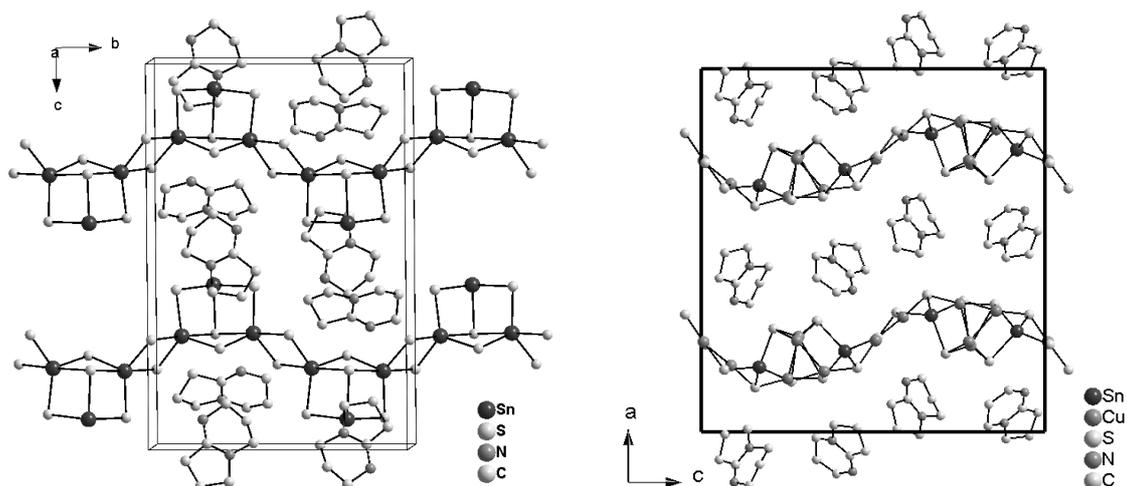


**Abb. 4.10:** Anordnung der wellenförmigen Anionenketten und protonierten Amine in  $(\text{DBNH})_2\text{Sn}_3\text{S}_6$  (links) sowie die gewellten Anionenschichten und ladungskompensierenden Kationen in  $(\text{DBNH})_2\text{Cu}_6\text{Sn}_2\text{S}_8$  (rechts). (Die Wasserstoffatome sind nicht abgebildet.)

Die optischen Bandlücken wurden mit der Kubelka-Munk-Methode zu 2.6 eV (I) und 1.84 eV (II) bestimmt, entsprechend der Farbe der jeweiligen Verbindung. In den Raman-Spektren werden die für Thiostannate typischen Resonanzen zwischen 400 und  $100\text{ cm}^{-1}$  beobachtet. Symmetrische Sn-S-Streckschwingungen treten bei  $367\text{ cm}^{-1}$  (I) bzw.  $362\text{ cm}^{-1}$  (II) auf. Bei  $336$  und  $313\text{ cm}^{-1}$  (I) sowie bei  $332\text{ cm}^{-1}$  (II) liegen die Sn-S<sub>bridging</sub>-Vibrationen, das Signal bei  $258\text{ cm}^{-1}$  (I) wird durch die Schwingung des Sn<sub>2</sub>S<sub>2</sub>-Rings hervorgerufen.

Die thermische Zersetzung von  $(\text{DBNH})_2\text{Sn}_3\text{S}_6$  (I) verläuft in zwei endothermen Schritten. Bei  $T_{\text{Onset}} = 229\text{ °C}$  ( $T_{\text{Peak}} = 234\text{ °C}$ ) beginnt der Abbau mit einem Massenverlust von 11.2 %, gefolgt von 21.5 % bei  $T_{\text{Onset}} = 288\text{ °C}$ . Der Gesamtverlust entspricht ungefähr der Emission von zwei Molekülen DBN und einem Molekül H<sub>2</sub>S pro Formeleinheit. Als Abbauprodukt kann SnS im Pulverdiffraktogramm identifiziert werden.  $(\text{DBNH})_2\text{Cu}_6\text{Sn}_2\text{S}_8$  (II) wird beginnend bei  $T_{\text{Onset}} = 218\text{ °C}$  mit einem einhergehenden Massenverlust von 28.9 % zersetzt. Dieser Massenabbau stimmt mit dem erwarteten Wert überein. Die Reflexe von CuS und SnS können im Pulverdiffraktogramm des Abbauprodukts identifiziert werden.

Gemischivalente Thiostannate sind recht selten, und interessanterweise koexistieren die neuen Verbindungen ( $(\text{DBNH})_2\text{Sn}_3\text{S}_6$  (I) und  $(\text{DBNH})_2\text{Cu}_6\text{Sn}_2\text{S}_8$  (II)) unter den gegebenen Reaktionsbedingungen. Zahlreiche Parameter wurden variiert, um die Synthese derart zu optimieren, dass nur eines der beiden

Thiostannate bevorzugt gebildet wird. Die kupferfreie Verbindung kann unter solvothermalen Bedingungen unter Verwendung von Sn, S und DBN dargestellt werden, während das kupferhaltige Thiostannat bisher nur im Gemisch mit **I** gebildet wird. Diese Beobachtungen werfen verschiedene Fragen auf wie z. B. ob **I** und **II** parallel kristallisieren oder ob eine der beiden Verbindungen in die andere umgewandelt wird. Um diese Fragen beantworten zu können, muss die Synthese unter realen Bedingungen mit einer geeigneten Sonde untersucht werden und zugleich stellt dieses System ein ideales Modell für zeitaufgelöste in-situ-Untersuchungen mit energiedispersiver Röntgenbeugung (EDXRD, vgl. Kap. 2.1.2) dar.

Für die in-situ-Beobachtungen mussten die Reaktionsbedingungen an das vorgegebene Volumen der in-situ-Zelle (vgl. Kap. 3.2) angepasst werden. Die Experimente wurden am Messplatz F3 (HASYLAB, DESY, vgl. Kap. 3.3) durchgeführt. Unter Rühren wurden die Verbindungen mit 30 mg Cu, 60 mg Sn und 50 mg S (0.5 : 0.5 : 1.5 mmol) in 1 mL DBN in einem Temperaturbereich von 140 bis 200 °C erhalten. Der Verlauf einer typischen Reaktion bei 160 °C ist in Abb. 4.11 dargestellt. Zunächst wurde die Temperaturabhängigkeit der Bildung von **I** und **II** untersucht. Dabei hat sich ergeben, dass die Induktionszeit – das ist die Zeit, die vergeht bis die ersten Reflexe im Diffraktogramm auftauchen – mit zunehmender Temperatur kürzer wird (Abb. 4.12).

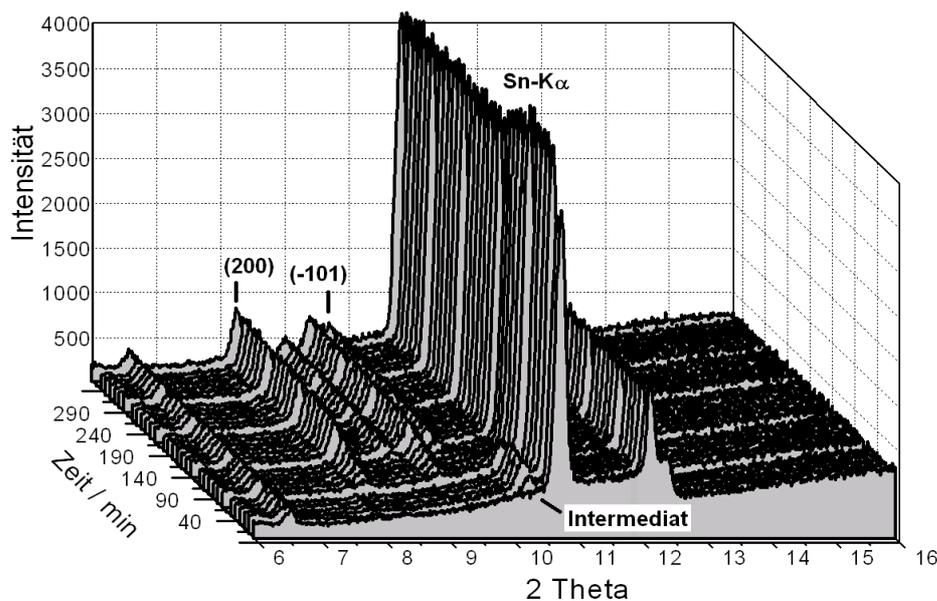


**Abb. 4.11:** Zeitaufgelöste Pulverdiffraktogramme einer Reaktion bei 160 °C. Die Sn-K $\alpha$ -Fluoreszenz, der Reflex des Intermediats, der (200)-Reflex von (DBNH) $_2$ Cu $_6$ Sn $_2$ S $_8$  (**II**) und der (-101)-Reflex von (DBNH) $_2$ Sn $_3$ S $_6$  (**I**) sind markiert. Die Energie wurde auf die Wellenlänge der Cu-K $\alpha$ -Strahlung umgerechnet. Der Escape-Peak des Ge-Detektors ist bei 6.6 ° 2 Theta zu finden.

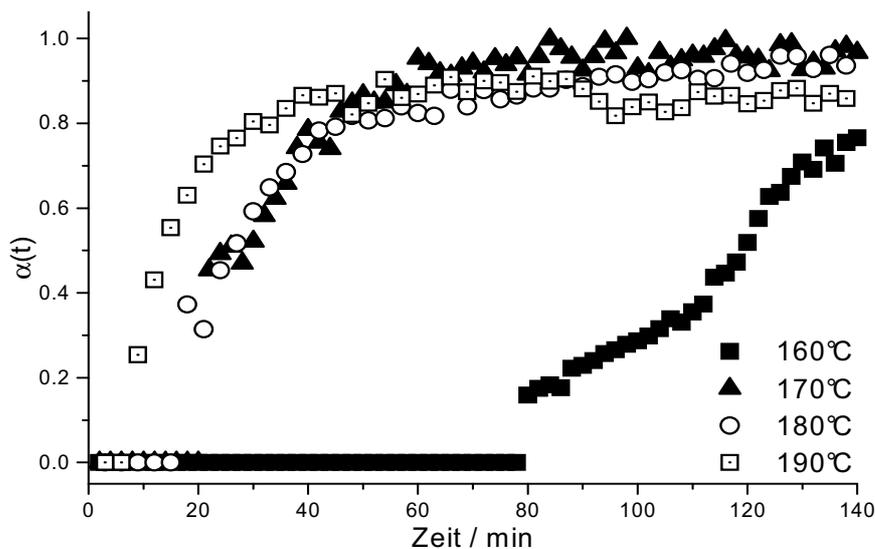


Abb. 4.12: Temperaturabhängigkeit der Kristallisation von  $(\text{DBNH})_2\text{Cu}_6\text{Sn}_2\text{S}_8$ .

Eine interessante Beobachtung wird bei tieferen Reaktionstemperaturen gemacht: nach einer kurzen Induktionszeit werden die Reflexe eines kristallinen Intermediats bzw. eines Precursors beobachtet. Die Reflexe dieses Intermediats verschwinden, wenn  $(\text{DBNH})_2\text{Cu}_6\text{Sn}_2\text{S}_8$  (II) gebildet wird. Bereits kurze Zeit später beginnt  $(\text{DBNH})_2\text{Sn}_3\text{S}_6$  (I) zu kristallisieren und anschließend nimmt die Intensität der Reflexe beider Verbindungen simultan zu, bis ein Gleichgewicht erreicht ist. In der  $\alpha(t)$  vs.  $t$  Kurve für den kristallinen Vorläufer, I und II wird deutlich, dass die Vorläuferverbindung nicht in direktem Zusammenhang mit I oder II steht. D. h., während der Reaktion findet keine Fest-Fest-Umwandlung des Precursors in eines der beiden Reaktionsprodukte statt.

Eine detaillierte Analyse des Reaktionsfortschritts  $\alpha$  vs. Reaktionszeit deutet auf Änderungen der Kristallisationsmechanismen während der Reaktionen in Abhängigkeit von der Temperatur hin. Zu Beginn ist das Wachstum von II diffusionskontrolliert. Mit fortschreitender Reaktion wird die Kristallisationskinetik komplizierter und scheint eher nukleationskontrolliert zu sein. Bei Synthesen ohne Kupfer verläuft die Produktbildung so schnell, dass nur qualitative Vergleiche gezogen werden können. Bei allen Temperaturen ist die Induktionszeit drastisch kürzer als bei Synthesen mit Cu, d. h. die Anwesenheit von Cu bzw. gelöster Cu-Spezies inhibiert die Kristallisation von I. Bei keiner Reaktion ohne Cu konnte das kristalline Intermediat beobachtet werden.

In weiteren Experimenten (ex-situ) wurde das Intermediat abgefangen und die ungefähre Zusammensetzung zu  $(\text{DBNH})\text{Cu}_2\text{Sn}_3\text{S}_6$  bestimmt. Alle Versuche, das

Intermediat in anschließenden Reaktionen zu den Zielverbindungen umzusetzen, waren nicht erfolgreich und es wurden überwiegend binäre Sulfide gebildet.

Alle Synthesen wurden mit elementarem Cu, Sn und S durchgeführt. In zukünftigen Arbeiten soll untersucht werden, ob  $(\text{DBNH})_2\text{Cu}_6\text{Sn}_2\text{S}_8$  ohne gleichzeitige Kristallisation von  $(\text{DBNH})_2\text{Sn}_3\text{S}_6$  darstellbar ist. Geplant sind Synthesen mit unterschiedlichen Kupfer- und Zinnverbindungen, d. h. Cu(I)-, Cu(II)-, Sn(II)- und Sn(IV)-Salzen mit unterschiedlichen Anionen. Die umfangreichen Erfahrungen mit solvothermalen Synthesen lassen vermuten, dass eine enorme Zahl an Versuchen notwendig ist, um die Zielverbindungen mit diesen Ausgangsmaterialien darzustellen. Allein der Wechsel von einem elementaren Edukt zu einer Verbindung erfordert eine Anpassung der Reaktionsbedingungen, welche empirisch durchgeführt werden muss. Solche empirischen Synthesen sind sehr zeitintensiv und konnten bisher nicht durchgeführt werden.

## Solvothermal syntheses of two new thioannates and an in-situ energy dispersive X-ray scattering study of their formation

Nicole Pienack, Christian Näther,<sup>[b]</sup> and Wolfgang Bensch\*<sup>[a]</sup>

**Abstract:** Two new thioannates (DBNH)<sub>3</sub>Sn<sub>3</sub>S<sub>6</sub> (**1**) and (DBNH)<sub>3</sub>Cu<sub>6</sub>Sn<sub>7</sub>S<sub>8</sub> (**2**) were synthesized under solvothermal conditions applying Cu, Sn, S and DBN (DBN = 1,5-diazabicyclo[4.3.0]non-7-ene). Compound **1** is a rare example of a mixed-valent thioannate. The Sn(II) species appears in the rare trigonal-pyramidal environment whereas Sn(IV) is in a tetrahedral coordination. The chain-anion is composed of alternating Sn<sub>3</sub>S<sub>4</sub> semi-cubes and Sn<sub>2</sub>S<sub>2</sub> rings. The structure of **2** consists of undulated anionic layers and amine molecules between the layers. The layers may be viewed as a heteroatom 6<sup>3</sup> graphene layer constructed by condensed CuS<sub>3</sub> triangles and SnS<sub>4</sub> tetrahedra. The two

thioannates coexist which was investigated with in-situ energy dispersive X-ray scattering under real solvothermal conditions. Prior to the formation of **1** and **2** a crystalline precursor appears which disappears after 60 min. Then reflections of **2** start to grow and reflections of **1** occur some time later. The two compounds grow simultaneously until equilibrium is reached. The appearance of a thioannate(IV) followed by the crystallization of a mixed-valent thioannate(II,IV) suggests complex redox reactions occurring under the solvothermal conditions. Syntheses without Cu in the reaction slurry lead to the formation of **1** within a very short time. The results of the in-situ studies

clearly indicate that the presence of Cu species in solution retards the nucleation and crystallization of **1**. The crystalline precursor was quenched with ex-situ experiments. All syntheses performed with this precursor do not lead to the crystallization of **1** or **2**, i.e., there is no direct relation between these three crystalline compounds. The spectroscopic and thermal properties of **1** and **2** are also discussed.

**Keywords:** Solvothermal Synthesis, Crystal Structure, in-situ X-Ray Diffraction, Mixed-valent Thioannate, Thioannates, Copper(I)thioannate

[a] Prof. Dr. W. Bensch  
University of Kiel  
Institute of Inorganic Chemistry  
Max-Eyth-Str. 2, 24118 Kiel, Germany  
Fax: (+) 49 431 880 1520  
E-mail: wbensch@ac.uni-kiel.de

[b] Nicole Pienack, Christian Näther  
University of Kiel  
Institute of Inorganic Chemistry  
Max-Eyth-Str. 2, 24118 Kiel, Germany

## Introduction

Applying the solvothermal route several thioannates have been synthesized using different amines as structure directing agents, e.g. in  $[\text{SnS}_2 \cdot \text{en}]$  (en = ethylenediamine) [1],  $(\text{C}_6\text{H}_{20}\text{N}_4)_2[\text{Sn}_2\text{S}_6] \cdot 2 \text{H}_2\text{O}$  [2],  $(\text{C}_2\text{H}_{10}\text{N}_2)(\text{C}_2\text{H}_9\text{N}_2)_2[\text{Sn}_2\text{S}_6]$  [3],  $\text{R}_2\text{Sn}_3\text{S}_7$  (R = tetramethylammonium TMA [4], R = diazabicyclooctane DABCO [5], R = ammonium / tetraethylammonium ATEA, tetraethylammonium TEA [6]),  $\text{R}'_2\text{Sn}_4\text{S}_9$  (R' = tetrapropylammonium TPA, tetrabutylammonium TBA [6]) and  $(\text{enH})_4[\text{Sn}_2\text{S}_6]$  [7]. Beside the interesting structural features, thioannates are candidates for catalysis applications and chemical sensing [8 - 10]. In addition, the integration of transition metals (TM) into the network alters the physical and chemical properties [11]. Thioannates containing transition metals are for example  $[\text{Ni}(\text{en})_3]_2\text{Sn}_2\text{S}_6$ ,  $[\text{Co}(\text{tren})]_2\text{Sn}_2\text{S}_6$  (tren = tris(2-aminoethyl)amine),  $[\text{Ni}(\text{tren})]_2\text{Sn}_2\text{S}_6$  [12],  $(1,4\text{-dabH}_2)\text{Ag}_2\text{Sn}_4\text{S}_4$  (1,4-dab = 1,4-diaminobutane) [13],  $(\text{DBUH})\text{CuSn}_3$  (DBU = 1,5-diazabicyclo[4.3.0]non-5-ene),  $(1,4\text{-dabH}_2)\text{Cu}_2\text{Sn}_4\text{S}_4$  [14],  $[\text{Ni}(\text{dien})_3]_2\text{Sn}_2\text{S}_6$  (dien = diethylenetriamine) [15] or  $[\text{M}(\text{en})_3]_2\text{Sn}_2\text{S}_6$  (M = Mn, Co, Zn) [16]. Sn(IV) is the most common oxidation state in thioannates and tin sulfides. Until now the number of mixed-valent Sn sulfides is limited with the most famous example  $\text{Sn}_2\text{S}_3$  containing Sn(II) and Sn(IV) [17]. But there are some other compounds like  $\text{K}_2\text{Sn}_4\text{Se}_8$  [18],  $\text{Rb}_2\text{Sn}_4\text{Se}_8$ ,  $\text{Cs}_2\text{Sn}_4\text{Se}_8$  [19],  $[\text{Sn}_2\text{I}_3(\text{NPPH}_3)_3]$  [20],  $[\text{Sn}(\mu_3\text{-NSnMe}_3)]_4$  [21],  $\text{In}_2\text{Sn}_3\text{S}_7$  [22],  $\text{In}_6\text{Sn}_8\text{S}_{19}$  [23],  $\text{Sn}_5\text{Sb}_2\text{S}_9$  [24] and  $\text{Cr}_2\text{Sn}_3\text{S}_7$  [25] featuring the coexistence of Sn(II) and Sn(IV).

The well-known problem of the solvothermal method is that in these heterogeneous multi-component processes many parameters like temperature, time, solvent, concentration etc. influence the product formation. Despite several efforts undertaken by different groups we are far from a deeper understanding of the reaction mechanisms occurring under solvothermal conditions [26]. The following example should illustrate the main problems of the solvothermal approach: syntheses performed with Sb, S, Ni and diethylenetriamine as structure director leads to a couple of compounds like  $[\text{Ni}(\text{dien})_2]_2\text{Sb}_4\text{S}_8$  [27],  $[\text{Ni}(\text{dien})_2]_2\text{Sb}_4\text{S}_9$  [28] or  $[\text{Ni}(\text{dien})_2]_3(\text{Sb}_3\text{S}_6)_2$  [29] under almost identical conditions.

In order to shed light on some aspects of the phenomena occurring under solvothermal conditions and to get more information about such 'black-box-reactions', kinetic analyses applying in-situ methods are necessary. During the last few years we successfully investigated several solvothermal reactions applying time resolved in-situ energy-dispersive X-ray diffraction (in-situ EDXRD) [30 - 36]. This technique facilitates investigations of the influence of different parameters onto the product formation under real reaction conditions [10, 37]. The occurrence, growth and decay of crystalline precursors or intermediates can directly be observed which is not possible with ex-situ experiments. In addition, it can be directly monitored whether such transient compounds are related to or necessary for the crystallization of the product. Finally, these studies supply the necessary reaction conditions for quenching such precursors and/or intermediates.

In our ongoing work in the field of the solvothermal syntheses of transition metal containing thioannates we studied solvothermal reactions applying Cu, Sn, S and 1,5-diazabicyclo[4.3.0]non-5-ene (DBN) as solvent and structure directing agent. An interesting observation made during the solvothermal syntheses is the

coexistence of two thioannates of which one is a Sn(II)/Sn(IV) mixed-valent compound without Cu and the second contains Cu and Sn(IV). This experimental finding requires a systematic study of the solvothermal reaction and therefore is appropriate for investigations using in-situ EDXRD.

In the paper we present the solvothermal syntheses of the two new thioannates  $(\text{DBNH})_2\text{Sn}_3\text{S}_6$  (1) and  $(\text{DBNH})_2\text{Cu}_6\text{Sn}_2\text{S}_8$  (2), their crystal structures, the thermal and spectroscopic properties and the results of the in-situ EDXRD studies.

## Results and Discussion

The new thioannate  $(\text{DBNH})_2\text{Sn}_3\text{S}_6$  (1) crystallizes in the monoclinic space group  $\text{P}2_1/n$  with all atoms located on general positions. The three unique Sn atoms are in different environments of S atoms. Sn(1) and Sn(2) are surrounded by 5 S atoms forming distorted rectangular pyramids (Fig. 1). The Sn-S bonds range from 2.3901(14) to 2.7024(13) Å for Sn(1) and from 2.3937(14) to 2.7157(13) Å for Sn(2), with corresponding S-Sn-S angles varying from 86.64(4) to 126.39(6)° (Table 1).

Table 1. Bond lengths [Å] for 1.

Sn(1)-S(4)	2.3901(14)
Sn(1)-S(6)	2.3927(14)
Sn(1)-S(3)	2.4149(12)
Sn(1)-S(2)	2.5367(14)
Sn(1)-S(1)	2.7024(13)
Sn(2)-S(5)	2.3937(14)
Sn(2)-S(2) <sup>a</sup>	2.4020(13)
Sn(2)-S(3)	2.4201(12)
Sn(2)-S(4) <sup>a</sup>	2.5222(14)
Sn(2)-S(1)	2.7157(13)
Sn(3)-S(1)	2.5059(13)
Sn(3)-S(5)	2.5335(16)
Sn(3)-S(6)	2.5511(17)

Symmetry transformations used to generate equivalent atoms:

<sup>a</sup>:  $-x+3/2, y+1/2, -z+1/2$

These values are in good agreement with literature data [38, 39]. Interestingly, Sn(3) is surrounded by only three S atoms to form a trigonal pyramidal  $\text{SnS}_3$  unit. This geometry is an indication for Sn(II) and the bond valence calculations confirm this assignment as well as the mixed-valent character of  $(\text{DBNH})_2\text{Sn}_3\text{S}_6$  (see Table 2; all parameters for the calculations were taken from ref. 40). The Sn-S bond lengths in the  $\text{SnS}_3$  pyramid are 2.5059(13), 2.5335(16) and 2.5511(17) Å (average Sn-S: 2.5302 Å) with the corresponding angles 88.02(4), 88.62(4) and 102.39(6)° (Table 2). Sn in a trigonal pyramidal environment is quite rare, but some examples are ottemannite  $\text{Sn}(\text{SnS}_3)$  [41],  $\text{C}_{25}\text{H}_{27}\text{NO}_3\text{SnS}_3$  [42],  $\text{C}_{42}\text{H}_{35}\text{AsSnS}_3$  [43], and  $\text{C}_{42}\text{H}_{35}\text{PSnS}_3$  [44]. In these compounds the Sn-S bond lengths are in the range of 2.532(10) to 2.765(2) Å and the S-Sn-S angles scatter from 83.59(2) to 96.87(3)°.

Table 2. valence bond calculations for  $(\text{DBNH})_2\text{Sn}_3\text{S}_6$  (1)

distances	oxidation state	$S=(R/R_0)^N$
	Sn(IV)	$(R/R_0)^N$
Sn(1)-S	2.39	1.00
	2.39	0.99
	2.41	0.94
	2.54	0.71
	2.70	0.49
		4.13

Sn(2)-S	Sn(IV)	(R/R <sub>0</sub> ) <sup>N</sup>
	2.39	0.99
	2.40	0.97
	2.42	0.93
	2.52	0.73
	2.72	0.48
		4.10

Sn(3)-S	Sn(II)	(R/R <sub>0</sub> ) <sup>N</sup>
	2.51	0.74
	2.53	0.70
	2.55	0.67
		2.11

with:	R <sub>0</sub>	N
Sn(II)	2.38	5.8
Sn(IV)	2.39	5.8

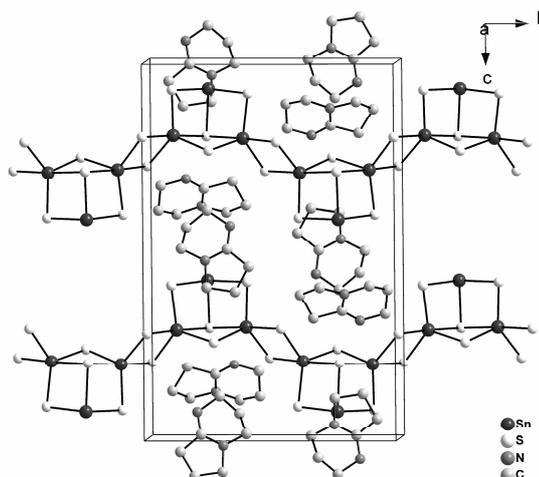


Figure 2: Packing in the *bc*-plane of (DBNH)<sub>2</sub>Sn<sub>3</sub>S<sub>6</sub> with undulated chains along [010]. H atoms are omitted for clarity.

The two SnS<sub>5</sub> pyramids and the SnS<sub>3</sub> group share common edges to form a so-called Sn<sub>3</sub>S<sub>4</sub> semi-cube (Fig. 1). Neighbored semi-cubes are joined via the terminal S atoms of the SnS<sub>5</sub> groups yielding a one-dimensional anionic [Sn<sub>3</sub>S<sub>6</sub>]<sup>2-</sup> chain running along [010] (Fig. 1). Alternatively, the structure of the chain may be viewed as alternating Sn<sub>3</sub>S<sub>4</sub> semi-cubes and Sn<sub>2</sub>S<sub>2</sub> rings.

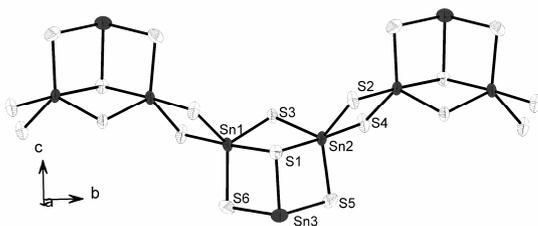


Figure 1: The anionic chain directed along [010] together with atom labelling. The displacement ellipsoids are drawn at the 50% probability level.

Within the chains the Sn<sub>3</sub>S<sub>4</sub> semi-cubes are arranged in a zig-zag-like fashion and the amine molecules are located in the cavities of neighbored chains (Fig. 2). In contrast to other compounds with Sn<sub>3</sub>S<sub>4</sub> units, the divalent Sn atom of the Sn<sub>3</sub>S<sub>4</sub> semi-cube in (DBNH)<sub>2</sub>Sn<sub>3</sub>S<sub>6</sub> is trigonally coordinated and has no contact to other sulfur atoms (see Fig. 1). Short S...H-N separations (S(1)-N(2): 3.388(17) Å and S(2)-N(4): 3.499(2) Å) indicate weak hydrogen bonding interactions.

An interesting observation is that the anionic chain of (DBNH)<sub>2</sub>Sn<sub>3</sub>S<sub>6</sub> shows similar structural motifs like those in the layered thiostannates R-SnS-1 and R-SnS-3 (R = organic molecule) [35, 36]. In these compounds two dimensional [Sn<sub>3</sub>S<sub>7</sub>]<sup>2-</sup> and [Sn<sub>4</sub>S<sub>9</sub>]<sup>2-</sup> anionic layers are observed containing also Sn<sub>3</sub>S<sub>4</sub> semi-cubes which are formed by interconnection of SnS<sub>4</sub> tetrahedra. The semi-cubes are joined via two S<sup>2-</sup> anions yielding anionic layers with pores consisting of 24 atoms (diameter: 10 Å). The organic molecules act as charge compensating cations and are located above/below the pores and between the layers [45]. In R-SnS-3 the Sn<sub>3</sub>S<sub>4</sub> units are joined by SnS<sub>4</sub> tetrahedra to form [Sn<sub>4</sub>S<sub>9</sub>]<sup>2-</sup> layers with elliptical pores measuring about 19.8 Å · 11.3 Å for TBA-SnS-3 (TBA = tetrabutylammonium) [6]. Instead of organic structure directors alkali metal ions were used for the synthesis of thiostannates like Rb<sub>2</sub>Sn<sub>3</sub>S<sub>7</sub> · 2 H<sub>2</sub>O or Cs<sub>4</sub>Sn<sub>5</sub>S<sub>12</sub> · 2 H<sub>2</sub>O [46, 47] which also contain Sn<sub>3</sub>S<sub>4</sub> groups as well as Sn<sub>2</sub>S<sub>2</sub> rings. In Cs<sub>4</sub>Sn<sub>5</sub>S<sub>12</sub> · 2 H<sub>2</sub>O two Sn<sub>3</sub>S<sub>4</sub> semi-cubes are connected via a common corner and with two bridging S<sup>2-</sup> anions to form the anionic layers containing elliptical pores with diameter of about 7.3 · 9.9 Å. In Rb<sub>2</sub>Sn<sub>3</sub>S<sub>7</sub> · 2 H<sub>2</sub>O the anionic layers are constructed by face-sharing semi-cubes and bridging Sn<sub>2</sub>S<sub>2</sub> rings.

The second new compound (DBNH)<sub>2</sub>Cu<sub>6</sub>Sn<sub>2</sub>S<sub>8</sub> (2) crystallizes in the non-centrosymmetric orthorhombic space group Pca2<sub>1</sub> with two unique Sn, six Cu and eight S atoms as well as two protonated DBN molecules. All atoms are located on general positions. The structure consists of undulated anionic layers in the (100) plane and protonated amine molecules acting as charge compensating cations between the layers (Fig. 3).

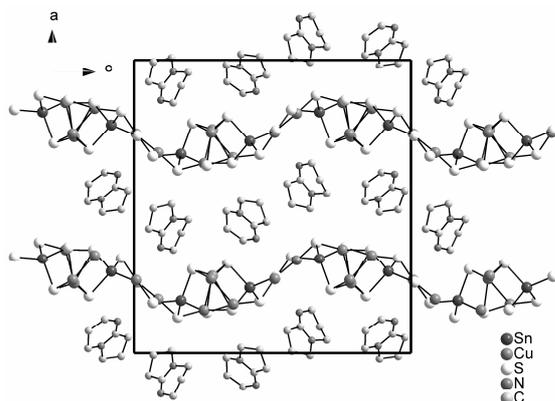


Figure 3: Arrangement of the undulated anionic layers and the cations in compound **2** (view along the *b*-axis). H atoms are omitted for clarity. Some DBN molecules are disordered and the split positions are not displayed.

Each Sn atom is in a tetrahedral environment of S atoms with Sn-S distances from 2.392(2) to 2.414(2) Å (Table 3) and S-Sn-S angles between 109.98(9) and 112.90(8)°, indicating a moderate deviation from ideal tetrahedral geometry. These values match well with data published in literature [12, 48].

Table 3. Bond lengths [Å] for **2**.

Sn(1)-S(2) <sup>a</sup>	2.392(2)	Cu(3)-S(4)	2.238(2)
Sn(1)-S(3)	2.405(2)	Cu(3)-S(8)	2.357(3)
Sn(1)-S(6)	2.407(2)	Cu(3)-S(5)	2.446(3)
Sn(1)-S(4)	2.414(2)	Cu(3)-Cu(4)	2.7755(18)
Sn(1)-Cu(6)	3.1678(18)	Cu(3)-Cu(5)	3.052(2)
Sn(2)-S(1) <sup>b</sup>	2.385(2)	Cu(4)-S(6) <sup>c</sup>	2.240(2)
Sn(2)-S(8)	2.408(2)	Cu(4)-S(2) <sup>a</sup>	2.246(2)
Sn(2)-S(5)	2.427(2)	Cu(4)-S(5)	2.295(2)
Sn(2)-Cu(3)	3.0951(13)	Cu(5)-S(7)	2.241(2)
		Cu(5)-S(5)	2.268(2)
		Cu(5)-S(6)	2.284(2)
		Cu(5)-Cu(6)	2.833(2)
		Cu(6)-S(8) <sup>d</sup>	2.200(3)
		Cu(6)-S(4)	2.260(3)
		S(1)-Cu(2) <sup>e</sup>	2.258(2)
		S(1)-Sn(2) <sup>f</sup>	2.385(2)

Symmetry transformations used to generate equivalent atoms:  
<sup>a</sup>:  $x, y+1, z$     <sup>b</sup>:  $-x+3/2, y, z-1/2$     <sup>c</sup>:  $-x+3/2, y, z+1/2$   
<sup>d</sup>:  $x, y-1, z$

All Cu atoms have bonds to three S atoms forming distorted Cu<sub>3</sub> triangles with the Cu atoms being located slightly above the planes of the three S atoms. The Cu-S bond lengths scatter between 2.200(3) and 2.446(3) Å (Table 3) and the corresponding angles are between 97.88(8) and 141.84(15)°. All values are in the typical range reported in literature [14, 49, 50].

The Cu(3) to Cu(6) atoms each have a Cu atom at relatively short distances ranging from 2.7755(18) to 3.052(2) Å (Table 3). These separations are longer than in Cu metal (2.556 Å). Some examples with comparable values for such relatively short Cu-Cu distances are (enH<sub>2</sub>)<sub>0.5</sub>Cu<sub>2</sub>SbS<sub>3</sub> (en = ethylenediamine), (1,3-dapH<sub>2</sub>)<sub>0.5</sub>Cu<sub>2</sub>SbS<sub>3</sub> (1,3-dap = 1,3-diaminopropane) [51], (C<sub>6</sub>N<sub>4</sub>H<sub>20</sub>)<sub>0.5</sub>Cu<sub>3</sub>Sb<sub>2</sub>S<sub>5</sub> [52] and (1,4-dabH<sub>2</sub>)Cu<sub>2</sub>SnS<sub>4</sub> (1,4-dab = 1,4-diaminobutane) [14]. In the literature d<sup>10</sup>-d<sup>10</sup> interactions are discussed for several sulfides [53], but in those cases the Cu-Cu distances are even shorter than in compound **2**.

Cu<sub>3</sub> triangles and SnS<sub>4</sub> tetrahedra are joined to form three different six-membered Cu<sub>2</sub>SnS<sub>3</sub> heterorings (6 MR): Cu(1)Cu(2)Sn(2)S<sub>3</sub> (6 MR A), Cu(2)Cu(4)Sn(1)S<sub>3</sub> (6 MR B), Cu(4)Cu(5)Sn(2)S<sub>3</sub> (6 MR C) which are condensed in the (100) plane (Fig. 4; left) yielding an undulated layer which may be viewed as a distorted graphene 6<sup>3</sup> layer. Along [001] the sequence of the rings is ...A-B-C... . Cu(3)S<sub>3</sub> and Cu(6)S<sub>3</sub> units do not participate in these rings and they are joined into chains along [010] by corner-sharing with each other and edge-sharing with the SnS<sub>4</sub> tetrahedra (Fig. 4, right). The chains and layers are connected via S atoms of the SnS<sub>4</sub> tetrahedra. This connection scheme leads to the formation of further heterorings like Cu(3)Cu(4)Cu(5)S<sub>3</sub> and Cu(4)Cu(6)Sn(2)S<sub>3</sub>.

The structural motif of condensed six-membered rings is found in layered thioantimonates like (C<sub>4</sub>N<sub>3</sub>H<sub>14</sub>)Cu<sub>3</sub>Sb<sub>2</sub>S<sub>5</sub> and (C<sub>6</sub>N<sub>4</sub>H<sub>20</sub>)<sub>0.5</sub>Cu<sub>3</sub>Sb<sub>2</sub>S<sub>5</sub> [49], but was never observed before in thioantimonates.

The amine molecules are located between the layers with an interlayer distance of about 7.5 Å. Short S...H-N separations (S(3)-N(4): 3.162(14) Å and S(3)-N(2): 3.313(27) Å) indicate weak hydrogen bonding interactions.

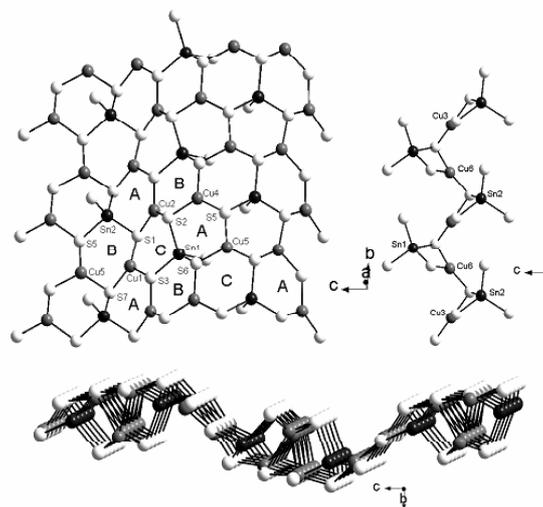


Figure 4: Condensation of the different heterorings in compound **2** forming the anionic layer (top, left). The chain made up by interconnection of Cu(3)S<sub>3</sub>, Cu(6)S<sub>3</sub> and SnS<sub>4</sub> tetrahedra (top, right). Bottom: undulated arrangement of a layer (view approximately along the *b*-axis).

#### In-situ EDXRD investigations

Solvothermal syntheses often deal with the problem that the products are not phase pure and sometimes even in one reaction mixture thiometalates with different compositions coexist. An example is the synthesis of [Ni(dien)<sub>2</sub>]Sb<sub>4</sub>S<sub>7</sub> · H<sub>2</sub>O where the product always contained [Ni(dien)<sub>2</sub>]<sub>3</sub>(SbS<sub>4</sub>)<sub>2</sub> [54] as the second phase. In the present case not only two different thioantimonates coexist but these two compounds have Sn in different oxidation states. In the syntheses elemental Sn and Cu are applied and obviously complex redox reactions lead to the formation of Sn(II)

and Sn(IV) in **1** and Sn(IV) in **2**. A broad variation of the synthesis conditions was performed to increase the yields and to find conditions where only compound **2** appears in the final product. But after about 50 syntheses without success the question raised whether the occurrence of the two products is an inherent "problem". Several scenarios can be imagined: (i) both compounds crystallize simultaneously and coexist due to a similar stability; (ii) one of the two compounds is formed first and the second starts to grow at later stages of the reaction; for instance, the Cu containing material (**2**) appears first and is partially dissolved providing the species for crystallization of **1**.

First the influence of the reaction temperature onto the crystallization of the two compounds was studied. Further studies were conducted without Cu to monitor the reaction progress of compound **1**. The energy range of the spectra was chosen to show at least two reflections of the final products respectively of each compound at the same time. A typical spectrum obtained at the end of a reaction with Cu, Sn, S and DBN shows the Sn-K $\alpha$  and Sn-K $\beta$  fluorescence as well as the Bragg peaks of the two compounds (Fig. 5).

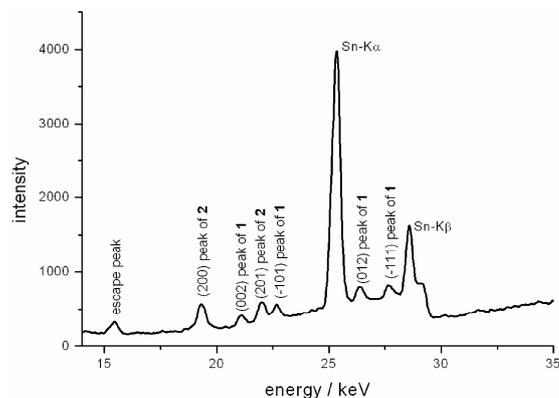


Figure 5: A typical powder pattern recorded at the beamline F3. The Bragg reflections of both compounds and the Sn fluorescence are labelled. The peak at ~ 15.5 keV is the escape peak of the Ge detector.

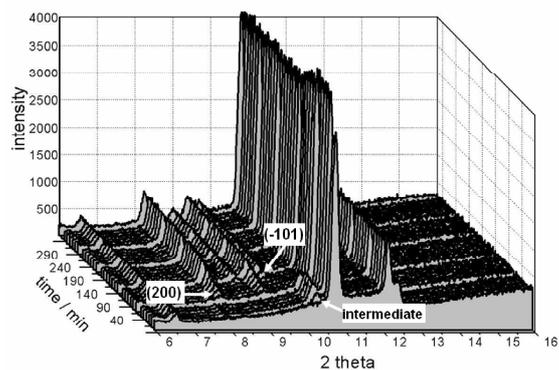


Figure 6: Time resolved powder diffraction patterns of a synthesis at 160 °C. The reflection of the crystalline precursor, the (-101) of  $(\text{DBNH})_2\text{Sn}_3\text{S}_6$  (**1**) and the (200) reflection of  $(\text{DBNH})_2\text{Cu}_6\text{Sn}_2\text{S}_8$  (**2**) are marked. The energy is converted to the  $2\theta$  scale applying Cu K $\alpha$  wavelength. The peak at ~  $6.6^\circ$   $2\theta$  is the escape peak of the Ge detector.

The progress of a typical reaction at 160 °C is shown as time-resolved spectra in Fig. 6. In the beginning of the reaction only Sn fluorescence are observable and a crystalline precursor starts to grow (marked in Fig. 6) after about 8 min. This precursor survives approximately 60 min and when this phase is disappeared, the (200) and (201) reflections of  $(\text{DBNH})_2\text{Cu}_6\text{Sn}_2\text{S}_8$  (**2**) become visible after 68 min and 72 min, respectively. After 110 min reaction time, the Cu free compound  $(\text{DBNH})_2\text{Sn}_3\text{S}_6$  (**1**) starts to grow with all reflections appearing at the same reaction time.

The time until the first crystallites are observed is the induction time  $t_0$  which depends on the reaction temperature. Increasing the temperature leads to a significant decrease of  $t_0$ . Typical for solid state kinetics are sigmoidal curves plotting the extent of reaction  $\alpha(t)$  versus time. The curves presenting the growth of the (200) reflection of  $(\text{DBNH})_2\text{Cu}_6\text{Sn}_2\text{S}_8$  (**2**) at different temperatures are shown in Fig. 7, and Fig. 8 displays the evolution of the crystalline transient species plotted together with the growth of the (200) reflection of **2** and the (-101) reflection of **1** at 160 °C.

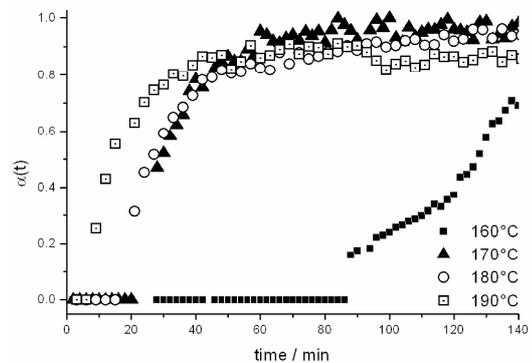


Figure 7: Temperature dependency of the crystallization of  $(\text{DBNH})_2\text{Cu}_6\text{Sn}_2\text{S}_8$  (**2**).

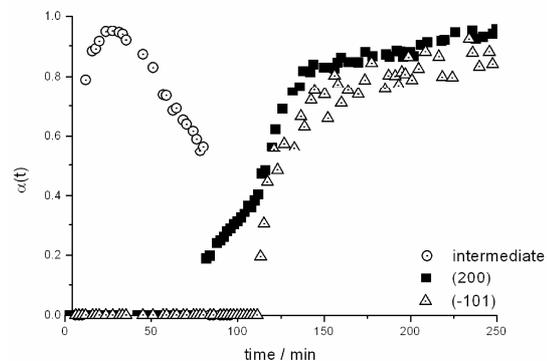


Figure 8: The extent of reaction  $\alpha(t)$  for the (200) reflection of  $(\text{DBNH})_2\text{Cu}_6\text{Sn}_2\text{S}_8$  (**2**), the (-101) reflection of  $(\text{DBNH})_2\text{Sn}_3\text{S}_6$  (**1**) and for the transient compound at 160 °C. Note that the scattering of the individual data points is due to the relatively low intensity of the (-101) peak and the reflection of the intermediate.

It is interesting to note that  $t_0$  for the formation of  $(\text{DBNH})_2\text{Cu}_6\text{Sn}_2\text{S}_8$  (**2**) is reduced by roughly 60 min when the temperature is raised from 160 to 170 °C (Fig. 7). For the reaction temperatures 170 – 190 °C,  $t_0$  is very similar and also the product growth is very fast at these temperatures. In addition, the reactions at higher temperatures are finished after about 100 min.

A comparison of the evolution of the extent of reaction for the transient crystalline phase and compounds **1** and **2** suggests that compound **2** starts to grow when the intermediate disappeared (Fig. 8). Extrapolating  $\alpha(t)$  of the precursor to longer reaction times indicates that the crossing point with  $\alpha(t)$  of  $(\text{DBNH})_2\text{Cu}_6\text{Sn}_2\text{S}_8$  is far below about  $\alpha = 0.2 - 0.3$ , or even at  $\alpha = 0$ . A possible interpretation of these findings is that the precursor is a metastable compound which is destroyed and the more stable compounds start to grow. Furthermore the first reflections of **1** appear when roughly 40% of compound **2** are formed. At longer reaction times both compounds are in equilibrium supporting the observation of the ex-situ syntheses presented above. Within the experimental accuracy no decrease of the intensity of reflections of **2** is observed indicating that **1** is not growing on the cost of **2**.

In the literature different models of the crystallization kinetics and the evaluation of appropriate data are well documented [55 - 59]. The analyses are done by integrating the intensities of the product reflections which are normalized against the intensities of the Sn-K $\alpha$  fluorescence. The experimental data are expressed as the extent of reaction and compared with the theoretical values for solid state kinetics.  $\alpha(t)$  is the ratio of the normalized intensity at time  $t$  to the intensity at time  $t_\infty$  and is defined by the following equation:

$$\alpha(t) = I_n(t) / I_n(t_\infty)$$

Using the Avrami-Eroféev expression the kinetic parameter for the reaction exponent  $m$  (Avrami exponent) and the rate constant  $k$  can be estimated. The kinetic parameters can also be extracted using the Sharp-Hancock plot (SH plot) [56]. The reaction exponent  $m$  corresponds to the slope of the curve and the rate constant  $k$  is the intercept with the y-axis. If the reaction follows one mechanism over the whole reaction time all experimental data points are on a straight line in a SH plot. Therefore, a change of the mechanism during a reaction can be detected immediately. For the evaluation of the kinetic data the induction time  $t_0$  was subtracted from the time  $t$ . In the following only the crystallization kinetics of  $(\text{DBNH})_2\text{Cu}_6\text{Sn}_2\text{S}_8$  (**2**) are discussed. The evaluation of the data of  $(\text{DBNH})_2\text{Sn}_3\text{S}_6$  (**1**) is difficult due to the relatively low intensity of the reflections and the overlap with reflections of  $(\text{DBNH})_2\text{Cu}_6\text{Sn}_2\text{S}_8$ . In principle, with the program calf3 (see experimental section) a deconvolution of superimposed reflections is possible and was also done. But the scattering of the intensity of the two reflections was too large for an unambiguous analysis of the crystallization kinetics.

The SH plot for the (200) peak of **2** at 160 °C is shown in Fig. 9.

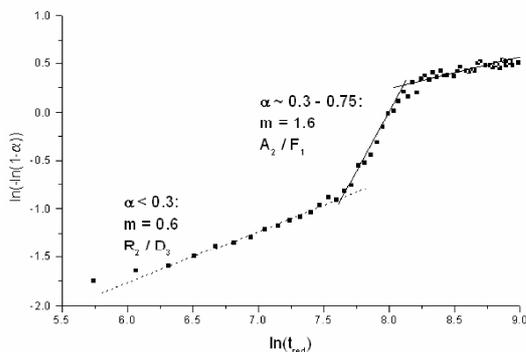


Fig. 9: Sharp-Hancock plot for the reaction at 160 °C using the (200) reflection of **2**. The lines are guides for the eyes.

The growth of **2** can be roughly divided into three different parts. Up to  $\alpha(t) \approx 0.3$ , the value for  $m$  is about 0.6 which is near models for diffusion control  $R_2/D_3$ . In the second part ( $0.3 < \alpha < 0.75$ )  $m$  increases to 1.6 indicating a change of mechanism. This value is in between the nucleation Avrami model  $A_2$  and a first order reaction  $F_1$ . For  $\alpha > 0.75$   $m$  decreases to about 0.4. The deviation of the values for  $m$  from the ideal values is not surprising because several strict conditions like random nucleation and no hard impingement have to be fulfilled before the Johnson-Mehl-Avrami (JMA) kinetics will hold. The JMA kinetics takes not into account that different reactions can occur parallel and/or successive. In addition, it is assumed that the reaction exponent  $m$  is temperature and time independent, which is not necessarily the case. In the present case it seems that no simple kinetics dominates the reaction. This is further evidenced by plotting  $t/t_{0.5}$  versus  $\alpha$  allowing a direct comparison with the established models (Fig. 10).

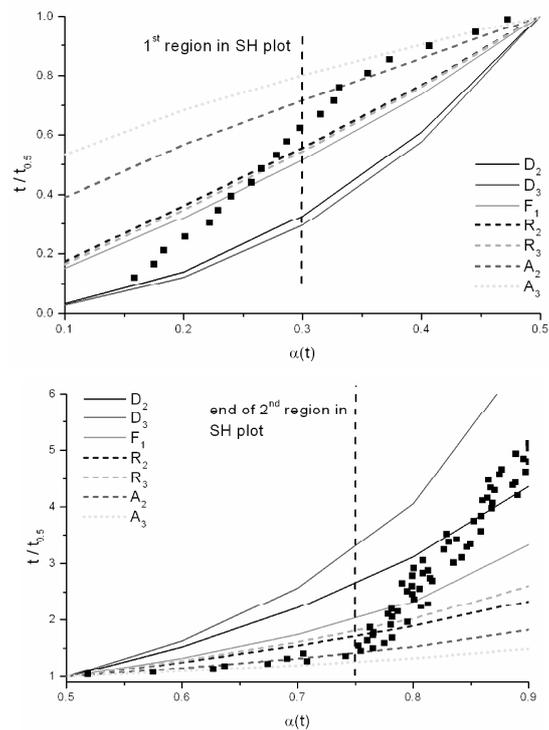


Fig. 10: Comparison of different kinetic models at 160 °C with the data for the (200) peak.

Analyzing the region between  $\alpha(t) = 0.1$  and  $0.5$  (Fig. 10, top) the experimental data points gradually shift from diffusion control to Avrami nucleation models  $A_2/A_3$  with increasing reaction time. In Figure 10 the data points between  $\alpha(t) = 0.4$  and  $0.75$  suggest that Avrami nucleation models dominate the kinetics. For the later stages of the reaction the data points scatter with a tendency toward a diffusion control. Two different cases can be distinguished for Avrami nucleation: all nuclei form instantaneously (zero order) or nuclei are added during the reaction progress (first order). The reaction exponent  $m$  contains both information and taking into account the two-dimensional nature of the crystals  $m \approx 1.6$  implies a two-dimensional growth and instantaneously formation of the nuclei.

The deviation of  $m$  from the ideal value 2 may be caused by heterogeneous nucleation on the walls of the glass tube.

For all temperatures a change of  $m$  is observed during the reaction progress with a tendency to later stages of the reaction where the change of  $m$  occurs. We note that only at  $T = 160$  and  $170$  °C the crystalline precursor appears. At higher temperatures no reflections of this transient species were detected and two possibilities can be envisaged as explanation for this observation: the crystalline transient compound is not formed at higher temperatures or the experimental time scale is too slow for the detection of this compound due to a very fast formation and disappearance.

The reactions performed without Cu are very fast and all reflections occur simultaneously after short induction times (Fig. 11), and a quantitative evaluation of the reaction kinetics is in this case not possible due to the fast reaction progress.

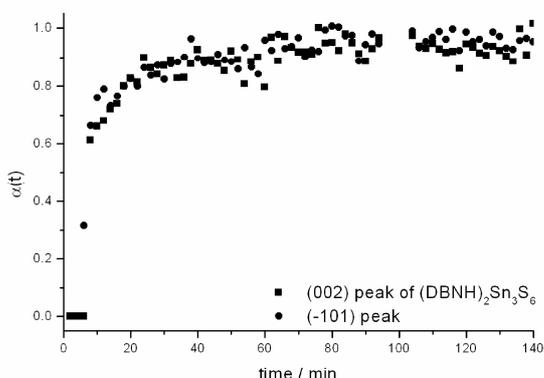


Fig. 11: Extent of reaction for compound **1** at 170 °C synthesized without Cu in the reaction mixture.

A qualitative comparison with the reactions using Cu, Sn, S and DBN clearly demonstrates that the induction time  $t_0$  is drastically reduced to 20 min at 160 °C (110 min with Cu) and to 4 min at 190 °C (42 min with Cu). In the competitive crystallization it seems that the formation of  $(\text{DBNH})_2\text{Cu}_6\text{Sn}_2\text{S}_8$  (**2**) is preferred and the growth of **1** is inhibited. Furthermore, in the temperature window from 140 to 190 °C no crystalline precursor or intermediate could be observed. This is a clear indication that the crystalline transient species must be associated with the presence of Cu in the reaction slurry (see below). In addition the presence of Cu is not required for the crystallization of the mixed-valent compound **1**, i.e., Cu is not involved in the redox reaction.

The sizes of the coherent scattering particles of both compounds can be estimated applying the Scherrer equation:

$$D_k = \frac{K \cdot \lambda \cdot 180/\pi}{d_{\text{FWHM}} \cdot \cos \theta}$$

with  $D_k$  average crystallite size,  $d_{\text{FWHM}}$  full width half maximum,  $\theta$  Bragg angle,  $\lambda$  wavelength and  $K$  the Scherrer constant (0.89 was used). The value for  $d_{\text{FWHM}}$  of the (200) peak of **2** ( $\theta = 4.14^\circ$ ) decreases from 0.22 to  $0.16^\circ$  during the reaction ( $t = 240$  min) leading to an increase of the coherent scattering domains from 36 to

49 nm. The  $d_{\text{FWHM}}$  for the (002) reflection of **1** ( $\theta = 4.72^\circ$ ) is reduced from  $0.2$  to  $0.17^\circ$  yielding sizes of 39 and 46 nm, respectively.

With ex-situ experiments the crystalline intermediate was isolated by quenching the reaction at different reaction times and the chemical composition was analyzed. For the intermediate quenched after 30, 40, 50 and 60 min EDX analyses give nearly identical ratios for Cu:Sn:S of about 2:1:6. The CHN content is in agreement with about one DBN molecule assuming  $\text{Cu}_2\text{SnS}_6$  as chemical composition of the inorganic part, i.e., the chemical formula of the intermediate is most likely  $(\text{DBNH})\text{Cu}_2\text{SnS}_6$ . Charge neutrality of this compound requires the presence of  $\text{S}_2^{2-}$  anions assuming Cu(I), Sn(IV) and a double protonated DBN molecule.

In further ex-situ experiments the role of the intermediate species for the formation of **1** and **2** was investigated. Treating the intermediate with DBN at 160 °C for 5 h, elemental crystalline Sn and an amorphous phase containing Cu, Sn and S are formed. The reaction under similar conditions adding also S produces Sn and Cu sulfides. But in the XRD a peak at  $7.7^\circ 2\theta$  is observed which cannot be explained with known Sn/Cu sulfides or the title compounds. Several experiments were conducted with the intermediate applying different reaction conditions. But in all cases the title compounds were not formed. Two important conclusions can be drawn from this observation: (i) in accordance with the results of the in-situ EDXRD investigations the transient crystalline compound can be regarded as a new material which is not necessary for the formation of **1** and **2**. (ii) Under the real solvothermal conditions soluble species are present which are important for the formation of **1** and **2**.

Further experiments were done to explore whether  $(\text{DBNH})_2\text{Sn}_3\text{S}_6$  (**1**) can be transformed to  $(\text{DBNH})_2\text{Cu}_6\text{Sn}_2\text{S}_8$  (**2**). Cu, S and DBN were added to a small amount of **1** and heated at 170 °C for 5 h. The EDX analysis yields a Cu/Sn/S ratio of 3/1/4, but the powder diffraction pattern confirms the presence of  $(\text{DBNH})_2\text{Sn}_3\text{S}_6$  (**1**) and  $(\text{DBNH})_2\text{Cu}_6\text{Sn}_2\text{S}_8$  (**2**).

### Spectroscopy

**Raman spectroscopy:** In the Raman spectra the resonances of compound **1** at 367, 336, 313 and 258  $\text{cm}^{-1}$  are in the typical region for Sn-S resonances [60, 61]. The symmetric Sn-S stretch vibration is located at 367  $\text{cm}^{-1}$  and symmetric Sn-S<sub>bridging</sub> modes appear at 336 and 313  $\text{cm}^{-1}$ . The resonance at 258  $\text{cm}^{-1}$  is caused by a  $\text{Sn}_2\text{S}_2$  ring vibration. For compound **2** only two modes are observed. The band at 362  $\text{cm}^{-1}$  is the symmetric Sn-S stretching and that at 332  $\text{cm}^{-1}$  the symmetric Sn-S<sub>bridging</sub> vibration. Surprisingly, no resonances or modes caused by Cu-S vibrations are observed.

**UV/Vis spectroscopy:** The optical band gap was determined from transformed UV/Vis diffuse reflectance spectra with the Kubelka-Munk-method. For **1**  $E_g$  amounts to 2.6 eV (477 nm) in agreement with the yellow color. The value for **2** of 1.84 eV (674 nm) is in accordance with the red color of the plates.

### Thermal Stability

Compound **1** decomposes in two steps. The first thermal reaction starts at  $T_{\text{onset}} = 229$  °C ( $T_{\text{peak}} = 234$  °C) and is associated

with a mass loss of 11.2 %. The next step occurs at  $T_{\text{onset}} = 288$  °C ( $T_{\text{peak}} = 310$  °C) with a weight change of 21.5 %. The difference between observed and calculated weight loss ( $-\Delta m_{\text{theo}}$  (2 DBN + 1 H<sub>2</sub>S) = 35.3 %) can be explained with a contamination (CHN) of the residue. The decomposition product is black and SnS was identified in the powder pattern.

The thermal decomposition of compound **2** starts at  $T_{\text{onset}} = 218$  °C ( $T_{\text{peak}} = 281$  °C) with a related weight loss of 28.9 % which is slightly higher than the calculated value ( $-\Delta m_{\text{theo}}$  (DBN + H<sub>2</sub>S) = 28.3 %). The obtained powder is black and contains a few percent of CHN. The compounds SnS and CuS were identified in the powder pattern.

### Conclusion

The aim of the synthetic work was the preparation of new copper containing thioannates. In the reaction products of all syntheses the new thioannates (DBNH)<sub>2</sub>Sn<sub>3</sub>S<sub>6</sub> (**1**) and (DBNH)<sub>2</sub>Cu<sub>6</sub>Sn<sub>2</sub>S<sub>8</sub> (**2**) were obtained simultaneously as yellow needles and red plates respectively. Long reaction times up to about one month were required for the crystallization of crystals suitable for the crystal structure determination. Stirring the reaction mixtures reduces the reaction times to a few hours and increases the yield, but as for the static syntheses both thioannates occurred in the reaction products. From a chemical point of view the simultaneous occurrence of the mixed-valent pure thioannate (DBNH)<sub>2</sub>Sn<sub>3</sub>S<sub>6</sub> (**1**) and a Sn(IV) containing Cu thioannate (DBNH)<sub>2</sub>Cu<sub>6</sub>Sn<sub>2</sub>S<sub>8</sub> (**2**) is of special interest. The syntheses were conducted applying elemental Cu, Sn and S and it is obvious that a complex redox reaction occurs during synthesis progress.

In the structure of the mixed-valent compound **1** the chains are constructed from alternating Sn<sub>3</sub>S<sub>4</sub> semi-cubes and Sn<sub>2</sub>S<sub>2</sub> rings. These structural motifs are related to those observed in R-SnS-1 and R-SnS-3 [6, 39, 45]. Whereas in R-SnS-1 and R-SnS-3 the primary building units contain only Sn(IV), in **1** a Sn(II) replaces a Sn atom of the Sn<sub>3</sub>S<sub>4</sub> semi-cube. This Sn(II) atom is in a trigonal pyramidal coordination which is quite rare. The layered structure of **2** may be viewed as an inorganic 6<sup>3</sup> graphene layer constructed by condensation of CuS<sub>3</sub> triangles and SnS<sub>4</sub> tetrahedra. Such a structural motif was never observed before in the structures of thioannates.

Despite a large variation of several synthesis parameters, compound **2** could not be obtained as phase pure product. In-situ EDXRD experiments not only reveal that **1** and **2** start to crystallize within a narrow time window but also highlights the occurrence of a crystalline precursor prior to formation of **1** and **2**. The detailed analysis of the data evidences that this precursor is a new metastable compound which is not simply transformed into the final products. This metastable compound was quenched with ex-situ syntheses but could not be transformed into one of the two stable compounds. In addition, the successful preparation of the mixed-valent compound without Cu in the reaction slurry demonstrates that neither the precursor nor Cu is directly involved in the complex redox reaction. The in-situ experiments also show that crystallization of **1** is retarded in the presence of Cu species in the solution. The results of in-situ experiments of reactions with only Sn, S, and DBN demonstrate that (DBNH)<sub>2</sub>Sn<sub>3</sub>S<sub>6</sub> is formed within a couple of minutes. The above presented results of the in-situ X-ray scattering experiments enhance our knowledge about solvothermal syntheses and also highlights the power of the in-situ approach. Such information cannot be acquired using only ex-situ syntheses.

Despite the large amount of information acquired during the studies several synthetic challenges are left open. For instance, it would be of great interest to synthesize the metastable precursor for structural characterization. The poor quality of the powder patterns of the quenched precursor prevented structure solution until now. The challenge is finding synthesis conditions where only this metastable compound is formed, or at least crystals of appropriate quality are present. It is also necessary synthesizing phase pure material of **2**. We note that all syntheses were performed applying the elements. Further explorative syntheses with different Cu and Sn compounds (Cu(I), Cu(II), Sn(II) and Sn(IV) salts) are under way. Due to our longstanding experience of solvothermal syntheses we know that changing the starting material requires a large number of experiments until the reaction conditions for the formation of a desired compound are established. In a relatively large number of cases we were never able synthesizing a thiometalate which was formerly obtained applying for instance the elements as educts.

### Experimental Section

#### Syntheses:

*General:* All chemicals were purchased (see below for purity and company) and used without further purifications. Both compounds were prepared under solvothermal conditions in teflon-lined steel autoclaves (inner volume: 30 mL). The crystalline reaction products were filtered off, washed with water and ethanol and dried in vacuum.

Synthesis of (DBNH)<sub>2</sub>Sn<sub>3</sub>S<sub>6</sub> (**1**) and (DBNH)<sub>2</sub>Cu<sub>6</sub>Sn<sub>2</sub>S<sub>8</sub> (**2**): 118.7 mg (1 mmol) Sn (99.5 %, Aldrich), 63.5 mg (1 mmol) Cu (99.5 %, Alfa Aesar), 105.8 mg (3.3 mmol) S in 3 mL of 1,5-diazabicyclo[4.3.0]non-5-ene (DBN) ( $\geq 98.0$  %, Fluka) were reacted for 27 d at 140 °C, followed by cooling to 25 °C in 30 h. In the reaction products yellow needles of **1** and red plates of **2** were found in a low yield. The compounds can also be obtained applying a reaction time of 5 d, but the quality of the crystals especially for **2** was not good enough for single crystal structure determination. During the optimization of the reaction conditions, the duration was elongated from 5 d over 10 and 15 d up to 27 d. In all syntheses Cu and Sn sulfides are the main products. A large number of syntheses was performed to increase the yield and also the homogeneity.

**1** can also be synthesized reacting 1 mmol Sn and 3 mmol S in 3 mL DBN for 20 d at 170 °C in a yield of ~10% based on Sn.

The different reaction products were manually separated and the homogeneity of both compounds was confirmed by X-ray powder diffraction. Elemental analyses (results in %): **1**: found: C 21.05, H 3.21, N 7.11; calculated: C 21.10, H 3.04, N 7.03; **2**: found: C 14.82, H 2.46, N 4.81; calculated: C 14.94, H 2.33, N 4.98.

#### Structure determination:

Intensity data were collected on a STOE IPDS-1 (Imaging Plate Diffraction System) with Mo K $\alpha$  radiation at room temperature. The structures were solved with direct methods using the program SHELXS-97 [62] and the refinements were done against F<sup>2</sup> with SHELXL-97 [63]. Anisotropic displacement parameters were used for all non-hydrogen atoms. The H atoms of the amines were positioned with idealized geometry and refined using a riding model and a fixed isotropic displacement parameter. In **2** some disorder of the DBN is present and the structure refinement was performed using a split model. Some selected refinement results are summarized in Table 4.

Tab. 4: Selected technical details of data collection and results of the structure refinement of the title compounds.

	(DBNH) <sub>2</sub> Sn <sub>3</sub> S <sub>6</sub>	(DBNH) <sub>2</sub> Cu <sub>6</sub> Sn <sub>2</sub> S <sub>8</sub>
Crystal system	Monoclinic	Orthorhombic
Space group	P2 <sub>1</sub> /n	Pca2 <sub>1</sub>
a / Å	9.5822(8)	21.3017(10)
b / Å	13.1199(7)	6.6837(3)
c / Å	19.9506(16)	19.9480(13)

$\alpha$	90	90
$\beta$	97.192(10)	90
$\gamma$	90	90
$V / \text{\AA}^3$	2488.4(3)	2840.1(3)
Z	4	4
Dcalculated / $\text{g/cm}^3$	2.132	2.632
$\mu / \text{mm}^{-1}$	3.501	6.734
Scan Range	$2.65 \leq \theta \leq 28.02^\circ$	$2.80 \leq \theta \leq 28.02^\circ$
Reflections collected	21603	16982
Refl. with $F_o > 4\sigma(F_o)$	1536	2160
Independent reflections	5831 [R(int) = 0.0589]	6810 [R(int) = 0.0636]
Goodness-of-fit on $F^2$	1.006	0.985
Final R indices [I > 2 $\sigma(I)$ ]	R1 = 0.0387, wR2 = 0.0874	R1 = 0.0441, wR2 = 0.1031
R indices (all data)	R1 = 0.0626, wR2 = 0.0958	R1 = 0.0597, wR2 = 0.1108
Res. Elec. Dens. / $\text{e.\AA}^{-3}$	0.928 / -0.971	1.667 / -1.634
Flack x parameter		-0.02(2)

Further crystallographic details have been deposited with the Cambridge Crystallographic Data Centre as publication no. CCDC XXXX (1) and CCDC XXX (2). Copies of the data can be obtained, free of charge, on application to CCDC, 12 Union Road, Cambridge CB2 1EZ, UK (mail: deposit@ccdc.ca.ac.uk).

#### Energy-dispersive X-Ray Diffraction (EDXRD):

All EDXRD experiments were carried out at the HASYLAB beamline F3 at DESY, Hamburg, Germany. The beamline station receives white synchrotron radiation from a bending magnet with  $E_c = 16.6$  keV and gives a positron beam energy of 4.5 GeV. The energy range from 6 to 60 keV exhibits a maximum at about 20 keV. A liquid nitrogen cooled solid-state germanium detector with a resolution of about 1% was used. The angle of the detector was fixed at approximately  $1.8^\circ$  which allowed the detection of the Bragg reflections and the observable  $d$ -spacing range was 3.1 to 32.3 Å given by  $E = 6.199/(d \cdot \sin\theta)$ . The beam was collimated to 200 x 200  $\mu\text{m}$  giving the best results. More experimental details can be found in [30, 31]. The in-situ investigations were conducted in glass tubes in special autoclaves with an internal diameter of 10 mm and a volume of 7 mL. The delay time between filling the mixture of the starting materials in the autoclave and starting the reaction was about 2 min and the reaction temperature was reached within 1 min. Time-resolved X-ray powder patterns with acceptable counting statistics could be recorded with acquisition times between 120 and 180 sec. Under stirring conditions the compounds were synthesized using 30 mg (0.47 mmol) Cu, 60 mg (0.5 mmol) Sn and 50 mg (1.55 mmol) S in 1 mL DBN at temperatures ranging from 140 to 200 °C. Compound 1 was prepared applying 60 mg Sn (0.5 mmol) and 50 mg S (1.55 mmol) in 1 mL DBN at temperatures between 140 and 190 °C. The resulting spectra were evaluated with EDXPOW [64] and the Origin6.0 program package. Due to some problems in integrating triple peaks of spectra series, we used the program "calf3" which was developed in close cooperation with A. Rothkirch (HASYLAB, DESY). It was written to support the energy calibration of beamline F3 and to evaluate spectra time series of in-situ EDXRD measurements. The routine is written in Interactive Data Language (IDL), ITT Visual Information Solutions, Boulder, CO, USA and runs also with IDL virtual machine. For the data evaluation of time series, an input file must be supplied which provides regions of interest for possible peak positions and (optional) regions for background. The data are background corrected by a polynomial assumption and regions of interest are scanned for diffraction/fluorescence peaks. The peaks are fitted to Gaussians (possible for single or even superimposed triple peaks) and separately integrated for every single spectrum. In addition, a normalization of the integrals to a reference can be applied (e.g. integral of fluorescence peak within a single spectrum). The derived coefficients and integrals are written to an output file as well as an illustration for first visual analysis. The integrals of the product reflections were normalized with the integrals of the intensity of the Sn- $K_{\alpha}$  fluorescence.

#### X-Ray Powder Diffraction

X-ray powder diffraction patterns were recorded in transmission mode with a STOE Stadi-P diffractometer equipped with an imaging plate position

sensitive detector (IP-PSD) and Ge monochromator using  $\text{Cu } K_{\alpha 1}$  ( $\lambda = 1.54056$  Å) radiation.

#### Thermal investigations:

DTA-TG experiments were carried out using a Netzsch STA 429 DTA-TG device. The samples were heated up to 500 °C with 4 K $\cdot$ min $^{-1}$  under a flow of argon (75 mL $\cdot$ min $^{-1}$ ) in  $\text{Al}_2\text{O}_3$  crucibles. The TG data were corrected for buoyancy and current effects.

#### Scanning electron microscopy (SEM)/ energy dispersive X-ray fluorescence (EDX):

A Philips ESEM XL30 equipped with an EDAX EDX system was used to determine the compositions.

#### Spectroscopic experiments:

**Infrared spectroscopy:** In the IR spectra the absorptions located at 3277 (m, -NH stretch), 3104 (m, -NH stretch), 2922 (s, -CH $_2$ ; m-s, -NH stretch), 1670 (m, -CC), 1567 (m-s, -NH), 1417, 1298, 1201 (m, -CN) and 1064 (m, -CN)  $\text{cm}^{-1}$  (1) respectively at 2920 (s, -CH $_2$ ; m-s, -NH stretch), 1670 (m, -CC), 1371, 1292, 1124 (m, -CN) and 1064 (m, -CN)  $\text{cm}^{-1}$  (2) are detected of the DBN molecules.

**Raman:** The data for the Raman spectra were collected in the region from 100 to 500  $\text{cm}^{-1}$  with a Bruker IFS 66 Fourier Transform Raman spectrometer (wavelength: 541.5 nm).

**UV/Vis:** Investigations were done at room temperature using a UV-VIS-NIR two-channel spectrometer Cary 5 from Varian Techtron Pty., Darmstadt. The absorption data were calculated with the Kubelka-Munk approach for diffuse reflectance data.  $\text{BaSO}_4$  powder was used as reference material.

#### Elemental analysis:

CHNS analyses were done using a EURO EA Elemental Analyzer, fabricated by EURO VECTOR Instruments and Software.

#### Acknowledgements

We thank the Hasylab, DESY, Hamburg, Germany, for the measurement times at the beamline F3. Thanks to Beatrix Seidlhofer and Elena Antonova (University of Kiel) for joining our measurements and thanks to André Rothkirch (HASYLAB, DESY, Hamburg) for his help.

- [1] M. Behrens, C. Näther, W. Bensch, *Z. Anorg. Allg. Chem.* **2002**, 628, 2160.
- [2] C. Näther, S. Scherb, W. Bensch, *Acta Cryst.* **2003**, E59, m280–m282.
- [3] A. Puls, C. Näther, W. Bensch, *Acta Cryst.* **2005**, E61, m868–m870.
- [4] J.B. Parise, Y. Ko, J. Rijnssenbeek, D.M. Nellis, K. Tan, S. Koch, *J. Chem. Soc., Chem. Commun.* **1994**, 527.
- [5] T. Jiang, A. Lough, G.A. Ozin, *Adv. Mater.* **1998**, 10, 42–46.
- [6] T. Jiang, A. Lough, G.A. Ozin, R.L. Bedard, R. Broach, *J. Mater. Chem.* **1998**, 8, 721–732.
- [7] S. Dehnen, C. Zimmermann, *Z. Anorg. Allg. Chem.* **2002**, 628, 2436–2439.
- [8] R.W.J. Scott, M.J. MacLachlan, G.A. Ozin, *Current Opinions in Solid State and Materials Science* **1999**, 4, 113–121.
- [9] T. Jiang, G.A. Ozin, *J. Mater. Chem.* **1997**, 7, 2213–2222.
- [10] R.J. Francis, S.J. Price, J.S.O. Evans, S. O'Brien, D. O'Hare, S.M. Clark, *Chem. Mater.* **1996**, 8, 2102–2108.
- [11] Y. An, M. Ji, M. Baiyin, X. Liu, C. Jia, D. Wang, *Inorg. Chem.* **2003**, 42, 4248–4249.
- [12] M. Behrens, S. Scherb, C. Näther, W. Bensch, *Z. Anorg. Allg. Chem.* **2003**, 629, 1367–1373.
- [13] N. Pienack, W. Bensch, *Z. Anorg. Allg. Chem.* **2006**, 632, 1733–1736.

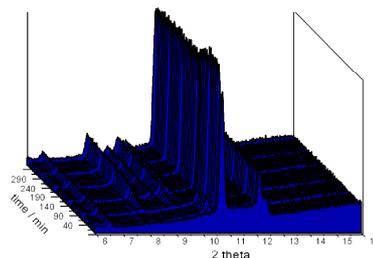
- [14] N. Pienack, C. Näther, W. Bensch, *Solid State Sci.* **2007**, *9*, 100-107.
- [15] D.X. Jia, J. Dai, Q.Y. Zhu, Y. Zhang, X.M. Gu, *Polyhedron* **2004**, *23*, 937-942.
- [16] M. Antonietti, G.A. Ozin, *Chem. Eur. J.* **2004**, *10*, 28-41.
- [17] M. Cruz, J. Morales, J.P. Espinos, J. Sanz, *J. Solid State Chem.* **2003**, *175*, 359-365.
- [18] K.O. Klepp, F. Fabian, *Z Naturforsch B* **1992**, *47*, 406-410.
- [19] K.O. Klepp, F. Fabian, *European Crystallographic Meeting* **1994**, *15*, 626-626.
- [20] S. Chitsaz, B. Neumüller, K. Dehnicke, *Z. Anorg. Allg. Chem.* **2000**, *626*, 318-815.
- [21] J.F. Eichler, O. Just, W.S. Rees, *Inorg. Chem.* **2006**, *45*, 6706-6712.
- [22] C. Adenis, J. Olivier-Fourcade, J.C. Jumas, E. Philippot, *Rev. Chim. Min.* **1986**, *23*, 735-745.
- [23] C. Adenia, J. Olivier-Fourcade, J.C. Jumas, E. Philippot, *Eur. J. Solid State Inorg. Chem.* **1988**, *25*, 413-423.
- [24] J.C. Jumas, J. Olivier-Fourcade, E. Philippot, M. Maurin, *Rev. Chim. Min.* **1979**, *16*, 48-59.
- [25] S. Jobic, P. le Boterf, R. Brec, G. Ouvrard, *J. Alloys Compd.* **1994**, *205*, 139-145.
- [26] R. Francis, D. O'Hare, *J. Chem. Soc., Dalton Trans.* **1998**, 3133.
- [27] W. Bensch, C. Näther, R. Stähler, *Chem. Commun.* **2001**, 477-478.
- [28] R. Stähler, B.D. Mosel, H. Eckert, W. Bensch, *Angew. Chem. Int. Ed.*, **2002**, *41*, 4487-4489.
- [29] R. Kiebach, F. Studt, C. Näther, W. Bensch, *Eur. J. Inorg. Chem.* **2004**, 2553-2556.
- [30] L. Engelke, M. Schaefer, M. Schur, W. Bensch, *Chem. Mater.* **2001**, *13*, 1383-1390.
- [31] L. Engelke, M. Schaefer, F. Porsch, W. Bensch, *Eur. J. Inorg. Chem.* **2003**, 506-513.
- [32] R. Kiebach, M. Schaefer, F. Porsch, W. Bensch, *Z. Anorg. Allg. Chem.* **2004**, *631*, 369-374.
- [33] R. Kiebach, N. Pienack, M.E. Ordolf, F. Studt, W. Bensch, *Chem. Mater.* **2006**, *18*, 1196-1205.
- [34] A. Michailovski, J.-D. Grunwaldt, A. Baiker, R. Kiebach, W. Bensch, G.R. Patzke, *Angew. Chem.* **2005**, *117*, 5787-5792.
- [35] A. Michailovski, R. Kiebach, W. Bensch, J.-D. Grunwaldt, A. Baiker, S. Komarneni, G.R. Patzke, *Chem. Mater.* **2007**, *19*, 185-197.
- [36] R. Kiebach, N. Pienack, W. Bensch, J.-D. Grunwaldt, A. Michailovski, A. Baiker, T. Fox, Y. Zhou, G.R. Patzke, *Chem. Mater.* **2008**, *20*, 3022-3033.
- [37] R.I. Walton, T. Loiseau, D. O'Hare, G. Férey, *Chem. Mater.* **1999**, *11*, 3201-3209.
- [38] K. Tan, Y. Ko, J.B. Parise, *Acta Cryst.* **1995**, *C51*, 398.
- [39] T. Jiang, A.J. Lough, G.A. Ozin, D. Young, R.L. Bedard, *Chem. Mater.* **1995**, *7*, 245-248.
- [40] O. Slupecki, I.D. Brown, *Acta Cryst.* **1982**, *B38*, 1078-1079.
- [41] R. Kniep, D. Mootz, U. Severin, H. Wunderlich, *Acta Cryst.* **1982**, *B 38*, 2022.
- [42] J.J. Vittal, P.A.W. Dean, *Acta Crystallogr. Sect.C: Cryst. Struct. Commun.* **1996**, *52*, 1180.
- [43] P.A.W. Dean, J.J. Vittal, N.C. Payne, *Can. J. Chem.* **1985**, *63*, 394.
- [44] G. Barone, T.G. Hibbert, M.F. Mahon, K.C. Molloy, I.P. Parkin, L.S. Price, I. Silaghi-Dumitrescu, *J. Chem. Soc., Dalton Trans.* **2001**, 3435.
- [45] T. Jiang, A. Lough, G.A. Ozin, R.L. Bedard, *J. Mater. Chem.* **1998**, *8*, 733-741.
- [46] W.S. Sheldrick, B. Schaaf, *Z. Anorg. Allg. Chem.* **1994**, *620*, 1041-1045.
- [47] T. Jiang, G.A. Ozin, *J. Mater. Chem.* **1998**, *8*, 1099-1108.
- [48] T. Jiang, G.A. Ozin, R.L. Bedard, *J. Mater. Chem.* **1998**, *8*, 1641-1648.
- [49] X. Chen, H. Wada, A. Sato, M. Mieno, *J. Solid State Chem.* **1998**, *139*, 144-151.
- [50] X. Chen, H. Wada, A. Sato, *Mater. Res. Bull.* **1999**, *34*, 239.
- [51] V. Spetzler, H. Rijnberk, C. Näther, W. Bensch, *Z. Anorg. Allg. Chem.* **2004**, *630*, 142-148.
- [52] V. Spetzler, C. Näther, W. Bensch, *Inorg. Chem.* **2005**, *44*, 5805-5812.
- [53] M. Jansen, *Angew. Chem.* **1987**, *99*, 1136-49.
- [54] R. Stähler, C. Näther, W. Bensch, *J. Solid State Chem.* **2003**, *174*, 264-275.
- [55] M.J. Avrami, *Chem. Phys.* **1939**, *7*, 1103-1112.
- [56] M.J. Avrami, *Chem. Phys.* **1940**, *8*, 212-224.
- [57] M.J. Avrami, *Chem. Phys.* **1941**, *9*, 177-184.
- [58] J.H. Sharp, G.W. Brindley, B.N. Narahari Achar, *J. Am. Cer. Soc.* **1966**, *47*, 379-382.
- [59] J.D. Hancock, J.H. Sharp, *J. Am. Cer. Soc.* **1972**, *55*, 74-76.
- [60] B. Krebs, W. Schiwy, *Z. Anorg. Allg. Chem.* **1973**, *398*, 63-71.
- [61] B. Krebs, S. Pohl, W. Schiwy, *Angew. Chem.* **1970**, *82*, 884-885.
- [62] G.M. Sheldrick, *SHELXS 97, Program for the Solution of Crystal Structures*, University of Göttingen, Germany, 1997.
- [63] G.M. Sheldrick, G.M., *SHELXL 97, Program for the Refinement of Crystal Structures*, University of Göttingen, Germany, 1997.
- [64] F. Porsch, *EDXPowd Version 3.155*, RTI GmbH, Paderborn, Germany, 2004.

Received: ((will be filled in by the editorial staff))  
Revised: ((will be filled in by the editorial staff))  
Published online: ((will be filled in by the editorial staff))

**A mixed-valent Sn(II)/Sn(IV) thioannate and a copper-containing Sn(IV) thioannate coexisting under solvothermal conditions.**

*N. Pienack, C. Näther, W. Bensch\**

**Solvothermal syntheses of two new thioannates and an in-situ energy dispersive X-ray scattering study of their formation**



The mixed-valent Sn(II)/Sn(IV) thioannate  $(\text{DBNH})_2\text{Sn}_3\text{S}_6$  and the Sn(IV) thioannate  $(\text{DBNH})_2\text{Cu}_6\text{Sn}_2\text{S}_8$  coexist under solvothermal conditions. The Sn(II) species shows a rare trigonal-pyramidal environment whereas Sn(IV) is in a trigonal-bipyramidal coordination resulting in chains made of alternating  $\text{Sn}_3\text{S}_4$  semi-cubes and  $\text{Sn}_2\text{S}_2$  rings. In the other compound the condensation of  $\text{CuS}_3$  triangles and  $\text{SnS}_4$  tetrahedra yields in undulated anionic layers which can be seen as heteroatom  $6^3$  graphene layers. The remarkable coexistence of the two thioannates was investigated with in-situ energy dispersive X-ray scattering under real reaction conditions. The appearance of a crystalline precursor is followed by the formation of the thioannate(IV). Short times later the crystallization of the mixed-valent Sn(II)/Sn(IV) thioannate started suggesting complex redox reactions occurring under the solvothermal conditions.

#### 4.2.2. EXAFS-Untersuchungen zur Bildung von $[\text{Co}(\text{C}_6\text{H}_{18}\text{N}_4)][\text{Sb}_2\text{S}_4]$

*Zusammenfassung der Veröffentlichung "Combined in-situ EDXRD/EXAFS Investigation of the Crystal Growth of  $[\text{Co}(\text{C}_6\text{H}_{18}\text{N}_4)][\text{Sb}_2\text{S}_4]$  under Solvothermal Conditions: Two Different Reaction Pathways Leading to the Same Product".*

Das Kristallwachstum und die Reaktionskinetik der Bildung des Thioantimonats  $[\text{Co}(\text{tren})][\text{Sb}_2\text{S}_4]$  (tren = Tris-(2-aminoethyl)-amin) unter solvothermalen Bedingungen wurden mit komplementären in-situ-EDXRD- und EXAFS-Messungen bei verschiedenen Temperaturen untersucht.

Die Schichtverbindung  $[\text{Co}(\text{tren})][\text{Sb}_2\text{S}_4]$  wird bei Temperaturen zwischen 105 °C - 130 °C ohne kristalline Zwischenprodukte, Precursoren oder Intermediate gebildet. Die Ergebnisse der EDXRD-Studie wurden bereits in der Dissertation von R. Kiebach [91] erörtert. Daher sollen nur die komplementär dazu durchgeführten EXAFS-Untersuchungen an der Sb-K-Kante an dieser Stelle diskutiert werden. Die Experimente wurden mit der in Kapitel 3.2 beschriebenen in-situ-Apparatur am Messplatz X1 (Hasylab, Desy, vgl. Kap. 3.4) durchgeführt. Bei einem typischen Experiment wurden 0.5 mmol Co, 0.5 mmol Sb und 1.5 mmol S in 2 mL 50%iger tren-Lösung eingesetzt.

Die Auswertung der EXAFS-Spektren ergibt, dass sich interessanterweise die lokale Umgebung um die Sb-Atome im Verlauf einer Reaktion nicht ändert. Variationen der Temperatur, des Amins oder des pH-Wertes beeinflussen dieses Ergebnis nicht. Da der Kantenhub direkt proportional zur Konzentration des untersuchten Absorberatoms ist, kann mit Hilfe des abnehmenden Kantenhubs die sinkende Sb-Konzentration verfolgt werden. Unter der Voraussetzung, dass das zu Beginn gelöste Antimon feste Produkte bildet, die sich absetzen und damit nicht mehr in der Lösung detektiert werden können, verläuft die Konzentrationsänderung sigmoidal (Abb. 4.13). Die in Lösung vorhandenen Spezies können identifiziert werden, indem für verschiedene  $\text{SbS}_x$ -Spezies berechnete EXAFS-Spektren mit den gemessenen verglichen, zusammen simuliert und angepasst werden. In der Literatur werden als Hauptspezies in alkalischer, sulfidischer Lösung die Spezies  $[\text{Sb}_2\text{S}_4]^{2-}$ ,  $[\text{SbS}_3]^{3-}$  und  $[\text{SbS}_4]^{3-}$  diskutiert [107, 108, 109]. Da die radiale Abstandsverteilung der Messungen nur eine Schale um das Sb anzeigt, kann die erste Spezies, für die zwei Schalen

sichtbar sein müssten, ausgeschlossen werden. Die Geometrien der verbleibenden Sb-Spezies wurden mit Gaussian98 [110] berechnet und optimiert.

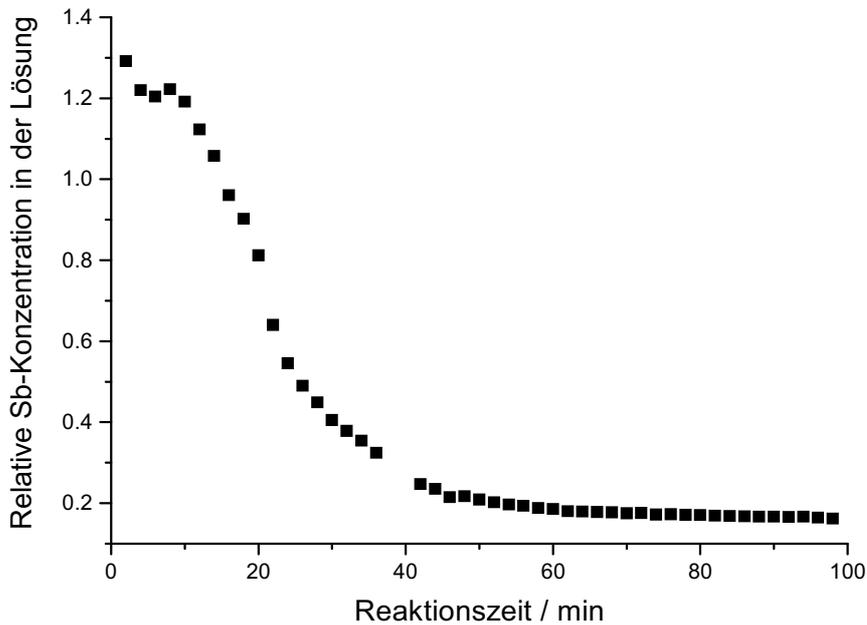


Abb. 4.13: Abnahme des Sb-Kantenhubs mit fortschreitender Reaktion.

Die optimierten  $\text{SbS}_3$ - bzw.  $\text{SbS}_4$ -Cluster wurden für die FEFF-Simulationen [104] herangezogen. Die Verfeinerungen (Abb. 4.14) mit variabler Koordinationszahl (zwischen 3 und 4) führen immer zu einer Koordinationszahl um 3.5. Dies ist ein guter Hinweis darauf, dass die beiden Spezies im Verhältnis von ca. 50 : 50 in der Lösung koexistieren.

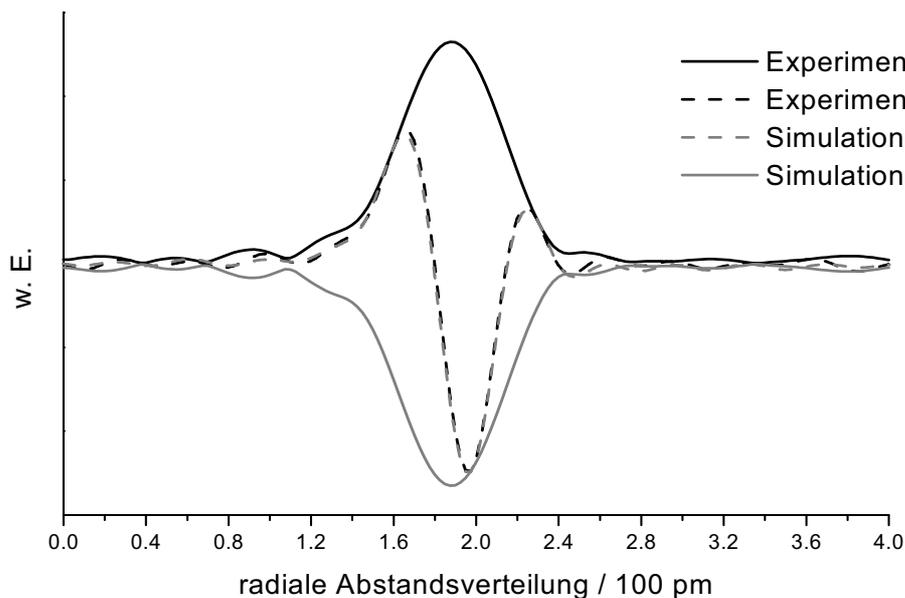


Abb. 4.14: Vergleich der radialen Abstandsverteilung (durchgezogene Linien) und der Fourier-Transformierten  $\chi(k)$  (gestrichelte Linien) der gemessenen (schwarz) und berechneten (grau) Daten. Die theoretischen Phasen und Amplituden wurden für  $\text{SbS}_3$ - und  $\text{SbS}_4$ -Einheiten simuliert.

Die EXAFS-Spektren belegen, dass sich die Sb-Nahordnung in Lösung bei allen durchgeführten Reaktionen nicht ändert und nur Monomere vorliegen. Kondensationen dieser Monomere führen wahrscheinlich zu  $Sb_xS_y$ -Einheiten, die als feste (amorphe) Zwischenprodukte oder Intermediate ausfallen und somit in Lösung nicht erfasst werden können. Für die Aufnahme der EXAFS-Spektren musste das Rühren des Reaktionsgemisches unterbrochen werden, da sonst die Spektren zu verrauscht und Auswertungen nicht möglich waren. Untersuchungen der festen, eventuell amorphen (Zwischen-) Produkte konnten daher nicht durchgeführt werden. Da bei den EDXRD-Untersuchungen kontinuierlich gerührt worden ist, sind die Reaktionsführungen nicht identisch, sondern müssen mit Sorgfalt und der notwendigen Skepsis verglichen werden.

Reproduced with permission from R. Kiebach, N. Pienack, M.-E. Ordolff, F. Studt, W. Bensch: Combined in-situ EDXRD/EXAFS Investigation of the Crystal Growth of  $[\text{Co}(\text{C}_6\text{H}_{18}\text{N}_4)][\text{Sb}_2\text{S}_4]$  under Solvothermal Conditions: Two Different Reaction Pathways Leading to the Same Product; *Chem. Mater.* **2006**, *18*, 1196-1205.

Copyright 2006 American Chemical Society.

1196

*Chem. Mater.* **2006**, *18*, 1196–1205

## Combined In Situ EDXRD/EXAFS Investigation of the Crystal Growth of $[\text{Co}(\text{C}_6\text{H}_{18}\text{N}_4)][\text{Sb}_2\text{S}_4]$ under Solvothermal Conditions: Two Different Reaction Pathways Leading to the Same Product

Ragnar Kiebach, Nicole Pienack, Marie-Eve Ordolff, Felix Studt, and Wolfgang Bensch\*

*Institute of Inorganic Chemistry, University of Kiel, Olshausenstrasse 40-60, 24098 Kiel, Germany*

*Received August 10, 2005. Revised Manuscript Received November 23, 2005*

The crystal growth and kinetics of the formation of  $[\text{Co}(\text{C}_6\text{H}_{18}\text{N}_4)][\text{Sb}_2\text{S}_4]$  were investigated under solvothermal conditions with combined in situ EDXRD (energy dispersive X-ray diffraction) and in situ EXAFS (extended X-ray absorption fine structure) at different temperatures. In the overwhelming number of reactions all product reflections occur simultaneously in the EDXRD spectra. A detailed analysis of the extent of reaction  $\alpha$  vs time clearly shows that the mechanism changes during the reaction. Such a change occurs at different temperatures after different reaction times. At the early stages the reactions are controlled by diffusion, and later the reaction exponents  $m$  suggest a more complex behavior. At the end of the formation of  $[\text{Co}(\text{C}_6\text{H}_{18}\text{N}_4)][\text{Sb}_2\text{S}_4]$  a second phase is formed which does not contain Co. The results of the in situ experiments suggest that  $[\text{Co}(\text{C}_6\text{H}_{18}\text{N}_4)][\text{Sb}_2\text{S}_4]$  is not only a metastable phase but rather that the second product crystallizes because the  $\text{Co}^{2+}$  concentration in solution is too low for further formation of  $[\text{Co}(\text{C}_6\text{H}_{18}\text{N}_4)][\text{Sb}_2\text{S}_4]$ . In the minor cases of the solvothermal reaction a very different growth was observed. At the beginning only one intense reflection occurs in the spectra and after a distinct time all other reflections start to grow simultaneously. This strange behavior indicates that disordered layers are formed at the beginning which start to arrange at later stages, yielding the three-dimensional long-range order. The in situ EXAFS experiments performed at the Sb K-edge demonstrate that, independent of the reaction time, the Sb/S ratio, and the amine applied, only the two species  $\text{SbS}_3$  and  $\text{SbS}_4$  are present in solution.

### Introduction

Cobalt-containing frameworks are of great interest in catalysis and a lot of research has been done in this field. Important catalysts are cobalt-containing acidic zeolites for hydrodesulfurization.<sup>1</sup> Thioantimonates(III) with zeotype structures are also possible candidates for catalytic applications. In recent years a large number of microporous thioantimonates(III)<sup>2–5</sup> have been synthesized. A good example to demonstrate the structural relationship between thioantimonates(III) and zeolites is the three-dimensional cobalt-containing compound  $[\text{Co}(\text{en})_3][\text{Sb}_{12}\text{S}_{19}]$ <sup>6</sup> with channels being comparable with those in ZSM-5. The combination of the useful properties of zeolites with manifold properties of thioantimonates(III) like tunable optical band gaps,<sup>7</sup> superconductivity,<sup>8</sup> or photoconductivity<sup>9</sup> should lead to a new

class of compounds with designed physical properties. Recently, we published the synthesis and structure of the layered compound  $[\text{Co}(\text{tren})][\text{Sb}_2\text{S}_4]$ <sup>10</sup> (tren = tris(2-aminoethyl)amine) in which  $\text{Co}^{2+}$  is part of the thioantimonate(III) network (Figure 1). Such a combination makes the material of interest for further applications and investigations are in progress. Microporous materials are synthesized under solvothermal conditions with organic molecules acting as structure directors. The final crystalline products often show a low density and can be regarded as kinetic controlled products.

Despite the importance of the solvothermal method for the synthesis of new materials such as catalysts, ion exchangers, and porous materials, the reaction mechanisms leading to the crystalline products are not well-understood. Compared to the enormous number of experiments performed under solvothermal conditions, experiments for understanding the mechanisms, the kinetics of solvothermal syntheses, and exploration of the influence of reaction parameters such as temperature, pH value, and volume are quite rare. In the past decade the number of publications<sup>11–16</sup> presenting results of in situ energy-dispersive X-ray diffraction (EDXRD) studies

\* To whom correspondence should be addressed. Tel: +49 431 880-2406. Fax: +49 431 880-1520. E-mail: wbensch@ac.uni-kiel.de.

- (1) Korányi, T. I.; Pham, N. G.; Jentys, A.; Vinek, H. *Stud. Surf. Sci. Catal.* **1997**, *106*, 509.
- (2) Stähler, R.; Näther, C.; Bensch, W. *J. Solid State Chem.* **2003**, *174*, 264.
- (3) Wang, X.; Liebau, F. *J. Solid State Chem.* **1994**, *111*, 385.
- (4) Spetzler, V.; Kiebach, R.; Näther, C.; Bensch, W. *Z. Anorg. Allg. Chem.* **2004**, *630*, 2398.
- (5) Kiebach, R.; Näther, C.; Bensch, W. *Z. Naturforsch.* **2004**, *59b*, 1314.
- (6) Vaquero, P.; Chippindale, A. M.; Powell, A. V. *Inorg. Chem.* **2004**, *43*, 7963.
- (7) Schaefer, M.; Stähler, R.; Kiebach, W.-R.; Näther, C.; Bensch, W. *Z. Anorg. Allg. Chem.* **2004**, *630*, 1816.
- (8) Lee, C.-S.; Safa-Sefat, A.; Greedan, J. E.; Kleinke, H. *Chem. Mater.* **2003**, *15*, 780.

- (9) Starrost, F.; Krasovskii, E. E.; Schattke, W.; Simon, U.; Wang, X.; Liebau, F. *Phys. Rev. Lett.* **1998**, *80*, 3316.
- (10) Stähler, R.; Bensch, W. *Eur. J. Inorg. Chem.* **2001**, 3073.
- (11) Kiebach, R.; Schaefer, M.; Porsch, F.; Bensch, W. *Z. Anorg. Allg. Chem.* **2005**, *631*, 369.
- (12) Engelke, L.; Schaefer, M.; Porsch, F.; Bensch, W. *Eur. J. Inorg. Chem.* **2003**, 506.

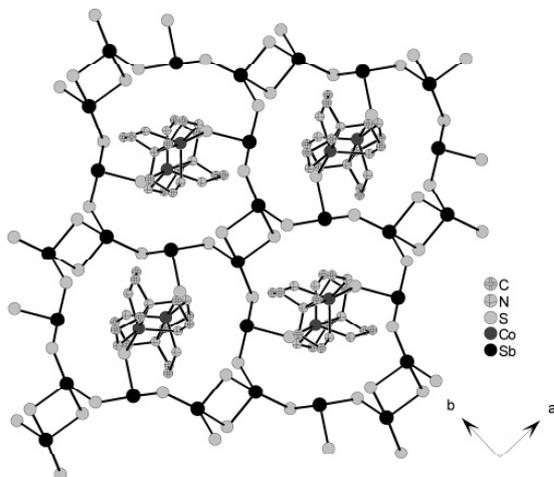


Figure 1. Crystal structure of  $[\text{Co}(\text{tren})][\text{Sb}_2\text{S}_4]$  viewed along the  $c$ -axis.

of solvothermal reaction has grown constantly, but the number of reports is still low. EDXRD is a powerful method to investigate the influence of different parameters onto the formation of crystalline products. Crystalline precursors and/or intermediates are detected without quenching the reaction and without workup of the product. But with EDXRD only crystalline phases can be detected, and amorphous phases and very small precursors in the liquid phase cannot be observed so this part of the reaction is still a kind of “black box”. Information from amorphous phases or molecules in solution can be acquired with extended X-ray absorption fine structure (EXAFS) experiments because data about the local structure and the local atomic coordination are collected.<sup>17–19</sup> The combination of these two complementary methods yields a much better understanding of the mechanisms occurring during chemical reactions.<sup>20–24</sup> Here we report the EDXRD/EXAFS studies of the system  $\text{Co}/\text{Sb}/\text{S}/\text{tren}$ , and the kinetic results of the crystal growth of  $[\text{Co}(\text{tren})][\text{Sb}_2\text{S}_4]$  are presented.

### Experimental Section

The compound  $[\text{Co}(\text{C}_6\text{H}_{18}\text{N}_4)][\text{Sb}_2\text{S}_4]$  is obtained by reacting elemental Co (29 mg, 0.5 mmol, Fluka, purum p.a.), Sb (61 mg,

0.5 mmol, Fluka, purum p.a.), and S (48 mg, 1.5 mmol, Fluka, purum p.a.) in 2 mL of an aqueous tren (purum, Fluka) solution (50%) as solvent. The temperature range for the experiments varied between 105 and 130 °C. Note that above 130 °C only  $[\text{Co}(\text{tren})\text{-Sb}_4\text{S}_7]$  is formed, below 105 °C no product growth could be observed within 5 h, and under static conditions the reaction required several days for completion. The reaction was studied at 105, 110, 115, 120, 125, and 130 °C under isothermal conditions. Additional experiments with  $\text{CoCl}_2 \cdot 6\text{H}_2\text{O}$  (119 mg, 0.5 mmol, Fluka) were carried out at 120 °C.

**Synchrotron Radiation Source for EDXRD Measurements.** HASYLAB Beamline F3 receives white synchrotron radiation from a bending magnet with a critical energy of 16 keV and gives a positron beam energy of 4.5 GeV. An energy range from 13.5 to 65 keV can be observed with a maximum at about 20 keV. The diffracted beam is monitored by a nitrogen-cooled solid-state germanium detector. The detector angle of approximately 1.90° allowed the detection of Bragg reflections with  $d$  spacing from 2.9 to 13.8 Å. The energy resolution  $\Delta d/d$  was about  $10^{-2}$  above 26 keV. The beam was collimated to 0.2 mm, giving the best results. More experimental details are found in refs 12 and 13. The in situ investigations were conducted with autoclaves containing glass liners with an internal diameter of 10 mm and a volume of 10 mL.

**Synchrotron Radiation Source for EXAFS Measurements.** The experiments were performed in transmission at the Sb K edge (30491 eV) at beamline X1 (HASYLAB). A Si(311) double crystal was used as monochromator and the measurement time was about 260 s for each scan. The storage ring operated with injection currents of 140 mA at 4.4 GeV. The stirring of the reaction mixture was interrupted every second spectrum for data acquisition of Sb in solution without influence of the solid phase.

Details of data reduction procedures for energy dispersive X-ray absorption spectra can be found in the literature.<sup>25,26</sup> The data analysis was done with WinXAS 3.0 following recommended procedures.<sup>27</sup> Pre-edge background subtraction and normalization were carried out fitting linear polynomials to the pre-edge and the post-edge region of the spectra, respectively. A smooth atomic background was obtained with a cubic spline refinement procedure. Fitting range in  $k$  space, number of splines, and  $k$  weighting were optimized to afford a rigid background curve at low  $k$  and minimization of low  $R$  peaks in the Fourier transformed signal. The radial distribution function  $FT(\chi(k))$  was obtained by Fourier-transforming the  $k^3$  weighted experimental extended fine structure (EXAFS)  $\chi(k)$ , multiplied by a Bessel window, into  $R$  space.

Calculation of theoretical EXAFS spectra and refinement of experimental data were carried out using theoretical backscattering phases and amplitudes obtained from the ab initio multiple-scattering code FEFF 7.<sup>28</sup> Parameters obtained with a least-squares fit of the standard EXAFS formula are  $S_0^2$ , the passive electron reduction factor,  $R_j$ , the interatomic distance, the Debye–Waller factor  $\sigma_j^2$ , and the coordination number CN.

EXAFS refinements were carried out in  $R$  space to the magnitude and imaginary parts of a Fourier-transformed  $k^3$  weighted experimental  $\chi(k)$ . Further details on the EXAFS refinement procedure employed can be found in ref 29.

- (13) Engelke, L.; Schaefer, M.; Schur, M.; Bensch, W. *Chem. Mater.* **2001**, *13*, 1383.  
 (14) Francis, R. J.; Price, J. S.; Evans, J. S. O.; O'Brien, S.; O'Hare, D. *Chem. Mater.* **1996**, *8*, 2102.  
 (15) Bray, H. J.; Redfern, S. A. T. *Phys. Chem. Miner.* **1999**, *591*.  
 (16) Christensen, A. N.; Bareges, A.; Nielsen, R. N.; Hazell, R. G.; Norby, P.; Hanson, J. C. *J. Chem. Soc., Dalton Trans.* **2001**, 1611.  
 (17) Penner-Hahn, J. E. *Coord. Chem. Rev.* **1999**, *190–192*, 1101.  
 (18) Burattini, E.; Dalba, G.; Fornasini, P. *Il Nuovo Cimento* **1986**, *7*, 293.  
 (19) Cervinka, L.; Smotlacha, O.; Bererová, J.; Tichý, L. *Non-Cryst. Solids* **1991**, *137–138*, 123.  
 (20) Sankar, G.; Rey, F.; Thomas, J. M.; Greaves, G. N.; Corma, A.; Dobson, B. R. *J. Chem. Soc., Chem. Commun.* **1994**, 2279.  
 (21) Thomas, J. M. *Angew. Chem.* **1999**, *111*, 3800.  
 (22) Rey, F.; Sankar, G.; Thomas, J. M.; Barrett, P. A.; Lewis, D. W.; Catlow, C. R. A.; Clark, S. M.; Greave, G. N. *Chem. Mater.* **1995**, *7*, 1435.  
 (23) Sankar, G.; Wright, P. A.; Natarajan, S.; Thomas, J. M.; Greaves, G. N.; Dent, A. J.; Dobson, B. R.; Ramsdale, C. A.; Jones, R. H. *J. Phys. Chem.* **1993**, *97*, 9550.  
 (24) Cora, F.; Sankar, G.; Catlow, C. R. A.; Thomas, J. M. *Chem. Commun.* **2002**, 734.

- (25) Ressler, T. *J. Phys. IV* **1997**, *7*, C2–C269.  
 (26) Ressler, T.; Hagelstein, M.; Hatje, U.; Metz, W. *J. Phys. Chem. B* **1997**, *101*, 6680.  
 (27) Koningsberger, D. C.; Prins, R. *X-Ray Absorption Spectroscopy, Chemical Analysis*, Wiley: New York, 1988.  
 (28) Rehr, J. J.; Booth, C. H.; Bridges, F.; Zabinsky, S. I. *Phys. Rev. Lett.* **1992**, *69*, 3397.  
 (29) Ressler, T.; Timpe, O.; Neisius, T.; Find, J.; Mestl, G.; Dieterle, M.; Schlögl, R. *J. Catal.* **2000**, *191*, 75.

The FT spectra showed only one shell and the fitting must be done with care. The parameters  $S_0^2$ , CN,  $R_j$ , and  $\sigma^2$  are correlated and some assumptions must be made to get reliable results. The factor  $S_0^2$  depends on the free path lengths which in turn scales with the temperature. The spectra were recorded at 130 °C and a fixed value of 1.05 is reasonable. For Sb-containing solutions different values for  $\sigma^2$  were reported which were used as the upper and lower limit during the refinements; i.e.,  $\sigma^2$  was freely refined within this range. The resulting magnitudes for  $\sigma^2$  (Table 3) are in excellent agreement with those reported in previous papers.<sup>30,31</sup> The interatomic distance  $R_j$  depends on  $E_0$  (zero point of the energy scale) which was fixed to 10 eV in accordance with literature data. Refinement of  $E_0$  with starting values far from 10 always yielded a value very near to 10. The spectra were then refined either with the  $\text{SbS}_3$  or the  $\text{SbS}_4$  unit with a freely varying CN. In both cases the value for CN was 3.6, giving lower reliability factors than using the same units with fixed coordination numbers. In the next step the spectra were refined with fixed coordination numbers but with a variable ratio of both species. The lowest reliability factor was obtained for a 1:1 mixture of  $\text{SbS}_3$  and  $\text{SbS}_4$ .

Reference measurements were done with a pressed pellet obtained by mixing about 100 mg  $[\text{Co}(\text{tren})][\text{Sb}_2\text{S}_4]$  with boron nitride (ratio 1:3). The in situ experiments were performed in the above-mentioned cell under autogenous pressure either under dynamic (with stirring) or static (without stirring) conditions. At the end of the reaction the solid product was used as the reference phase.

For Sb references in the liquid phase 3.04 g (25 mmol) of Sb and 2.4 g (75 mmol) of S were dissolved in 100 mL of a 50% aqueous diethylenediamine solution and heated under reflux for 2 h. The resulting parent solution (A1) was diluted with 50 vol % water (A2). This solution was again diluted with 50 vol % water, yielding A3, and this procedure was continued until solution A15 was obtained, which contained 0.003% of solution A1.

**Density Functional Theory Calculations.** Spin-restricted DFT calculations using Becke's three-parameter hybrid functional with the correlation functional of Lee, Yang, and Parr (B3LYP)<sup>32–34</sup> were performed for the singlet ground state of  $\text{SbS}_3^{3-}$  and  $\text{SbS}_4^{5-}$ . The LANL2DZ basis set was used for the calculations. It applies Dunning/Huzinaga full double- $\zeta$  (D95) basis functions<sup>35</sup> on the first row and Los Alamos effective core potentials plus DZ functions on all other atoms.<sup>36,37</sup> All computational procedures were used as they are implemented in the Gaussian 98 package.<sup>38</sup>

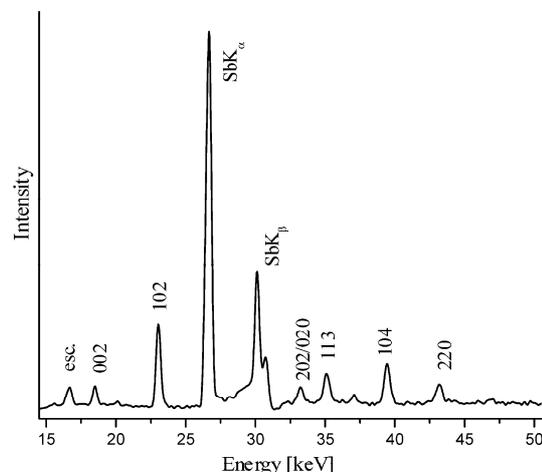


Figure 2. Energy dispersive diffraction pattern of  $[\text{Co}(\text{tren})][\text{Sb}_2\text{S}_4]$ . The indices of the reflections and the Sb fluorescence are marked.

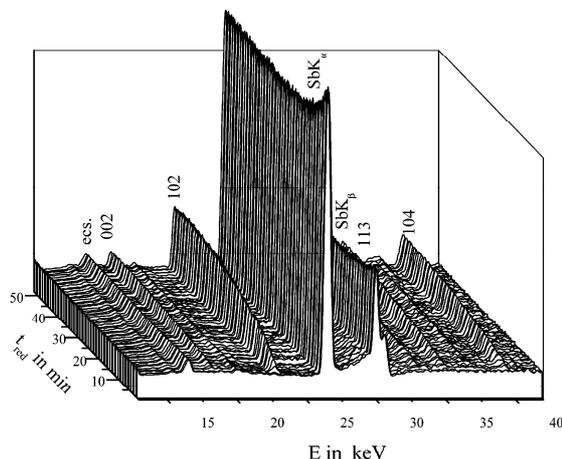


Figure 3. Time-resolved powder pattern recorded at 120 °C. The indices of the most intense lines of the product phase and the Sb K $\alpha$  fluorescence line are marked.

## Results and Discussion

**EDXRD.** In the spectra several reflections of the product and the Sb resonance are monitored simultaneously (Figure 2). A typical sequence of time-resolved spectra is shown in Figure 3. After an induction time,  $t_{\text{ind}}$ , which strongly depends on the reaction temperature, product peaks starts to grow. Note that the Sb resonance at 26.6 and 31.1 keV as well as an escape peak at 16.5 keV are immediately visible in the spectra. The (102) reflection with the highest intensity corresponds to the layers of the compound. A quantitative analysis of the growth rates shows an identical behavior for different reflections and confirms an isotropic crystallite growth (see also below). In the spectra no hints are seen for the occurrence of crystalline precursors or intermediates. Compared to  $t_{\text{ind}}$  the half-life time  $t_{0.5}$  of crystallization is short and is about 15% of the time necessary to complete the reaction (Table 1). The first step of the kinetic analysis is the integration of one or several product reflections using a Gaussian function and measuring the corresponding areas.

- (30) Frederick, J.; Mosselmans, W.; Helz, G. R.; Patrick, R. A. D.; Charnock, J. M.; Vaughan, D. J. *Appl. Geochem.* **2000**, *15*, 879.  
 (31) Oelkers, E. H.; Sherman, D. M.; Ragnarsdottir, K. M.; Collins, C. *Chem. Geol.* **1998**, *151*, 21.  
 (32) Becke, A. D. *Phys. Rev. A* **1988**, *38*, 3098.  
 (33) Becke, A. D. *J. Chem. Phys.* **1993**, *98*, 1372.  
 (34) Becke, A. D. *J. Chem. Phys.* **1993**, *98*, 5648.  
 (35) Dunning, T. H., Jr.; Hay, P. J. In *Modern Theoretical Chemistry*; Schaefer, H. F., III, Ed.; Plenum: New York, 1976.  
 (36) Hay, P. J.; Wadt, W. R. *J. Chem. Phys.* **1985**, *82*, 270.  
 (37) Wadt, W. R.; Hay, P. J. *J. Chem. Phys.* **1985**, *82*, 284.  
 (38) Frisch, M. J.; Trucks, G. W.; Schlegel, H. B.; Scuseria, G. E.; Robb, M. A.; Cheeseman, J. R.; Zakrzewski, V. G.; Montgomery, J. A., Jr.; Stratmann, R. E.; Burant, J. C.; Dapprich, S.; Millam, J. M.; Daniels, A. D.; Kudin, K. N.; Strain, M. C.; Farkas, O.; Tomasi, J.; Barone, V.; Cossi, M.; Cammi, R.; Mennucci, B.; Pomelli, C.; Adamo, C.; Clifford, S.; Ochterski, J.; Petersson, G. A.; Ayala, P. Y.; Cui, Q.; Morokuma, K.; Salvador, P.; Dannenberg, J. J.; Malick, D. K.; Rabuck, A. D.; Raghavachari, K.; Foresman, J. B.; Cioslowski, J.; Ortiz, J. V.; Baboul, A. G.; Stefanov, B. B.; Liu, G.; Liashenko, A.; Piskorz, P.; Komaromi, I.; Gomperts, R.; Martin, R. L.; Fox, D. J.; Keith, T.; Al-Laham, M. A.; Peng, C. Y.; Nanayakkara, A.; Challacombe, M.; Gill, P. M. W.; Johnson, B.; Chen, W.; Wong, M. W.; Andres, J. L.; Gonzalez, C.; Head-Gordon, M.; Replogle, E. S.; Pople, J. A. *Gaussian98*, Rev. A.11; Gaussian, Inc.: Pittsburgh, PA, 2001.

Crystal Growth of  $[Co(C_6H_{18}N_4)][Sb_2S_4]$

Chem. Mater., Vol. 18, No. 5, 2006 1199

Table 1. Kinetic Data Obtained by the Analysis with Sharp-Hancock Plots

$T$ in °C	induction time <sup>a</sup> in min	reaction time <sup>b</sup> in min	half-life time <sup>c</sup> in min	$m$	$k[s^{-1}] \times 10^{-4}$
105 $\alpha < 0.71$	204	200	18	0.57	5.20
$\alpha > 0.71$				0.85	4.29
110 $\alpha < 0.77$	113	133	17	0.66	5.45
$\alpha > 0.77$				1.29	4.43
115 $\alpha < 0.75$	101	62	15	0.59	6.39
$\alpha > 0.75$				1.23	4.64
120 $\alpha < 0.68$	83	47	9	0.70	8.74
$\alpha > 0.68$				1.65	8.28
125 $\alpha < 0.53$	66	45	9	0.67	10.13
$\alpha > 0.53$				0.98	11.18
130 $\alpha < 0.67$	56	38	7	0.55	10.74
$\alpha > 0.67$				1.41	10.81

<sup>a</sup> Induction time: time between reaction start and occurrence of first product peaks. <sup>b</sup> Reaction time: time between first occurrence of product peaks and end of reaction ( $\alpha = 1$ ). <sup>c</sup> Half-life time: time between first occurrence of product peaks and  $\alpha = 0.5$ .

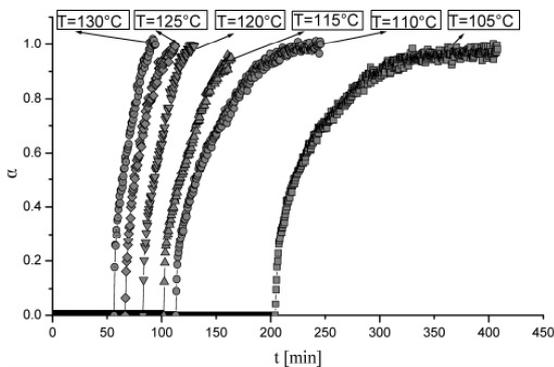


Figure 4. Extent of reaction  $\alpha$  versus time for the (102) reflection at different reaction times.

These are then converted to the extent of reaction  $\alpha$  using the relation  $\alpha(t) = I_n(t)/I_n(t_\infty)$ , with  $I_n(t)$  being the intensity of the reflection at time  $t$  and  $I_n(t_\infty)$  is the intensity of this reflection at the end of the reaction ( $t = \infty$ ). In the present analysis the previously integrated intensities at time  $t$  were divided by the intensity of the Sb K $\alpha$  resonance peak at the same time  $t$  to get the normalized intensity relative to the beam intensity; i.e., the data are very accurate due to the correction for fluctuation of primary beam intensity.

The plot of  $\alpha$  vs reaction time  $t$  (Figure 4, Table 1) shows a strong temperature dependence of  $t_{ind}$ . At 130 °C the value for  $t_{ind}$  is 56 min and increases by a factor of 4 at 105 °C ( $t_{ind} = 204$  min). It is remarkable that the data are reproducible on a very high level despite the long induction period at 105 °C, and according to experimental results the variation of  $t_{ind}$  is less than 5 min (<2.5%) at 105 °C.

**Kinetic Analysis.** Kinetic analyses are performed by fitting the experimental data to a theoretical expression relating the extent of reaction  $\alpha$  vs time. Several kinetic expressions applied to solid-state kinetics are reported, and the general shape of their curves is well-documented. A detailed description of the procedure for the evaluation of the data was presented for instance in ref 12.

The kinetic evaluation was performed after subtraction of  $t_{ind}$  from time  $t$  and the reduced reaction time ( $t_{red}$ ) is obtained. The kinetic data for different reaction temperatures are

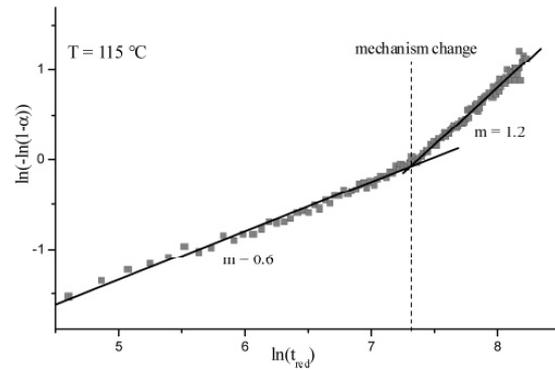


Figure 5. Sharp-Hancock plot for the data at  $T = 115$  °C.

Table 2. Rate Equations for Solid-State Reactions Reported in the Literature

growth model	rate equation $f(\alpha) = kt$	$m$
Diffusion-Controlled		
$D_1(\alpha)$	$\alpha^2 = 0.25 (t/t_{0.5})$	0.62
$D_2(\alpha)$	$(1 - \alpha) \ln(1 - \alpha) + \alpha = 0.1534 (t/t_{0.5})$	0.57
$D_3(\alpha)$ [Jander]	$[1 - (1 - \alpha)^{1/3}]^2 = 0.0425 (t/t_{0.5})$	0.54
$D_4(\alpha)$	$1 - 2\alpha/3 - (1 - \alpha)^{2/3} = 0.0367 (t/t_{0.5})$	0.57
[Ginstling-Brounshtein]		
Phase-Boundary-Controlled		
$R_2(\alpha)$	$1 - (1 - \alpha)^{1/2} = 0.2929 (t/t_{0.5})$	1.11
$R_3(\alpha)$	$1 - (1 - \alpha)^{1/3} = 0.2063 (t/t_{0.5})$	1.07
First Order		
$F1(\alpha)$	$[-\ln(1 - \alpha)] = 0.6931 (t/t_{0.5})$	1.00
Nucleation [Avrami-Eroevéef]		
$A2(\alpha)$	$[-\ln(1 - \alpha)]^{1/2} = 0.8326 (t/t_{0.5})$	2.00
$A3(\alpha)$	$[-\ln(1 - \alpha)]^{1/3} = 0.885 (t/t_{0.5})$	3.00

summarized in Table 1. When  $\ln[-\ln(1 - \alpha)]$  is plotted vs  $\ln(t)$  (the so-called Sharp-Hancock plot, abbreviated SH) a straight line is obtained for that part of the reaction which follows the same mechanism.<sup>39-41</sup> A change of the mechanism results in a change of the slope of the curve. From the slope of the linear part of the curve the reaction exponent  $m$  can be evaluated (often called the Avrami exponent) and the intercept with the y axis gives the rate constant  $k$  [ $s^{-1}$ ]. The exponent  $m$  is then related to the type of nucleation and growth process taking place, including the morphology of the reaction product, i.e., whether the crystals are fibers, needles, plates, sheets, spheres, or polygons. The exponent  $m$  also includes the type of nucleation, i.e., whether the nuclei all develop at once or continuous nucleation with a constant rate occurs.<sup>42,43</sup>

The SH plot for data obtained at  $T = 115$  °C (Figure 5) clearly shows that the growth can be divided into two different parts. Up to  $\alpha \approx 0.77$  the reaction exponent  $m$  has a value of 0.59 corresponding to a diffusion controlled growth mechanism (Table 2), and in the second part ( $\alpha > 0.77$ )  $m$  increases to about 1.23. For reactions at  $T \leq 110$  °C the experimental points are on a straight line nearly over

(39) Hancock, J. D.; Sharp, J. H. *J. Am. Ceram. Soc.* **1972**, *55*, 74.

(40) Sharp, J. H.; Brindley, G. W.; Narahari Achar, B. N. *J. Am. Ceram. Soc.* **1966**, *379*.

(41) Mohamed, B. M.; Sharp, J. H. *J. Mater. Sci.* **1997**, *1595*.

(42) Brown, P. W.; Pommersheim, J.; Frohnsdorff, G. *Cem. Concr. Res.* **1985**, *15*, 35.

(43) Thomas, J. J.; Jennings, H. M. *Chem. Mater.* **1999**, *11*, 1907.

1200 *Chem. Mater.*, Vol. 18, No. 5, 2006

Kiebach et al.

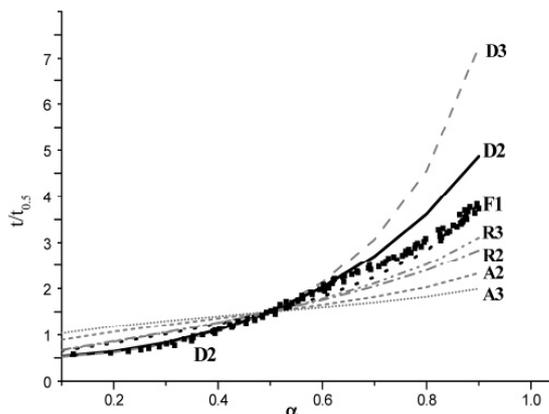


**Figure 6.** Comparison of experimental  $t/t_{0.5}$  data as a function of  $\alpha$  (black squares) with different theoretical models for  $T = 115$  °C. The letters with the numbers are abbreviations of the different models listed in Table 2.

the whole reaction, and only just before the end a slight deviation seems to occur. The nucleation and growth are mainly controlled by diffusion and a first-order process may influence the growth at the latest stages of the reaction. It must be kept in mind that the discussion of possible mechanisms based on the exponent  $m$  is not always straightforward. The values for  $m$  often deviate severely from the theoretical values listed in Table 2 and there are several reasons for these experimental findings. The simplest assumption is that reactions with different mechanisms proceed in parallel and/or in succession, yielding values different from theoretical ones.<sup>44–46</sup> We note that the values for  $m$  discussed above deviate from theoretical values, but they are in the range for diffusion-controlled mechanisms during the first stage of the reactions with stronger deviations from theoretical values for the later stage. The rate constant  $k$  and the half-life time exhibit a clear temperature dependence. While the half-life time decreases with increasing temperatures, the value for the rate constant increases (Table 2).

More detailed and rigorous analyses were performed comparing all models listed in Table 2 with the experimental data.<sup>47–49</sup> A plot of the experimental  $t/t_{0.5}$  data ( $t/t_{0.5}$  is the reaction time at  $\alpha = 0.5$ ) vs  $\alpha$  (Figure 6) allows a direct comparison with the different models under consideration. For  $T > 110$  °C (Figure 6,  $T = 115$  °C) the experimental data  $\alpha < 0.7$  are in accordance with a diffusion control followed by a change toward the first-order mechanism F1 for  $\alpha > 0.7$ . When the time-dependent behavior of a reaction is scaled to 33%, a better discrimination between the models is possible for higher values of  $\alpha$ . Hence, the plot of  $t/t_{0.33}$  vs  $\alpha$  (Figure 7,  $T = 115$  °C) confirms the change of the mechanism at later stages of the reaction. For  $T \leq 110$  °C the analysis of the data (Figure 8) suggests that diffusion (D2 and/or D3) is the rate-limiting process for the crystal

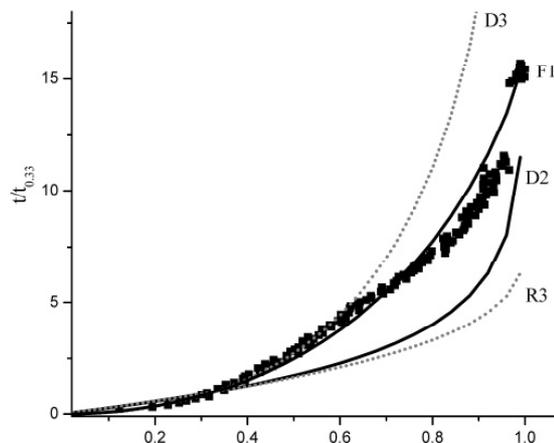


**Figure 7.** Comparison of experimental  $t/t_{0.33}$  data as a function of  $\alpha$  (black squares) with different theoretical models for  $T = 115$  °C. The letters with the numbers are abbreviations of the different models listed in Table 2.

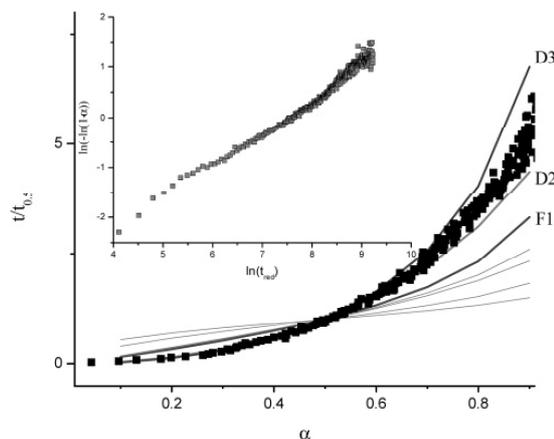


**Figure 8.** Comparison of experimental  $t/t_{0.5}$  data as a function of  $\alpha$  (black squares) with different theoretical models for  $T = 105$  °C. The letters with the numbers are abbreviations of the different models listed in Table 2. Inset: Sharp-Hancock plot for the data at  $T = 105$  °C.

growth, but a definite decision is not possible, in agreement with the results from the SH analysis (Figure 9). The deviations discussed above are also observed in the so-called Austin-Rickett plots<sup>50</sup> (Figure 10).

The activation energy  $E_A$  was determined with the Arrhenius equation using the  $k$  values of the first part of the reactions (Table 2). The plot  $\ln k$  vs  $1/T$  yields a straight line and  $E_A = 42$  kJ/mol is obtained (Figure 11). This result is comparable with values found in the literature.<sup>13,15</sup>

At the end of the formation of  $[\text{Co}(\text{tren})][\text{Sb}_2\text{S}_4]$ , reflections of a second crystalline phase appear in the spectra and several new reflections start to grow simultaneously (Figure 12). This phenomenon is independent from temperature and is observed at the latest stages of every reaction. The second phase was identified as  $[\text{tren}]_x[\text{Sb}_{21}\text{S}_{34}]$ . Unfortunately, the (102) reflection of  $[\text{Co}(\text{tren})][\text{Sb}_2\text{S}_4]$  and the (004/013) peak of the second phase coincide. Hence, the end of crystallization of  $[\text{Co}(\text{tren})][\text{Sb}_2\text{S}_4]$  was evaluated with the (002)

(44) Pradell, T.; Crespo, D.; Clavaguera, N.; Clavaguera-Mora, M. T. *J. Phys. Condens. Matter* **1998**, *10*, 3833.

(45) Fanfoni, M.; Tomellini, M. *Il Nuovo Cimento* **1998**, *20*, 1171.

(46) Castro, M.; Domínguez-Adame, F.; Sánchez, A.; Podríguez, T. *Appl. Phys. Lett.* **1999**, *75*, 2205.

(47) Avrami, M. *J. Chem. Phys.* **1939**, *7*, 1103.

(48) Avrami, M. *J. Chem. Phys.* **1940**, *8*, 212.

(49) Avrami, M. *J. Chem. Phys.* **1941**, *9*, 177.

(50) Austin, J. B.; Rickett, R. L. *Trans. AIME* **1939**, *135*, 396.

Crystal Growth of  $[\text{Co}(\text{C}_6\text{H}_{18}\text{N}_4)][\text{Sb}_2\text{S}_4]$

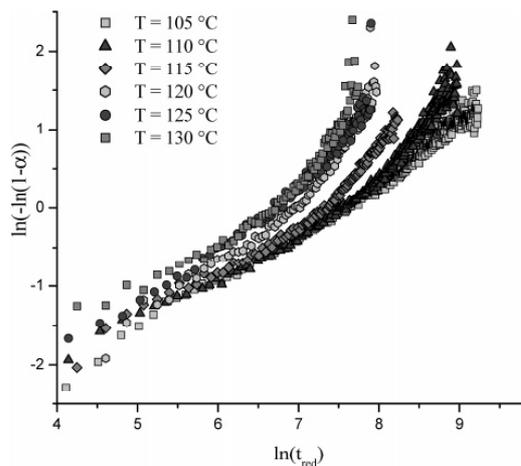


Figure 9. Sharp-Hancock plots for all temperatures.

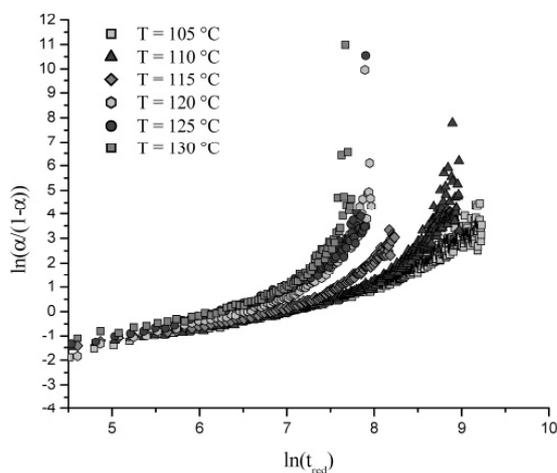


Figure 10. Austin-Rickett plots for all temperatures.

reflection and for the second phase  $[\text{tren}]_x[\text{Sb}_{21}\text{S}_{34}]$  the overlapping (202)/(-212) peak was used (Figure 12). The integrated intensity of the (002) peak of  $[\text{Co}(\text{tren})][\text{Sb}_2\text{S}_4]$  passes a maximum which was then defined as the end of the formation of this phase. Exactly at this time the second phase starts to grow and the amount of the first compound starts to decrease (Figure 13).

An in situ experiment was performed for 14 h after the intensity of reflections of  $[\text{Co}(\text{tren})][\text{Sb}_2\text{S}_4]$  just started to decrease to prove whether  $[\text{Co}(\text{tren})][\text{Sb}_2\text{S}_4]$  is only a kind of intermediate. During the first 6 h the intensity of (002) of  $[\text{Co}(\text{tren})][\text{Sb}_2\text{S}_4]$  drops and an equilibrium between the two phases is reached (Figure 13). This may be explained on the basis of a partial dissolution/amorphization of  $[\text{Co}(\text{tren})][\text{Sb}_2\text{S}_4]$  and the simultaneous crystallization of the new phase. On a microscopic level the following may occur. At the point where the intensities of  $[\text{Co}(\text{tren})][\text{Sb}_2\text{S}_4]$  start to decrease, the concentration of dissolved  $\text{Co}^{2+}$  cations is too low for further crystallization, and the transition metal free compound starts to crystallize. The formation of this new phase influences the equilibrium between solid  $[\text{Co}(\text{tren})][\text{Sb}_2\text{S}_4]$

Chem. Mater., Vol. 18, No. 5, 2006 1201

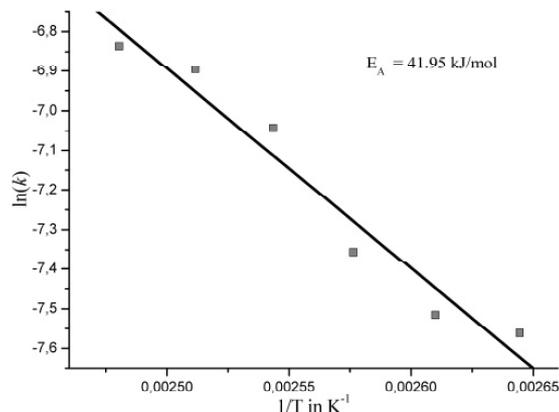


Figure 11. Arrhenius plot of  $\ln k$  vs  $1/T$  [ $\text{K}^{-1}$ ] for the first stage of the reaction, determined from Sharp Hancock plots.

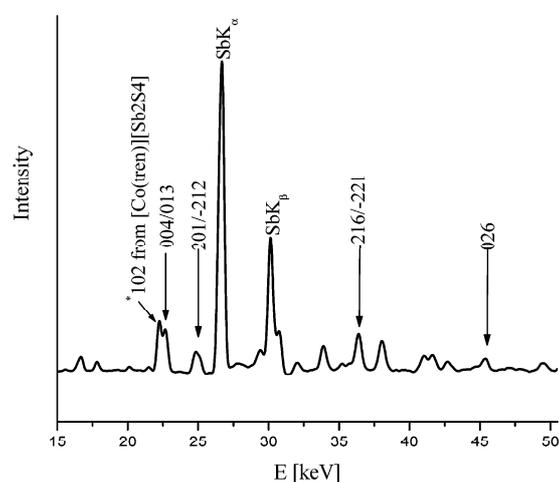


Figure 12. Energy dispersive diffraction patterns of  $[\text{Co}(\text{tren})][\text{Sb}_2\text{S}_4]$  and the second phase. The indices of reflections of the second phase are indicated. Additionally the (102) reflection of  $[\text{Co}(\text{tren})][\text{Sb}_2\text{S}_4]$  is marked.

and the solution because the concentration of  $\text{Sb}^{3+}/\text{S}^{2-}$  is lowered due to crystallization of  $[\text{tren}]_x[\text{Sb}_{21}\text{S}_{34}]$ . The strong reduction of the concentration of  $\text{Sb}^{3+}/\text{S}^{2-}$  is accompanied by the partial dissolution of the Co-containing compound, yielding a new equilibrium for this complex system. To prove that  $[\text{Co}(\text{tren})][\text{Sb}_2\text{S}_4]$  is not only dissolved by tren, the solid compound was filtered off after the reaction was complete and 2 mL of pure tren was added. No change in the spectra was observed within the next 4 h. The ratio between the two phases was constant, demonstrating that the pH value and the concentration of tren do not alter the equilibrium.

In about one-third of the in situ experiments highly interesting observations for reactions performed at  $T \leq 120$  °C were made; i.e., a very different growth behavior of the reaction product was observed (Figure 14). After a temperature-dependent induction time only the (102) reflection starts to grow (Figure 14), and after another 28 min all other peaks of  $[\text{Co}(\text{tren})][\text{Sb}_2\text{S}_4]$  occur and grow simultaneously. The position of the (102) reflection is slightly shifted to smaller energy values at the early stages of reaction (23.27 keV) and reaches 23.05 keV found in the other experiments

1202 *Chem. Mater.*, Vol. 18, No. 5, 2006

Kiebach et al.

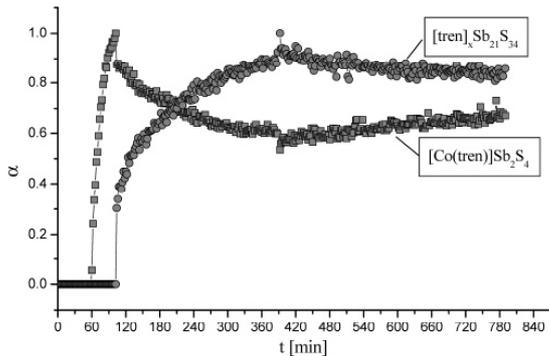


**Figure 13.** Extent of reaction  $\alpha$  versus time for the (002) reflection of  $[\text{Co}(\text{tren})]\text{Sb}_2\text{S}_4$  and the (202/-212) reflections of the second phase  $[\text{tren}]_x\text{Sb}_{21}\text{S}_{34}$ .

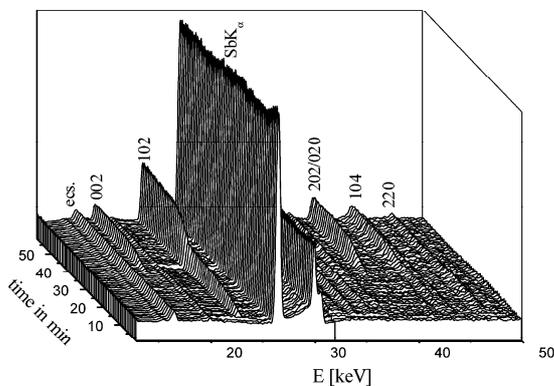


**Figure 14.** Time-resolved powder patterns recorded at 120 °C showing the different growth behavior. The indices of the most intense lines of the product phase and the Sb  $K\alpha$  fluorescence line are marked.

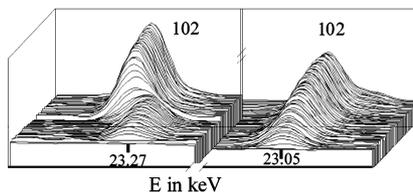


**Figure 15.** Comparison of the (102) reflection for the two different growth behaviors at 120 °C. Left: unusual growth behavior with peak shift; right: with normal growth mechanism.

discussed above (Figure 15). The most possible “parameter” responsible for this unusual observation is the ferromagnetic behavior of elemental Co. The slurry is stirred with a magnetic stirrer bar (see Experimental Section). When Co sticks at the surface of this bar, the dissolution of Co at  $T \leq 120$  °C seems to have a random component. This effect is negligible for  $T > 120$  °C due to faster dissolution of Co, yielding a concentration of  $\text{Co}^{2+}$  ions which is large enough for the nucleation and crystallization following the mechanisms presented above. We proved the hypothesis of this phenomenon and performed in situ experiments with  $\text{CoCl}_2 \cdot 6\text{H}_2\text{O}$  as Co source. In all these experiments product growth proceeds following the reaction paths discussed in the previous section. This experimental finding supports our assumption that the velocity of dissolu-

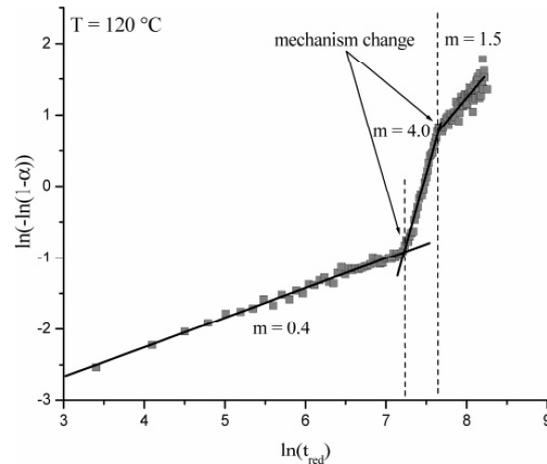


**Figure 16.** Sharp-Hancock plot for the data at  $T = 120$  °C for the product formed by the second reaction path.

tion of elemental cobalt has a significant influence on the reaction mechanism.

The SH analysis of the data gives evidence that the crystallization kinetics occurs in three different steps, each being characterized by a different reaction exponent  $m$  (Figure 16). The values for  $m$  are about 0.4 ( $\alpha < 0.33$ ) and 1.5 ( $\alpha > 0.88$ ) for the first and third stage and deviate from the ideal values listed in Table 2. In the second part of the reaction where all peaks grow simultaneously the value for  $m$  of 4.0 is unusually large, but may be explained on the basis of constant nucleation.<sup>51</sup> An identical behavior was observed by O’Hare and co-workers<sup>14</sup> during the formation of the thioantimonate TMA-SnS1 and was explained by strongly disordered layers which at later stages of reaction start to arrange, yielding the three-dimensional long-range order.

**EXAFS Measurements.** In the past decades many experiments were devoted to identify the soluble species of antimony sulfides in alkaline solutions. Different species were postulated, e.g.,  $\text{SbS}_2^-$ ,  $\text{Sb}_2\text{S}_4^{2-}$ ,  $\text{Sb}_4\text{S}_7^{2-}$ ,<sup>52</sup>  $\text{SbS}_3^{3-}$ , and  $\text{SbS}_4^{3-}$ ,<sup>30,52,53</sup> and  $\text{Sb}_2\text{S}_6^{2-}$ .<sup>53</sup> But until now it is not clear how Sb atoms are coordinated in basic sulfur-containing solutions. For a better understanding of the building mechanisms of thioantimonates it is important to identify primary building units existing in reaction solutions using EXAFS experiments.

**Reference Measurements.** Solutions with different concentrations of Sb/S in diethylenetriamine were used as references (see Experimental Section). The edge jump scales linearly with the Sb concentration; i.e., lower Sb contents yield smaller jumps. The temperature effect onto the edge jump can be neglected. Interestingly, the spectra exhibit only different intensities of the peaks but no differences were observed for the shape of the XANES or EXAFS. This result shows that the coordination sphere of Sb is the same for all concentrations.

(51) Davies, A. T.; Sankar, G.; Catlow, C. R.; Clark, S. M. *J. Phys. Chem. B* **1997**, *101*, 10115.

(52) Wood, S. A. *Geochim. Cosmochim. Acta* **1989**, *53*, 237.

(53) Helz, G. R.; Valerio, M. S.; Capps, N. E. *Environ. Sci. Technol.* **2002**, *36*, 943.

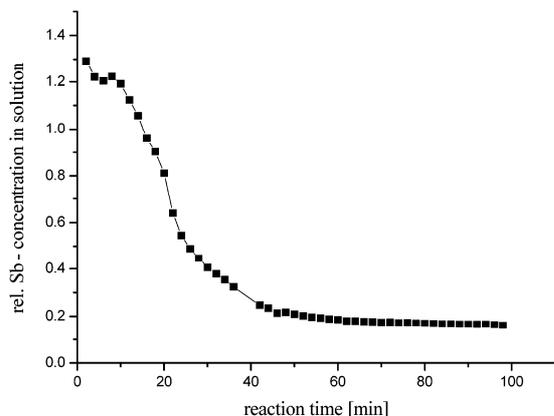


Figure 17. Evolution of the Sb K edge jump during the reaction.

**Measurements during the Formation of  $[\text{Co}(\text{tren})][\text{Sb}_2\text{S}_4]$ .** The evolution of the Sb edge height during the reaction at 120 °C is shown in Figure 17. After a short induction time a maximum of the absorption jump  $\Delta\mu x$  of 1.3 was reached and after 60 min the value decreased to 0.2. The change of the edge jump time proceeds not in a linear way but has a sigmoidal shape reminiscent of the curve for the extent of reaction presented in Figure 4. The two curves cannot be compared directly due to the different experimental conditions. The stirring was interrupted to collect the XAFS data (see Experimental Section); i.e., this interruption increases the reaction time. At the beginning of the reaction elemental Sb is dissolved and the Sb content in solution is very high. Within a few minutes the Sb content decreases dramatically, indicating that a solid product is formed which must be amorphous because it is not seen in EDXRD experiments. Hence, it can be assumed that long before crystallization of  $[\text{Co}(\text{tren})][\text{Sb}_2\text{S}_4]$  an amorphous precursor is formed. The quality of EXAFS spectra of this amorphous solid was not good enough for an evaluation and the composition of the precursor is not known.

**Evaluation of the Spectra.** During the whole reaction only two different types of spectra were observed. At the beginning the spectra are similar to those recorded for reference A1 (see Experimental Section) and at the end the spectra are similar to those obtained with pellets of crystalline  $[\text{Co}(\text{tren})][\text{Sb}_2\text{S}_4]$  (Figure 18). This observation suggests that  $[\text{Co}(\text{tren})][\text{Sb}_2\text{S}_4]$  is either soluble or that small particles are present in the solution which do not sediment during the time after stirring was stopped. In another experiment the solution was not stirred for 2 h and care was taken that only the solution was investigated with EXAFS. Interestingly, the spectra were identical to those recorded at the beginning of the reaction, demonstrating that  $[\text{Co}(\text{tren})][\text{Sb}_2\text{S}_4]$  is not dissolved and the spectra obtained at the end of the reaction were caused by small particles of  $[\text{Co}(\text{tren})][\text{Sb}_2\text{S}_4]$ .

Reactions with other Sb/S/amine slurries were also investigated (0.5 mmol of Sb, 1.5 mmol of S in 2 mL of 50% 2-aminoethylpiperazine at 160 °C; 0.5 mmol of Sb, 0.5 mmol of Mn, 1.2 mmol of S in 2 mL of 100% dien at 120 °C) to monitor the influence of the amine onto the formation of the  $\text{SbS}_x$  species. But for all solutions the spectra were

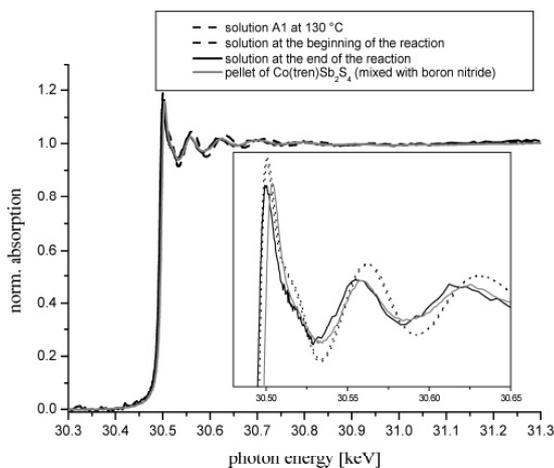


Figure 18. Changes of EXAFS spectra during the reaction.

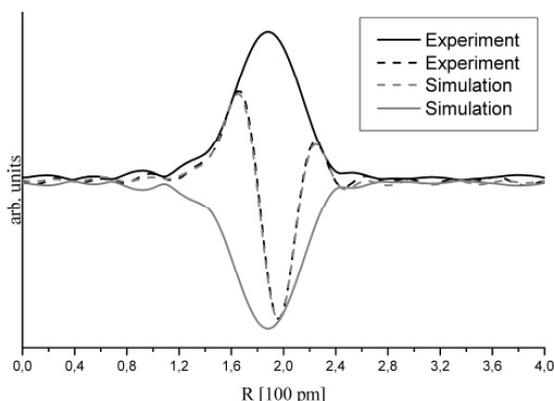


Figure 19. Experimental and simulated Fourier transformed  $\chi(k)$ . Theoretical phases and amplitudes calculated with  $\text{SbS}_3$  and  $\text{SbS}_4$  units.

Table 3. Results from EXAFS Simulations with Standard Deviations Given in Parentheses

	$\text{SbS}_3$	$\text{SbS}_4$	$\text{SbS}_3$	$\text{SbS}_4$
residual	3.51	3.59	1.60	3.58
coordination number	3 (fixed)	4 (fixed)	3.6 (free)	3.5 (free)
$\sigma^2/\text{\AA}^2$	0.00189(3)	0.00386(4)	0.00308(2)	0.00295(3)

similar; i.e., the environment of Sb in sulfur-containing amine solutions is identical. Temperature, volume, pH value, and the kind of amine have no measurable influence on the dissolved  $\text{SbS}_x$  species, which is a quite remarkable and surprising result.

**Simulations of EXAFS Spectra.** The species in solution may be identified comparing simulated EXAFS spectra for different  $\text{SbS}_x$  species with the experimental data. In the literature<sup>43–45</sup> mainly three different structural species were suggested, i.e., a  $\text{Sb}_2\text{S}_6^{6-}$  ring, the  $\text{SbS}_3^{3-}$  group, and a  $\text{SbS}_4^{3-}$  unit. The existence of the  $\text{Sb}_2\text{S}_6^{6-}$  ring can be ruled out because the radial distance distribution (Figure 19) shows only one shell around Sb, but a  $\text{Sb}_2\text{S}_6^{6-}$  ring requires a second shell, accounting for the Sb–Sb coordination. The two other models were simulated with Gaussian98 (see above) and protonated sulfur atoms had no influence on the geometry. The structurally optimized clusters were used for FEFF

1204 Chem. Mater., Vol. 18, No. 5, 2006

Kiebach et al.

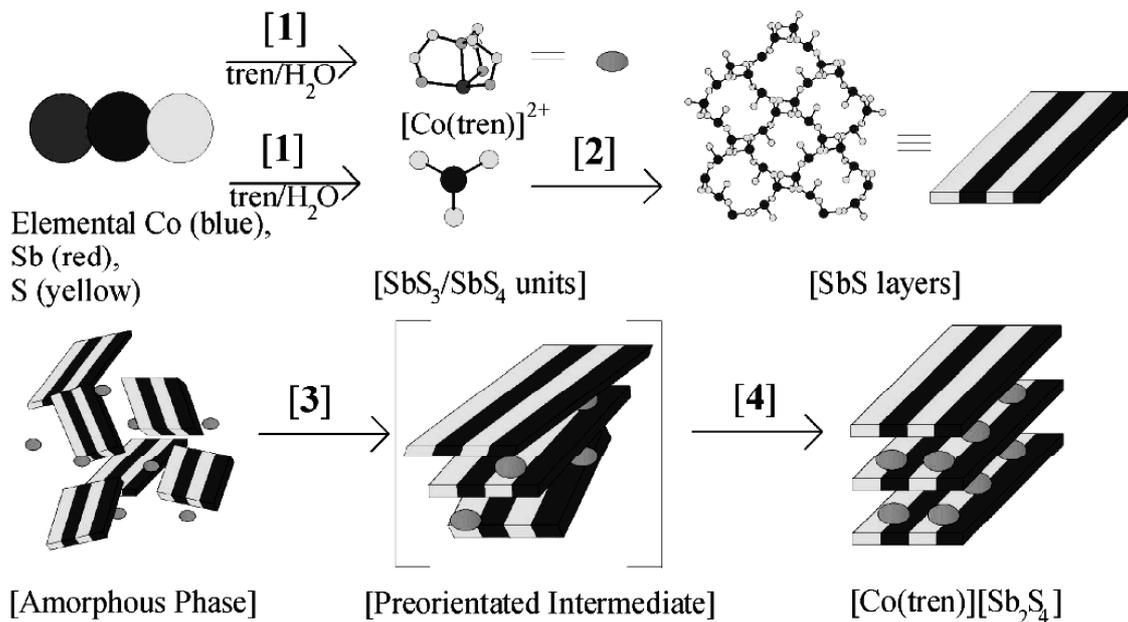


Figure 20. Reaction scheme for the formation of  $[\text{Co}(\text{tren})][\text{Sb}_2\text{S}_4]$ .

calculations (see Experimental Section) and the results are summarized in Table 3.

The refinements performed with freely varying coordination numbers (CN) for either  $\text{SbS}_3$  or  $\text{SbS}_4$  always yield a value for CN near 3.5, suggesting that both species coexist in solution. Therefore, the spectrum was simulated containing a 1:1 mixture of  $\text{SbS}_3$  and  $\text{SbS}_4$  groups and the resulting  $\text{FT}(\chi(k))$  together with the theoretical XAFS function utilizing phases and amplitudes is shown in Figure 19. The calculated EXAFS function fits perfectly with the experimental  $\chi(k)$  for both the phase and the amplitude. This result suggests that only these two groups are present in solution.

### Conclusion

The synthesis of compounds under solvothermal conditions is in most cases a black box method; i.e., after a distinct reaction time the reaction vessels are removed from the furnaces and the products are then characterized. The products often consist of mixtures of different compounds and optimization of the synthesis is time-consuming because several reaction parameters have to be varied. In addition, crystalline precursors or intermediates may crystallize at short reaction times, which will never be "seen" using the conventional synthesis procedure. Such kinetically less stable compounds may have interesting physicochemical properties. In the present contribution we demonstrated that in situ EDXRD experiments are powerful for monitoring the evolution of the formation of a distinct compound so that phase-pure materials can be prepared. But for basic research the reaction mechanisms and kinetics occurring under solvothermal conditions are more interesting. A rigorous analysis of the results recorded as a function of different reaction parameters provides information about the kinetics and give

hints about the reaction mechanisms. For the present system diffusion is the rate-limiting step, and at later stages the reaction exponents indicate more complex kinetics/mechanisms. When the synthesis of the title compound is performed with elemental Co at  $T \leq 120^\circ\text{C}$ , a random dissolution of Co influences the reaction path, which was immediately detected in the EDXRD spectra. At the beginning only the (102) reflection of the product starts to grow and slightly shifts with reaction time and at later stages of the reaction all other peaks of  $[\text{Co}(\text{tren})][\text{Sb}_2\text{S}_4]$  occur and grow simultaneously. These observations are reminiscent of a mechanism where first strong disordered layers are formed which then start to arrange during reaction progress, yielding the three-dimensional long-range ordered material.

The combination of in situ EDXRD with in situ EXAFS experiments provides information about the reaction starting from the very early stages until products start to crystallize. We have shown that the starting material is dissolved within a short period. According to the EXAFS analysis, only two different species are present in the solution. A drastic decrease of dissolved antimony species indicates that a solid product is formed which is not detected in the EDXRD spectra; i.e., the particle sizes are too small and/or the solid is amorphous.

Taking all results into account, possible reaction pathways can be postulated which is depicted in Figure 20. At the beginning of the reaction the starting material is very quickly dissolved (see Figure 20 path 1) and it can be assumed that Co is coordinated by the amine, yielding a  $[\text{Co}(\text{tren})]^{2+}$  complex. According to the EXAFS results, monomeric  $\text{SbS}_x$  units with  $x = 3$  and 4 are formed. Further condensation (see path 2 in Figure 20) via common corners and/or edges leads to larger SbS aggregates, which precipitate and a solid amorphous phase is formed. For temperatures  $\leq 120^\circ\text{C}$  a

*Crystal Growth of [Co(C<sub>6</sub>H<sub>18</sub>N<sub>4</sub>)]Sb<sub>2</sub>S<sub>4</sub>*

*Chem. Mater., Vol. 18, No. 5, 2006 1205*

preorientation (see path 3 in Figure 20) of the layers occurs and only the (102) reflection of the product starts to grow in the X-ray powder pattern. In contrast to this observation the normal reaction path does not proceed via this step and all product reflections grow simultaneously, which is sketched in Figure 20 as path 4.

**Acknowledgment.** The financial support of this work by the state of Schleswig-Holstein and the Deutsche Forschungsgemeinschaft (DFG) are acknowledged. We also thank Julia Wienold and Ulrich Ponkratz for their help at the beamlines X1 and F3 at HASYLAB.

CM051788T

### **4.3. Ergebnisse und Publikationen aus Kooperationen**

#### **4.3.1. EDXRD-Untersuchungen zur Bildung von W/Mo-Oxiden**

*Zusammenfassung der Veröffentlichung „Hydrothermal Formation of W/Mo-Oxides: A Multidisciplinary Study of Growth and Shape“.*

Hier werden die Ergebnisse der EDXRD-Untersuchungen diskutiert, die im Rahmen der Kooperation mit der Arbeitsgruppe von Frau Prof. G. Patzke erzielt worden sind.

Die Reaktionen wurden am Messplatz F3 (Kap. 3.3) in der in Kapitel 3.2 beschriebenen in-situ-Apparatur durchgeführt. Bei einem typischen Experiment (Verhältnis Mo : W = 1 : 1) wurden 298 mg  $(\text{NH}_4)_6[\text{H}_2\text{W}_{12}\text{O}_{40}] \cdot \sim 3 \text{ H}_2\text{O}$  und 14 mg  $\text{MoO}_3 \cdot 2 \text{ H}_2\text{O}$  in 1.5 mL 25%iger Essigsäure eingesetzt.

Die Einflüsse der Reaktionstemperatur sowie der Verhältnisse der Edukte auf die Produktbildung  $(\text{NH}_4)_x(\text{W},\text{Mo})\text{O}_3$  sollten untersucht werden. Zuerst wurde die Temperatur zwischen 170 und 190 °C variiert. Bei allen Reaktionen erfolgt eine sehr schnelle Auflösung der Edukte, so dass keine Reflexe der Edukte beobachtbar sind. Für W : Mo-Verhältnisse  $< 1$  wird die Bildung eines sehr kurzlebigen Intermediats beobachtet. Nach der temperaturabhängigen Induktionszeit beginnt das Wachstum der Produktreflexe. Mit zunehmender Reaktionstemperatur werden die Induktionszeiten kürzer, die Reaktionszeit verkürzt sowie das Intermediat rascher aufgelöst. Das Wachstum des Intermediats und des Produkts zeigen für verschiedene Reflexe ähnliches Verhalten, so dass von einem isotropen Wachstum der Kristallite beider Phasen ausgegangen werden kann. Die Induktionszeit hängt bei geringeren Konzentrationen der W-Spezies nicht nur von der Temperatur, sondern auch vom Verhältnis der Edukte ab. Wird der W-Anteil erhöht, so werden die Induktions- und Reaktionszeit verlängert. Ausgehend von einem Verhältnis für W : Mo = 1 : 1 wird für die Kurven des Reaktionsfortschritts  $\alpha$  der Auflösung des Intermediats und der Bildung des Produkts ein Schnittpunkt bei  $\alpha = 0.5$  erhalten, der von der Reaktionstemperatur unabhängig ist. Das ist ein sehr deutlicher Hinweis darauf, dass das Auflösen des Intermediats und die Produktbildung korreliert sind, d. h. es ist möglich, dass eine direkte Umwandlung des Intermediats in das Produkt  $(\text{NH}_4)_x(\text{W},\text{Mo})\text{O}_3$  stattfindet. Die Auflösung bzw. Amorphisierung des Intermediats könnte allerdings auch

gleichzeitig mit der Produktbildung innerhalb einer so schnellen Zeitskala erfolgen, die im Experiment nicht erfasst werden kann. Bei einem W : Mo-Verhältnis von 1 : 3 wird nur 20% des Intermediats umgesetzt und es liegt im Produktgemisch neben  $(\text{NH}_4)_x(\text{W},\text{Mo})\text{O}_3$  vor. Interessant ist zudem, dass die großen Halbwertsbreiten der Produktreflexe die Abmessungen der Kristallite im nanoskaligen Bereich widerspiegeln bzw. bestätigen.

Die kinetischen Analysen ergeben, dass während der Bildung von  $(\text{NH}_4)_x(\text{W},\text{Mo})\text{O}_3$ -Stäbchen kein Wechsel des dominierenden Mechanismus erfolgt. Werden die experimentellen Daten mit verschiedenen, etablierten Modellen der Festkörperkinetik verglichen, so kann von einem zweidimensionalen Wachstum der Nuklei ausgegangen werden. Die Produktbildung von  $(\text{NH}_4)_x(\text{W},\text{Mo})\text{O}_3$  verläuft also unter Keimbildungskontrolle, gefolgt vom geschwindigkeitsbestimmenden Schritt des Verbrauchs bzw. der Aufzehrung der W-Spezies.

Reproduced with permission from R. Kiebach, N. Pienack, W. Bensch, J.-D. Grunwaldt, A. Michailovski, A. Baiker, T. Fox, Y. Zhou, G. R. Patzke: Hydrothermal Formation of W/Mo-Oxides: A Multidisciplinary Study of Growth and Shape; *Chem. Mater.* **2008**, *20*, 3022-3033.

Copyright 2008 American Chemical Society.

3022

*Chem. Mater.* **2008**, *20*, 3022-3033

## Hydrothermal Formation of W/Mo-Oxides: A Multidisciplinary Study of Growth and Shape

Ragnar Kiebach,<sup>†</sup> Nicole Pienack,<sup>†</sup> Wolfgang Bensch,<sup>†</sup> Jan-Dierk Grunwaldt,<sup>‡,§</sup> Alexej Michailovski,<sup>‡</sup> Alfons Baiker,<sup>‡</sup> Thomas Fox,<sup>||</sup> Ying Zhou,<sup>||</sup> and Greta R. Patzke<sup>\*||</sup>

*Institute of Inorganic Chemistry, University of Kiel, Olshausenstrasse 40, D-24098 Kiel, Germany, Institute for Chemical and Bioengineering, Department of Chemistry and Applied Biosciences, ETH Zurich, Hönggerberg-HCI, CH-8093 Zurich, Switzerland, and Institute of Inorganic Chemistry, University of Zurich, Wintherturerstrasse 190, CH-8057 Zurich, Switzerland*

Received September 28, 2007. Revised Manuscript Received January 30, 2008

The hydrothermal formation of mixed nanoscale W/Mo-oxides with the hexagonal tungsten bronze (HTB) structure has been investigated by in situ EDXRD (energy dispersive X-ray diffraction). Compared to the binary oxide systems, they display intermediate kinetics with a nucleation-controlled mechanism dominated by the slow growing tungsten component. Furthermore, the thermal stability of nanostructured W/Mo-HTB compounds has been monitored through combined in situ X-ray absorption spectroscopy (XAS) and XRD in reducing and oxidizing atmospheres. Their transformation into other mixed nanostructures was only observed above 300 °C in O<sub>2</sub>- and H<sub>2</sub>-containing atmospheres. In addition, the shape of nanoscale hexagonal W/Mo-oxides can be expanded into a variety of morphologies via the use of alkali chlorides as hydrothermal additives. The alkali cations exert a two-fold role as internal stabilizers and external shape control agents. Their mobility within the channels of the W/Mo-oxide host framework has been investigated by solid state NMR spectroscopy.

### 1. Introduction

Transition metal oxides (TMOs) play an important role in modern materials chemistry. Their almost unlimited number of structural options is both a blessing and a curse.<sup>1</sup> While the ongoing discovery of new TMO structures continues to bring forward substances with key properties and applications (e.g., superconductors, semiconductors, magnetic materials, or fast ion conductors), it can be extremely difficult to prepare the according TMOs in a predictive manner on a larger scale.<sup>2</sup> This applies especially for downscaling TMO-based materials to nanoscopic dimensions.<sup>3</sup> For this purpose, solvo- and hydrothermal methods are a powerful tool due to their exceptional parameter tuning options that can be adapted and optimized to bring forward a wide spectrum of materials that may be difficult to access with conventional preparative methods, for example, nanoparticles, metastable compounds/ or hybrid materials.<sup>4</sup> However, at the moment, too little is known about the mechanisms occurring under hydrothermal conditions to predict the products resulting

from a new experimental setup in a general fashion. Therefore, in situ investigations of hydrothermal reactions are essential to fully explore their potential for morphology control in materials synthesis.<sup>5,6</sup>

In our previous work, we have focused on the investigation of the formation of nanoscale molybdenum<sup>7</sup> and tungsten oxides<sup>8</sup> with in situ XAS (EXAFS, extended X-ray absorption fine structure and XANES, X-ray absorption near-edge structure) and EDXRD (energy dispersive X-ray diffraction) techniques. In addition, we have demonstrated that the nanoscale morphology of hexagonal tungsten bronzes (HTBs) can be adjusted through the use of alkali cations as additives.<sup>8</sup> Furthermore, we have developed a convenient one-step hydrothermal approach to mixed nanostructured W/Mo-oxides starting from readily available precursor materials.<sup>9</sup>

In the present study, these previous analytical and synthetic results are applied on the formation of nanostructured W/Mo-HTBs.<sup>9</sup> Generally, ternary and higher TMOs often benefit from a "synergistic" effect, because the combination of two or more oxides can substantially enhance the properties of

\* To whom correspondence should be addressed. Phone: +41 44 63 54691. Fax: +41 44 63 56802. E-mail: greta.patzke@aci.uzh.ch.

<sup>†</sup> University of Kiel.

<sup>‡</sup> ETH Zurich.

<sup>§</sup> Present address: Department of Chemical and Biochemical Engineering, Technical University of Denmark, DK-2800 Kgs. Lyngby, Denmark.

<sup>||</sup> University of Zurich.

- (1) Rao, C. N. R.; Raveau, B. *Transition Metal Oxides*, 2nd ed.; Wiley-VCH: New York, 1998.
- (2) (a) Rao, C. N. R.; Deepak, F. L.; Gundiah, G.; Govindaraj, A. *Prog. Solid State Chem.* **2005**, *31*, 5. (b) Niederberger, M.; Garnweitner, G.; Pinna, N.; Neri, G. *Prog. Solid State Chem.* **2005**, *33*, 59. (c) Patzke, G. R.; Krumeich, F.; Nesper, R. *Angew. Chem., Int. Ed.* **2003**, *42*, 972.
- (3) (a) Mann, S. *Angew. Chem., Int. Ed.* **2000**, *39*, 3392. (b) Wang, T. P.; Antonietti, M.; Cölfen, H. *Chem. Eur. J.* **2006**, *12*, 5722.

- (4) (a) Byrappa, K.; Yoshimura, M. *Handbook of Hydrothermal Technology*; Noyes: Park Ridge, NJ, 2001. (b) Demazeau, G. *J. Mater. Chem.* **1999**, *9*, 15.

- (5) Cheetham, A. K.; Mellot, C. F. *Chem. Mater.* **1997**, *9*, 229.

- (6) (a) Walton, R. I.; O'Hare, D. *Chem. Commun.* **2000**, 2283. (b) Morris, R. E.; Weigel, S. J.; Norby, P.; Hanson, J. C.; Cheetham, A. K. *J. Synchrotron Radiat.* **1996**, *3*, 301.

- (7) (a) Michailovski, A.; Grunwaldt, J.-D.; Baiker, A.; Kiebach, R.; Bensch, W.; Patzke, G. R. *Angew. Chem., Int. Ed.* **2005**, *44*, 5643. (b) Grunwaldt, J.-D.; Ramin, M.; Rohr, M.; Michailovski, A.; Patzke, G. R.; Baiker, A. *Rev. Sci. Instrum.* **2005**, *76*, 054104.

- (8) Michailovski, A.; Kiebach, R.; Bensch, W.; Grunwaldt, J. D.; Baiker, A.; Komarneni, S.; Patzke, G. R. *Chem. Mater.* **2007**, *19*, 185.

- (9) Michailovski, A.; Krumeich, F.; Patzke, G. R. *Chem. Mater.* **2004**, *16*, 1433.

Table 1. Recent Developments in the Materials Chemistry of Mixed W/Mo-Oxides

target compound	synthetic pathway	properties/applications	reference
thin MoO <sub>3</sub> /WO <sub>3</sub> films	APCVD of metal carbonyls	working electrodes in electrochromic devices	24
mixed W/Mo-oxide films	cathodic electrodeposition from aqueous solutions	enhanced electrochromism and lithium intercalation	25
nanosized mixed W/Mo-oxide thin films	RF-magnetron sputtering	morphology-dependent sensor response towards CO	26,27
MoO <sub>3</sub> -WO <sub>3</sub> composites	sintering/calcination methods	humidity sensors/T-dependent surface barriers	28,29
Mo-doped HTBs	hydrothermal methods	immobilization of radio cesium and strontium	30

the binary components. Over the past years, considerable progress has been achieved in the development of catalysts,<sup>10,11</sup> sensors,<sup>12</sup> electrochromic materials,<sup>13</sup> and other applications of mixed W/Mo-oxides (for selected examples cf. Table 1).

In the analytical part of the paper, we characterize the growth process of mixed W/Mo-HTBs with in situ EDXRD methods. Next, the redox chemistry of nanoscale hexagonal W/Mo-oxides is investigated with complementary in situ X-ray diffraction and in situ EXAFS/XANES spectroscopy. X-ray absorption spectroscopic techniques have been proven to be an efficient tool in the synthesis of oxide materials in general,<sup>14</sup> and for the analysis of the detailed structural features of Mo- and W-oxides in particular.<sup>7,15</sup> In this way, the effect of thermal treatment in oxygen- and hydrogen-containing atmospheres on the phase and morphology of the mixed oxide materials was monitored. The resulting information about the stability and the structural transformations of W/Mo-based nanomaterials provides new insights for a more rational synthesis of oxide-based catalysts.<sup>16</sup>

The following synthetic section of the manuscript illustrates the importance of a flexible TMO structural motif for nanoscale morphology control with additive substances.<sup>17,18</sup> Whereas major progress has been achieved in the additive-controlled synthesis of metal nanoparticles,<sup>17</sup> the search for perfect TMO-additive matches is still a major challenge: While organic additives and bio-macromolecules can exert powerful shaping effects in principle,<sup>19</sup> they often decompose at the reaction temperatures required for hydrothermal oxide formation. Secondly, many additives alter the target TMO structure through unwanted side reactions. However, the hexagonal channels of the HTB structure are stabilized through the intercalation of alkali cations,<sup>20</sup> and this turns the reaction between TMO and additive into a specific preparative asset to generate W/Mo-oxide materials with a

wide spectrum of morphologies. Generally, the HTB framework easily undergoes redox and diffusion processes: On the one hand, oxygen atoms can diffuse in and out of the tunnels via complex pathways.<sup>20</sup> Furthermore, there is also a delicate interplay between the degree of occupation of the hexagonal tunnels, for example, by alkali cations, and according vacancies in the W sublattice.<sup>20</sup> The mobility of Li<sup>+</sup>, Na<sup>+</sup>, and Cs<sup>+</sup> in the channel systems of the W/Mo-HTB structure was investigated in terms of solid state NMR spectroscopy. Recently, composite materials of W/Mo-HTBs and polyacrylonitrile have attracted considerable interest for the immobilization of radioactive Sr<sup>2+</sup> and Cs<sup>+</sup>, and <sup>133</sup>Cs MAS NMR spectroscopy revealed the presence of different Cs species in the saturated samples.<sup>21</sup> However, the incorporation of alkali cations into the HTB channels has seldom been studied in terms of NMR spectroscopy, because the majority of the investigations have been focused on other tungsten oxide systems.<sup>22,23</sup>

To the best of our knowledge, only very few detailed studies were reported applying a combination of advanced in situ techniques as well as ex situ characterization on the hydrothermal synthesis and nanoscale morphochemistry of mixed W/Mo-oxides. We have chosen this model system to investigate whether hydrothermal synthetic guidelines can be transferred from binary to ternary TMO systems. In the long term, we aim for general strategies for the controlled design of oxide materials. For this purpose, we work towards a systematic hydrothermal "toolbox" approach to TMO nanomaterials that is based on mechanistic insights.

## 2. Experimental Procedures

**2.1. Hydrothermal Experiments.** The mixed W/Mo-oxide materials were prepared according to standard hydrothermal

- (10) Mestl, G. *J. Raman Spectrosc.* **2002**, *33*, 333.  
 (11) Ovsitser, O.; Uchida, Y.; Mestl, G.; Weinberg, G.; Blume, A.; Jäger, J.; Dieterle, M.; Hibt, H.; Schlögl, R. *J. Mol. Catal. A* **2002**, *185*, 291.  
 (12) Prasad, A. K.; Gouma, P. I. *J. Mater. Sci.* **2003**, *38*, 4347.  
 (13) Ivanova, T.; Gesheva, K. A.; Popkirov, G.; Ganchev, M.; Tzvetkova, E. *Mater. Sci. Eng. B* **2005**, *119*, 232.  
 (14) (a) Beale, A. M.; Reilly, L. M.; Gopinathan, S. *Appl. Catal. A* **2007**, *325*, 290. (b) Huwe, H.; Fröba, M. *Carbon* **2007**, *45*, 304. (c) Opre, Z.; Grunwaldt, J.-D.; Mallat, T.; Baiker, A. *J. Mol. Catal. A* **2005**, *242*, 224.  
 (15) (a) Schlögl, R.; Knop-Gericke, A.; Hävecker, M.; Wild, U.; Frickel, D.; Ressler, T.; Jentoft, R. E.; Wienold, J.; Mestl, G.; Blume, A.; Timpe, O.; Uchida, Y. *Top. Catal.* **2001**, *15*, 219. (b) Purans, J.; Kuzmin, A.; Parent, P.; Laffon, C. *Electrochim. Acta* **2001**, *46*, 1973.  
 (16) Giebler, L.; Kampe, P.; Wirth, A.; Adams, A. H.; Kunert, J.; Fuess, H.; Vogel, H. *J. Mol. Catal. A* **2006**, *259*, 309.  
 (17) Pileni, M. P. *J. Phys. Chem. C* **2007**, *111*, 9019.  
 (18) Rajam, S.; Mann, S. *J. Chem. Soc., Chem. Commun.* **1990**, 1789.  
 (19) (a) Komarneni, S.; Gao, F.; Lu, Q. Y. *Langmuir* **2005**, *21*, 6002. (b) Welzel, T.; Meyer-Zaika, W.; Epple, M. *Chem. Commun.* **2004**, 1204.

- (20) (a) Guo, J. D.; Reis, K. P.; Whittingham, M. S. *Solid State Ionics* **1992**, *53–56*, 305. (b) Reis, K. P.; Prince, E.; Whittingham, M. S. *Chem. Mater.* **1992**, *4*, 307. (c) Tsuyumoto, I.; Kishimoto, A.; Kudo, T. *Solid State Ionics* **1993**, *59*, 211.  
 (21) Griffith, C. S.; Sebesta, F.; Hanna, J. V.; Yee, P.; Drabarek, E.; Smith, M. E.; Luca, V. *J. Nucl. Mater.* **2006**, *358*, 151.  
 (22) (a) Whittle, K. R.; Lumpkin, G. R.; Ashbrook, S. E. *J. Solid State Chem.* **2006**, *179*, 512. (b) Dubson, M. A.; Holcomb, D. F. *Phys. Rev. B* **1986**, *34*, 25.  
 (23) Xia, Y.; Machida, N.; Wu, X.; Lakeman, C.; van Willen, L.; Lange, F.; Levi, C.; Eckert, H. *J. Phys. Chem. B* **1997**, *101*, 9180.  
 (24) Gesheva, K. A.; Ivanova, T. *Chem. Vap. Deposition* **2006**, *12*, 231.  
 (25) Kondrachova, L.; Hahn, B. P.; Vijayaraghavan, G.; Williams, R. D.; Stevenson, K. J. *Langmuir* **2006**, *22*, 10490.  
 (26) Vomiero, A.; Della Mea, G.; Ferroni, M.; Martinelli, G.; Roncarati, G.; Guidi, V.; Comini, E.; Sberveglieri, G. *Mat. Sci. Eng. B* **2003**, *101*, 216.  
 (27) Morandi, S.; Ghiotti, G.; Chiorino, A.; Bonelli, B.; Comini, E.; Sberveglieri, G. *Sens. Actuators, B* **2005**, *111–112*, 28.  
 (28) Pokhrel, S.; Nagaraja, K. S. *Phys. Status Solidi* **2003**, *2*, 343.  
 (29) Malagù, C.; Carotta, M. C.; Morandi, S.; Gherardi, S.; Ghiotti, G.; Giberti, A.; Martinelli, G. *Sens. Actuators, B* **2006**, *118*, 94.

3024 *Chem. Mater.*, Vol. 20, No. 9, 2008

Kiebach et al.

procedures. For experiments with a M:W/Mo-ratio of 60:1, 40 mg (0.13 mmol of W) of  $(\text{NH}_4)_6[\text{H}_2\text{W}_{12}\text{O}_{40}] \cdot \sim 3\text{H}_2\text{O}$  (ammonium metatungstate, in the following: AMT), 20 mg of  $\text{MoO}_3 \cdot 2\text{H}_2\text{O}$  (0.11 mmol of Mo), 10 mL of 25 vol % acetic acid (HAc), and 15 mmol of MCl (M = Li–Cs) were added to a Teflon-lined stainless-steel autoclave with a capacity of 23 mL. The autoclave was then sealed, heated for 2 days at 180 °C, and subsequently cooled to room temperature. The resulting precipitate was collected by filtration, washed with distilled  $\text{H}_2\text{O}$ , EtOH, and acetone, and dried in air. Experiments with a lower M:W/Mo-ratio of 2.5:1 started from 148 mg of AMT (0.60 mmol of W), 58 mg of  $\text{MoO}_3 \cdot 2\text{H}_2\text{O}$  (0.32 mmol of Mo), 2 mL of 25 vol % HAc, and 2 mmol of MCl (M = Li–Cs), following the above-mentioned hydrothermal routine.

**2.2. Analytical Methods.** X-ray powder diffraction analyses were conducted on a STOE STADI-P2 diffractometer in transmission mode (flat sample holders, Ge monochromated Cu  $K\alpha_1$  radiation) equipped with a position-sensitive detector (resolution ca.  $0.01^\circ$  in  $2\theta$ ).

For scanning electron microscopy (SEM), performed on a LEO 1530 (FEG) microscope with 1 keV electrons, samples were dispersed in ethanol and subsequently deposited on a silicon wafer. A CamScan CS-44 electron microscope with an EDAX-Phoenix energy-dispersive X-ray spectrometer (EDXS) was employed for approximate elemental analyses. The scanning transmission electron microscopy (STEM) images were recorded on a Philips Tecnai 30F microscope, operated at 300 kV (field emission cathode). In the STEM mode, the electron beam was placed on a selected spot, and an elemental analysis by energy-dispersive X-ray spectroscopy (EDS, EDAX detector) was performed there. Elemental analyses were conducted on a Leco CHN(S)-932 instrument.

**2.3. In Situ EDXRD Experiments.** All in situ EDXRD experiments were performed at HASYLAB Beamline F3, which receives white synchrotron radiation from a bending magnet with a critical energy of 16 keV and gives a positron beam energy of 4.5 GeV. An energy range from 13.5 to 65 keV can be observed with a maximum at about 20 keV. The diffracted beam is monitored by a nitrogen cooled solid state germanium detector. The detector angle was chosen so that all important Bragg reflections can be detected. The  $d$ -spacing range is given by  $E = 6.199/(d \sin \theta)$ . With a detector angle of approximately  $3^\circ$  the observable  $d$ -spacing range is 2.9 Å to 13.8 Å. The energy resolution  $\Delta d/d$  is about  $10^{-2}$  above 26 keV. The beam was collimated to 0.1 mm giving the best results. More experimental details can be found in refs 31 and 32. For the in situ investigations autoclaves with glass liners with an internal diameter of 10 mm and a volume of 10 mL were used. A typical experiment (ratio Mo:W = 1:1) was performed by using 298 mg of  $(\text{NH}_4)_6[\text{H}_2\text{W}_{12}\text{O}_{40}] \cdot \sim 3\text{H}_2\text{O}$  (AMT), 144 mg  $\text{MoO}_3 \cdot 2\text{H}_2\text{O}$ , and 1.5 mL 25% HAc as reactants.

**2.4. In Situ XRD and EXAFS Experiments.** XANES and EXAFS (X-ray absorption near edge structure) and EXAFS data were collected at the Norwegian-Swiss Beamline (SNBL, BM01B) of the European Synchrotron Radiation Facility, ESRF, Grenoble, France. The electron energy is typically 6.0 GeV and the ring current was between 150 and 200 mA. A Si(111) crystal was used as channel-cut monochromator. Harmonic rejection was performed by a double-bounce gold coated mirror system. EXAFS data were collected in transmission mode at room temperature and at elevated temperatures. Three ionization chambers were used for detecting the incoming  $I(0)$ , the transmitted  $I(t)$ , and the through the reference

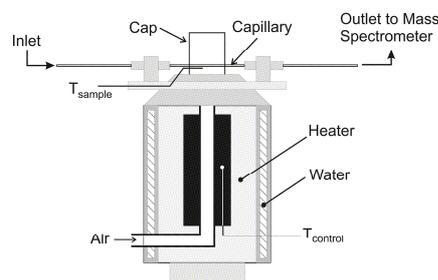


**Figure 1.** Schematic view of the in situ cell used in the present combined EXAFS/XRD studies.

transmitted  $I(\text{ref})$ , X-rays. Spectra were taken around the Mo K-edge (20.000 keV), using a Mo foil as a reference. They were taken in the energy range of 19.850 to 21.000 keV. The raw data were energy-calibrated, background corrected, and normalized using the WINXAS 3.0 software.<sup>33</sup>

The XRD data were collected at a wavelength  $\lambda = 0.5 \text{ \AA}$  using a Si(111) double-crystal as monochromator and a two-circle diffractometer equipped with six counting chains (a Si-111 analyzer crystal is mounted in front of each detector, Na–I scintillation counter) and an intrinsic resolution (FWHM) of approximately  $0.01^\circ$ . The spectra were taken using a specially designed and home-built (Figure 1, cf. ref 34) in situ cell, which consists of a sample holder with quartz capillary, a gas blower for heating of the system, a gas supply, and a mass spectrometer for on-line gas analysis. The sample was loaded in the glass microreactor (quartz capillary, Markröhrchen, Hilgenberg GmbH) between two glass wool plugs of 1.0 mm diameter as already described by Clausen et al.<sup>35</sup> The capillary is heated by a hot gas stream (here air, 300–400 L/h) with a commercially available gas blower (Cyberstar S.A., France, 220 V, 1000 W, provided by SNBL). The maximum temperature is 1000 °C. The temperature of the heater ( $T_{\text{control}}$ ) was measured by a thermocouple at the heating element in order to control a constant temperature ramp. The actual sample temperature ( $T_{\text{sample}}$ ) was monitored just below the sample. The heater is embedded in ceramics, and the outer side of the oven could be cooled by water or air in order to prevent the surroundings from warming up (e.g., important for ionization chambers). The capillary was enclosed in a Kapton cap around the in situ cell just above the heater where the hot stream of air passed out of the oven to improve the temperature homogeneity.

Typically a flow of 20 mL/min was fed over the catalysts using mass flow controllers (Brooks). Usually, pre-mixed gasses (oxidation in 20%  $\text{O}_2/\text{He}$ , reduction in 5%  $\text{H}_2/\text{He}$ ) were utilized. The whole assembly (in situ cell, heater) was mounted on a small  $x, z$ -table ( $x = \text{translation}$ ,  $z = \text{height}$ ) to align the sample in the X-ray beam.

**2.5. Solid State NMR Spectroscopy.** The NMR spectra were recorded at room temperature on a Bruker DRX-500-spectrometer, which has been modified for solid state capability with MAS sample spinning up to 15 kHz (4 mm rotors) and high power  $^1\text{H}$  decoupling. The NMR frequencies were 194.41 MHz for  $^7\text{Li}$  ( $I = 3/2$ ,  $\text{QM} = 0.045$ ), 132.32 MHz for  $^{23}\text{Na}$  ( $I = 3/2$ ,  $\text{QM} = 0.12$ ), 163.61 MHz for  $^{87}\text{Rb}$  ( $I = 3/2$ ,  $\text{QM} = 0.12$ ), and 65.61 MHz for  $^{133}\text{Cs}$  ( $I = 7/2$ ,  $\text{QM} = 0.003$ ).

(30) Luca, V.; Griffith, C. S.; Drabarek, E.; Chronis, H. *J. Nucl. Mater.* **2006**, 358, 139.

(31) (a) Avrami, M. *J. Chem. Phys.* **1939**, 7, 1103. (b) Avrami, M. *J. Chem. Phys.* **1940**, 8, 212. (c) Avrami, M. *J. Chem. Phys.* **1941**, 9, 177.

(32) Engelke, L.; Schaefer, M.; Schur, M.; Bensch, W. *Chem. Mater.* **2001**, 13, 1383.

(33) Ressler, T. *J. Synchrotron Radiat.* **1998**, 5, 118.

(34) (a) Grunwaldt, J. D.; Caravati, M.; Hannemann, S.; Baiker, A. *Phys. Chem. Chem. Phys.* **2004**, 6, 3037. (b) Grunwaldt, J.-D.; van Vegten, N.; Baiker, A. *Chem. Commun.* **2007**, 4635.

(35) Clausen, B.S.; Gråbæk, G.; Steffensen, G.; Hansen, P. L.; Topsøe, H. *Catal. Lett.* **1993**, 20, 23.

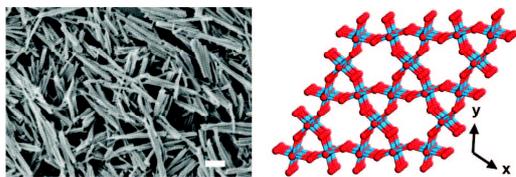


Figure 2. Representative image of W/Mo-oxide rods (left; scale bar = 200 nm) and the tunnel motif of the HTB structure (right).

### 3. Experimental Results

**3.1. Hydrothermal Formation of Nanostructured W/Mo-Oxides.** The direct hydrothermal reaction of ammonium metatungstate (AMT,  $(\text{NH}_4)_6[\text{H}_2\text{W}_{12}\text{O}_{40}] \cdot 3\text{H}_2\text{O}$ ) with  $\text{MoO}_3 \cdot 2\text{H}_2\text{O}$  in acetic acid at 180 °C affords anisotropic  $(\text{NH}_4)_x(\text{W},\text{Mo})\text{O}_3$  particles after 2 days (Figure 2, left).<sup>9</sup> In this procedure, the starting materials are directly transferred into the autoclave without any further pre-treatment. To investigate the influence of homogeneous precursor solutions on the morphology of the product and on the nucleation process, the synthetic protocol was modified as follows: First, clear acidified solutions of AMT and ammonium heptamolybdate  $(\text{NH}_4)_6\text{Mo}_7\text{O}_{24} \cdot 4\text{H}_2\text{O}$ , respectively, were prepared. These solutions were then transferred into the autoclave in the according ratios, and in a series of hydrothermal experiments (180 °C, 2 d) the molar W/Mo-ratio was increased in steps of 10% (metal% in the starting material). In the range between 0% and 60% W, mixtures of microcrystalline starting materials and anisotropic  $(\text{NH}_4)_x(\text{W},\text{Mo})\text{O}_3$  with the HTB structural motif are obtained (Figure 2, right). At higher W/Mo-ratios, the W/Mo-HTBs are exclusively formed, and the smallest rods display diameters in the range of 20–30 nm and lengths around 100 nm. Although the use of homogeneous starting materials might suggest the opposite trend, the nanoparticles obtained from this approach exhibit a stronger tendency towards agglomeration than those formed from the direct reaction of  $\text{MoO}_3 \cdot 2\text{H}_2\text{O}$  with AMT with no further pre-treatment. Therefore, the one-step pathway starting from AMT and  $\text{MoO}_3 \cdot 2\text{H}_2\text{O}$  was selected for the following morphological and mechanistic studies.

**3.2. Time-Dependent Conversion of AMT and  $\text{MoO}_3 \cdot 2\text{H}_2\text{O}$  into Nanostructured  $(\text{NH}_4)_x(\text{W},\text{Mo})\text{O}_3$ : In Situ EDXRD Investigations.** In our previous studies, we have performed kinetic and mechanistic studies on the growth of  $\text{MoO}_3$  nanorods<sup>7</sup> and nanostructured HTB tungstates.<sup>8</sup> As these reactions display different results, a kinetic analysis of the mixed W/Mo system provides an excellent opportunity to investigate the parameters which are the decisive factors for the different reaction types and therewith a possible control of the morphology and structure of the product. In situ EDXRD using synchrotron radiation has proven to be an especially powerful method for studying the kinetics of crystallization processes and evaluating their mechanisms.<sup>31,32</sup> The direct monitoring of synthetic processes is superior to ex situ observations, because it permits the collection of much more data with no quenching steps involved. Here, in situ EDXRD measurements are employed to investigate the influence of two main parameters, firstly the influence of the reaction temperature (170–90 °C) and secondly the ratio

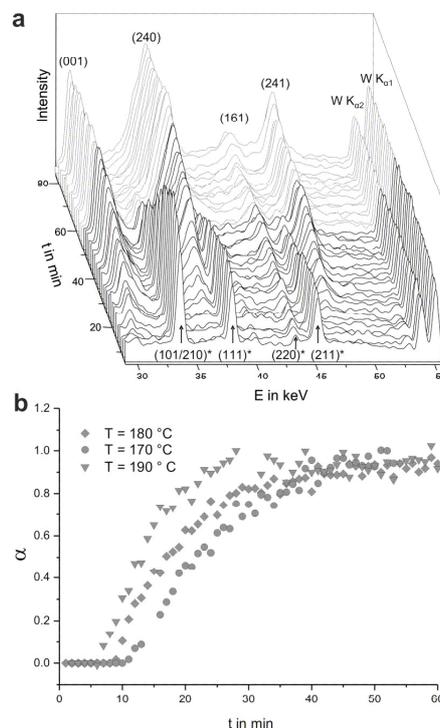


Figure 3. (a) Time-resolved energy-dispersive X-ray powder diffraction pattern of  $(\text{NH}_4)_x(\text{W},\text{Mo})\text{O}_3$  nanorod formation. The indices of the most intense lines of the intermediate and the product phase and W  $K\alpha$  and  $K\beta$  fluorescence lines are marked. (b) Extent of reaction  $\alpha$  versus time for the formation of  $(\text{NH}_4)_x(\text{W},\text{Mo})\text{O}_3$  rods at different temperatures.

of the educts (W:Mo = 1:3, 1:1, 3:1). In the energy range chosen several reflections of the product and the W resonances (immediately visible) are monitored simultaneously, and the sequence of time resolved spectra is shown in Figure 3a. In all experiments no reflections of the reactants were observed, indicating a very fast dissolution of the W and the Mo sources. Interestingly, for W:Mo ratios < 1 the first observed reflections (Figure 3a) point to the formation of a hexagonal intermediate phase with the structural motif of  $(\text{NH}_4)_{0.94}\text{H}_{3.3}\text{Mo}_{5.3}\text{O}_{18}$ .<sup>36</sup> The growth of this Mo-rich intermediate is finished within 2 min so that a kinetic evaluation of this phase is not possible due its rapid formation. After an induction time,  $t_{\text{ind}}$ , the product peaks of  $(\text{NH}_4)_x(\text{W},\text{Mo})\text{O}_3$  start to grow. As expected, an increase of the reaction temperature leads in all cases to a decrease of the induction time (range: 10 min (190 °C)–23 min (170 °C)) and overall reaction time (range: 55 min (190 °C)–105 min (170 °C); Figures 3 and 4) and to a faster dissolution of the intermediate.

The integrated intensities of the product and intermediate reflections were normalized against the intensity of the most intense W  $K\alpha$  resonance. Quantitative analysis of the growth rates shows identical behavior for different reflections and confirms an isotropic crystallite growth for both phases. The

(36) Guo, J. D.; Zavalij, P.; Whittingham, M. S. *J. Solid State Chem.* **1995**, *117*, 323.

(37) Kiebach, R.; Pienack, N.; Ordolff, M. E.; Studt, F.; Bensch, W. *Chem. Mater.* **2006**, *18*, 1196.

3026 Chem. Mater., Vol. 20, No. 9, 2008

Kiebach et al.

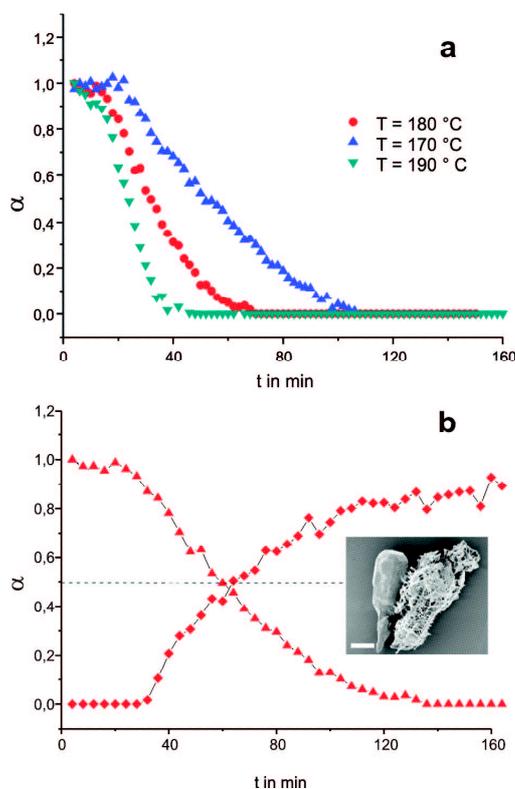


**Figure 4.** Temperature-dependent dissolution of the AMT starting material (a) and the correlation between the dissolution of AMT and the formation of the product at  $170^\circ\text{C}$  together with a SEM image (inset, scale bar =  $2\ \mu\text{m}$ ) illustrating the nucleation-controlled formation process of  $(\text{NH}_4)_x(\text{W},\text{Mo})\text{O}_3$  rods (b).

plots of the extent of reaction  $\alpha$  (ratio of the normalized intensity at the reaction time  $t$  by the intensity at the time  $t_{0.5}$ ) against the reaction time  $t$  (Figures 3 and 4) demonstrate that the induction time  $t_{\text{ind}}$  depends not only on the reaction temperature but for low W concentration also on the ratio of the educts. The general trend in these cases is that higher induction and longer reaction times are found for increasing W amounts. As presented in Figure 4b, the dissolution of the intermediate and the formation of the product seem to be strongly correlated: Starting from an initial W:Mo ratio of 1:1, the curves of the extent of the reaction for product dissolution and intermediate formation meet for all investigated reaction temperatures exactly at  $\alpha = 0.5$ . This highly interesting observation suggests a direct transformation of the intermediate to the final product via a solid–solid transformation. But one can also imagine that the intermediate is dissolved/becomes amorphous and the product crystallization occurs promptly which cannot be resolved within the time resolution of the experiment. For experiments where the Mo content is increased to a ratio of W:Mo = 1:3, only 20% of the intermediate dissolves (not depicted) and the final product contains both phases.

Another interesting feature is the large FWHM of the reflections of the  $(\text{NH}_4)_x(\text{W},\text{Mo})\text{O}_3$  product, which is four times larger than the one of the intermediate compound that

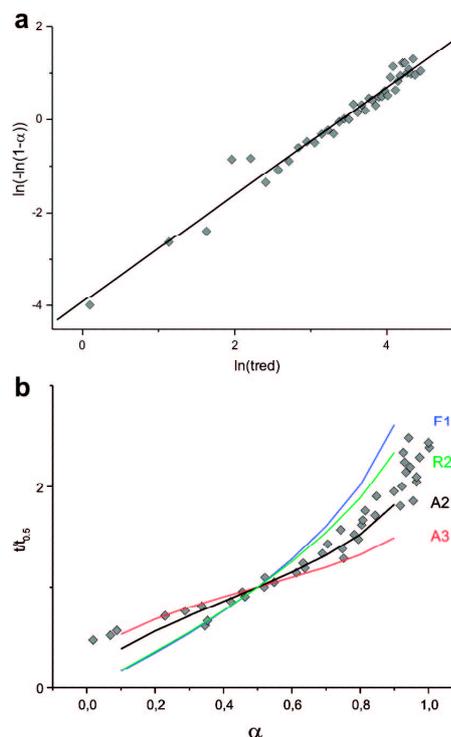


**Figure 5.** (a) Sharp–Hancock plot and (b) comparison of the evolution of experimental  $t/t_{0.5}$  data as a function of  $\alpha$  (gray squares) with different theoretical models.

is isostructural with  $(\text{NH}_4)_{0.94}\text{H}_3.3\text{Mo}_{5.3}\text{O}_{18}$ . Thus, the size of the monitored crystalline phase can be considered as nano-sized material, a result which is in line with the SEM measurements (cf. Figure 2).

The kinetic evaluation of the formation of  $(\text{NH}_4)_x(\text{W},\text{Mo})\text{O}_3$  rods was performed after subtracting the induction time  $t_0$  from time  $t$ . When  $\ln[-\ln(1-\alpha)]$  versus  $\ln(t)$  is plotted (the so-called Sharp–Hancock plot, abbreviated SH) a straight line is obtained for that part of the reaction which follows the same mechanism.<sup>31</sup> A change in the mechanism during the reaction leads to a change in the slope of the curve.

During the formation of  $(\text{NH}_4)_x(\text{W},\text{Mo})\text{O}_3$  rods, no change of the reaction mechanism could be observed over the entire range of experiments, and the experimental points are on a straight line over the whole reaction. A representative example is shown for the reaction at  $170^\circ\text{C}$  in Figure 5a (W/Mo = 1:1). Also the slope of SH plot, from which the reaction exponent can be calculated, is comparable for the entire range of experiments. The values found for the reaction exponent are in the same range of the one published for the W system. For further discussion and an overview about the different models compare refs 8 and 37.

A more detailed analysis is available comparing different established models with the experimental data.<sup>31</sup> The most appropriate model is selected by plotting the experimental  $t/t_{0.5}$  data ( $t_{0.5}$  is the reaction time at  $\alpha = 0.5$ ) versus  $\alpha$ . This procedure permits a direct comparison

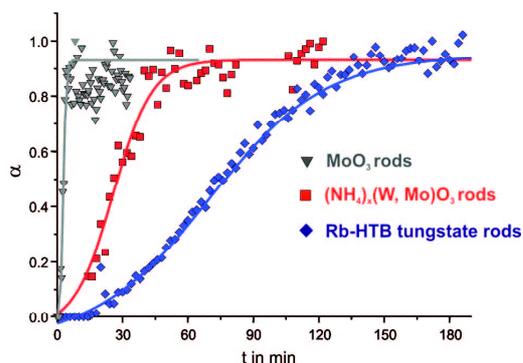


**Figure 6.** Extent of reaction  $\alpha$  versus time for the growth of  $\text{MoO}_3$  rods,  $(\text{NH}_4)_x(\text{W, Mo})\text{O}_3$  rods and nanostructured Rb-HTB tungstates.

with different models under consideration. The experimental data fit best with the two-dimensional growth of nuclei (model A2), and this result is in line with the above-mentioned SH plot (Figure 5). At the very early stages of the reaction up to about  $\alpha \approx 0.4$  the curve fits well with the three-dimensional growth of nuclei (A3) which can be also rationalized. First small 3D particles are formed (A3) which then exhibit a preferred 2D growth (A2), in accordance with the anisotropic morphology of the materials (see Figure 2). Indeed the kinetic data should be interpreted with some care because several strict conditions have to be fulfilled before the Johnson–Mehl–Avrami kinetics will hold. Nevertheless, the analysis presented above is on a solid scientific ground because important requirements like random nucleation and no hard impingement can be safely assumed. Especially the latter event leads to significant deviations from JMA kinetics. The results are in line with experiments performed under static conditions, because they often display crystals of the starting material with up-grown fibers (cf. inset Figure 4b). The growth curves for the hydrothermal formation of  $\text{MoO}_3$  rods, nanostructured  $(\text{NH}_4)_x(\text{W, Mo})\text{O}_3$ , and Rb-HTB rods as a representative example are compared in Figure 6. Whereas the formation of  $\text{MoO}_3$  fibers proceeds quantitatively within several minutes via a quick dissolution–precipitation sequence, the nucleation-controlled growth of nanostructured alkali HTBs takes between 2 and 5 h to completion, depending on the cation involved. Consequently, the  $(\text{NH}_4)_x(\text{W, Mo})\text{O}_3$  rods are formed through nucleation control, thereby following the rate-determining consumption step of the tungstate material. In terms of reaction time, they exhibit intermediate kinetics so that the reaction is finished after approximately 1 h.

**3.3. Oxidation/Reduction of Nanostructured W/Mo-Oxides: In Situ XRD and EXAFS.** **3.3.1. Thermal Treatment in  $\text{O}_2/\text{He}$  Atmosphere.** A representative sample of nanostructured oxide with the composition  $(\text{NH}_4)_{0.22}(\text{W}_{0.43}\text{Mo}_{0.57})\text{O}_3$  (containing 50 wt % BN) was subjected to thermal treatment in an atmosphere of 20%  $\text{O}_2$  in He at a heating rate of  $5\text{ }^\circ\text{C min}^{-1}$ . During the oxidation, in situ XRD data were taken (Figure 7a) and complemented by EXAFS measurements at selected temperatures (RT, 250  $^\circ\text{C}$ , 500  $^\circ\text{C}$ ). From room temperature to 390  $^\circ\text{C}$ , the HTB-structural motif

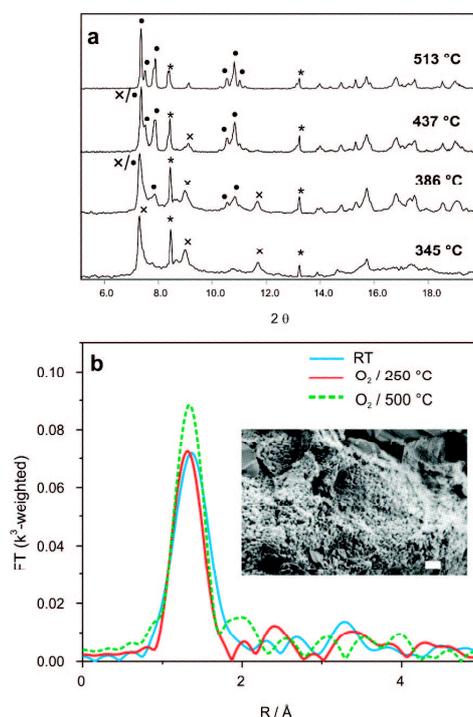


**Figure 7.** (a) In situ XRD monitoring of the treatment of nanostructured  $(\text{NH}_4)_{0.22}(\text{W}_{0.43}\text{Mo}_{0.57})\text{O}_3$  (containing 50 wt % BN) in oxygen atmosphere ( $\lambda = 0.5\text{ \AA}$ , key reflections: \* = BN, x = HTB-phase, • = monoclinic W/Mo-oxide). (b) In situ EXAFS spectra at the Mo K-edge (Fourier transformed) during the treatment of nanostructured  $(\text{NH}_4)_{0.22}(\text{W}_{0.43}\text{Mo}_{0.57})\text{O}_3$  in oxygen atmosphere together with a representative SEM image of the resulting product (inset, scale bar = 500 nm).

experiences a slight broadening of the reflections and changes in their relative intensities. Whereas the intensity of the (001) and (110) reflections increases, the reflections (101) and (200) become less intense. In the temperature range between 390 and 510  $^\circ\text{C}$ , the HTB structure is gradually transformed into a mixed oxide that displays close resemblance to monoclinic  $\text{WO}_3$  with a distorted  $\text{ReO}_3$  motif (JCPDS No. 43-1305). The key XRD patterns illustrating the temperature-dependent transformation are displayed in Figure 7a.

These structural changes are reflected in the Fourier transformed EXAFS data (Figure 7b): The data suggest an onset of structural changes can be observed at 500  $^\circ\text{C}$ , but only small changes of the local structure at the Mo absorber atom occur at 250  $^\circ\text{C}$ , also supported by XANES data (cf. ESI). The obtained mixed monoclinic W/Mo-oxide still exhibits nanostructures in the range of 100 nm (cf. inset in Figure 7b). During the oxidation process, the W/Mo-ratio increased from 0.75 to 1 according to EDX analyses of the product. Given that the experimental error of the EDX method is about 3 atom %, this points to a very small loss of molybdenum.

**3.3.2. Thermal Treatment in  $\text{H}_2/\text{He}$  Atmosphere.** A sample of  $(\text{NH}_4)_{0.22}(\text{W}_{0.43}\text{Mo}_{0.57})\text{O}_3$  (50 wt % BN) was heated in an atmosphere of 7 vol %  $\text{H}_2$  in Ar. In the temperature range

3028 Chem. Mater., Vol. 20, No. 9, 2008

Kiebach et al.

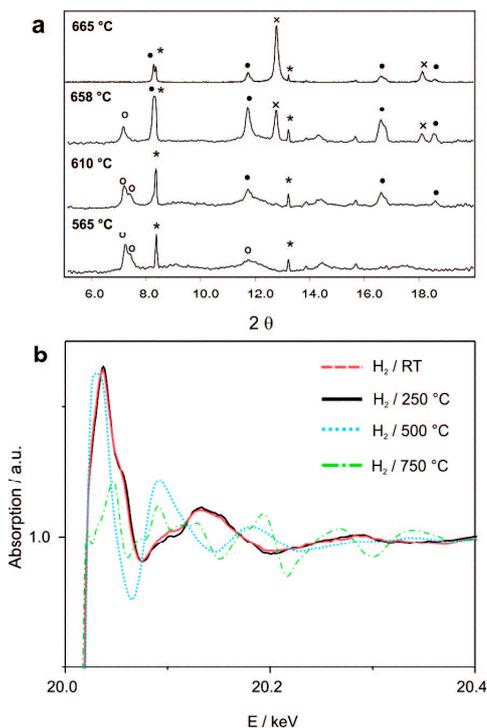


**Figure 8.** (a) In situ XRD monitoring of the treatment of  $(\text{NH}_4)_{0.22}(\text{W}_{0.43}\text{Mo}_{0.57})\text{O}_3$  (containing 50 wt % BN) in a hydrogen atmosphere ( $\lambda = 0.5 \text{ \AA}$ , key reflections: \* = BN, ○ = HTB structure, ● =  $\text{WO}_2$ -based motif, × = Mo–W alloy with W-structure). (b) In situ XANES spectra at the Mo K-edge during treatment of  $(\text{NH}_4)_{0.22}(\text{W}_{0.43}\text{Mo}_{0.57})\text{O}_3$  (containing 50 wt % BN) in 5%  $\text{H}_2/\text{He}$  atmosphere.

between 295 and 500 °C, both in situ XRD and XANES/EXAFS measurements at the Mo K edge indicate only minor structural alterations (cf. Figure 8).

Note, however, that at 500 °C the near edge structure of the Mo K-edge already changed significantly, also indicated by the Fourier transformed EXAFS data (cf. ESI). Above 500 °C, the reduction to a metallic compound sets in that is structurally related to tungsten (JCPDS No. 4-806). In parallel, a mixed dioxide intermediate is formed that displays a  $\text{WO}_2$ -based structural motif (JCPDS No. 2-414). After heating to 700 °C, the entire sample is transformed into a mixed metal with a W/Mo ratio of 1 that is isostructural with metallic W (Figure 9). The formation of a metallic Mo–W alloy is also supported by both the XANES (Figure 8b) and EXAFS data. This Mo–W alloy shows a nanostructured morphology consisting of agglomerated particles with diameters of 50 nm and below (cf. inset in Figure 9).

**3.4. Influence of Alkali Halides on the Morphology of Nanostructured W/Mo-Oxides.** **3.4.1. Reaction of AMT/MoO<sub>3</sub>·2H<sub>2</sub>O Systems in the Presence of MCl.** To investigate the effect of alkali chlorides on the morphology of nanostructured hexagonal W/Mo-oxides, an excess of MCl (M = Li–Cs) was added to the AMT/MoO<sub>3</sub>·2H<sub>2</sub>O hydrothermal system at 180 °C for 2 d of reaction time (M/(W/Mo) = 60:1). As shown in Figure 10, the different alkali chlorides bring forward a wide spectrum of morphologies. The general trends among the mixed W/Mo-alkali oxides (cf. Tables S2

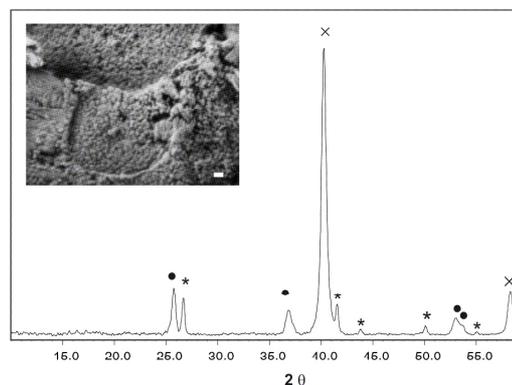


**Figure 9.** XRD pattern and a representative SEM image (inset, scale bar = 100 nm) of the product obtained after treatment of  $(\text{NH}_4)_{0.22}(\text{W}_{0.43}\text{Mo}_{0.57})\text{O}_3$  (containing 50 wt % BN) in 5%  $\text{H}_2/\text{He}$  atmosphere (key reflections: \* = BN, ● =  $\text{WO}_2$ -based motif, × = Mo–W alloy with W-structure).

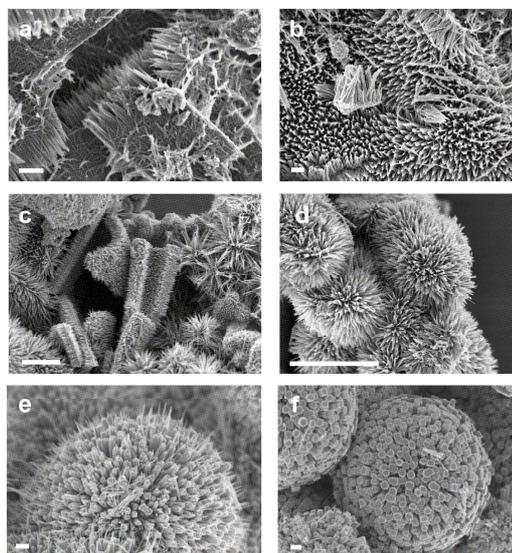


**Figure 10.** Representative SEM images of nanostructured (a) Li-W/Mo-HTB oxides, (b) Na-W/Mo-HTB oxides, nanostructured K-W/Mo-HTB oxides (c,d) and hierarchically grown Rb-W/Mo-HTB oxides (e,f) obtained from high initial M:W/Mo ratios (60:1); scale bar = 200 nm.

and S3, Supporting Information) can be compared to those observed among the binary hexagonal alkali tungstates,<sup>8</sup> whereas LiCl and NaCl favor the decomposition of micro-scale intermediates into fibrous products (Figure 10a,b), RbCl and CsCl induce a hierarchical nanostructuring on three levels that leads to the formation of complex spherical aggregates (Figures 10 and 11).

When the hydrothermal reaction is performed with RbCl, very small nanorods (ca. 20 nm in diameter) are organized into cylindrical bundles with diameters around 100 nm (Figure 10e,f). These nanorods assemble into regular spherical aggregates, and their shape can be further altered applying CsCl (Figure 11). In the presence of KCl, a transition from fibrous growth to the organization into flower-like patterns

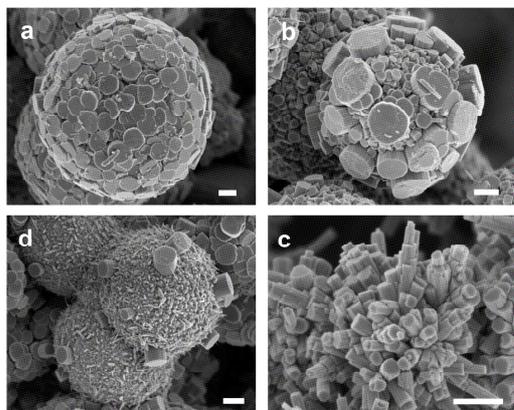


**Figure 11.** (a–d) Representative SEM images of nanostructured Cs-W/Mo oxides displaying spherical growth patterns (scale bar = 200 nm, M:W/Mo-ratio = 60:1).

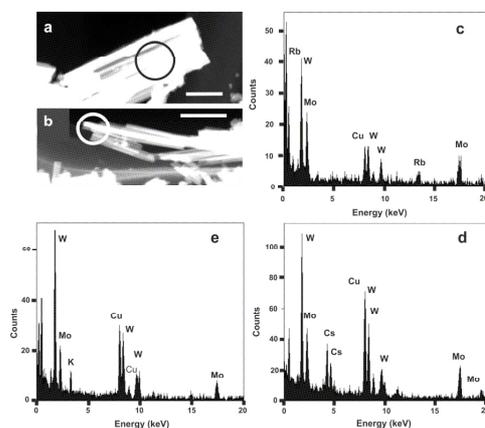


**Figure 12.** TEM images (scale bar = 100 nm) and EDX spot analyses of nanostructured K-W/Mo-HTB oxides (a,e), Rb-W/Mo-HTB oxides (b,c), and Cs-W/Mo oxides (d).

can be observed (Figure 10c,d). The products obtained in the MCl/AMT/MoO<sub>3</sub>·2H<sub>2</sub>O hydrothermal systems (M = Li–Rb) display the HTB structural motif. With CsCl, however, a small amount of pyrochlore (P-type) tungstate is obtained as a side product, and more detailed TEM characterizations are in progress. Previous studies in the CsCl/AMT hydrothermal system have shown that considerable optimization work is required to suppress the formation of P tungstates completely.<sup>8</sup>

Thus, the individual morphological trends of the alkali chlorides deteriorate when they are used in lower contents in the starting material: an initial M/(W/Mo)-ratio of 2.5:1 (M = Li–Cs) afforded strongly agglomerated spherical patterns of the alkali W/Mo-HTB oxides (cf. ESI for background analytical data).

The ratios of the metal atoms in the above-mentioned M-W/Mo oxides (M = Li–Cs) were analyzed with EDX spot analyses (Figure 12), verifying the simultaneous presence of W, Mo, and the respective alkali cation (K–Cs) in a single nanorod. The presence of Li and Na in the products was evidenced in terms of solid state NMR investigations

(for details cf. section 3.5). In the Li-based systems, the W/Mo-ratio points to an approximately 1:1 distribution of both elements in the product. This also applies for most areas of the Na-containing W/Mo-HTB oxides, but specific parts of the sample display a slight excess of W. On the basis of the overall atomic percent of metallic cations, the products obtained with KCl contain approximately 15–18 atom % K, whereas the HTB framework is enriched in tungsten. RbCl is incorporated to a similar extent (17–20 atom %) into a less homogeneous HTB structure that exhibits a wider variation of the W/Mo-ratio. Finally, the Cs-W/Mo oxides contain around 20 atom % Cs in a Mo-enriched environment. Small amounts of stabilizing ammonium cations from the AMT starting material are also included in the IITB channels. The amount of NH<sub>4</sub><sup>+</sup> decreases consequently with the size of the alkali cation, as has been reported for the alkali HTB systems (for details cf. ESI).<sup>8</sup>

**3.4.2. Influence of the Reaction Time and Temperature on the AMT/MoO<sub>3</sub>·2H<sub>2</sub>O Systems.** As outlined above, the formation of alkali HTBs takes between 2 and 5 h, whereas the growth of W/Mo-IITB oxides is completed after approximately 1 h of reaction time. Therefore, the reaction in the MCl/AMT/MoO<sub>3</sub>·2H<sub>2</sub>O (M = Li–Cs) systems was stopped after 5 or 16 h, respectively, of treatment at 180 °C. After this time, the formation of alkali W/Mo-HTBs was finished in none of the systems. In the presence of LiCl, the formation of a mixed compound exhibiting the orthorhombic (O) tungstate structural motif precedes the conversion into the HTB phase, and the process takes more than 16 h. After 5 h, the Li–W/Mo oxides display an unusual growth pattern: A considerable amount of the sample is transformed into intersecting disk-shaped microcrystals that display further internal nanostructuring (Figure 13a,b). With NaCl, the formation of fibrous HTB already sets in after 5 h of reaction time (Figure 13c), but considerable amounts of the products still show a structure that is closely related to the hexagonal molybdate motif.<sup>36</sup> Here, the structural conversion is almost complete after 16 h. The addition of KCl to the AMT/MoO<sub>3</sub>·2H<sub>2</sub>O system leads to the formation of a compound with very low crystallinity after 5 h exhibiting a remote structural resemblance to the HTB target material. However, the characteristic spherical growth patterns are already present in the product (Figure 13d), together with hollow microcrystals decaying into nanorods. The crystallinity and purity of the compound is substantially improved after 16 h. RbCl, however, does not give rise to pure HTB formation after 5 h of treatment, and a complex mixture of phases is formed, including Rb<sub>2</sub>Mo<sub>4</sub>O<sub>13</sub>, Rb-P-tungstate, and a phase displaying an orthorhombic mixed W/Mo oxide motif. Nevertheless, considerable parts of the sample are already organized into spherical aggregates after 5 h (Figure 13e). After 16 h of treatment, this mixture contains increasing amounts of the HTB phase. On the other hand, the addition of CsCl favors the formation of a HTB/P-based mixed oxide product, and the XRD patterns recorded after 5 h and 16 h of reaction time show close resemblance to those obtained after 2 d of reaction time (cf. section 3.4.1). The same holds for the sample morphology after 5 h (Figure 13f).

3030 Chem. Mater., Vol. 20, No. 9, 2008

Kiebach et al.

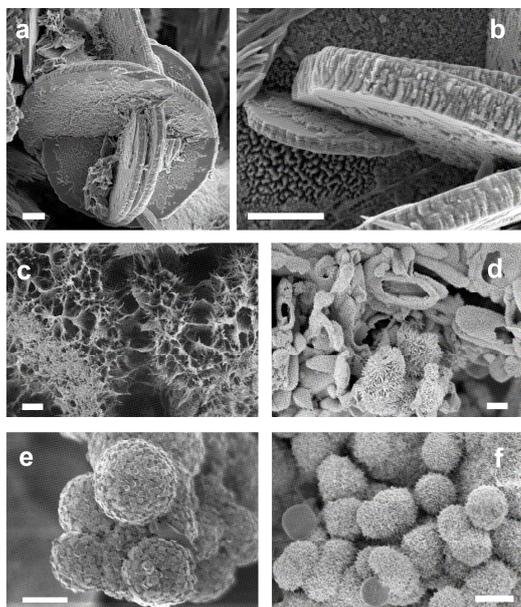


**Figure 13.** Representative SEM images of products formed after 5 h of hydrothermal treatment: (a,b) Li-W/Mo oxides (scale bar = 1  $\mu\text{m}$ ), (c) Na-W/Mo oxides, (d) K-W/Mo oxides, (e) Rb-W/Mo oxides, and (f) Cs-W/Mo oxides (c-f: scale bar = 2  $\mu\text{m}$ ).

Furthermore, the formation of W/Mo-HTBs in the presence of alkali chlorides was investigated at 120  $^{\circ}\text{C}$  (cf. ESD). Whereas  $(\text{NH}_4)_x(\text{W},\text{Mo})\text{O}_x$  HTB-rods with only very few remaining impurities are formed after 4 d of hydrothermal treatment at 100  $^{\circ}\text{C}$  from  $\text{AMT}/\text{MoO}_3 \cdot 2\text{H}_2\text{O}$  starting materials,<sup>9</sup> the conversion into M-W/Mo HTB-nanostructured materials (M = Li–Cs) requires higher temperatures and/or longer reaction times. These results point to a very complex interaction of the alkali chlorides with the  $\text{AMT}/\text{MoO}_3 \cdot 2\text{H}_2\text{O}$  hydrothermal system that requires detailed kinetic monitoring, and further investigations are in progress. Unlike the alkali HTB compounds that follow basically the same nucleation controlled mechanism, the formation pathways for alkali W/Mo-HTBs vary with the different MCl additives.

**3.5. Solid State NMR Spectroscopy on Alkali W/Mo-HTB Oxides.** Solid state NMR spectroscopy has been carried out in order to find evidence for mobility of the alkali metal sites within the transition metal oxides. All incorporated alkali metals ( $^7\text{Li}$ ,  $^{23}\text{Na}$ ,  $^{87}\text{Rb}$ , and  $^{133}\text{Cs}$ ) have half integer quadrupolar nuclear spins. Therefore, their solid state NMR spectra are dominated by the interaction of the quadrupolar moment with the electric field gradient. Chemical shift anisotropy and dipolar interactions are negligible in non-spherical symmetric environments. Furthermore, the central transition ( $\pm 1/2$ ) of non-integer spins is not affected by first order quadrupolar interactions, and MAS need only remove the much smaller second order effects leading to line narrowing by approximately a factor of four in rigid systems of low symmetry. The non-central transitions of half integer quadrupolar spins are suppressed as a result of first order

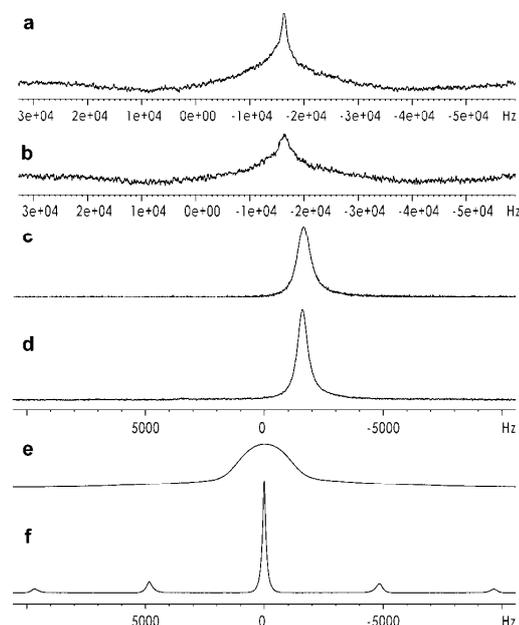


**Figure 14.** Solid state  $^{133}\text{Cs}$  NMR spectra of Cs-W/Mo-HTB oxide (a) with MAS and (b) without MAS and solid state  $^{23}\text{Na}$  NMR spectra of (c) Na-W/Mo HTB-oxide without MAS, (d) Na-W/Mo HTB-oxide with MAS, (e) NaCl without MAS, and (f) NaCl with MAS.

quadrupolar interactions and have therefore no influence onto the line shape.<sup>38</sup>

In our NMR studies the MAS line width dependency of the incorporated alkali chloride and comparison with the pure rigid chloride served as a probe for mobility. Line widths in the typical range of some kHz with high sensitivity to MAS are an indication for rigid systems. In contrast, narrow lines below 1 kHz with low sensitivity to MAS are evidence for diffusion, which averages the quadrupolar interactions in the solid environment within the NMR time scale, in the rapid mode leading to line shapes even as in the liquid phase. Furthermore,  $^7\text{Li}$   $T_1$  time measurements were carried out for the lithiated systems, applying the inversion recovery method.<sup>39</sup> The obtained  $T_1$  data served as an additional, sensitive probe for the dynamic behavior of the appropriate lithium sites. Generally, quadrupolar  $T_1$  relaxation is more efficient in dynamic systems with low symmetry, compared with rigid, symmetric systems, due to time-dependent spin lattice interactions, which occur in fluctuating environments.<sup>40</sup>

Cs-W/Mo-HTB oxide shows a broad  $^{133}\text{Cs}$  line (3.1 kHz) at 5 kHz MAS,  $-240$  ppm shifted relatively to CsCl (Figure 14a, b). Without MAS the line width increases up to 5.8 kHz, being in the typical range of a static system with lower symmetry as in pure CsCl, where the line width is 76 Hz at 5 kHz MAS and 840 Hz in the static rotor. Also the large chemical shift difference to pure CsCl indicates the

(38) Fyfe, C. A. *Solid State NMR for Chemists*; Guelph: Ontario, Canada, 1983.

(39) Cowan, B. *Nuclear Magnetic Resonance and Relaxation*; Cambridge University Press: New York, 1997.

(40) Abragam, A. *Principles of Nuclear Magnetism*, Clarendon Press, Oxford, 1986.

absence of isolated CsCl units and is evidence for the incorporation of Cs into the W/Mo oxide lattice.

In contrast to pure NaCl the  $^{23}\text{Na}$  resonance of the Na-W/Mo-HTB oxide (Figure 14c, d) is just slightly affected by MAS (510 Hz vs 660 Hz with and without MAS), being additionally much sharper as in the case of NaCl without MAS (660 Hz vs 2.6 kHz). That is in good agreement with the mobility of sodium which causes averaging effects leading to a fourfold sharper line, compared with the NaCl reference (Figure 14e, f). The chemical shift difference of 12 ppm relative to NaCl is not as significant as in the case of Cs relative to CsCl. Nevertheless, the line shape differences of Na-W/Mo-HTB oxide and pure NaCl (510 Hz vs. 160 Hz) at 5 kHz MAS show that the sodium environment in Na-W/Mo-HTB oxide is of lower symmetry, and therefore, no NaCl lattice is present.

Comparison of the  $^7\text{Li}$  signals of Li-W/Mo-HTB oxide and Li-HTB tungstate suggests a higher lithium mobility in the latter one, where the line width without MAS amounts to 230 Hz in contrast to 5.8 kHz in Li-W/Mo-HTB oxide (Figure 15). In contrast to the sodium and cesium species, the NMR spectra of the lithiated compounds are influenced by chemical shift anisotropy (csa) effects rather than by quadrupolar interactions. Therefore, broad rotation side band patterns are observed under MAS conditions. This is evidence for a quasi-spherical symmetry with small electric field gradients at the lithium sites, resulting in just small quadrupolar interactions which are insignificant with respect to the csa effects. The presence of rotation side bands under MAS conditions not only for Li-W/Mo-HTB oxide but also in the case of Li-HTB tungstate indicates for the latter that there is rather a hindered lithium reorientation instead of free diffusion which would completely wipe out csa effects.

Li-W/Mo-HTB and Li-HTB tungstate show narrow  $^7\text{Li}$  line widths (<70 Hz) under MAS conditions and two lithium sites with a chemical shift difference of 1.8 ppm could be distinguished for Li-HTB tungstate. The sharper line at lower field shows a narrow rotation side band pattern in contrast to the much broader high field signal with its large rotation side band extension. These differences are due to different environmental symmetries and site mobilities, as shown with  $^7\text{Li}$   $T_1$  time measurements. The sharp low field signal of Li-HTB tungstate exhibits a  $T_1$  time of just 469 ms, which is some orders of magnitude smaller than that one of  $^7\text{Li}$  in pure LiCl (449 s). In contrast, the broad high field component of Li-HTB tungstate ranges with a  $T_1$  time of 12.1 s between the values of pure LiCl and the Li-HTB tungstate component in the fast exchange mode. In the case of Li-W/Mo-HTB the  $^7\text{Li}$   $T_1$  time amounts to 481 ms, which is comparable with the value of Li-HTB tungstate in the fast mode. This suggests a lower symmetry of the Li-W/Mo-HTB site which compensates the low lithium mobility and gives rise to a  $T_1$  value, which is as short as the one of Li-HTB tungstate. Although  $^{87}\text{Rb}$  has a high NMR sensitivity and a nuclear quadrupolar moment comparable with  $^{23}\text{Na}$  and is therefore easy to detect, attempts to observe it in the W/Mo oxide framework were not successful. Under MAS conditions the RuCl reference showed a  $^{87}\text{Rb}$  line shape pattern similar to that of NaCl already after four scans, but the spectrum of

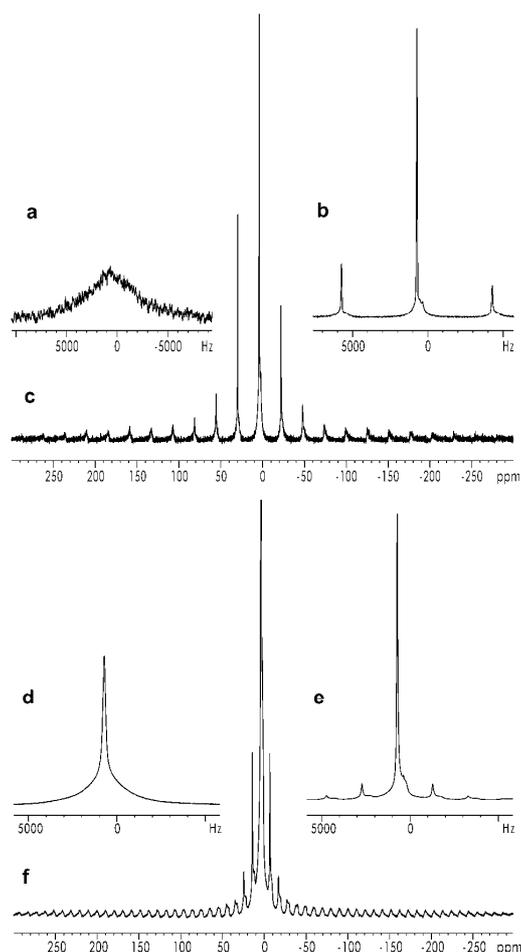


**Figure 15.** Solid state  $^7\text{Li}$  NMR spectra of Li-W/Mo-HTB oxide (a) without MAS and (b,c) with MAS compared to solid state  $^7\text{Li}$  NMR spectra of Li-HTB oxide (d) without MAS and (e,f) with MAS.

Rb-W/Mo-HTB oxide did not reveal any  $^{87}\text{Rb}$  resonance even after 80 000 scans. This may be due to a tight fixation of rubidium in a low symmetric environment, leading to strong quadrupolar couplings causing line widths which exceed the limits of the NMR facility that was used. Isolated RbCl units do obviously not exist in the framework, because they should lead to an intense line pattern similar to pure RbCl.

#### 4. Discussion

Mixed nanoscale W/Mo-HTB oxides are accessible from AMT and  $\text{MoO}_3 \cdot 2\text{H}_2\text{O}$  in a one-step hydrothermal reaction within approximately 1 h of reaction time at 180 °C. In situ EDXRD studies revealed that the kinetics of W/Mo-HTB nanorod growth is slower than that observed for the formation of  $\text{MoO}_3$  fibers but faster than the growth process of nanostructured tungstates. Therefore, the slower growing tungstate component of the hydrothermal system determines both the nucleation-controlled formation mechanism and the overall reaction kinetics.<sup>7,8</sup> As a result, anisotropic W/Mo-

HTB oxides are obtained that are intermediate with respect to both the aspect ratio and the growth velocity of the binary Mo- and W-oxide nanomaterials. Other than in the binary systems, a hexagonal intermediate phase ( $(\text{NH}_4)_{0.94}\text{H}_{3.3}\text{Mo}_{5.3}\text{O}_{18}$ ) could be identified in the course of the in situ EDXRD investigations. These results point out that the “construction” of ternary nanoparticles with a specific phase and morphology from binary hydrothermal systems is in principle possible. However, the underlying reaction mechanism may be different, and therefore each hydrothermal system must be studied individually. The present results furthermore indicate that much more information is required before the combination of hydrothermal processes and the general application of synthetic principles can be employed as a true “design” approach towards nanostructured materials. This holds especially for the complex redox and structural chemistry of ternary systems containing transition metal oxides, as has been illustrated in a recent in situ study on the formation of bismuth molybdate catalysts.<sup>41</sup> Even though in situ analyses provide the most valuable mechanistic insights, the optimization of materials is still a challenging interplay of established synthetic principles and concrete parameter optimizations in a given system. Furthermore, the hydrothermal formation of W/Mo-HTB oxides can be steered through the use of alkali chlorides as additives.<sup>42</sup> As has been observed for the formation of nanoscopic alkali HTBs, the individual alkali cations exhibit different morphological profiles:<sup>8</sup> whereas the addition of LiCl and NaCl directs the W/Mo-HTB oxides into fibrous structures, KCl as an additive induces an arrangement of these nanofibers into spherical patterns. This tendency is intensified with RbCl and CsCl, thereby resulting in a hierarchical organization of nanorods on three levels into microspheres. Among the hydrothermal reaction parameters, the type and concentration of the alkali additive exerts the most pronounced influence on the resulting morphology, followed by the reaction temperature and the reaction time. More detailed investigations concerning the effect of time and temperature on the phase of the product unraveled that the formation of mixed alkali W/Mo-HTB oxides displays different kinetics from the additive-free hydrothermal system. Further kinetic investigations are therefore in progress to shed light on the complex relations between cation incorporation, morphology control and the resulting growth kinetics. The preliminary results indicate that the presence of alkali cations further complicates the formation mechanisms of the resulting nanostructured W/Mo-HTB oxides: The individual cations display different kinetic profiles, and—other than in our previous studies—they also seem to change in the reaction mechanism. While the formation of hierarchical nanopatterns, for example, in the recently investigated  $\text{BaWO}_4$  system,<sup>43</sup> can easily be classified on the basis of electron microscopy studies and other ex situ data as “oriented aggregation mechanism” with nucleation control, it takes considerably more effort to assign

all intermediates and steps occurring in the formation process. The present results are a step towards such understanding, but the precise interaction of the different alkali cations with the planes of the different growing mixed W/Mo-oxide intermediates probably requires additional calculation methods. However, this effort is worthwhile to fully exploit the numerous applications of W/Mo materials in catalysis, sensor technology, and the construction of smart electrochromic materials. Especially for the production of nanostructured catalysts that benefit from the synergistic interaction of the two transition metal oxides, information about the thermal stability of the W/Mo-HTB framework and its follow-up reactions in different reactions is of key importance. Complementary in situ XRD and EXAFS techniques provide an excellent opportunity to monitor the onset of structural changes in nanoscale W/Mo HTB oxides and their subsequent transformation into other nanomaterials in oxidizing and reducing atmospheres. In the  $\text{O}_2/\text{He}$  atmosphere, the mixed oxide material can be handled up to 390 °C without major structural changes, and a monoclinic structural motif is formed at higher temperatures. The thermal resilience is even higher in an  $\text{H}_2/\text{He}$  environment: Above 500 °C, the gradual formation of a nanostructured mixed W/Mo-metal sets in. Fourier transformed EXAFS data allowed monitoring these gradual structural changes individually for the local structure around the different absorber atoms before the net structural alterations are evident from the XRD patterns. This provides very detailed information for the thermal treatment and synthetic use of mixed W/Mo-HTBs.

As additive substances are key morphological tools in nanomaterials synthesis, their interaction with the structure of the target material needs to be studied in detail. In the case of alkali W/Mo-HTBs, solid state NMR spectroscopy illustrates that the interaction of the different intercalated alkali cations with the host W/Mo-channel structure influences not only the external morphology but also the cationic mobility within the channel system. Whereas the small  $\text{Li}^+$  cations can occupy two sites with different environments and mobilities, the sodium cations display significant mobility only on the larger site. Consequently,  $\text{Cs}^+$  ions are highly stabilizing yet less mobile. Interestingly, the substitution of W by Mo in the HTB channel framework also affects the mobility of the cations, as has been demonstrated comparing Li-W/Mo HTB oxides with their Mo-free analogues.

## 5. Conclusion

This study presents a multidisciplinary investigation of the hydrothermal kinetics, morphochemistry, and follow-up treatment of nanostructured W/Mo-HTB oxides. It demonstrates how preparative processes and analytical methods applied on the binary oxide systems can be extended upon the complex task of the controlled synthesis of ternary nanomaterials. On the preparative level, the use of readily available ionic additives opens up a wide spectrum of nanoscale morphologies. In situ EDXRD methods have proven to be a powerful tool to track down an intermediate compound in the nucleation-controlled formation of mixed W/Mo-HTBs. Concerning the follow-up treatment of the W/Mo-oxide nanomaterials in different atmospheres, a

(41) Beale, A.M.; Le, M. T.; Hoste, S.; Sankar, G. *Solid State Sci.* **2005**, *7*, 1141.

(42) Michailovski, A.; Krumeich, F.; Patzke, G. R. *Helv. Chim. Acta* **2004**, *87*, 1029.

(43) Luo, Y.; Tu, Y.; Yu, B.; Liu, J.; Li, J.; Jia, Z. *Mater. Lett.* **2007**, *61*, 5250.

combination of in situ EXAFS and in situ XRD is required to keep track of the complex structural transformations. The results are currently applied on the development of W/Mo-HTB-based catalysts.

The complex interplay between the internal W/Mo substitution in the hexagonal channel structure, the external morphological influence of the additive cation, and its mobility in the resulting mixed nanomaterials is furthermore investigated with the help of solid state NMR spectroscopy. All in all, alkali W/Mo-HTB compounds are excellent model systems for deriving structure-morphology relationships that are essential for the future design of nanomaterials and the results yield some rules of thumb for the synthesis of nanoparticles with a special shape and size. Further investigations on different oxidic systems are required to show whether some general rules can be formulated allowing a better control of the size, shape, and morphology of the nanosized materials.

**Acknowledgment.** We thank the Swiss-Norwegian beamlines at ESRF for providing beamtime for the in situ EXAFS/XRD measurements. H. Emmerich and W. van Beek (SNBL) are

acknowledged for their kind support during the experiments. We gratefully acknowledge HASYLAB (DESY, Hamburg, Germany) for providing beamtime at beamline F3 for in situ EDXRD experiments. We thank Prof. Dr. Reinhard Nesper (Laboratory of Inorganic Chemistry, ETH Zurich) for the support of this work. The authors acknowledge support of the Electron Microscopy ETH Zurich, EMEZ. We thank Dr. Frank Krumeich, EMEZ, for STEM and EDX analyses. We are grateful to Heinz Spring, Institute of Inorganic Chemistry, University of Zurich, for elemental analyses. Financial support by the Swiss National Science Foundation (SNF Professorship PP002-114711/1 and MaNEP - Materials with Novel Electronic Properties) and by the University of Zurich is gratefully acknowledged.

**Supporting Information Available:** In situ XANES/EXAFS spectra of W/Mo-HTB oxide, elemental analyses concerning the ammonium content of alkali W/Mo-HTB oxides, preparative details of the hydrothermal preparation of alkali W/Mo HTBs (SEM images and tables), and additional EDX spot analyses of nanostructured alkali W/Mo HTBs (PDF). This material is available free of charge via the Internet at <http://pubs.acs.org>.

CM7028036

### 4.3.2. EDXRD-Untersuchungen zur Bildung von Bi<sub>2</sub>O<sub>3</sub>-Nanodrähten sowie nanostrukturierter W/Mo-HTB-Oxide

In Kooperation mit Frau Prof. G. Patzke wurden auch folgende Reaktionen mit in-situ-EDXRD untersucht: die Bildung von Bi<sub>2</sub>O<sub>3</sub>-Nanodrähten aus  $\alpha$ -Bi<sub>2</sub>O<sub>3</sub>-Pulver sowie die Bildung nanostrukturierter W/Mo-HTB-Oxide. Die Versuche wurden am Messplatz F3 (Kap. 3.3) in der in Kapitel 3.2 beschriebenen in-situ-Apparatur durchgeführt.

Da sich die beiden Manuskripte noch im Stadium der Vorbereitung befinden, sollen an dieser Stelle nur die wichtigsten Ergebnisse schlaglichtartig zusammengefasst werden.

Die Bildung von  $\alpha$ - und  $\beta$ -Bi<sub>2</sub>O<sub>3</sub>-Nanodrähten aus Bi<sub>2</sub>O<sub>3</sub>-Pulver in Gegenwart von K<sub>2</sub>SO<sub>4</sub> wurde bei 160 °C untersucht. Nach 30 min war die Reaktion abgeschlossen. Aufgrund der guten Kristallinität und Streukraft des Materials konnte eine Zeitauflösung von 20 sec pro Spektrum erzielt werden. Bei den Reaktionen konnten keine Auflösungsprozesse oder kristallinen Intermediate beobachtet werden. Die Produkte zeigen die gleichen Spektren wie die Edukte. Daher kann angenommen werden, dass die Nanodrähte in Wasser durch eine durch K<sub>2</sub>SO<sub>4</sub>-unterstützte Fest-Fest-Reaktion gebildet werden, bei der das Wachstum aus ungelösten  $\alpha$ -Bi<sub>2</sub>O<sub>3</sub>-Partikeln beginnt.

Die Morphologie der W/Mo-HTB-Oxide (HTB = Hexagonal Tungsten Bronze) kann durch die Zugabe von Alkalichloriden als Additive modifiziert werden. Die Synthese nanokristalliner W/Mo-HTB-Oxide sowie der Einfluss der Alkalichloride als Additive auf Produktmorphologie und Bildungsmechanismen wurden mit in-situ-EDXRD verfolgt. Die Zugabe von LiCl und NaCl führt zur Ausbildung faserartiger Strukturen und KCl als Additiv ermöglicht den Übergang zu sphärischen Partikeln, wobei die Tendenz zu kugelartigen Morphologien mit RbCl und CsCl noch zunimmt.

Ein typisches Experiment (mit einem Verhältnis von Mo : W = 1 : 2 mmol) wurde mit 148 mg (NH<sub>4</sub>)<sub>6</sub>[H<sub>2</sub>W<sub>12</sub>O<sub>40</sub>] · ~ 3 H<sub>2</sub>O, 58 mg MoO<sub>3</sub> · 2 H<sub>2</sub>O, 2 mmol ACl (A = Li -

Cs) in 1.5 mL 25 %iger Essigsäure bei 180 °C durchgeführt. Die Aufnahmezeit pro Spektrum betrug 120 sec.

Die Auswertung der Spektren ergibt, dass die Kristalle ohne Vorzugsorientierung wachsen, d. h. es liegt isotropes Wachstum vor. Mit zunehmender Intensität der Produktreflexe wird eine simultane Abnahme der Intensität der Eduktreflexe (Schnittpunkt der Kurven bei einem Reaktionsfortschritt von  $\alpha = 0.5$ ) beobachtet. Bei Zugabe von KCl, RbCl und CsCl erfolgt die Auflösung der Edukte so schnell, dass zwar eine weitere Auswertung erfolgt ist, die Resultate allerdings mit Vorsicht zu betrachten sind. In Abb. 4.15 sind das Wachstum des (002)-Reflexes sowie die unterschiedlichen Induktionszeiten in Abhängigkeit der verschiedenen Additive dargestellt. Die Induktionszeiten werden durch die Alkalimetallionen verkürzt und die Reaktionen laufen schneller ab. Die Vermutung, dass die Kristallisationsprozesse mit der Natur der Additive variieren, konnte bestätigt werden. Der Mechanismus des Produktwachstums hängt vom entsprechenden Alkalimetallion ab.

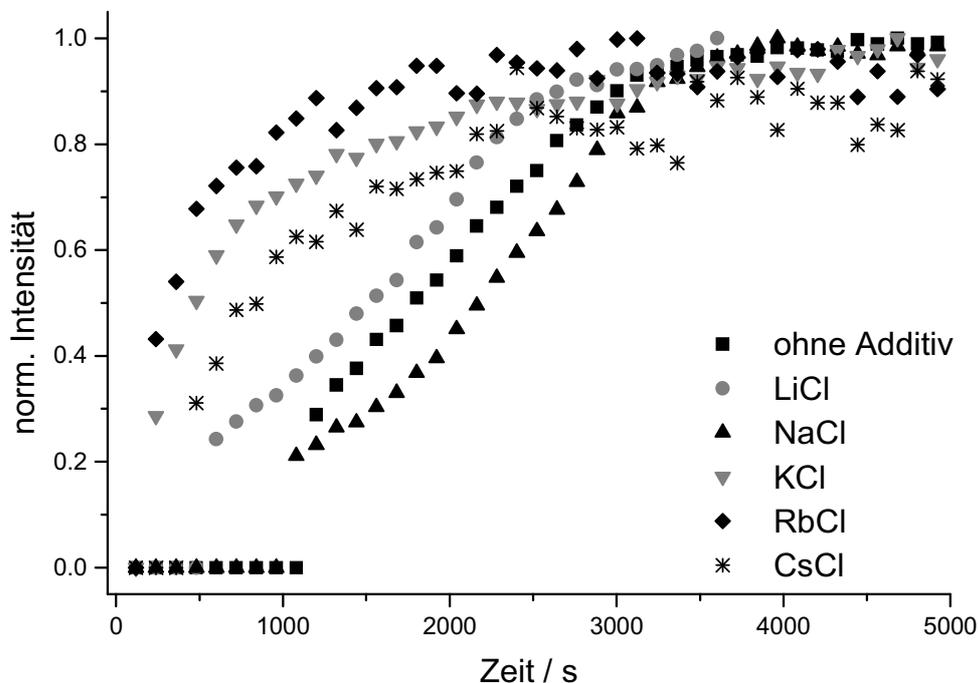


**Abb. 4.15:** Verlauf des Wachstums des (002)-Reflexes unter Zugabe verschiedener Alkalimetallionen.

Bei der Reaktion mit LiCl wird zu Beginn das Wachstum durch Diffusionskontrolle bestimmt und geht im weiteren Verlauf in nukleationskontrollierte Mechanismen

über. Ein vergleichbares Verhalten wird auch bei den Reaktionen ohne Additive erhalten. Mit NaCl scheint zuerst Phasengrenzkontrolle vorzuliegen und mit fortschreitender Reaktion dominieren dann nukleationskontrollierte Mechanismen. Interessanterweise werden für KCl, RbCl und CsCl als Additive vergleichbare Mechanismen beobachtet. Die Synthesen zeigen im Vergleich zu LiCl oder NaCl keinen Mechanismuswechsel und die Bildung wird durch Diffusion kontrolliert. Bemerkenswert ist zudem, dass sich die Ergebnisse der EDXRD-Untersuchungen in den TEM-Aufnahmen widerspiegeln. Die faserartige Produktmorphologie der Synthesen ohne Additiv ähnelt denen mit LiCl- und NaCl-Zusatz und eher sphärische Nanopartikel werden durch KCl-, RbCl- und CsCl-Zugabe ausgebildet.



## 5. Zusammenfassung und Ausblick

Die Darstellung und Charakterisierung neuer Thiostannate durch die Integration von Übergangsmetallkationen war ein wesentliches Ziel dieser Arbeit. Die Synthesen erwiesen sich als erfolgreich und es konnten 13 neue Thiostannate, davon zwölf mit integrierten Übergangsmetallkationen, dargestellt werden. Anfängliche experimentelle Probleme konnten beseitigt werden, so dass die Synthesen deutlich erfolgreicher verliefen. Das synthetische Potential zur Darstellung neuer, funktionalisierter Thiostannate ist noch lange nicht erschöpft, und in den letzten Jahren wurde eine große Anzahl an Übergangsmetall- aber auch lanthanoidenhaltigen Chalkogenidometallaten synthetisiert und charakterisiert. Die Wahl neuer strukturdirigierender Reagenzien sowie geschickte Variationen der Synthesebedingungen sollten das Auffinden neuer Verbindungen ermöglichen, welche weitere Untersuchungen der Struktur-Eigenschafts-Beziehungen erlauben.

Die Integration von Kupfer in die anionischen Ketten oder Schichten ist in den Thiostannaten  $(\text{DBUH})\text{CuSnS}_3$ ,  $(1,4\text{-dabH}_2)\text{Cu}_2\text{SnS}_4$ ,  $(\text{DBNH})_2\text{Cu}_6\text{Sn}_2\text{S}_8$  und  $(\text{dienH}_2)\text{Cu}_2\text{Sn}_2\text{S}_6$  gelungen. Die Elemente Kupfer, Zinn und Schwefel wurden in (nahezu) reinen Aminen (vgl. verwendete Chemikalien, Kap. 3.5) bei allen Synthesen ein- und umgesetzt. Die Reaktionsprodukte enthalten neben den Thiostannaten oft diverse Zinn- und Kupfersulfide und die Ausbeuten sind zum Teil gering. Die Versuche zur Syntheseoptimierung waren oft nicht sehr erfolgreich, so dass durch „trial and error“ Vorgehen der/die Parameter erfasst werden musste/n, welche die Bildung der Zielverbindungen positiv beeinflussen. Bei den Synthesen hat sich herausgestellt, dass die Wahl des strukturdirigierenden Reagenz von entscheidender Bedeutung ist. Cyclische Amine wie beispielsweise 1,8-Diazabicyclo[5.4.0]undec-7-en (DBU) sind durch andere Eigenschaften gekennzeichnet als langkettige wie 1,4-Diaminobutan (1,4-dab). Die unterschiedlichen Siedepunkte oder Viskositäten sind dabei ebenso wichtig wie die Fähigkeit, Protonen abfangen zu können. Zusätzlich spielt sicher das Redoxpotential der Amine eine wichtige Rolle, was bis heute schlecht verstanden bzw. nicht hinreichend untersucht ist.

Die Strukturen von  $(\text{DBUH})\text{CuSnS}_3$  und  $(1,4\text{-dabH}_2)\text{Cu}_2\text{SnS}_4$  sind sehr verschieden, obwohl in beiden Verbindungen eindimensionale Anionenketten von protonierten Aminmolekülen umgeben sind. Zwei  $\text{SnS}_4$ -Tetraeder in  $(\text{DBUH})\text{CuSnS}_3$  bilden durch Verknüpfung über eine gemeinsame Kante eine  $\text{Sn}_2\text{S}_6$ -Einheit aus. Benachbarte  $\text{Sn}_2\text{S}_6$ -Gruppen sind mit  $\text{CuS}_2$ -Hanteln zu anionischen  $[\text{CuSnS}_3]^-$ -Ketten verbunden. Im Vergleich dazu sind in  $(1,4\text{-dabH}_2)\text{Cu}_2\text{SnS}_4$  die  $\text{SnS}_4$ -Tetraeder mit zwei  $\text{CuS}_3$ -Einheiten zu anionischen  $[\text{Cu}_2\text{SnS}_4]^{2-}$ -Ketten verknüpft. Die unterschiedlichen sekundären Baueinheiten (secondary building units, SBU) und bezüglich Cu auch primären Baueinheiten (primary building units, PBU) könnten dadurch erklärt werden, dass DBU nur einfach protoniert wird, während 1,4-dab zwei positive Ladungen trägt. Bis jetzt sind allerdings die Einflüsse der Amine auf die Bildung der PBU/SBU in Lösung und deren Stabilität nur unzureichend untersucht worden.

1,5-Diazabicyclo[4.3.0]non-5-en (DBN) kommt neben DBU in der organischen Chemie oft als Nukleophil zum Einsatz. Die Erwartungen, dass die kleineren Moleküle Auswirkungen auf mögliche Kristallstruktur haben, konnte nachgewiesen werden. Die Schichtverbindung  $(\text{DBNH})_2\text{Cu}_6\text{Sn}_2\text{S}_8$  kristallisiert in der nicht-zentrosymmetrischen Raumgruppe  $\text{Pca}2_1$ . Die Struktur besteht aus wellenförmigen Anionenschichten und protonierten Aminmolekülen zwischen diesen Schichten. Die Verknüpfung der  $\text{SnS}_4$ -Tetraeder mit den  $\text{CuS}_3$ -Einheiten führt zur Ausbildung von  $6^3$ -Graphitschichten, die bislang noch nicht bei Thiostannaten beobachtet worden sind. Darüber hinaus werden im Reaktionsprodukt nicht nur Sulfide als weitere Reaktionsprodukte gefunden, sondern noch eine interessante „Nebenphase“ beobachtet. Hierbei handelt es sich um das übergangsmetallfreie, gemischtvalente  $\text{Sn(II)/Sn(IV)}$ -Thiostannat  $(\text{DBNH})_2\text{Sn}_3\text{S}_6$ . Anionische Ketten alternierender  $\text{Sn}_3\text{S}_4$ -Halbwürfel und  $\text{Sn}_2\text{S}_2$ -Ringe bilden die wesentlichen Strukturmerkmale, und die ladungskompensierenden Kationen sind in den Ausbuchtungen benachbarter Ketten lokalisiert. Bei weiteren Synthesen konnte nachgewiesen werden, dass für die Bildung der gemischtvalenten Verbindung die Gegenwart von Kupfer nicht erforderlich ist. Das Auftreten gemischtvalenter Thiostannate ist recht selten. Besonders bemerkenswert ist, dass diese Verbindung in Koexistenz mit einem kupferhaltigen Thiostannat unter den gewählten Reaktionsbedingungen auftritt. Der Frage, welche Parameter die Bildung dieser beiden Verbindungen

beeinflussen, wurde mit den in-situ-Experimenten mit energiedispersiver Röntgenbeugung untersucht.

Als weiterer, langkettiger „Strukturdirektor“ wurde das Amin Diethylentriamin (dien) verwendet. Kristalle der Verbindung  $(\text{dienH}_2)\text{Cu}_2\text{Sn}_2\text{S}_6$  konnten nach anfänglichen experimentellen Schwierigkeiten schließlich von ausreichender Qualität dargestellt werden, so dass die Strukturbestimmung möglich war. Das Thiostannat kristallisiert in Form schwarzer Plättchen und kann unter dynamischen Bedingungen in guten Ausbeuten phasenrein dargestellt werden. Die Struktur besteht aus  $[\text{Cu}_2\text{Sn}_2\text{S}_6]^{2-}$ -Schichten und protonierten Aminmolekülen als ladungskompensierende Kationen, die zwischen den Schichten lokalisiert sind. Das  $[\text{Cu}_2\text{Sn}_2\text{S}_6]^{2-}$ -Schichtanion ist aus allseitig eckenverknüpften  $\text{CuS}_4$ -Tetraedern aufgebaut, die von Ketten eckenverknüpfter  $\text{SnS}_4$ -Tetraeder sandwichartig umgeben sind. Die Verbindung ist ein direkter Halbleiter mit einer optischen Bandlücke von 1.51 eV. Obgleich der spezifische Widerstand des Thiostannats recht groß ist, konnten orientierende Widerstands- bzw. Leitfähigkeitsmessungen durchgeführt werden. Der spezifische Widerstand nimmt unter UV-Belichtung um den Faktor 3 ab. Vorläufige Ergebnisse dieser Untersuchungen belegen die Photoleitfähigkeit des Materials, die viel versprechende Anwendungen nach sich ziehen könnte.

Das Amin Diethylentriamin ist in  $(\text{dienH}_2)\text{Cu}_2\text{Sn}_2\text{S}_6$  zwischen den Schichten lokalisiert. Die Idee, den Schichtabstand durch „Vergrößerung“ der strukturdirigierenden Reagenzien zu verändern, konnte mit den Aminen Triethylentetramin (trien) und Tetraethylenpentamin (tepa) nicht erfolgreich realisiert werden. Die Synthesen mit Kupfer (oder Cu-Verbindungen) waren nicht erfolgreich, was darauf hindeutet, dass die optimalen Synthesebedingungen noch nicht ermittelt werden konnten.

Da in den vier Thiostannaten das Kupfer in der Oxidationsstufe +I vorliegt, könnten Cu(I)-Edukte (z. B.  $\text{CuCl}$  oder  $\text{Cu}_2\text{S}$ ) als alternative Eduktquellen zum Einsatz kommen. Einige Versuche mit zweiwertigen Kupfersalzen wurden bereits mit Erfolg durchgeführt. So kann beispielsweise  $(\text{dienH}_2)\text{Cu}_2\text{Sn}_2\text{S}_6$  ebenfalls mit Cu oder  $\text{CuCl}_2 \cdot 2 \text{H}_2\text{O}$ , Sn oder  $\text{SnS}_2$  und S in vergleichbarer Ausbeute dargestellt werden, wobei allerdings die Kristallqualität bei den Synthesen mit den Elementen besser ist. Unter Verwendung anderer strukturdirigierender Reagenzien und

anderer Edukte sollten weitere kupferhaltige Thiostannate mit interessanten Eigenschaften darstellbar sein.

Ausgehend von den Bedingungen der bereits erhaltenen Verbindungen wurden weitere Variationen der Synthesen durchgeführt. Silber als ebenfalls chalkophiles Element konnte erfolgreich bei Verwendung von 1,4-Diaminobutan in anionische Thiostannat-Ketten integriert werden. Die Verbindung  $(1,4\text{-dabH}_2)\text{Ag}_2\text{SnS}_4$  ist zu  $(1,4\text{-dabH}_2)\text{Cu}_2\text{SnS}_4$  isostrukturell. Dies ist erstaunlich, da bisher keine isostrukturellen kupfer- und silberhaltigen Thiometallate beobachtet werden konnten. Anzumerken ist auch noch, dass die Synthesen mit Kupfer oder Silber oft zur Kristallisation binärer oder ternärer Sulfide geführt haben. Das ist ein deutlicher Hinweis darauf, dass diese dichten Phasen auch unter solvothormalen Bedingungen sehr stabil sind.

Im Vergleich zu anderen Übergangsmetallen weist Mangan eine ähnliche Affinität zu Schwefel wie zu Stickstoff auf. Die Annahme hat sich mit der Synthese der Verbindung  $(1,4\text{-dabH})_2\text{MnSnS}_4$  als richtig erwiesen.  $(1,4\text{-dabH})_2\text{MnSnS}_4$  wurde unter analogen Bedingungen wie  $(1,4\text{-dabH}_2)\text{Cu}_2\text{SnS}_4$  und  $(1,4\text{-dabH}_2)\text{Ag}_2\text{SnS}_4$  erhalten, weist allerdings einen anderen, neuartigen Strukturtyp auf. Es ist zudem das erste Thiostannat, in dem  $\text{Mn}^{2+}$ -Kationen in die anionischen Ketten integriert sind. Das wesentliche Strukturmotiv kann mit der Substitution eines  $\text{SnS}_4$ -Tetraeders durch einen  $\text{MnS}_4$ -Tetraeder in dem Thiostannat-Anion  $[\text{Sn}_2\text{S}_6]^{4-}$  erklärt werden. Die resultierenden  $[\text{MnSnS}_6]$ -Einheiten bilden durch Kantenverknüpfung eindimensionale Ketten, die von einfach protonierten Aminmolekülen umgeben sind.

Üblicherweise bestehen die in der Literatur beschriebenen manganhaltigen Thiostannate aus  $[\text{Mn}(\text{Amin})_x]^{2+}$ -Komplexen und  $[\text{Sn}_2\text{S}_6]^{4-}$ -Anionen (vgl. Kap. 1.3). Synthesen mit 1,2-Diaminocyclohexan (1,2-dach) führten zur Bildung der neuen Thiostannate  $[\text{Mn}(1,2\text{-dach})_2(\text{H}_2\text{O})]_2\text{Sn}_2\text{S}_6$  und  $[\text{Mn}(1,2\text{-dach})_2]\text{Sn}_2\text{S}_6 \cdot 2(1,2\text{-dach})$ . Die Kristallisation der Verbindungen ist dabei abhängig von der Konzentration des Amins. Niedrige Konzentrationen führen zur Ausbildung diskreter  $[\text{Mn}(1,2\text{-dach})_2(\text{H}_2\text{O})]_2\text{Sn}_2\text{S}_6$ -Einheiten, wohingegen bei höheren Konzentrationen die eindimensionale Verbindung  $[\text{Mn}(1,2\text{-dach})_2]\text{Sn}_2\text{S}_6 \cdot 2(1,2\text{-dach})$  bevorzugt wird. In  $[\text{Mn}(1,2\text{-dach})_2(\text{H}_2\text{O})]_2\text{Sn}_2\text{S}_6$  sind die  $\text{Mn}^{2+}$ -Kationen von zwei Aminmolekülen und einem Wassermolekül komplexiert und haben eine Bindung zu einem S-Atom des Thiostannat-Anions. Als Teil der anionischen

Ketten agieren die  $[\text{Mn}(\text{Amin})_x]^{y+}$ -Komplexe in  $[\text{Mn}(1,2\text{-dach})_2]\text{Sn}_2\text{S}_6 \cdot 2$  (1,2-dach) und  $[\text{Mn}(\text{trien})]_2\text{SnS}_4 \cdot 4 \text{H}_2\text{O}$ .

Beim Einsatz von Triethylentetramin konnte die Verbindung  $[\text{Mn}(\text{trien})]_2\text{SnS}_4 \cdot 4 \text{H}_2\text{O}$  dargestellt werden. Die Struktur besteht aus  $\text{SnS}_4$ -Tetraedern, die  $\text{Mn}^{2+}$ -zentrierte Doppeloktaeder verknüpfen. Zwei der vier S-Atome des  $[\text{SnS}_4]^{4-}$ -Anions sind  $\mu_3$ -verbrückend. Die resultierende ladungsneutrale Kette kann als Koordinationspolymer angesehen werden mit den Doppeloktaedern als Knoten und den Anionen als Linker.

Im Gegensatz zu den Versuchen mit Kupfer konnten mit Mangan und den Aminen Triethylentetramin sowie Tetraethylenpentamin neue Verbindungen synthetisiert werden. Da manganhaltige Thio- und Selenidostannate mit tepa bereits publiziert wurden, wurden bei weiteren Synthesen andere Übergangsmetalle eingesetzt und die Thiostannate  $[\text{Co}(\text{tepa})]_2\text{Sn}_2\text{S}_6$ ,  $[\text{Fe}(\text{tepa})]_2\text{Sn}_2\text{S}_6$  und  $[\text{Ni}(\text{tepa})]_2\text{Sn}_2\text{S}_6$  dargestellt. In allen Verbindungen werden isolierte  $[\text{M}(\text{tepa})]_2\text{Sn}_2\text{S}_6$ -Einheiten ( $\text{M} = \text{Co}, \text{Fe}, \text{Ni}$ ) beobachtet, in denen ein  $[\text{Sn}_2\text{S}_6]^{4-}$ -Anion zwei  $[\text{M}(\text{tepa})]^{2+}$ -Kationen verknüpft. Die nickelhaltige Verbindung kristallisiert interessanterweise in einem anderen Strukturtyp als die beiden anderen, die zueinander isostrukturell sind. Vermutlich sind unterschiedliche Wechselwirkungen wie  $\text{S} \cdots \text{H}$ -Bindungen sowie Packungseffekte dafür verantwortlich.

Nicht nur bei den manganhaltigen Thiostannaten, die in Abhängigkeit von der Konzentration des 1,2-Diaminocyclohexans gebildet werden, spielt das Lösungsmittel Wasser eine wichtige Rolle. Was aber passiert, wenn statt Wasser z. B. Methanol zum Einsatz kommt? Der Zusatz anderer Lösungsmittel ist ein weiterer Parameter, der bei den Synthesen berücksichtigt werden sollte. Die Salze von DBN und DBU sind zudem ionische Flüssigkeiten, die als neue strukturdirigierende Reagenzien zu den reinen Aminen verwendet werden könnten.

Die Auswirkungen der zahlreichen Parameter solvothormaler Synthesen auf die Produktbildung sind immer noch schlecht verstanden. Im Rahmen dieser Arbeit sind einige in-situ-Untersuchungen zu den Bildungsmechanismen mit energiedispersiver Röntgenbeugung (EDXRD) durchgeführt worden. Die Kristallisation der beiden Thiostannate  $(\text{DBNH})_2\text{Sn}_3\text{S}_6$  und  $(\text{DBNH})_2\text{Cu}_6\text{Sn}_2\text{S}_8$  wurde temperaturabhängig verfolgt. Bei niedrigen Reaktionstemperaturen sind die

Induktionszeiten lang und eine kristalline Vorläuferverbindung bzw. ein Intermediat wird beobachtet. Nach Verschwinden des Intermediats beginnt die Kristallisation von  $(\text{DBNH})_2\text{Cu}_6\text{Sn}_2\text{S}_8$  und kurze Zeit später die Bildung von  $(\text{DBNH})_2\text{Sn}_3\text{S}_6$ . Die Menge dieser beiden Verbindungen nimmt mit zunehmender Reaktionsdauer zu bis ein Gleichgewicht erreicht ist. Eine eingehende Analyse belegt, dass das Intermediat nicht über eine einfache Umwandlung in eines der beiden Produkte überführt wird. Zu Beginn der Reaktionen ist das Wachstum der kupferhaltigen Verbindung  $(\text{DBNH})_2\text{Cu}_6\text{Sn}_2\text{S}_8$  diffusionskontrolliert, wird jedoch mit fortschreitender Reaktion komplizierter und kann eher mit nukleationskontrollierten Modellen beschrieben werden. Die Kristallisationskinetik der gemischtvalenten Verbindung  $(\text{DBNH})_2\text{Sn}_3\text{S}_6$  konnte nicht genauer analysiert werden, da die Reflexe nur eine geringe Intensität aufweisen und mit denen der Cu-haltigen Verbindung überlappen. Mit dem Programm calf3 (vgl. Kap. 6.3, S. 239) konnte eine Auflösung der überlappenden Reflexe erzielt werden, allerdings ist eine weitere Auswertung aufgrund der geringen Intensität der Reflexe und der starken Streuung der Messwerte nicht sinnvoll. Bei Synthesen ohne Kupfer verlaufen die Reaktionen so schnell, dass nur qualitative Vergleiche gezogen werden können. Die deutlich kürzere Induktionszeit bei den Synthesen ohne Cu ist ein klarer Hinweis, dass die Kristallisation der gemischtvalenten Verbindung in Gegenwart von Cu inhibiert ist. Interessant ist auch, dass die Bildung von  $(\text{DBNH})_2\text{Sn}_3\text{S}_6$  ohne kristallinen Vorläufer/Intermediat erfolgt.

Drei Projekte wurden in Kooperation mit der Arbeitsgruppe von Frau Prof. Greta Patzke (ETH Zürich) durchgeführt. Das erste beschäftigt sich mit der Bildung von W/Mo-Oxiden. Die Einflüsse der Reaktionstemperatur sowie der Verhältnisse der Edukte auf die Produktbildung  $((\text{NH}_4)_x(\text{W},\text{Mo})\text{O}_3)$  wurden mit in-situ-EDXRD untersucht. In dem zweiten Projekt wurde mit in-situ-EDXRD-Untersuchungen die Bildung von nanostrukturiertem  $\alpha$ - und  $\beta$ - $\text{Bi}_2\text{O}_3$  aus  $\text{Bi}_2\text{O}_3$ -Pulver unter Zusatz von  $\text{K}_2\text{SO}_4$  verfolgt. Das letzte Projekt befasst sich mit der Synthese nanokristalliner W/Mo-HTB-Oxide (HTB = Hexagonal Tungsten Bronze) sowie den Einfluss der Alkalichloride als Additive auf Produktmorphologie und Bildungsmechanismen. Die unterschiedlichen Projekte demonstrieren eindrücklich die Möglichkeiten, allerdings auch die Grenzen der Methode. In-situ-Untersuchungen solvothermalen Reaktionen mit EDXRD liefern wertvolle Informationen über die

Kristallisationskinetik und Reaktionsabläufe. Kurzlebige Intermediate können detektiert und später ex-situ im Labor abgefangen und charakterisiert werden. Sind die Reaktionen zu schnell, kann eine kinetische Auswertung nicht erfolgen. Allerdings werden mit der Beugung nur kristalline Stoffe erfasst und die vor der Nukleation ablaufenden Prozesse, welche für die Produktbildung von entscheidender Bedeutung sind, können nicht erfasst werden.

Besonders leistungsfähig ist die Kombination sich ergänzender Methoden. Die Bildung des Thioantimonats  $[\text{Co}(\text{tren})][\text{Sb}_2\text{S}_4]$  wurde unter solvothermalen Bedingungen mit in-situ-EDXRD- und EXAFS-Messungen bei verschiedenen Temperaturen untersucht. Die in Lösung vorhandenen Antimonspezies konnten mit den EXAFS-Daten erfasst werden. Solche Untersuchungen sind z. B. für die Bildung der beiden Thiostannate  $(\text{DBNH})_2\text{Sn}_3\text{S}_6$  und  $(\text{DBNH})_2\text{Cu}_6\text{Sn}_2\text{S}_8$  durchaus sinnvoll. Für solche Experimente muss jedoch die vorhandene in-situ-Zelle modifiziert werden, um die häufiger aufgetretenen Probleme mit dem Rühren der Gemische zu beseitigen. Änderungen am Aufbau der Apparatur sollen Abhilfe schaffen, indem der magnetische Rührstab durch einen mechanischen Rührer ausgetauscht wird. Ob nach dieser Modifizierung die Reaktionsgefäße vergrößert und/oder die Materialien angepasst werden müssen, bleibt vorerst offen. Allerdings sind in-situ-Experimente, welche das Studium der Reaktionen vor der Kristallisation erlauben, von fundamentaler Bedeutung für das Verständnis solvothormaler Synthesen. Abschreckexperimente als Alternative zu in-situ-Untersuchungen bergen die Gefahr, dass der „wahre“ Reaktionszustand nicht eingefroren wird. Alternativen zu in-situ-EXAFS-Untersuchungen könnten in-situ-Raman- und/oder -IR-Experimente sein. Für solche Experimente müssen jedoch die apparativen Voraussetzungen geschaffen werden. Eine besondere Herausforderung an eine solche Messzelle stellen die Reaktionsbedingungen dar: hohe pH-Werte und autogener Druck erfordern hohe Ansprüche an z. B. Lichtleiter, welche prinzipiell für Raman/IR-Spektroskopie geeignet sind. Auf diesem Gebiet müssen noch Entwicklungsarbeiten geleistet werden.



## 6. Anhang

### 6.1. Publikationsliste

#### 6.1.1. Publikationen

*Combined in-situ EDXRD/EXAFS Investigation of the Crystal Growth of [Co(C<sub>6</sub>H<sub>18</sub>N<sub>4</sub>)]Sb<sub>2</sub>S<sub>4</sub> under Solvothermal Conditions: Two Different Reaction Pathways Leading to the Same Product,*

R. Kiebach, N. Pienack, M.-E. Ordolff, F. Studt, W. Bensch;  
*Chem. Mater.* **2006**, 18, 1196-1205.

*The New Silver Thiostannate (1,4-dabH<sub>2</sub>)Ag<sub>2</sub>SnS<sub>4</sub>: Solvothermal Synthesis, Crystal Structure and Spectroscopic Properties,*

N. Pienack, W. Bensch;  
*Z. Anorg. Allg. Chem.* **2006**, 632, 1733-1736.

*Two New Copper Thiostannates Synthesised Under Solvothermal Conditions: Crystal Structures, Spectroscopic and Thermal Properties of (DBUH)CuSnS<sub>3</sub> and (1,4-dabH<sub>2</sub>)Cu<sub>2</sub>SnS<sub>4</sub>,*

N. Pienack, C. Näther, W. Bensch;  
*Solid State Sci.* **2007**, 9, 100-107.

*(1,4-dabH)<sub>2</sub>MnSnS<sub>4</sub>: The first thiostannate with integrated Mn<sup>2+</sup> ions in an anionic chain structure,*

N. Pienack, K. Möller, C. Näther, W. Bensch;  
*Solid State Sci.* **2007**, 9, 1110-1114.

*Hydrothermal Formation of W/Mo-Oxides: A Multidisciplinary Study of Growth and Shape,*

R. Kiebach, N. Pienack, W. Bensch, J.-D. Grunwaldt, A. Michailovski, A. Baiker, T. Fox, Y. Zhou, G. R. Patzke;  
*Chem. Mater.* **2008**, 20, 3022-3033.

*The Layered Thiostannate (dienH<sub>2</sub>)Cu<sub>2</sub>Sn<sub>2</sub>S<sub>6</sub> – a Photoconductive Inorganic-Organic Hybrid Compound,*

N. Pienack, A. Puls, C. Näther, W. Bensch;

*Inorg. Chem.*, angenommen am 30.07.08.

*Solvothermal syntheses, crystal structures and selected optical properties of [M(C<sub>8</sub>N<sub>5</sub>H<sub>23</sub>)<sub>2</sub>Sn<sub>2</sub>S<sub>6</sub> (M = Co, Fe, Ni; C<sub>8</sub>N<sub>5</sub>H<sub>23</sub> = tetraethylenepentamine),*

N. Pienack, S. Lehmann, H. Lühmann, M. El-Madani, C. Näther, W. Bensch;

*Z. Anorg. Allg. Chem.*, angenommen am 02.07.08.

*Solvothermal syntheses of two new thiostannates and an in-situ energy dispersive X-ray scattering study of their formation,*

N. Pienack, C. Näther, W. Bensch;

*Chem. Eur. J.*, eingereicht am 19.09.08.

*The Influence of the Amine Concentration onto Product Formation: Crystal Structures, Thermal Stability and Spectroscopic Properties of Two New Manganese Thiostannates Obtained under Solvothermal Conditions,*

N. Pienack, C. Näther, W. Bensch;

*Z. Naturforsch. B.*, angenommen am 08.09.08.

*The thiostannate coordination polymer {[Mn(trien)]<sub>2</sub>SnS<sub>4</sub>} · 4 H<sub>2</sub>O exhibiting a hitherto unknown binding mode of the [SnS<sub>4</sub>]<sup>4-</sup> tetrahedron,*

N. Pienack, C. Näther, W. Bensch;

*Inorg. Chem.*, eingereicht am 19.09.08.

### 6.1.2. Tagungsbeiträge

*Combined In-situ Energy-Dispersive X-ray Diffraction and In-situ EXAFS Studies of the Crystallisation of [Co(tren)][Sb<sub>2</sub>S<sub>4</sub>] Under Solvothermal Conditions,*

R. Kiebach, M. E. Ordolff, N. Pienack, W. Bensch;

DESY, Annual Report **2005**.

*A Combined in-situ EDXRD/EXAFS Investigation of the Crystal Growth of [Co(C<sub>6</sub>H<sub>18</sub>N<sub>4</sub>)] [Sb<sub>2</sub>S<sub>4</sub>] under Solvothermal Conditions: Two Different Reaction Pathways Leading to the Same Product,*

R. Kiebach, N. Pienack, M.-E. Ordolff, F. Studt, W. Bensch;

DESY, User Meeting **2006**.

*Zwei Kupfer-Thiostannate: (DBUH)CuSnS<sub>3</sub> und (1,4-dabH<sub>2</sub>)Cu<sub>2</sub>SnS<sub>4</sub>,*

N. Pienack, C. Näther, W. Bensch;

Vortragstagung der GDCh-Fachgruppe Festkörperchemie und Materialforschung, Aachen, September **2006**.

*Untersuchung der Kristallisationskinetik von [Ni(tren)]SnS<sub>3</sub> mit in-situ EDXRD in Abhängigkeit von den Edukten,*

M. Ordolff, N. Pienack, W. Bensch;

Deutsche Tagung für Forschung mit Synchrotronstrahlung, Neutronen und Ionenstrahlen an Großgeräten, Universität Hamburg, Oktober **2006**.

*In-situ EXAFS investigations of the formation of Ni(C<sub>6</sub>N<sub>4</sub>H<sub>18</sub>)SnS<sub>3</sub> under solvothermal conditions,*

N. Pienack, M.-E. Ordolff, W. Bensch;

DESY, Annual Report **2006**.

*Investigating the influence of different educts on the formation of [Ni(C<sub>6</sub>N<sub>4</sub>H<sub>18</sub>)]SnS<sub>3</sub> using in-situ EDXRD,*

M.-E. Ordolff, N. Pienack, W. Bensch;

DESY, Annual Report **2006**.

*Das erste Thiostannat mit Mangan in der Anionenkette: (1,4-dabH)<sub>2</sub>MnSnS<sub>4</sub>,*

N. Pienack, K. Möller, W. Bensch;

15. Jahrestagung der Deutschen Gesellschaft für Kristallographie, Bremen, März **2007**.

*The formation of Ni(C<sub>6</sub>N<sub>4</sub>H<sub>18</sub>)SnS<sub>3</sub>: in-situ EXAFS investigations under solvothermal conditions,*

N. Pienack, M.-E. Ordolff, W. Bensch;

Faraday Discussion 136: Crystal Growth and Nucleation, London, April **2007**.

*In-situ EDXRD investigations of the formation of Fe(C<sub>6</sub>H<sub>18</sub>N<sub>4</sub>)Sb<sub>4</sub>S<sub>7</sub> and [Fe(C<sub>6</sub>H<sub>18</sub>N<sub>4</sub>)]FeSbS<sub>4</sub> under solvothermal conditions,*

B. Seidlhofer, E. Antonova, N. Pienack, W. Bensch;

DESY, Annual Report **2007**.

*The influence of temperature onto the formation of two new thiostannates in one reaction mixture,*

N. Pienack, E. Antonova, B. Seidlhofer, W. Bensch;

DESY, Annual Report **2007**.

*In-situ EXAFS investigations of the effect of reactants onto the formation of Ni(C<sub>6</sub>N<sub>4</sub>H<sub>18</sub>)SnS<sub>3</sub> under solvothermal conditions,*

N. Pienack, M.-E. Ordolff, E. Antonova, B. Seidlhofer, W. Bensch;

DESY, Annual Report **2007**.

*(dienH)<sub>2</sub>Sn<sub>3</sub>S<sub>7</sub> – ein Thiostannat des R-SnS-1-Typs mit interessantem Verhalten gegenüber Cs<sup>+</sup>-Kationen,*

N. Pienack, W. Bensch;

14. Vortragstagung der GDCh-Fachgruppe Festkörperchemie und Materialforschung, Bayreuth, September **2008**.

## 6.2. Strukturdaten / Messprotokolle

### 6.2.1. Messprotokoll für die Verbindung (DBUH)CuSnS<sub>3</sub>

Table 1. Crystal data and structure refinement for (DBUH)CuSnS<sub>3</sub> (C<sub>9</sub>H<sub>16</sub>N<sub>2</sub>; DBU = 1,8-Diazabicyclo[5.4.0]undec-7-en).

Identification code	(DBUH)CuSnS <sub>3</sub> (np336)	
Empirical formula	C <sub>9</sub> H <sub>17</sub> N <sub>2</sub> CuSnS <sub>3</sub>	
Crystal colour, – Habitués:	yellow needles	
Formula weight	431.66 g/mol	
Temperature	293(2) K	
Wavelength	0.71073 Å	
Crystal system	Monoclinic	
Space group	P2 <sub>1</sub> /n	
Unit cell dimensions	a = 9.2541(10) Å	α = 90°
	b = 8.6190(7) Å	β = 92.803(16)°
	c = 18.135(2) Å	γ = 90°
Volume	1444.7(3) Å <sup>3</sup>	
Z	4	
Density (calculated)	1.985 g/cm <sup>3</sup>	
Absorption coefficient	3.610 mm <sup>-1</sup>	
F(000)	848	
Crystal size	0.12 · 0.10 · 0.08 mm <sup>3</sup>	
Theta range for data collection	2.25 to 30.04°	
Index ranges	0 ≤ h ≤ 13, -12 ≤ k ≤ 12, -25 ≤ l ≤ 25	
Reflections collected	8629	
Independent reflections	4215 [R(int) = 0.0230]	
Completeness to theta = 30.04°	99.9 %	
Refinement method	Full-matrix least-squares on F <sup>2</sup>	
Data / restraints / parameters	4215 / 0 / 146	
Goodness-of-fit on F <sup>2</sup>	0.989	
Final R indices [I > 2σ(I)]	R1 = 0.0208, wR2 = 0.0465	
R indices (all data)	R1 = 0.0371, wR2 = 0.0496	
Extinction coefficient	0.00405(18)	
Largest diff. peak and hole	0.362 and -0.383 e.Å <sup>-3</sup>	

Table 2. Atomic coordinates ( $\cdot 10^4$ ) and equivalent isotropic displacement parameters ( $\text{\AA}^2 \cdot 10^3$ ).  $U(\text{eq})$  is defined as one third of the trace of the orthogonalized  $U_{ij}$  tensor.

	x	y	z	U(eq)
Sn(1)	9319(1)	1750(1)	5160(1)	31(1)
Cu(1)	11064(1)	5044(1)	5790(1)	38(1)
S(1)	9872(1)	3171(1)	6244(1)	42(1)
S(2)	7532(1)	3025(1)	4399(1)	40(1)
S(3)	8602(1)	-870(1)	5497(1)	43(1)
N(1)	4629(2)	3946(2)	6878(1)	38(1)
C(1)	5073(2)	3679(2)	6212(1)	35(1)
N(2)	5983(2)	4596(2)	5897(1)	48(1)
C(2)	6609(3)	5964(3)	6255(2)	64(1)
C(3)	6622(3)	5762(4)	7072(2)	70(1)
C(4)	5182(3)	5263(3)	7314(2)	61(1)
C(5)	3600(2)	2917(3)	7232(1)	42(1)
C(6)	4185(3)	1331(3)	7417(1)	51(1)
C(7)	4206(4)	222(3)	6776(2)	67(1)
C(8)	5091(3)	752(3)	6142(2)	61(1)
C(9)	4559(3)	2269(3)	5790(1)	47(1)

Table 3. Bond lengths [ $\text{\AA}$ ] and angles [ $^\circ$ ].

Sn(1)-S(1)	2.3508(6)	S(2)-Sn(1)-S(3)#1	113.91(2)
Sn(1)-S(2)	2.3715(6)	S(1)-Sn(1)-S(3)	108.86(2)
Sn(1)-S(3)#1	2.4332(6)	S(2)-Sn(1)-S(3)	112.59(2)
Sn(1)-S(3)	2.4399(6)	S(3)#1-Sn(1)-S(3)	93.758(18)
Cu(1)-S(1)	2.1419(6)	S(1)-Cu(1)-S(2)#2	166.27(2)
Cu(1)-S(2)#2	2.1496(6)	Cu(1)-S(1)-Sn(1)	99.59(2)
S(2)-Cu(1)#2	2.1496(6)	Cu(1)#2-S(2)-Sn(1)	92.39(2)
S(3)-Sn(1)#1	2.4332(6)	Sn(1)#1-S(3)-Sn(1)	86.242(18)
N(1)-C(1)	1.314(3)	C(1)-N(1)-C(4)	121.1(2)
N(1)-C(4)	1.462(3)	C(1)-N(1)-C(5)	122.25(18)
N(1)-C(5)	1.472(3)	C(4)-N(1)-C(5)	116.63(18)
C(1)-N(2)	1.307(3)	N(2)-C(1)-N(1)	122.2(2)
C(1)-C(9)	1.500(3)	N(2)-C(1)-C(9)	117.46(19)
N(2)-C(2)	1.453(3)	N(1)-C(1)-C(9)	120.31(19)
C(2)-C(3)	1.492(4)	C(1)-N(2)-C(2)	123.1(2)
C(3)-C(4)	1.487(4)	N(2)-C(2)-C(3)	109.5(2)
C(5)-C(6)	1.502(3)	C(4)-C(3)-C(2)	111.3(3)
C(6)-C(7)	1.505(4)	N(1)-C(4)-C(3)	111.1(2)
C(7)-C(8)	1.515(4)	N(1)-C(5)-C(6)	114.31(19)
C(8)-C(9)	1.525(4)	C(5)-C(6)-C(7)	115.1(2)
		C(6)-C(7)-C(8)	115.0(2)
S(1)-Sn(1)-S(2)	111.25(2)	C(7)-C(8)-C(9)	113.6(2)
S(1)-Sn(1)-S(3)#1	115.24(2)	C(1)-C(9)-C(8)	113.2(2)

Symmetry transformations used to generate equivalent atoms:

#1 -x+2,-y,-z+1 #2 -x+2,-y+1,-z+1

Table 4. Anisotropic displacement parameters ( $\text{\AA}^2 \cdot 10^3$ ). The anisotropic displacement factor exponent takes the form:  $-2\pi^2[h^2 a^{*2} U_{11} + \dots + 2 h k a^* b^* U_{12}]$ .

	$U_{11}$	$U_{22}$	$U_{33}$	$U_{23}$	$U_{13}$	$U_{12}$
Sn(1)	34(1)	25(1)	33(1)	-1(1)	3(1)	-4(1)
Cu(1)	46(1)	31(1)	38(1)	0(1)	0(1)	0(1)
S(1)	58(1)	35(1)	33(1)	-1(1)	-4(1)	-8(1)
S(2)	40(1)	43(1)	36(1)	5(1)	-2(1)	-4(1)
S(3)	42(1)	29(1)	58(1)	2(1)	21(1)	-8(1)
N(1)	41(1)	35(1)	37(1)	-5(1)	5(1)	-1(1)
C(1)	35(1)	34(1)	35(1)	3(1)	2(1)	1(1)
N(2)	52(1)	41(1)	50(1)	7(1)	13(1)	-6(1)
C(2)	59(2)	38(1)	96(2)	2(1)	15(2)	-12(1)
C(3)	66(2)	51(2)	93(2)	-25(2)	1(2)	-13(1)
C(4)	69(2)	50(2)	64(2)	-25(1)	8(1)	-5(1)
C(5)	39(1)	51(1)	38(1)	0(1)	12(1)	4(1)
C(6)	58(2)	55(1)	41(1)	11(1)	10(1)	0(1)
C(7)	98(2)	37(1)	69(2)	0(1)	27(2)	-9(1)
C(8)	85(2)	39(1)	62(2)	-14(1)	29(2)	-3(1)
C(9)	54(1)	57(1)	30(1)	-6(1)	6(1)	-14(1)

Table 5. Hydrogen coordinates ( $\cdot 10^4$ ) and isotropic displacement parameters ( $\text{\AA}^2 \cdot 10^3$ ).

	x	y	z	U(eq)
H(1N2)	6353	4358	5486	57
H(2A)	6045	6874	6112	77
H(2B)	7589	6115	6102	77
H(3A)	7341	4992	7223	84
H(3B)	6890	6735	7311	84
H(4A)	5262	4974	7832	73
H(4B)	4507	6122	7262	73
H(5A)	2743	2805	6906	51
H(5B)	3306	3406	7683	51
H(6A)	3607	879	7794	61
H(6B)	5165	1442	7626	61
H(7A)	3218	50	6590	80
H(7B)	4585	-766	6954	80
H(8A)	5068	-51	5766	73
H(8B)	6089	882	6320	73
H(9A)	4891	2330	5292	56
H(9B)	3510	2266	5758	56

### 6.2.2. Messprotokoll für die Verbindung (DBNH)<sub>2</sub>Sn<sub>3</sub>S<sub>6</sub>

Table 1. Crystal data and structure refinement for (DBNH)<sub>2</sub>Sn<sub>3</sub>S<sub>6</sub> (C<sub>7</sub>H<sub>12</sub>N<sub>2</sub>; DBN = 1,5-Diazabicyclo[4.3.0]non-5-en).

Identification code	(DBNH) <sub>2</sub> Sn <sub>3</sub> S <sub>6</sub> (NP 404)	
Empirical formula	(C <sub>14</sub> H <sub>26</sub> N <sub>4</sub> )Sn <sub>3</sub> S <sub>6</sub>	
Crystal colour, – Habitués:	yellow needles	
Formula weight	798.82 g/mol	
Temperature	293(2) K	
Wavelength	0.71073 Å	
Crystal system	Monoclinic	
Space group	P2 <sub>1</sub> /n	
Unit cell dimensions	a = 9.5822(8) Å	α = 90°
	b = 13.1199(7) Å	β = 97.192(10)°
	c = 19.9506(16) Å	γ = 90°
Volume	2488.4(3) Å <sup>3</sup>	
Z	4	
Density (calculated)	2.132 g/cm <sup>3</sup>	
Absorption coefficient	3.501 mm <sup>-1</sup>	
F(000)	1536	
Crystal size	0.13 · 0.10 · 0.07 mm <sup>3</sup>	
Theta range for data collection	2.65 to 28.02°	
Index ranges	-12 ≤ h ≤ 12, -16 ≤ k ≤ 16, -26 ≤ l ≤ 26	
Reflections collected	21603	
Independent reflections	5831 [R(int) = 0.0589]	
Completeness to theta = 28.02°	96.7 %	
Refinement method	Full-matrix least-squares on F <sup>2</sup>	
Data / restraints / parameters	5831 / 0 / 245	
Goodness-of-fit on F <sup>2</sup>	1.006	
Final R indices [I > 2σ(I)]	R1 = 0.0387, wR2 = 0.0874	
R indices (all data)	R1 = 0.0626, wR2 = 0.0958	
Extinction coefficient	0.00068(16)	
Largest diff. peak and hole	0.928 and -0.971 e.Å <sup>-3</sup>	

Table 2. Atomic coordinates ( $\cdot 10^4$ ) and equivalent isotropic displacement parameters ( $\text{\AA}^2 \cdot 10^3$ ).  $U(\text{eq})$  is defined as one third of the trace of the orthogonalized  $U_{ij}$  tensor.

	x	y	z	U(eq)
Sn(1)	2705(1)	993(1)	2005(1)	27(1)
Sn(2)	2692(1)	3758(1)	2082(1)	26(1)
Sn(3)	4218(1)	2457(1)	733(1)	41(1)
S(1)	4781(1)	2384(1)	1993(1)	29(1)
S(2)	786(1)	-318(1)	2082(1)	35(1)
S(3)	1338(1)	2339(1)	2430(1)	27(1)
S(4)	4253(1)	9(1)	2785(1)	36(1)
S(5)	2635(2)	3964(1)	887(1)	41(1)
S(6)	2563(2)	947(1)	799(1)	48(1)
N(1)	-553(5)	2331(4)	3772(2)	41(1)
C(1)	-1697(7)	2387(7)	3326(3)	56(2)
N(2)	-2390(8)	1655(9)	3078(4)	101(3)
C(2)	-2067(10)	3516(11)	3135(5)	116(5)
N(3)	3746(5)	2252(4)	5301(2)	41(1)
C(3)	-1105(10)	4072(7)	3753(5)	82(3)
N(4)	3965(7)	3263(5)	4384(3)	58(2)
C(4)	87(7)	3338(6)	3928(3)	53(2)
C(5)	73(7)	1360(5)	3974(3)	50(2)
C(6)	-1071(8)	595(6)	3891(5)	67(2)
C(7)	-1912(9)	667(8)	3254(5)	86(3)
C(8)	3750(6)	3131(5)	5011(3)	43(1)
C(9)	3436(10)	3970(6)	5467(4)	65(2)
C(10)	3235(8)	3417(6)	6128(3)	56(2)
C(11)	3460(8)	2294(5)	6010(3)	52(2)
C(12)	4248(9)	2364(6)	3970(4)	67(2)
C(13)	4929(10)	1558(7)	4408(4)	72(2)
C(14)	4097(8)	1319(5)	4985(4)	56(2)

Table 3. Bond lengths [ $\text{\AA}$ ] and angles [ $^\circ$ ].

Sn(1)-S(4)	2.3901(14)	C(2)-C(3)	1.618(15)
Sn(1)-S(6)	2.3927(14)	N(3)-C(8)	1.290(8)
Sn(1)-S(3)	2.4149(12)	N(3)-C(14)	1.437(8)
Sn(1)-S(2)	2.5367(14)	N(3)-C(11)	1.475(8)
Sn(1)-S(1)	2.7024(13)	C(3)-C(4)	1.501(11)
Sn(2)-S(5)	2.3937(14)	N(4)-C(8)	1.305(8)
Sn(2)-S(2)#1	2.4020(13)	N(4)-C(12)	1.484(10)
Sn(2)-S(3)	2.4201(12)	C(5)-C(6)	1.480(10)
Sn(2)-S(4)#1	2.5222(14)	C(6)-C(7)	1.421(12)
Sn(2)-S(1)	2.7157(13)	C(8)-C(9)	1.483(9)
Sn(3)-S(1)	2.5059(13)	C(9)-C(10)	1.537(10)
Sn(3)-S(5)	2.5335(16)	C(10)-C(11)	1.511(10)
Sn(3)-S(6)	2.5511(17)	C(12)-C(13)	1.472(10)
S(2)-Sn(2)#2	2.4020(13)	C(13)-C(14)	1.513(11)
S(4)-Sn(2)#2	2.5222(14)		
N(1)-C(1)	1.324(8)	S(4)-Sn(1)-S(6)	126.39(6)
N(1)-C(5)	1.444(8)	S(4)-Sn(1)-S(3)	119.09(5)
N(1)-C(4)	1.474(9)	S(6)-Sn(1)-S(3)	113.99(6)
C(1)-N(2)	1.235(12)	S(4)-Sn(1)-S(2)	89.41(4)
C(1)-C(2)	1.559(14)	S(6)-Sn(1)-S(2)	95.35(5)
N(2)-C(7)	1.406(13)	S(3)-Sn(1)-S(2)	92.63(5)

S(4)-Sn(1)-S(1)	88.44(4)	C(1)-N(1)-C(4)	112.3(6)
S(6)-Sn(1)-S(1)	87.57(5)	C(5)-N(1)-C(4)	125.8(5)
S(3)-Sn(1)-S(1)	86.64(4)	N(2)-C(1)-N(1)	125.8(9)
S(2)-Sn(1)-S(1)	177.04(4)	N(2)-C(1)-C(2)	123.1(9)
S(5)-Sn(2)-S(2)#1	124.84(5)	N(1)-C(1)-C(2)	111.1(7)
S(5)-Sn(2)-S(3)	115.23(5)	C(1)-N(2)-C(7)	118.4(8)
S(2)#1-Sn(2)-S(3)	119.31(5)	C(1)-C(2)-C(3)	98.7(6)
S(5)-Sn(2)-S(4)#1	96.11(5)	C(8)-N(3)-C(14)	123.4(6)
S(2)#1-Sn(2)-S(4)#1	89.48(4)	C(8)-N(3)-C(11)	114.1(5)
S(3)-Sn(2)-S(4)#1	92.31(5)	C(14)-N(3)-C(11)	122.4(5)
S(5)-Sn(2)-S(1)	86.27(5)	C(4)-C(3)-C(2)	103.4(7)
S(2)#1-Sn(2)-S(1)	89.53(4)	C(8)-N(4)-C(12)	119.4(6)
S(3)-Sn(2)-S(1)	86.24(4)	N(1)-C(4)-C(3)	104.0(6)
S(4)#1-Sn(2)-S(1)	177.58(5)	N(1)-C(5)-C(6)	106.9(5)
S(1)-Sn(3)-S(5)	88.02(4)	C(7)-C(6)-C(5)	112.6(7)
S(1)-Sn(3)-S(6)	88.62(4)	N(2)-C(7)-C(6)	114.5(8)
S(5)-Sn(3)-S(6)	102.39(6)	N(3)-C(8)-N(4)	123.9(6)
Sn(3)-S(1)-Sn(1)	88.16(4)	N(3)-C(8)-C(9)	112.1(6)
Sn(3)-S(1)-Sn(2)	88.41(4)	N(4)-C(8)-C(9)	123.9(6)
Sn(1)-S(1)-Sn(2)	84.15(4)	C(8)-C(9)-C(10)	103.4(6)
Sn(2)#2-S(2)-Sn(1)	90.15(4)	C(11)-C(10)-C(9)	107.0(6)
Sn(1)-S(3)-Sn(2)	97.35(4)	N(3)-C(11)-C(10)	103.4(5)
Sn(1)-S(4)-Sn(2)#2	90.77(5)	C(13)-C(12)-N(4)	109.8(6)
Sn(2)-S(5)-Sn(3)	95.34(5)	C(12)-C(13)-C(14)	111.4(7)
Sn(1)-S(6)-Sn(3)	94.30(5)	N(3)-C(14)-C(13)	109.4(6)
C(1)-N(1)-C(5)	121.1(6)		

Symmetry transformations used to generate equivalent atoms:

#1  $-x+3/2, y+1/2, -z+1/2$  #2  $-x+3/2, y-1/2, -z+1/2$

Table 4. Anisotropic displacement parameters ( $\text{\AA}^2 \cdot 10^3$ ). The anisotropic displacement factor exponent takes the form:  $-2\pi^2 [h^2 a^{*2} U_{11} + \dots + 2 h k a^* b^* U_{12}]$ .

	$U_{11}$	$U_{22}$	$U_{33}$	$U_{23}$	$U_{13}$	$U_{12}$
Sn(1)	34(1)	16(1)	30(1)	-2(1)	2(1)	2(1)
Sn(2)	31(1)	15(1)	31(1)	1(1)	0(1)	-3(1)
Sn(3)	45(1)	48(1)	32(1)	2(1)	15(1)	-1(1)
S(1)	25(1)	27(1)	34(1)	0(1)	2(1)	0(1)
S(2)	30(1)	20(1)	52(1)	7(1)	-9(1)	-2(1)
S(3)	29(1)	18(1)	35(1)	-1(1)	9(1)	-2(1)
S(4)	29(1)	22(1)	52(1)	6(1)	-6(1)	-2(1)
S(5)	51(1)	37(1)	33(1)	11(1)	-2(1)	4(1)
S(6)	71(1)	42(1)	30(1)	-11(1)	4(1)	-12(1)
N(1)	33(2)	52(3)	38(2)	-1(2)	5(2)	4(2)
C(1)	31(3)	92(6)	46(4)	-5(3)	6(3)	-5(3)
N(2)	46(4)	167(11)	87(6)	-6(6)	-3(4)	13(5)
C(2)	62(6)	222(14)	67(5)	54(7)	23(4)	85(8)
N(3)	38(3)	38(3)	41(3)	4(2)	-8(2)	1(2)
C(3)	82(6)	45(5)	132(8)	0(5)	62(6)	9(4)
N(4)	75(4)	48(4)	50(3)	14(2)	4(3)	8(3)
C(4)	43(4)	67(5)	51(4)	-10(3)	13(3)	-2(3)
C(5)	46(4)	59(5)	45(3)	5(3)	6(3)	12(3)
C(6)	47(4)	53(5)	103(6)	12(4)	15(4)	9(3)
C(7)	34(4)	102(8)	123(8)	-35(6)	10(5)	1(4)
C(8)	36(3)	43(4)	46(3)	0(3)	-6(2)	0(2)
C(9)	85(6)	41(5)	65(4)	-2(3)	-3(4)	4(4)
C(10)	57(4)	55(5)	55(4)	-7(3)	2(3)	-5(3)

C(11)	54(4)	57(5)	42(3)	4(3)	-2(3)	1(3)
C(12)	70(5)	84(6)	45(4)	1(4)	0(3)	20(4)
C(13)	94(6)	71(6)	47(4)	-5(3)	-1(4)	34(5)
C(14)	66(5)	36(4)	61(4)	-10(3)	-13(3)	8(3)

Table 5. Hydrogen coordinates ( $\cdot 10^4$ ) and isotropic displacement parameters ( $\text{\AA}^2 \cdot 10^3$ ).

	x	y	z	U(eq)
H(2)	-3147	1749	2805	151
H(2A)	-3060	3658	3138	139
H(2B)	-1788	3700	2700	139
H(3A)	-765	4725	3614	98
H(3B)	-1627	4175	4134	98
H(4)	3942	3865	4212	87
H(4A)	840	3466	3656	64
H(4B)	457	3388	4402	64
H(5A)	500	1385	4441	60
H(5B)	794	1186	3692	60
H(6A)	-664	-82	3941	81
H(6B)	-1664	689	4246	81
H(7A)	-1369	419	2908	104
H(7B)	-2721	223	3256	104
H(9A)	2587	4331	5287	78
H(9B)	4210	4450	5537	78
H(10A)	3910	3663	6495	68
H(10B)	2295	3535	6243	68
H(11A)	4252	2036	6313	62
H(11B)	2627	1904	6074	62
H(12A)	3372	2111	3731	80
H(12B)	4856	2560	3637	80
H(13A)	5869	1775	4588	86
H(13B)	5013	946	4142	86
H(14A)	3244	955	4816	67
H(14B)	4650	888	5312	67

### 6.2.3. Messprotokoll für die Verbindung (1,4-dabH<sub>2</sub>)Cu<sub>2</sub>SnS<sub>4</sub>

Table 1. Crystal data and structure refinement for (C<sub>4</sub>H<sub>12</sub>N<sub>2</sub>H<sub>2</sub>)Cu<sub>2</sub>SnS<sub>4</sub> (C<sub>4</sub>H<sub>12</sub>N<sub>2</sub>; 1,4-dab = 1,4-Diaminobutan).

Identification code	(C <sub>4</sub> H <sub>12</sub> N <sub>2</sub> H <sub>2</sub> )Cu <sub>2</sub> SnS <sub>4</sub> (NP 445)	
Empirical formula	(C <sub>4</sub> H <sub>14</sub> N <sub>2</sub> )Cu <sub>2</sub> SnS <sub>4</sub>	
Crystal colour, – Habitués	dark yellow needles	
Formula weight	464.18 g/mol	
Temperature	293(2) K	
Wavelength	0.71073 Å	
Crystal system	Tetragonal	
Space group	P4 <sub>2</sub> /n	
Unit cell dimensions	a = 14.5392(15) Å	α = 90°
	b = 14.5392(15) Å	β = 90°
	c = 11.4776(12) Å	γ = 90°
Volume	2426.2(4) Å <sup>3</sup>	
Z	8	
Density (calculated)	2.542 g/cm <sup>3</sup>	
Absorption coefficient	6.163 mm <sup>-1</sup>	
F(000)	1792	
Crystal size	0.13 · 0.10 · 0.06 mm <sup>3</sup>	
Theta range for data collection	2.26 to 25.02°	
Index ranges	-16 ≤ h ≤ 5, -16 ≤ k ≤ 17, -11 ≤ l ≤ 13	
Reflections collected	5424	
Independent reflections	2135 [R(int) = 0.1214]	
Completeness to theta = 25.02°	99.6 %	
Refinement method	Full-matrix least-squares on F <sup>2</sup>	
Data / restraints / parameters	2135 / 0 / 114	
Goodness-of-fit on F <sup>2</sup>	1.025	
Final R indices [I > 2σ(I)]	R1 = 0.0751, wR2 = 0.1772	
R indices (all data)	R1 = 0.1132, wR2 = 0.1988	
Extinction coefficient	0.0002(3)	
Largest diff. peak and hole	1.687 and -2.321 e.Å <sup>-3</sup>	

Table 2. Atomic coordinates ( $\cdot 10^4$ ) and equivalent isotropic displacement parameters ( $\text{\AA}^2 \cdot 10^3$ ).  $U(\text{eq})$  is defined as one third of the trace of the orthogonalized  $U_{ij}$  tensor.

	x	y	z	U(eq)
Sn(1)	2271(1)	5746(1)	3700(1)	15(1)
Cu(1)	2418(1)	6452(2)	390(2)	24(1)
Cu(2)	3516(2)	7340(1)	1941(2)	24(1)
S(1)	3168(3)	5821(3)	1951(3)	18(1)
S(2)	3168(3)	5921(3)	5421(3)	20(1)
S(3)	1084(3)	6893(3)	3643(4)	18(1)
S(4)	1608(3)	4264(3)	3852(4)	29(1)
N(2)	4643(10)	4344(10)	8664(14)	30(3)
N(1)	3644(12)	3121(14)	3731(19)	55(5)
C(4)	4272(14)	3670(13)	7862(19)	38(5)
C(3)	4222(17)	3700(30)	4490(20)	104(16)
C(2)	3934(15)	3340(15)	5778(19)	43(5)
C(1)	4478(14)	3911(14)	6637(17)	36(5)

Table 3. Bond lengths [ $\text{\AA}$ ] and angles [ $^\circ$ ].

Sn(1)-S(4)	2.367(4)	S(1)-Cu(1)-S(3)#2	112.37(16)
Sn(1)-S(2)	2.380(4)	S(2)#1-Cu(1)-Cu(2)	116.23(15)
Sn(1)-S(1)	2.397(4)	S(1)-Cu(1)-Cu(2)	52.95(12)
Sn(1)-S(3)	2.401(4)	S(3)#2-Cu(1)-Cu(2)	115.12(13)
Cu(1)-S(2)#1	2.246(5)	S(2)#1-Cu(1)-Cu(2)#3	51.37(12)
Cu(1)-S(1)	2.290(5)	S(1)-Cu(1)-Cu(2)#3	89.13(12)
Cu(1)-S(3)#2	2.305(5)	S(3)#2-Cu(1)-Cu(2)#3	153.53(14)
Cu(1)-Cu(2)	2.718(3)	Cu(2)-Cu(1)-Cu(2)#3	65.00(10)
Cu(1)-Cu(2)#3	2.845(3)	S(2)#1-Cu(1)-Cu(1)#3	80.25(13)
Cu(1)-Cu(1)#3	3.057(4)	S(1)-Cu(1)-Cu(1)#3	111.21(12)
Cu(2)-S(1)	2.265(4)	S(3)#2-Cu(1)-Cu(1)#3	101.38(11)
Cu(2)-S(2)#2	2.272(5)	Cu(2)-Cu(1)-Cu(1)#3	58.69(7)
Cu(2)-S(3)#3	2.323(5)	Cu(2)#3-Cu(1)-Cu(1)#3	54.70(7)
Cu(2)-Cu(1)#3	2.845(3)	S(1)-Cu(2)-S(2)#2	126.93(17)
Cu(2)-Cu(2)#3	2.991(4)	S(1)-Cu(2)-S(3)#3	121.29(16)
S(2)-Cu(1)#4	2.246(5)	S(2)#2-Cu(2)-S(3)#3	107.52(16)
S(2)-Cu(2)#5	2.272(5)	S(1)-Cu(2)-Cu(1)	53.78(12)
S(3)-Cu(1)#5	2.305(5)	S(2)#2-Cu(2)-Cu(1)	87.74(13)
S(3)-Cu(2)#3	2.323(5)	S(3)#3-Cu(2)-Cu(1)	157.79(14)
N(2)-C(4)	1.45(3)	S(1)-Cu(2)-Cu(1)#3	119.89(14)
N(1)-C(3)	1.47(4)	S(2)#2-Cu(2)-Cu(1)#3	50.56(12)
C(4)-C(1)	1.48(3)	S(3)#3-Cu(2)-Cu(1)#3	110.44(12)
C(3)-C(2)	1.62(4)	Cu(1)-Cu(2)-Cu(1)#3	66.61(10)
C(2)-C(1)	1.51(3)	S(1)-Cu(2)-Cu(2)#3	86.04(14)
S(4)-Sn(1)-S(2)	105.03(16)	S(2)#2-Cu(2)-Cu(2)#3	105.89(13)
S(4)-Sn(1)-S(1)	108.95(15)	S(3)#3-Cu(2)-Cu(2)#3	99.94(11)
S(2)-Sn(1)-S(1)	113.08(14)	Cu(1)-Cu(2)-Cu(2)#3	59.56(8)
S(4)-Sn(1)-S(3)	109.99(15)	Cu(1)#3-Cu(2)-Cu(2)#3	55.44(7)
S(2)-Sn(1)-S(3)	110.03(14)	Cu(2)-S(1)-Cu(1)	73.26(14)
S(1)-Sn(1)-S(3)	109.65(14)	Cu(2)-S(1)-Sn(1)	99.82(15)
S(2)#1-Cu(1)-S(1)	123.22(17)	Cu(1)-S(1)-Sn(1)	114.49(18)
S(2)#1-Cu(1)-S(3)#2	119.52(17)	Cu(1)#4-S(2)-Cu(2)#5	78.07(15)
		Cu(1)#4-S(2)-Sn(1)	103.00(16)

Cu(2)#5-S(2)-Sn(1)	112.66(18)	N(2)-C(4)-C(1)	111.7(17)
Cu(1)#5-S(3)-Cu(2)#3	117.68(18)	N(1)-C(3)-C(2)	102(3)
Cu(1)#5-S(3)-Sn(1)	96.39(15)	C(1)-C(2)-C(3)	106.6(19)
Cu(2)#3-S(3)-Sn(1)	100.18(16)	C(4)-C(1)-C(2)	112.6(17)

Symmetry transformations used to generate equivalent atoms:

#1  $y-1/2, -x+1, z-1/2$  #2  $-y+1, x+1/2, z-1/2$  #3  $-x+1/2, -y+3/2, z$

#4  $-y+1, x+1/2, z+1/2$  #5  $y-1/2, -x+1, z+1/2$

Table 4. Anisotropic displacement parameters ( $\text{\AA}^2 \cdot 10^3$ ). The anisotropic displacement factor exponent takes the form:  $-2\pi^2 [h^2 a^{*2} U_{11} + \dots + 2 h k a^* b^* U_{12}]$ .

	$U_{11}$	$U_{22}$	$U_{33}$	$U_{23}$	$U_{13}$	$U_{12}$
Sn(1)	18(1)	16(1)	12(1)	-1(1)	1(1)	-1(1)
Cu(1)	24(1)	28(1)	19(1)	1(1)	-1(1)	1(1)
Cu(2)	25(1)	25(1)	20(1)	-2(1)	-2(1)	1(1)
S(1)	23(2)	18(2)	13(2)	-1(2)	4(2)	3(2)
S(2)	26(2)	22(2)	13(2)	0(2)	-6(2)	3(2)
S(3)	22(2)	21(2)	12(2)	0(2)	-1(2)	6(2)
S(4)	35(2)	19(2)	34(3)	3(2)	7(2)	-8(2)
N(2)	29(7)	33(8)	29(8)	13(7)	2(7)	18(6)
N(1)	36(9)	73(13)	54(12)	14(12)	7(10)	4(9)
C(4)	34(10)	28(10)	53(13)	-4(9)	-4(10)	12(8)
C(3)	32(13)	230(40)	53(16)	-80(20)	-14(12)	50(20)
C(2)	42(12)	49(12)	39(12)	1(10)	-6(10)	-9(10)

Table 5. Hydrogen coordinates ( $\cdot 10^4$ ) and isotropic displacement parameters ( $\text{\AA}^2 \cdot 10^3$ ).

	x	y	z	U(eq)
H(2A)	4507	4172	9389	36
H(2B)	4392	4891	8521	36
H(2C)	5250	4381	8584	36
H(1A)	3758	3271	2994	65
H(1B)	3052	3216	3887	65
H(1C)	3778	2530	3842	65
H(4A)	3611	3632	7965	46
H(4B)	4531	3072	8037	46
H(3A)	4083	4344	4389	125
H(3B)	4870	3594	4339	125
H(2A)	3280	3423	5903	52
H(2B)	4081	2693	5867	52
H(1A)	5129	3821	6494	43
H(1B)	4340	4556	6513	43

**6.2.4. Messprotokoll für die Verbindung (1,4-dabH<sub>2</sub>)Ag<sub>2</sub>SnS<sub>4</sub>**Table 1. Crystal data and structure refinement for (C<sub>4</sub>H<sub>14</sub>N<sub>2</sub>)Ag<sub>2</sub>SnS<sub>4</sub> (C<sub>4</sub>H<sub>12</sub>N<sub>2</sub>; 1,4-dab = 1,4-Diaminobutan).

Identification code	(C <sub>4</sub> H <sub>14</sub> N <sub>2</sub> )Ag <sub>2</sub> SnS <sub>4</sub> (NP 517)	
Empirical formula	(C <sub>4</sub> H <sub>14</sub> N <sub>2</sub> )Ag <sub>2</sub> SnS <sub>4</sub>	
Crystal colour, – Habitués	light yellow needles	
Formula weight	552.84 g/mol	
Temperature	293(2) K	
Wavelength	0.71073 Å	
Crystal system	Tetragonal	
Space group	P4 <sub>2</sub> /n	
Unit cell dimensions	a = 14.7847(8) Å	α = 90°
	b = 14.7847(8) Å	β = 90°
	c = 11.9087(6) Å	γ = 90°
Volume	2603.1(2) Å <sup>3</sup>	
Z	8	
Density (calculated)	2.821 g/cm <sup>3</sup>	
Absorption coefficient	5.486 mm <sup>-1</sup>	
F(000)	2080	
Crystal size	0.14 · 0.11 · 0.08 mm <sup>3</sup>	
Theta range for data collection	2.59 to 28.05°	
Index ranges	-18 ≤ h ≤ 19, -19 ≤ k ≤ 19, -14 ≤ l ≤ 15	
Reflections collected	24124	
Independent reflections	3143 [R(int) = 0.0426]	
Completeness to theta = 28.05°	99.5 %	
Refinement method	Full-matrix least-squares on F <sup>2</sup>	
Data / restraints / parameters	3143 / 0 / 119	
Goodness-of-fit on F <sup>2</sup>	1.042	
Final R indices [I > 2sigma(I)]	R1 = 0.0269, wR2 = 0.0678	
R indices (all data)	R1 = 0.0335, wR2 = 0.0711	
Extinction coefficient	0.00252(14)	
Largest diff. peak and hole	1.599 and -1.342 e.Å <sup>-3</sup>	

Table 2. Atomic coordinates ( $\cdot 10^4$ ) and equivalent isotropic displacement parameters ( $\text{\AA}^2 \cdot 10^3$ ).  $U(\text{eq})$  is defined as one third of the trace of the orthogonalized  $U_{ij}$  tensor.

	x	y	z	U(eq)
Sn(1)	7222(1)	4414(1)	1204(1)	16(1)
Ag(1)	6455(1)	2404(1)	-363(1)	33(1)
Ag(2)	7311(1)	3501(1)	-2189(1)	31(1)
S(1)	5992(1)	3358(1)	1276(1)	22(1)
S(2)	8097(1)	4191(1)	-452(1)	24(1)
S(3)	8105(1)	4327(1)	2883(1)	22(1)
S(4)	6612(1)	5903(1)	1054(1)	25(1)
N(1)	5713(3)	5285(2)	8636(3)	30(1)
N(2)	6779(3)	6310(3)	3714(3)	30(1)
C(1)	6014(3)	5491(3)	6604(3)	28(1)
C(2)	6571(3)	5990(3)	5729(3)	30(1)
C(3)	6282(3)	5755(3)	4557(3)	28(1)
C(4)	6319(3)	5707(3)	7784(3)	30(1)

Table 3. Bond lengths [ $\text{\AA}$ ] and angles [ $^\circ$ ].

Sn(1)-S(2)	2.3826(9)	S(1)-Ag(1)-S(3)#2	106.27(3)
Sn(1)-S(4)	2.3846(9)	S(2)#1-Ag(1)-Ag(2)	112.07(3)
Sn(1)-S(3)	2.3919(9)	S(1)-Ag(1)-Ag(2)	112.15(2)
Sn(1)-S(1)	2.3982(9)	S(3)#2-Ag(1)-Ag(2)	52.34(2)
Ag(1)-S(2)#1	2.4514(10)	S(2)#1-Ag(1)-Ag(1)#1	79.58(3)
Ag(1)-S(1)	2.5029(10)	S(1)-Ag(1)-Ag(1)#1	102.76(2)
Ag(1)-S(3)#2	2.6019(10)	S(3)#2-Ag(1)-Ag(1)#1	113.96(2)
Ag(1)-Ag(2)	2.9926(5)	Ag(2)-Ag(1)-Ag(1)#1	61.942(10)
Ag(1)-Ag(1)#1	3.1021(7)	S(2)#1-Ag(1)-Ag(2)#1	53.35(2)
Ag(1)-Ag(2)#1	3.1377(5)	S(1)-Ag(1)-Ag(2)#1	159.96(3)
Ag(2)-S(3)#2	2.4921(10)	S(3)#2-Ag(1)-Ag(2)#1	82.65(2)
Ag(2)-S(1)#3	2.5099(10)	Ag(2)-Ag(1)-Ag(2)#1	58.793(13)
Ag(2)-S(2)	2.5829(10)	Ag(1)#1-Ag(1)-Ag(2)#1	57.315(10)
Ag(2)-Ag(2)#1	3.0117(6)	S(3)#2-Ag(2)-S(1)#3	133.97(3)
Ag(2)-Ag(1)#1	3.1378(5)	S(3)#2-Ag(2)-S(2)	120.16(3)
S(1)-Ag(2)#4	2.5099(10)	S(1)#3-Ag(2)-S(2)	100.83(3)
S(2)-Ag(1)#1	2.4514(10)	S(3)#2-Ag(2)-Ag(1)	55.74(2)
S(3)-Ag(2)#5	2.4921(10)	S(1)#3-Ag(2)-Ag(1)	162.10(2)
S(3)-Ag(1)#5	2.6019(10)	S(2)-Ag(2)-Ag(1)	79.77(2)
N(1)-C(4)	1.489(5)	S(3)#2-Ag(2)-Ag(2)#1	87.11(2)
N(2)-C(3)	1.490(5)	S(1)#3-Ag(2)-Ag(2)#1	100.30(2)
C(1)-C(4)	1.510(6)	S(2)-Ag(2)-Ag(2)#1	107.72(2)
C(1)-C(2)	1.519(6)	Ag(1)-Ag(2)-Ag(2)#1	63.010(10)
C(2)-C(3)	1.500(6)	S(3)#2-Ag(2)-Ag(1)#1	116.15(2)
		S(1)#3-Ag(2)-Ag(1)#1	105.88(2)
S(2)-Sn(1)-S(4)	105.73(3)	S(2)-Ag(2)-Ag(1)#1	49.59(2)
S(2)-Sn(1)-S(3)	112.81(4)	Ag(1)-Ag(2)-Ag(1)#1	60.743(14)
S(4)-Sn(1)-S(3)	108.63(3)	Ag(2)#1-Ag(2)-Ag(1)#1	58.197(9)
S(2)-Sn(1)-S(1)	110.53(3)	Sn(1)-S(1)-Ag(1)	97.59(3)
S(4)-Sn(1)-S(1)	108.52(4)	Sn(1)-S(1)-Ag(2)#4	101.62(3)
S(3)-Sn(1)-S(1)	110.41(3)	Ag(1)-S(1)-Ag(2)#4	98.00(3)
S(2)#1-Ag(1)-S(1)	130.48(3)	Sn(1)-S(2)-Ag(1)#1	104.15(4)
S(2)#1-Ag(1)-S(3)#2	117.92(3)	Sn(1)-S(2)-Ag(2)	118.24(4)

Ag(1)#1-S(2)-Ag(2)	77.06(3)	C(4)-C(1)-C(2)	112.0(3)
Sn(1)-S(3)-Ag(2)#5	98.75(3)	C(3)-C(2)-C(1)	111.8(4)
Sn(1)-S(3)-Ag(1)#5	118.53(4)	N(2)-C(3)-C(2)	111.0(3)
Ag(2)#5-S(3)-Ag(1)#5	71.92(3)	N(1)-C(4)-C(1)	111.5(3)

Symmetry transformations used to generate equivalent atoms:

#1  $-x+3/2, -y+1/2, z$  #2  $-y+1, x-1/2, z-1/2$  #3  $y+1/2, -x+1, z-1/2$

#4  $-y+1, x-1/2, z+1/2$  #5  $y+1/2, -x+1, z+1/2$

Table 4. Anisotropic displacement parameters ( $\text{\AA}^2 \cdot 10^3$ ). The anisotropic displacement factor exponent takes the form:  $-2\pi^2 [h^2 a^{*2} U_{11} + \dots + 2 h k a^* b^* U_{12}]$ .

	$U_{11}$	$U_{22}$	$U_{33}$	$U_{23}$	$U_{13}$	$U_{12}$
Sn(1)	18(1)	15(1)	14(1)	0(1)	0(1)	2(1)
Ag(1)	32(1)	29(1)	38(1)	-3(1)	4(1)	-1(1)
Ag(2)	27(1)	25(1)	42(1)	3(1)	5(1)	1(1)
S(1)	20(1)	24(1)	24(1)	0(1)	0(1)	-3(1)
S(2)	30(1)	22(1)	20(1)	-4(1)	8(1)	-3(1)
S(3)	23(1)	24(1)	19(1)	0(1)	-5(1)	0(1)
S(4)	33(1)	18(1)	23(1)	-2(1)	-5(1)	9(1)
N(1)	35(2)	30(2)	24(2)	0(1)	0(1)	8(1)
N(2)	32(2)	36(2)	23(2)	-3(1)	4(1)	2(1)
C(1)	33(2)	27(2)	25(2)	5(2)	-2(2)	4(2)
C(2)	33(2)	36(2)	22(2)	1(2)	1(2)	-1(2)
C(3)	32(2)	25(2)	28(2)	-1(2)	2(2)	4(2)
C(4)	34(2)	31(2)	25(2)	3(2)	-1(2)	3(2)

Table 5. Hydrogen coordinates ( $\cdot 10^4$ ) and isotropic displacement parameters ( $\text{\AA}^2 \cdot 10^3$ ).

	x	y	z	U(eq)
H(1A)	5909	5422	9321	45
H(1B)	5716	4687	8547	45
H(1C)	5153	5493	8547	45
H(2A)	6598	6159	3026	46
H(2B)	7370	6211	3779	46
H(2C)	6664	6894	3833	46
H(1A)	5383	5656	6520	34
H(1B)	6065	4845	6477	34
H(2A)	6507	6637	5842	36
H(2B)	7205	5837	5824	36
H(3A)	6399	5119	4418	34
H(3B)	5638	5858	4479	34
H(4A)	6931	5488	7892	36
H(4B)	6322	6358	7890	36

### 6.2.5. Messprotokoll für die Verbindung (1,4-dabH)<sub>2</sub>MnSnS<sub>4</sub>

Table 1. Crystal data and structure refinement for (1,4-dabH)<sub>2</sub>MnSnS<sub>4</sub> (C<sub>8</sub>H<sub>12</sub>N<sub>2</sub>; 1,4-dab = 1,4-Diaminobutan).

Identification code	(C <sub>8</sub> H <sub>26</sub> N <sub>4</sub> ) MnSnS <sub>4</sub> (km 348)	
Empirical formula	C <sub>8</sub> H <sub>26</sub> N <sub>4</sub> MnSnS <sub>4</sub>	
Crystal colour, – Habitués	pale yellow rods	
Formula weight	480.20 g/mol	
Temperature	293(2) K	
Wavelength	0.71073 Å	
Crystal system	orthorhombic	
Space group	Fdd2	
Unit cell dimensions	a = 22.8124(15) Å	α = 90°
	b = 24.7887(16) Å	β = 90°
	c = 6.4153(6) Å	γ = 90°
Volume	3627.8(5) Å <sup>3</sup>	
Z	8	
Density (calculated)	1.758 g/cm <sup>3</sup>	
Absorption coefficient	2.524 mm <sup>-1</sup>	
F(000)	1928	
Crystal size	0.07 · 0.10 · 0.14 mm <sup>3</sup>	
Theta range for data collection	2.43 to 30.02°	
Index ranges	-32 ≤ h ≤ 2, -34 ≤ k ≤ 2, -9 ≤ l ≤ 9	
Reflections collected	3122	
Independent reflections	2636 [R(int) = 0.0179]	
Completeness to theta = 30.02°	99.9 %	
Refinement method	Full-matrix least-squares on F <sup>2</sup>	
Data / restraints / parameters	2636 / 1 / 86	
Goodness-of-fit on F <sup>2</sup>	1.046	
Final R indices [I > 2σ(I)]	R1 = 0.0184, wR2 = 0.0494	
R indices (all data)	R1 = 0.0217, wR2 = 0.0504	
Absolute structure parameter	-0.01(2)	
Extinction coefficient	0.00229(6)	
Largest diff. peak and hole	0.476 and -0.732 e.Å <sup>-3</sup>	

Table 2. Atomic coordinates ( $\cdot 10^4$ ) and equivalent isotropic displacement parameters ( $\text{\AA}^2 \cdot 10^3$ ).  $U(\text{eq})$  is defined as one third of the trace of the orthogonalized  $U_{ij}$  tensor.

	x	y	z	U(eq)
Sn(1)	5000	5000	8824	18(1)
Mn(1)	5000	5000	3832(2)	24(1)
S(1)	4201(1)	5017(1)	6433(1)	24(1)
S(2)	4961(1)	4262(1)	11233(1)	23(1)
N(1)	3802(1)	6304(1)	6767(3)	32(1)
N(2)	6080(1)	6396(1)	4998(4)	36(1)
C(3)	5281(1)	7015(1)	6076(4)	36(1)
C(1)	4273(1)	6702(1)	7195(4)	31(1)
C(4)	5793(1)	6923(1)	4625(4)	37(1)
C(2)	4792(1)	6601(1)	5782(4)	36(1)

Table 3. Bond lengths [ $\text{\AA}$ ] and angles [ $^\circ$ ].

Sn(1)-S(1)#1	2.3832(7)	S(2)-Sn(1)-Mn(1)	130.170(19)
Sn(1)-S(1)	2.3832(7)	S(1)#1-Sn(1)-Mn(1)#2	130.058(18)
Sn(1)-S(2)#1	2.3958(7)	S(1)-Sn(1)-Mn(1)#2	130.058(19)
Sn(1)-S(2)	2.3958(7)	S(2)#1-Sn(1)-Mn(1)#2	49.830(19)
Sn(1)-Mn(1)	3.2027(13)	S(2)-Sn(1)-Mn(1)#2	49.830(19)
Sn(1)-Mn(1)#2	3.2126(13)	Mn(1)-Sn(1)-Mn(1)#2	180.000(1)
Mn(1)-S(1)#1	2.4724(14)	S(1)#1-Mn(1)-S(1)	95.09(7)
Mn(1)-S(1)	2.4724(14)	S(1)#1-Mn(1)-S(2)#3	116.145(14)
Mn(1)-S(2)#3	2.4761(14)	S(1)-Mn(1)-S(2)#3	117.928(14)
Mn(1)-S(2)#4	2.4761(14)	S(1)#1-Mn(1)-S(2)#4	117.928(14)
Mn(1)-Sn(1)#4	3.2126(13)	S(1)-Mn(1)-S(2)#4	116.145(14)
S(2)-Mn(1)#2	2.4761(14)	S(2)#3-Mn(1)-S(2)#4	95.36(7)
N(1)-C(1)	1.485(3)	S(1)#1-Mn(1)-Sn(1)	47.54(3)
N(2)-C(4)	1.482(3)	S(1)-Mn(1)-Sn(1)	47.54(3)
C(3)-C(4)	1.510(3)	S(2)#3-Mn(1)-Sn(1)	132.32(4)
C(3)-C(2)	1.528(3)	S(2)#4-Mn(1)-Sn(1)	132.32(4)
C(1)-C(2)	1.511(3)	S(1)#1-Mn(1)-Sn(1)#4	132.46(3)
		S(1)-Mn(1)-Sn(1)#4	132.46(3)
S(1)#1-Sn(1)-S(1)	99.88(4)	S(2)#3-Mn(1)-Sn(1)#4	47.68(4)
S(1)#1-Sn(1)-S(2)#1	113.596(15)	S(2)#4-Mn(1)-Sn(1)#4	47.68(4)
S(1)-Sn(1)-S(2)#1	115.467(15)	Sn(1)-Mn(1)-Sn(1)#4	180.0
S(1)#1-Sn(1)-S(2)	115.467(15)	Sn(1)-S(1)-Mn(1)	82.51(3)
S(1)-Sn(1)-S(2)	113.595(15)	Sn(1)-S(2)-Mn(1)#2	82.49(3)
S(2)#1-Sn(1)-S(2)	99.66(4)	C(4)-C(3)-C(2)	112.80(19)
S(1)#1-Sn(1)-Mn(1)	49.942(18)	N(1)-C(1)-C(2)	110.27(17)
S(1)-Sn(1)-Mn(1)	49.942(18)	N(2)-C(4)-C(3)	112.01(19)
S(2)#1-Sn(1)-Mn(1)	130.170(19)	C(1)-C(2)-C(3)	112.78(19)

Symmetry transformations used to generate equivalent atoms:

#1 -x+1,-y+1,z #2 x,y,z+1 #3 -x+1,-y+1,z-1

#4 x,y,z-1

Table 4. Anisotropic displacement parameters ( $\text{\AA}^2 \cdot 10^3$ ). The anisotropic displacement factor exponent takes the form:  $-2\pi^2 [h^2 a^{*2} U_{11} + \dots + 2 h k a^* b^* U_{12}]$ .

	$U_{11}$	$U_{22}$	$U_{33}$	$U_{23}$	$U_{13}$	$U_{12}$
Sn(1)	19(1)	21(1)	14(1)	0	0	1(1)
Mn(1)	27(1)	28(1)	16(1)	0	0	-2(1)
S(1)	20(1)	31(1)	21(1)	2(1)	-2(1)	0(1)
S(2)	28(1)	21(1)	21(1)	2(1)	-4(1)	-1(1)
N(1)	28(1)	31(1)	37(1)	-4(1)	5(1)	5(1)
N(2)	29(1)	40(1)	39(1)	3(1)	2(1)	-1(1)
C(3)	32(1)	31(1)	45(1)	-4(1)	-6(1)	-1(1)
C(1)	28(1)	32(1)	33(1)	-5(1)	-2(1)	5(1)
C(4)	32(1)	40(1)	41(1)	8(1)	-3(1)	-6(1)
C(2)	31(1)	36(1)	41(1)	-11(1)	3(1)	-3(1)

Table 5. Hydrogen coordinates ( $\cdot 10^4$ ) and isotropic displacement parameters ( $\text{\AA}^2 \cdot 10^3$ ).

	x	y	z	U(eq)
H(1A)	3715	6308	5414	48
H(1B)	3484	6389	7501	48
H(1C)	3923	5976	7128	48
H(2A)	6134	6351	6360	54
H(2B)	6425	6390	4351	54
H(3A)	5124	7374	5837	43
H(3B)	5419	6999	7505	43
H(1A)	4396	6672	8639	37
H(1B)	4125	7064	6971	37
H(4A)	5656	6939	3194	45
H(4B)	6078	7209	4818	45
H(2A)	4661	6611	4343	43
H(2B)	4946	6244	6055	43

### 6.2.6. Messprotokoll für die Verbindung (DBNH)<sub>2</sub>Cu<sub>6</sub>Sn<sub>2</sub>S<sub>8</sub>

Table 1. Crystal data and structure refinement for (DBNH)<sub>2</sub>Cu<sub>6</sub>Sn<sub>2</sub>S<sub>8</sub> (C<sub>7</sub>H<sub>12</sub>N<sub>2</sub>; DBN = 1,5-Diazabicyclo[4.3.0]non-5-en).

Identification code	(DBNH) <sub>2</sub> Cu <sub>6</sub> Sn <sub>2</sub> S <sub>8</sub> (NP 524a)	
Empirical formula	C <sub>14</sub> H <sub>26</sub> N <sub>4</sub> Cu <sub>6</sub> Sn <sub>2</sub> S <sub>8</sub>	
Crystal colour, – Habitués	red plates	
Formula weight	1125.49 g/mol	
Temperature	293(2) K	
Wavelength	0.71073 Å	
Crystal system	Orthorhombic	
Space group	Pca2 <sub>1</sub>	
Unit cell dimensions	a = 21.3017(10) Å	α = 90°
	b = 6.6837(3) Å	β = 90°
	c = 19.9480(13) Å	γ = 90°
Volume	2840.1(3) Å <sup>3</sup>	
Z	4	
Density (calculated)	2.632 g/cm <sup>3</sup>	
Absorption coefficient	6.734 mm <sup>-1</sup>	
F(000)	2160	
Crystal size	0.14 · 0.10 · 0.07 mm <sup>3</sup>	
Theta range for data collection	2.80 to 28.02°	
Index ranges	-23 ≤ h ≤ 28, -8 ≤ k ≤ 8, -26 ≤ l ≤ 26	
Reflections collected	16982	
Independent reflections	6810 [R(int) = 0.0636]	
Completeness to theta = 28.02°	99.5 %	
Refinement method	Full-matrix least-squares on F <sup>2</sup>	
Data / restraints / parameters	6810 / 1 / 326	
Goodness-of-fit on F <sup>2</sup>	0.985	
Final R indices [I > 2sigma(I)]	R1 = 0.0441, wR2 = 0.1031	
R indices (all data)	R1 = 0.0597, wR2 = 0.1108	
Absolute structure parameter	-0.02(2)	
Extinction coefficient	0.00093(14)	
Largest diff. peak and hole	1.667 and -1.634 e.Å <sup>-3</sup>	

Table 2. Atomic coordinates ( $\cdot 10^4$ ) and equivalent isotropic displacement parameters ( $\text{\AA}^2 \cdot 10^3$ ).  $U(\text{eq})$  is defined as one third of the trace of the orthogonalized  $U_{ij}$  tensor.

	x	y	z	$U(\text{eq})$
Sn(1)	7774(1)	4665(1)	9182(1)	18(1)
Sn(2)	8213(1)	9737(1)	6695(1)	17(1)
Cu(1)	6834(1)	4606(2)	10873(1)	26(1)
Cu(2)	7479(1)	-629(2)	10080(1)	27(1)
Cu(3)	7480(1)	7411(2)	7785(1)	35(1)
Cu(4)	8333(1)	9474(2)	8578(1)	27(1)
Cu(5)	8531(1)	4402(2)	7530(1)	28(1)
Cu(6)	7379(1)	2491(2)	7835(1)	64(1)
S(1)	6710(1)	7881(3)	10677(1)	22(1)
S(2)	8234(1)	-2251(3)	9538(1)	24(1)
S(3)	7406(1)	2767(3)	10128(1)	22(1)
S(4)	6944(1)	5126(3)	8372(1)	23(1)
S(5)	8613(1)	7773(3)	7624(1)	21(1)
S(6)	8520(1)	2770(3)	8535(1)	29(1)
S(7)	8773(1)	2817(3)	6574(1)	23(1)
S(8)	7157(1)	10114(3)	7109(1)	25(1)
N(1)	4760(6)	7950(19)	3813(5)	53(3)
N(2)	3910(13)	8770(40)	4407(12)	51(5)
C(1)	4348(13)	7450(50)	4335(14)	40(6)
N(2')	4096(11)	7340(30)	4668(11)	41(5)
C(1')	4262(12)	8410(50)	4142(12)	34(4)
C(2)	4467(8)	5600(20)	4779(7)	57(4)
C(3)	5110(10)	5240(40)	4537(11)	98(8)
C(4)	5194(7)	6270(30)	3865(7)	62(4)
C(5)	4838(10)	9590(30)	3339(11)	90(7)
C(6)	4238(11)	10760(40)	3360(10)	100(8)
C(7)	3849(7)	10330(20)	3939(7)	51(3)
N(11)	9569(6)	3150(19)	1417(6)	53(3)
N(12)	8614(6)	3890(20)	968(8)	76(4)
C(11)	9098(6)	2880(20)	1004(6)	47(3)
C(12)	9234(9)	980(20)	533(8)	71(5)
C(13)	9932(10)	700(30)	697(9)	73(5)
C(14)	10075(9)	1720(30)	1356(9)	83(6)
C(15)	9553(11)	4700(30)	1959(10)	92(6)
C(16)	9102(11)	6280(30)	1705(11)	107(8)
C(17)	8529(11)	5530(30)	1415(9)	83(6)

Table 3. Bond lengths [ $\text{\AA}$ ] and angles [ $^\circ$ ].

Sn(1)-S(2)#1	2.392(2)	Cu(1)-S(7)#3	2.249(2)
Sn(1)-S(3)	2.405(2)	Cu(1)-S(3)	2.282(2)
Sn(1)-S(6)	2.407(2)	Cu(2)-S(2)	2.220(3)
Sn(1)-S(4)	2.414(2)	Cu(2)-S(1)#4	2.258(3)
Sn(1)-Cu(6)	3.1678(18)	Cu(2)-S(3)	2.277(2)
Sn(2)-S(1)#2	2.385(2)	Cu(3)-S(4)	2.238(2)
Sn(2)-S(7)#1	2.392(2)	Cu(3)-S(8)	2.357(3)
Sn(2)-S(8)	2.408(2)	Cu(3)-S(5)	2.446(3)
Sn(2)-S(5)	2.427(2)	Cu(3)-Cu(4)	2.7755(18)
Sn(2)-Cu(3)	3.0951(13)	Cu(3)-Cu(5)	3.052(2)
Cu(1)-S(1)	2.239(2)	Cu(4)-S(6)#1	2.240(2)

Cu(4)-S(2)#1	2.246(2)	S(1)-Cu(1)-S(3)	118.42(9)
Cu(4)-S(5)	2.295(2)	S(7)#3-Cu(1)-S(3)	115.21(8)
Cu(5)-S(7)	2.241(2)	S(2)-Cu(2)-S(1)#4	124.57(9)
Cu(5)-S(5)	2.268(2)	S(2)-Cu(2)-S(3)	123.83(10)
Cu(5)-S(6)	2.284(2)	S(1)#4-Cu(2)-S(3)	111.58(9)
Cu(5)-Cu(6)	2.833(2)	S(4)-Cu(3)-S(8)	132.35(11)
Cu(6)-S(8)#4	2.200(3)	S(4)-Cu(3)-S(5)	129.74(10)
Cu(6)-S(4)	2.260(3)	S(8)-Cu(3)-S(5)	97.88(8)
S(1)-Cu(2)#1	2.258(2)	S(4)-Cu(3)-Cu(4)	112.01(8)
S(1)-Sn(2)#3	2.385(2)	S(8)-Cu(3)-Cu(4)	97.82(7)
S(2)-Cu(4)#4	2.246(2)	S(5)-Cu(3)-Cu(4)	51.68(6)
S(2)-Sn(1)#4	2.392(2)	S(4)-Cu(3)-Cu(5)	90.68(8)
S(6)-Cu(4)#4	2.240(2)	S(8)-Cu(3)-Cu(5)	128.59(8)
S(7)-Cu(1)#2	2.249(2)	S(5)-Cu(3)-Cu(5)	47.13(5)
S(7)-Sn(2)#4	2.392(2)	Cu(4)-Cu(3)-Cu(5)	86.70(5)
S(8)-Cu(6)#1	2.200(3)	S(4)-Cu(3)-Sn(2)	165.39(8)
N(1)-C(1')	1.28(3)	S(8)-Cu(3)-Sn(2)	50.22(6)
N(1)-C(1)	1.40(3)	S(5)-Cu(3)-Sn(2)	50.29(5)
N(1)-C(4)	1.459(18)	Cu(4)-Cu(3)-Sn(2)	79.69(4)
N(1)-C(5)	1.46(2)	Cu(5)-Cu(3)-Sn(2)	81.03(4)
N(2)-C(1)	1.29(4)	S(6)#1-Cu(4)-S(2)#1	123.61(9)
N(2)-C(7)	1.41(3)	S(6)#1-Cu(4)-S(5)	114.18(9)
C(1)-C(2)	1.54(3)	S(2)#1-Cu(4)-S(5)	118.48(8)
N(2')-C(1')	1.32(3)	S(6)#1-Cu(4)-Cu(3)	125.70(9)
N(2')-C(2)	1.42(3)	S(2)#1-Cu(4)-Cu(3)	99.78(8)
C(1')-C(7)	1.61(4)	S(5)-Cu(4)-Cu(3)	56.75(7)
C(2)-C(3)	1.47(2)	S(7)-Cu(5)-S(5)	121.53(9)
C(3)-C(4)	1.52(2)	S(7)-Cu(5)-S(6)	121.58(8)
C(5)-C(6)	1.50(2)	S(5)-Cu(5)-S(6)	113.71(9)
C(6)-C(7)	1.45(2)	S(7)-Cu(5)-Cu(6)	99.75(8)
N(11)-C(11)	1.310(16)	S(5)-Cu(5)-Cu(6)	119.79(9)
N(11)-C(14)	1.45(2)	S(6)-Cu(5)-Cu(6)	65.61(9)
N(11)-C(15)	1.50(2)	S(7)-Cu(5)-Cu(3)	128.50(8)
N(12)-C(11)	1.233(18)	S(5)-Cu(5)-Cu(3)	52.26(7)
N(12)-C(17)	1.43(2)	S(6)-Cu(5)-Cu(3)	99.25(8)
C(11)-C(12)	1.61(2)	Cu(6)-Cu(5)-Cu(3)	68.03(5)
C(12)-C(13)	1.53(3)	S(8)#4-Cu(6)-S(4)	141.84(15)
C(13)-C(14)	1.51(3)	S(8)#4-Cu(6)-Cu(5)	111.71(9)
C(15)-C(16)	1.51(3)	S(4)-Cu(6)-Cu(5)	96.08(8)
C(16)-C(17)	1.44(3)	S(8)#4-Cu(6)-Sn(1)	161.09(10)
		S(4)-Cu(6)-Sn(1)	49.42(7)
S(2)#1-Sn(1)-S(3)	110.79(7)	Cu(5)-Cu(6)-Sn(1)	75.27(5)
S(2)#1-Sn(1)-S(6)	109.98(9)	Cu(1)-S(1)-Cu(2)#1	115.94(11)
S(3)-Sn(1)-S(6)	110.98(7)	Cu(1)-S(1)-Sn(2)#3	110.60(9)
S(2)#1-Sn(1)-S(4)	112.90(8)	Cu(2)#1-S(1)-Sn(2)#3	99.74(9)
S(3)-Sn(1)-S(4)	110.71(8)	Cu(2)-S(2)-Cu(4)#4	103.43(10)
S(6)-Sn(1)-S(4)	101.11(9)	Cu(2)-S(2)-Sn(1)#4	105.57(10)
S(2)#1-Sn(1)-Cu(6)	139.15(6)	Cu(4)#4-S(2)-Sn(1)#4	103.14(9)
S(3)-Sn(1)-Cu(6)	109.70(6)	Cu(2)-S(3)-Cu(1)	126.93(10)
S(6)-Sn(1)-Cu(6)	58.66(8)	Cu(2)-S(3)-Sn(1)	118.06(9)
S(4)-Sn(1)-Cu(6)	45.33(7)	Cu(1)-S(3)-Sn(1)	113.66(8)
S(1)#2-Sn(2)-S(7)#1	109.11(8)	Cu(3)-S(4)-Cu(6)	94.26(10)
S(1)#2-Sn(2)-S(8)	114.30(8)	Cu(3)-S(4)-Sn(1)	93.64(9)
S(7)#1-Sn(2)-S(8)	114.24(8)	Cu(6)-S(4)-Sn(1)	85.25(10)
S(1)#2-Sn(2)-S(5)	110.15(7)	Cu(5)-S(5)-Cu(4)	122.77(10)
S(7)#1-Sn(2)-S(5)	111.51(8)	Cu(5)-S(5)-Sn(2)	116.54(9)
S(8)-Sn(2)-S(5)	97.04(8)	Cu(4)-S(5)-Sn(2)	105.89(8)
S(1)#2-Sn(2)-Cu(3)	111.83(6)	Cu(5)-S(5)-Cu(3)	80.61(8)
S(7)#1-Sn(2)-Cu(3)	138.98(6)	Cu(4)-S(5)-Cu(3)	71.58(8)
S(8)-Sn(2)-Cu(3)	48.77(6)	Sn(2)-S(5)-Cu(3)	78.86(7)
S(5)-Sn(2)-Cu(3)	50.85(6)	Cu(4)#4-S(6)-Cu(5)	120.29(11)
S(1)-Cu(1)-S(7)#3	124.08(10)	Cu(4)#4-S(6)-Sn(1)	112.29(10)

Cu(5)-S(6)-Sn(1)	103.06(9)	N(2')-C(2)-C(1)	33.3(12)
Cu(5)-S(7)-Cu(1)#2	98.33(10)	C(3)-C(2)-C(1)	95.4(14)
Cu(5)-S(7)-Sn(2)#4	101.91(9)	C(2)-C(3)-C(4)	109.1(16)
Cu(1)#2-S(7)-Sn(2)#4	103.46(10)	N(1)-C(4)-C(3)	109.7(13)
Cu(6)#1-S(8)-Cu(3)	96.57(11)	N(1)-C(5)-C(6)	106.2(15)
Cu(6)#1-S(8)-Sn(2)	95.81(10)	C(7)-C(6)-C(5)	113.7(15)
Cu(3)-S(8)-Sn(2)	81.01(8)	N(2)-C(7)-C(6)	128.8(17)
C(1')-N(1)-C(1)	32.9(14)	N(2)-C(7)-C(1')	36.0(14)
C(1')-N(1)-C(4)	132.1(18)	C(6)-C(7)-C(1')	92.8(13)
C(1)-N(1)-C(4)	99.3(17)	C(11)-N(11)-C(14)	115.2(13)
C(1')-N(1)-C(5)	104.1(18)	C(11)-N(11)-C(15)	122.2(14)
C(1)-N(1)-C(5)	136.9(18)	C(14)-N(11)-C(15)	122.3(14)
C(4)-N(1)-C(5)	123.7(11)	C(11)-N(12)-C(17)	119.4(16)
C(1)-N(2)-C(7)	120(3)	N(12)-C(11)-N(11)	126.9(16)
N(2)-C(1)-N(1)	112(3)	N(12)-C(11)-C(12)	123.3(15)
N(2)-C(1)-C(2)	127(3)	N(11)-C(11)-C(12)	109.8(12)
N(1)-C(1)-C(2)	121(2)	C(13)-C(12)-C(11)	98.5(12)
C(1')-N(2')-C(2)	115(2)	C(14)-C(13)-C(12)	108.9(14)
N(1)-C(1')-N(2')	120(3)	N(11)-C(14)-C(13)	102.8(12)
N(1)-C(1')-C(7)	121(2)	N(11)-C(15)-C(16)	104.7(13)
N(2')-C(1')-C(7)	119(2)	C(17)-C(16)-C(15)	115.5(19)
N(2')-C(2)-C(3)	126.8(15)	N(12)-C(17)-C(16)	114.3(17)

Symmetry transformations used to generate equivalent atoms:

#1  $x, y+1, z$  #2  $-x+3/2, y, z-1/2$  #3  $-x+3/2, y, z+1/2$

#4  $x, y-1, z$

Table 4. Anisotropic displacement parameters ( $\text{\AA}^2 \cdot 10^3$ ). The anisotropic displacement factor exponent takes the form:  $-2\pi^2 [h^2 a^{*2} U_{11} + \dots + 2 h k a^* b^* U_{12}]$ .

	$U_{11}$	$U_{22}$	$U_{33}$	$U_{23}$	$U_{23}$	$U_{12}$
Sn(1)	28(1)	11(1)	17(1)	0(1)	1(1)	-2(1)
Sn(2)	25(1)	10(1)	15(1)	1(1)	-1(1)	-1(1)
Cu(1)	35(1)	17(1)	26(1)	1(1)	-2(1)	0(1)
Cu(2)	37(1)	21(1)	22(1)	-2(1)	0(1)	1(1)
Cu(3)	49(1)	29(1)	26(1)	3(1)	1(1)	-14(1)
Cu(4)	36(1)	17(1)	29(1)	-1(1)	1(1)	-2(1)
Cu(5)	34(1)	19(1)	30(1)	-4(1)	1(1)	-3(1)
Cu(6)	117(2)	29(1)	45(1)	-14(1)	39(1)	-22(1)
S(1)	39(1)	13(1)	16(1)	-1(1)	4(1)	-4(1)
S(2)	37(1)	13(1)	22(1)	-5(1)	6(1)	-5(1)
S(3)	34(1)	11(1)	20(1)	1(1)	7(1)	-1(1)
S(4)	25(1)	20(1)	26(1)	3(1)	1(1)	-1(1)
S(5)	33(1)	12(1)	18(1)	1(1)	-1(1)	1(1)
S(6)	50(2)	11(1)	26(1)	-1(1)	14(1)	2(1)
S(7)	37(1)	14(1)	19(1)	2(1)	-1(1)	-5(1)
S(8)	24(1)	21(1)	29(1)	-1(1)	-1(1)	2(1)
N(1)	50(7)	68(7)	40(5)	-11(5)	15(5)	3(6)
N(2)	57(16)	52(14)	43(11)	-13(10)	-11(11)	-4(12)
C(1)	39(15)	51(16)	31(14)	12(11)	8(11)	-6(12)
N(2')	52(13)	32(10)	40(10)	6(8)	24(10)	-3(9)
C(1')	36(13)	44(13)	21(10)	-10(10)	8(10)	-1(11)
C(2)	61(9)	49(7)	59(8)	17(6)	28(7)	3(6)
C(3)	71(12)	119(17)	102(15)	58(13)	43(11)	19(11)
C(4)	48(8)	85(11)	54(8)	29(7)	17(6)	24(8)
C(5)	90(14)	84(13)	96(13)	38(11)	46(12)	42(11)
C(6)	87(15)	117(17)	95(14)	35(12)	30(12)	55(13)

C(7)	55(8)	50(7)	47(6)	10(5)	6(6)	15(6)
N(11)	40(6)	58(7)	62(7)	-7(5)	-12(5)	11(5)
N(12)	49(8)	84(9)	95(9)	47(8)	-11(7)	0(7)
C(11)	26(6)	65(8)	49(6)	29(6)	-3(5)	-6(5)
C(12)	85(13)	62(9)	66(9)	7(7)	-11(8)	-37(9)
C(13)	81(13)	63(9)	76(11)	10(8)	14(9)	24(9)
C(14)	62(11)	111(15)	76(11)	20(10)	-20(9)	33(11)
C(15)	84(14)	111(16)	81(13)	-27(11)	-33(11)	-3(12)
C(16)	106(18)	107(16)	108(15)	-67(14)	-25(14)	29(14)
C(17)	97(16)	71(11)	82(12)	-8(9)	-19(11)	24(10)

Table 5. Hydrogen coordinates ( $\cdot 10^4$ ) and isotropic displacement parameters ( $\text{\AA}^2 \cdot 10^3$ ).

	x	y	z	U(eq)
H(2)	3655	8687	4741	61
H(2')	3788	7663	4924	50
H(2A)	4452	5905	5254	68
H(2B)	4185	4500	4677	68
H(2C)	4217	4494	4610	68
H(2D)	4486	5425	5261	68
H(3A)	5183	3816	4489	117
H(3B)	5411	5767	4857	117
H(4A)	5623	6745	3823	75
H(4B)	5115	5325	3506	75
H(5A)	4913	9084	2891	108
H(5B)	5189	10432	3469	108
H(6A)	4338	12181	3360	120
H(6B)	4000	10484	2956	120
H(7A)	3851	11543	4204	61
H(7B)	3426	10199	3764	61
H(7C)	3421	9988	3819	61
H(7D)	3854	11374	4275	61
H(12)	8330	3600	677	91
H(12A)	8986	-174	662	85
H(12B)	9166	1279	63	85
H(13A)	10030	-716	728	88
H(13B)	10188	1276	344	88
H(14A)	10070	766	1724	99
H(14B)	10480	2379	1344	99
H(15A)	9967	5260	2032	110
H(15B)	9404	4124	2377	110
H(16A)	8995	7153	2076	129
H(16B)	9318	7079	1372	129
H(17A)	8250	5123	1773	100
H(17B)	8327	6613	1173	100

### 6.2.7. Messprotokoll für die Verbindung (dienH<sub>2</sub>)Cu<sub>2</sub>Sn<sub>2</sub>S<sub>6</sub>

Table 1. Crystal data and structure refinement for (C<sub>4</sub>N<sub>3</sub>H<sub>15</sub>)Cu<sub>2</sub>Sn<sub>2</sub>S<sub>6</sub> (C<sub>4</sub>N<sub>3</sub>H<sub>14</sub>; dien = Diethylentriamin).

Identification code	(C <sub>4</sub> N <sub>3</sub> H <sub>15</sub> )Cu <sub>2</sub> Sn <sub>2</sub> S <sub>6</sub> (np388)	
Empirical formula	(C <sub>4</sub> N <sub>3</sub> H <sub>15</sub> )Cu <sub>2</sub> Sn <sub>2</sub> S <sub>6</sub>	
Crystal colour, – Habitués	black plates	
Formula weight	662.01 g/mol	
Temperature	293(2) K	
Wavelength	0.71073 Å	
Crystal system	Tetragonal	
Space group	I $\bar{4}$ m2	
Unit cell dimensions	a = 7.8793(3) Å	$\alpha = 90^\circ$
	b = 7.8793(3) Å	$\beta = 90^\circ$
	c = 24.9955(15) Å	$\gamma = 90^\circ$
Volume	1551.80(13) Å <sup>3</sup>	
Z	4	
Density (calculated)	2.834 g/cm <sup>3</sup>	
Absorption coefficient	6.673 mm <sup>-1</sup>	
F(000)	1256	
Crystal size	0.15 · 0.10 · 0.05 mm <sup>3</sup>	
Theta range for data collection	2.71 to 28.03°	
Index ranges	-9 ≤ h ≤ 10, -10 ≤ k ≤ 10, -32 ≤ l ≤ 30	
Reflections collected	6243	
Independent reflections	1078 [R(int) = 0.0578]	
Completeness to theta = 28.03°	99.7 %	
Refinement method	Full-matrix least-squares on F <sup>2</sup>	
Data / restraints / parameters	1078 / 0 / 57	
Goodness-of-fit on F <sup>2</sup>	1.052	
Final R indices [I > 2σ(I)]	R1 = 0.0417, wR2 = 0.0979	
R indices (all data)	R1 = 0.0471, wR2 = 0.1018	
Absolute structure parameter	0.02(6)	
Extinction coefficient	0.0037(4)	
Largest diff. peak and hole	3.923 and -1.949 e.Å <sup>-3</sup>	

Table 2. Atomic coordinates ( $\cdot 10^4$ ) and equivalent isotropic displacement parameters ( $\text{\AA}^2 \cdot 10^3$ ).  $U(\text{eq})$  is defined as one third of the trace of the orthogonalized  $U_{ij}$  tensor.

	x	y	z	U(eq)
Sn(1)	0	0	1519(1)	13(1)
Sn(2)	5000	0	1502(1)	14(1)
Cu	2541(1)	2459(1)	2500	21(1)
S(1)	0	2564(3)	2005(1)	15(1)
S(2)	5000	2594(3)	1972(1)	15(1)
S(3)	2478(4)	0	904(1)	22(1)
N(1)	2451(12)	5000	1267(4)	27(2)
C(1)	2740(20)	5000	698(6)	75(6)
C(2)	1580(30)	5000	348(6)	140(14)
N(2)	0	6070(20)	491(6)	25(3)

Table 3. Bond lengths [ $\text{\AA}$ ] and angles [ $^\circ$ ].

Sn(1)-S(1)	2.357(2)	S(2)#2-Sn(2)-S(3)	107.44(4)
Sn(1)-S(1)#1	2.357(2)	S(2)-Sn(2)-S(3)#2	107.44(4)
Sn(1)-S(3)#1	2.485(3)	S(2)#2-Sn(2)-S(3)#2	107.44(4)
Sn(1)-S(3)	2.485(3)	S(3)-Sn(2)-S(3)#2	106.13(12)
Sn(2)-S(2)	2.359(2)	S(2)-Cu-S(2)#3	113.04(11)
Sn(2)-S(2)#2	2.359(2)	S(2)-Cu-S(1)	113.88(5)
Sn(2)-S(3)	2.486(3)	S(2)#3-Cu-S(1)	106.61(7)
Sn(2)-S(3)#2	2.486(3)	S(2)-Cu-S(1)#4	106.61(7)
Cu-S(2)	2.3464(13)	S(2)#3-Cu-S(1)#4	113.88(5)
Cu-S(2)#3	2.3464(13)	S(1)-Cu-S(1)#4	102.51(11)
Cu-S(1)	2.3555(12)	Cu-S(1)-Cu#5	116.43(8)
Cu-S(1)#4	2.3555(12)	Cu-S(1)-Sn(1)	103.93(6)
S(1)-Cu#5	2.3555(12)	Cu#5-S(1)-Sn(1)	103.93(6)
S(2)-Cu#6	2.3464(13)	Cu#6-S(2)-Cu	111.32(8)
N(1)-C(1)	1.441(16)	Cu#6-S(2)-Sn(2)	103.95(6)
N(1)-H(1N1)	0.8900	Cu-S(2)-Sn(2)	103.95(6)
N(1)-H(2N1)	0.8900	Sn(1)-S(3)-Sn(2)	104.86(8)
C(1)-C(2)	1.27(3)	C(1)-N(1)-H(1N1)	109.1
C(1)-H(1)	0.9699	C(1)-N(1)-H(2N1)	109.6
C(2)-N(2)#7	1.54(2)	H(1N1)-N(1)-H(2N1)	109.5
C(2)-N(2)	1.54(2)	C(2)-C(1)-N(1)	124.3(17)
C(2)-H(2A)	0.9600	C(2)-C(1)-H(1)	105.6
C(2)-H(2B)	0.9599	N(1)-C(1)-H(1)	106.8
N(2)-C(2)#7	1.54(2)	C(1)-C(2)-N(2)#7	115.1(13)
N(2)-N(2)#7	1.68(4)	C(1)-C(2)-N(2)	115.1(13)
N(2)-H(1N2)	0.9000	N(2)#7-C(2)-N(2)	66.1(16)
		C(1)-C(2)-H(2A)	108.2
S(1)-Sn(1)-S(1)#1	117.98(10)	N(2)#7-C(2)-H(2A)	43.0
S(1)-Sn(1)-S(3)#1	108.58(4)	N(2)-C(2)-H(2A)	107.3
S(1)#1-Sn(1)-S(3)#1	108.58(4)	C(1)-C(2)-H(2B)	110.2
S(1)-Sn(1)-S(3)	108.58(4)	N(2)#7-C(2)-H(2B)	131.8
S(1)#1-Sn(1)-S(3)	108.58(4)	N(2)-C(2)-H(2B)	108.4
S(3)#1-Sn(1)-S(3)	103.59(11)	H(2A)-C(2)-H(2B)	107.5
S(2)-Sn(2)-S(2)#2	120.16(11)	C(2)#7-N(2)-C(2)	107.3(18)
S(2)-Sn(2)-S(3)	107.44(4)	C(2)#7-N(2)-N(2)#7	57.0(8)

C(2)-N(2)-N(2)#7	57.0(8)	C(2)-N(2)-H(1N2)	109.6
C(2)#7-N(2)-H(1N2)	109.6	N(2)#7-N(2)-H(1N2)	147.5

Symmetry transformations used to generate equivalent atoms:

#1 -x,-y,z #2 -x+1,-y,z #3 -y+1/2,x-1/2,-z+1/2  
 #4 -y+1/2,x+1/2,-z+1/2 #5 y-1/2,-x+1/2,-z+1/2  
 #6 y+1/2,-x+1/2,-z+1/2 #7 -x,-y+1,z

Table 4. Anisotropic displacement parameters ( $\text{\AA}^2 \cdot 10^3$ ). The anisotropic displacement factor exponent takes the form:  $-2\pi^2[h^2 a^{*2}U_{11} + \dots + 2 h k a^* b^* U_{12}]$ .

	$U_{11}$	$U_{22}$	$U_{33}$	$U_{23}$	$U_{13}$	$U_{12}$
Sn(1)	10(1)	14(1)	15(1)	0	0	0
Sn(2)	11(1)	16(1)	15(1)	0	0	0
Cu	21(1)	21(1)	21(1)	0(1)	0(1)	0(1)
S(1)	11(1)	15(1)	18(1)	-2(1)	0	0
S(2)	11(1)	16(1)	17(1)	-1(1)	0	0
S(3)	14(1)	38(1)	13(1)	0	0(1)	0
N(1)	19(4)	31(4)	31(4)	0	0(4)	0
C(1)	49(10)	140(20)	31(7)	0	-7(7)	0
C(2)	89(17)	310(40)	21(6)	0	6(9)	0
N(2)	30(8)	23(7)	21(7)	15(6)	0	0

Table 5. Hydrogen coordinates ( $\cdot 10^4$ ) and isotropic displacement parameters ( $\text{\AA}^2 \cdot 10^3$ ).

	x	y	z	U(eq)
H(1N1)	3445	5000	1436	40
H(2N1)	1867	4078	1358	40
H(1)	3438	4013	619	90
H(2A)	1201	3851	298	168
H(2B)	2010	5393	11	168
H(1N2)	0	7030	298	30

### 6.2.8. Messprotokoll für die Verbindung $[\text{Mn}(\text{trien})]_2\text{SnS}_4 \cdot 4 \text{H}_2\text{O}$

Table 1. Crystal data and structure refinement for  $[\text{Mn}(\text{trien})]_2\text{SnS}_4 \cdot 4 \text{H}_2\text{O}$  ( $\text{C}_6\text{H}_{18}\text{N}_4$ ; trien = Triethylentetramin).

Identification code	$[\text{Mn}(\text{trien})]_2\text{SnS}_4 \cdot 4 \text{H}_2\text{O}$ (np736)	
Empirical formula	$(\text{C}_6\text{H}_{18}\text{N}_4)_2\text{Mn}_2\text{SnS}_4 \cdot 4 \text{H}_2\text{O}$	
Crystal colour, – Habitués	yellow needles	
Formula weight	721.36 g/mol	
Temperature	170(2) K	
Wavelength	0.71073 Å	
Crystal system	Monoclinic	
Space group	$P2_1/c$	
Unit cell dimensions	$a = 10.8446(9) \text{ \AA}$	$\alpha = 90^\circ$
	$b = 20.9740(10) \text{ \AA}$	$\beta = 113.487(8)^\circ$
	$c = 13.2746(9) \text{ \AA}$	$\gamma = 90^\circ$
Volume	$2769.2(3) \text{ \AA}^3$	
Z	4	
Density (calculated)	$1.730 \text{ g/cm}^3$	
Absorption coefficient	$2.128 \text{ mm}^{-1}$	
F(000)	1472	
Crystal size	$0.15 \cdot 0.11 \cdot 0.07 \text{ mm}^3$	
Theta range for data collection	2.28 to $28.11^\circ$	
Index ranges	$-14 \leq h \leq 14, -24 \leq k \leq 27, -13 \leq l \leq 17$	
Reflections collected	15023	
Independent reflections	6549 [R(int) = 0.0520]	
Completeness to theta = $28.11^\circ$	96.9 %	
Refinement method	Full-matrix least-squares on $F^2$	
Data / restraints / parameters	6549 / 0 / 281	
Goodness-of-fit on $F^2$	0.984	
Final R indices [ $l > 2\sigma(l)$ ]	R1 = 0.0369, wR2 = 0.0854	
R indices (all data)	R1 = 0.0584, wR2 = 0.0924	
Extinction coefficient	0.0026(3)	
Largest diff. peak and hole	0.669 and $-0.955 \text{ e.\AA}^{-3}$	

Table 2. Atomic coordinates ( $\cdot 10^4$ ) and equivalent isotropic displacement parameters ( $\text{\AA}^2 \cdot 10^3$ ).  $U(\text{eq})$  is defined as one third of the trace of the orthogonalized  $U_{ij}$  tensor.

	x	y	z	U(eq)
Sn(1)	5796(1)	4594(1)	7812(1)	13(1)
Mn(2)	4976(1)	4116(1)	4780(1)	15(1)
Mn(1)	6956(1)	5167(1)	10861(1)	15(1)
S(1)	5183(1)	5368(1)	8893(1)	14(1)
S(2)	4258(1)	4847(1)	5969(1)	14(1)
S(3)	8068(1)	4717(1)	8041(1)	17(1)
S(4)	5359(1)	3541(1)	8245(1)	18(1)
N(1)	8505(3)	5641(2)	10297(3)	20(1)
N(2)	7688(3)	6110(2)	11915(3)	18(1)
N(3)	8088(3)	4836(2)	12660(3)	19(1)
N(4)	7996(3)	4258(2)	10693(3)	21(1)
N(5)	7165(3)	3846(2)	5651(3)	22(1)
N(6)	5380(3)	3555(2)	3455(3)	20(1)
N(7)	2863(3)	3867(2)	3511(3)	19(1)
N(8)	4381(3)	3206(2)	5504(3)	19(1)
C(1)	8349(4)	6335(2)	10393(3)	20(1)
C(2)	8640(4)	6471(2)	11585(4)	22(1)
C(3)	8277(4)	5959(2)	13103(3)	23(1)
C(4)	9047(4)	5333(2)	13300(3)	22(1)
C(5)	8683(4)	4201(2)	12675(4)	24(1)
C(6)	9157(4)	4139(2)	11750(4)	21(1)
C(7)	7695(4)	3686(2)	4813(4)	24(1)
C(8)	6702(4)	3240(2)	3968(4)	25(1)
C(9)	4233(4)	3130(2)	2878(4)	23(1)
C(10)	2934(4)	3514(2)	2573(3)	22(1)
C(11)	2164(4)	3539(2)	4116(4)	27(1)
C(12)	2999(4)	2992(2)	4826(4)	25(1)
O(1)	5648(3)	3179(2)	10667(3)	31(1)
O(2)	9995(4)	2429(2)	5769(4)	46(1)
O(3)	8122(4)	2473(2)	6787(3)	45(1)
O(4)	8344(3)	3176(2)	8635(3)	30(1)

Table 3. Bond lengths [ $\text{\AA}$ ] and angles [ $^\circ$ ].

Sn(1)-S(3)	2.3736(9)	Mn(1)-N(2)	2.370(3)
Sn(1)-S(4)	2.3782(10)	Mn(1)-S(1)	2.5874(11)
Sn(1)-S(2)	2.4070(10)	Mn(1)-S(1)#2	2.7115(10)
Sn(1)-S(1)	2.4275(9)	S(1)-Mn(1)#2	2.7115(10)
Mn(2)-N(5)	2.259(3)	S(2)-Mn(2)#1	2.6581(11)
Mn(2)-N(6)	2.298(3)	N(1)-C(1)	1.476(5)
Mn(2)-N(7)	2.299(3)	N(2)-C(3)	1.480(5)
Mn(2)-N(8)	2.341(3)	N(2)-C(2)	1.481(5)
Mn(2)-S(2)	2.5359(11)	N(3)-C(5)	1.476(5)
Mn(2)-S(2)#1	2.6581(11)	N(3)-C(4)	1.479(5)
Mn(1)-N(4)	2.271(3)	N(4)-C(6)	1.487(5)
Mn(1)-N(3)	2.315(3)	N(5)-C(7)	1.479(6)
Mn(1)-N(1)	2.317(3)	N(6)-C(9)	1.473(5)

N(6)-C(8)	1.475(5)	N(2)-Mn(1)-S(1)	113.56(9)
N(7)-C(11)	1.476(6)	N(4)-Mn(1)-S(1)#2	98.44(9)
N(7)-C(10)	1.476(5)	N(3)-Mn(1)-S(1)#2	83.01(9)
N(8)-C(12)	1.478(5)	N(1)-Mn(1)-S(1)#2	168.97(9)
C(1)-C(2)	1.511(6)	N(2)-Mn(1)-S(1)#2	112.05(8)
C(3)-C(4)	1.522(6)	S(1)-Mn(1)-S(1)#2	82.09(3)
C(5)-C(6)	1.514(6)	Sn(1)-S(1)-Mn(1)	102.69(3)
C(7)-C(8)	1.525(6)	Sn(1)-S(1)-Mn(1)#2	104.10(4)
C(9)-C(10)	1.531(6)	Mn(1)-S(1)-Mn(1)#2	97.91(3)
C(11)-C(12)	1.532(6)	Sn(1)-S(2)-Mn(2)	103.84(4)
S(3)-Sn(1)-S(4)	111.50(3)	Sn(1)-S(2)-Mn(2)#1	111.54(4)
S(3)-Sn(1)-S(2)	111.71(3)	Mn(2)-S(2)-Mn(2)#1	92.45(3)
S(4)-Sn(1)-S(2)	109.05(3)	C(1)-N(1)-Mn(1)	105.8(2)
S(3)-Sn(1)-S(1)	111.49(3)	C(3)-N(2)-C(2)	111.7(3)
S(4)-Sn(1)-S(1)	110.50(3)	C(3)-N(2)-Mn(1)	110.6(2)
S(2)-Sn(1)-S(1)	102.21(3)	C(2)-N(2)-Mn(1)	111.2(3)
N(5)-Mn(2)-N(6)	77.38(13)	C(5)-N(3)-C(4)	115.1(3)
N(5)-Mn(2)-N(7)	148.79(13)	C(5)-N(3)-Mn(1)	109.5(3)
N(6)-Mn(2)-N(7)	76.20(12)	C(4)-N(3)-Mn(1)	110.1(2)
N(5)-Mn(2)-N(8)	89.47(13)	C(6)-N(4)-Mn(1)	108.4(3)
N(6)-Mn(2)-N(8)	93.69(13)	C(7)-N(5)-Mn(2)	108.4(2)
N(7)-Mn(2)-N(8)	76.00(12)	C(9)-N(6)-C(8)	115.7(3)
N(5)-Mn(2)-S(2)	110.71(10)	C(9)-N(6)-Mn(2)	109.2(3)
N(6)-Mn(2)-S(2)	170.20(9)	C(8)-N(6)-Mn(2)	108.8(3)
N(7)-Mn(2)-S(2)	97.45(9)	C(11)-N(7)-C(10)	115.9(3)
N(8)-Mn(2)-S(2)	91.94(9)	C(11)-N(7)-Mn(2)	106.6(2)
N(5)-Mn(2)-S(2)#1	88.59(10)	C(10)-N(7)-Mn(2)	111.1(2)
N(6)-Mn(2)-S(2)#1	87.13(9)	C(12)-N(8)-Mn(2)	112.1(2)
N(7)-Mn(2)-S(2)#1	106.31(9)	N(1)-C(1)-C(2)	107.1(3)
N(8)-Mn(2)-S(2)#1	177.68(9)	N(2)-C(2)-C(1)	109.5(3)
S(2)-Mn(2)-S(2)#1	87.55(3)	N(2)-C(3)-C(4)	110.0(3)
N(4)-Mn(1)-N(3)	76.67(13)	N(3)-C(4)-C(3)	107.3(3)
N(4)-Mn(1)-N(1)	82.90(13)	N(3)-C(5)-C(6)	110.9(3)
N(3)-Mn(1)-N(1)	107.90(12)	N(4)-C(6)-C(5)	108.5(3)
N(4)-Mn(1)-N(2)	134.10(12)	N(5)-C(7)-C(8)	108.7(3)
N(3)-Mn(1)-N(2)	74.09(12)	N(6)-C(8)-C(7)	109.7(3)
N(1)-Mn(1)-N(2)	73.56(12)	N(6)-C(9)-C(10)	108.4(3)
N(4)-Mn(1)-S(1)	103.64(9)	N(7)-C(10)-C(9)	113.1(3)
N(3)-Mn(1)-S(1)	164.98(9)	N(7)-C(11)-C(12)	112.2(3)
N(1)-Mn(1)-S(1)	86.95(9)	N(8)-C(12)-C(11)	110.7(3)

Symmetry transformations used to generate equivalent atoms:

#1 -x+1,-y+1,-z+1 #2 -x+1,-y+1,-z+2

Table 4. Anisotropic displacement parameters ( $\text{\AA}^2 \cdot 10^3$ ). The anisotropic displacement factor exponent takes the form:  $-2\pi^2 [h^2 a^{*2} U_{11} + \dots + 2 h k a^* b^* U_{12}]$ .

	$U_{11}$	$U_{22}$	$U_{33}$	$U_{23}$	$U_{13}$	$U_{12}$
Sn(1)	13(1)	13(1)	12(1)	1(1)	5(1)	0(1)
Mn(2)	18(1)	13(1)	14(1)	-1(1)	6(1)	1(1)
Mn(1)	14(1)	16(1)	13(1)	0(1)	4(1)	-1(1)
S(1)	14(1)	17(1)	12(1)	-1(1)	6(1)	1(1)
S(2)	16(1)	13(1)	12(1)	1(1)	6(1)	1(1)
S(3)	14(1)	20(1)	19(1)	-1(1)	7(1)	-1(1)
S(4)	18(1)	15(1)	20(1)	3(1)	8(1)	-1(1)
N(1)	18(2)	23(2)	17(2)	-1(1)	5(1)	-3(1)
N(2)	14(1)	20(2)	19(2)	-1(1)	5(1)	0(1)
N(3)	17(2)	23(2)	16(2)	3(1)	6(1)	0(1)
N(4)	22(2)	21(2)	20(2)	-1(1)	8(1)	0(1)
N(5)	25(2)	20(2)	21(2)	0(1)	8(1)	4(1)
N(6)	32(2)	13(2)	17(2)	-1(1)	12(1)	2(1)
N(7)	22(2)	15(2)	17(2)	0(1)	5(1)	0(1)
N(8)	24(2)	15(2)	17(2)	1(1)	6(1)	2(1)
C(1)	19(2)	21(2)	18(2)	5(2)	4(2)	-2(1)
C(2)	24(2)	20(2)	22(2)	0(2)	7(2)	-4(2)
C(3)	22(2)	28(2)	19(2)	-4(2)	9(2)	-7(2)
C(4)	16(2)	32(2)	14(2)	1(2)	0(1)	-2(2)
C(5)	26(2)	23(2)	21(2)	8(2)	8(2)	4(2)
C(6)	18(2)	21(2)	23(2)	4(2)	6(2)	3(2)
C(7)	20(2)	23(2)	31(2)	2(2)	12(2)	5(2)
C(8)	33(2)	19(2)	27(2)	2(2)	17(2)	6(2)
C(9)	30(2)	14(2)	23(2)	-5(2)	11(2)	-2(2)
C(10)	29(2)	19(2)	13(2)	-4(2)	2(2)	-3(2)
C(11)	18(2)	32(2)	32(3)	-2(2)	10(2)	-1(2)
C(12)	27(2)	24(2)	26(2)	1(2)	11(2)	-9(2)
O(1)	46(2)	22(2)	27(2)	2(1)	15(1)	-2(1)
O(2)	37(2)	46(2)	54(3)	-8(2)	17(2)	5(2)
O(3)	57(2)	46(2)	39(2)	-8(2)	28(2)	-10(2)
O(4)	24(2)	24(2)	46(2)	2(1)	19(1)	4(1)

Table 5. Hydrogen coordinates ( $\cdot 10^4$ ) and isotropic displacement parameters ( $\text{\AA}^2 \cdot 10^3$ ).

	x	y	z	U(eq)
H(1A)	9364	5514	10738	24
H(1B)	8334	5532	9583	24
H(2)	6938	6366	11777	22
H(3)	7453	4790	12963	22
H(4A)	7405	3921	10529	25
H(4B)	8289	4300	10134	25
H(5A)	7643	4181	6075	27
H(5B)	7250	3501	6102	27
H(6)	5430	3847	2946	24
H(7)	2413	4248	3243	23
H(8A)	4974	2882	5549	23
H(8B)	4450	3293	6204	23
H(1A)	7422	6468	9920	24
H(1B)	8985	6570	10164	24
H(2A)	9575	6344	12051	27
H(2B)	8546	6933	11687	27
H(3A)	7552	5926	13376	27
H(3B)	8892	6306	13511	27
H(4A)	9797	5368	13057	27
H(4B)	9423	5225	14092	27
H(5A)	8006	3868	12598	28
H(5B)	9453	4137	13387	28
H(6A)	9880	4452	11849	26
H(6B)	9520	3705	11751	26
H(7A)	8581	3474	5166	29
H(7B)	7812	4079	4449	29
H(8A)	7039	3131	3398	30
H(8B)	6613	2841	4331	30
H(9A)	4239	2768	3357	27
H(9B)	4298	2958	2206	27
H(10A)	2862	3821	1986	27
H(10B)	2158	3220	2277	27
H(11A)	1297	3369	3585	33
H(11B)	1966	3851	4592	33
H(12A)	2567	2834	5310	30
H(12B)	3030	2636	4347	30
H(1O1)	5537	3520	10954	47
H(2O1)	5501	3258	10009	47
H(1O2)	9486	2469	6104	69
H(2O2)	9477	2265	5173	69
H(1O3)	8223	2581	7425	67
H(2O3)	7442	2236	6598	67
H(1O4)	7549	3190	8588	45
H(2O4)	8389	3559	8472	45

### 6.2.9. Messprotokoll für die Verbindung $[\text{Mn}(1,2\text{-dach})_2(\text{H}_2\text{O})]_2\text{Sn}_2\text{S}_6$

Table 1. Crystal data and structure refinement for  $[\text{Mn}(1,2\text{-dach})_2(\text{H}_2\text{O})]_2\text{Sn}_2\text{S}_6$  ( $\text{C}_6\text{N}_2\text{H}_{14}$ ; 1,2-dach = 1,2-Diaminocyclohexan).

Identification code	$[\text{Mn}(\text{C}_6\text{N}_2\text{H}_{14})_2(\text{H}_2\text{O})]_2\text{Sn}_2\text{S}_6$ (np768)	
Empirical formula	$\text{C}_{24}\text{H}_{56}\text{N}_8 \text{H}_4\text{O}_2 \text{Mn}_2\text{Sn}_2\text{S}_6$	
Crystal colour, – Habitués	dark brown rods	
Formula weight	1032.42 g/mol	
Temperature	293(2) K	
Wavelength	0.71073 Å	
Crystal system	Monoclinic	
Space group	C2/c	
Unit cell dimensions	$a = 23.7500(18)$ Å	$\alpha = 90^\circ$
	$b = 15.5655(16)$ Å	$\beta = 113.532(8)^\circ$
	$c = 12.1072(9)$ Å	$\gamma = 90^\circ$
Volume	$4103.6(6)$ Å <sup>3</sup>	
Z	4	
Density (calculated)	1.671 g/cm <sup>3</sup>	
Absorption coefficient	2.143 mm <sup>-1</sup>	
F(000)	2088	
Crystal size	0.14 · 0.11 · 0.08 mm <sup>3</sup>	
Theta range for data collection	2.62 to 28.16°	
Index ranges	-31 ≤ h ≤ 31, -20 ≤ k ≤ 20, -15 ≤ l ≤ 15	
Reflections collected	25198	
Independent reflections	4943 [R(int) = 0.0614]	
Completeness to theta = 28.16°	98.0 %	
Absorption correction	Numerical	
Max. and min. transmission	0.7614 and 0.6164	
Refinement method	Full-matrix least-squares on F <sup>2</sup>	
Data / restraints / parameters	4943 / 0 / 196	
Goodness-of-fit on F <sup>2</sup>	1.049	
Final R indices [I > 2σ(I)]	R1 = 0.0381, wR2 = 0.0923	
R indices (all data)	R1 = 0.0457, wR2 = 0.0958	
Largest diff. peak and hole	1.386 and -1.201 e.Å <sup>-3</sup>	

Table 2. Atomic coordinates ( $\cdot 10^4$ ) and equivalent isotropic displacement parameters ( $\text{\AA}^2 \cdot 10^3$ ).  $U(\text{eq})$  is defined as one third of the trace of the orthogonalized  $U_{ij}$  tensor.

	x	y	z	U(eq)
Sn(1)	2165(1)	1825(1)	5646(1)	26(1)
Mn(1)	1671(1)	-570(1)	5995(1)	30(1)
S(1)	1516(1)	703(1)	4550(1)	36(1)
S(2)	2293(1)	1841(1)	7656(1)	41(1)
S(3)	3126(1)	1778(1)	5335(1)	35(1)
N(1)	1413(2)	-1744(2)	6818(3)	36(1)
N(2)	772(2)	-1067(3)	4529(4)	73(2)
C(1)	859(2)	-2198(3)	5976(4)	48(1)
C(2)	439(2)	-1596(4)	5052(6)	67(2)
C(3)	-146(2)	-2019(4)	4187(6)	72(2)
C(4)	-455(3)	-2539(5)	4826(8)	90(2)
C(5)	-53(3)	-3136(4)	5716(7)	80(2)
C(6)	529(2)	-2724(4)	6584(5)	61(1)
N(3)	2380(2)	-1280(2)	5527(3)	36(1)
N(4)	2574(1)	-347(2)	7611(3)	33(1)
C(7)	2950(2)	-766(3)	6068(4)	44(1)
C(8)	3110(2)	-666(3)	7407(4)	43(1)
C(9)	3680(2)	-101(3)	7987(5)	52(1)
C(10)	4215(2)	-387(5)	7692(6)	79(2)
C(11)	4051(3)	-543(5)	6420(6)	81(2)
C(12)	3486(1)	-1117(2)	5837(2)	52(1)
O(1)	1265(1)	262(2)	7070(2)	46(1)

Table 3. Bond lengths [ $\text{\AA}$ ] and angles [ $^\circ$ ].

Sn(1)-S(2)	2.3294(10)	C(4)-C(5)	1.454(10)
Sn(1)-S(1)	2.3561(9)	C(4)-H(4A)	0.9700
Sn(1)-S(3)#1	2.4415(9)	C(4)-H(4B)	0.9700
Sn(1)-S(3)	2.4582(10)	C(5)-C(6)	1.506(8)
Mn(1)-N(3)	2.268(3)	C(5)-H(5A)	0.9700
Mn(1)-N(1)	2.279(3)	C(5)-H(5B)	0.9700
Mn(1)-N(4)	2.281(3)	C(6)-H(6A)	0.9700
Mn(1)-N(2)	2.297(4)	C(6)-H(6B)	0.9700
Mn(1)-O(1)	2.302(3)	N(3)-C(7)	1.481(5)
Mn(1)-S(1)	2.5707(10)	N(3)-H(3C)	0.9000
S(3)-Sn(1)#1	2.4415(9)	N(3)-H(3D)	0.9000
N(1)-C(1)	1.482(5)	N(4)-C(8)	1.477(5)
N(1)-H(1A)	0.9000	N(4)-H(4C)	0.9000
N(1)-H(1B)	0.9000	N(4)-H(4D)	0.9000
N(2)-C(2)	1.450(7)	C(7)-C(12)	1.510(5)
N(2)-H(2A)	0.9000	C(7)-C(8)	1.518(6)
N(2)-H(2B)	0.9000	C(7)-H(7)	0.9800
C(1)-C(2)	1.494(7)	C(8)-C(9)	1.529(6)
C(1)-C(6)	1.512(6)	C(8)-H(8)	0.9800
C(1)-H(1)	0.9800	C(9)-C(10)	1.518(7)
C(2)-C(3)	1.516(7)	C(9)-H(9A)	0.9700
C(2)-H(2)	0.9800	C(9)-H(9B)	0.9700
C(3)-C(4)	1.499(10)	C(10)-C(11)	1.450(9)
C(3)-H(3A)	0.9700	C(10)-H(10A)	0.9700
C(3)-H(3B)	0.9700	C(10)-H(10B)	0.9700

C(11)-C(12)	1.530(6)	C(5)-C(4)-H(4A)	108.6
C(11)-H(11A)	0.9700	C(3)-C(4)-H(4A)	108.6
C(11)-H(11B)	0.9700	C(5)-C(4)-H(4B)	108.6
C(12)-H(12A)	0.9700	C(3)-C(4)-H(4B)	108.6
C(12)-H(12B)	0.9700	H(4A)-C(4)-H(4B)	107.6
O(1)-H(1O1)	0.9459	C(4)-C(5)-C(6)	113.1(5)
O(1)-H(2O1)	1.1034	C(4)-C(5)-H(5A)	109.0
		C(6)-C(5)-H(5A)	109.0
S(2)-Sn(1)-S(1)	112.25(3)	C(4)-C(5)-H(5B)	109.0
S(2)-Sn(1)-S(3)#1	113.07(3)	C(6)-C(5)-H(5B)	109.0
S(1)-Sn(1)-S(3)#1	113.02(4)	H(5A)-C(5)-H(5B)	107.8
S(2)-Sn(1)-S(3)	114.76(4)	C(5)-C(6)-C(1)	113.7(5)
S(1)-Sn(1)-S(3)	109.37(4)	C(5)-C(6)-H(6A)	108.8
S(3)#1-Sn(1)-S(3)	92.99(3)	C(1)-C(6)-H(6A)	108.8
N(3)-Mn(1)-N(1)	94.27(12)	C(5)-C(6)-H(6B)	108.8
N(3)-Mn(1)-N(4)	75.54(11)	C(1)-C(6)-H(6B)	108.8
N(1)-Mn(1)-N(4)	94.14(12)	H(6A)-C(6)-H(6B)	107.7
N(3)-Mn(1)-N(2)	101.34(18)	C(7)-N(3)-Mn(1)	105.3(2)
N(1)-Mn(1)-N(2)	74.85(13)	C(7)-N(3)-H(3C)	110.7
N(4)-Mn(1)-N(2)	168.43(14)	Mn(1)-N(3)-H(3C)	110.7
N(3)-Mn(1)-O(1)	159.32(11)	C(7)-N(3)-H(3D)	110.7
N(1)-Mn(1)-O(1)	87.58(11)	Mn(1)-N(3)-H(3D)	110.7
N(4)-Mn(1)-O(1)	83.79(11)	H(3C)-N(3)-H(3D)	108.8
N(2)-Mn(1)-O(1)	99.02(17)	C(8)-N(4)-Mn(1)	112.5(2)
N(3)-Mn(1)-S(1)	97.18(9)	C(8)-N(4)-H(4C)	109.1
N(1)-Mn(1)-S(1)	157.66(9)	Mn(1)-N(4)-H(4C)	109.1
N(4)-Mn(1)-S(1)	107.26(8)	C(8)-N(4)-H(4D)	109.1
N(2)-Mn(1)-S(1)	84.11(11)	Mn(1)-N(4)-H(4D)	109.1
O(1)-Mn(1)-S(1)	88.41(7)	H(4C)-N(4)-H(4D)	107.8
Sn(1)-S(1)-Mn(1)	107.72(4)	N(3)-C(7)-C(12)	114.3(3)
Sn(1)#1-S(3)-Sn(1)	87.01(3)	N(3)-C(7)-C(8)	108.8(3)
C(1)-N(1)-Mn(1)	113.7(3)	C(12)-C(7)-C(8)	111.4(3)
C(1)-N(1)-H(1A)	108.8	N(3)-C(7)-H(7)	107.3
Mn(1)-N(1)-H(1A)	108.8	C(12)-C(7)-H(7)	107.3
C(1)-N(1)-H(1B)	108.8	C(8)-C(7)-H(7)	107.3
Mn(1)-N(1)-H(1B)	108.8	N(4)-C(8)-C(7)	110.4(3)
H(1A)-N(1)-H(1B)	107.7	N(4)-C(8)-C(9)	113.2(4)
C(2)-N(2)-Mn(1)	110.7(3)	C(7)-C(8)-C(9)	110.3(4)
C(2)-N(2)-H(2A)	109.5	N(4)-C(8)-H(8)	107.6
Mn(1)-N(2)-H(2A)	109.5	C(7)-C(8)-H(8)	107.6
C(2)-N(2)-H(2B)	109.5	C(9)-C(8)-H(8)	107.6
Mn(1)-N(2)-H(2B)	109.5	C(10)-C(9)-C(8)	113.2(4)
H(2A)-N(2)-H(2B)	108.1	C(10)-C(9)-H(9A)	108.9
N(1)-C(1)-C(2)	111.0(4)	C(8)-C(9)-H(9A)	108.9
N(1)-C(1)-C(6)	114.4(4)	C(10)-C(9)-H(9B)	108.9
C(2)-C(1)-C(6)	112.5(4)	C(8)-C(9)-H(9B)	108.9
N(1)-C(1)-H(1)	106.1	H(9A)-C(9)-H(9B)	107.8
C(2)-C(1)-H(1)	106.1	C(11)-C(10)-C(9)	113.8(5)
C(6)-C(1)-H(1)	106.1	C(11)-C(10)-H(10A)	108.8
N(2)-C(2)-C(1)	111.4(4)	C(9)-C(10)-H(10A)	108.8
N(2)-C(2)-C(3)	117.0(5)	C(11)-C(10)-H(10B)	108.8
C(1)-C(2)-C(3)	113.4(4)	C(9)-C(10)-H(10B)	108.8
N(2)-C(2)-H(2)	104.5	H(10A)-C(10)-H(10B)	107.7
C(1)-C(2)-H(2)	104.5	C(10)-C(11)-C(12)	113.7(5)
C(3)-C(2)-H(2)	104.5	C(10)-C(11)-H(11A)	108.8
C(4)-C(3)-C(2)	112.3(5)	C(12)-C(11)-H(11A)	108.8
C(4)-C(3)-H(3A)	109.1	C(10)-C(11)-H(11B)	108.8
C(2)-C(3)-H(3A)	109.1	C(12)-C(11)-H(11B)	108.8
C(4)-C(3)-H(3B)	109.1	H(11A)-C(11)-H(11B)	107.7
C(2)-C(3)-H(3B)	109.1	C(7)-C(12)-C(11)	110.7(3)
H(3A)-C(3)-H(3B)	107.9	C(7)-C(12)-H(12A)	109.5
C(5)-C(4)-C(3)	114.6(5)	C(11)-C(12)-H(12A)	109.5

C(7)-C(12)-H(12B)	109.5	Mn(1)-O(1)-H(1O1)	114.2
C(11)-C(12)-H(12B)	109.5	Mn(1)-O(1)-H(2O1)	102.8
H(12A)-C(12)-H(12B)	108.1	H(1O1)-O(1)-H(2O1)	95.8

Symmetry transformations used to generate equivalent atoms:

#1  $-x+1/2, -y+1/2, -z+1$

Table 4. Anisotropic displacement parameters ( $\text{\AA}^2 \cdot 10^3$ ). The anisotropic displacement factor exponent takes the form:  $-2\pi^2[h^2 a^{*2}U_{11} + \dots + 2 h k a^* b^* U_{12}]$ .

	$U_{11}$	$U_{22}$	$U_{33}$	$U_{23}$	$U_{13}$	$U_{12}$
Sn(1)	38(1)	19(1)	21(1)	1(1)	13(1)	-3(1)
Mn(1)	34(1)	28(1)	29(1)	1(1)	13(1)	-4(1)
S(1)	54(1)	26(1)	25(1)	-1(1)	13(1)	-12(1)
S(2)	72(1)	29(1)	25(1)	-3(1)	22(1)	-10(1)
S(3)	40(1)	26(1)	41(1)	10(1)	19(1)	6(1)
N(1)	39(2)	34(2)	33(2)	3(1)	14(1)	-3(1)
N(2)	63(3)	76(3)	51(3)	28(2)	-9(2)	-30(2)
C(1)	44(2)	47(2)	49(3)	3(2)	13(2)	-12(2)
C(2)	50(3)	58(3)	71(4)	18(3)	1(3)	-16(2)
C(3)	46(3)	78(4)	63(4)	8(3)	-7(2)	-14(2)
C(4)	45(3)	88(4)	122(6)	-3(4)	18(3)	-14(3)
C(5)	66(3)	89(5)	82(5)	1(3)	28(3)	-32(3)
C(6)	59(3)	65(3)	58(3)	5(2)	23(2)	-17(2)
N(3)	44(2)	36(2)	28(2)	-5(1)	16(1)	0(1)
N(4)	40(2)	32(1)	28(2)	-2(1)	14(1)	-2(1)
C(7)	43(2)	49(2)	42(2)	-5(2)	21(2)	-2(2)
C(8)	42(2)	48(2)	37(2)	-3(2)	14(2)	2(2)
C(9)	42(2)	59(3)	47(3)	-8(2)	11(2)	-6(2)
C(10)	38(2)	109(5)	84(5)	-24(4)	19(3)	-7(3)
C(11)	44(3)	121(6)	84(5)	-8(4)	33(3)	-7(3)
C(12)	49(2)	60(3)	53(3)	-2(2)	27(2)	11(2)
O(1)	60(2)	40(2)	46(2)	9(1)	30(2)	7(1)

Table 5. Hydrogen coordinates ( $\cdot 10^4$ ) and isotropic displacement parameters ( $\text{\AA}^2 \cdot 10^3$ ).

	x	y	z	U(eq)
H(1A)	1731	-2113	7068	43
H(1B)	1347	-1578	7468	43
H(2A)	537	-618	4142	88
H(2B)	857	-1377	3988	88
H(1)	1005	-2608	5535	58
H(2)	301	-1192	5514	81
H(3A)	-426	-1579	3708	86
H(3B)	-49	-2390	3643	86
H(4A)	-633	-2149	5223	108
H(4B)	-788	-2861	4232	108
H(5A)	52	-3603	5304	96
H(5B)	-273	-3379	6167	96
H(6A)	803	-3169	7062	73
H(6B)	431	-2355	7128	73
H(3C)	2439	-1815	5837	43
H(3D)	2259	-1317	4723	43
H(4C)	2621	219	7773	40
H(4D)	2559	-613	8259	40
H(7)	2860	-191	5709	52
H(8)	3211	-1238	7773	52
H(9A)	3574	486	7715	62
H(9B)	3806	-109	8854	62
H(10A)	4532	51	7965	94
H(10B)	4386	-910	8135	94
H(11A)	4397	-811	6321	97
H(11B)	3974	3	6001	97
H(12A)	3377	-1147	4976	62
H(12B)	3580	-1693	6163	62
H(1O1)	1361	68	7865	69
H(2O1)	1576	822	7329	69

### 6.2.10. Messprotokoll für die Verbindung [Mn(C<sub>6</sub>N<sub>2</sub>H<sub>14</sub>)<sub>2</sub>]Sn<sub>2</sub>S<sub>6</sub> · 2 C<sub>6</sub>N<sub>2</sub>H<sub>15</sub>

Table 1. Crystal data and structure refinement for [Mn(C<sub>6</sub>N<sub>2</sub>H<sub>14</sub>)<sub>2</sub>]Sn<sub>2</sub>S<sub>6</sub> · 2 C<sub>6</sub>N<sub>2</sub>H<sub>15</sub> (C<sub>6</sub>N<sub>2</sub>H<sub>14</sub>; 1,2-dach = 1,2-Diaminocyclohexan).

Identification code	[Mn(C <sub>6</sub> N <sub>2</sub> H <sub>14</sub> ) <sub>2</sub> ]Sn <sub>2</sub> S <sub>6</sub> · 2 C <sub>6</sub> N <sub>2</sub> H <sub>15</sub> (np771)	
Empirical formula	C <sub>24</sub> H <sub>58</sub> N <sub>8</sub> Mn Sn <sub>2</sub> S <sub>6</sub>	
Crystal colour, – Habitués	yellow needles	
Formula weight	943.46 g/mol	
Temperature	293(2) K	
Wavelength	0.71073 Å	
Crystal system	Triclinic	
Space group	P $\bar{1}$	
Unit cell dimensions	a = 7.3019(6) Å	$\alpha$ = 76.877(10)°
	b = 11.1798(9) Å	$\beta$ = 74.719(9)°
	c = 13.2837(11) Å	$\gamma$ = 82.872(10)°
Volume	1016.36(14) Å <sup>3</sup>	
Z	1	
Density (calculated)	1.541 g/cm <sup>3</sup>	
Absorption coefficient	1.860 mm <sup>-1</sup>	
F(000)	479	
Crystal size	0.56 · 0.25 · 0.07 mm <sup>3</sup>	
Theta range for data collection	2.72 to 28.00°	
Index ranges	-9 ≤ h ≤ 9, -14 ≤ k ≤ 14, -17 ≤ l ≤ 17	
Reflections collected	10307	
Independent reflections	4838 [R(int) = 0.0574]	
Completeness to theta = 28.00°	98.5 %	
Refinement method	Full-matrix least-squares on F <sup>2</sup>	
Data / restraints / parameters	4838 / 0 / 224	
Goodness-of-fit on F <sup>2</sup>	0.953	
Final R indices [I > 2σ(I)]	R1 = 0.0370, wR2 = 0.0793	
R indices (all data)	R1 = 0.0622, wR2 = 0.0873	
Largest diff. peak and hole	0.828 and -1.212 e.Å <sup>-3</sup>	

Table 2. Atomic coordinates ( $\cdot 10^4$ ) and equivalent isotropic displacement parameters ( $\text{\AA}^2 \cdot 10^3$ ).  $U(\text{eq})$  is defined as one third of the trace of the orthogonalized  $U_{ij}$  tensor.

	x	y	z	$U(\text{eq})$
Sn(1)	-1151(1)	6380(1)	5061(1)	27(1)
Mn(1)	0	10000	5000	35(1)
S(1)	-386(2)	7652(1)	6050(1)	37(1)
S(2)	-3652(2)	7089(1)	4236(1)	35(1)
S(3)	-1638(2)	4334(1)	6195(1)	39(1)
N(1)	-1126(5)	9787(3)	3619(3)	32(1)
N(2)	2697(5)	9510(3)	3819(3)	36(1)
C(1)	522(13)	9829(8)	2640(7)	34(2)
C(2)	2235(11)	9047(8)	2984(7)	31(2)
C(1')	310(20)	9193(14)	2906(10)	40(3)
C(2')	2190(20)	9647(14)	2759(11)	44(3)
C(3)	3860(8)	9030(5)	1996(4)	58(1)
C(4)	3400(20)	8496(13)	1171(10)	64(3)
C(5)	1640(30)	9298(15)	840(15)	73(5)
C(4')	3190(50)	9190(30)	872(15)	91(8)
C(5')	1410(50)	8680(20)	1020(20)	92(10)
C(6)	-54(9)	9320(6)	1794(4)	59(2)
N(3)	6692(5)	4313(3)	3659(3)	38(1)
N(4)	5528(8)	2082(4)	3193(4)	68(1)
C(7)	6315(6)	4295(4)	2606(4)	39(1)
C(8)	6641(7)	2982(5)	2397(4)	47(1)
C(9)	6274(9)	2994(7)	1315(5)	72(2)
C(10)	7465(12)	3887(8)	419(6)	92(2)
C(11)	7193(12)	5167(8)	643(6)	92(2)
C(12)	7563(9)	5187(6)	1728(4)	63(2)

Table 3. Bond lengths [ $\text{\AA}$ ] and angles [ $^\circ$ ].

Sn(1)-S(2)	2.3373(10)	C(1)-C(2)	1.545(11)
Sn(1)-S(1)	2.3432(10)	C(1)-H(1)	0.9800
Sn(1)-S(3)#1	2.4454(12)	C(2)-C(3)	1.522(10)
Sn(1)-S(3)	2.4462(11)	C(2)-H(2)	0.9800
Mn(1)-N(2)	2.266(4)	C(1')-C(2')	1.47(2)
Mn(1)-N(2)#2	2.266(4)	C(1')-C(6)	1.542(12)
Mn(1)-N(1)	2.267(3)	C(1')-H(1A)	0.9800
Mn(1)-N(1)#2	2.267(3)	C(2')-C(3)	1.564(15)
Mn(1)-S(1)#2	2.6888(11)	C(2')-H(2A)	0.9800
Mn(1)-S(1)	2.6888(11)	C(3)-C(4)	1.487(14)
S(3)-Sn(1)#1	2.4454(12)	C(3)-C(4')	1.66(2)
N(1)-C(1')	1.424(13)	C(3)-H(3A)	0.9700
N(1)-C(1)	1.517(10)	C(3)-H(3B)	0.9700
N(1)-H(1A)	0.8789	C(3)-H(3C)	0.9700
N(1)-H(1B)	0.8796	C(3)-H(3D)	0.9700
N(2)-C(2)	1.453(9)	C(4)-C(5)	1.57(2)
N(2)-C(2')	1.518(15)	C(4)-H(4A)	0.9700
N(2)-H(2A)	0.8733	C(4)-H(4B)	0.9700
N(2)-H(2B)	0.8764	C(5)-C(6)	1.52(2)
C(1)-C(6)	1.537(9)	C(5)-H(5A)	0.9700

C(5)-H(5B)	0.9700	C(1)-N(1)-H(1A)	99.5
C(4')-C(5')	1.43(4)	Mn(1)-N(1)-H(1A)	110.1
C(4')-H(4C)	0.9700	C(1')-N(1)-H(1B)	94.1
C(4')-H(4D)	0.9700	C(1)-N(1)-H(1B)	119.5
C(5')-C(6)	1.51(3)	Mn(1)-N(1)-H(1B)	110.7
C(5')-H(5C)	0.9700	H(1A)-N(1)-H(1B)	107.8
C(5')-H(5D)	0.9700	C(2)-N(2)-C(2')	25.9(5)
C(6)-H(6A)	0.9700	C(2)-N(2)-Mn(1)	110.3(4)
C(6)-H(6B)	0.9700	C(2')-N(2)-Mn(1)	107.0(6)
C(6)-H(6C)	0.9700	C(2)-N(2)-H(2A)	99.5
C(6)-H(6D)	0.9700	C(2')-N(2)-H(2A)	123.1
N(3)-C(7)	1.500(5)	Mn(1)-N(2)-H(2A)	110.0
N(3)-H(3C)	0.8900	C(2)-N(2)-H(2B)	117.5
N(3)-H(3D)	0.8900	C(2')-N(2)-H(2B)	97.1
N(3)-H(3E)	0.8900	Mn(1)-N(2)-H(2B)	110.8
N(4)-C(8)	1.434(8)	H(2A)-N(2)-H(2B)	107.9
N(4)-H(4C)	0.8900	N(1)-C(1)-C(6)	109.7(6)
N(4)-H(4D)	0.8900	N(1)-C(1)-C(2)	108.0(6)
C(7)-C(12)	1.524(8)	C(6)-C(1)-C(2)	110.8(6)
C(7)-C(8)	1.534(6)	N(1)-C(1)-H(1)	109.4
C(7)-H(7)	0.9800	C(6)-C(1)-H(1)	109.4
C(8)-C(9)	1.527(7)	C(2)-C(1)-H(1)	109.4
C(8)-H(8)	0.9800	N(2)-C(2)-C(3)	114.5(6)
C(9)-C(10)	1.517(11)	N(2)-C(2)-C(1)	109.8(6)
C(9)-H(9A)	0.9700	C(3)-C(2)-C(1)	108.3(6)
C(9)-H(9B)	0.9700	N(2)-C(2)-H(2)	108.0
C(10)-C(11)	1.507(11)	C(3)-C(2)-H(2)	108.0
C(10)-H(10A)	0.9700	C(1)-C(2)-H(2)	108.0
C(10)-H(10B)	0.9700	N(1)-C(1')-C(2')	111.4(11)
C(11)-C(12)	1.540(9)	N(1)-C(1')-C(6)	114.7(9)
C(11)-H(11A)	0.9700	C(2')-C(1')-C(6)	107.8(11)
C(11)-H(11B)	0.9700	N(1)-C(1')-H(1A)	107.6
C(12)-H(12A)	0.9700	C(2')-C(1')-H(1A)	107.6
C(12)-H(12B)	0.9700	C(6)-C(1')-H(1A)	107.6
S(2)-Sn(1)-S(1)	117.27(4)	C(1')-C(2')-N(2)	111.2(10)
S(2)-Sn(1)-S(3)#1	110.78(4)	C(1')-C(2')-C(3)	114.8(11)
S(1)-Sn(1)-S(3)#1	112.59(4)	N(2)-C(2')-C(3)	108.6(9)
S(2)-Sn(1)-S(3)	111.68(4)	C(1')-C(2')-H(2A)	107.3
S(1)-Sn(1)-S(3)	108.22(4)	N(2)-C(2')-H(2A)	107.3
S(3)#1-Sn(1)-S(3)	93.82(4)	C(3)-C(2')-H(2A)	107.3
N(2)-Mn(1)-N(2)#2	180.000(1)	C(4)-C(3)-C(2)	114.0(8)
N(2)-Mn(1)-N(1)	77.76(13)	C(4)-C(3)-C(2')	118.2(8)
N(2)#2-Mn(1)-N(1)	102.24(13)	C(2)-C(3)-C(2')	25.0(5)
N(2)-Mn(1)-N(1)#2	102.24(13)	C(4)-C(3)-C(4')	28.8(9)
N(2)#2-Mn(1)-N(1)#2	77.76(13)	C(2)-C(3)-C(4')	114.9(12)
N(1)-Mn(1)-N(1)#2	180.000(1)	C(2')-C(3)-C(4')	106.0(13)
N(2)-Mn(1)-S(1)#2	86.95(10)	C(4)-C(3)-H(3A)	108.8
N(2)#2-Mn(1)-S(1)#2	93.05(10)	C(2)-C(3)-H(3A)	108.8
N(1)-Mn(1)-S(1)#2	84.60(9)	C(2')-C(3)-H(3A)	84.6
N(1)#2-Mn(1)-S(1)#2	95.40(9)	C(4')-C(3)-H(3A)	82.0
N(2)-Mn(1)-S(1)	93.05(9)	C(4)-C(3)-H(3B)	108.8
N(2)#2-Mn(1)-S(1)	86.95(10)	C(2)-C(3)-H(3B)	108.8
N(1)-Mn(1)-S(1)	95.40(9)	C(2')-C(3)-H(3B)	124.3
N(1)#2-Mn(1)-S(1)	84.60(9)	C(4')-C(3)-H(3B)	129.1
S(1)#2-Mn(1)-S(1)	180.00(2)	H(3A)-C(3)-H(3B)	107.7
Sn(1)-S(1)-Mn(1)	113.54(4)	C(4)-C(3)-H(3C)	81.7
Sn(1)#1-S(3)-Sn(1)	86.18(4)	C(2)-C(3)-H(3C)	85.6
C(1')-N(1)-C(1)	28.7(6)	C(2')-C(3)-H(3C)	110.5
C(1')-N(1)-Mn(1)	109.8(5)	C(4')-C(3)-H(3C)	110.5
C(1)-N(1)-Mn(1)	108.6(4)	H(3A)-C(3)-H(3C)	155.4
C(1')-N(1)-H(1A)	122.9	H(3B)-C(3)-H(3C)	47.9
		C(4)-C(3)-H(3D)	122.3

C(2)-C(3)-H(3D)	123.1	C(5)-C(6)-H(6D)	82.7
C(2')-C(3)-H(3D)	110.5	C(1)-C(6)-H(6D)	81.6
C(4')-C(3)-H(3D)	110.5	C(1')-C(6)-H(6D)	108.2
H(3A)-C(3)-H(3D)	46.8	H(6A)-C(6)-H(6D)	157.8
H(3B)-C(3)-H(3D)	60.9	H(6B)-C(6)-H(6D)	49.6
H(3C)-C(3)-H(3D)	108.7	H(6C)-C(6)-H(6D)	107.4
C(3)-C(4)-C(5)	106.9(9)	C(7)-N(3)-H(3C)	109.5
C(3)-C(4)-H(4A)	110.3	C(7)-N(3)-H(3D)	109.5
C(5)-C(4)-H(4A)	110.3	H(3C)-N(3)-H(3D)	109.5
C(3)-C(4)-H(4B)	110.3	C(7)-N(3)-H(3E)	109.5
C(5)-C(4)-H(4B)	110.3	H(3C)-N(3)-H(3E)	109.5
H(4A)-C(4)-H(4B)	108.6	H(3D)-N(3)-H(3E)	109.5
C(6)-C(5)-C(4)	111.6(12)	C(8)-N(4)-H(4C)	109.1
C(6)-C(5)-H(5A)	109.3	C(8)-N(4)-H(4D)	109.3
C(4)-C(5)-H(5A)	109.3	H(4C)-N(4)-H(4D)	109.5
C(6)-C(5)-H(5B)	109.3	N(3)-C(7)-C(12)	109.5(4)
C(4)-C(5)-H(5B)	109.3	N(3)-C(7)-C(8)	110.3(4)
H(5A)-C(5)-H(5B)	108.0	C(12)-C(7)-C(8)	112.0(4)
C(5')-C(4')-C(3)	113.1(18)	N(3)-C(7)-H(7)	108.3
C(5')-C(4')-H(4C)	109.0	C(12)-C(7)-H(7)	108.3
C(3)-C(4')-H(4C)	109.0	C(8)-C(7)-H(7)	108.3
C(5')-C(4')-H(4D)	109.0	N(4)-C(8)-C(9)	109.2(5)
C(3)-C(4')-H(4D)	109.0	N(4)-C(8)-C(7)	115.5(4)
H(4C)-C(4')-H(4D)	107.8	C(9)-C(8)-C(7)	109.2(4)
C(4')-C(5')-C(6)	107(2)	N(4)-C(8)-H(8)	107.6
C(4')-C(5')-H(5C)	110.3	C(9)-C(8)-H(8)	107.6
C(6)-C(5')-H(5C)	110.3	C(7)-C(8)-H(8)	107.6
C(4')-C(5')-H(5D)	110.3	C(10)-C(9)-C(8)	112.5(5)
C(6)-C(5')-H(5D)	110.3	C(10)-C(9)-H(9A)	109.1
H(5C)-C(5')-H(5D)	108.5	C(8)-C(9)-H(9A)	109.1
C(5')-C(6)-C(5)	27.0(12)	C(10)-C(9)-H(9B)	109.1
C(5')-C(6)-C(1)	120.7(14)	C(8)-C(9)-H(9B)	109.1
C(5)-C(6)-C(1)	109.3(9)	H(9A)-C(9)-H(9B)	107.8
C(5')-C(6)-C(1')	116.3(14)	C(11)-C(10)-C(9)	111.6(6)
C(5)-C(6)-C(1')	118.9(9)	C(11)-C(10)-H(10A)	109.3
C(1)-C(6)-C(1')	27.6(5)	C(9)-C(10)-H(10A)	109.3
C(5')-C(6)-H(6A)	82.8	C(11)-C(10)-H(10B)	109.3
C(5)-C(6)-H(6A)	109.8	C(9)-C(10)-H(10B)	109.3
C(1)-C(6)-H(6A)	109.8	H(10A)-C(10)-H(10B)	108.0
C(1')-C(6)-H(6A)	82.3	C(10)-C(11)-C(12)	112.1(6)
C(5')-C(6)-H(6B)	120.7	C(10)-C(11)-H(11A)	109.2
C(5)-C(6)-H(6B)	109.8	C(12)-C(11)-H(11A)	109.2
C(1)-C(6)-H(6B)	109.8	C(10)-C(11)-H(11B)	109.2
C(1')-C(6)-H(6B)	122.8	C(12)-C(11)-H(11B)	109.2
H(6A)-C(6)-H(6B)	108.3	H(11A)-C(11)-H(11B)	107.9
C(5')-C(6)-H(6C)	108.2	C(7)-C(12)-C(11)	109.7(5)
C(5)-C(6)-H(6C)	125.8	C(7)-C(12)-H(12A)	109.7
C(1)-C(6)-H(6C)	124.7	C(11)-C(12)-H(12A)	109.7
C(1')-C(6)-H(6C)	108.2	C(7)-C(12)-H(12B)	109.7
H(6A)-C(6)-H(6C)	50.5	C(11)-C(12)-H(12B)	109.7
H(6B)-C(6)-H(6C)	57.8	H(12A)-C(12)-H(12B)	108.2
C(5')-C(6)-H(6D)	108.2		

Symmetry transformations used to generate equivalent atoms:

#1 -x,-y+1,-z+1 #2 -x,-y+2,-z+1

Table 4. Anisotropic displacement parameters ( $\text{\AA}^2 \cdot 10^3$ ). The anisotropic displacement factor exponent takes the form:  $-2\pi^2[h^2 a^{*2}U_{11} + \dots + 2 h k a^* b^* U_{12}]$ .

	$U_{11}$	$U_{22}$	$U_{33}$	$U_{23}$	$U_{13}$	$U_{12}$
Sn(1)	26(1)	18(1)	41(1)	-9(1)	-14(1)	3(1)
Mn(1)	38(1)	38(1)	34(1)	-20(1)	-13(1)	5(1)
S(1)	47(1)	26(1)	49(1)	-15(1)	-25(1)	4(1)
S(2)	34(1)	29(1)	49(1)	-10(1)	-22(1)	5(1)
S(3)	35(1)	24(1)	48(1)	-5(1)	0(1)	3(1)
N(1)	37(2)	28(2)	36(2)	-13(1)	-12(2)	0(1)
N(2)	38(2)	34(2)	40(2)	-14(2)	-12(2)	3(1)
C(1)	52(5)	24(3)	28(4)	-6(3)	-16(4)	-1(4)
C(2)	37(4)	22(3)	29(4)	-3(3)	-5(3)	0(3)
C(1')	55(8)	46(7)	23(6)	-17(6)	-13(6)	10(7)
C(2')	55(8)	37(7)	34(7)	-2(6)	-6(6)	2(7)
C(3)	58(3)	67(3)	44(3)	-20(3)	-1(3)	5(3)
C(4)	75(8)	79(8)	35(7)	-26(6)	-5(6)	11(7)
C(5)	91(10)	88(10)	59(9)	-50(10)	-37(8)	20(10)
C(4')	140(20)	110(19)	22(9)	-18(10)	-11(12)	-10(20)
C(5')	140(20)	95(18)	56(14)	-59(16)	-20(14)	20(20)
C(6)	81(4)	68(3)	40(3)	-24(3)	-24(3)	2(3)
N(3)	37(2)	38(2)	46(2)	-18(2)	-18(2)	3(2)
N(4)	87(4)	52(3)	76(4)	-38(2)	-20(3)	1(2)
C(7)	29(2)	51(2)	43(3)	-21(2)	-15(2)	9(2)
C(8)	38(3)	55(3)	60(3)	-34(3)	-19(2)	11(2)
C(9)	65(4)	106(5)	68(4)	-54(4)	-27(3)	6(3)
C(10)	94(6)	139(7)	52(4)	-45(4)	-19(4)	2(5)
C(11)	93(6)	129(7)	48(4)	3(4)	-21(4)	-17(5)
C(12)	64(4)	80(4)	45(3)	-10(3)	-13(3)	-13(3)

Table 5. Hydrogen coordinates ( $\cdot 10^4$ ) and isotropic displacement parameters ( $\text{\AA}^2 \cdot 10^3$ ).

	x	y	z	U(eq)
H(1A)	-1795	10461	3404	39
H(1B)	-1874	9174	3814	39
H(2A)	3289	8848	4110	43
H(2B)	3469	10106	3622	43
H(1)	858	10682	2349	40
H(2)	1862	8202	3279	37
H(1A)	377	8313	3228	48
H(2A)	2113	10529	2447	53
H(3A)	4215	9867	1684	70
H(3B)	4953	8560	2209	70
H(3C)	4077	8167	2304	70
H(3D)	5024	9436	1868	70
H(4A)	3090	7647	1456	77
H(4B)	4479	8519	558	77
H(5A)	1997	10132	520	87
H(5B)	1283	8965	311	87
H(4C)	3093	10053	550	110
H(4D)	4168	8784	382	110
H(5C)	1506	7797	1309	111
H(5D)	1064	8807	348	111
H(6A)	-467	8494	2093	71
H(6B)	-1104	9835	1570	71
H(6C)	-1279	9005	1885	71
H(6D)	-145	10189	1473	71
H(3C)	5959	3794	4172	57
H(3D)	6430	5070	3788	57
H(3E)	7910	4084	3641	57
H(4C)	5745	2075	3823	82
H(4D)	5862	1343	3030	82
H(7)	4981	4575	2632	47
H(8)	7984	2718	2358	57
H(9A)	6555	2172	1166	87
H(9B)	4937	3219	1344	87
H(10A)	8797	3602	326	110
H(10B)	7113	3906	-240	110
H(11A)	5902	5495	635	110
H(11B)	8054	5694	84	110
H(12A)	8892	4954	1713	75
H(12B)	7279	6013	1869	75

**6.2.11. Messprotokoll für die Verbindung [Co(tepa)]<sub>2</sub>Sn<sub>2</sub>S<sub>6</sub>**Table 1. Crystal data and structure refinement for [Co(tepa)]<sub>2</sub>Sn<sub>2</sub>S<sub>6</sub> (C<sub>8</sub>N<sub>5</sub>H<sub>23</sub>; tepa = Tetraethylenpentamin).

Identification code	[Co(tepa)] <sub>2</sub> Sn <sub>2</sub> S <sub>6</sub> (np839)
Empirical formula	C <sub>16</sub> N <sub>10</sub> H <sub>46</sub> Co <sub>2</sub> Sn <sub>2</sub> S <sub>6</sub>
Crystal colour, – Habitués:	red needles
Formula weight	926.23 g/mol
Temperature	293(2) K
Wavelength	0.71073 Å
Crystal system	Tetragonal
Space group	I4 <sub>1</sub> /a
Unit cell dimensions	a = 25.9729(15) Å      α = 90° b = 25.9729(15) Å      β = 90° c = 9.8942(5) Å        γ = 90°
Volume	6674.5(6) Å <sup>3</sup>
Z	8
Density (calculated)	1.843 g/cm <sup>3</sup>
Absorption coefficient	2.858 mm <sup>-1</sup>
F(000)	3696
Crystal size	0.12 · 0.09 · 0.07 mm <sup>3</sup>
Theta range for data collection	2.20 to 28.08°
Index ranges	-34 ≤ h ≤ 34, -34 ≤ k ≤ 34, -12 ≤ l ≤ 12
Reflections collected	37804
Independent reflections	3922 [R(int) = 0.0445]
Completeness to theta = 28.08°	96.6 %
Absorption correction	Numerical
Max. and min. transmission	0.6701 and 0.6201
Refinement method	Full-matrix least-squares on F <sup>2</sup>
Data / restraints / parameters	3922 / 0 / 163
Goodness-of-fit on F <sup>2</sup>	1.050
Final R indices [I > 2σ(I)]	R1 = 0.0270, wR2 = 0.0633
R indices (all data)	R1 = 0.0372, wR2 = 0.0665
Largest diff. peak and hole	0.427 and -0.824 e.Å <sup>-3</sup>

Table 2. Atomic coordinates ( $\cdot 10^4$ ) and equivalent isotropic displacement parameters ( $\text{\AA}^2 \cdot 10^3$ ).  $U(\text{eq})$  is defined as one third of the trace of the orthogonalized  $U_{ij}$  tensor.

	x	y	z	$U(\text{eq})$
Sn(1)	9803(1)	5474(1)	1027(1)	20(1)
Co(1)	9366(1)	4309(1)	3566(1)	22(1)
S(1)	9483(1)	5287(1)	3203(1)	25(1)
S(2)	10638(1)	5051(1)	688(1)	24(1)
S(3)	9869(1)	6326(1)	353(1)	29(1)
N(1)	9043(1)	3935(1)	1798(3)	30(1)
N(2)	8535(1)	4542(1)	3642(3)	29(1)
N(3)	9226(1)	4428(1)	5732(3)	31(1)
N(4)	9514(1)	3524(1)	4412(3)	29(1)
N(5)	10152(1)	4179(1)	3029(4)	42(1)
C(1)	8527(1)	4135(1)	1442(4)	35(1)
C(2)	8226(1)	4224(1)	2722(4)	36(1)
C(3)	8338(1)	4594(2)	5018(4)	42(1)
C(4)	8774(1)	4771(2)	5934(4)	41(1)
C(5)	9166(1)	3926(1)	6421(4)	37(1)
C(6)	9569(1)	3563(1)	5886(4)	37(1)
C(7)	9976(1)	3313(1)	3751(4)	35(1)
C(8)	10390(1)	3725(1)	3653(4)	34(1)

Table 3. Bond lengths [ $\text{\AA}$ ] and angles [ $^\circ$ ].

Sn(1)-S(3)	2.3174(7)	S(1)-Sn(1)-S(2)#1	110.57(3)
Sn(1)-S(1)	2.3582(8)	S(2)-Sn(1)-S(2)#1	93.97(2)
Sn(1)-S(2)	2.4558(7)	N(5)-Co(1)-N(1)	95.59(12)
Sn(1)-S(2)#1	2.4602(7)	N(5)-Co(1)-N(3)	115.04(12)
Co(1)-N(5)	2.138(3)	N(1)-Co(1)-N(3)	141.83(10)
Co(1)-N(1)	2.170(3)	N(5)-Co(1)-N(4)	77.58(10)
Co(1)-N(3)	2.196(3)	N(1)-Co(1)-N(4)	87.65(10)
Co(1)-N(4)	2.239(2)	N(3)-Co(1)-N(4)	77.98(10)
Co(1)-N(2)	2.242(2)	N(5)-Co(1)-N(2)	166.07(11)
Co(1)-S(1)	2.5826(8)	N(1)-Co(1)-N(2)	77.06(10)
S(2)-Sn(1)#1	2.4602(7)	N(3)-Co(1)-N(2)	76.71(10)
N(1)-C(1)	1.481(4)	N(4)-Co(1)-N(2)	113.46(9)
N(2)-C(3)	1.460(5)	N(5)-Co(1)-S(1)	90.45(8)
N(2)-C(2)	1.468(4)	N(1)-Co(1)-S(1)	111.96(7)
N(3)-C(5)	1.479(4)	N(3)-Co(1)-S(1)	90.99(7)
N(3)-C(4)	1.484(4)	N(4)-Co(1)-S(1)	158.12(7)
N(4)-C(6)	1.470(4)	N(2)-Co(1)-S(1)	81.59(7)
N(4)-C(7)	1.472(4)	Sn(1)-S(1)-Co(1)	111.80(3)
N(5)-C(8)	1.469(4)	Sn(1)-S(2)-Sn(1)#1	86.03(2)
C(1)-C(2)	1.506(5)	C(1)-N(1)-Co(1)	112.6(2)
C(3)-C(4)	1.522(5)	C(3)-N(2)-C(2)	116.1(3)
C(5)-C(6)	1.504(5)	C(3)-N(2)-Co(1)	113.1(2)
C(7)-C(8)	1.520(4)	C(2)-N(2)-Co(1)	110.77(19)
		C(5)-N(3)-C(4)	112.6(3)
S(3)-Sn(1)-S(1)	119.06(3)	C(5)-N(3)-Co(1)	110.1(2)
S(3)-Sn(1)-S(2)	108.76(3)	C(4)-N(3)-Co(1)	110.2(2)
S(1)-Sn(1)-S(2)	110.10(3)	C(6)-N(4)-C(7)	112.8(3)
S(3)-Sn(1)-S(2)#1	111.47(3)	C(6)-N(4)-Co(1)	108.89(19)

C(7)-N(4)-Co(1)	108.27(19)	N(3)-C(4)-C(3)	109.1(3)
C(8)-N(5)-Co(1)	115.1(2)	N(3)-C(5)-C(6)	108.5(3)
N(1)-C(1)-C(2)	108.9(3)	N(4)-C(6)-C(5)	109.0(3)
N(2)-C(2)-C(1)	108.9(2)	N(4)-C(7)-C(8)	110.0(3)
N(2)-C(3)-C(4)	108.9(3)	N(5)-C(8)-C(7)	107.2(3)

Symmetry transformations used to generate equivalent atoms:

#1 -x+2,-y+1,-z

Table 4. Anisotropic displacement parameters ( $\text{\AA}^2 \cdot 10^3$ ). The anisotropic displacement factor exponent takes the form:  $-2\pi^2[h^2 a^{*2}U_{11} + \dots + 2 h k a^* b^* U_{12}]$ .

	$U_{11}$	$U_{22}$	$U_{33}$	$U_{23}$	$U_{13}$	$U_{12}$
Sn(1)	21(1)	17(1)	21(1)	-1(1)	1(1)	2(1)
Co(1)	22(1)	23(1)	22(1)	1(1)	-3(1)	-2(1)
S(1)	31(1)	22(1)	23(1)	-2(1)	5(1)	-5(1)
S(2)	20(1)	26(1)	28(1)	-6(1)	-3(1)	3(1)
S(3)	32(1)	18(1)	38(1)	2(1)	7(1)	4(1)
N(1)	31(1)	32(1)	26(2)	0(1)	-3(1)	-3(1)
N(2)	23(1)	27(1)	36(2)	1(1)	-2(1)	-4(1)
N(3)	31(1)	33(1)	31(2)	-2(1)	-4(1)	-10(1)
N(4)	33(1)	24(1)	30(2)	2(1)	-8(1)	-9(1)
N(5)	27(1)	35(1)	65(2)	20(1)	2(1)	1(1)
C(1)	33(2)	37(2)	36(2)	3(1)	-11(1)	-6(1)
C(2)	23(1)	40(2)	46(2)	0(2)	-9(1)	-6(1)
C(3)	28(2)	53(2)	45(2)	-6(2)	6(1)	1(1)
C(4)	41(2)	48(2)	34(2)	-11(2)	6(2)	1(2)
C(5)	46(2)	41(2)	24(2)	6(1)	-1(1)	-14(1)
C(6)	48(2)	33(2)	29(2)	10(1)	-11(1)	-9(1)
C(7)	40(2)	26(1)	41(2)	-1(1)	-9(1)	3(1)
C(8)	28(2)	33(2)	41(2)	5(1)	-5(1)	3(1)

Table 5. Hydrogen coordinates ( $\cdot 10^4$ ) and isotropic displacement parameters ( $\text{\AA}^2 \cdot 10^3$ ).

	x	y	z	U(eq)
H(1A)	9257	3982	1092	36
H(1B)	9021	3594	1954	36
H(2)	8524	4865	3288	35
H(3)	9506	4588	6087	38
H(4)	9240	3317	4220	35
H(5A)	10172	4147	2125	51
H(5B)	10337	4459	3263	51
H(1A)	8348	3889	873	42
H(1B)	8560	4455	945	42
H(2A)	7904	4397	2515	43
H(2B)	8146	3897	3146	43
H(3A)	8205	4266	5330	50
H(3B)	8060	4843	5037	50
H(4A)	8867	5123	5720	49
H(4B)	8665	4758	6870	49
H(5A)	8825	3788	6251	44
H(5B)	9208	3969	7389	44
H(6A)	9909	3691	6111	44
H(6B)	9527	3227	6296	44
H(7A)	9888	3191	2852	42
H(7B)	10104	3022	4267	42
H(8A)	10519	3809	4545	41
H(8B)	10674	3603	3105	41

**6.2.12. Messprotokoll für die Verbindung [Fe(tepa)]<sub>2</sub>Sn<sub>2</sub>S<sub>6</sub>**Table 1. Crystal data and structure refinement for [Fe(tepa)]<sub>2</sub>Sn<sub>2</sub>S<sub>6</sub> (C<sub>8</sub>N<sub>5</sub>H<sub>23</sub>; tepa = Tetraethylenpentamin).

Identification code	[Fe(tepa)] <sub>2</sub> Sn <sub>2</sub> S <sub>6</sub> (np872)
Empirical formula	C <sub>16</sub> N <sub>10</sub> H <sub>46</sub> Fe <sub>2</sub> Sn <sub>2</sub> S <sub>6</sub>
Crystal colour, – Habitués	yellow needles
Formula weight	920.07 g/mol
Temperature	293(2) K
Wavelength	0.71073 Å
Crystal system	Tetragonal
Space group	I4 <sub>1</sub> /a
Unit cell dimensions	a = 25.9640(16) Å      α = 90° b = 25.9640(16) Å      β = 90° c = 9.9936(6) Å        γ = 90°
Volume	6737.0(7) Å <sup>3</sup>
Z	8
Density (calculated)	1.814 g/cm <sup>3</sup>
Absorption coefficient	2.708 mm <sup>-1</sup>
F(000)	3680
Crystal size	0.12 · 0.09 · 0.05 mm <sup>3</sup>
Theta range for data collection	2.69 to 28.12°
Index ranges	-34 ≤ h ≤ 34, -32 ≤ k ≤ 34, -12 ≤ l ≤ 13
Reflections collected	31747
Independent reflections	4080 [R(int) = 0.0487]
Completeness to theta = 28.12°	98.9 %
Absorption correction	Numerical
Refinement method	Full-matrix least-squares on F <sup>2</sup>
Data / restraints / parameters	4080 / 0 / 163
Goodness-of-fit on F <sup>2</sup>	1.005
Final R indices [I > 2σ(I)]	R1 = 0.0368, wR2 = 0.0870
R indices (all data)	R1 = 0.0462, wR2 = 0.0915
Largest diff. peak and hole	0.485 and -1.370 e.Å <sup>-3</sup>

Table 2. Atomic coordinates ( $\cdot 10^4$ ) and equivalent isotropic displacement parameters ( $\text{\AA}^2 \cdot 10^3$ ).  $U(\text{eq})$  is defined as one third of the trace of the orthogonalized  $U_{ij}$  tensor.

	x	y	z	U(eq)
Sn(1)	9801(1)	5475(1)	1020(1)	23(1)
Fe(1)	9376(1)	4309(1)	3540(1)	26(1)
S(1)	9492(1)	5286(1)	3186(1)	29(1)
S(2)	10640(1)	5058(1)	670(1)	27(1)
S(3)	9858(1)	6328(1)	353(1)	33(1)
N(1)	10173(1)	4161(1)	2940(4)	42(1)
N(2)	9533(1)	3521(1)	4424(3)	33(1)
N(3)	9226(1)	4427(1)	5740(3)	36(1)
N(4)	8526(1)	4540(1)	3653(3)	34(1)
N(5)	9025(1)	3948(1)	1764(3)	33(1)
C(1)	10408(2)	3719(2)	3645(4)	39(1)
C(2)	9999(2)	3307(1)	3777(4)	40(1)
C(3)	9584(2)	3564(2)	5893(4)	42(1)
C(4)	9174(2)	3922(2)	6410(4)	42(1)
C(5)	8774(2)	4763(2)	5927(4)	46(1)
C(6)	8336(2)	4583(2)	5020(5)	46(1)
C(7)	8213(1)	4232(2)	2734(4)	41(1)
C(8)	8506(2)	4148(2)	1447(4)	41(1)

Table 3. Bond lengths [ $\text{\AA}$ ] and angles [ $^\circ$ ].

Sn(1)-S(3)	2.3192(8)	S(3)-Sn(1)-S(1)	118.91(3)
Sn(1)-S(1)	2.3605(9)	S(3)-Sn(1)-S(2)	108.89(3)
Sn(1)-S(2)	2.4573(8)	S(1)-Sn(1)-S(2)	109.95(3)
Sn(1)-S(2)#1	2.4655(8)	S(3)-Sn(1)-S(2)#1	111.63(3)
Fe(1)-N(1)	2.188(3)	S(1)-Sn(1)-S(2)#1	110.67(3)
Fe(1)-N(5)	2.206(3)	S(2)-Sn(1)-S(2)#1	93.90(3)
Fe(1)-N(3)	2.254(3)	N(1)-Fe(1)-N(5)	95.53(13)
Fe(1)-N(2)	2.266(3)	N(1)-Fe(1)-N(3)	117.07(13)
Fe(1)-N(4)	2.289(3)	N(5)-Fe(1)-N(3)	140.44(11)
Fe(1)-S(1)	2.5786(9)	N(1)-Fe(1)-N(2)	77.18(12)
S(2)-Sn(1)#1	2.4655(8)	N(5)-Fe(1)-N(2)	90.23(11)
N(1)-C(1)	1.476(5)	N(3)-Fe(1)-N(2)	76.92(12)
N(2)-C(3)	1.478(5)	N(1)-Fe(1)-N(4)	166.18(13)
N(2)-C(2)	1.480(5)	N(5)-Fe(1)-N(4)	75.62(11)
N(3)-C(5)	1.475(5)	N(3)-Fe(1)-N(4)	75.46(12)
N(3)-C(4)	1.478(5)	N(2)-Fe(1)-N(4)	112.94(11)
N(4)-C(6)	1.457(5)	N(1)-Fe(1)-S(1)	91.48(9)
N(4)-C(7)	1.465(5)	N(5)-Fe(1)-S(1)	110.86(8)
N(5)-C(8)	1.478(5)	N(3)-Fe(1)-S(1)	91.16(8)
C(1)-C(2)	1.512(5)	N(2)-Fe(1)-S(1)	157.10(8)
C(3)-C(4)	1.505(6)	N(4)-Fe(1)-S(1)	82.05(8)
C(5)-C(6)	1.526(6)	Sn(1)-S(1)-Fe(1)	111.69(3)
C(7)-C(8)	1.511(6)	Sn(1)-S(2)-Sn(1)#1	86.10(3)
		C(1)-N(1)-Fe(1)	113.3(2)

C(3)-N(2)-C(2)	112.9(3)	C(8)-N(5)-Fe(1)	113.6(2)
C(3)-N(2)-Fe(1)	109.6(2)	N(1)-C(1)-C(2)	107.6(3)
C(2)-N(2)-Fe(1)	108.4(2)	N(2)-C(2)-C(1)	110.3(3)
C(5)-N(3)-C(4)	113.2(3)	N(2)-C(3)-C(4)	109.0(3)
C(5)-N(3)-Fe(1)	110.0(2)	N(3)-C(4)-C(3)	109.2(3)
C(4)-N(3)-Fe(1)	109.7(2)	N(3)-C(5)-C(6)	109.6(3)
C(6)-N(4)-C(7)	116.2(3)	N(4)-C(6)-C(5)	109.2(3)
C(6)-N(4)-Fe(1)	113.2(2)	N(4)-C(7)-C(8)	109.4(3)
C(7)-N(4)-Fe(1)	111.3(2)	N(5)-C(8)-C(7)	109.1(3)

Symmetry transformations used to generate equivalent atoms:

#1 -x+2,-y+1,-z

Table 4. Anisotropic displacement parameters ( $\text{\AA}^2 \cdot 10^3$ ). The anisotropic displacement factor exponent takes the form:  $-2\pi^2[h^2 a^{*2}U_{11} + \dots + 2 h k a^* b^* U_{12}]$ .

	$U_{11}$	$U_{22}$	$U_{33}$	$U_{23}$	$U_{13}$	$U_{12}$
Sn(1)	24(1)	20(1)	24(1)	-1(1)	1(1)	2(1)
Fe(1)	25(1)	28(1)	26(1)	2(1)	-2(1)	-2(1)
S(1)	34(1)	26(1)	26(1)	-2(1)	5(1)	-5(1)
S(2)	23(1)	29(1)	30(1)	-5(1)	-2(1)	2(1)
S(3)	37(1)	21(1)	41(1)	2(1)	7(1)	4(1)
N(1)	31(2)	38(2)	57(2)	12(2)	3(2)	2(1)
N(2)	36(2)	29(1)	32(2)	3(1)	-9(1)	-8(1)
N(3)	38(2)	36(2)	33(2)	-3(1)	-1(1)	-9(1)
N(4)	28(1)	30(1)	44(2)	1(1)	-2(1)	-3(1)
N(5)	34(2)	35(2)	31(2)	3(1)	-2(1)	-5(1)
C(1)	31(2)	44(2)	42(2)	6(2)	-4(2)	5(2)
C(2)	48(2)	27(2)	44(2)	-3(2)	-10(2)	2(2)
C(3)	51(2)	40(2)	35(2)	10(2)	-9(2)	-12(2)
C(4)	53(2)	45(2)	29(2)	7(2)	2(2)	-16(2)
C(5)	46(2)	53(2)	39(2)	-10(2)	6(2)	-1(2)
C(6)	31(2)	59(3)	49(3)	-9(2)	4(2)	-2(2)
C(7)	26(2)	47(2)	49(2)	1(2)	-8(2)	-11(2)
C(8)	38(2)	44(2)	39(2)	6(2)	-13(2)	-9(2)

Table 5. Hydrogen coordinates ( $\cdot 10^4$ ) and isotropic displacement parameters ( $\text{\AA}^2 \cdot 10^3$ ).

	x	y	z	U(eq)
H(1A)	10182	4100	2053	50
H(1B)	10363	4444	3101	50
H(2)	9262	3311	4235	39
H(3)	9504	4590	6097	43
H(4)	8514	4866	3321	41
H(5A)	9232	4000	1054	40
H(5B)	9003	3606	1900	40
H(1A)	10527	3825	4523	47
H(1B)	10699	3589	3142	47
H(2A)	9912	3175	2898	48
H(2B)	10132	3024	4308	48
H(3A)	9922	3696	6121	50
H(3B)	9545	3227	6301	50
H(4A)	8836	3779	6231	51
H(4B)	9210	3964	7370	51
H(5A)	8864	5116	5712	55
H(5B)	8663	4752	6854	55
H(6A)	8209	4252	5324	55
H(6B)	8054	4828	5054	55
H(7A)	7892	4410	2548	49
H(7B)	8131	3903	3141	49
H(8A)	8323	3904	886	49
H(8B)	8535	4470	962	49

**6.2.13. Messprotokoll für die Verbindung [Ni(tepa)]<sub>2</sub>Sn<sub>2</sub>S<sub>6</sub>**Table 1. Crystal data and structure refinement for [Ni(C<sub>8</sub>N<sub>5</sub>H<sub>23</sub>)<sub>2</sub>Sn<sub>2</sub>S<sub>6</sub> (C<sub>8</sub>N<sub>5</sub>H<sub>23</sub>; tepa = Tetraethylenpentamin).

Identification code	[Ni(tepa)] <sub>2</sub> Sn <sub>2</sub> S <sub>6</sub> (npm198z)	
Empirical formula	C <sub>16</sub> N <sub>10</sub> H <sub>46</sub> Ni <sub>2</sub> Sn <sub>2</sub> S <sub>6</sub>	
Crystal colour, – Habitués	purple “fish bones”	
Formula weight	925.79 g/mol	
Temperature	293(2) K	
Wavelength	0.71073 Å	
Crystal system	Monoclinic	
Space group	P2 <sub>1</sub> /n	
Unit cell dimensions	a = 9.1425(7) Å	α = 90°
	b = 13.1394(7) Å	β = 93.002(9)°
	c = 13.0750(10) Å	γ = 90°
Volume	1568.50(19) Å <sup>3</sup>	
Z	2	
Density (calculated)	1.960 g/cm <sup>3</sup>	
Absorption coefficient	3.183 mm <sup>-1</sup>	
F(000)	928	
Crystal size	0.12 · 0.10 · 0.07 mm <sup>3</sup>	
Theta range for data collection	2.72 to 28.12°	
Index ranges	-12 ≤ h ≤ 12, -16 ≤ k ≤ 17, -17 ≤ l ≤ 16	
Reflections collected	10386	
Independent reflections	3027 [R(int) = 0.0529]	
Completeness to theta = 28.12°	79.0 %	
Refinement method	Full-matrix least-squares on F <sup>2</sup>	
Data / restraints / parameters	3027 / 0 / 164	
Goodness-of-fit on F <sup>2</sup>	1.028	
Final R indices [I > 2σ(I)]	R1 = 0.0347, wR2 = 0.0881	
R indices (all data)	R1 = 0.0434, wR2 = 0.0920	
Extinction coefficient	0.0078(6)	
Largest diff. peak and hole	0.803 and -0.895 e.Å <sup>-3</sup>	

Table 2. Atomic coordinates ( $\cdot 10^4$ ) and equivalent isotropic displacement parameters ( $\text{\AA}^2 \cdot 10^3$ ).  $U(\text{eq})$  is defined as one third of the trace of the orthogonalized  $U_{ij}$  tensor.

	x	y	z	U(eq)
Sn(1)	5183(1)	70(1)	3711(1)	19(1)
S(1)	6339(1)	982(1)	5179(1)	26(1)
S(2)	6796(1)	-946(1)	2865(1)	39(1)
S(3)	3604(1)	1085(1)	2676(1)	27(1)
Ni(1)	2172(1)	2472(1)	3582(1)	17(1)
N(1)	445(4)	2071(3)	2539(2)	22(1)
C(1)	-622(5)	1422(3)	3048(3)	27(1)
C(2)	155(5)	824(3)	3918(3)	27(1)
N(2)	1094(4)	1490(3)	4575(3)	24(1)
C(3)	283(5)	2096(4)	5322(3)	35(1)
C(4)	-218(5)	3117(4)	4897(4)	39(1)
N(3)	916(4)	3616(3)	4310(3)	29(1)
C(5)	1952(6)	4258(4)	4927(4)	37(1)
C(6)	3224(6)	3640(4)	5394(3)	36(1)
N(4)	3866(4)	2946(3)	4637(3)	27(1)
C(7)	5039(5)	3382(4)	4051(4)	39(1)
C(8)	4466(5)	4024(4)	3173(4)	42(1)
N(5)	3212(4)	3517(3)	2616(3)	30(1)

Table 3. Bond lengths [ $\text{\AA}$ ] and angles [ $^\circ$ ].

Sn(1)-S(2)	2.3129(12)		
Sn(1)-S(3)	2.3420(10)	S(2)-Sn(1)-S(3)	116.18(5)
Sn(1)-S(1)	2.4556(11)	S(2)-Sn(1)-S(1)	113.35(4)
Sn(1)-S(1)#1	2.4832(11)	S(3)-Sn(1)-S(1)	113.65(4)
S(1)-Sn(1)#1	2.4832(11)	S(2)-Sn(1)-S(1)#1	110.42(5)
S(3)-Ni(1)	2.5698(12)	S(3)-Sn(1)-S(1)#1	107.90(4)
Ni(1)-N(1)	2.099(3)	S(1)-Sn(1)-S(1)#1	92.65(3)
Ni(1)-N(2)	2.112(3)	Sn(1)-S(1)-Sn(1)#1	87.35(3)
Ni(1)-N(4)	2.114(3)	Sn(1)-S(3)-Ni(1)	116.79(4)
Ni(1)-N(5)	2.125(3)	N(1)-Ni(1)-N(2)	83.50(13)
Ni(1)-N(3)	2.145(3)	N(1)-Ni(1)-N(4)	177.23(14)
N(1)-C(1)	1.479(5)	N(2)-Ni(1)-N(4)	97.37(14)
C(1)-C(2)	1.528(6)	N(1)-Ni(1)-N(5)	96.94(14)
C(2)-N(2)	1.471(5)	N(2)-Ni(1)-N(5)	177.38(15)
N(2)-C(3)	1.487(6)	N(4)-Ni(1)-N(5)	82.06(14)
C(3)-C(4)	1.514(8)	N(1)-Ni(1)-N(3)	93.58(14)
C(4)-N(3)	1.475(6)	N(2)-Ni(1)-N(3)	82.94(15)
N(3)-C(5)	1.476(6)	N(4)-Ni(1)-N(3)	83.94(15)
C(5)-C(6)	1.521(7)	N(5)-Ni(1)-N(3)	94.45(16)
C(6)-N(4)	1.487(6)	N(1)-Ni(1)-S(3)	84.63(10)
N(4)-C(7)	1.466(6)	N(2)-Ni(1)-S(3)	96.64(10)
C(7)-C(8)	1.497(7)	N(4)-Ni(1)-S(3)	97.85(11)
C(8)-N(5)	1.484(6)	N(5)-Ni(1)-S(3)	85.97(12)

N(3)-Ni(1)-S(3)	178.20(11)	C(4)-N(3)-Ni(1)	109.1(3)
C(1)-N(1)-Ni(1)	110.1(2)	C(5)-N(3)-Ni(1)	107.5(3)
N(1)-C(1)-C(2)	109.9(3)	N(3)-C(5)-C(6)	111.7(4)
N(2)-C(2)-C(1)	111.3(3)	N(4)-C(6)-C(5)	112.4(3)
C(2)-N(2)-C(3)	114.0(3)	C(7)-N(4)-C(6)	115.7(4)
C(2)-N(2)-Ni(1)	106.3(2)	C(7)-N(4)-Ni(1)	107.8(3)
C(3)-N(2)-Ni(1)	109.9(3)	C(6)-N(4)-Ni(1)	108.3(3)
N(2)-C(3)-C(4)	112.7(3)	N(4)-C(7)-C(8)	112.6(4)
N(3)-C(4)-C(3)	112.1(4)	N(5)-C(8)-C(7)	110.7(4)
C(4)-N(3)-C(5)	114.8(4)	C(8)-N(5)-Ni(1)	110.9(3)

Symmetry transformations used to generate equivalent atoms:

#1 -x+1,-y,-z+1

Table 4. Anisotropic displacement parameters ( $\text{\AA}^2 \cdot 10^3$ ). The anisotropic displacement factor exponent takes the form:  $-2\pi^2 [h^2 a^{*2} U_{11} + \dots + 2 h k a^* b^* U_{12}]$ .

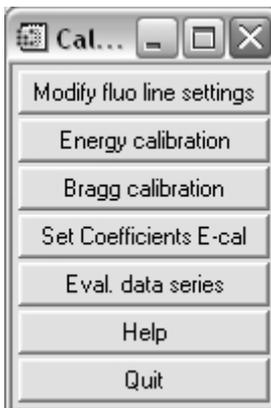
	$U_{11}$	$U_{22}$	$U_{33}$	$U_{23}$	$U_{13}$	$U_{12}$
Sn(1)	16(1)	18(1)	23(1)	-1(1)	-1(1)	1(1)
S(1)	24(1)	26(1)	26(1)	3(1)	-5(1)	-9(1)
S(2)	24(1)	31(1)	62(1)	-17(1)	10(1)	0(1)
S(3)	30(1)	31(1)	21(1)	2(1)	-2(1)	9(1)
Ni(1)	18(1)	18(1)	16(1)	2(1)	0(1)	0(1)
N(1)	20(2)	24(2)	22(2)	3(1)	-5(1)	-1(1)
C(1)	18(2)	28(2)	35(2)	0(2)	-4(2)	-4(2)
C(2)	28(2)	22(2)	30(2)	7(2)	-2(2)	-4(2)
N(2)	19(2)	27(2)	25(2)	9(1)	1(1)	-1(1)
C(3)	33(2)	53(3)	21(2)	-2(2)	9(2)	-7(2)
C(4)	31(2)	50(3)	38(3)	-11(2)	10(2)	8(2)
N(3)	35(2)	32(2)	20(2)	-2(1)	2(1)	15(2)
C(5)	50(3)	22(2)	39(3)	-9(2)	4(2)	6(2)
C(6)	54(3)	31(2)	22(2)	-3(2)	-12(2)	-11(2)
N(4)	29(2)	24(2)	27(2)	6(1)	-11(1)	-3(1)
C(7)	22(2)	37(3)	56(3)	3(2)	-10(2)	-7(2)
C(8)	29(2)	37(3)	59(3)	18(2)	6(2)	-7(2)
N(5)	29(2)	33(2)	29(2)	15(2)	-1(2)	-1(2)

Table 5. Hydrogen coordinates ( $\cdot 10^4$ ) and isotropic displacement parameters ( $\text{\AA}^2 \cdot 10^3$ ).

	x	y	z	U(eq)
H(1N1)	-4	2637	2295	27
H(2N1)	801	1732	2007	27
H(1A)	-1079	955	2554	33
H(1B)	-1383	1844	3318	33
H(2A)	-569	501	4328	32
H(2B)	748	292	3633	32
H(1N2)	1775	1101	4925	29
H(3A)	911	2205	5933	42
H(3B)	-564	1712	5517	42
H(4A)	-1093	3022	4455	47
H(4B)	-468	3556	5458	47
H(1N3)	464	4010	3816	35
H(5A)	1439	4583	5469	44
H(5B)	2328	4788	4496	44
H(6A)	3978	4100	5665	43
H(6B)	2887	3240	5959	43
H(1N4)	4226	2388	4977	32
H(7A)	5626	2834	3791	47
H(7B)	5670	3794	4505	47
H(8A)	4156	4679	3428	50
H(8B)	5241	4142	2708	50
H(1N5)	3532	3185	2069	36
H(2N5)	2561	3990	2389	36

### 6.3. Programmroutine calf3

Die Programmroutine calf3 wurde in enger Zusammenarbeit mit André Rothkirch (Hasylab, DESY) entwickelt und dient der Energiekalibrierung für energie-dispersive Röntgenbeugungsmessungen (EDXRD) am Messplatz F3 sowie der weiteren Auswertung der zeitaufgelösten in-situ-EDXRD-Untersuchungen. Die Programmroutine ist in Interactive Data Language (IDL), ITT Visual Information Solutions, Boulder, CO, USA, geschrieben und kann ebenfalls mit der IDL virtual machine benutzt werden. Es sind verschiedene Optionen wie Energiekalibrierung, Bragg-Winkelkalibrierung und die Auswertung zeitaufgelöster Spektren in die Routine integriert (Abb. 6.1).



**Abb. 6.1:** Das Startmenü von calf3.

Für die Energiekalibrierung muss eine Messdatei mit Röntgenfluoreszenzlinien eingelesen werden, welche graphisch dargestellt wird. Die Programmroutine fragt ausgewählte Fluoreszenzen ab, die der Nutzer in der Graphik des Messfiles markieren muss. Anschließend wird eine lineare Regression durchgeführt und die Koeffizienten der Energiekalibrierung ausgegeben. Die markierten Fluoreszenzlinien, das Anpassen mit Gaußfunktionen sowie die lineare Regression mit den Koeffizienten werden am Bildschirm visualisiert und können als Datei gespeichert werden. Die Einstellung der Abfrage der Fluoreszenzen kann bei Bedarf über den Menüpunkt „Modify fluo line setting“ geändert werden. Typischerweise wird für die Energiekalibrierung am Messplatz F3 ein Kalibrierglas mit den Elementen Molybdän, Zinn, Barium, Wolfram und Gadolinium benutzt wird, weshalb einige Fluoreszenzen davon als Standardeinstellungen vorgegeben werden. Für die Auswertung der Zeitreihen der in-situ-Untersuchungen ist eine

Parameterdatei erforderlich, in welcher die Randbedingungen zur Analyse der Messungen angegeben werden müssen. Diese Parameterdatei beinhaltet unter anderem die Pfadangaben zu den Dateien verschiedener Messungen, die Koeffizienten aus der Energiekalibrierung, die Bereiche für eine Untergrundkorrektur (optional), die erwarteten Peakpositionen, die zulässigen Abweichungen davon, die Arten der Peaks und die Bedingungen für z. B. Dreifachpeaks. Zur Auswertung wird die Parameterdatei eingelesen und ggfs. für jede Messung durch Anpassung eines Polynoms an ausgewählte Bereiche des Spektrums eine Untergrundkorrektur durchgeführt. Die interessierenden Bereiche werden anschließend nach Beugungs- und Fluoreszenzpeaks abgesucht. Die Peaks werden mit Gaußfunktionen angefitet und separat für jedes einzelne Spektrum integriert (so z. B. in Abb. 6.2). Dies ist sowohl für einfache als auch für überlagernde Dreifachpeaks möglich, was für unsere Untersuchungen zur Bildung von  $(\text{DBNH})_2\text{Sn}_3\text{S}_6$  und  $(\text{DBNH})_2\text{Cu}_6\text{Sn}_2\text{S}_8$  (vgl. Kap. 4.2.1, S. 128) unumgänglich war, da die Produktreflexe nahe beieinander lagen und nicht immer aufgelöst werden konnten. Zusätzlich können mittels `calcf3` die Integrale auf eine Referenz normiert werden (z. B. auf das Integral der Fluoreszenzlinie). Die abgeleiteten Koeffizienten und Integrale werden in eine Ausgabedatei geschrieben und eine Illustration (Postscript Datei) erlaubt eine erste visuelle Beurteilung der Peakanpassung (Abb. 6.2).

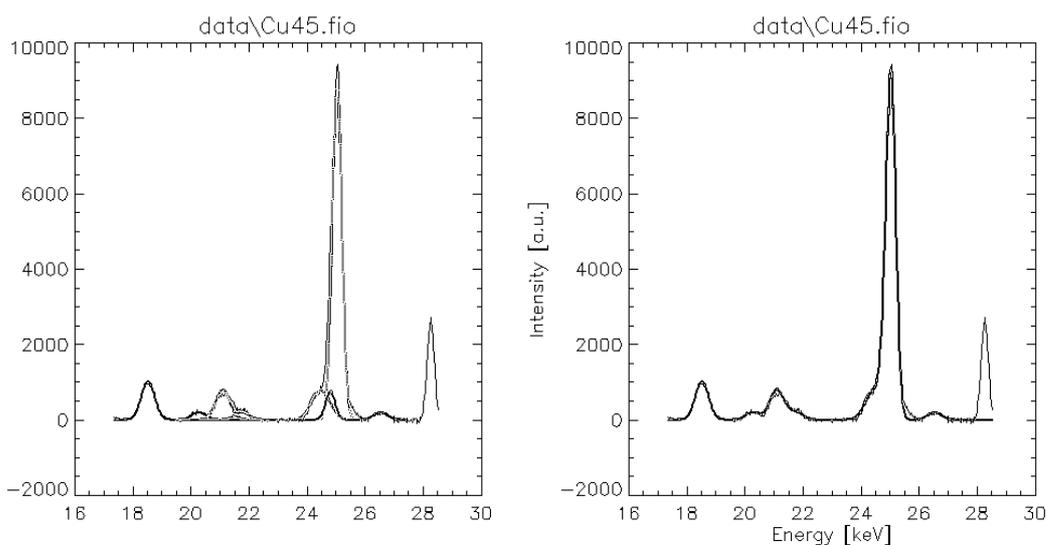


**Abb. 6.2:** Ausschnitt einer Ausgabe von `calcf3`, die auch in einer Postscriptdatei (für eine visuelle Beurteilung der Peakanpassung) erfolgt (links: Anpassung der einzelnen Reflexe und Fluoreszenzen; rechts: Gesamtanpassung). Die gezeigten Messungen stammen aus den EDXRD-Untersuchungen zur Bildung von  $(\text{DBNH})_2\text{Sn}_3\text{S}_6$  und  $(\text{DBNH})_2\text{Cu}_6\text{Sn}_2\text{S}_8$ .

## Danksagung

Die vorliegende Arbeit wurde in der Zeit vom Februar 2005 bis September 2008 am Institut für Anorganische Chemie der Christian-Albrechts-Universität zu Kiel angefertigt.

An dieser Stelle möchte ich mich bei allen Institutsangehörigen bedanken, die mich während dieser Zeit auf die eine oder andere Weise unterstützt haben.

Mein besonderer Dank gilt Herrn Prof. Dr. Wolfgang Bensch für die Bereitstellung des interessanten Themas, seine Unterstützung in allen wissenschaftlichen Fragestellungen und die vielen Diskussionen und Anregungen.

Der gesamten Arbeitsgruppe danke ich für die ständige Diskussions- und Hilfsbereitschaft (ggfs. auch über die Arbeit hinaus), die nette Arbeitsatmosphäre und die gute Zusammenarbeit.

Meine Arbeit wurde zudem durch einige Kooperationen außerhalb unseres Instituts unterstützt. Dank gebührt Dr. Christian Knittlmayer und Prof. Dr. Werner Weppner (Technische Fakultät, CAU Kiel), Dr. André Rothkirch (Hasylab, DESY) sowie Prof. Dr. Greta Patzke (ETH Zürich).

## **Erklärung**

Hiermit versichere ich an Eides statt, dass ich die vorliegende Arbeit selbständig – abgesehen von der Beratung durch meinen wissenschaftlichen Lehrer – und nur unter Verwendung der angegebenen Hilfsmittel angefertigt habe.

Die Dissertation wird ausschließlich an dieser Stelle zur Promotion vorgelegt.

Zusätzlich erkläre ich, dass ich noch keinen Promotionsversuch, weder an dieser oder an einer anderen Hochschule, unternommen habe.

Kiel, September 2008

Nicole Pienack

## 7. Literatur

---

- [1] A.K. Cheetham, G. Férey, T. Loiseau, *Angew. Chem.* **1999**, *111*, 3466.
- [2] W.S. Sheldrick, *J. Chem. Soc., Dalton Trans.* **2000**, 3041.
- [3] B. Krebs, *Angew. Chem.* **1983**, *95*, 113.
- [4] B. Krebs, S. Pohl, W. Schiwy, *Z. Anorg. Allg. Chem.* **1972**, *393*, 241.
- [5] B. Krebs, W. Schiwy, *Z. Anorg. Allg. Chem.* **1973**, *398*, 63.
- [6] W.S. Sheldrick, M. Wachhold, *Angew. Chem.* **1997**, *109*, 214.
- [7] W. Schiwy, S. Pohl, B. Krebs, *Z. Anorg. Allg. Chem.* **1973**, *402*, 77.
- [8] E. Ruzin, S. Jakobi, S. Dehnen, *Z. Anorg. Allg. Chem.* **2008**, *634*, 995.
- [9] W.S. Sheldrick, *Z. Anorg. Allg. Chem.* **1988**, *562*, 23.
- [10] W.S. Sheldrick, B. Schaaf, *Z. Anorg. Allg. Chem.* **1994**, *620*, 1041.
- [11] J. Liao, M.G. Kanatzidis, *Chem. Mater.* **1993**, *5*, 1561.
- [12] J. Liao, C. Varotsis, M.G. Kanatzidis, *Inorg. Chem.* **1993**, *32*, 2453.
- [13] J.C. Jumas, E. Philippot, M. Maurin, *J. Solid State Chem.* **1975**, *14*, 152.
- [14] R.L. Bedard, S.T. Wilson, L.D. Vail, J.M. Bennett, E.M. Flanigen, *Studies in Surface Science and Catalysis* **1989**, *49*, 375.
- [15] R.L. Bedard, L.D. Vail, S.T. Wilson, E.M. Flanigen, *U.S. Patent* **1989**, 4880761.
- [16] R.L. Bedard, L.D. Vail, S.T. Wilson, E.M. Flanigen, *U.S. Patent* **1990**, 4933068.
- [17] T. Jiang, G.A. Ozin, *J. Mater. Chem.* **1998**, *8*, 1099.
- [18] J.B. Parise, Y. Ko, J. Rijssenbeek, D.M. Nellis, K. Tan, S. Koch, *J. Chem. Soc., Chem. Commun.* **1994**, 527.
- [19] T. Jiang, A. Lough, G.A. Ozin, *Adv. Mater.* **1998**, *10*, 42.
- [20] C.L. Bowes, S. Petrov, G. Vovk, D. Young, G.A. Ozin, R.L. Bedard, *J. Mater. Chem.* **1998**, *8*, 711.
- [21] T. Jiang, G.A. Ozin, A. Verma, R.L. Bedard, *J. Mater. Chem.* **1998**, *8*, 1649.
- [22] R.W.J. Scott, M.J. MacLachlan, G.A. Ozin, *Curr. Opin. Solid State Mater. Sci.* **1999**, *4*, 113.
- [23] T. Jiang, A. Lough, G.A. Ozin, R.L. Bedard, R. Broach, *J. Mater. Chem.* **1998**, *8*, 721.
- [24] H. Ahari, G.A. Ozin, R.L. Bedard, S. Petrov, D. Young, *Adv. Mater.* **1995**, *7*, 370.

- 
- [25] Ö. Dag, H. Ahari, N. Coombs, T. Jiang, P.P. Aroca-Ouellette, S. Petrov, I. Sokolov, A. Verma, G. Vovk, D. Young, G.A. Ozin, C. Reber, Y. Pelletier, R.L. Bedard, *Adv. Mater.* **1997**, 9, 1133.
- [26] T. Jiang, A. Lough, G.A. Ozin, R.L. Bedard, *J. Mater. Chem.* **1998**, 8, 733.
- [27] P. Enzel, G.S. Henderson, G.A. Ozin, R.L. Bedard, *Adv. Mater.* **1995**, 7, 64.
- [28] T. Jiang, A.J. Lough, G.A. Ozin, D. Young, R.L. Bedard, *Chem. Mater.* **1995**, 7, 245.
- [29] Y. Ko, K. Tan, D.M. Nellis, S. Koch, J.B. Parise, *J. Solid State Chem.* **1995**, 114, 506.
- [30] Y. Ko, C.L. Cahill, J.B. Parise, *J. Chem. Soc., Chem. Commun.* **1994**, 69.
- [31] M. Behrens, C. Näther, W. Bensch, *Z. Anorg. Allg. Chem.* **2002**, 628, 2160.
- [32] S. Dehnen, C. Zimmermann, *Z. Anorg. Allg. Chem.* **2002**, 628, 2463.
- [33] C. Näther, S. Scherb, W. Bensch, *Acta Cryst.* **2003**, E59, m280.
- [34] A. Puls, C. Näther, W. Bensch, *Acta Cryst.* **2005**, E61, m868.
- [35] T. Jiang, G.A. Ozin, R.L. Bedard, *Adv. Mater.* **1995**, 7, 166.
- [36] A. Müller, J. Schimanski, M. Römer, H. Bögge, F.W. Baumann, W. Eltzner, E. Krickemeyer, U. Billerbeck, *Chimia* **1985**, 39, 25.
- [37] C.L. Teske, *Z. Anorg. Allg. Chem.* **1976**, 419, 67.
- [38] C.L. Teske, *Z. Anorg. Allg. Chem.* **1980**, 460, 163.
- [39] S.I. Chykhrij, L.V. Sysa, O.V. Parasyuk, L.V. Piskach, *J. Alloys Comp.* **2000**, 307, 124.
- [40] O. Palchik, R.G. Iyer, J.H. Liao, M.G. Kanatzidis, *Inorg. Chem.* **2003**, 42, 5052.
- [41] M.J. Manos, R.G. Iyer, E. Quarez, J.H. Liao, M.G. Kanatzidis, *Angew. Chem.* **2005**, 117, 3618.
- [42] M. Daszkiewicz, L.D. Gulay, A. Pietraszko, V.Ya. Shemet, *J. Solid State Chem.* **2007**, 180, 2053.
- [43] T. Jiang, G.A. Ozin, *J. Mater. Chem.* **1997**, 7, 2213.
- [44] K.K. Rangan, P.N. Trikalitis, C. Canlas, T. Bakas, D.P. Weliky, M.G. Kanatzidis, *Nano Letters* **2002**, 2, 513.
- [45] W. Bensch, M. Schur, *Eur. J. Solid State Inorg. Chem.* **1996**, 33, 1149.
- [46] M. Behrens, S. Scherb, C. Näther, W. Bensch, *Z. Anorg. Allg. Chem.* **2003**, 629, 1367.

- 
- [47] D.X. Jia, Y. Zhang, J. Dai, Q.Y. Zhu, Y.M. Gu, *Z. Anorg. Allg. Chem.* **2004**, 630, 313.
- [48] D.X. Jia, J. Dai, Q.Y. Zhu, Y. Zhang, X.M. Gu, *Polyhedron* **2004**, 23, 937.
- [49] M.L. Fu, G.C. Guo, B. Liu, A.Q. Wu, J.S. Huang, *Chin. J. Inorg. Chem.* **2005**, 21, 25.
- [50] M. Baiyin, L. Ye, Y. An, X. Liu, C. Jia, G. Ning, *Bull. Chem. Soc. Jpn.* **2005**, 78, 1283.
- [51] Y. Wang, M. Baiyin, S. Li, X. Liu, Y. An, G. Ning, *Chem. Res. Chinese U.* **2006**, 22, 411.
- [52] Y. An, B. Menghe, L. Ye, M. Ji, X. Liu, G. Ning, *Inorg. Chem. Commun.* **2005**, 8, 301.
- [53] Q. Zhao, D. Jia, Y. Zhang, L. Song, J. Dai, *Inorg. Chim. Acta* **2007**, 360, 1895.
- [54] D.X. Jia, A.M. Zhu, J. Deng, Y. Zhang, *Z. Anorg. Allg. Chem.* **2007**, 633, 1246.
- [55] A. D. Compaan, *Solar Energy Materials & Solar Cells* **2006**, 90, 2170.
- [56] A. Goetzberger, C. Hebling, H.W. Schock, *Mater. Sci. Eng.* **2003**, R40, 1.
- [57] J. Xiao, Y. Xie, Y. Xiong, R. Tang, Y. Qian, *J. Mater. Chem.* **2001**, 11, 1417.
- [58] A. Lafond, J.A. Cody, M. Souilah, C. Guillot-Deudon, R. Kiebach, W. Bensch, *Inorg. Chem.* **2007**, 46, 1502.
- [59] M. Schaefer, R. Stähler, R. Kiebach, C. Näther, W. Bensch, *Z. Anorg. Allg. Chem.* **2004**, 630, 1816.
- [60] M. Schaefer, L. Engelke, W. Bensch, *Z. Anorg. Allg. Chem.* **2003**, 629, 1912.
- [61] M. Schur, C. Näther, W. Bensch, *Z. Naturforsch.* **2001**, 56b, 79.
- [62] L. Engelke, R. Stähler, M. Schur, C. Näther, W. Bensch, R. Pöttgen, M.H. Möller, *Z. Naturforsch.* **2004**, 59b, 869.
- [63] M. Schur, W. Bensch, *Z. Naturforsch.* **2002**, 57b, 1.
- [64] A. Puls, C. Näther, W. Bensch, *Z. Anorg. Allg. Chem.* **2006**, 632, 1239.
- [65] J. Zhou, G.Q. Bian, J. Dai, Y. Zhang, A. Tang, Q.Y. Zhu, *Inorg. Chem.* **2007**, 46, 1541.
- [66] X.M. Gu, J. Dai, D.X. Jia, Y. Zhang, Q.Y. Zhu, *Cryst. Growth & Design* **2005**, 5, 1845.
- [67] R. Francis, D. O'Hare, *J. Chem. Soc., Dalton Trans.* **1998**, 3133.

- 
- [68] R.J. Francis, S.J. Price, J.S.O Evans, S. O'Brien, D. O'Hare, S.M. Clark, *Chem. Mater.* **1996**, *8*, 2102.
- [69] L. Engelke, M. Schaefer, M. Schur, W. Bensch, *Chem. Mater.* **2001**, *13*, 1383.
- [70] L. Engelke, M. Schaefer, F. Porsch, W. Bensch, *Eur. J. Inorg. Chem.* **2003**, 506.
- [71] R. Kiebach, N. Pienack, M.E. Ordolff, F. Studt, W. Bensch, *Chem. Mater.* **2006**, *18*, 1196.
- [72] [http://hasylab.desy.de/e70/e207/e3452/index\\_eng.html](http://hasylab.desy.de/e70/e207/e3452/index_eng.html) (Stand: 14.07.04).
- [73] [http://hasylab.desy.de/facilities/doris\\_iii/machine/index\\_eng.html](http://hasylab.desy.de/facilities/doris_iii/machine/index_eng.html) (Stand: 07.07.08)
- [74] R.I. Walton, T. Loiseau, D. O'Hare, G. Férey, *Chem. Mater.* **1999**, *11*, 3201.
- [75] L.X. Chen, *Angew. Chem.* **2004**, *116*, 2946.
- [76] D.E. Sayers, E.A. Stern, F. Lytle, *Phys. Rev. Lett.* **1971**, *27*, 1204.
- [77] D.E. Sayers, F.W. Lytle, M. Weissbluth, P. Pianetta, *J. Chem. Phys.* **1975**, *62*, 2514.
- [78] P.A. Lee, J.B. Pendry, *Phys. Rev. B* **1975**, *11*, 2795.
- [79] F.W. Lytle, D.E. Sayers, E.A. Stern, *Phys. Rev. B* **1975**, *11*, 4825.
- [80] E.A. Stern, D.E. Sayers, F.W. Lytle, *Phys. Rev. B* **1975**, *11*, 4836.
- [81] B.K. Teo, *EXAFS: Basic Principles and Data Analysis*, Springer-Verlag, Berlin, Heidelberg, New York, Tokyo, **1986**.
- [82] F. Sauerwald, *Dissertation*, Universität Marburg, **2005**.
- [83] J. Schwenzel, *Dissertation*, Universität Kiel, **2003**.
- [84] V. Spetzler, *Dissertation*, Universität Kiel, **2006**.
- [85] [http://www.ionic-systems.de/Geraete/KC\\_02.html](http://www.ionic-systems.de/Geraete/KC_02.html) (Stand: 07.07.08)
- [86] A. Rabenau, *Angew. Chem.* **1985**, *97*, 1017.
- [87] [http://hasylab.desy.de/facilities/doris\\_iii/beamlines/f3/index\\_eng.html](http://hasylab.desy.de/facilities/doris_iii/beamlines/f3/index_eng.html) (Stand: 07.07.08)
- [88] [http://hasylab.desy.de/facilities/doris\\_iii/beamlines/a2/software/spectra\\_online/index\\_eng.html](http://hasylab.desy.de/facilities/doris_iii/beamlines/a2/software/spectra_online/index_eng.html) (Stand: 07.07.08)
- [89] M. Schaefer, *Dissertation*, Universität Kiel, **2003**.
- [90] L. Engelke, *Dissertation*, Universität Kiel, **2002**.
- [91] R. Kiebach, *Dissertation*, Universität Kiel, **2005**.

- 
- [92] [http://hasylab.desy.de/facilities/doris\\_iii/beamlines/x1\\_roemo\\_ii/beamline/index\\_eng.html](http://hasylab.desy.de/facilities/doris_iii/beamlines/x1_roemo_ii/beamline/index_eng.html) (Stand: 07.07.08)
- [93] Stoe & Cie. *WinXPow, Version 1.2*, Stoe & Cie GmbH, Darmstadt, **2001**.
- [94] G.M. Sheldrick, *SHELXS 97, Program for the solution of crystal structures*, Universität Göttingen, **1997**.
- [95] G.M. Sheldrick, *SHELXL 97, Program for the refinement of crystal structures*, Universität Göttingen, **1997**.
- [96] Stoe & Cie. *X-Red, Version 1.11*, Stoe & Cie GmbH, Darmstadt, **1998**.
- [97] Stoe & Cie. *X-Shape, Version 1.03*, Stoe & Cie GmbH, Darmstadt, **1998**.
- [98] A.L. Spek. *PLATON, A multipurpose crystallographic tool*, Utrecht University, Utrecht, The Netherlands, **2000**.
- [99] K. Brandenburg, *DIAMOND, Version 2.1e*, Crystal Impact GbR, Bonn, **1999**; *DIAMOND, Version 3.1f*, Crystal Impact GbR, Bonn, **2008**.
- [100] Netzsch, *Netzsch TA Windows Software*, Version 4.1.2, Selb, **2001**.
- [101] INFICON, *QUADSTAR 422*, Version 6.03, Inficon AG, **2001**.
- [102] F. Porsch, *EDXPowd, Version 3.155*, RTI GmbH, Paderborn, **2002**.
- [103] T. Ressler, *WinXAS, Version 3.1*, **2004**.
- [104] J.J. Rehr, F. Vila, M. Prange, J. Kas, Y. Takimoto, A. Sorini, K. Jorissen, B. Ravel, M. Newville, *FEFF Project*, **2006**.
- [105] M. Newville, *Iffffit, Version 1.2.2*, University of Chicago, **2003**.
- [106] H. Kolanoski, *Vorlesung „Detektoren in der Teilchenphysik“* **2007**, <http://www-zeuthen.desy.de/~kolanosk/det07/skripte/halbl01.pdf> (Stand: 14.07.08).
- [107] S.A. Wood, *Geochim. Cosmochim. Acta* **1989**, 53, 237.
- [108] J.A. Tossell, *Geochim. Cosmochim. Acta* **1994**, 58, 5093.
- [109] J.F.W. Mosselmans, G.R. Helz, R.A.D. Patrick, J.M. Charnock, D.J. Vaughan, *Appl. Geochem.* **2000**, 15, 879.
- [110] M.J. Frisch, G.W. Trucks, H.B. Schlegel, G.E. Scuseria, M.A. Robb, J.R. Cheeseman, V.G. Zakrzewski, J.A.Jr. Montgomery, R.E. Stratmann, J.C. Barrant, S. Dapprich, J.M. Millam, A.D. Daniels, K.N. Kudin, M.C. Strain, O. Farkas, J. Tomasi, V. Barone, M. Cossi, R. Cammi, B. Mennucci, C. Pomelli, C. Adamo, S. Clifford, J. Ochterski, G.A. Petersson, P.Y. Ayala, Q. Cui, K. Morokuma, P. Salvador, J.J. Dannenberg, D.K. Malick, A.D. Rabuck, K. Raghavachari, J.B. Foresman, J. Cioslowski, J.V. Ortiz, A.G.

---

Baboul, B.B. Stefanov, G. Liu, A. Liashenko, P. Piskorz, I. Komaromi, R. Gomperts, R.L. Martin, D.J. Fox, T. Keith, M.A. Al-Laham, C.Y. Peng, A. Nanayakkara, M. Challacombe, P.M.W. Gill, B. Johnson, W. Chen, M.W. Wong, J.L. Andres, C. Gonzalez, M. Head-Gordon, E.S. Replogle, J.A. Pople, *Gaussian98, Rev. A.11*, Gaussian, Inc. Pittsburgh, PA, **2001**.

# Lebenslauf

Nicole Pienack

---

## Persönliche Angaben

Geburtsdatum	29.09.1977
Geburtsort	Flensburg
Staatsangehörigkeit	Deutsch
Familienstand	Ledig

## Ausbildung

02/2005 – 09/2008	<b>Christian-Albrechts-Universität zu Kiel</b> Promotion im Fachbereich Anorganischer Chemie (Prof. Dr. W. Bensch)
10/1997 – 12/2004	<b>Christian-Albrechts-Universität zu Kiel</b> Studiengang Höheres Lehramt Mathematik / Chemie Studiengang Chemie-Diplom (ab WS 00/01) Abschluss als Diplom-Chemikerin (21.12.2004)
08/1988 – 06/1997	<b>Gymnasium Satrup</b> Hochschulreifeprüfung 1997
1984 – 1988	<b>Grund- und Hauptschule Tarp</b>